



HAL
open science

The palaeo-glaciers and palaeo-lakes from the Bolivian Altiplano as climatic archives for the last deglaciation

Léo Martin

► **To cite this version:**

Léo Martin. The palaeo-glaciers and palaeo-lakes from the Bolivian Altiplano as climatic archives for the last deglaciation. Earth Sciences. Université de Lorraine, 2016. English. NNT : 2016LORR0058 . tel-01752256

HAL Id: tel-01752256

<https://hal.univ-lorraine.fr/tel-01752256>

Submitted on 21 Jun 2018

HAL is a multi-disciplinary open access archive for the deposit and dissemination of scientific research documents, whether they are published or not. The documents may come from teaching and research institutions in France or abroad, or from public or private research centers.

L'archive ouverte pluridisciplinaire **HAL**, est destinée au dépôt et à la diffusion de documents scientifiques de niveau recherche, publiés ou non, émanant des établissements d'enseignement et de recherche français ou étrangers, des laboratoires publics ou privés.



AVERTISSEMENT

Ce document est le fruit d'un long travail approuvé par le jury de soutenance et mis à disposition de l'ensemble de la communauté universitaire élargie.

Il est soumis à la propriété intellectuelle de l'auteur. Ceci implique une obligation de citation et de référencement lors de l'utilisation de ce document.

D'autre part, toute contrefaçon, plagiat, reproduction illicite encourt une poursuite pénale.

Contact : ddoc-theses-contact@univ-lorraine.fr

LIENS

Code de la Propriété Intellectuelle. articles L 122. 4

Code de la Propriété Intellectuelle. articles L 335.2- L 335.10

http://www.cfcopies.com/V2/leg/leg_droi.php

<http://www.culture.gouv.fr/culture/infos-pratiques/droits/protection.htm>



UNIVERSITÉ DE LORRAINE

École doctorale R.P.2.E

Centre de Recherches Pétrographiques et Géochimiques

Thèse de doctorat présentée et soutenue publiquement pour l'obtention du titre de
Docteur de l'Université de Lorraine (Spécialité: Géosciences)

par **Léo Martin**

Les paléoglaciers et les paléolacs de l'Altiplano, archives climatiques de la dernière déglaciation

Soutenance publique prévue le 13 Mai 2016 devant le jury composé de Mmes et MM.

Directeurs de thèse:

Dr. Pierre-Henri BLARD, CRPG (Nancy, France)

Dr. Jérôme LAVÉ, CRPG (Nancy, France)

Rapporteurs:

Pr. Mathias VUILLE, University at Albany (USA)

Pr. Arjen STROEVEN, Stockholms Universitet (Suède)

Examinatrices:

Dr. Florence SYLVESTRE, CEREGE (Aix-en-Provence, France)

Dr. Irene SCHIMMELPFENNIG, CEREGE (Aix-en-Provence, France)

Invités:

Dr. Vincent JOMELLI, LGP (Meudon, France)

Dr. Thomas CONDOM, LTHE (Grenoble, France)

CENTRE DE RECHERCHES PÉTROGRAPHIQUES ET GÉOCHIMIQUES, 15 RUE NOTRE-DAME DES
PAUVRES, 54500 VANDOEUVRE-LÈS-NANCY, FRANCE

Résumé

La période Quaternaire (2.6 Ma - Présent) est caractérisée par une forte variabilité climatique mondiale et l'alternance d'épisodes glaciaires et interglaciaires. La période tardiglaciaire (il y a 20 à 11 ka) voit se succéder des réorganisations rapides et abruptes du climat à différentes échelles. Deux épisodes froids dans l'hémisphère Nord sont synchrones du développement des paléolacs géants Tauca (17 - 14 ka) et Coipasa (13 - 11.5 ka) sur l'Altiplano bolivien. L'Altiplano est un haut plateau bordé par les Cordillères Orientale et Occidentale des Andes. Les flancs des volcans et des massifs montagneux y présentent de nombreuses preuves d'une activité glaciaire passée intense. Ces géomorphologies glaciaires, ainsi que les lignes de rivage abandonnées des paléolacs constituent de précieuses archives pour comprendre le climat passé. L'exploitation couplée de ces deux archives est au cœur de cette thèse.

Après des chapitres introductifs, le chapitre 4 porte sur la calibration du taux de production du ^{10}Be in situ dans les Hautes Andes Tropicales. Ce paramètre géochimique est nécessaire à l'emploi de la méthode des âges d'exposition utilisée dans cette thèse afin de reconstruire l'histoire des paléoglaciers. Un nouveau taux de $4.07 \pm 0.18 \text{ at.g}^{-1}.\text{a}^{-1}$ est établi à partir de l'âge et de la concentration en ^{10}Be du fan-delta de Challapata situé sur le flanc de Cerro Azanaques (18.9°S - 66.7°W). Une synthèse des taux andins est également menée et conduit à proposer un jeu de données de référence pour la calibration du ^{10}Be in-situ dans cette région.

Le chapitre 5 porte sur le développement d'un code de calcul pour les âges d'exposition. Les programmes existant à ce jour n'incluent pas les dernières avancées dans le domaine et obligent les utilisateurs à se servir de paramètres sans pouvoir les choisir et les discuter. Dans cette optique, le programme CREp offre une grande flexibilité de paramétrage. Il est de plus couplé à une base de données en ligne de taux de production afin de proposer les choix les plus pertinents pour cette valeur clé du calcul. Le programme CREp est disponible sur Internet.

Le chapitre 6 présente 4 chronologies glaciaires basées sur les âges d'exposition dans la vallée du Zongo (16.2°S - 68.1°W), au Cerro Tunupa (19.8°S - 67.6°W), au Nevado Sajama (18.1°S - 68.9°W) et au Cerro Luxar (21.0°S - 68.0°W). Elles sont couplées à une reconstitution des températures moyennes basée sur la modélisation croisée lac-glaciers. Les résultats indiquent 2 comportements glaciaires différents au cours du tardiglaciaire entre le Nord et le Sud et suggèrent une variabilité spatiale importante des précipitations. Des refroidissements de 4 - 4.5 °C et 2.5 °C sont respectivement associés aux stades Tauca et Coipasa.

Le dernier chapitre est consacré à la reconstitution du champ des précipitations sur l'Altiplano durant le stade Tauca. La modélisation croisée permet d'observer les variations de précipitation par rapport au présent pour 8 sites répartis sur l'Altiplano et d'en déduire une carte des précipitations synthétique pour la période considérée. Ces variations indiquent des précipitations 1.7 à 3.1 fois supérieures à l'actuel. La répartition des pluies révèle un apport accru de l'humidité en provenance de l'Est, et suggère une intensification et une expansion vers le sud des vents d'Est, en cohérence avec plusieurs observations actuelles et passées.

Abstract

The Quaternary period (2.6 Ma - Present) is characterized by rapid and strong worldwide climate variability and the alternating pattern of glacial and interglacial periods. Rapid and abrupt climatic reorganisations follow one another at different scales during the late glacial period (20 - 11 ka ago). Two cold episodes in the Northern Hemisphere are coeval with the rise of giant palaeo-lakes Tauca (17 - 14 ka) and Coipasa (13 - 11.5 ka) over the Bolivian Altiplano. The Altiplano is a high plateau surrounded by the eastern and western cordilleras of the Andes. The flanks of the volcanoes and mountainous massifs in the area exhibit substantial evidence of intense past glacial activity. These glacial geomorphologies, along with the abandoned palaeo-lake shorelines represent valuable archive to understand the past climate. The coupled study of these 2 archives is at the heart of this thesis project.

After introductory chapters, the chapter 4 deals with the calibration of in situ ^{10}Be production rate in the High Tropical Andes. This geochemical parameter is required to make use of the exposure age method, which is applied in this thesis to reconstruct the palaeo-glaciers history. A new production rate of $4.07 \pm 0.18 \text{ at.g}^{-1}.\text{yr}^{-1}$ is derived from the age and ^{10}Be concentration of the Challapata fan-delta, on the flank of Cerro Azanaques (18.9°S - 66.7°W). A review of the Andean production rates is also presented and leads to propose a reference calibration dataset for the in situ ^{10}Be production rate in the region.

The chapter 5 deals with the development of a calculation code for exposure ages. Actual programs do not account for the latest advances in this domain and force users to use fixed parameters without being able to change or discuss them. In this view the CREp program offers an important flexibility in the parameterization. Furthermore, it is coupled with an online production rate database so as to offer the most relevant choices concerning the key parameters of the calculation. The CREp program is available online.

The chapter 6 presents 4 exposure age based glacial chronologies in the Zongo Valley (16.2°S - 68.1°W), Cerro Tunupa (19.8°S - 67.6°W), Nevado Sajama (18.1°S - 68.9°W) and Cerro Luxar (21.0°S - 68.0°W). They are coupled with lake and glacier modelling to reconstruct mean temperature evolution. Results indicate 2 different glacial behaviors during the lateglacial period between the North and the South of the Altiplano and suggest an important spatial variability of the precipitations. Coolings of 4 - 4.5 °C and 2.5 °C are respectively associated to the Tauca and Coipasa Highstands.

The last chapter presents a reconstitution of the Altiplano precipitation field during the Tauca Highstand. The lake and glacier cross-modelling enables to derive the increase of precipitations from past to present for 8 sites distributed over the Altiplano and to infer a synthetic precipitation field for the period. These variations indicate 1.7 to 3.1 times stronger precipitations compared to present. The rain spatial distribution reveals enhanced moist input from the East and suggests a strengthening and southward expansion of the easterly winds, in consistence with actual and past observations.

C'est dans les vieux karsts qu'on fait les meilleures soupes.
Nicho B.

Remerciements

Sacrée aventure humaine que ces 3 années et demie de thèse. Tant de gens à remercier, mais je sens mes doigts, (un petit peu) lassés de la rédaction, retrouver un nouvel élan et s'agiter avec plaisir sur le clavier au moment de rédiger cette partie.

Mes premiers remerciements vont bien entendu à PH qui m'a pris en thèse en 2012 alors que je n'y connaissais rien ni en Cosmos ni en Paléoclim. Il m'a énormément appris pendant ces 3 années et demie et m'a complètement inclus dans le projet GALAC. Je ne me doutais pas en commençant de l'importance de cette transmission et je lui en suis très reconnaissant. Merci pour m'avoir fait découvrir l'Altiplano en vrai, m'avoir fait voyager à Vienne, à San Francisco, ... que d'aventures ! Je remercie ensuite Jérôme pour son encadrement de "chercheur senior" comme il l'appelle, très intéressant et enrichissant - particulièrement dans son application du principe schumpétérien de la destruction créatrice ☺. Je plaisante, mais c'était une grande chance de pouvoir te soumettre mes différents travaux, ça m'a fait beaucoup avancer. J'ai énormément apprécié travailler avec vous deux, je suis bien content qu'on se soit si bien entendu et qu'on ait pu partager des moments également hors de la science, notamment ces nombreux footings qui ont constitués 99% de mes activités non-scientifiques de ces derniers mois. Un grand merci à vous deux !

Je remercie ensuite mon Jury. En premier lieu mes rapporteurs Mathias Vuille et Arjen Stroeven qui ont accepté de venir de loin pour écouter ce que j'avais à dire, merci pour le temps et l'énergie qu'ils m'ont consacré. Merci à mes examinatrices Florence Sylvestre et Irène Schimmelpfennig pour l'intérêt qu'elles ont porté à mes travaux. Et merci aux invités Vincent Jomelli et Thomas Condom qui ont également été des collaborateurs avec qui j'ai eu du plaisir à travailler.

Je remercie la Région Lorraine et l'ANR pour le financement de mes travaux de thèse.

Merci au CRPG dans son ensemble pour fournir un cadre de travail aussi agréable et stimulant aux thésards. Merci aux directeurs, à Christian et à Raph pour l'attention témoignée sur cette fin de thèse. Merci à Isabelle, Aurélie, Martine, Cathy, Corinne et Odile pour l'aide et l'efficacité formidable du service administratif, ainsi que pour leur bonne humeur, c'était toujours un plaisir de venir vous voir. Merci à Bruno, Yannick et Marie Lorraine pour l'indispensable Service Général, et son rôle aussi Général que précieux. Merci à Larry pour toutes ses contributions informatiques et pour tout ce qu'il m'a appris sur les versions successives de Mac OS. Merci au SARM pour toutes les belles mesures.

Merci aux enseignants chercheurs qui m'ont permis d'intervenir dans leur cours dans le cadre de mon monitorat et demi ATER. J'ai pris beaucoup de plaisir à m'acquitter de mes charges d'enseignement. Merci à Yves Géraud pour les belles journées de stage terrain dans ce petit coin de paradis des Alpes Maritimes. Merci à Emilie et Pierre pour cette bonne semaine passée à Ploumanac'h. Un grand merci à Bernard pour la géochimie, j'ai pris beaucoup de plaisir à faire ces TD. Je garde également un très bon souvenir de cette superbe semaine à San Francisco dans notre appart de choix. Merci Julien pour la géomorpho, pour le regard bienveillant qu'il a toujours porté sur mon parcours en thèse et pour les centaines de km de footings qu'on a fait ensemble. Merci à l'équipe gaz rares, pour l'aide au cours des longues journées à essayer de faire marcher le SFT. Pete qui nous manque terriblement, Bouch toujours près à rendre service, Laurent, toujours près à dire une petite méchanceté ;-). Merci à Manu qui m'a fourni mes premières armes au labo avec le broyage, le tamisage et la séparation des minéraux. Merci à Tix pour l'aide sur le MEB.

Merci aussi à l'incroyable Aster Team du CEREGE, pour toutes les mesures ^{10}Be et pour vos accueils chaleureux à Aix, un grand merci à George, à Maurice, Karim, Régis (qui ne fait pas partie de l'Aster team) et bien sûr au Grand Chef Didier, merci pour les conseils, les relectures, le comité de mi-thèse, tu es à mon avis un des parrains de cette thèse (je ne sais pas vraiment ce que ça veut dire mais c'est sincère). Merci également à Amaëlle Landais d'avoir fait partie de mon comité de mi thèse. Merci à Maayt, Véro et Abdul pour l'aventure incroyable qu'a été cette mission en Bolivie où les paysages se sont avérés aussi beaux que le poulet toxique.

Un grand merci à tous ceux à qui je n'ai pas directement collaboré scientifiquement mais qui font que c'est toujours un grand plaisir de venir au labo. En premier lieu à mes petits poulets du bureau, mon vieux Rémi et mes chers Romain et Guillaume (merci pour l'aide informatique !!) avec qui on a partagé tant de bons moments ainsi que les délires les plus farfelus. Vous avez rendu cette thèse terriblement drôle et vivante, on a bien ri. Yves Marrocchi est bien entendu indissociable des conneries racontées dans ce bureau, président de l'association des amis du bureau, merci pour les bêtises en tout genre. Trésorier de l'association David B. et son traditionnel "Guillaume, je peux te poser une question ?". Ce bureau et son ambiance légendaire me resteront longtemps précieux.

Merci aux étudiants dont j'ai croisé la route. A mon petit Flo Gallo avec qui j'ai passé de très bons moments au labo Be et à Aix. Merci à Marie, Amandine, Mélo pour leur pêche. Merci aux anciens, Guillaume, Maia, Sarah, Camille, Martin (pour l'animation d'un certain fan club "scientifiquement merdique !"), Merci à Bombom. Merci aux grands cosmogénistes devant l'Eternel Puch et Dimitri pour leurs instructions et nombreux conseils. Merci aux plus jeunes qui se rapprochent doucement mais sûrement du bout de la planche, Jesse (Sup MF ?), Gaëlle, Rémi, Christine, Yumi, Prescillia, Léa, Imène, Paul, Lionel, les 2 Sebs, Thomas, bon courage à vous !

Merci à Damien C et Monsieur Martin pour la bonne humeur partagée et les virées au BBC auxquelles j'envisage de faire mon grand retour bientôt. Merci à Thomas, Gaston, Aymeric, Johan pour les échanges chaleureux plus ou moins déjantés au détour d'un couloir ou à la cafèt. Merci à tous gens qui participe à la bonne humeur prégnante un peu partout dans le labo, François, Michel, Evelyne, Lyderic, Mary, Catherine, Pierre, Nordine, Abdallah, ... j'ai peur d'oublier du monde, merci à tous ! Merci à Jean Marc Montel qui, en plus être un super directeur, m'a toujours été de très bon conseil quand j'en avais besoin.

En dehors de la science, mes premiers remerciements vont bien entendu à mes parents, pour un millier de choses, mais principalement pour leur affection, leur soutien et tout ce qu'ils continuent à m'apprendre de la vie. Merci à mon frère Jerry O'Hagan pour toutes ses folies (et pour les pilules que je vais lui mettre au tennis). Merci également à mes vieilles tantes Momo et Zouzou pour leur soutien, je réserve déjà pour de longues et paisibles vacances chez Milou cet été ! Merci à mes grands parents, à mes cousins, mon cher Edzi Mohy, vivement une petite soirée jeux vidéos ! Mes petits cousins, mes oncles et tantes, bon ça va finir par faire un peu cassé, des gros bécots à tout le monde !

Il y a aussi une bande inoxydable de potes qu'il faut que je remercie pour l'ensemble de son œuvre. Un crew formé dans des temps immémoriaux et qui vivra encore pour des millénaires. Le Greg, le Yannou, le Miguelito, le Tots, l'Audrey, le Bebs et bien sûr Flo et Quentin avec qui j'ai passée 2 années magiques en coloc. Merci à Emilie pour tout ce que nous avons partagé et qui m'est très précieux.

Merci aux potes de prépa et de géol pour tous ces moments géniaux qu'on a déjà passé ensemble et pour toutes les soirées qu'on va encore se faire. Merci à ma petite Less qui m'a fait des corrections depuis l'autre bout du monde. Merci à mes chers Léa, Salim, Fab, Julien pour nos sorties nancéiennes. Merci à tous mes potes géoliens qui me manquent mais que j'ai bien envie de venir voir ! Benjy, Loulou, Nico, Ben, Caca, Ivan, La Bourse, Baptiste, Cazou, Adri, Caro, Ched, Matthieu, Paulo, Coco, Nono, Toto... Merci aux prépas, Aurélie, Maxou, Oc, Antoine, ...

Merci à Nicho Beix auteur de la citation qui ouvre ce manuscrit, aux frangines Allé, Rémichta Callypso Fléta, Hyacinth Schnock et Daphné Schwartz, vivement notre prochaine soirée ! Merci à ma chère Elsa (un petit ciné bientôt ?). Merci bien sûr à Alejandra, et à toute la Olson family, j'espère qu'on va se revoir bientôt.

Merci aux villarois, à mon cher Plonplon pour le sens du rythme, merci à Patrick (reprise des répèts ?) Fred, Rémy, Marie, tout l'atelier pour tous les boeufs, tous les concerts faits et à faire. Merci à mon petit Thomas Schuh, le coach FR, promis je reviens à l'entraînement bientôt.

Et puis parce qu'une thèse c'est aussi pas mal de moments seul, chez soi ou face à son clavier (ou ses pyroxènes), je voudrais aussi remercier un tas de gens qui ne me connaissent pas mais qui, sans le savoir, ont passé un nombre d'heures incalculable à mes cotés et qui sont devenus indissociables de ces 4 années. Bill Frisell qui représente 80% de la bande son de cette thèse (demandez à mes collègues

de bureau) et plein d'autres. Merci à François Angelier, litterature-audio.com et à Ned Stark (je tenais à rendre mon manuscrit avant le début de la saison 6).

Et enfin merci à Chouchounet et Double-Zou pour leurs ronrons chaleureux, leurs poils soyeux, leur art de la sieste et la fraîcheur inimitable avec laquelle ils observent le monde.

A mes grands parents Lulu, Nini, Michel et Roger
que j'embrasse bien fort

Note sur la structure du manuscrit

Ce manuscrit est rédigé en français en et anglais. Le résumé long, l'introduction et la présentation des âges d'exposition sont en français, ainsi que la conclusion. Le cœur du manuscrit est composé de 4 articles rédigés en anglais qui correspondent aux chapitres 4 à 7. Le premier a été accepté et publié dans une revue à comité de lecture. Il est présenté sous sa forme finale. Les trois autres articles sont en préparation en vue d'une soumission.

Les parties en français possèdent une bibliographie commune à la fin du manuscrit. Les articles possèdent leur structure et bibliographie propres. Ils peuvent être abordés indépendamment du reste du manuscrit. Il en va de même pour les annexes qui présentent les articles qui ont fait l'objet d'une collaboration (2 publiés et 2 soumis). Etant donné que chaque article possède sa propre méthodologie, ce manuscrit ne contient pas non plus de méthodologie globale.

Note on the structure of the manuscript

This manuscript is written both in French and English. The long abstract, the introduction, the presentation of the exposure ages and the conclusion are in French. The heart of the manuscript is composed of 4 articles written in English. They correspond to chapter 4 to 7. The first one is accepted in a peer-review journal, and presented under its final layout. The 3 others are in preparation.

The parts that are written in French share a common bibliography at the end of the manuscript. The articles have their own inner structure and bibliography. They can be addressed independently from the rest of the manuscript. The same applies to the Appendices, which present co-authored articles (2 are accepted and 2 have been submitted). Considering that each article includes an introduction and a methodology section, this manuscript possesses a short synthetic introduction and no methodology chapter. My personal contribution to the presented works is exposed in the first Appendix.

The draft papers presented in chapters 6 and 7 have been written in the last moments of this thesis so as to present the most recent climatic results that were computed. For this reason, several points of the methodology and results will need further development. Particularly, the methodology applied to the ages scatter is still in reflexion and the approach proposed here will be replaced by a consistent method for all sites.

Concerning the climatic inversions, all the uncertainties haven't been propagated yet in the final results and some sensitivity tests are still to be done. Some methodological points are still in development relatively to the incidence of the age uncertainties in the climatic inversions and the variability of the inversion results for a common period.

These shortcomings were considered of minor importance relatively to the significance of the presented results. The future amendments should bring more robustness to the investigations; yet, they are not expected to bring significant modifications in the major results and conclusions reported.

Table des matières

1	Résumé Long	15
1.1	Introduction	16
1.2	Calibration d'un taux de production ^{10}Be	18
1.3	Programme CREp	19
1.4	Chronologies glaciaires et paléotempératures	20
1.5	Precipitations pendant le haut niveau Tauca	21
1.6	Conclusion	21
2	Introduction	23
2.1	Contexte paléoclimatique	23
2.1.1	Variabilité du climat mondial et archives climatiques	23
2.1.2	La dernière déglaciation	24
2.1.3	La dernière déglaciation en Amérique du Sud	26
2.2	Les paléoglaciers, traceurs paléoclimatiques continentaux	27
2.2.1	La Dynamique glaciaire est pilotée par le climat	27
2.2.2	Les morphologies glaciaires témoignent de l'histoire du glacier	27
2.2.3	Les enregistrements des glaciers des Andes Tropicales pendant le tardiglaciaire	28
2.2.4	L'inversion climatique et le couplage avec les lacs	29
3	Présentation des âges d'exposition	31
3.1	Les âges d'exposition et la formation des isotopes cosmogéniques	31
3.2	Les âges d'exposition et le taux de production	32
3.3	Les modèles de spatialisation et de calibration du taux de production	34
4	Etude de Calibration pour le ^{10}Be in situ	37
5	Le programme CREp	55
6	Chronologies glaciaires et Paléotempératures	127
7	Champ des précipitations pendant le haut niveau Tauca	199
8	Conclusions et Perspectives	241
9	Annexes	247
9.1	Personal Contribution	248
9.1.1	Sampling	248
9.1.2	Sample preparation and measurements	248
9.1.3	Other contribution	248
9.1.4	Co-authorship	248
9.2	Ages d'exposition à Chiar-Khota	249
9.3	Collaborations	252
9.3.1	Blard et al. (2014)	252
9.3.2	Jomelli et al. (2014)	267
9.3.3	Delunel et al. (2016)	286
9.3.4	Zumaque et al. (Submitted)	305

Chapitre 1

Résumé Long

Sommaire

1.1	Introduction	16
1.2	Calibration d'un taux de production ^{10}Be	18
1.3	Programme CREp	19
1.4	Chronologies glaciaires et paléotempératures	20
1.5	Precipitations pendant le haut niveau Tauca	21
1.6	Conclusion	21

1.1 Introduction

La période Quaternaire (2.6 Ma - Présent) est caractérisée par une forte variabilité climatique mondiale et l'alternance d'épisodes glaciaires et interglaciaires. La période tardiglaciaire s'étend entre le Dernier Maximum Glaciaire (il y a environ 20 000 ans) et l'Holocène, débuté il y a 11 700 ans. Cette période voit se succéder des réorganisations rapides et abruptes du climat à différentes échelles. L'hémisphère Nord connaît deux épisodes froids : le stade Heinrich 1 (18.5 - 14.5 ka) et le Dryas Récent (12.9 - 11.7 ka) (Andersen et al., 2004). Ces épisodes sont caractérisés par un ralentissement de la circulation thermohaline (McManus et al., 2004), ainsi que par des modulations de l'intensité et de la localisation des moussons (Wang et al., 2001, 2004). Le climat sud américain connaît également d'importantes modifications. Dans le sud de l'Altiplano (Bolivie), ces périodes sont synchrones du développement des paléolacs géants Tauca (17 - 14 ka) et Coipasa (13 - 11.5 ka) aujourd'hui disparus (Sylvestre et al., 1999; Blard et al., 2011; Placzek et al., 2006). Ces différentes évolutions sont présentées dans la Figure 1.1.

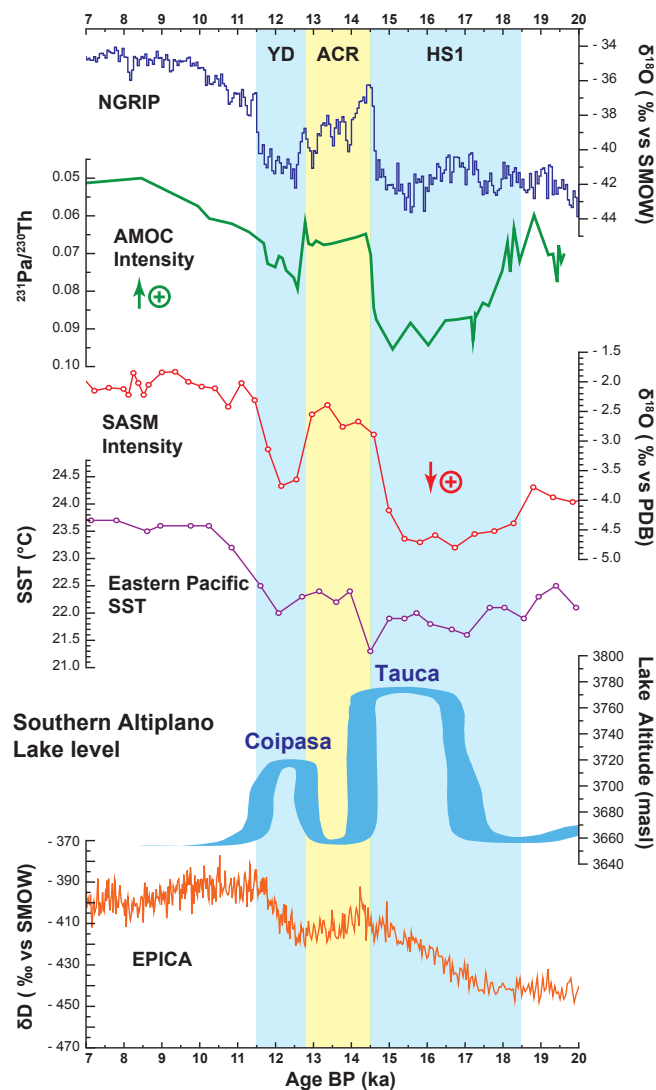


FIGURE 1.1 : Mise en contexte de la période tardiglaciaire par différents signaux paléoclimatiques. NGRIP : $\delta^{18}\text{O}$ (‰ vs. SMOW) dans les glaces du Groenland (Andersen et al., 2004); AMOC : $^{231}\text{Pa}/^{230}\text{Th}$ dans les sédiments de l'Atlantique Nord (McManus et al., 2004); Botuvera Cave : $\delta^{18}\text{O}$ (‰ vs. PDB) dans les spéléothèmes de la grotte Botuvera au Brésil (Wang et al., 2007); SST : Températures de surface dans le Pacifique Est (Dubois et al., 2009); Lake Level : Élévation des Lacs de l'Altiplano Sud (Blard et al., 2011; Placzek et al., 2006; Sylvestre et al., 1999); EPICA : δD (‰ vs. SMOW) from EPICA Dome C ice core (Jouzel et al., 2007).

L'Altiplano est un haut plateau (altitude moyenne 4000 m) bordé par les Cordillères Orientale et Occidentale des Andes, principalement localisé en Bolivie. Sa configuration topographique en fait un bassin endoréique de 196 000 km² constitué de 4 sous-bassins se succédant d'amont en aval et du Nord au Sud : le bassin versant du Titicaca, celui du Poopo, du Coipasa et d'Uyuni. L'Altiplano connaît actuellement un fort gradient de précipitations Nord - Sud (800 mm de pluie par an sur le bassin versant du Lac Titicaca contre 50 à 200 mm par an à la frontière avec l'Argentine et le Chili). Sa localisation en haute altitude et à des latitudes tropicales fait que les températures y sont basses et varient peu au long de l'année. L'aridité actuelle fait que de nombreux sommets culminant à plus de 6000 m au Sud de l'Altiplano - comme l'Uturuncu - ne présentent pas de glaciers. Toutefois, les volcans et les massifs de l'Altiplano présentent des preuves abondantes d'une activité glaciaire passée intense. Ces géomorphologies glaciaires ainsi que les lignes de rivage laissées par les paléolacs constituent de précieuses archives climatiques pour documenter le tardiglaciaire. L'interprétation couplée de ces 2 archives est au cœur du projet GALAC porté par Pierre-Henri BLARD, dans lequel s'inscrit cette thèse. Les différents sites étudiés dans cette thèse sont présentés en Figure 1.2.

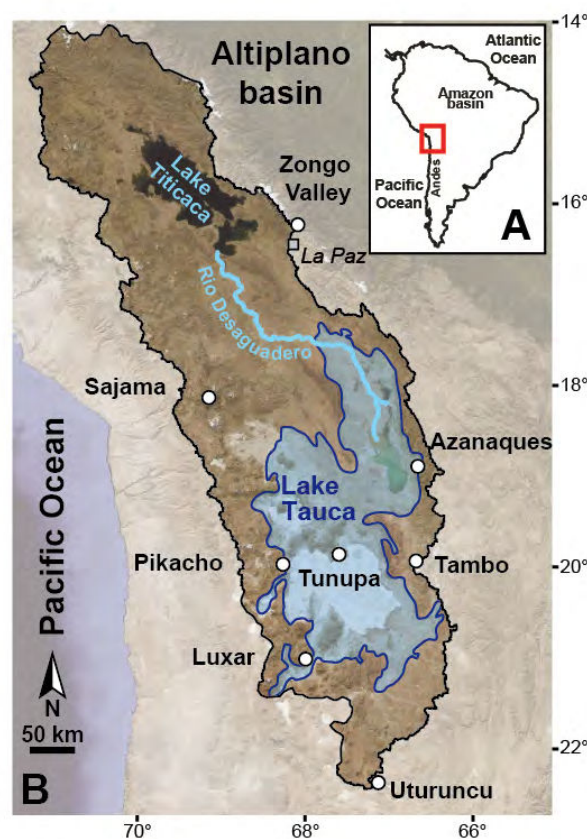


FIGURE 1.2 : L'Altiplano et les sites étudiés pendant cette thèse. A - Localisation générale de l'Altiplano en Amérique du Sud. Les points blancs indiquent les sites. Les contours noirs et bleus indiquent respectivement les limites de l'Altiplano et du paléolac Tauca. Le lac Titicaca et le Rio Desaguadero sont indiqués en turquoise.)

L'exploitation de données paléoclimatologiques inclut deux volets nécessaires et complémentaires : la géochronologie et l'interprétation. Aussi, les chapitres 4 et 5 de cette thèse portent sur des développements méthodologiques relatifs au calcul d'âges d'exposition ; méthode particulièrement appropriée à la datation des moraines et des polis glaciaires. Les deux chapitres suivants couplent ces datations à des méthodes d'inversions climatiques afin d'apporter des contraintes sur les conditions de précipitation et de températures sur la période étudiée.

1.2 Calibration d'un taux de production du ^{10}Be in situ dans les Hautes Andes Tropicales

Les reconstructions des dynamiques des paléoglaciers présentées dans ce manuscrit reposent sur la méthode des âges d'exposition. Cette méthode permet de déterminer le temps qu'a passé une roche à la surface de la Terre grâce à la mesure de la concentration en certains atomes, les isotopes cosmogéniques, dans une de ses phases minérales. Ces éléments - tels que le ^{10}Be ou le ^3He - sont créés par l'interaction des éléments des minéraux avec le flux cosmique en provenance de l'Espace. Le calcul d'un âge par cette méthode géochimique nécessite la connaissance a priori d'un paramètre indispensable, le taux de production. **Cette valeur représente la vitesse à laquelle s'accumulent les isotopes cosmogéniques dans les minéraux des roches à la surface de la Terre.** Le taux de production varie en fonction de nombreux paramètres. Les principaux sont l'altitude, la latitude, les conditions de pression et l'activité du champ magnétique terrestre. De nombreux modèles de spatialisation permettent de tenir compte de ces variations mais ils ne produisent pas tous les mêmes résultats. Une manière de minimiser l'impact de ces modèles sur le calcul des âges d'exposition est d'utiliser un taux de calibration proche en espace et en âge des objets à dater. Dans cette optique, le premier chantier de cette thèse a consisté en l'établissement d'un nouveau taux de production sur l'Altiplano.

Une étude de calibration in situ nécessite de déterminer indépendamment l'âge et la concentration en isotopes cosmogéniques d'un objet géologique. Le fan-delta de Challapata, situé sur un flanc de Cerro Azanaques est la formation sédimentaire qui a permis l'établissement de ce nouveau taux. Ce cône d'épandage s'est établi lors d'une avancée glaciaire synchrone du Haut niveau du lac Tauca. Il s'étend jusqu' au paléolac et se transforme progressivement en delta lacustre dans sa partie distale. Nous avons prolongé les premières descriptions de ce fan-delta (Clapperton et al., 1997; Clayton and Clapperton, 1997, 1995) pour préciser le cadre temporel de la construction du fan-delta. Un calcul bayésien se basant sur l'âge du haut niveau lacustre ainsi que sur les datations de Clayton and Clapperton, (1995) nous a permis d'établir un âge de 16.07 ± 0.64 ka avant le présent. Nous avons échantillonné 15 rochers appartenant au fan-delta pour établir la concentration moyenne du quartz en ^{10}Be . Nos mesures indiquent une concentration de $4.92 \pm 0.05 \times 10^5$ at.g $^{-1}$. Ces 2 valeurs combinées donnent un taux local de 30.8 ± 1.3 at.g $^{-1}$.a $^{-1}$. Ramenée à des conditions de hautes latitudes et au niveau de la mer (conditions standard pour les taux de production) grâce aux modèles évoqués plus haut, cette valeur est de 3.76 ± 0.15 at.g $^{-1}$.a $^{-1}$. Les taux déjà établis pour les Hautes Andes Tropicales (Blard et al., 2013; Kelly et al., 2013) ont été recalculés afin de proposer un jeu de données de calibration homogène et d'en dériver un taux de production de référence pour la région. Ce taux s'établit à 3.74 ± 0.09 at.g $^{-1}$.a $^{-1}$. Ces résultats sont résumés dans la Figure 1.3 (détails de calcul et procédure de mise aux conditions standards dans le manuscrit).

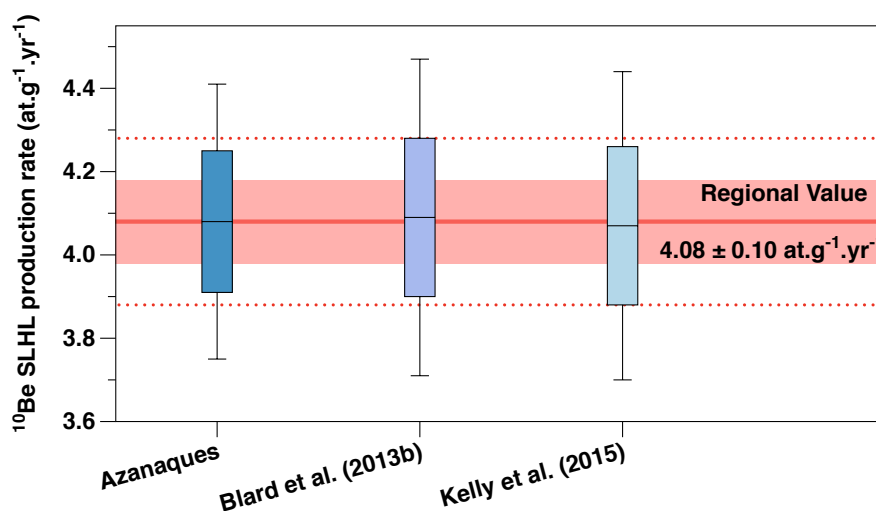


FIGURE 1.3 : Les taux de production ^{10}Be in situ des Hautes Andes Tropicales et la valeur moyenne qui en est déduite (en rouge-rose). Les boîtes et la plage rose indiquent l'incertitude associée à 1σ , les moustaches et les pointillés indiquent l'incertitude à 2σ .

1.3 Développement d'un programme en ligne pour le calcul des âges d'exposition ^3He et ^{10}Be

Les âges d'exposition sont de plus en plus utilisés dans de nombreux domaines de la géologie de surface et des sciences qui lui sont connexes. Les utilisateurs de la méthode peuvent soit calculer leurs âges eux même soit utiliser un des différents programmes déjà publiés comme CRONUS-Earth (Balco et al., 2008). Pourtant, la détermination d'âges d'exposition est une procédure qui requiert de nombreux calculs ainsi qu'une connaissance de l'influence des différents paramètres évoqués précédemment sur le taux de production. C'est pourquoi, les programmes de calculs sont très utilisés et deviennent centraux dans la production scientifique. Cependant, les programmes actuellement disponibles n'incluent pas les dernières avancées dans le domaine et laissent peu de liberté quant au paramétrage des calculs. Le choix du taux de production est, par exemple, central pour le calcul et - comme évoqué plus haut - l'utilisation d'un taux régional permet de calculer des âges robustes et moins dépendants des modèles de spatialisation. Or les programmes actuels ne donnent pas accès à des valeurs régionales. De plus, les différents modèles et bases de données utilisés pour la dépendance à l'altitude, à la latitude, à l'atmosphère, et au champ magnétique terrestre ne fournissent pas les mêmes résultats. Le choix d'un modèle ou d'une base de données au détriment d'un ou d'une autre impacte le résultat final. Il est important que l'utilisateur puisse évaluer l'importance de tels choix.

Dans cette optique, le programme CREp a été conçu afin de proposer une grande souplesse de paramétrisation et de tenir compte des derniers résultats comparatifs sur les modèles et les bases de données à employer. Il est également relié à une base de données en ligne des taux de production. Cette base est régulièrement mise à jour et donne accès à tous les taux de production publiés qui remplissent certains critères de qualité (Figure 1.4). Le programme est simple à utiliser et permet d'exporter les âges calculés ainsi que les densités de probabilités (non triviales) associées sous format tableur. Le programme CREp a été mis en ligne par les soins de l'entreprise Studio 1D3P : CREp

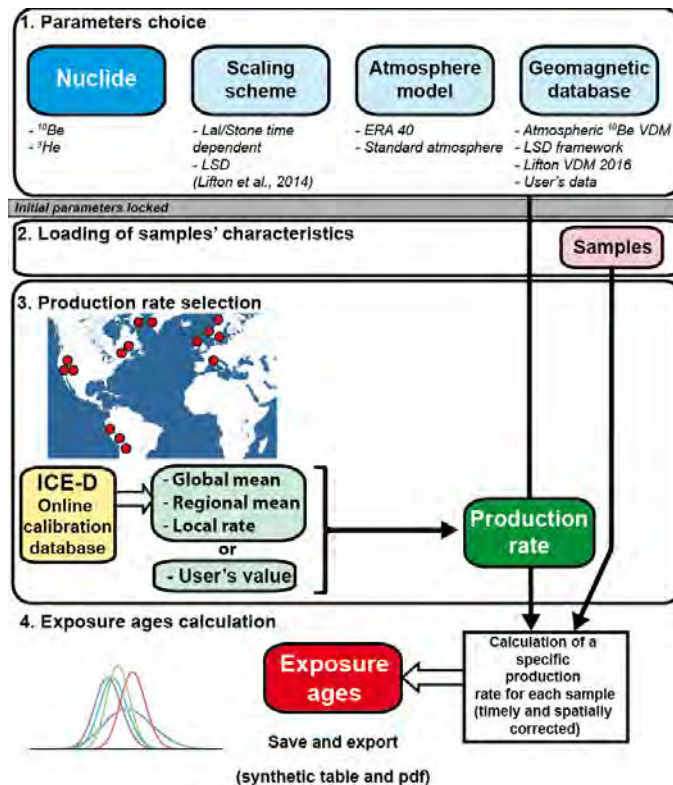


FIGURE 1.4 : Principe de fonctionnement du programme CREp et lien avec la base de données de taux de production en ligne. Référence pour les modèles et données : "Lal modified" (Balco et al., 2008; Lal, 1991; Stone, 2000), LSD (Lifton et al., 2014), ERA40 (Uppala et al., 2005), Standard Atm. (N.O.A.A., 1976), Atmospheric ^{10}Be (Muscheler et al., 2005), Lifton (2015), LSD framework (Lifton et al., 2014).

1.4 Présentation de 4 chronologies glaciaires couplées à des inversions de températures

Le chapitre 6 présente de nouveaux jeux de données d'âges d'expositions pour les sites du Nevado Sajama et du Cerro Luxar et il étend les datations déjà réalisées dans la vallée du Zongo (Jomelli et al., 2011; Smith et al., 2005) et au Cerro Tunupa (Blard et al., 2009, 2013). De nouvelles datations ^{14}C de lignes de rivage sur l'île Incahuasi (20.2°S - 67.6°W) réalisées sur de la calcite de biohermes sont également présentées. Ces nouvelles datations indiquent que le Haut niveau du lac Coipasa a atteint 3720 m, soit 15 m plus haut que cela avait été rapporté précédemment (Blard et al., 2011; Placzek et al., 2006; Sylvestre et al., 1999)

Nous avons profité de ces âges d'exposition pour calculer les Altitudes des Lignes d'Equilibre (ELA) associées aux moraines datées, en utilisant la méthode AAR avec une valeur de 0.55 à 0.65 provenant d'observations glaciologiques actuelles dans les Hautes Andes Tropicales (Sorucu et al., 2009). Ces ELA, ainsi que des observations sur le climat actuel sont utilisées dans une méthode d'inversion des précipitations et températures afin de reconstruire l'évolution des températures aux 4 sites pour la période tardiglaciaire. Les 13 moraines étudiées dans la Vallée du Zongo couvrent toute la période tardiglaciaire. La vallée connaît un Dernier Maximum Glaciaire Local (LLGM) autour de 17 ka, suivi par un très faible recul jusqu'à 13.5 ka. Pendant cette période, l'ELA passe de 4540 à 4640 m et les écarts de température par rapport au présent (ΔT vs. Présent) de -4.3 à -3.7 °C. La période de 13.5 à 10 ka marque un retrait massive avec des ELAs synchrones du Dryas Récent et du début de l'Holocène autour de 4800 m et un ΔT vs. Présent associé de -2.5 à -3°C.

Le Nevado Sajama, Cerro Tunupa et Cerro Luxar présentent des comportements globalement semblables. Ils enregistrent un LLGM autour de 16 ka au début du Haut niveau Tauca suivi par un retrait, soit pendant la seconde moitié du Haut niveau (Sajama, Luxar), soit pendant la régression (Tunupa). Cerro Luxar connaît un retrait massive sans stabilisation plus tardive. Le Nevado Sajama et Cerro Tunupa présentent tous les deux des moraines autour de 12-13 ka. Pendant toute la période, les ELAs du Sajama et du Luxar s'élèvent de 4740 à plus de 4800 m. L'ELA du Tunupa monte de 4450 à 4680 m. La reconstruction des ΔT vs. Présent présentent des résultats très dispersés entre ces sites pour le Haut niveau Tauca (-6.5 à -3.5°C vs. Présent), probablement dus à des anomalies de répartition spatiale de la pluie. Le ΔT le plus robuste pour cette période est d'environ, -4 à -4.5°C (Figure 1.5).

La répartition des moraines Tauca identifiées dans ce chapitre et dans d'autres publications (Zech et al., 2009, 2007b) ainsi que celle des ces anomalies de température suggèrent que les changements hydrologiques majeurs synchrones du stade HS1 étaient pilotés par un transport d'humidité en provenance de l'Est du bassin via un renforcement et une expansion vers le Sud des vents d'Est.

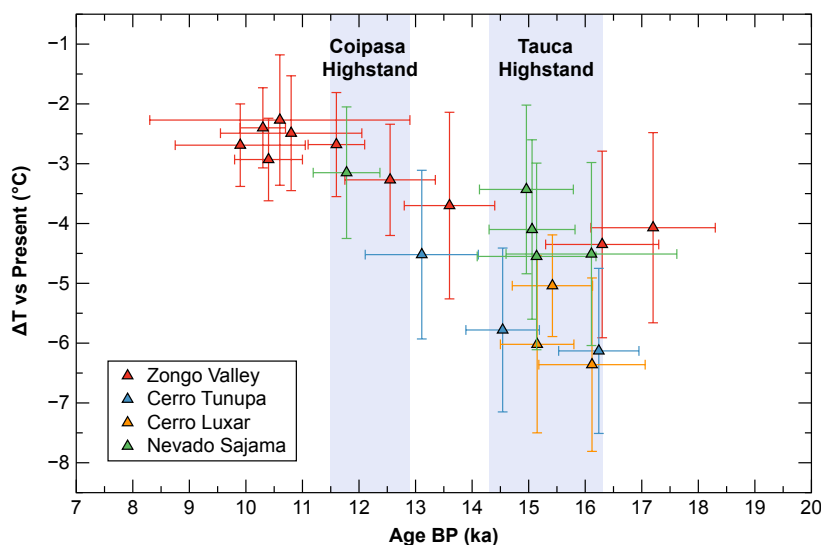


FIGURE 1.5 : Reconstitutions des écarts de température par rapport au Présent pour les 4 sites étudiés. Les bandes bleues indiquent les hauts niveaux Tauca et Coipasa.

1.5 Reconstitution du champ des précipitations pendant le Haut niveau Tauca

Dans un premier temps, de nouveaux âges d'exposition sont présentés pour Cerro Azanaques (18.9°S - 66.7°W), Cerro Tambo (19.9°S - 66.6°W) et Cerro Pikacho (19.9°S - 68.3°W). Ils sont ensuite combinés avec les résultats du chapitre précédent pour identifier 8 moraines synchrones du Haut niveau Tauca dans différentes vallées glaciaires réparties sur l'Altiplano. L'ELA est calculée pour chaque moraine à l'aide de la méthode AAR (gamme de valeurs : 0.55 - 0.65). Elles sont principalement situées entre 4500 et 4600 m avec 3 valeurs plus hautes entre 4700 et 5300 m.

Ces ELAs sont utilisées ainsi que des observations climatiques actuelles dans la méthode de modélisation croisée glacier - lac afin de reconstruire le champ des précipitations sur l'Altiplano pendant le Haut niveau Tauca. Cette reconstitution apporte des contraintes quantitatives sur les pluies pendant le Tauca, qui se sont avérées 1.7 à 3.1 fois plus élevées qu'à l'actuel. De plus, cette répartition indique des pluies très importantes dans le Nord et le long de la Cordillère Orientale (1000 à 1800 mm.a⁻¹) alors que le Sud Ouest de l'Altiplano reste relativement aride (environ 300 mm.a⁻¹). Ceci indique un apport majeur d'humidité par l'Est, franchissant la cordillère Orientale jusqu'à 19°S (Figure 1.6). En cohérence avec des observations actuelles (Garreaud et al., 2003; Vuille, 1999) et de nouveaux résultats sur l'évolution de la Zone de Convergence Sud Atlantique (Strikis et al., 2015) et la ceinture des vents d'Ouest (Montade et al., 2015) pendant HS1, nous proposons que ce transport résulte d'une intensification et d'une expansion vers le Sud des vents d'Ouest.

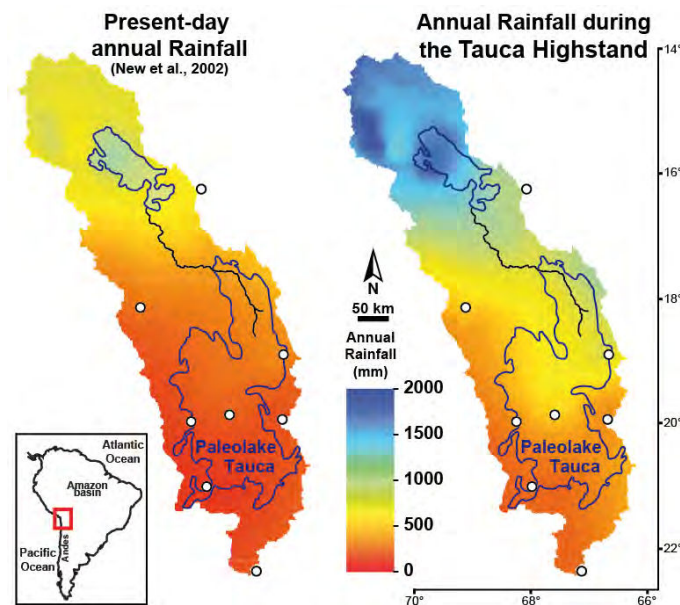


FIGURE 1.6 : Comparaison de la pluviométrie annuelle moyenne actuelle (données de New et al. (2002) et de la pluviométrie reconstituée pour le Haut niveau Tauca. Les deux cartes sont sur la même échelle de couleur. Les points blancs indiquent les sites glaciaires étudiés. Les contours bleus indiquent les lacs Titicaca et Tauca. Le tracé noir indique le Rio Desaguadero.

1.6 Conclusion

Cette thèse a contribué à documenter la dynamique continentale du climat des Hautes Andes Tropicales pendant la période Tardiglaciaire en apportant (i) de nouveaux outils méthodologiques vis à vis du calcul d'âges d'exposition, (ii) de nouvelles contraintes temporelles sur les paléo-extensions glaciaires, ainsi que des reconstitutions spatiales et temporelles des précipitations et températures pour la période.

La détermination d'un nouveau taux de production pour le ¹⁰Be in situ ainsi que l'homogénéisation des taux pour la région ont permis de proposer un taux de production régional robuste pour le calcul des âges d'exposition sur les lithologies présentant du quartz. Le développement du programme CREP

doit à terme permettre aux utilisateurs de bénéficier d'une base exhaustive des taux de production locaux en ^3He et ^{10}Be et de tester l'influence des choix de paramétrisation sur les âges calculés.

Les résultats paléoclimatiques mettent en évidence le comportement particulier des glaciers du sud de l'Altiplano pendant les Hauts niveaux lacustres et l'importance de la répartition des précipitations dans la dynamique glaciaire. Ces précipitations abondantes et synchrones des événements froids de l'hémisphère Nord semblent être permises par une modification du régime des vents en faveur des vents d'Est, favorisant un transport accru de l'humidité depuis l'Est du bassin.

Chapitre 2

Introduction

Sommaire

2.1	Contexte paléoclimatique	23
2.1.1	Variabilité du climat mondial et archives climatiques	23
2.1.2	La dernière déglaciation	24
2.1.3	La dernière déglaciation en Amérique du Sud	26
2.2	Les paléoglaciers, traceurs paléoclimatiques continentaux	27
2.2.1	La Dynamique glaciaire est pilotée par le climat	27
2.2.2	Les morphologies glaciaires témoignent de l'histoire du glacier	27
2.2.3	Les enregistrements des glaciers des Andes Tropicales pendant le tardiglaciaire	28
2.2.4	L'inversion climatique et le couplage avec les lacs	29

Les travaux réalisés dans le cadre de cette thèse sont présentés dans les chapitres 4 à 7 sous forme d'articles scientifiques qui comportent tous une introduction, un état de l'art et une méthodologie en rapport avec les différents sujets abordés. Afin d'éviter des répétitions inutiles, cette introduction se fixe donc comme objectif de présenter le cadre général et les problématiques abordées de ces travaux de thèse de manière brève et synthétique. Le lecteur trouvera les détails nécessaires à une compréhension approfondie dans le corps des différents chapitres.

2.1 Contexte paléoclimatique

2.1.1 Variabilité du climat mondial et archives climatiques

Les premières observations géologiques des morphologies glaciaires des Alpes suisses au XIX^{ème} siècle par Horace-Bénédict de Saussure, Jean-Pierre Perraudin, Jean de Charpentier et Ignace Venetz ont permis d'établir que les glaciers de cette région avaient connu une extension beaucoup plus importante par le passé. Elles inspirèrent le jeune Louis Agassiz qui - dans son Etude sur les glaciers (1840) - généralisa l'idée d'une période passée plus froide qu'aujourd'hui ayant permis l'expansion des glaciers qui fut nommée âge de la glace (Foucault, 2009). Ces travaux marquent le premier constat d'un climat ayant connu des fluctuations de grande ampleur sur de longues échelles de temps.

Depuis ces observations paléoclimatologiques pionnières, les archives climatiques se sont diversifiées et les techniques de datation se sont perfectionnées. Ces progrès ont permis de préciser notre connaissance des variations spatio-temporelles du climat. Parmi les différentes époques géologiques, la période Quaternaire - actuellement en cours depuis 2.6 millions d'années - est caractérisée par une forte variabilité climatique mondiale et l'alternance d'épisodes glaciaires et interglaciaires. Ces périodes correspondent respectivement à des phases de croissance et de retrait des calottes de glaces et des glaciers. La dernière période glaciaire, entamée il y a environ 115 000 ans, a pris fin il y a 11 700 ans. Elle a connu son apogée - l'extension maximale des calottes et des glaciers - il y a environ 20 000 ans au cours de Dernier Maximum Glaciaire. Ces variations sont enregistrées par les isotopes de l'oxygène présents dans le squelette carbonaté des foraminifères benthiques présents dans les sédiments marins (Figure 2.1).

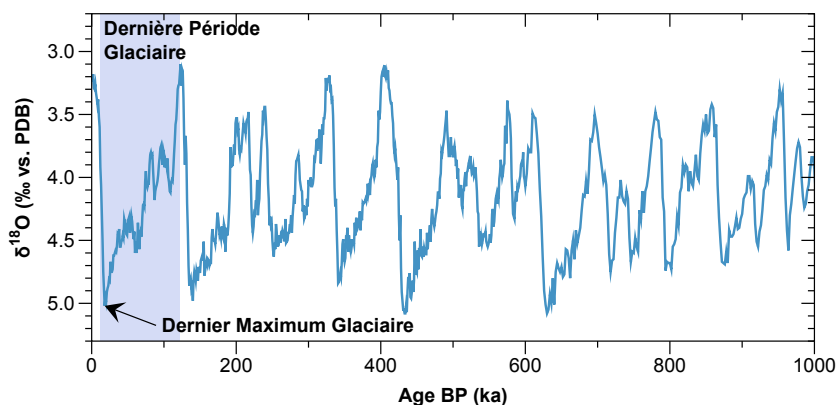


FIGURE 2.1 : Composition isotopique en oxygène des tests de foraminifères benthiques au cours du dernier million d'années (Lisiecki and Raymo, 2005). Les oscillations entre périodes glaciaires et interglaciaires sont caractérisées par l'alternance des valeurs hautes et basses du $\delta^{18}\text{O}$. La zone bleutée montre la dernière période glaciaire. Le dernier pic il y a 20 000 ans correspond au Dernier Maximum Glaciaire. Le présent est à gauche.

Le $\delta^{18}\text{O}$ des foraminifères benthiques constitue une archive de référence pour le Quaternaire. Cet exemple est l'occasion de préciser les problématiques propres aux archives climatiques. En effet, une archive climatique doit permettre de répondre aux questions :

- Quels sont les phénomènes climatiques en lien avec les grandeurs observées ?
- Quel âge ont ces observations ? A quelle résolution temporelle donnent-elles accès ?
- A quelle échelle spatiale nous apportent-elles des informations sur le climat ?

Dans ce premier exemple, la grandeur observée est la composition isotopique de l'oxygène du test carbonaté des foraminifères. Cette composition varie en fonction de la taille des calottes de glace qui séquestrent de l'eau riche en ^{16}O en dehors de l'océan, ainsi qu'en fonction de la température de l'eau de mer à partir de laquelle la calcite a cristallisé. L'enregistrement tel qu'il a été publié (Lisiecki and Raymo, 2005) couvre les 5 derniers millions d'années avec une précision inférieure au siècle. Les variations observées sont mondiales car la courbe présentée moyenne les résultats obtenus à partir de 57 forages répartis dans les différents océans du Globe. Ces 3 questions sont importantes car il existe une grande diversité d'archives climatiques qui peuvent apporter des informations sur différents paramètres de l'atmosphère, l'océan, la cryosphère, ou encore la faune et la flore. De plus, ces archives couvrent des échelles temporelles allant de la centaine aux millions d'années et des échelles spatiales allant de la vallée à la planète entière. Il n'est pas question ici de faire une présentation détaillée de toutes les archives climatiques existantes à ce jour, cependant ces problématiques de signification et de cadre spatio-temporel sont importantes pour la comparaison des archives entre elles. Comparaison qui permet de reconstituer et comprendre l'histoire du climat. Ces observations montrent également le rôle central de la datation dans toute production de donnée paléoclimatique. La datation doit notamment fournir une précision à même de reconstituer une succession d'événement et de lui donner un timing afin d'identifier les possibles liens de causalité(s) entre les événements qui se succèdent (Barker et al., 2015).

2.1.2 La dernière déglaciation

La transition entre le Dernier Maximum Glaciaire et l'interglaciaire actuel, nommé Holocène, ne correspond pas à un réchauffement monotone des températures à la surface du globe. Cette période, le Tardiglaciaire ou dernière déglaciation, est marquée par des oscillations climatiques courtes et abruptes selon des schémas différents dans l'hémisphère Nord et Sud (Blunier and Brook, 2001; Broecker, 1998; Jouzel et al., 1995).

De la même manière que pour le $\delta^{18}\text{O}$ des foraminifères benthiques, ces variations sont enregistrées par une grande variété d'archives climatiques. Le $\delta^{18}\text{O}$ et δD des glaces du Groenland et de l'Antarctique, qui sont des proxys de la température, montrent des évolutions différentes (Andersen et al. (2004); Jouzel et al. (2007), Figure 2.2). Au Groenland, un réchauffement abrupt a lieu vers 14.7 suivi

à 12.9 ka d'un refroidissement subit de 1200 ans : le Dryas Récent (YD, en bleu sur la Figure 2.2). La fin du Dryas Récent marque la fin de la dernière période glaciaire et le passage à l'Holocène. L'Antarctique enregistre un réchauffement progressif depuis 19 ka, suivi d'une baisse des températures de 14.2 à 12.7 ka, l'Antarctic Cold Reversal (ACR, en jaune sur la Figure 2.2). S'ensuivent une remontée abrupte et une stabilisation des températures.

La période 18.5-14.5 ka est une période froide pour l'hémisphère Nord, durant laquelle les calottes de l'hémisphère Nord vèlent des quantités importantes d'icebergs qui envahissent l'Atlantique Nord jusqu'aux latitudes du Portugal (Bard et al., 2000; Bond et al., 1992; Heinrich, 1988). Cette période est nommée Heinrich Stadial 1 (HS1, en bleu sur la Figure 2.2) du nom d'un des premiers chercheurs impliqués dans la découverte de ce phénomène. Les périodes HS1 et YD sont également caractérisées par des ralentissements de l'activité de la circulation thermohaline, enregistrés par le rapport $^{231}\text{Pa}/^{230}\text{Th}$ des sédiments marins (McManus et al. (2004), Figure 2.2).

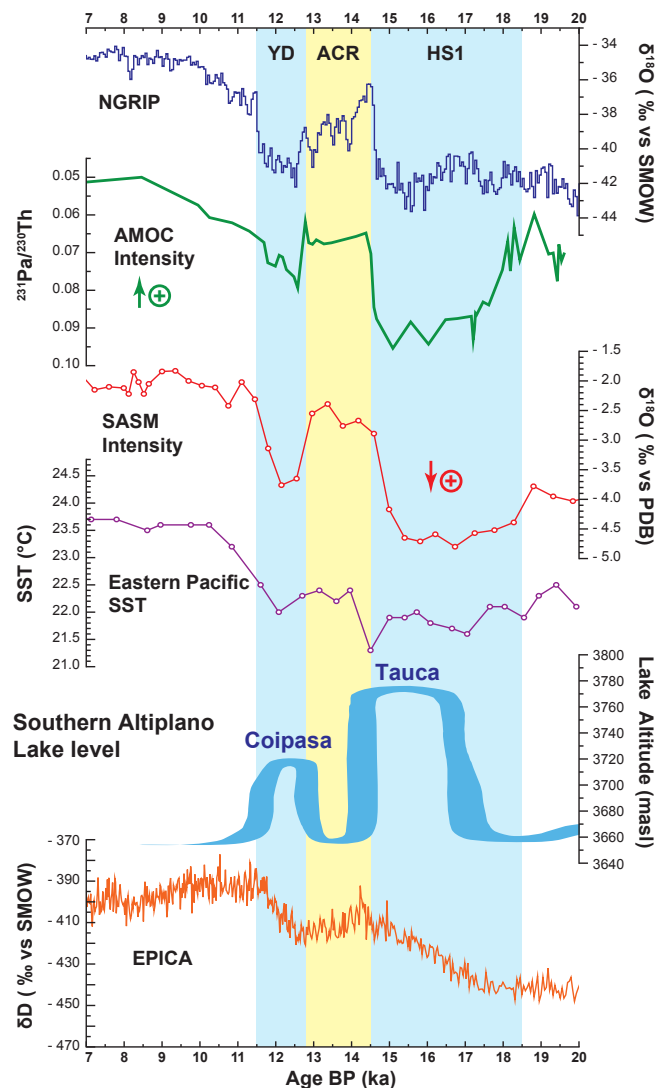


FIGURE 2.2 : Mise en contexte de la période tardiglaciaire par différents signaux paléoclimatiques. NGRIP : $\delta^{18}\text{O}$ (‰ vs. SMOW) dans les glaces du Groenland (Andersen et al., 2004); AMOC : $^{231}\text{Pa}/^{230}\text{Th}$ dans les sédiments de l'Atlantique Nord (McManus et al., 2004); Botuvera Cave : $\delta^{18}\text{O}$ (‰ vs. PDB) dans les spéléothèmes de la grotte Botuvera au Brésil (Wang et al., 2007); SST : Températures de surface dans le Pacifique Est (Dubois et al., 2009); Lake Level : Élévation des Lacs de l'Altiplano Sud (Blard et al., 2011; Placzek et al., 2006; Sylvestre et al., 1999); EPICA : δD (‰ vs. SMOW) from EPICA Dome C ice core (Jouzel et al., 2007)

La circulation thermohaline joue un rôle central dans la répartition de la chaleur à la surface du globe entre l'Equateur et les pôles. Elle exporte vers le Nord des eaux de surfaces chaudes ce qui a pour conséquences de réchauffer l'hémisphère Nord et de refroidir l'hémisphère Sud (Crowley, 1992). La variabilité du fonctionnement de ce "tapis roulant" est suspectée d'être un acteur majeur des oscillations climatiques tardiglaciaires (Broecker, 1998; Mix et al., 1986). Récemment différentes études de modélisation ont corroboré cette hypothèse et permis de proposer des mécanismes liant la circulation thermohaline au climat (Banderas et al., 2014; Zhang et al., 2014). En accord avec de nouvelles observations, elles mettent notamment l'accent sur l'importance de la modification de la répartition des vents d'ouest dans ces changements (De Deckker et al., 2012; Denton et al., 2010; Buizert and Schmittner, 2015).

Les systèmes de moussons connaissent également des modulations dans leur fonctionnement pendant ces périodes, associées à des déplacements vers le Sud de la zone de convergence intertropicale (Gibbons et al., 2014; Ivanochko et al., 2005). Ce qui a pour conséquence un affaiblissement de l'intensité des moussons sur l'Inde, la mer d'Arabie (Sirocko et al., 1996; Zorzi et al., 2015) et la Chine (Han et al., 2015; Wang et al., 2001).

2.1.3 La dernière déglaciation en Amérique du Sud

En Amérique du Sud, les périodes YD et HS1 sont synchrones d'une intensification de la mousson Sud-Américaine, marquée par une excursion négative du $\delta^{18}\text{O}$ dans la calcite des stalagmites de la grotte de Botuvera au Sud du Brésil (Wang et al. (2007), Figure 2.2).

Ces réorganisations atmosphériques sont synchrones du développement de grands paléolacs sur l'Altiplano : le Lac Tauca qui atteint une superficie de 56 700 km², équivalente à celle du lac Michigan et le Lac Coipasa, atteignant 32 300 km², l'équivalent du lac Tanganyika (Blard et al., 2011; Placzek et al., 2006; Sylvestre et al., 1999; Servant and Fontes, 1978). Ces hauts niveaux (Figure 2.2) sont identifiés et datés grâce aux nombreux éléments attestant d'une paléo ligne de rivage, principalement les biohermes, qui sont des concrétions carbonatées résultant de la précipitation de calcite par des algues.

Différents proxys montrent également une réponse synchrone de ces 2 événements. C'est le cas des radiations gamma mesurées lors d'un carottage dans le Salar des Uyuni qui traces l'abondance de boue et donc les périodes humides (Baker et al., 2001a). C'est également le cas de l'abondance du plancton et des diatomées benthiques dans les sédiments du lac Titicaca (Baker et al., 2001b) qui indique une baisse de niveau lacustre à la fin du haut niveau Tauca et une remontée à l'initiation du Coipasa. Le $\delta^{18}\text{O}$ des glaces du Sajama enregistre des sauts rapides à partir de l'initiation du haut niveau Tauca avec un maximum au début de la régression. La fin de Dryas Récent est très nettement marquée par une stabilisation dans des valeurs moins négatives de $\delta^{18}\text{O}$ (Thompson et al., 1998). Toutefois, en plus de la température, ce dernier signal intègre d'autres variables de premier ordre telle que l'évaporation des paléolacs, ce qui le rend dur à interpréter (Quesada et al., 2015).

Ainsi, il est maintenant bien établi que le cycle hydrologique tropical a subi des réorganisations importantes pendant la déglaciation, notamment en Amérique du Sud. Mais les modalités exactes de ces perturbations sont encore mal connues. La variabilité spatiale des précipitations est d'ailleurs peu documentée pour le moment alors qu'elle constitue un paramètre central de ces modifications atmosphériques. Aucune observation n'a jusqu'à présent permis de reconstituer un paléo-champ de précipitations avec une résolution spatiale suffisante.

Par ailleurs, les variations de température pendant la déglaciation sont assez bien connues pour les eaux de surface des océans, mais on ne peut pas en dire autant pour les températures atmosphériques au niveau des surfaces continentales de haute altitude. Quelle a été l'amplitude de ces variations ?

Or les enregistrements géomorphologiques des paléoglaciers des Andes tropicales constituent une source d'informations paléoclimatiques à même de documenter ces deux aspects. Leur utilisation est détaillée dans la section suivante.

2.2 Les paléoglaciers, traceurs paléoclimatiques continentaux

La section suivante présente des notions générales sur les glaciers qu'il est possible de trouver dans de nombreux ouvrages. Une présentation détaillée est fournie par [Paterson \(1994\)](#).

2.2.1 La Dynamique glaciaire est pilotée par le climat

Les glaciers de montagne se forment par l'accumulation prolongée de la neige qui se transforme progressivement en glace. La masse de glace flue, sous l'effet de la gravité, selon la pente sur laquelle elle s'est formée. Le processus par lequel un glacier gagne de la masse, principalement grâce aux précipitations neigeuses est appelé accumulation. Il favorise l'expansion de la langue glaciaire vers l'aval. Le processus inverse correspond à l'ablation, il est principalement le fait de la fonte et de la sublimation. Le gradient thermique altitudinal de l'atmosphère et la répartition des précipitations organisent le glacier en une zone d'accumulation située en amont et une zone d'ablation en aval. Dans les régions où le climat présente une importante saisonnalité, le découpage de ces zones varie avec les saisons. L'altitude à laquelle le bilan de masse annuel du glacier est nul est appelée altitude de la ligne d'équilibre (Figure 2.3).

La position du glacier dans la vallée s'ajuste donc en fonction des variations de sa masse imposées par le climat. Dans les périodes plus froides et plus humides, la ligne d'équilibre s'abaisse et le glacier s'étend en aval. Le phénomène inverse se produit dans les périodes plus chaude et plus sèches.

2.2.2 Les morphologies glaciaires témoignent de l'histoire du glacier

Le frottement créé par le fluage de la glace sur le substratum est un important agent érosif. Il arrache de la matière à la surface rocheuse et déplace ces débris vers l'aval. Cette activité d'érosion et de transport sédimentaire des glaciers est responsable de la mise en place des modelés glaciaires. Il existe une grande variété de modelés glaciaires dont une description exhaustive et détaillée est fournie par l'ouvrage *Glacial Geology* de M. Bennett et N. Glasser ([Bennett and Glasser, 2009](#)).

Les principales morphologies glaciaires étudiées dans le cadre de cette thèse sont les moraines et les roches moutonnées. Les moraines sont constituées des matériaux que la langue de glace transporte de l'amont vers l'aval, et qu'elle dépose dans la partie terminale de la zone d'ablation. La granulométrie des dépôts morainiques est très hétéroclite, les argiles y côtoient les blocs métriques à décimétriques. La limite inférieure de la langue met en place des moraines frontales, elles occupent le talweg, perpendiculairement à l'écoulement. Les moraines frontales sont parfois en connexion avec les moraines latérales mises en places par les flancs de la langue glaciaire. Elles sont disposées parallèlement à l'écoulement (Figure 2.3). La moraine située la plus en aval est appelée moraine terminale, elle marque l'extension maximale atteinte par un glacier. Les moraines plus récentes qui se sont formées en amont sont des moraines de récession. Elles se forment à l'occasion de stabilisation ou de ré-avancées mineures, alors que le glacier connaît un recul sur une plus longue échelle de temps. Quand un glacier avance sur ces anciennes moraines, il peut les éroder et les faire disparaître, ce qui rend l'enregistrement morainique parfois lacunaire.

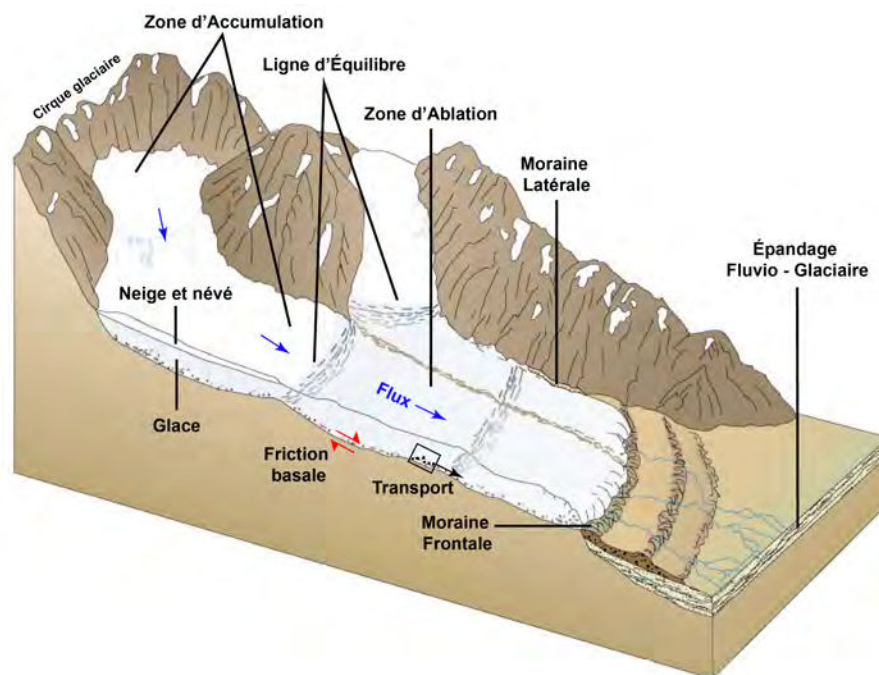


FIGURE 2.3 : Les différentes caractéristiques d'un glacier de montagne (modifié d'après Christopherson (2010)).

Les roches moutonnées sont des portions du substratum qui n'ont pas été transportées par le glacier mais qui ont subi son effet abrasif. Elles peuvent présenter une forme convexe asymétrique ou encore des stries qui témoignent du rabotage glaciaire.

Les moraines et les roches moutonnées constituent donc des marqueurs de l'histoire d'un glacier. Elles permettent de tracer l'évolution de son expansion qui est elle même dictée par le climat. L'utilisation des paléoglaciers comme archives climatiques nécessite donc de dater l'abandon des moraines et des roches moutonnées par le glacier afin de donner un cadre temporel à cet enregistrement climatique.

2.2.3 Les enregistrements des glaciers des Andes Tropicales pendant le tardiglaciaire

Les importants progrès méthodologiques et analytiques concernant l'utilisation des âges d'exposition (voir chapitres 4 et 5) qui ont eu lieu depuis 30 ans ont permis de systématiser leur utilisation pour dater des morphologies glaciaires. Ainsi, de nombreuses publications ont rapporté des chronologies glaciaires couvrant la dernière déglaciation dans les Andes tropicales (e.g. Farber et al., 2005; Glasser et al., 2009; Hall et al., 2009; May et al., 2011; Smith et al., 2011, 2005; Smith and Rodbell, 2010; Zech et al., 2009, 2007b). Cependant, l'idiosyncrasie des dynamiques glaciaires rend les enregistrements morainiques très divers et il est dur d'en faire émerger une vision globale. Cette diversité est probablement due à la "disparité d'échelle" qui existe entre les conditions climatiques locales qui influencent la dynamique glaciaire et les conditions régionales, et globales (Mölg and Kaser, 2011).

Afin d'extraire une tendance globale des différents jeux de données des chronologies glaciaires, Jomelli et al. (2014) a rassemblé et recalculé de manière homogène tous les âges disponibles entre 15 ka et l'Holocène. Le jeu d'âges ainsi calculé met en évidence que les glaciers andins montrent des enregistrements morainiques synchrones de l'Antarctic Cold Reversal propre à l'hémisphère Sud et également du Younger Dryas observé en premier lieu dans l'hémisphère Nord. Cependant, le stade ACR étant enregistré un plus grand nombre de fois, il est identifié comme ayant la plus forte empreinte sur les glaciers des Andes Tropicales (Figure 2.4). L'article est présent en annexe du manuscrit avec les autres articles auxquels ces travaux de thèse ont contribué.

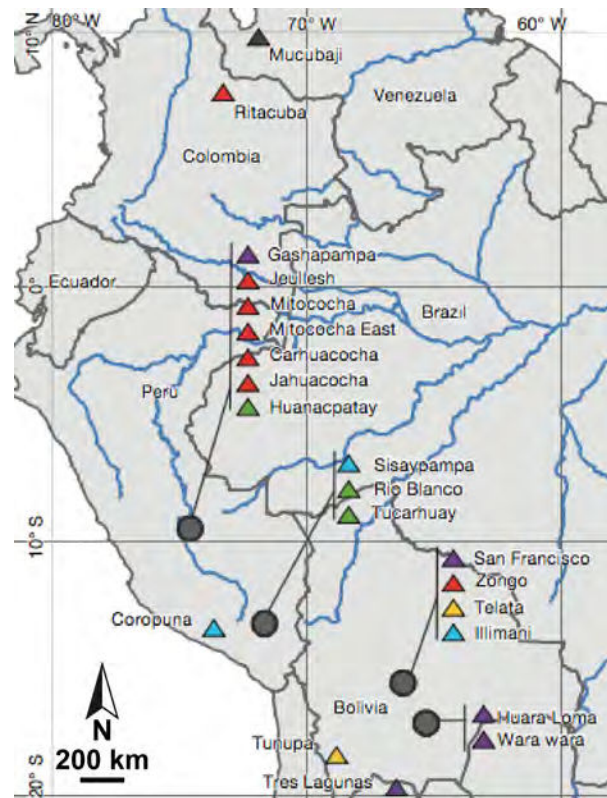


FIGURE 2.4 : Comparaison des avancées glaciaires couvrant la fin de la période tardiglaciaire. Les symboles violets indiquent des âges plus vieux ou synchrones de l'Antarctic Cold Reversal (ACR) (compte tenu des barres d'erreur). Les rouges sont synchrones de l'ACR; les oranges sont les âges compatibles avec l'ACR et le Younger Dryas (YD); les bleus sont synchrones du YD, les verts sont Holocènes; les noirs ont été rejetés. (Modifiée d'après Jomelli et al. (2014)).

2.2.4 L'inversion climatique et le couplage avec les lacs

Afin de compléter la comparaison des chronologies glaciaires, il est possible d'inverser les anciennes extensions des glaciers afin de retrouver les conditions climatiques qui leurs étaient associées. Cette démarche permet ainsi de proposer des résultats facilement comparables entre eux ainsi qu'avec d'autres archives climatiques, et facilement interprétables. Ils sont donc plus à même d'améliorer notre compréhension du climat.

Cette démarche a déjà fait l'objet de plusieurs études sur l'Altiplano (voir chapitre 6) et notamment celle de Blard et al. (2009) qui a utilisé une modélisation couplée des glaciers et des lacs pour contraindre les conditions de précipitation et de température pendant le haut niveau du lac Tauca. Cette démarche inédite s'est révélée particulièrement efficace car elle permet de confronter les contraintes climatiques de premier ordre sur les extensions glaciaires et lacustres à l'aide de modèles adaptés au contexte d'inversions paléoclimatiques pour lesquels peu de données sont disponibles. Cette étude a permis de contraindre des températures environ 6.5 °C inférieures à l'actuelle et des précipitations 1.6 à 3 fois supérieures au niveau du volcan Tunupa situé au Nord du Salar des Uyuni (voir chapitre 6). Ce sont ces premiers résultats qui ont motivé le développement du projet de recherche ANR GALAC porté par Pierre-Henri Blard et dans le cadre duquel s'inscrit cette thèse. Elle reprend la même approche tant du point de vue de la datation que de l'inversion climatique (avec quelques variations).

La dernière déglaciation est donc une période propice à l'investigation paléoclimatologique et à la compréhension des interactions entre les différents rouages de la machine climatique globale. Pendant cette période les systèmes climatiques continentaux connaissent des perturbations majeures à l'instar de l'Altiplano qui voit se développer et disparaître de grands paléolacs. Les glaciers dont la dynamique est pilotée par le

climat laissent dans le paysage des traces de leurs extensions passées qui peuvent être utilisées comme des archives climatiques. En couplant la modélisation des paléoglaciers et des paléolacs de l'Altiplano, il est possible d'inverser les conditions de précipitation et de température enregistrées par ces archives et ainsi de reconstituer l'histoire du climat en domaine continental.

Toutefois le potentiel d'une archive à documenter le climat passé est lié à la possibilité de dater cette archive afin de donner un cadre temporel aux observations. C'est pourquoi les premiers chapitres 4 et 5 de cette thèse présentent des développements méthodologiques concernant la technique utilisée pour la datation des modelés glaciaires. Les deux chapitres suivants présentent des études paléoclimatiques qui ont bénéficié de ces développements.

Chapitre 3

Présentation des âges d'exposition

Sommaire

3.1	Les âges d'exposition et la formation des isotopes cosmogéniques . . .	31
3.2	Les âges d'exposition et le taux de production	32
3.3	Les modèles de spatialisation et de calibration du taux de production	34

Dans cette thèse, l'âge d'abandon des morphologies glaciaires (moraines, roches moutonnées) par le glacier est déterminé par la méthode d'âge d'exposition. Cette section n'a pas pour but de constituer une méthodologie détaillée à ce sujet. Elle vise à présenter au lecteur étranger de la méthode ses principaux concepts et problématiques afin de bien appréhender les motivations des travaux présentés dans les chapitres 4 et 5, ainsi que les résultats des chapitres 6 et 7.

3.1 Les âges d'exposition et la formation des isotopes cosmogéniques

La méthode d'âge d'exposition repose sur la mesure de la concentration des minéraux des roches en atomes appelés isotopes cosmogéniques. Ces isotopes se forment par l'interaction du flux cosmique en provenance de l'espace avec des éléments initialement présents dans les minéraux des roches. Comme ce flux s'atténue avec la profondeur (il devient négligeable ou bout de quelques mètres), seules les roches à la surface de la Terre accumulent des isotopes cosmogéniques. Il est donc possible de déterminer le temps passé par une roche à la surface de la Terre à partir de sa concentration en isotopes cosmogéniques (Gosse et al., 1995; Smith et al., 2005). Parmi les différents isotopes étudiés aujourd'hui, ces travaux de thèse utilisent le ^{10}Be mesuré dans le quartz et le ^3He dans les pyroxènes.

Le flux cosmiques peut être décomposé en un flux primaire et un flux secondaire. Le flux primaire est principalement composé de protons, de particules alpha (noyaux de ^4He) et d'électrons (Gosse and Phillips, 2001). Le champ magnétique terrestre agit comme une barrière qui dévie une partie de ce flux primaire en provenance de l'espace. Cette capacité de barrière dépend de l'intensité du champ magnétique terrestre (Dunai, 2001). Or cette intensité varie au cours du temps (Guyodo and Valet, 1999). Les périodes de fort champ magnétique sont donc associées à une plus faible production d'isotopes cosmogéniques. La relation inverse a lieu pendant les périodes de faible champ magnétique.

En entrant dans l'atmosphère terrestre, ce flux primaire interagit avec les éléments qui la composent (O et N). Cette interaction donne lieu à une cascade de réactions nucléaires dans la colonne atmosphérique qui est responsable de la production de nouvelles particules telles que le ^{14}C . Ce ^{14}C est donc un isotope cosmogénique atmosphérique. Il est utilisé fréquemment pour les datations archéologiques. Parmi les nouvelles particules créées, on trouve également des neutrons de haute énergie, des neutrons thermiques (moins énergétiques) et des muons. Ce sont ces particules qui, en parvenant à la surface de la Terre, vont à leur tour créer des réactions nucléaires avec les éléments présents dans les minéraux des roches et créer les isotopes cosmogéniques, concernés pour les âges

d'exposition. Ces isotopes n'étant plus formés dans l'atmosphère, mais dans les mailles cristallines des minéraux, ils sont appelés isotopes cosmogéniques In Situ. Les muons et les neutrons thermiques viennent s'intégrer à la structure d'un noyau et créent des réactions de capture. Les neutrons de haute énergie percutent des noyaux, les amenant à se décomposer en noyaux fils plus légers. Cette réaction est appelée spallation. Un résumé du processus de formation des isotopes cosmogéniques est présenté en Figure 3.1. La formation des isotopes cosmogéniques est présentée de manière détaillée dans le livre de T.J. Dunai (Dunai, 2010).

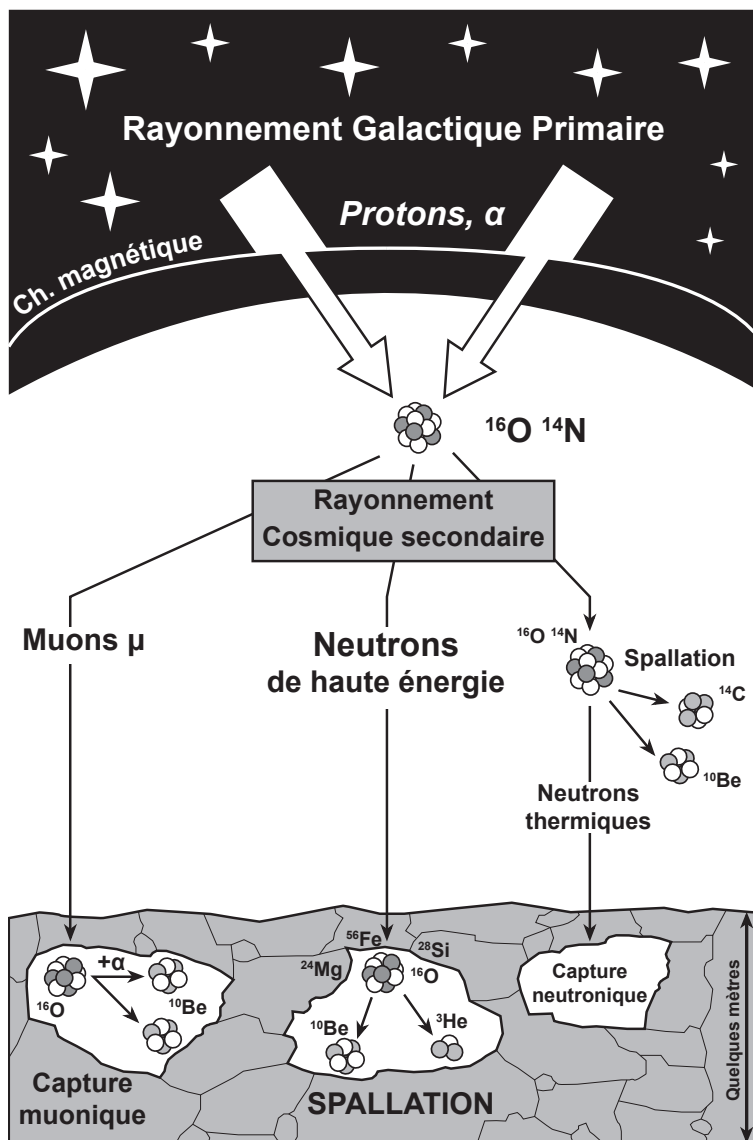


FIGURE 3.1 : Formation des isotopes cosmogéniques, à partir d'une figure de Pierre-Henri Blard.

3.2 Les âges d'exposition et le taux de production

La détermination d'un âge à partir d'une concentration en isotopes cosmogéniques nécessite de connaître la vitesse à laquelle se sont accumulés les isotopes cosmogéniques dans le minéral. Par analogie, pour savoir depuis combien de temps se remplit une baignoire, il ne suffit pas de connaître le niveau d'eau dans la baignoire, mais également le débit de remplissage de celle-ci. En première approximation, cette vitesse est considérée constante au cours du temps. Elle est appelée **taux de production**. Elle est homogène à un nombre d'atomes d'isotopes cosmogéniques créés par gramme de minéral et par an.

Spatialement, le taux de production varie avec la latitude, l'altitude et les anomalies de pression atmosphérique (Lal, 1991; Stone, 2000). La latitude détermine l'angle d'incidence du flux cosmique avec les lignes de champs magnétique de la Terre. A l'équateur, les particules cosmiques se présentent orthogonalement aux lignes de champ, ce qui maximise l'effet répulsif du champ. Aux pôles, le flux est davantage tangentiel aux lignes de champs et l'énergie requise pour arriver jusqu'à la surface de la Terre est plus faible. L'altitude module l'épaisseur de la colonne d'air à traverser par le flux cosmique. Le flux cosmique est atténué au cours de son interaction avec l'atmosphère terrestre. Plus un endroit est bas et plus la production d'isotopes cosmogéniques en surface est faible. Le rôle des anomalies de pression est similaire. La pression peut être envisagée comme une valeur de densité de l'atmosphère. Dans les zones de hautes pressions, le flux cosmique traverse une atmosphère plus dense et s'atténue plus rapidement avant d'avoir atteint la surface. Ainsi, un taux de production au sommet du mont Mc Kinley - Denali est 100 fois supérieur à un taux sur une plage des Galápagos ou des Maldives (un utilisant le modèle de Lal-Stone cité précédemment). Cette situation fait qu'il n'est pas possible de déterminer la valeur d'un taux de production indépendamment de sa situation géographique. Par défaut, les taux de production sont couramment exprimés dans les conditions suivantes : en hautes latitudes et au niveau de la mer (SLHL, pour Sea Level High Latitude). La dépendance spatiale des taux de production est résumée dans la Figure 3.2.

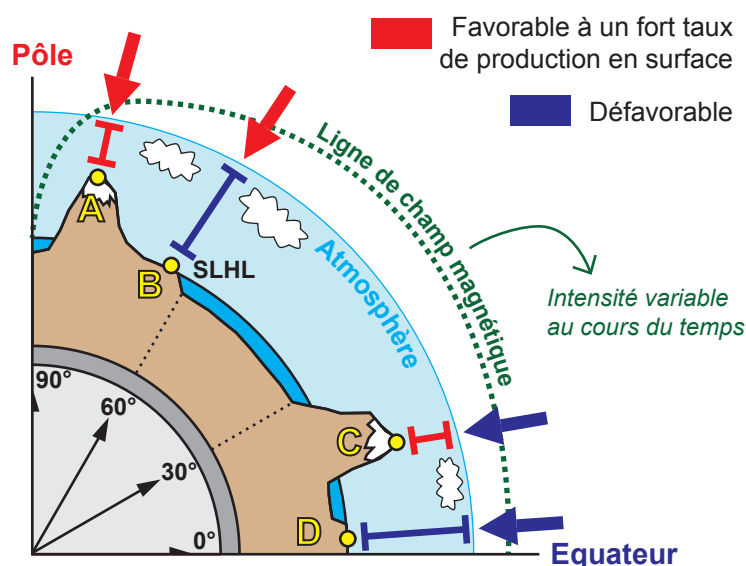


FIGURE 3.2 : Dépendance spatiale du taux de production. La production est maximale en A, en haute altitude et latitude. Elle est minimale en D, au niveau de la mer et à l'équateur. Les situations B et C sont intermédiaires aux deux autres cas, toutefois l'influence de l'altitude est prédominante sur celle de la latitude.

La dépendance du flux cosmique à l'intensité du champ magnétique terrestre induit des variations temporelles du taux de production. C'est pourquoi le calcul d'âge d'exposition, au même titre que la normalisation des taux aux conditions SLHL, fait également intervenir une correction qui permet de prendre en compte l'incidence de ces variations sur l'âge (Dunai, 2001). Ces calculs se basent sur des reconstitutions de l'activité du champ magnétique issues de différents proxys tels que le ^{10}Be atmosphérique (Muscheler et al., 2005) ou encore les propriétés magnétiques des minéraux dans les sédiments marins et lacustres (Laj et al., 2004). Le plus souvent, ces reconstitutions assimilent le fonctionnement du champ magnétique terrestre à celui d'un dipôle virtuel dont le moment magnétique est parallèle à l'axe des pôles magnétiques. Ainsi ces reconstitutions font références à la valeur du moment dipolaire axial virtuel du champ magnétique terrestre (VDM en anglais pour Virtual Dipolar Moment). Différentes reconstitutions utilisées dans les chapitres 4 et 5 de cette thèse sont présentés dans la Figure 3.3.

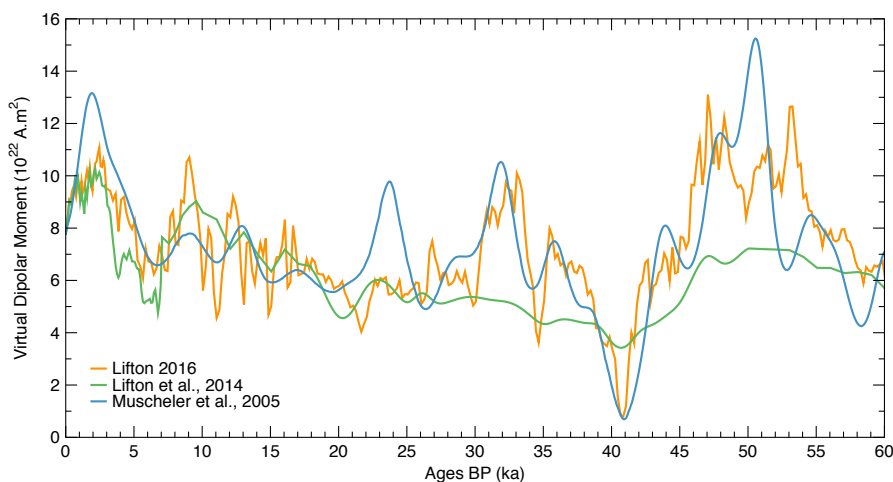


FIGURE 3.3 : Exemple de trois reconstitutions du moment dipolaire virtuel du champ magnétique terrestre (VDM) sur les soixante derniers milliers d'années.

3.3 Les modèles de spatialisation et de calibration du taux de production

La détermination d'âge d'exposition précise et robuste nécessite une bonne connaissance du taux de production localement, sur le lieu d'échantillonnage. Dans la pratique, le géochronologue choisit un taux de production connu exprimé dans les conditions SLHL. Il utilise ensuite des modèles de mise à l'échelle (scaling models en anglais) afin de déterminer le taux de production local et de tenir compte des variations du champs magnétique. Différents modèles de mise à l'échelle ont été développés depuis les années 90 (Dunai, 2001; Lal, 1991; Lifton et al., 2014, 2005; Desilets and Zreda, 2003; Desilets et al., 2006) . Ils sont présentés en détail dans les chapitres 4 et 5 de cette thèse.

Ces modèles ne produisent pas les mêmes résultats et l'utilisation d'un modèle plutôt que d'un autre introduit une part de subjectivité dans le calcul d'âge d'exposition. Il en va de même pour le choix de la reconstruction du champ magnétique et du modèle d'atmosphère. Une manière de réduire ce biais consiste à utiliser un taux de production proche spatialement et temporellement du site à dater. Une telle configuration permet de limiter la dépendance des taux calculés aux modèles de mise à l'échelle. Cette idée est développée plus en détail dans l'introduction de l'article présenté en chapitre 4 (voir la première figure).

Ce sont ces constats qui ont motivé les développements méthodologiques présentés dans les chapitres 4 et 5. Dans le chapitre 4 un nouveau taux de production sur l'Altiplano pour le ^{10}Be in situ est établi. Ce nouveau résultat est couplé à un travail d'homogénéisation des données relatives aux études précédentes de calibration dans les hautes Andes tropicales afin de proposer un jeu de taux de production de référence ainsi qu'un taux synthétique pour la région. Dans le chapitre 5, un nouveau programme en ligne de calcul d'âge d'exposition est présenté. Partant du constat que les programmes actuels ne laissent pas suffisamment de possibilités aux utilisateurs dans (i) le choix du taux de production utilisée pour le calcul, (ii) le paramétrage de la mise à l'échelle des taux, nous avons développé un programme afin de proposer les différents modèles et taux de production les plus à jour.

Dans les chapitres 6 et 7, les âges d'exposition sont utilisés pour documenter le climat de l'Altiplano au cours de la dernière déglaciation.

NOTE : les âges sont exprimés en milliers d'années depuis le présent. Ils sont donc mentionnés sous la forme "15 ka BP" pour "Before Present" ou "15 ka" de manière implicite.

Chapitre 4

Calibration d'un taux de production du ^{10}Be in situ dans les Hautes Andes Tropicales

Le taux de production est un paramètre central du calcul d'âge d'exposition. Il est essentiel d'en connaître précisément la valeur pour produire des âges robustes. Une valeur erronée du taux de production est source d'erreurs systématiques sur les âges calculés et une incertitude significative sur cette valeur impliquera également d'importantes incertitudes sur ces âges.

La détermination d'un nouveau taux de production nécessite de pouvoir étudier un même objet géomorphologique sous 2 aspects complémentaires. Il est nécessaire de (i) déterminer sa concentration en isotopes cosmogéniques, (ii) déterminer son âge indépendamment de cette concentration. C'est notamment possible grâce à une autre méthode géochimique telle que la méthode $^{40}\text{Ar}/^{39}\text{Ar}$ utilisée pour la calibration du taux de San Pedro présentée en Annexe. Il est alors possible d'établir un taux de production local à l'aide de ces 2 grandeurs (ainsi que la demie-vie dans le cas des isotopes radioactifs). Cette valeur est associée à la situation géographique du site de calibration et à son âge. Il est ensuite possible d'en dériver une valeur standard aux conditions SLHL à l'aide des modèles de mise à l'échelle.

Lors d'un calcul d'âge d'exposition, le taux de production est calculé pour l'échantillon à dater à partir de sa valeur standard SLHL en utilisant les modèles de mise à l'échelle dans une transformation complémentaire à celle qui vient d'être évoquée. D'un point de vue calculatoire, il est donc possible d'utiliser un taux établi à partir d'une coulée de lave islandaise vieille de 100 000 ans pour dater une moraine Holocène sur l'Altiplano, pour peu que l'on soit en possession d'une reconstitution suffisamment longue de l'intensité du champ magnétique terrestre. Toutefois dans un tel cas de figure, l'âge calculé est très dépendant du modèle de mise à l'échelle choisi et de tous les paramètres qu'on lui adjoint (e.g. modèle d'atmosphère, base paléomagnétique). En revanche, lorsque l'on utilise un taux qui a été déterminé sur un objet proche de l'endroit à dater en espace (de l'ordre de la centaine de km horizontalement et de 1000 m verticalement) et en temps (quelques milliers d'années), la dépendance au modèle est beaucoup plus faible. En effet, dans ce deuxième cas, le passage du taux SLHL au taux adapté pour la datation est symétrique de celui effectué en amont pour passer du taux local (au site de calibration) au taux SLHL. Plus les sites de calibration et de datation sont proches et plus les 2 transformations tendent à s'annuler (plus on tend à utiliser le taux local). L'utilisation d'un taux calibré dans la même région que le site à dater permet donc de réduire considérablement l'empreinte du modèle sur la valeur finale du taux de production. Cette notion est illustrée par la figure 1 de l'article.

De plus des phénomènes atmosphériques synoptiques tels que le Bolivian High (Anticyclone de haute altitude observé pendant l'été Austral sur l'Altiplano) ou la dépression d'Islande sont à même d'influencer durablement la production en isotopes cosmogéniques sans que les modèles de mise à l'échelle puissent en tenir compte. Il y a donc un grand intérêt à contraindre précisément les taux de production dans une région avant de les utiliser.

Les lithologies rencontrées sur l'Altiplano sont variées et nous ont amené à utiliser des âges d'exposition se basant sur le ^3He dans les pyroxènes pour les lithologies basiques rencontrées dans le sud de l'Altiplano du Sajama à l'Uturuncu, mais également le ^{10}Be dans les quartz pour les lithologies granitiques et granodioritiques du Zongo et d'Azanaques ou celles silicoclastiques du Tambo. L'étude de [Blard et al. \(2013\)](#) sur le Tunupa a établi un taux de production pour le ^3He de $134 \pm 5 \text{ at.g}^{-1}.\text{a}^{-1}$ en accord avec celui déterminé par Delunel. et al (Submitted) sur une coulée de lave sur le San Pedro au Nord du Chili ($129 \pm 14 \text{ at.g}^{-1}.\text{a}^{-1}$). Ces résultats sont exprimés, une fois n'est pas coutume, dans les conditions SLHL et en utilisant la procédure de mise à l'échelle se basant sur (i) le modèle de Lal-Stone dépendant du temps, (ii) l'atmosphère spatialisée ERA-40, (iii) la reconstruction géomagnétique de [Muscheler et al. \(2005\)](#). Pour le ^{10}Be , [Blard et al. \(2013\)](#) et [Kelly et al. \(2013\)](#) ont établi des taux respectifs de $4.14 \pm 0.20 \text{ at.g}^{-1}.\text{a}^{-1}$ et $4.01 \pm 18 \text{ at.g}^{-1}.\text{a}^{-1}$ à l'extrême Sud et Nord du bassin de l'Altiplano.

Le développement de l'utilisation des âges d'exposition pour dater les moraines est symptomatique du fait qu'il existe peu de méthodes permettant de dater facilement les morphologies glaciaires. Aussi les sites permettant de réaliser ces datations indépendamment des isotopes cosmogéniques sont rares et précieux pour asseoir les valeurs locales des taux de production.

Dans l'étude présentée ici, nous avons tiré parti des observations de [Clayton and Clapperton \(1995, 1997\)](#); [Clapperton et al. \(1997\)](#) sur le synchronisme entre le haut niveau du lac Tauca et une avancée glaciaire enregistrée sur les flancs de Cerro Azanaques, à l'Est de l'Altiplano. Ces auteurs ont décrit la mise en place d'un fan d'épandage glaciaire synchrone de cette avancée ayant atteint le lac. Cette disposition particulière est attestée par les observations sédimentaires réalisées le long des chenaux qui incisent le fan et dans lesquels on observe une progression à partir de faciès proximaux de type till (moraine) jusqu'au faciès distaux de delta à l'interface avec le paléolac. Nous avons combiné nos observations aux premières pour préciser les relations chronologiques entre le fan-delta et le lac Tauca. Les foresets du delta, qui sont des faciès sous marins, sont situés entre 3760 m et 3770 m d'altitude. Ceci indique que la mise en place du fan a eu lieu au plus haut niveau du Tauca, pour lequel un important jeu de données d'âges existe ([Blard et al., 2011](#); [Placzek et al., 2006](#); [Sylvestre et al., 1999](#)). De plus des faciès lacustres sont observés en superpositions des faciès fluviaux du delta, indiquant que le haut niveau du Tauca constitue un âge minimal pour la formation. [Clayton and Clapperton \(1995\)](#) ont également effectué des datations ^{14}C sur des horizons tourbeux situés sous le till du fan-delta et qui le pré-date ($16.1 \pm 0.1 \text{ ka BP}$ and $17.1 \pm 0.2 \text{ ka BP}$ après calibration).

Nous avons utilisés ces relations chronologiques et les données d'âges associées (âge du plus haut niveau Tauca, et âge des échantillons de tourbe) pour calculer l'âge du fan en appliquant une méthode bayésienne de probabilités conditionnelles. En considérant une densité de probabilité d'âge dérivée des datations du haut niveau Tauca, et une autre dérivée des 2 âges ^{14}C dans la tourbe, nous avons calculé une densité d'âge pour le fan-delta. Nous avons ainsi pu établir l'âge du fan à $16.1 \pm 0.6 \text{ ka}$. Nous avons également échantillonné 15 blocs appartenant à la partie proximale du fan -delta pour en déterminer la concentration en ^{10}Be . La préparation des échantillons a été effectuée par Régis Braucher au CEREGE et moi-même au CRPG et les mesures à l'AMS ont été réalisées par les membres de l'ASTER team, également au CEREGE. Nous avons ainsi obtenu une concentration de $4.92 \pm 0.05 \times 10^5 \text{ at.g}^{-1}$. En couplant cette valeur à l'âge du fan-delta, nous obtenons un taux de production local de $30.8 \pm 1.3 \text{ at.g}^{-1}.\text{a}^{-1}$. Ramené aux conditions ce taux est de $4.07 \pm 0.18 \text{ at.g}^{-1}.\text{a}^{-1}$.

Nous avons souhaité pouvoir proposer ce nouveau taux, accompagné des autres taux déjà publiés, pour cela, nous avons recalculé à l'aide d'une méthodologie homogène les 3 taux. Ceci a abouti à la création d'un jeu de données de calibration de référence, duquel nous avons déduit un taux synthétique SLHL de $4.08 \pm 0.10 \text{ at.g}^{-1}.\text{a}^{-1}$ pour la région des hautes Andes tropicales (suivant la même procédure de standardisation).

Cette étude de calibration a fait l'objet d'une publication dans le journal *Quaternary Geochronology* en 2015. Le chapitre suivant est donc présenté en langue anglaise et reprend la mise en page de l'article tel qu'il a été publié.



Contents lists available at ScienceDirect

Quaternary Geochronology

journal homepage: www.elsevier.com/locate/quageo

Research paper

In situ cosmogenic ^{10}Be production rate in the High Tropical Andes



L.C.P. Martin ^{a,*}, P.-H. Blard ^{a,*}, J. Lavé ^a, R. Braucher ^b, M. Lupker ^{c,d}, T. Condom ^e,
J. Charreau ^a, V. Mariotti ^a, ASTER Team ^{b,1}, E. Davy ^a

^a CRPG, UMR7358 CNRS – Université de Lorraine, 54500 Vandoeuvre-lès-Nancy, France

^b Aix-Marseille Université, CNRS-IRD-Collège de France, UM 34 CEREGE, Technopôle de l'Arbois, BP80, 13545 Aix-en-Provence, France

^c ETH, Inst. f. Geochemie und Petrologie, Clausiusstrasse 25, 8092 Zurich, Switzerland

^d ETH, Geological Institute, Sonneggstrasse 5, 8092 Zurich, Switzerland

^e IRD, LTHE, UMR 5564, CNRS, Univ. Grenoble Alpes, G-INP, 38000 Grenoble, France

ARTICLE INFO

Article history:

Received 30 January 2015

Received in revised form

22 June 2015

Accepted 29 June 2015

Available online 6 July 2015

Keywords:

Cosmogenic ^{10}Be

Production rate

Calibration

Bolivian Altiplano

Azanaques

Challapata fan-delta

Lake Tauca

ABSTRACT

Continental climate change during the late glacial period has now been widely documented thanks to Cosmic-Ray Exposure (CRE) dating of glacial features. The accuracy of these CRE ages mainly relies on *a priori* knowledge of the production rate of the cosmogenic nuclide that has accumulated in a specific mineral. To produce unequivocal and accurate chronologies of glacier fluctuations during the late glacial period, it is crucial that the cosmogenic nuclide production rates are better constrained, particularly in the high tropics where existing spatial and temporal scaling models show significant discrepancies. Here we report a new production rate established at low latitude (19°S) and high elevation (3800 masl) on the Challapata fan-delta, at the edge of the Paleolake Tauca, on the flank of Cerro Azanaques (Bolivia). Sedimentological evidence for synchronicity with the Tauca Lake highstand along with U–Th and ^{14}C measurements established that the fan-delta is 16.07 ± 0.64 kyr BP old. In situ-produced ^{10}Be concentrations measured in 15 boulders lying on the fan-delta yield a mean ^{10}Be concentration of $4.92 \pm 0.05 \times 10^5$ at g^{-1} . A local in situ ^{10}Be production rate of 30.8 ± 1.3 at $\text{g}^{-1} \text{yr}^{-1}$ is thus obtained at 3800 masl and 19°S . Application of the “Lal-modified” scaling scheme to this Azanaques production rate, using a standard atmosphere and the Muscheler et al. (2005) geomagnetic reconstruction, leads to a Sea Level High Latitude (SLHL) in situ ^{10}Be production rate of 3.76 ± 0.15 at $\text{g}^{-1} \text{yr}^{-1}$ (1σ uncertainty). In addition, we propose a reference in situ ^{10}Be calibration dataset for the region that combines the production rates of this study with those of Blard et al. (2013b) and Kelly et al. (2015). This dataset of three calibration sites shows a good consistency and yields a regional in situ ^{10}Be production rate of 3.74 ± 0.09 at $\text{g}^{-1} \text{yr}^{-1}$ using the same scaling.

© 2015 Elsevier B.V. All rights reserved.

1. Introduction

The growing number of studies based on terrestrial cosmogenic nuclides evidence their importance in modern Earth Surface Sciences. This expanding interest can be explained by the wide fields of application of cosmogenic nuclides, including Cosmic-Ray Exposure (CRE) dating, and estimation of burial ages and denudation rates. CRE dating of glacial landscapes has significantly improved our knowledge of glacial chronologies and has provided

tight constraints on the evolution of the continental climate since the Last Glacial Maximum in many settings (e.g. Barrows et al., 2011; Blard et al., 2007; Gosse et al., 1995; Jomelli et al., 2014; Licciardi et al., 2009; Smith et al., 2005). This is of particular interest for the tropical Andes since this region is thought to play a key role in the dynamics of the Atlantic Meridional Overturning Circulation (Leduc et al., 2007). The determination of a CRE age relies on *a priori* knowledge of the production rate of the measured cosmogenic nuclide in a specific mineral. This production rate depends on spatial parameters, namely the latitude, altitude and depth of the sample, and also varies with time due to temporal fluctuations in the Earth's magnetic field. Several scaling models have therefore been proposed for converting Sea Level High Latitude (SLHL) production rates into production rates for different sampling locations (Desilets et al., 2006; Dunai, 2001; Lal, 1991;

* Corresponding authors. CRPG, 15 rue Notre Dame des Pauvres, 54501 Vandoeuvre-lès-Nancy, France.

E-mail addresses: leom@crpg.cnrs-nancy.fr (L.C.P. Martin), blard@crpg.cnrs-nancy.fr (P.-H. Blard).

¹ M. Arnold, G. Aumaître, D. L. Bourlès, K. Keddadouche.

Lifton et al., 2005; Stone, 2000). However, discrepancies between the different proposed models are often difficult to assess and biases are introduced that ultimately affect the accuracy of the CRE dating. Even though Lifton et al. (2014) have proposed a new scaling model that aims to reconcile the different published models, the use of production rates calibrated from independently-dated geomorphological surfaces remains necessary. An effective way to overcome scaling discrepancies is to use a “local” calibration site; “local” meaning close, both in space (a few hundreds of km horizontally and less than 1000 m in elevation) and time (a few ka for Pleistocene moraines), to the studied site. In this case, scaling from the Sea Level High Latitude (SLHL) production rate to the local object to be dated is symmetric to the scaling originally used to convert the local production rate to a SLHL production rate (Fig. 1) (Balco et al., 2008; Licciardi et al., 2009). This dramatically reduces the impact of the scaling model on the CRE age.

In this study, we present a new ^{10}Be production rate from a calibration site located at 18.91°S - 66.76°W and 3800 m asl in the tropical Andes, on the Bolivian Altiplano. The motivation for this work is twofold: first, to enrich the worldwide database of production rates and thus improve the accuracy of CRE dating methods, and second, to provide a new local calibration site to chronologically anchor palaeoclimatic and geomorphologic studies in the central Andes. The calibration feature is the Challapata fan-delta, a glaciogenic fan that shows sedimentological evidence for synchronicity between its deposition and the highest level reached by the Paleolake Tauca (Clapperton et al., 1997; Clayton and Clapperton, 1997). Sedimentological evidence and ^{14}C ages constrain this synchronicity and enable emplacement of the fan-delta to be dated. The local in situ ^{10}Be production rate is then derived from measurement of the ^{10}Be concentrations of 15 boulders embedded in the fan. This calibrated local in situ ^{10}Be production rate is then scaled to the Sea Level High Latitude conditions and compared with an updated and homogenized dataset of regional production rates (Blard et al., 2013a; Kelly et al., 2015). The dataset exhibits good internal consistency and can therefore be taken as a reference calibration dataset for in situ ^{10}Be production rates in the High Tropical Andes.

2. Geologic setting of the “Azanaques” calibration site

2.1. The Altiplano and the Paleolake Tauca shorelines

The Altiplano is a wide intermontane plateau, covering an area of 196 000 km² and delimited by the eastern and the western Andes cordilleras (Fig. 2). Latitudinally, it spans from 15.5°S (Peru) to 22.5°S (Bolivia), and it ranges in elevation from 3658 masl in the middle of the plateau to 6542 masl at Sajama volcano. Due to its configuration, the Altiplano is an endorheic basin, which is today dry but was covered by large paleolakes (>50 000 km²) during the wettest periods of the Quaternary (Placzek et al., 2006; Sylvestre et al., 1999).

Of the several lake episodes that have occurred during the last 120 ka, the Lake Tauca episode was the widest and deepest (~120 m) (Placzek et al., 2006). U–Th and ^{14}C dating of the shorelines has enabled the timing of the Tauca cycle to be constrained and the transgression (18–16 ka BP) and regression phases of the lake (14.5–13.5 ka) to be bracketed (Blard et al., 2013b). During its highstand (16–15 ka BP), the level of the lake reached a maximum altitude of 3770 masl and covered a surface of 55 000 km². Two shorelines have been unequivocally identified at elevations of 3770 and 3760 masl and accurate dating of these has indicated that the highstand lasted from 15.8 to 14.9 ka BP (Blard et al., 2013b, 2011; Placzek et al., 2006; Sylvestre et al., 1999). These U–Th and ^{14}C ages are used in this study to independently date the cosmogenic ^{10}Be calibration site (Section 3.1).

2.2. Cerro Azanaques and the Challapata fan-delta

Located at mid-latitude on the eastern Altiplano, Cerro Azanaques (19.96°S , 66.70°W) culminates at 5140 masl on the eastern flank of the Poopo basin (Fig. 2). Cerro Azanaques is the summit of a wide granodiorite massif that formed during the upper Oligocene/lower Miocene (Clayton and Clapperton, 1995; K–Ar age of 23.7 ± 1.6 Ma, GEOBOL, 1994). Though not glaciated today, Cerro Azanaques presents clear geomorphic and sedimentological evidence for intense glacial activity during the Quaternary.

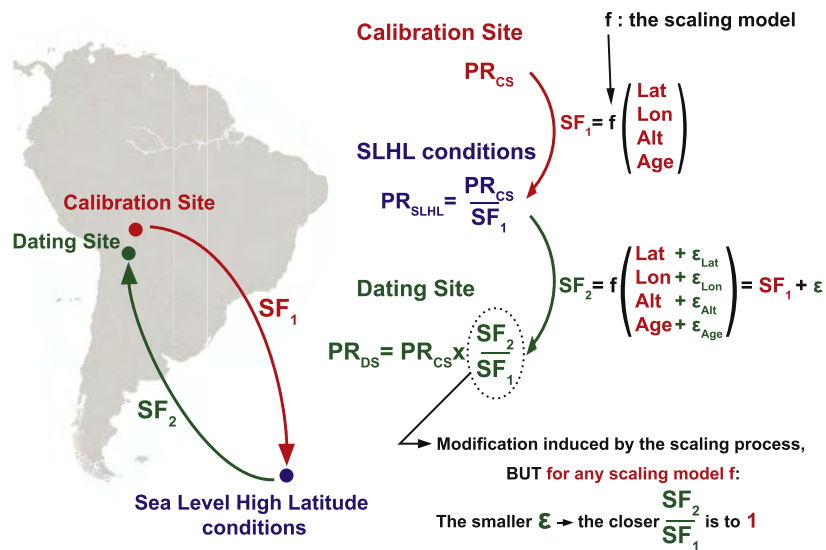


Fig. 1. The benefit of using regional calibration sites. When the calibration site and the site to be dated are close, the SF_1 scaling factor that transforms the production rate determined at the calibration site (PR_{CS}) into a Sea Level High Latitude production rate (PR_{SLHL}) is close to the SF_2 scaling factor that transforms the SLHL production rate into the site to be dated (PR_{DS}). Consequently, the SF_2/SF_1 ratio, which quantifies the modification induced by the scaling process, is close to 1. In this case, small inaccuracies in the scaling factors SF_1 or SF_2 are cancelled-out.

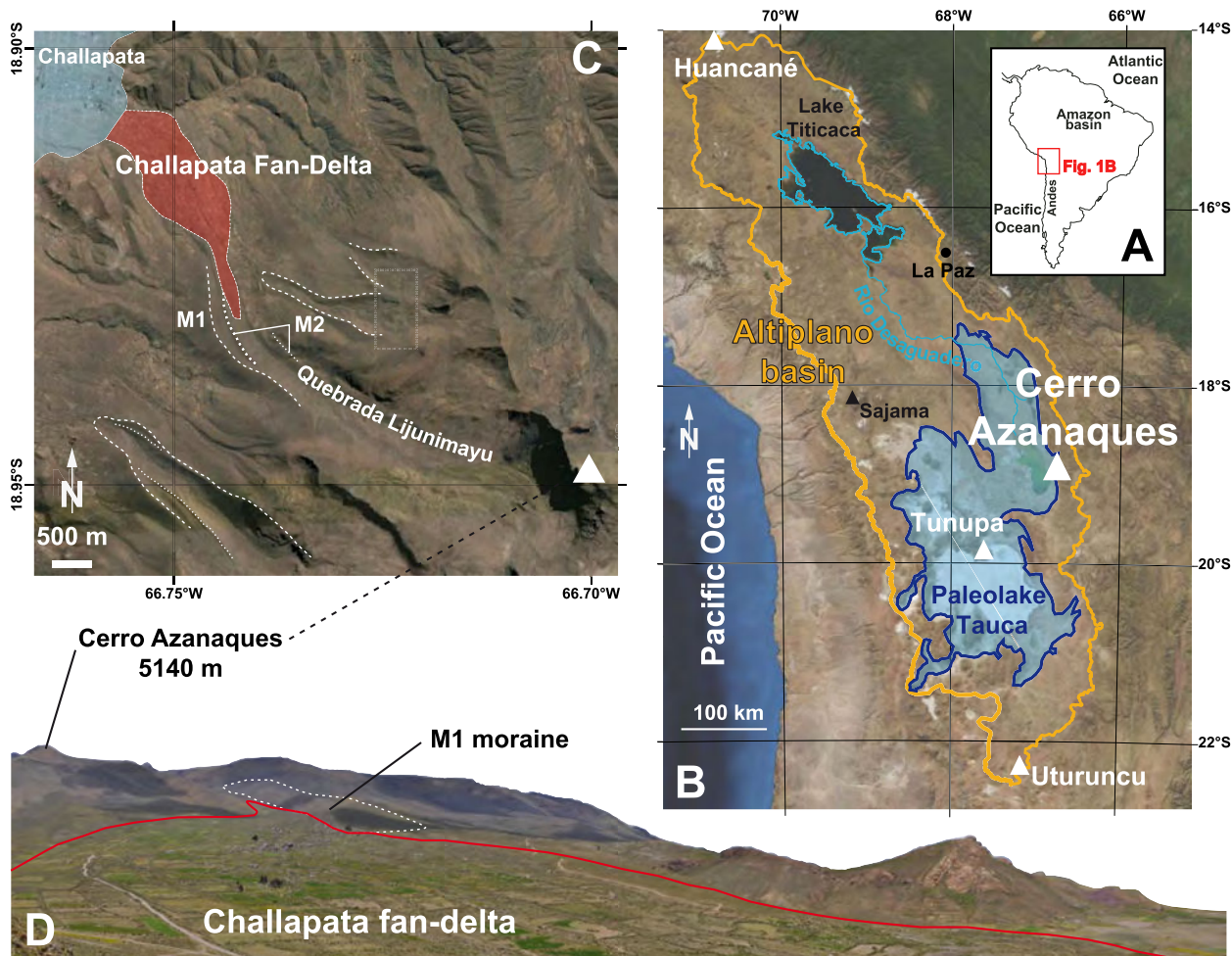


Fig. 2. Location of the Challapata fan-delta. (A) Location of the Altiplano Basin in South America. (B) Cerro Azanaques in the Altiplano Basin, at the edge of Paleolake Tauca. The other sites marked in white are the calibration sites of [Blard et al. \(2013a,b\)](#) (Uturuncu and Tunupa) and [Kelly et al., 2015](#) (Huancané valley). (C) Mapping of the glacial and lacustrine features. In red, the Challapata fan-delta below Cerro Azanaques and in blue, the Lake Tauca extent (3770 m shoreline). The thick dotted lines correspond to the older M1 stage moraines, and the thin dotted lines represent the more recent M2 moraines, which spread into a large frontal lobe where the glacier exited the Quebrada onto a gently sloping piedmont. (D) Panorama of the Challapata fan-delta (in red). (For interpretation of the references to colour in this figure legend, the reader is referred to the web version of this article.)

Five glacial advances on Cerro Azanaques were mapped and described in [Clayton and Clapperton \(1995\)](#), [Clapperton et al. \(1997\)](#) and [Clayton and Clapperton \(1997\)](#). In this study, only two of these are considered. The first advance built up the highest and most massive lateral moraines, which can reach up to 100 m in height (M1 moraines in [Fig. 2](#), thick dashed lines). These moraines and the associated glacial valley channel the flow path of the Rio Lijunimayu, the main stream that drains from the cirque below the Azanaques summit. Buttressed by these M1 moraines, the second advance built up smaller lateral moraines as well as a distal fan-shaped deposit composed of diamicton and containing large blocks up to 5 m in size. This landform evolves into coarse fluvio-glacial deposits further downstream, at the outlet of the Quebrada Lijunimayu (M2 moraines and the Challapata fan-delta on [Fig. 2](#)).

Small modern channels, flowing toward the Poopo Basin, cut the glaciogenic fan that formed during the M2 stage and expose the stratigraphy of the formation in its distal part ([Fig. 3](#)) ([Clapperton et al., 1997](#); [Clayton and Clapperton, 1997](#)). Progressing downstream, these authors reported a continuous transition from

diamict to coarse topset facies, followed by fine foreset and bottomset facies. The continuity and interfingering of the different facies from the glaciogenic material to the prograding Gilbert delta allowed these authors to establish the coeval deposition of these units, which they named the Challapata fan-delta ([Clapperton et al., 1997](#); [Clayton and Clapperton, 1997, 1995](#)).

[Fig. 3](#) summarizes observations made during our successive field campaigns (between 2010 and 2013) across the Challapata fan-delta. We combined our observations with the facies descriptions (Units A to F) proposed in [Clapperton et al. \(1997\)](#) and [Clayton and Clapperton \(1997\)](#). The facies evolution observed along ephemeral streams that incise the fan-delta shows a transition from glacial till to fluvial Gilbert-delta-type facies, interrupted by observation lacunas that mainly result from recent torrential deposits. These recent deposits of torrential debris are often observed in erosive contact with the fan-delta material (Unit A), including till material upstream of Challapata (Photograph 5 in [Fig. 3](#)). Downstream, the coarse glacio-fluvial gravels of the Unit C (Photograph 3) evolve into the smaller pebbles and gravels of the upper part of the Unit E foresets (Photograph 4). Our observations are in good agreement with the first

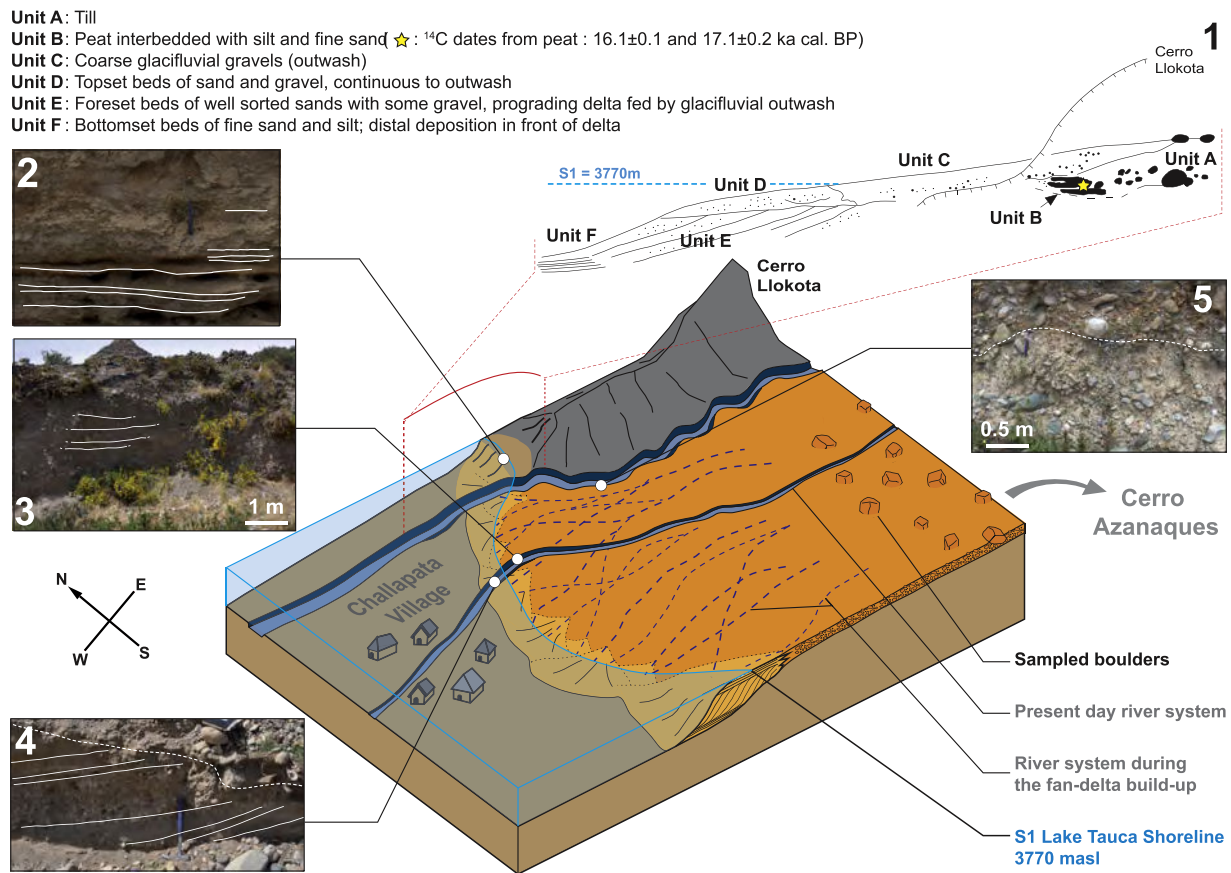


Fig. 3. Structure and facies description of the Challapata fan-delta. 1 – Cross-section of the fan-delta in the northern river, modified from Clayton and Clapperton (1997) and Clapperton et al. (1997). The river-cut shows the downstream transition from glaciogenic to Gilbert-delta facies. 2 – Lacustrine facies that can be found above glaci-fluvial facies of the fan-delta. 3 – Crudely bedded coarse gravels corresponding to Unit C. 4 – Summit of foresets (Unit E). 5 – Till material (Unit A). The upper part of the formation is in erosive contact with torrential deposits (white dashed line).

descriptions of the Challapata fan-delta presented by Clapperton et al. (1997) and Clayton and Clapperton (1997), and support their interpretation that the deposition of the glaciogenic fan material was bounded by a shore deposit environment on its distal part. Since this interfingering of diamict and lake sediments lies at between 3780 and 3750 masl, it clearly marks the overall synchronicity of the fan-delta deposition and the Lake Tauca Highstand.

2.3. Age constraints on the Challapata fan-delta

Additional observations and absolute dating provide the precise timing of the fan build-up during the Lake Tauca Highstand. The highest coarse topsets stand at between 3760 and 3770 masl and this facies corresponds to underwater delta deposits (Lønne and Nemeč, 2004; Machlus et al., 2000; Nemeč et al., 1999). When the topsets of the fan delta were deposited, the level of the lake must therefore have been higher than 3760 masl (Fig. 3). Furthermore, the highest lacustrine facies that we mapped (Photograph 2 in Fig. 3) can be found at 3770 masl, above the fluvial material of the fan delta, on the right bank of the Ljunimayu ephemeral stream, in front of Challapata. Consequently, the 3770-masl level of Lake Tauca provides a minimum age constraint for these fluvial-material proximal units of the fan-delta. The absolute age of the highest level of the Lake Tauca Highstand (shoreline S1; Figs. 3) – 15.5 ka BP – is well constrained by concordant U–Th and ^{14}C data (Blard et al., 2013b).

Clayton and Clapperton (1997) reported two dating studies undertaken at the base and the summit of a peat layer overlain by diamict-type material of the fan-delta (Fig. 3, Element 1, Unit B). The dating yielded ^{14}C ages of 13.30 ± 0.09 and 14.02 ± 0.10 ka BP for the summit and the base of the peat layer, i.e. calibrated ages of 16.1 ± 0.1 ka BP and 17.1 ± 0.2 ka BP, respectively (IntCal13, OxCal 4.2, Ramsey, 2009; Reimer, 2013). These ^{14}C ages provide a maximum age constraint for the age of the upper and most distal sequence of the fan-delta, and in particular for the large meter-size boulders that were deposited by the paleoglacier at the top of the till material of the fan delta (see implications in Section 3.1 and 4.1). Note that the above conclusion is entirely based on Clayton and Clapperton's observations and sampling, as during our field campaigns we were unable to find the peat layer and exact outcrop described by Clapperton et al. (1997) and Clayton and Clapperton (1997). This may have been due to changes to the riverbed and/or to anthropogenic development along both banks over the last fifteen years, which would have affected the outcrops and thus led to a loss of stratigraphic information.

3. Material and methods

3.1. Absolute dating of the Challapata fan-delta

We determined the age of the fan-delta using the minimum and the maximum age limits presented in Section 2.3. Since we

Table 1
Age data used to constrain the age of the Challapata fan-delta.

Age constraint	Object	Sample	Material	Dating method	Reference	Latitude (°S)	Longitude (°W)	Altitude ^a (m)	¹⁴ C age ^b (yr)	Calendar age ^c (ka BP)
Minimum Age ^e	S1 shoreline	Hua-44c ^d	Tufa	¹⁴ C	Sylvestre et al., 1999; Blard et al., 2011	19.55800	68.00600	3770	12686 ± 31	15.2 ± 0.1
		T-7	Tufa	¹⁴ C	Blard et al., 2013b	18.57340	66.87100	3775	13000 ± 60	15.6 ± 0.1
		U-5u	Littoridina	¹⁴ C	Placzek et al., 2006a, 2006b	20.11027	68.22923	3772	12596 ± 60	15.0 ± 0.1
		Chig1-1	Littoridina	¹⁴ C	Placzek et al., 2006a, 2006b	21.03910	68.25253	3760	13494 ± 73	16.3 ± 0.1
		Hua-44	Tufa	U–Th	Blard et al., 2011	19.55800	68.00600	3770	–	15.6 ± 0.3
		T-7	Tufa	U–Th isochrone	Blard et al., 2011	18.57340	66.87100	3775	–	15.5 ± 0.1
Maximum Age ^f	Challapata fan-delta	A-7574	Peat	¹⁴ C	Clayton and Clapperton, 1997; Clapperton et al., 1997	≈ 18.905 ^g	≈ 66.755 ^g	3800 ^g	13300 ± 95	16.1 ± 0.1
		A-7573	Peat	¹⁴ C	Clayton and Clapperton, 1997; Clapperton et al., 1997	≈ 18.905 ^g	≈ 66.755 ^g	3800 ^g	14015 ± 95	17.1 ± 0.2

^a Elevation uncertainty is about 10 m. Only outcrops where two successive shorelines are identified have been selected (see discussion in Blard et al., 2013b).

^b ¹⁴C dates are given as uncalibrated ages.

^c Present refers to the sampling year: 2010. Radiocarbon ages are calibrated using IntCal13. U–Th ages include a correction for detrital ²³⁰Th (Blard et al., 2011; Placzek et al., 2006b). Uncertainties are given at the 1 σ level.

^d Weighted mean of two aliquots.

^e The minimum age constraint is based on sedimentological inference between the Lake Tauca Highstand, corresponding to the S1 shoreline, and the fan build-up (as presented in Section 3.1.).

^f The maximum age constraint is given by the dating of peat material that is stratigraphically older than the fan-delta (as presented in Section 3.1.).

^g Precise values are not available, the given values have been estimated from the detailed logs in Clapperton et al. (1997) and Clayton and Clapperton (1997).

established that the 3770-masl Lake Tauca level is synchronous with or younger than the fan-delta build-up, we used the absolute dating of the so-called ‘S1 shoreline’ reported in Blard et al. (2013b) to determine the minimum age (Section 2.3). Four carbonate samples from S1 have been dated with radiocarbon-dating and two of these have also been dated with the U–Th method (Blard et al., 2013b, 2011; Placzek et al., 2006; Sylvestre et al., 1999). The maximum age of the fan-delta is given by the two ¹⁴C dates presented by Clayton and Clapperton (1997). All of these radiocarbon ages have been re-calibrated with IntCal13 calibration dataset and the OxCal 4.2 program, (Ramsey, 2009; Reimer, 2013).

We then applied the same Bayesian approach as Blard et al.

(2013b) to determine the age of the fan, using the minimum and maximum age dataset. First, two composite probability density functions were calculated for the minimum age and maximum age of the fan-delta. Each function was obtained by normalizing the sum of the probability density functions of each set of sample age (Equation (1)):

$$\text{for } t \in \mathbb{R}, \quad F_{\text{MinAge}}(t) = \frac{1}{n} \sum_{i=1}^n f_{\text{MinAge},i}(t) \quad (1)$$

where F_{MinAge} is the probability density function for the minimum

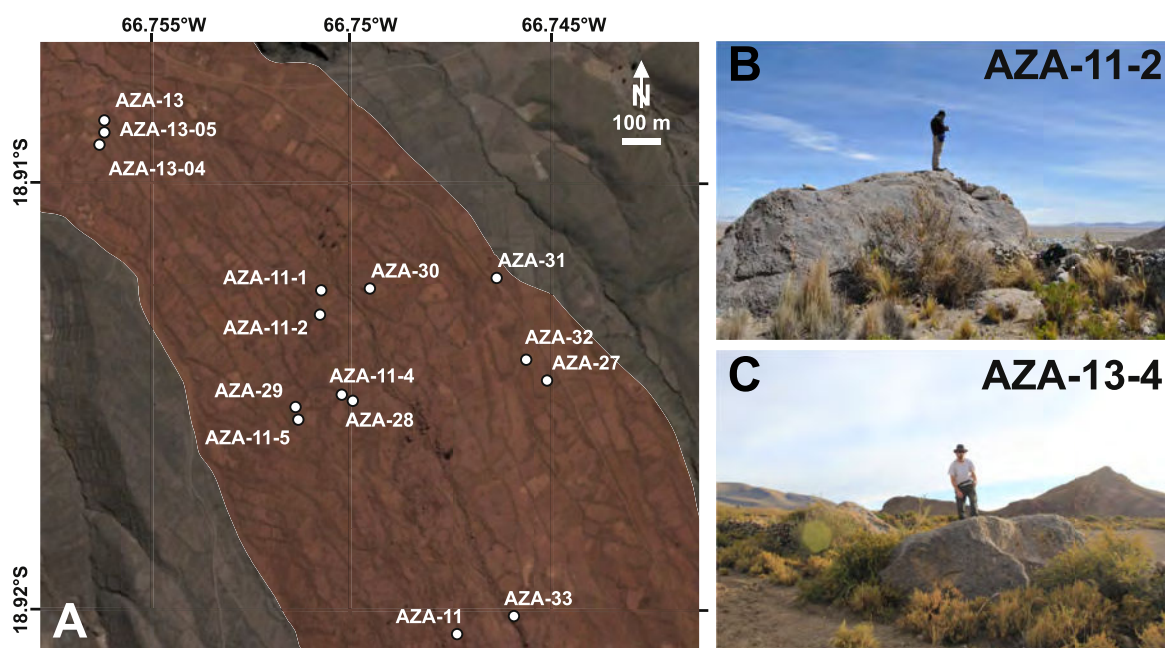


Fig. 4. The boulders sampled on the fan-delta. (A) Location of the boulders on the fan. (B) and (C) Field photographs of boulders AZA-11-2 and AZA-13-4.

age of the fan-delta, $f_{\text{MinAge},i}$ is the probability density function for the age of sample i , and n is the number of available samples.

When two dates were available for the same sample (one radiocarbon and one U–Th age), the normalized sum of the two probability density functions was calculated first.

The same equation was used to establish the F_{MaxAge} function.

To compute the probability density function of the Challapata fan-delta, $F_{\text{fan-delta}}$, we then calculated the product of the integrals of the F_{MinAge} and F_{MaxAge} functions (Equation (2)):

$$F_{\text{fan-delta}}(t) = \int_t^{\infty} F_{\text{MaxAge}}(\tau) d\tau \times \int_0^t F_{\text{MinAge}}(\tau) d\tau \quad (2)$$

In this calculation, $F_{\text{fan-delta}}$ is established based on the assumption that for a value of t taken between the minimum and the maximum age, the closer t is to one of these age-limits, the less probable the build-up of the fan is (see Section 5.2 for discussion about the use of Bayesian formulas).

The mean value associated with $F_{\text{Fan-Delta}}$ is the age of the Challapata fan-delta. The data used for calculating the age of the fan-delta are presented in Table 1.

3.2. Measurement of ¹⁰Be concentrations

Fifteen boulders found embedded in the fan-delta between 3802 and 3987 masl were selected and sampled. We favoured large angular granite boulders (three to five meters high) to avoid boulders that may have been recently brought to the surface by deflation of the diamict matrix (Fig. 4). The sampled surfaces of the boulders had a thickness less than or equal to 4 cm (Table 2). Many boulder tops presented flat or slightly sloping surfaces, with a generally smooth and clean aspect and without any evidence for exfoliation or physical weathering. This suggests that they have experienced only negligible denudation (i.e. less than a few mm) since their deposition.

The samples were then processed at CRPG (Nancy, France) and at CEREGE (Aix-en-Provence, France), for measurement of their in situ produced cosmogenic ¹⁰Be concentration in the quartz mineral fraction. Of the fifteen samples, two were chosen for replicate analyses (AZA-13 and AZA-28). Eleven samples were processed at CRPG and six at CEREGE (Table 2). Samples were first crushed and then sieved to collect the 200–800 μm fraction. The quartz was concentrated from this fraction by magnetic separation and then isolated through selective dissolution in an H₂SiF₆-HCl concentrated solution. Once pure quartz had been obtained, 30% of the mass of each sample was dissolved during three successive HF leaching steps in order to remove any atmospheric ¹⁰Be contamination from the quartz (Brown et al., 1991; Kober et al., 2005). We then added 150–300 mg of ⁹Be carrier (⁹Be concentration: 2020 ppm at CRPG, 3066 ppm at CEREGE) to the samples and dissolved them completely in concentrated HF. To extract the beryllium, samples underwent three alkaline fractionated precipitations alternated with two separations on ionic-exchange columns and a final dehydration at 700 °C.

The resulting BeO was mixed with niobium powder, introduced into a copper cathode, pressed and then finally measured at the French national AMS facility ASTER (CEREGE, Aix-en-Provence, France). During each analytical session, the measured ¹⁰Be/⁹Be ratios were normalized to the ¹⁰Be/⁹Be ratio of the SRM 4325 NIST reference material (¹⁰Be/⁹Be: $(2.79 \pm 0.03) \times 10^{-11}$, Nishiizumi et al., 2007). During the three analytical sessions, the blank values were $(1.1 \pm 0.5) \times 10^{-15}$, $(2.7 \pm 1.7) \times 10^{-15}$ and $(1.5 \pm 0.4) \times 10^{-15}$, respectively. These yielded maximum blank corrections of the sample ¹⁰Be/⁹Be ratios of 1%, 6% and 2%, respectively.

Table 2
¹⁰Be concentrations from 15 boulders of the Challapata fan-delta. The AZA-33 sample was rejected because it was outside the three-sigma limit. Samples AZA-30 and AZA-32 were later rejected because they were two-sigma outliers among the 14 remaining samples.

Sample	Latitude Dec°	Longitude Dec°	Altitude masl	Thickness cm	Preparation Lab	Dissolved Quartz g	Carrier ⁹ Be 10 ¹⁹ at	¹⁰ Be ^a 10 ⁵ at g ⁻¹	Depth correction ^b	Lal-Stone factor ^c	¹⁰ Be Normalized ^d 10 ⁵ at g ⁻¹	Impact of the elevation normalization (%) ^e
AZA-11	-18.92045	-66.74732	3930	1.5	CEREGE	10.77	2.11	5.05 ± 0.27	0.99	8.69	4.80 ± 0.25	6.2
AZA-13	-18.90822	-66.75647	3808	1.0	CRPG	6.23	4.12	5.12 ± 0.21	0.99	8.18	5.14 ± 0.21	0.4
AZA-13 ^R	-18.90822	-66.75647	3808	1.0	CEREGE	10.10	2.07	4.71 ± 0.26	0.99	8.69	4.73 ± 0.26	0.4
AZA-27	-18.91465	-66.74508	3930	2.5	CRPG	3.24	4.18	5.30 ± 0.33	0.98	8.69	5.07 ± 0.31	6.2
AZA-28	-18.91512	-66.74990	3909	2.0	CRPG	4.13	4.16	4.77 ± 0.30	0.98	8.60	4.60 ± 0.29	5.3
AZA-28 ^R	-18.91512	-66.74990	3909	2.0	CEREGE	4.11	2.10	5.47 ± 0.20	0.98	8.60	5.27 ± 0.19	5.3
AZA-29	-18.91557	-66.75127	3899	4.0	CRPG	10.70	4.14	5.52 ± 0.31	0.97	8.56	5.43 ± 0.31	4.8
AZA-31	-18.91223	-66.74630	3908	1.0	CRPG	40.11	4.15	5.24 ± 0.15	0.99	8.60	5.01 ± 0.15	5.2
AZA-11-01	-18.91252	-66.75071	3903	2.0	CRPG	11.29	2.04	4.98 ± 0.15	0.98	8.58	4.81 ± 0.14	5.0
AZA-11-02	-18.91309	-66.75075	3909	2.0	CRPG	13.29	2.01	4.98 ± 0.15	0.98	8.60	4.80 ± 0.14	5.3
AZA-11-04	-18.91500	-66.75015	3935	3.0	CRPG	43.22	2.04	5.01 ± 0.15	0.98	8.71	4.81 ± 0.14	6.5
AZA-11-05	-18.91552	-66.75131	3899	3.0	CRPG	6.80	4.10	5.36 ± 0.22	0.98	8.56	5.23 ± 0.22	4.8
AZA-13-04	-18.90891	-66.75649	3804	2.5	CRPG	5.97	4.18	4.14 ± 0.72	0.98	8.17	4.22 ± 0.73	0.2
AZA-13-05	-18.90844	-66.75645	3802	2.0	CRPG	9.01	4.17	4.76 ± 0.16	0.98	8.16	4.84 ± 0.16	0.1
AZA-30	-18.91248	-66.74950	3895	2.5	CEREGE	4.63	2.10	7.01 ± 0.15	0.98	8.54	6.82 ± 0.15	4.6
AZA-32	-18.91418	-66.74557	3909	2.0	CEREGE	2.99	2.10	6.70 ± 0.35	0.98	8.60	6.45 ± 0.34	5.3
AZA-33	-18.92003	-66.74595	3987	2.0	CEREGE	9.12	2.13	16.57 ± 0.68	0.98	8.94	15.36 ± 0.63	8.8

^R Replicates.

^a One sigma uncertainty.

^b Depth correction calculated with an attenuation length of 160 g cm⁻² and a density of 2.7 g cm⁻³.

^c Calculated for a standard atmosphere.

^d Concentrations corrected for the depth and the topographic shielding (= 1 for all samples) and normalized with the Lal-Stone model at 3800 masl, 18.91°S.

^e Relative difference between the normalized concentration and the depth-and-shielding-corrected concentration.

4. Results

4.1. Age of the Challapata fan-delta

Fig. 5 displays the results of the calculation presented in Section 3.1. Graph (A) shows the F_{MinAge} and F_{MaxAge} probability density functions derived from the S1 shoreline and the ^{14}C peat dating, respectively. The two distributions are multimodal and overlap at around 16 ka. Graph (B) presents $F_{\text{fan-delta}}$, which is the age probability density function of the Challapata fan-delta obtained from Equation (2). The distribution of $F_{\text{fan-delta}}$ is bimodal and the highest mode is centred on 15.83 ka BP. This mode is 1.5% lower than the mean value (and 1.2% lower than the median), indicating that the central tendency parameters are tightly clustered (and are in fact indistinguishable at the one-sigma interval (15.46–16.74 ka BP)). Unlike the mode, the median and mean values account for the whole distribution. We thus retain the mean value of 16.07 ka BP. To handle simple values, the uncertainty is taken as the half of the one-sigma interval. Thus, we establish an age of 16.07 ± 0.64 ka BP (1σ) for the Challapata fan-delta.

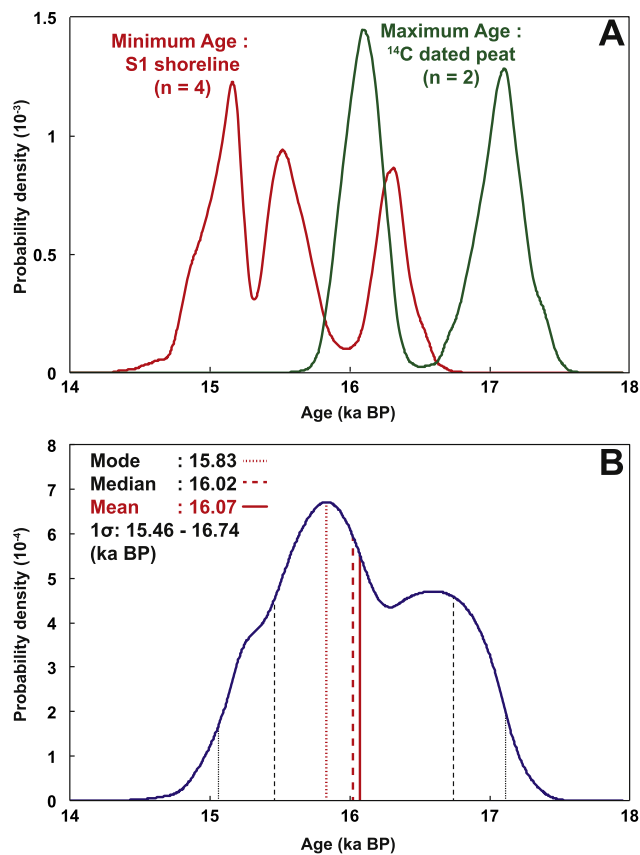


Fig. 5. Age of the Challapata fan-delta. (A) Age constraints for the Challapata fan-delta. Minimum age constraint: the red line shows the F_{MinAge} probability density function derived from the dating of the S1 Taucu shoreline. Maximum age constraint: the green curve shows the F_{MaxAge} probability density function derived from ^{14}C dating on peat. (B) The age probability density function for the Challapata fan-delta derived from the functions presented in (A). Red lines show the central tendency parameters; black lines indicate the one-sigma and two-sigma intervals. See Section 3.1 and Table 1 for methods and data. (For interpretation of the references to colour in this figure legend, the reader is referred to the web version of this article.)

4.2. In situ cosmogenic ^{10}Be concentrations of the Challapata fan-delta boulders

The ^{10}Be results are presented in Table 2. The fifteen samples and replicates were processed in different laboratories: eleven samples at CRPG and six at CEREGE (Table 2). The replicates of samples AZA-13 and AZA-28 can be used to assess the agreement between CRPG and CEREGE. Since their concentrations agree within uncertainty, we can conclude that the procedures used at the two laboratories yield similar results (Table 2). All concentrations were first corrected for sampling thickness and topographic shielding and then normalized to a reference point at 3800 masl, 18.91°S using the Lal-Stone scaling factors with a standard atmosphere (Lal, 1991; Stone, 2000). This normalization allows us to compare the ^{10}Be concentrations of boulders located at different altitudes (from 3802 to 3897 masl) and positions (the maximum distance between two samples is about 1.5 km). This correction has limited impact on the measured ^{10}Be as it represents on average only 4% (1σ) of the measured concentration. Therefore, the choice of the scaling model used for this correction does not affect the accuracy of the final values. AZA-33 is the only sample whose ^{10}Be concentration lies outside the three-sigma interval. It was therefore considered as an outlier and excluded from our analysis.

The probability density functions (PDF) of the 14 remaining samples and their sum are plotted on Fig. 6A. The summed PDF offers a synthetic view of the results and shows a clear mode at around 5×10^5 at g^{-1} with a secondary peak at around 7×10^5 at g^{-1} . This second peak is produced by two samples, AZA-30 and AZA-32, that fall outside the two-sigma interval defined by the main peak at 5×10^5 at g^{-1} . The two samples clearly suggest that the two boulders have been affected by previous exposure and ^{10}Be inheritance. They were therefore removed from the mean calculation. The weighted mean (Fig. 6B) was then calculated by multiplying the individual PDFs (excluding AZA-30, 32 and 33). The mean, median and mode of this distribution all give a value of 4.92×10^5 at g^{-1} . For a one-sigma uncertainty, the ^{10}Be concentration of the Challapata fan-delta is thus $(4.92 \pm 0.05) \times 10^5$ at g^{-1} at 18.91°S and 3800 masl.

4.3. Local and reference ^{10}Be production rates derived from the Challapata fan (19°S , 3800 m)

The ^{10}Be concentration and age of the Challapata fan-delta were then used to calculate a local in situ ^{10}Be production rate P (in at $\text{g}^{-1} \text{yr}^{-1}$):

$$P = \frac{\lambda \cdot C}{1 - e^{-\lambda t}} \quad (3)$$

where C is the cosmogenic in situ ^{10}Be concentration of the fan-delta in at g^{-1} , t is the age of the fan-delta in yr and λ is the decay constant of ^{10}Be in yr^{-1} (Chmeleff et al., 2010; Korschinek et al., 2010; for the whole study). Based on our field observations, we assume zero surface denudation.

Using the fan-delta age established at 16.07 ± 0.64 ka BP, the calculated in situ ^{10}Be production rate is 30.8 ± 1.3 at $\text{g}^{-1} \text{yr}^{-1}$ (1σ) at 18.91°S , 66.76°W and at an altitude of 3800 m. A SLHL time integrated production rate can be derived from this local production rate using various models. We studied several possible scaling schemes and proposed a wide range of Sea Level High Latitude in situ ^{10}Be production rates. These are detailed in Appendix A.1, along with an evaluation of the different scaling models. For conciseness, we report only the production rate obtained using the

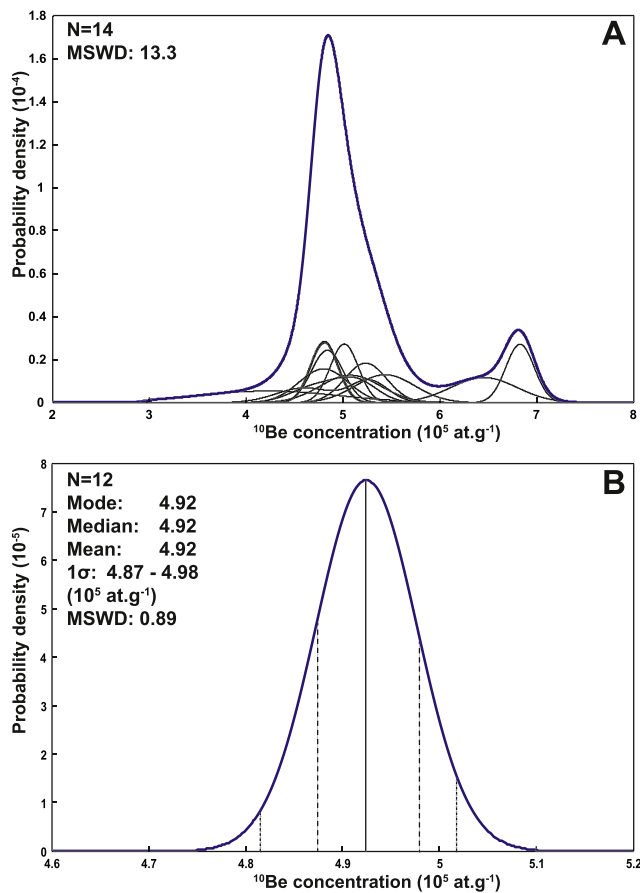


Fig. 6. ^{10}Be results for the Challapata fan-delta. (A) The probability density functions (PDF) of individual samples, except for AZA-33 ($15.36 \times 10^5 \text{ at.g}^{-1}$, rejected), are the thin black curves, and the sum of the different PDF is represented by the thick blue curve. (B) Weighted mean of the measurements after the two-sigma rejection of AZA-30 and AZA-32. The dashed lines indicate the one-sigma and two-sigma intervals. (For interpretation of the references to colour in this figure legend, the reader is referred to the web version of this article.)

“Lal modified” scaling scheme (Balco et al., 2008), a standard atmosphere and the Muscheler et al. (2005) geomagnetic reconstruction. This yielded a SLHL in situ ^{10}Be production rate of $3.76 \pm 0.15 \text{ at.g}^{-1} \text{ yr}^{-1}$ (1σ uncertainty).

5. Discussion

5.1. Accuracy of the Azanaques ^{10}Be production rate

The accuracy of the Azanaques production rate relies both on the determination of the ^{10}Be concentration of the fan-delta and on the fan-delta dating.

The minimum age used to constrain the age of the Challapata fan-delta was not obtained from direct dating of the fan itself but was instead derived from stratigraphic correlation with the highest level reached by the Lake Tauca. Because the Gilbert delta facies belongs to the distal part of the Challapata fan-delta, a hypothesis of progressive build-up of the fan from its proximal to distal part over a wide time span must be considered. However, the distribution of $F_{\text{fan-delta}}$ (centred on 16 ka BP (Fig. 5) with a low uncertainty of 4%) invalidates such a hypothesis.

The ^{10}Be concentrations of the fan-delta boulders lie within a narrow range within analytical uncertainty (Fig. 6). The boulders

exhibited no traces of denudation and the distribution of the data confirms this interpretation. The statistical distribution also clearly shows that three of the boulders were affected by pre-exposure (AZA-30, AZA-32 and AZA-33). These samples were therefore excluded in our calculation, in order to avoid overestimating the actual ^{10}Be concentration. The MSWD values validate this approach. Before rejection of AZA-30 and AZA-32 ($N = 14$), the MSWD is 13.3. This indicates an over-dispersion that cannot be explained by the analytical uncertainties alone (the MSWD is significantly greater than 1). After their rejections, the MSWD is 0.89, indicating that the ^{10}Be concentrations of the boulders are in good agreement within analytical uncertainties ($\text{MSWD} \approx 1$) (Fig. 6).

We also tested the possibility that boulders deposition was polygenic and occurred over a wide timespan. For this, we plotted the ^{10}Be concentration of the boulders versus their axial distance on the fan-delta (Fig. 7A) and versus the transversal distance on the fan (Fig. 7B).

Fig. 7 unequivocally shows that the ^{10}Be concentrations are not controlled by the position of the boulders on the fan. Therefore, the observed data scatter cannot result from a slow progressive build-up of the fan-delta from its proximal to distal part, or from its eastern to western part. The ^{10}Be concentrations of the boulders suggest that build-up of the fan occurred over a timespan that was short enough to be considered as instantaneous.

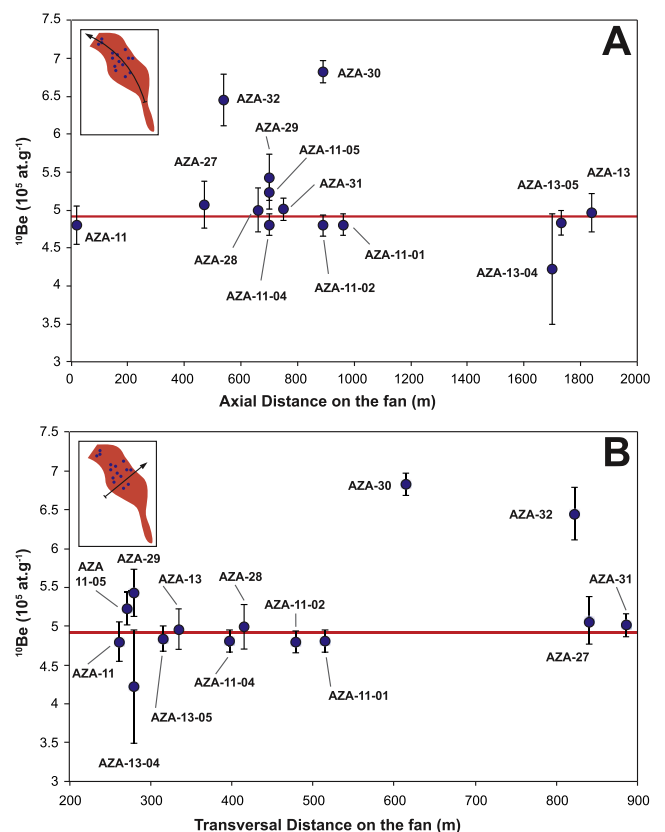


Fig. 7. Distribution of ^{10}Be normalized concentrations across the fan-delta. AZA-33 has been excluded. The red line indicates the mean value used to calculate the production rate. (A) ^{10}Be concentrations of the boulders versus the axial distance on the fan-delta. (B) ^{10}Be concentrations of the boulders versus the transversal distance on the fan-delta. (For interpretation of the references to colour in this figure legend, the reader is referred to the web version of this article.)

Table 3
Updated cosmogenic ^3He and ^{10}Be data from Uturuncu (Blard et al., 2014, 2013a).

Sample	Altitude (m)	Latitude ($^{\circ}\text{S}$)	Longitude ($^{\circ}\text{W}$)	Sample thickness (cm)	$^3\text{He}^{\text{a}}$ (10^7 at g^{-1})	^{10}Be (10^6 at g^{-1})	^3He age $^{\text{b}}$ (ka)	$^3\text{He}/^{10}\text{Be}$ production ratio $^{\text{c}}$
UTU – 6B	4846	22.31302	67.19997	3	5.72 ± 0.15	1.82 ± 0.09	29 ± 1	31.1 ± 1.8
UTU – 6D	4840	22.31307	67.20042	4	5.77 ± 0.37	1.80 ± 0.05	29 ± 1	31.8 ± 2.3
UTU – 7C	4830	22.31547	67.19847	4	11.10 ± 0.18	3.69 ± 0.36	51 ± 1	29.7 ± 2.9
UTU – 8A	4820	22.31775	67.20207	4	11.85 ± 0.12	3.45 ± 0.11	54 ± 2	33.9 ± 1.1
UTU – 8D	4815	22.31682	67.20008	4	6.97 ± 0.10	2.17 ± 0.06	35 ± 1	31.9 ± 1.1
UTU – 9A	4813	22.31983	67.20222	4	7.15 ± 0.09	1.96 ± 0.08	37 ± 1	36.1 ± 1.5
							Mean	32.4 ± 0.9

This table is an updated version of Table 1 published in (Blard et al., 2013a).

All samples are dacite moraine boulders (Blard et al., 2013a, 2014). Cosmogenic ^3He was measured in pyroxenes while ^{10}Be was measured in quartz (Blard et al., 2013a). Uncertainties are given at the 1σ level. These include external and internal reproducibilities, as well as the error arising from the blank correction.

^a ^3He exposure ages were calculated using the cosmogenic ^3He production rate calibrated on the Altiplano (Blard et al., 2013a) and the time-dependent scaling of (Lal, 1991; Stone, 2000) (see Blard et al., 2014 for details).

^b Blank $^{10}\text{Be}/^9\text{Be}$ ratios of the Uturuncu session were remeasured, and yielded a new value of $(0.4 \pm 1) \times 10^{-15}$, which increased the ^{10}Be concentrations initially published in (Blard et al., 2013a) by less than 2%.

^c The $^3\text{He}/^{10}\text{Be}$ production ratio was computed after correcting the measured $^3\text{He}/^{10}\text{Be}$ ratio for the time-integrated decay of ^{10}Be , using an half-life of 1.39×10^6 yr (Chmeleff et al., 2010; Korschinek et al., 2010).

5.2. Homogenization of the different High Tropical Andes calibration datasets

With the existing regional cosmogenic ^{10}Be calibration studies of Blard et al. (2013a) and Kelly et al. (2015) (locations on Fig. 2) and this new Azanaques calibration site, three calibration datasets for in situ ^{10}Be production rates are now available in the High Tropical Andes. We aim now to homogenize these data in order to obtain a regional calibration dataset for in situ ^{10}Be production rates for the High Tropical Andes. Accordingly, the data of Blard et al. (2013a) and Kelly et al. (2015) have been recalculated as follows.

In order to use the most up-to-date data, the ^{14}C ages used to determine the Blard et al. (2013a) and Kelly et al. (2015) production rates have all been recalibrated with IntCal13 (OxCal 4.2, Ramsey, 2009; Reimer, 2013). The statistical method for age estimation presented in Section 3.1 (Equation (2)) was then applied to both sites. A detailed discussion of the Bayesian statistical calculation is presented in Appendix A.2.

Blard et al. (2013a) calculated an in situ ^{10}Be production rate by multiplying the ^3He production rate established from the Tunupa volcano with the $^3\text{He}/^{10}\text{Be}$ production ratio measured in the moraines of the Uturuncu volcano at 4900 m, 22°S (Blard et al., 2013a). Table 3 presents an updated version of these data.

For recalculation of the Kelly et al. (2015) production rate, we retained the 5×10^{-4} cm/yr denudation rate correction, without introducing any uncertainty associated with this correction. This

correction shifts the computed production rates upward by 5%.

As we did for the Azanaques production rate and for the ^3He data of Blard et al. (2013a), we recalculated the ^{10}Be concentrations of Kelly et al. (2015) using weighted means.

These recalculations all have limited impact on the local production rate values however. The published value of 43.3 ± 2.7 at $\text{g}^{-1} \text{yr}^{-1}$ for the Kelly et al. (2015) production rate increases to 45.2 ± 2.1 at $\text{g}^{-1} \text{yr}^{-1}$ (4% increase) and the Blard et al. (2013a) production rate increases from 30.0 ± 1.4 to 30.8 ± 1.4 at $\text{g}^{-1} \text{yr}^{-1}$ (3% increase). The complete homogenized calibration data are presented in Table 4.

Various SLHL values for these three sites, along with their weighted mean values, are proposed in Appendix A.1. The weighted mean of the three production rates can be considered as a regional SLHL value. Using the “Lal modified” (Balco et al., 2008) scaling scheme with a standard atmosphere and the Muscheler et al. (2005) geomagnetic reconstruction, we obtain a mean SLHL in situ ^{10}Be production rate of 3.74 ± 0.09 at $\text{g}^{-1} \text{yr}^{-1}$ for the region (dispersion of the three SLHL production rates 0.9%). The three production rates derived with this scaling scheme are presented in Fig. 8.

5.3. Consistency of the reference calibration dataset

In order to investigate the internal consistency of the reference calibration dataset presented in Table 4, we tested its ability to produce an unequivocal Sea Level High Latitude production rate.

Table 4
Reference calibration dataset for in situ ^{10}Be production rate in the High Tropical Andes.

Calibration data	This study	Blard et al., 2013a and ^b	Kelly et al., 2015
Site	Cerro Azanaques (Bolivia)	Cerro Tunupa/Uturuncu (Bolivia)	Huancané Valley (Peru)
Altitude ^d	(masl)	3800	4857
Latitude ^d	(dec $^{\circ}$)	-18.910	-13.947
Longitude ^d	(dec $^{\circ}$)	-66.756	-70.892
Age ^e	(ka)	16.07 ± 0.64	12.26 ± 0.56
Concentration ^f	(at g^{-1})	$(4.92 \pm 0.05) \times 10^5$	$(5.24 \pm 0.04) \times 10^5$
Erosion	(cm a^{-1})	0	5×10^{-4}
Local PR	at $\text{g}^{-1} \text{yr}^{-1}$	30.8 ± 1.3	45.2 ± 2.1

^a ^{10}Be production rate derived by dividing the Cerro Tunupa ^3He production rate (Blard et al., 2013a) by the Uturuncu $^3\text{He}/^{10}\text{Be}$ production ratio of 32.40 ± 0.90 (Blard et al., 2013a).

^b Cerro Tunupa data for ^3He calibration.

^c Uturuncu P_{10} .

^d Reference point used to normalize cosmogenic nuclide concentrations.

^e Computed with the bayesian approach described in Section 3.1.

^f Weighted mean of the normalized concentrations.

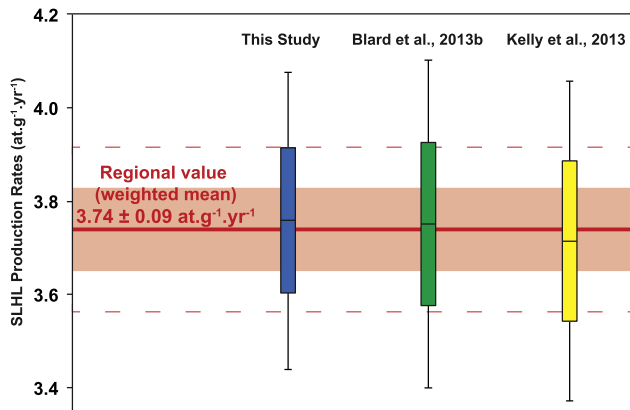


Fig. 8. The homogenized SLHL production rates and a proposed regional production rate. The scaling has been conducted using the “Lal modified” model (Balco et al., 2008), for a standard atmosphere and using the Muscheler et al. (2005) geomagnetic reconstruction. For the local points, the coloured boxes indicate the one-sigma interval and the black bars indicate the two-sigma interval. For the regional value, the light red area represents the one-sigma interval and the red dotted lines mark the two-sigma interval. (For interpretation of the references to colour in this figure legend, the reader is referred to the web version of this article.)

This approach involves the use of scaling schemes, and thus the efficiency of one scaling scheme relative to another will also contribute to the consistency of the data in SLHL conditions. To address this issue, several scaling schemes were used to conduct a test, the results of which are presented in Table 5. The results also show how the different scaling schemes can reconcile the three calibration studies of our reference dataset.

We adjusted a single SLHL production rate to the three datasets using a weighted least-squares method (Table 5). To do this, we compared the ages determined using this fitted SLHL production rate with the real ages of the calibration objects. We then calculated the goodness-of-fit for each scaling scheme. The lower the goodness-of-fit value, the better the fit of the SLHL production rate to the three sites. If this statistical parameter is less than 1, then the

data show good consistency (Strutz, 2011). The lowest dispersion is produced using the “Lal modified” scaling model, particularly when combined with the ERA-40 (Uppala et al., 2005) atmosphere model (Table 5). Regarding geomagnetic models, the GLOPIS-75 and the Muscheler et al. (2005) databases yield the best results.

These results are consistent with those of another test that we conducted on the scaling parameters. The last column of Table A.1.3 (Appendix 1) shows the standard deviations of the three SLHL production rates calculated for each of the three local production rates. The key result is that, for any scaling scheme, the three SLHL production rates are in good agreement, with a dispersion of less than 2% for most of them. This result is coherent with the fact that for each scaling scheme, the three production rates are always in agreement at one sigma.

To compare the in situ ¹⁰Be production rates derived from the High Tropical Andes dataset with production rates calibrated in other regions, we chose the regional mean production rate of $3.74 \pm 0.09 \text{ at.g}^{-1} \text{ yr}^{-1}$, scaled using the “Lal modified” scaling model with a standard atmosphere and the geomagnetic reconstruction of Muscheler et al. (2005). This model yielded a good agreement between the three sites (Table 5). In addition, the Muscheler et al. (2005) geomagnetic model presents many advantages and provides values that are intermediate between those derived using other scaling schemes (Appendix A.1). Finally, standard atmosphere is the most widely used atmosphere model in calibration studies (see the review that follows) and thus allows the widest comparison of published SLHL production rates.

This High Tropical Andes ¹⁰Be production rate of $3.74 \pm 0.09 \text{ at.g}^{-1} \text{ yr}^{-1}$ is statistically consistent with recently established regional ¹⁰Be production rates from intermediate to high latitude sites, as summarized in Young et al. (2013). These production rates were established in north-eastern North America ($3.85 \pm 0.19 \text{ at.g}^{-1} \text{ yr}^{-1}$, at 50–400 m a.s.l., >42°N, Balco et al., 2009), New Zealand ($3.79 \pm 0.10 \text{ at.g}^{-1} \text{ yr}^{-1}$, at 1000 m a.s.l., 44°S, Putnam et al., 2010), Patagonia ($3.70 \pm 0.11 \text{ at.g}^{-1} \text{ yr}^{-1}$, at 300 m, 50°S, Kaplan et al., 2011), Norway (3.63 ± 0.15 and $4.04 \pm 0.20 \text{ at.g}^{-1} \text{ yr}^{-1}$, at 100 m a.s.l., 69°N, Fenton et al. (2011) recalculated in Young et al. (2013)), and in the Arctic

Table 5

Internal consistency of the reference calibration dataset and efficiency of the scaling schemes to reconcile the data.

Scaling model	Atmosphere model ^c	Geomagnetic reconstruction ^d	Fitting a SLHL P ₁₀ to the 3 datasets ^e		Fitted SLHL P ₁₀ ⁱ at g ⁻¹ yr ⁻¹
			goodness of fit ^h	Mean	
“Lal modified” ^a	Standard atmosphere	Muscheler et al., 2005	3.0	4.2	3.74
		GLOPIS-75 ^e	0.1		
		LSD framework ^f	9.6		
ERA-40 atmosphere	ERA-40 atmosphere	Muscheler et al., 2005	0.9	2.1	4.08
		GLOPIS-75	1.0		
		LSD framework	4.3		
LSD ^b	Standard atmosphere	Muscheler et al., 2005	10.8	34.5	3.94
		GLOPIS-75	5.9		
		LSD framework	86.8		
ERA-40 atmosphere	ERA-40 atmosphere	Muscheler et al., 2005	5.9	26.1	4.32
		GLOPIS-75	2.4		
		LSD framework	69.9		

^a Being the Lal-Stone model (Lal, 1991; Stone, 2000) integrating a geomagnetic time correction through the formula taken from Nishiizumi et al. (1989).

^b From Lifton et al. (2014).

^c Both model implementations were taken from the LSD matlab code presented in Lifton et al. (2014).

^d All the VDM values used are normalized to the actual value of $7.746 \times 10^{22} \text{ A m}^{-2}$ from the 2010 DGRFs (Finlay et al., 2010) as in Lifton et al. (2014).

^e From Laj et al. (2004).

^f For the “Lal modified” model, the CALS7k.2 (Korte et Constable, 2005) and the CALS3k.3 (Korte et al., 2009) data used in the LSD framework is the M/M₀ VDM ratio.

^g A least squares method was used to determine a SLHL P₁₀ that best fitted the three calibration datasets for each scaling scheme, a small Goodness of fit indicates a better fit.

^h χ^2 residual divided by the degree of freedom.

ⁱ Mean value of the three production rates.

(3.96 ± 0.15 at $g^{-1} yr^{-1}$, 100–300 m a.s.l., 70°S, Young et al., 2013). The values correspond to SLHL production rates scaled with the “Lal modified” scheme, but the SINT-800 (Guyodo and Valet, 1999) field intensity reconstruction was used in these studies rather than that of Muscheler et al. (2005). However, given that the correction for temporal variations in the geomagnetic field has limited impact on high latitude low altitude production rates (Dunai, 2001; Balco et al., 2008), comparison with the proposed reference value remains relevant.

We recommend using this reference calibration dataset for CRE dating in the High Tropical Andes over periods ranging from the LGM to the Holocene. Concerning the different scaling schemes, the user should choose the one he or she considers most relevant. The narrow uncertainty associated with the weighted mean of the three SLHL production rates for any scaling scheme (2.4% at 1σ) now offers the opportunity to establish precise and accurate glacial chronologies. By inducing a 1σ uncertainty of less than 400 years for an age span of 15 ka BP, this new synthetic rate may offer high enough precision to establish synchronicity between the build up of moraine and global climatic events, and, for example, to distinguish Antarctic Cold Reversal from Younger Dryas moraines (Jomelli et al., 2014).

However, the geological scatter induced by denudation and/or pre-exposure may remain a significant source of inaccuracy and uncertainty if these are not considered by a cautious sampling and by analyzing a statistically large enough sample population (at least 5 different boulders from each moraine).

6. Conclusion

We reported a new production rate for ^{10}Be in quartz in the High Tropical Andes (18.91°S – 66.76°W – 3800m). The new calibration site, the Challapata fan-delta, is located on the Cerro Azanaques massif. The site is a glaciogenic fan that evolves into a Gilbert type delta in its distal part, at the edge of the Paleolake Taucá. The occurrence of delta type facies at the highest altitudes reached by Lake Taucá has enabled us to determine the age of the fan-delta (16.07 ± 0.64 ka, 1σ) using robust ^{14}C and U–Th ages from lacustrine shorelines (Blard et al., 2011; Placzek et al., 2006; Sylvestre et al., 1999) and ^{14}C dating of peat (Clapperton et al., 1997; Clayton and Clapperton, 1997). Measurement of the ^{10}Be concentrations in 15 boulders on the fan has allowed us to determine a local Azanaques in situ ^{10}Be production rate of 30.8 ± 1.3 at $g^{-1} yr^{-1}$ (3800 masl, 18.9°S). Once scaled to Sea Level High Latitude, this corresponds to a SLHL production rate of 3.76 ± 0.15 at $g^{-1} yr^{-1}$ for a standard atmosphere, using the “Lal modified” model (Balco et al., 2008; Lal, 1991; Stone, 2000) in conjunction with the Muscheler et al. (2005) geomagnetic field intensity reconstruction. The local Azanaques production rate was then compared to the production rates of Blard et al. (2013b) and Kelly et al. (2015), having first updated these two earlier datasets in order to homogenize the methodologies of the different studies and produce a coherent dataset. The homogenized dataset is proposed as a reference to calculate a regional ^{10}Be SLHL production rate for the High Tropical Andes. From this dataset, we derive a synthetic value of 3.74 ± 0.09 at $g^{-1} yr^{-1}$ for a standard atmosphere, using the “Lal modified” model with the Muscheler et al. (2005) geomagnetic field intensity reconstruction. We recommend use of this reference calibration dataset for determining CRE ages in the High Tropical Andes from the LGM to the Holocene period.

Acknowledgement

This work was funded by the INSU EVE-LEFE program and the ANR Jeunes Chercheurs GALAC project “ANR-11-JS56-011-01”. We

greatly appreciated the logistical support of the IRD of La Paz (Bolivia) during our field trips conducted between 2010 and 2013. R. Hemelsdaël, L. Ménabréaz and N. Lifton are thanked for useful discussions about Gilbert delta formation, paleomagnetic reconstructions and the LSD model, respectively. R. Joussemet and the STEVAL crew (GeoRessources, Nancy) are acknowledged for their technical support for sample crushing and mineral separation. The ASTER French national AMS facility (CEREGE, Aix-en-Provence) is supported by the INSU/CNRS, the ANR through the “Equipements d’Excellence” program, IRD and CEA. Careful readings by Alice Williams greatly improved the manuscript. We are grateful to an anonymous reviewer for constructive comments and suggestions. This is CRPG contribution 2391.

Appendices

A.1. Discussion of the different scaling schemes

The first scaling models relied on nuclear emulsion and cloud chambers (Lal, 1991; Stone, 2000) for measurement of secondary cosmic-ray fluxes whereas the more recent models rely on data obtained from neutron monitors (Desilets and Zreda, 2003; Desilets et al., 2006; Dunai, 2001; Lifton et al., 2005). For a review, see Lifton et al., (2014).

The Lal-Stone scaling scheme provides a better description of the current atmospheric attenuation of neutrons at low geomagnetic latitude than any of the neutron-monitor-based models (Lifton et al., 2014). Furthermore, this scheme has also been more widely used in recent calibration studies (e.g. Blard et al., 2013a, 2013b; Fenton et al., 2011; Kaplan et al., 2011; Young et al., 2013). We therefore favoured this model for computing the SLHL production rates. Since past variations in geomagnetic field intensity have a non-negligible impact on cosmogenic nuclide production rates at low latitudes (Balco et al., 2008; Gosse and Phillips, 2001; Lal, 1991), we used the so called “Lal-modified” (Balco et al., 2008) version of the Lal-Stone scaling scheme. This model includes the Nishiizumi et al. (1989) corrections for temporal variations in the geomagnetic field. In addition, we also tested different geomagnetic field intensity reconstructions in the present study.

The Lifton-Sato-Dunai (LSD) model (Lifton et al., 2014) aimed to reconcile the two types of scaling model by deriving scaling factors from integrals of neutron and proton fluxes, calculated using the PHITS-based Analytical Radiation Model in the Atmosphere (PARMA) model, in conjunction with locally consistent neutron and proton excitation functions (Lifton et al., 2014; Sato et al., 2008). The LSD model is consistent with observed cosmogenic neutron data for high and low geomagnetic latitudes. It also includes corrections for temporal variations in geomagnetic and solar intensity. As the LSD model brought about significant improvements, we also used this model to convert our calibrated production rate to SLHL conditions.

In order to keep our study concise, we chose to restrict our comparison to these two scaling models (the Lal-Stone time-dependent model and the LSD model), since these are, respectively, the most widely used and the most up-to-date models available.

In comparing the Lal-Stone and LSD scaling schemes, we also assessed the effect of using different atmosphere models and paleomagnetic field intensity reconstructions. Two atmosphere models were examined. First, a regional atmosphere model was derived from the ERA-40 dataset produced by the European Centre for Medium-Range Weather Forecasts. This model is based on a re-analysis of meteorological data over 45 years (Uppala et al., 2005). The model was implemented using the Matlab © function published by Lifton et al. (2014). The second model we considered was the U.S. standard atmosphere model from (National Oceanic and Atmospheric Administration, 1976) as proposed by Stone (2000)

(using the following parameters: sea level pressure = 1013.25 hPa; sea level temperature = 288.15 K; adiabatic lapse rate = 0.0065 K m⁻¹). To address the potential impact of the geomagnetic time correction, three different paleomagnetic field intensity datasets were considered. In the first dataset, that of [Muscheler et al. \(2005\)](#), the virtual axial dipole moment (VDM) is reconstructed from atmospheric ¹⁰Be and ³⁶Cl concentrations trapped in the Greenland ice. This VDM reconstruction has a high temporal resolution (less than 500 years) and its absolute dating is robust. Moreover, ice-based VDM reconstructions are more sensitive than sediment-based VDM reconstructions, as the characteristic closing time to record the Earth magnetic field and its intensity in sediment may be long (sometimes over 1000 yrs) and can thus smooth out the original signal and induce a phase shift. The atmospheric ¹⁰Be proxy has in particular proven its ability to correctly capture the amplitude of geomagnetic dipole events such as the Laschamp low (see [Ménabréaz et al. \(2012\)](#) for discussion).

The second geomagnetic framework examined here was derived from the LSD model, as proposed in its original form in [Lifton et al. \(2014\)](#). This composite database combines the geomagnetic reconstructions of the CALS7k.2 and CALS3k.3 model for the 0–7 ka

resolution VDM reconstructions (GLOPIS-75 and [Muscheler et al. \(2005\)](#)) and one composite dataset ([Lifton et al., 2014](#)).

It should be noted that the “Lal modified” model and the LSD model each use different inputs for the 0–7 ka period. While the “Lal modified” model always uses the M/M₀ ratio (the virtual axial dipole moment normalized to the actual value), the LSD model only uses it beyond 7 ka BP. Between 0 and 7 ka BP, the LSD model directly uses spatialized cut-off rigidity values from CALS7k.2 and CALS3k.3. Therefore, when we used the LSD model with the GLOPIS-75 or the [Muscheler et al. \(2005\)](#) reconstruction, we derived the cut-off rigidity from the M/M₀ ratio over the whole time span. For this, we used the relationship initially proposed by [Lifton et al. \(2014\)](#) beyond 7 ka BP.

Conversely, when using the “Lal modified” model with the LSD geomagnetic framework, a global M/M₀ value is derived from CALS7k.2 and CALS3k.3 over the 0–7 ka BP period, leading to a loss of the quadrupolar local influences on the geomagnetic field. Since the effect of these differences is small on ages older than 15 ka BP, we consider the comparison to still be relevant to our discussion.

The different considerations regarding the geomagnetic data used in the scaling models are summarized in [Table A.2.1](#).

Table A.1.1
Geomagnetic reconstructions and their input in the scaling models.

Geomagnetic reconstruction	Reference	“Lal modified” model ^a Input: M/M ₀ ^b	LSD model Input: R _c ^c
Muscheler et al., 2005	Muscheler et al. (2005)	M/M ₀ from Muscheler et al. (2005)	R _c derived from the Muscheler et al. (2005) M/M ₀ with the relation of Lifton et al. (2014) ^d
LSD framework	Lifton et al. (2014)	0–7 ka period: Global M/M ₀ derived from CALS7k.2 and CALS3k.3 After 7 ka: M/M ₀ ratios from GLOPIS-75	0–7 ka period: R _c from CALS7k.2 and CALS3k.3 7–18 ka period: R _c derived from the GLOPIS-75 M/M ₀ with the relation of Lifton et al. (2014)
GLOPIS-75	Laj et al. (2004)	M/M ₀ from GLOPIS-75	R _c derived from the GLOPIS-75 M/M ₀ with the relation of Lifton et al. (2014)

^a Being the Lal-Stone model ([Lal, 1991; Stone, 2000](#)) integrating a geomagnetic time correction through the formula taken from [Nishiizumi et al., 1989](#).

^b The virtual axial dipole moment normalized to the actual value of 7.746×10^{22} A m⁻² ([Finlay et al., 2010](#)).

^c Effective vertical cutoff rigidity.

^d Equation (2) in [Lifton et al. \(2014\)](#).

period ([Korte et al., 2009, 2005](#)), and the GLOPIS-75 reconstruction for 7–18 ka period ([Laj et al., 2004](#)).

Finally, the third magnetic database we consider is the GLOPIS-75 ([Laj et al., 2004](#)) reconstruction only database.

The VDM test thus allows us to compare the effects of two high-

Following [Lifton et al. \(2014\)](#), the M₀ value used in the tested models is 7.746×10^{22} A m⁻², taken from the 2010 DGRF ([Finlay et al., 2010](#)).

The different SLHL Azanaques production rates calculated using the different databases and scaling schemes are presented in [Table A.1.2](#).

Table A.1.2
Azanaques SLHL (Sea Level High Latitude) production rates.

Type of production rate	Atmosphere model ^c	Geomagnetic data ^d	Scaling factor [–]	Production rate at g ⁻¹ yr ⁻¹
Local Production Rate ($4.92 \pm 0.05 \times 10^5$ at g ⁻¹ – 16.07 ± 0.64 ka BP – 18.91°S – 66.76°W – 3800 masl)	–	–	–	30.8 ± 1.3
SLHL Production rate: “Lal modified” model ^a	Standard atmosphere	Muscheler et al., 2005	8.189	3.76 ± 0.15
		GLOPIS-75 ^e	7.847	3.92 ± 0.16
	ERA-40 atmosphere	LSD framework ^f	8.356	3.68 ± 0.15
		Muscheler et al., 2005	7.533	4.08 ± 0.17
		GLOPIS-75	7.224	4.26 ± 0.17
		LSD framework	7.684	4.00 ± 0.16
Standard atmosphere	Muscheler et al., 2005	7.610	4.04 ± 0.17	
	GLOPIS-75	7.281	4.22 ± 0.17	
	LSD framework	8.247	3.73 ± 0.15	
	Muscheler et al., 2005	6.961	4.42 ± 0.18	
SLHL Production rate: LSD model ^b	ERA-40 atmosphere	GLOPIS-75	6.665	4.61 ± 0.19
		LSD framework	7.538	4.08 ± 0.17

^a Being the Lal-Stone model ([Lal, 1991; Stone, 2000](#)) integrating a geomagnetic time correction through the formula taken from [Nishiizumi et al. \(1989\)](#).

^b From [Lifton et al. \(2014\)](#).

^c Both model implementations were taken from the LSD matlab code presented in [Lifton et al. \(2014\)](#).

^d All the VDM values used are normalized to the actual value of 7.746×10^{22} A m⁻² from the 2010 DGRFs ([Finlay et al., 2010](#)) as in [Lifton et al. \(2014\)](#).

^e From [Laj et al. \(2004\)](#).

^f For the “Lal modified” model, the CALS7k.2 ([Korte et Constable, 2005](#)) and the CALS3k.3 ([Korte et al., 2009](#)) data used in the LSD framework is the M/M₀ VDM ratio.

Depending on the scaling scheme used, the SLHL production rates range from 3.68 to 4.61 at $g^{-1} yr^{-1}$ (Table 3). The LSD scaling scheme yields production rates whose mean value of 4.19 ± 0.17 at $g^{-1} yr^{-1}$ is 6% higher than that obtained using the “Lal modified” model (3.95 ± 0.16 at $g^{-1} yr^{-1}$). For the atmosphere models, the ERA-40 local atmosphere model also tends to yield production rates (mean of 4.24 ± 0.17 at $g^{-1} yr^{-1}$) that are higher than those given by the standard atmosphere (mean of 3.89 ± 0.16 at $g^{-1} yr^{-1}$). Regarding the geomagnetic reconstructions, the GLOPIS-75 dataset yields a mean production rate (4.25 ± 0.17 at $g^{-1} yr^{-1}$) that is significantly higher than that obtained using the LSD framework (3.87 ± 0.16 at $g^{-1} yr^{-1}$). The Muscheler et al. (2005) reconstruction yields intermediate values,

SLHL production rate calculation. For better consistency and simplicity, a single VDM proxy is therefore preferred, when possible.

The local production rates of Blard et al. (2013b) and Kelly et al. (2015) have been scaled to SLHL following the same procedures as those used for scaling the Azanaques production rate. The same muonic scaling (Stone, 2000, using the Braucher et al. (2011) spallation/muonic production rate ratio) was applied to each site to simplify the calculation. Modification of the muonic scaling has negligible impact on the SLHL production rates, and affects only the third or fourth significant figure in the computed values. The resulting in situ ^{10}Be SLHL production rates are presented in Table A.1.3. For each scaling scheme, the three production rates are compatible within uncertainty.

Table A.1.3

Updated and homogenized production rates and reference ^{10}Be production rate proposed for the High Tropical Andes.

Scaling model	Atmosphere model ^c	Geomagnetic reconstruction ^d	This study	Blard et al., 2013b	Kelly et al., 2015	Weighted mean of the three sites at $g^{-1} yr^{-1}$ 2.4%	Dispersion of the 3 SLHL P10 ^h	
			at $g^{-1} yr^{-1}$ 1 σ uncertainty ^g : 4.1%	at $g^{-1} yr^{-1}$ 4.7%	at $g^{-1} yr^{-1}$ 4.6%		in %	Mean
“Lal modified” model ^a	Standard atmosphere	Muscheler et al., 2005	3.76	3.75	3.71	3.74	0.9	0.8
		GLOPIS-75 ^e	3.92	3.90	3.92	3.91	0.1	
		LSD framework ^f	3.68	3.64	3.60	3.64	1.4	
ERA-40 atmosphere	Muscheler et al., 2005	4.08	4.09	4.07	4.08	0.6	0.7	
	GLOPIS-75	4.26	4.24	4.29	4.26	0.4		
	LSD framework	4.00	3.96	3.95	3.97	1.0		
LSD model ^b	Standard atmosphere	Muscheler et al., 2005	4.04	4.04	3.95	4.01	1.6	2.3
		GLOPIS-75	4.22	4.21	4.13	4.19	1.2	
		LSD framework	3.73	3.70	3.47	3.63	4.2	
ERA-40 atmosphere	Muscheler et al., 2005	4.42	4.43	4.36	4.40	1.3	2.0	
	GLOPIS-75	4.61	4.61	4.55	4.59	0.8		
	LSD framework	4.08	4.06	3.83	3.98	3.8		

^a Being the Lal-Stone model (Lal, 1991; Stone, 2000) integrating a geomagnetic time correction through the formula taken from Nishiizumi et al. (1989).

^b From Lifton et al. (2014).

^c Both model implementations were taken from the LSD matlab code presented in Lifton et al. (2014).

^d All the VDM values used are normalized to the actual value of $7.746 \times 10^{22} A.m^{-2}$ from the 2010 DGRFs (Finlay et al., 2010) as in Lifton et al. (2014).

^e From Laj et al. (2004).

^f For the “Lal modified” model, the CALS7k.2 (Korte et Constable, 2005) and the CALS3k.3 (Korte et al., 2009) data used in the LSD framework is the M/M₀ VDM ratio.

^g uncertainties have been homogenized using the same methods.

^h the standard deviation divided by the mean for the three Sea Level High Latitude (SLHL) production rates.

with a mean of 4.08 ± 0.17 at $g^{-1} yr^{-1}$.

This variability between the different SLHL production rates demonstrates the very strong influence of the selected scaling scheme. Indeed, there is a 20% difference between the lowest and the highest SLHL values (3.68 ± 0.15 and 4.61 ± 0.19 at $g^{-1} yr^{-1}$) (Table A.1.2). The scaling scheme, the atmosphere and the geomagnetic field intensity reconstruction models effect the final values to comparable extents, producing 6%, 8% and 9% differences between the mean values, respectively. An unexpected and important difference arises between the SLHL production rates derived from the composite geomagnetic reconstruction that partly relies on GLOPIS-75 (called “LSD framework” in this study) and the SLHL production rates determined using GLOPIS-75 alone. It should be noted that the SLHL production rates deduced using the Muscheler et al. (2005) VDM values range between those of the two geomagnetic reconstructions mentioned above. This suggests that the variability in the proxies and the methods used for geomagnetic reconstruction induce important disparities between the M/M₀ reconstructions. Therefore, rather than being a synthetic solution, the use of a composite reconstruction could be an additional source of noise for the

A.2. Discussion of the Bayesian methods used for age calculation

Blard et al. (2013b) and Kelly et al. (2015) dated the calibration object using stratigraphical bracketing by ^{14}C and U–Th dated features (peats or lake shorelines). The method used in Blard et al. (2013b) is also used in this study (Section 3.1). It differs from that used by Kelly et al. (2015). To produce a density probability function of the age of the calibration object, both methods calculate two sub-functions with the age dataset. One sub-function leads to the maximum limiting age of the dated object, the other leads to the minimum limiting age. These two sub-functions are then multiplied to obtain the probability density function of the calibration object. In this study and in Blard et al. (2013b), the sub-functions were computed by summing the probability density functions of all individual sample ages, and then integrating this sum (see Equation (2), Section 3.1.). In Kelly et al. (2015) the sub-functions were computed by multiplying the integrals of the probability density functions of each individual sample ages as in Equation (A.1):

fort $\in \mathbb{R}$,

$$pdf_{\text{calibrationObj}}(t) = \prod_{i \in \text{OlderObj}} \int_t^{\infty} pdf_i(\tau) d\tau \times \prod_{j \in \text{YoungerObj}} \int_0^t pdf_j(\tau) d\tau \quad (\text{A1})$$

Due to the bounds of the integrals, multiplying integrals (Equation (A.1)) tends to attribute a higher weight to ages that closely bracket the age of the calibration site. In other words, an old sample age belonging to the oldest bracketing object will have no impact on the final product, whereas the youngest ages in the dataset will have a major impact on the final age. The situation is symmetric with respect to the ages of the younger object. This difference in the weight attributed to each sample is valid if we assume that the variability of the age dataset of a peat land or a shoreline only arises from a continuous build up of the object. However, the geochemical dating methods may also be affected by analytical scatter and potential inaccuracies, such as the possibility that ¹⁴C behaves as an open system and undergoes exchange with modern ¹⁴C, or has been contaminated by older carbon. Similarly, the correction for detrital ²³⁰Th can also be a source of inaccuracy for U–Th ages. Therefore, Equation (A.1) may be considered less conservative than Equation (2). The fact that this method may be too optimistic is clearly apparent in the narrow shape of the final probability density functions of the calculated age (Table A.1; Fig. 6 in Kelly et al. (2015)). Table A.1 presents the age calculation for the three calibration sites, carried out using the two bayesian methods. Depending on the dataset, Equation (A.1) yields uncertainties that are around or inferior to 1% whereas Equation (2) yields uncertainties of around 4%. The last column in Table A.1 shows the ratio of the relative errors of the two methods. Equation (A.1) induces uncertainties that are on average 7 times lower than those obtained using Equation (2):

Table A.2.1

Uncertainties associated with the two different bayesian approaches for determination of the age of the calibration object.

Source	Equation	Mean age (a)	1σ uncertainty (a)	1σ uncertainty (% of the mean value)	Uncertainty ratio (2)/(A.1) ^a
This study	Equation 2	16070	±640	4.0%	3
	Equation A.1	15850	±210	1.3%	
Blard et al., 2013a	Equation 2	15260	±540	3.5%	8
	Equation A.1	15380	±70	0.4%	
Kelly et al., 2015	Equation 2	12260	±560	4.6%	9
	Equation A.1	12350	±60	0.5%	
Mean					7

^a Ratio of the 1σ uncertainties (% of the mean value) given by Equations (2) and (A.1).

However, the computation defined by Equation (2), by firstly summing all of the available probability density functions, preserves a widest range of possible ages. This larger interval can be considered more conservative since all of the samples are equally weighted in the calculation. These observations thus led to our choice of Equation (2) for calculating the age of the calibration surfaces.

References

Balco, G., Briner, J., Finkel, R.C., Rayburn, J., Ridge, J.C., Schaefer, J.M., 2009. Regional beryllium-10 production rate calibration for late-glacial northeastern North

- America. *Quat. Geochronol.* 4, 93–107. <http://dx.doi.org/10.1016/j.quageo.2008.09.001>.
- Balco, G., Stone, J.O., Lifton, N., Dunai, T.J., 2008. A complete and easily accessible means of calculating surface exposure ages or erosion rates from ¹⁰Be and ²⁶Al measurements. *Quat. Geochronol.* 3, 174–195. <http://dx.doi.org/10.1016/j.quageo.2007.12.001>.
- Barrows, T.T., Hope, G.S., Prentice, M.L., Fifield, L.K., Tims, S.G., 2011. Late pleistocene glaciation of the Mt Giluwe volcano, Papua New Guinea. *Quat. Sci. Rev.* 30, 2676–2689. <http://dx.doi.org/10.1016/j.quascirev.2011.05.022>.
- Blard, P.-H., Braucher, R., Lavé, J., Bourlès, D., 2013a. Cosmogenic ¹⁰Be production rate calibrated against ³He in the high Tropical Andes (3800–4900 m, 20–22° S). *Earth Planet. Sci. Lett.* 382, 140–149. <http://dx.doi.org/10.1016/j.epsl.2013.09.010>.
- Blard, P.-H., Lave, J., Farley, K., Ramirez, V., Jimenez, N., Martin, L.C.P., Charreau, J., Tibari, B., Fornari, M., 2014. Progressive glacial retreat in the Southern Altiplano (Utruncu volcano, 22°S) between 65 and 14ka constrained by cosmogenic ³He dating. *Quat. Res.* 82, 209–221. <http://dx.doi.org/10.1016/j.yqres.2014.02.002>.
- Blard, P.-H., Lavé, J., Pik, R., Wagnon, P., Bourlès, D., 2007. Persistence of full glacial conditions in the central Pacific until 15,000 years ago. *Nature* 449, 591–594. <http://dx.doi.org/10.1038/nature06142>.
- Blard, P.-H., Lavé, J., Sylvestre, F., Placzek, C.J., Claude, C., Galy, V., Condom, T., Tibari, B., 2013b. Cosmogenic ³He production rate in the high tropical Andes (3800 m, 20°S): Implications for the local last glacial maximum. *Earth Planet. Sci. Lett.* 377–378, 260–275. <http://dx.doi.org/10.1016/j.epsl.2013.07.006>.
- Blard, P.-H., Sylvestre, F., Tripathi, A.K., Claude, C., Causse, C., Coudrain, A., Condom, T., Seidel, J.-L., Vimeux, F., Moreau, C., Dumoulin, J.-P., Lavé, J., 2011. Lake high-stands on the Altiplano (Tropical Andes) contemporaneous with Heinrich 1 and the Younger Dryas: new insights from ¹⁴C, U–Th dating and δ¹⁸O of carbonates. *Quat. Sci. Rev.* 30, 3973–3989. <http://dx.doi.org/10.1016/j.quascirev.2011.11.001>.
- Braucher, R., Merchel, S., Borgomano, J., Bourlès, D.L., 2011. Production of cosmogenic radionuclides at great depth: a multi element approach. *Earth Planet. Sci. Lett.* 309, 1–9. <http://dx.doi.org/10.1016/j.epsl.2011.06.036>.
- Brown, E.T., Edmond, J.M., Raisbeck, G.M., Yiu, F., Kurz, M.D., Brook, E.J., 1991. Examination of surface exposure ages of Antarctic moraines using in situ produced ¹⁰Be and ²⁶Al. *Geochim. Cosmochim. Acta* 55, 2269–2283. [http://dx.doi.org/10.1016/0016-7037\(91\)90103-C](http://dx.doi.org/10.1016/0016-7037(91)90103-C).
- Chmieleff, J., von Blanckenburg, F., Kossert, K., Jakob, D., 2010. Determination of the ¹⁰Be half-life by multicollector ICP-MS and liquid scintillation counting. *Nucl. Instruments Methods Phys. Res. Sect. B Beam Interact. Mater. Atoms* 268, 192–199. <http://dx.doi.org/10.1016/j.nimb.2009.09.012>.
- Clapperton, C., Clayton, J., Benn, D., 1997. Late quaternary glacier advances and palaeolake highstands in the Bolivian Altiplano. *Quat.* 6182, 49–59.
- Clayton, J.D., Clapperton, C.M., 1995. The last glacial cycle and palaeolake synchrony in the southern Volivian Altiplano: Cerro Azanaques case study.
- Clayton, J.D., Clapperton, C.M., 1997. Broad synchrony of a Late-glacial glacier advance and the highstand of palaeolake Tauca in the Bolivian Altiplano. *J. Quat. Sci.* 12, 169–182. [http://dx.doi.org/10.1016/S0012-821X\(02\)01088-9](http://dx.doi.org/10.1002/(SICI)1099-1417(199705)06<12:::Desilets, D., Zreda, M., 2003. Spatial and temporal distribution of secondary cosmic-ray nucleon intensities and applications to in situ cosmogenic dating. <i>Earth Planet. Sci. Lett.</i> 206, 21–42. <a href=).
- Desilets, D., Zreda, M., Prabu, T., 2006. Extended scaling factors for in situ cosmogenic nuclides: new measurements at low latitude. *Earth Planet. Sci. Lett.* 246, 265–276. <http://dx.doi.org/10.1016/j.epsl.2006.03.051>.
- Dunai, T., 2001. Influence of secular variation of the geomagnetic field on production rates of in situ produced cosmogenic nuclides. *Earth Planet. Sci. Lett.* 193, 197–212. [http://dx.doi.org/10.1016/S0012-821X\(01\)00503-9](http://dx.doi.org/10.1016/S0012-821X(01)00503-9).
- Fenton, C.R., Hermanns, R.L., Blikra, L.H., Kubik, P.W., Bryant, C., Niedermann, S., Meixner, A., Goethals, M.M., 2011. Regional ¹⁰Be production rate calibration for the past 12ka deduced from the radiocarbon-dated Grøtlandsura and Russenes rock avalanches at 69° N, Norway. *Quat. Geochronol.* 6, 437–452. <http://dx.doi.org/10.1016/j.quageo.2011.04.005>.
- Finlay, C.C., Maus, S., Beggan, C.D., Bondar, T.N., Chambodut, A., Chernova, T.A., Chulliat, A., Golovkov, V.P., Hamilton, B., Hamoudi, M., Holme, R., Hulot, G., Kuang, W., Langlais, B., Lesur, V., Lowes, F.J., Lühr, H., Macmillan, S., Manda, M., McLean, S., Manoj, C., Menvielle, M., Michaelis, I., Olsen, N., Rauberg, J., Rother, M., Sabaka, T.J., Tangborn, a., Tøffner-Clausen, L., Thébaud, E., Thomson, A.W.P., Wardinski, I., Wei, Z., Zvereva, T.I., 2010. International geomagnetic reference field: the eleventh generation. *Geophys. J. Int.* 183, 1216–1230. <http://dx.doi.org/10.1111/j.1365-246X.2010.04804.x>.
- GEOBOL – Servicio Geológico de Bolivia, 1994. *Mapas Tematicos de Recursos Minerales de Bolivia. Hoja Uncia SE-19-12 1:250,000. Publication SGB II-MTB-2B.*
- Gosse, J.C., Klein, J., Lawn, B., Middleton, R., Evenson, E.B., 1995. Beryllium-10 dating of the duration and retreat of the last pinedale glacial sequence. *Science* 268, 1329–1333. <http://dx.doi.org/10.1126/science.268.5215.1329>.
- Gosse, J.C., Phillips, F.M., 2001. Terrestrial in situ cosmogenic nuclides: theory and application. *Quat. Sci. Rev.* 20, 1475–1560. [http://dx.doi.org/10.1016/S0277-3791\(00\)00171-2](http://dx.doi.org/10.1016/S0277-3791(00)00171-2).
- Guyodo, Y., Valet, J., 1999. Global changes in intensity of the Earth's magnetic field during the past 800 kyr. *Nature* 399, 249–252. <http://dx.doi.org/10.1038/20420>.
- Jomelli, V., Favier, V., Vuille, M., Braucher, R., Martin, L., Blard, P.-H., Colose, C., Brunstein, D., He, F., Khodri, M., Bourlès, D.L., Leanni, L., Rinterknecht, V., Grancher, D., Francou, B., Ceballos, J.L., Fonseca, H., Liu, Z., Otto-Bliessner, B.L., 2014. A major advance of tropical Andean glaciers during the Antarctic cold reversal. *Nature*. <http://dx.doi.org/10.1038/nature13546>.
- Kaplan, M.R., Strelin, J.A., Schaefer, J.M., Denton, G.H., Finkel, R.C., Schwartz, R.,

- Putnam, A.E., Vandergoes, M.J., Goehring, B.M., Travis, S.G., 2011. In-situ cosmogenic ^{10}Be production rate at Lago Argentino, Patagonia: implications for late-glacial climate chronology. *Earth Planet. Sci. Lett.* 309, 21–32. <http://dx.doi.org/10.1016/j.epsl.2011.06.018>.
- Kelly, M.A., Lowell, T.V., Applegate, P.J., Phillips, F.M., Schaefer, J.M., Smith, C.A., Kim, H., Leonard, K.C., Hudson, A.M., 2015. A locally calibrated, late glacial ^{10}Be production rate from a low-latitude, high-altitude site in the Peruvian Andes. *Quat. Geochronol.* 26, 70–85. <http://dx.doi.org/10.1016/j.quageo.2013.10.007>.
- Kober, F., Ivy-Ochs, S., Leya, I., Baur, H., Magna, T., Wieler, R., Kubik, P.W., 2005. In situ cosmogenic ^{10}Be and ^{21}Ne in sanidine and in situ cosmogenic ^3He in Fe–Ti-oxide minerals. *Earth Planet. Sci. Lett.* 236, 404–418. <http://dx.doi.org/10.1016/j.epsl.2005.05.020>.
- Korschinek, G., Bergmaier, A., Faestermann, T., Gerstmann, U.C., Knie, K., Rugel, G., Wallner, A., Dillmann, I., Dollinger, G., von Gostomski, C.L., Kossert, K., Maiti, M., Poutivsev, M., Remmert, A., 2010. A new value for the half-life of ^{10}Be by Heavy-Ion Elastic Recoil Detection and liquid scintillation counting. *Nucl. Instrum. Methods Phys. Res. Sect. B Beam Interact. Mater. Atoms* 268, 187–191. <http://dx.doi.org/10.1016/j.nimb.2009.09.020>.
- Korte, M., Donadini, F., Constable, C.G., 2009. Geomagnetic field for 0–3 ka: 2. A new series of time-varying global models. *Geochem. Geophys. Geosystems* 10. <http://dx.doi.org/10.1029/2008GC002297> n/a–n/a.
- Korte, M., Genevey, A., Constable, C.G., Frank, U., Schnepf, E., 2005. Continuous geomagnetic field models for the past 7 millennia: 1. A new global data compilation. n/a–n/a *Geochem. Geophys. Geosystems* 6. <http://dx.doi.org/10.1029/2004GC000800>.
- Laj, C., Kissel, C., Beer, J., 2004. Geophysical Monograph Series. High Resolution Global Paleointensity Stack since 75 kyr (GLOPIIS-75) Calibrated to Absolute Values. *Timescales Paleomagn. F.*, vol. 145, pp. 255–265. <http://dx.doi.org/10.1029/145GM19>.
- Lal, D., 1991. Cosmic ray labeling of erosion surfaces: in situ nuclide production rates and erosion models. *Earth Planet. Sci. Lett.* 104, 424–439. [http://dx.doi.org/10.1016/0012-821X\(91\)90220-C](http://dx.doi.org/10.1016/0012-821X(91)90220-C).
- Leduc, G., Vidal, L., Tachikawa, K., Rostek, F., Sonzogni, C., Beaufort, L., Bard, E., 2007. Moisture transport across Central America as a positive feedback on abrupt climatic changes. *Nature* 445, 908–911. <http://dx.doi.org/10.1038/nature05578>.
- Licciardi, J.M., Schaefer, J.M., Taggart, J.R., Lund, D.C., 2009. Holocene glacier fluctuations in the Peruvian Andes indicate northern climate linkages. *Science* 325, 1677–1679. <http://dx.doi.org/10.1126/science.1175010>.
- Lifton, N.A., Bieber, J.W., Clem, J.M., Duldig, M.L., Evenson, P., Humble, J.E., Pyle, R., 2005. Addressing solar modulation and long-term uncertainties in scaling secondary cosmic rays for in situ cosmogenic nuclide applications. *Earth Planet. Sci. Lett.* 239, 140–161. <http://dx.doi.org/10.1016/j.epsl.2005.07.001>.
- Lifton, N., Sato, T., Dunai, T.J., 2014. Scaling in situ cosmogenic nuclide production rates using analytical approximations to atmospheric cosmic-ray fluxes. *Earth Planet. Sci. Lett.* 386, 149–160. <http://dx.doi.org/10.1016/j.epsl.2013.10.052>.
- Lønne, I., Nemeč, W., 2004. High-arctic fan delta recording deglaciation and environment disequilibrium. *Sedimentology* 51, 553–589. <http://dx.doi.org/10.1111/j.1365-3091.2004.00636.x>.
- Machlus, M., Enzel, Y., Goldstein, S.L., Marco, S., Stein, M., 2000. Reconstructing low levels of Lake Lisan by correlating fan-delta and lacustrine deposits. *Quat. Int.* 73–74, 137–144. [http://dx.doi.org/10.1016/S1040-6182\(00\)00070-7](http://dx.doi.org/10.1016/S1040-6182(00)00070-7).
- Ménabréaz, L., Bourlés, D.L., Thouveny, N., 2012. Amplitude and timing of the Laschamp geomagnetic dipole low from the global atmospheric ^{10}Be overproduction: contribution of authigenic $^{10}\text{Be}/^9\text{Be}$ ratios in west equatorial Pacific sediments. *J. Geophys. Res.* 117, B11101. <http://dx.doi.org/10.1029/2012JB009256>.
- Muscheler, R., Beer, J., Kubik, P.W., Synal, H.-A., 2005. Geomagnetic field intensity during the last 60,000 years based on ^{10}Be and ^{36}Cl from the Summit ice cores and ^{14}C . *Quat. Sci. Rev.* 24, 1849–1860. <http://dx.doi.org/10.1016/j.quascirev.2005.01.012>.
- National Oceanic and Atmospheric Administration, 1976. *U.S. Standard Atmosphere*. US Government Printing Office.
- Nemeč, W., Lønne, I., Blikra, L.H., 1999. The Kregnes moraine in Gauldalen, west-central Norway: anatomy of a Younger Dryas proglacial delta in a palaeofjord basin. *Boreas* 28, 454–476. <http://dx.doi.org/10.1080/030094899421975>.
- Nishiizumi, K., Imamura, M., Caffee, M.W., Southon, J.R., Finkel, R.C., McAninch, J., 2007. Absolute calibration of ^{10}Be AMS standards. *Nucl. Instrum. Methods Phys. Res. Sect. B Beam Interact. Mater. Atoms* 258, 403–413. <http://dx.doi.org/10.1016/j.nimb.2007.01.297>.
- Nishiizumi, K., Winterer, E.L., Kohl, C.P., Klein, J., Middleton, R., Lal, D., Arnold, J.R., 1989. Cosmic ray production rates of ^{10}Be and ^{26}Al in quartz from glacially polished rocks. *J. Geophys. Res.* 94, 17907. <http://dx.doi.org/10.1029/JB094iB12p17907>.
- Placzek, C., Quade, J., Patchett, P.J., 2006. Geochronology and stratigraphy of late Pleistocene lake cycles on the southern Bolivian Altiplano: implications for causes of tropical climate change. *Geol. Soc. Am. Bull.* 118, 515–532. <http://dx.doi.org/10.1130/B25770.1>.
- Putnam, A.E., Schaefer, J.M., Barrell, D.J.A., Vandergoes, M., Denton, G.H., Kaplan, M.R., Finkel, R.C., Schwartz, R., Goehring, B.M., Kelley, S.E., 2010. In situ cosmogenic ^{10}Be production-rate calibration from the Southern Alps, New Zealand. *Quat. Geochronol.* 5, 392–409. <http://dx.doi.org/10.1016/j.quageo.2009.12.001>.
- Ramsey, C.B., 2009. Bayesian analysis of radiocarbon dates Christopher Bronk Ramsey. *Radiocarbon* 51, 337–360. http://dx.doi.org/10.2458/azu_js_rc.v51i1.3494.
- Reimer, P., 2013. IntCal13 and Marine13 radiocarbon age calibration curves 0–50,000 Years cal BP. *Radiocarbon* 55, 1869–1887. http://dx.doi.org/10.2458/azu_js_rc.v55.16947.
- Sato, T., Yasuda, H., Niita, K., Endo, A., Sihver, L., 2008. Development of PARMA: PHITS-based analytical radiation model in the atmosphere. *Radiat. Res.* 170, 244–259. <http://dx.doi.org/10.1667/JR1094.1>.
- Smith, J.A., Seltzer, G.O., Farber, D.L., Rodbell, D.T., Finkel, R.C., 2005. Early local last glacial maximum in the tropical Andes. *Science* 308, 678–681. <http://dx.doi.org/10.1126/science.1107075>.
- Stone, J.O., 2000. Air pressure and cosmogenic isotope production. *J. Geophys. Res.* 105, 23753. <http://dx.doi.org/10.1029/2000JB900181>.
- Strutz, T., 2011. Data Fitting and Uncertainty. <http://dx.doi.org/10.1007/978-3-8348-9813-5>.
- Sylvestre, F., Servant, M., Servant-Vildary, S., Causse, C., Fournier, M., Ybert, J.-P., 1999. Lake-Level chronology on the southern Bolivian Altiplano (18°–23°S) during late-glacial time and the Early holocene. *Quat. Res.* 51, 54–66. <http://dx.doi.org/10.1006/qres.1998.2017>.
- Uppala, S.M., Källberg, P.W., Simmons, A.J., Andrae, U., Bechtold, V.D.C., Fiorino, M., Gibson, J.K., Haseler, J., Hernandez, A., Kelly, G.A., Li, X., Onogi, K., Saarinen, S., Sokka, N., Allan, R.P., Andersson, E., Arpe, K., Balmaseda, M.A., Beljaars, A.C.M., Berg, L., De, Van, Bidlot, J., Bormann, N., Caires, S., Chevallier, F., Dethof, A., Dragosavac, M., Fisher, M., Fuentes, M., Hagemann, S., Hólm, E., Hoskins, B.J., Isaksen, I., Janssen, P.A.E.M., Jenne, R., McNally, A.P., Mahfouf, J.-F., Morcrette, J.-J., Rayner, N.A., Saunders, R.W., Simon, P., Sterl, A., Trenberth, K.E., Untch, A., Vasiljevic, D., Viterbo, P., Woollen, J., 2005. The ERA-40 re-analysis. *Q. J. R. Meteorol. Soc.* 131, 2961–3012. <http://dx.doi.org/10.1256/qj.04.176>.
- Young, N.E., Schaefer, J.M., Briner, J.P., Goehring, B.M., 2013. A ^{10}Be production-rate calibration for the Arctic. *J. Quat. Sci.* 28, 515–526. <http://dx.doi.org/10.1002/jqs.2642>.

Chapitre 5

Développement d'un programme en ligne pour le calcul des âges d'exposition ^3He et ^{10}Be

Nous avons déjà évoqué l'importance de l'utilisation des taux de production locaux dans les calculs d'âges d'exposition, ainsi que la variabilité sur les résultats produits par l'utilisation des différents modèles de mise à l'échelle. Ce sont ces mêmes problématiques qui ont motivé le développement du programme CREp présenté dans ce chapitre.

Ce projet de programme s'est construit tout au long de cette thèse. La nécessité de développer un programme de calcul automatisé des âges d'expositions s'est présentée en constatant que les programmes alors en ligne (notamment le programme CRONUS, très utilisé) ne permettaient pas de choisir le taux de production ou encore la base de données géomagnétiques pour les calculs. Nous souhaitons tester des paramètres différents de ceux alors proposés par CRONUS. La première version en ligne de code Matlab© a été développée pour calculer des âges d'expositions avec (i) les taux de production andins pour le ^3He et le ^{10}Be , (ii) le modèle de Lal-Stone dépendant du temps (Lal, 1991; Stone, 2000; Balco et al., 2008), (iii) l'atmosphère andine déterminée par Farber et al. (2005), (iv) le VDM de Muscheler et al. (2005). C'est cette version qui a été utilisée pour calculer les âges d'exposition à Cerro Uturuncu (Blard et al., 2014) et pour recalculer tous les âges d'exposition Sud Américains présentés dans la synthèse des ages andins (Jomelli et al., 2014). Ces deux articles sont présentés en Annexes de ce manuscrit.

Le modèle LSD (Lifton et al., 2014) a été publié en 2014 avec ses codes sources dans le même langage. L'article présentant le modèle propose une synthèse des différents types de modèles existants à la lumière des nouveaux développements menés. Il existe 3 groupes de modèles :

- ceux basés sur la mesure du flux cosmique à l'aide de plaques d'émulsion photographiques et de chambres à brouillard (Lal, 1991; Stone, 2000)
- ceux basés sur la mesure du flux à l'aide de détecteurs de neutrons (Dunai, 2001; Lifton et al., 2005; Desilets and Zreda, 2003; Desilets et al., 2006)
- le modèle LSD, basé sur le calcul ab initio du flux cosmique (Lifton et al., 2014).

Cette synthèse montre que les modèles basés sur les détecteurs de neutrons ont tendance à surévaluer le flux cosmique alors que les modèles plus anciens à émulsion et chambre à brouillard sont plus robustes et cohérents avec le nouveau modèle présenté. Ce dernier propose également de réaliser les calculs de mise à l'échelle avec le modèle d'atmosphère spatialisé ERA-40 (Uppala et al., 2005) qui permet de calculer des pressions à l'aide de paramètres atmosphériques spatialisés.

Une deuxième version du code a donc été développée de manière à ce qu'il puisse utiliser (i) les modèles de mise à l'échelle de Lal-Stone et LSD, (ii) l'atmosphère ERA-40 et l'atmosphère standard des Etats Unis (très utilisée par le passé), (iii) n'importe quelle reconstitution dipolaire du champ magnétique terrestre.

En vue d'une publication, le code a fait ensuite l'objet du développement d'une interface graphique sous Matlab, avec l'ajout d'une interface pour la calibration de taux de production. En parallèle, une première base de données mondiale des taux de production a été développée par Pierre Henri Blard et Romain Delunel et incorporée au programme afin de pouvoir choisir parmi les différents taux de productions établis partout dans le monde. Cette base de données est notamment discutée dans l'article Delunel et al., (Submitted) présenté en Annexe de ce manuscrit.

Considérant qu'un calculateur en ligne serait plus utile et pratique qu'une version Matlab (nécessitant de posséder une licence), un dernier développement a consisté à porter en ligne le code et la base de données des taux de production. Cette base de données en ligne a été développée par Pierre Henri Blard, Greg Balco et Nat Lifton. La mise en ligne du code a été conçue de manière à faire dialoguer un site internet avec le logiciel Octave, équivalent libre de droits de Matlab. Ce changement a, dans un premier temps, nécessité une refonte du code pour un tel fonctionnement. Dans un second temps, la gestion du site, sa communication avec l'utilisateur, avec la base de données des taux de production en ligne et avec Octave a été confiée à l'entreprise de web développement Studio 1D 3P (<http://crep.cprg.cnrs-nancy.fr>).

Le programme CREp va faire l'objet d'une soumission au journal Quaternary Geochronology. Pour cette raison, il est présenté sous forme de manuscrit d'article en langue anglaise.

1 **The CREP program and the ICE-D production rate calibration**
2 **database: a fully parameterizable and updated online tool to**
3 **compute exposure ages from cosmogenic ^3He and ^{10}Be**
4

5
6 L.C.P. Martin^a, P.-H. Blard^{1*}, G. Balco^b, J. Lavé^a, R. Delunel^c, N. Lifton^d, V. Laurent^e
7
8

9 a CRPG, UMR 7358, CNRS, Université de Lorraine, Vandoeuvre-lès-Nancy, France

10 b Berkeley Geochronological Center, Berkeley, CA, USA

11 c Institute of Geological Sciences, University of Bern, Bern, Switzerland

12 d Purdue University, West Lafayette, IN, USA

13 e 1D3P Studio, Nancy, France
14

15 * Corresponding author:
16

17 CRPG

18 15 rue Notre Dame des Pauvres

19 54501 Vandoeuvre-lès-Nancy

20 FRANCE
21
22
23

24 email: leom@crpg.cnrs-nancy.fr, blard@crpg.cnrs-nancy.fr, balcs@bgc.org

25 cell: +33 6 40 22 47 32

26 office: + 33 3 83 59 42 46
27
28

29 **Submitted to Quaternary Geochronology on June 8th**
30
31

32 7354 words (main text)

33 7 Tables

34 5 Figures

35 2 Appendices (3386 words)

36 Supplementary files: Matlab version of the CREP's code (zipped)

37 Link of the online version: <http://crep.crpg.cnrs-nancy.fr>
38
39
40
41

42 **Keywords:** cosmic-ray exposure age computation; cosmogenic ^{10}Be ; ^3He , scaling model;
43 atmosphere model; geomagnetic reconstruction model; production rate parameterization
44

45 Highlights

46

47 - CREp (Cosmic Ray Exposure program) is a new Octave/Matlab© tool for exposure age
48 computation

49

- Online version of CREp: crep.crpq.cnrs-nancy.fr

50

- This program includes both the Lal/Stone time dependent scaling model (Lal, 1991 ;

51

Stone, 2000), and the LSD model (Lifton et al., 2014).

52

- Users can choose between the standard atmosphere pressure, or the ERA40
53 atmosphere model.

54

- Time dependent correction may be done using several different Virtual Dipole
55 Moment databases.

56

- CREp is linked to an online database of production rate calibration data (ICE-D), so
57 reference production rates are dynamically available to the calculator as the database is
58 updated.

59

- Users can either select global, regional or local production rates to compute exposure
60 ages.

61

- The statistical dispersion of the SLHL production rates are rather similar for the
62 Lal/Stone and LSD models. The impact of the tested atmospheric model and the
63 geomagnetic database is also limited.

64 **Abstract**

65 Over the last decades, cosmogenic exposure dating has permitted major advances in
66 many fields of Earth surface sciences and particularly in paleoclimatology. Yet,
67 exposure age calculation remains a complicated and dense procedure. It requires
68 numerous choices of parameterization and the use of an accurate production rate.

69 This study describes the CREp program and the ICE-D production rate online
70 database. This system is designed so that the CREp calculator will automatically reflect
71 the current state of this global calibration database production rate, ICE-D. ICE-D will
72 be regularly updated in order to incorporate new calibration data and reflect the current
73 state of the available literature.

74 CREp is a Octave/Matlab© online code that computes Cosmic Ray Exposure (CRE)
75 ages for ^3He and ^{10}Be , available at crep.crpq.cnrs-nancy.fr. A stand-alone version of the
76 CREp code is also released with the present article. Note however that only the online
77 version is connected to the online database ICE-D. The CREp program offers the
78 possibility to calculate ages with two scaling models: i.e. the empirical Lal-Stone time-
79 dependent model

80 (Balco et al., 2008; Lal, 1991; Stone, 2000) with the muon parameters of (Braucher et
81 al., 2011), and the Lifton-Sato-Dunai (LSD) theoretical model (Lifton et al., 2014). The
82 default atmosphere model is the ERA-40 database (Uppala et al., 2005), but one may
83 also use the standard atmosphere for comparison (N.O.A.A., 1976) to apply the
84 atmospheric correction. To perform the time-dependent correction, users may import
85 their own geomagnetic database for paleomagnetic corrections or opt for one of the
86 three proposed datasets (Lifton, 2016; Lifton et al., 2014; Muscheler et al., 2005).

87 For the important choice of the production rate, CRE-p is linked to a database of

88 production rate calibration data that is part of the ICE-D (Informal Cosmogenic-nuclide
89 Exposure-age Database) project (<http://calibration.ice-d.org>). This database includes
90 published empirical calibration rate studies that are publicly available at present,
91 comprising those of the CRONUS-Earth and CRONUS-EU projects, as well as studies
92 from other projects. In the present study, the efficacy of the different scaling models has
93 also been evaluated looking at the statistical dispersion of the computed Sea Level High
94 Latitude (SLHL) production rates. Lal/Stone and LSD models have comparable
95 efficacies, and the impact of the tested atmospheric model and the geomagnetic
96 database is also limited.

97 Users however have several possibilities to select the production rate: 1) using a
98 worldwide mean value, 2) a regionally averaged value (not available in region with no
99 data), 3) a local unique value, which can be chosen among the existing dataset or
100 imported by the user, or 4) any combination of single or multiple calibration data.

101 If a global mean is chosen, the 1σ uncertainty arising from the production rate is about
102 5% for ^{10}Be and 10% for ^3He .

103 CREP is able to calculate a large number of ages in a reasonable time (typically < 30
104 seconds for 50 samples). The user may export a summary table of the computed ages
105 and the density probability function associated with each age (in the form of a
106 spreadsheet format).

107 **1. Introduction**

108 *1.1. Cosmic-Rays Exposure age calculation*

109 Over the last decades, the development of Cosmic Ray Exposure dating method has
110 permitted major advances in many fields of Earth sciences, notably in paleoclimatology
111 (e.g. Barrows et al., 2011; Blard et al., 2011, 2007; Gosse et al., 1995; Jomelli et al.,
112 2014; Licciardi et al., 2009; Smith et al., 2005) tectonics (e.g. Palumbo et al., 2004; Ritz
113 et al., 1995), paleoaltimetry (e.g. Blard et al., 2006) landscape evolution (e.g. Brown et
114 al., 1995; Riebe et al., 2000) or sediment transfer in the plain (e.g. Lupker et al., 2012;
115 Wittmann and Blanckenburg, 2009).

116 The calculation of accurate and precise CRE ages requires a good knowledge of the
117 production rate of the cosmogenic nuclide in a specific mineral at a place to be dated,
118 over the time frame of interest. Yet, in most cases, this local production rate is
119 computed from calibration sites that may be located hundreds or thousands kilometres
120 away from the studied place, on objects that are sometimes significantly older or
121 younger than the dated surface. As production rates vary with latitude, altitude, and also
122 with time due to temporal fluctuations in the Earth's magnetic field, a complicated
123 scaling procedure is necessary to obtain the appropriate production rate for dating. The
124 usual method consists of, first, converting the reference production rate at a calibration
125 site into a Sea Level High Latitude (SLHL) rate, corrected for the past geomagnetic
126 activity over the calibration time period. Then, this SLHL production rate is rescaled to
127 the location of the surface to be dated (Balco et al., 2008; Gosse and Phillips, 2001). For
128 calculation consistency, these two transformations must be done using the same scaling
129 scheme. This scaling scheme implies a model describing spatial variation in the cosmic
130 ray flux, an atmosphere model, a reconstruction of the past geomagnetic activity, and an

131 accurate model linking this paleomagnetic activity with the production of cosmogenic
132 nuclides (Balco et al., 2008; Lifton et al., 2014; Dunai, 2001). Therefore, exposure age
133 computation is not unique and the choices of the scaling framework and corresponding
134 reference production rate may significantly impact the computed ages.

135

136 *1.2. Published calculation software and recent advances in CRE dating*

137 Over the last twenty years, several programs have been published to enable the
138 calculations that are required to compute exposure ages: the WebCN online program
139 (Ma et al., 2007), the Cosmocalc Excel © add-in (Vermeesch, 2007), the CRONUS-
140 Earth online calculators (Balco et al., 2008; Marrero et al., 2016), the ACE Python-
141 based software (Zweck et al., 2012) and other tools (Phillips et al., 2001;
142 Schimmelpfennig et al., 2011). All of these tools are based on different approaches.

143 Yet, since the publication of these programs, the cosmogenic nuclide community has
144 produced new developments and results that have improved the accuracy of exposure
145 ages. Importantly, several new production rate calibration studies are now published
146 each year, improving the method's accuracy in several regions. Incorporating this new
147 information into an exposure-age calculation scheme represents a challenge in data
148 assimilation.

149 The default SLHL production rate used in the original CRONUS calculator for ^{10}Be is
150 a global average deduced from several calibration sites ($\sim 4.5 \text{ at.g}^{-1}.\text{yr}^{-1}$ with the Lm
151 scaling) (Balco et al., 2008). However, recent calibration studies yielded significantly
152 lower SLHL ^{10}Be production rates ($< 4 \text{ at.g}^{-1}.\text{yr}^{-1}$ for the same scaling scheme) (e.g.
153 Blard et al., 2015; Fenton et al., 2011; Kaplan et al., 2011; Putnam et al., 2010; Stroeven
154 et al., 2015; Young et al., 2013; Martin et al., 2015). Moreover, statistical analyses

155 highlighted the imperfections of scaling schemes to fit the production rates in certain
156 regions, notably at high elevations low latitudes (Borchers et al., 2016; Lifton et al.,
157 2014). This observation tends to suggest that the use of local calibration rate is more
158 pertinent to compute accurate ages. Indeed, using a production rate derived from a
159 calibration site that is both close in space and time to the site to date lowers the
160 dependence of the production rate value to the scaling procedure (Balco et al., 2008;
161 Licciardi et al., 2009). In this regard, the ongoing enrichment of the worldwide database
162 of production rate is likely to efficiently improve the accuracy of CRE dating. Our
163 opinion is that an online calculator connected to a regularly updated database is the most
164 efficient mean to achieve this goal.

165 The new theoretical LSD model and the associated publication (Lifton et al., 2014)
166 brought important insights on the inaccuracies of former scaling models. Neutron-
167 monitor based models (Desilets and Zreda, 2003; Desilets et al., 2006; Dunai, 2001;
168 Lifton et al., 2005) are prone to overestimate the altitude dependence of cosmogenic-
169 nuclide production while the older Lal-Stone model turned out to be robust and in good
170 agreement with the LSD model. This is due to the multiplicity effect affecting neutron
171 monitor data: this bias is indeed larger at high cutoff rigidities, for altitude above 3 km
172 (Lifton et al., 2014). (Borchers et al., 2016) confirmed these observations: using a least
173 square criterion, they showed that the Lal-Stone models (with and without geomagnetic
174 time corrections) and the LSD models are much more efficient than neutron-monitor
175 based models (Desilets and Zreda, 2003; Dunai, 2001; Lifton et al., 2005) in predicting
176 the spatial variability of production rates. With the LSD model, Lifton et al. (2014) also
177 came up with a new 2D atmosphere model derived from the ERA-40 meteorological
178 reanalysis (Uppala et al., 2005). Similarly to the NCEP/NCAR 2-D reanalysis (Balco et

179 al., 2008), ERA-40 provides a globally consistent alternative to the independently
180 determined pre-existing local atmosphere parameters (e.g. Farber et al., 2005 for the
181 Andean atmosphere).

182 The impact of geomagnetic variations on cosmogenic nuclide production rates may be
183 accounted using various reconstructions of the geomagnetic activity. So far, the initial
184 CRONUS-Earth calculator (Balco et al., 2008) relies on a composite framework
185 including the Yang et al. (2000), Korte et Constable (2005a) and SINT800 (Guyodo and
186 Valet, 1999) reconstructions whereas the Lifton et al. (2014) LSD model uses
187 CALS3k.3 (Korte et al., 2009), CALS7k.2 (Korte et Constable, 2005a), GLOPIS-75
188 (Laj et al., 2004) and PADM2M (Ziegler et al., 2011). Yet Martin et al. (2015), Delunel
189 et al. (2016) and Lifton (2016) showed that the choice of the geomagnetic database is
190 likely to influence the ability of a scaling scheme to fit a set of production rates to
191 SLHL values.

192

193 *1.3 The CREp program and the ICE-D production rate calibration database*

194 This overview raises the critical importance of the choice of the production rate and
195 the impact of the wide scaling possibilities on exposure age computation. Therefore, it
196 is crucial for the users to be able to test various production rates among the most
197 relevant values and to perform sensitivity test on the scaling choices using the most
198 efficient models. For this purpose, we present the CREp program, a Octave/Matlab©
199 program that allows exposure ages computation for ^3He and ^{10}Be using a large choice of
200 parameterization possibilities. CREp is linked with the ICE-D production rate
201 calibration database, a new online database that compiles all existing calibration studies.
202 This innovation makes CREp a flexible and easily updatable online calculator.

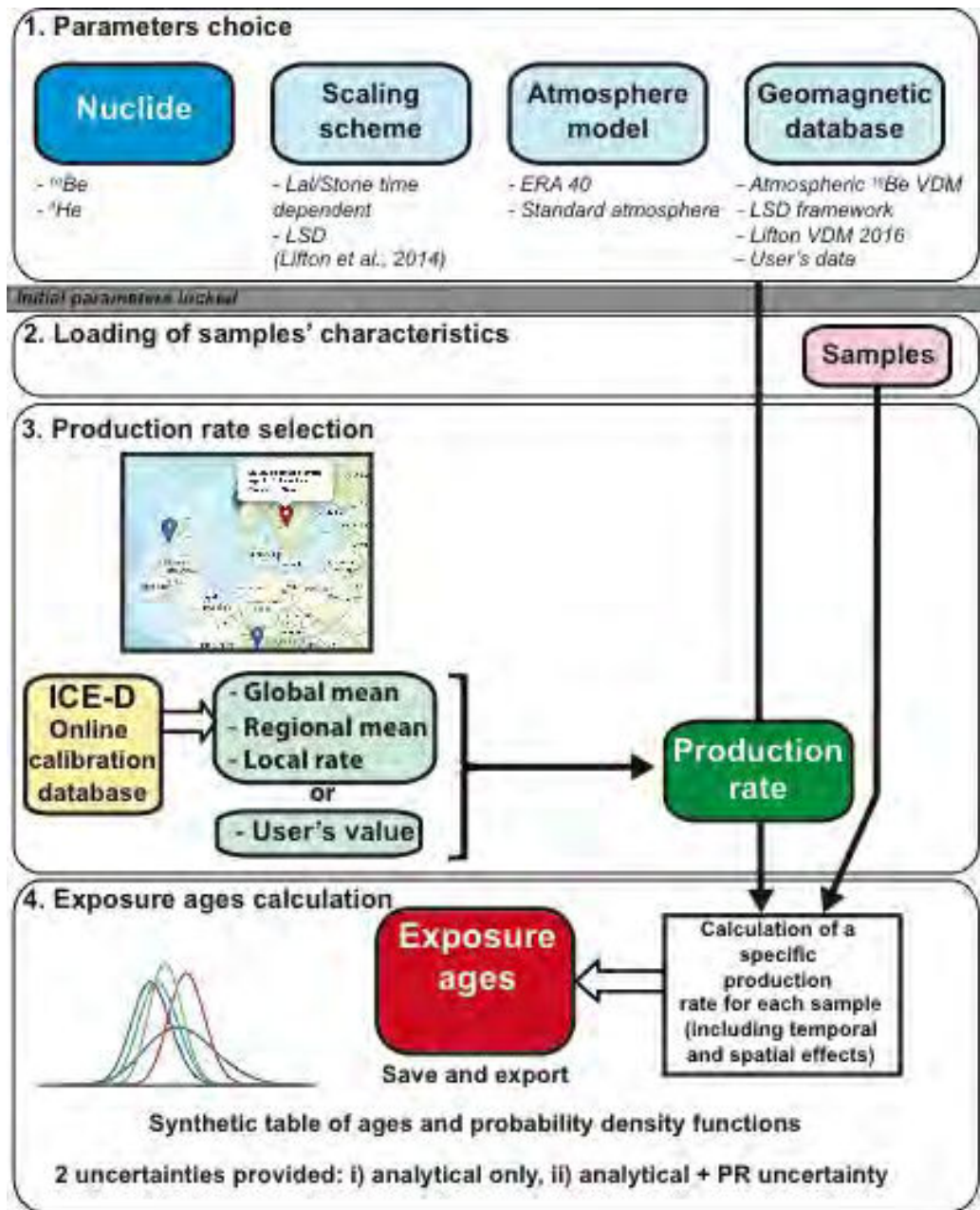
203 **2. Description of CREp**

204 CREp exists in the form of a Matlab© codes released as supplementary material of the
205 present article. An Octave online version of CREp is also available at [crep.crpq.cnrs-](http://crep.crpq.cnrs-nancy.fr)
206 [nancy.fr](http://crep.crpq.cnrs-nancy.fr). The online version should be favoured, since it will incorporate the most
207 recent developments, notably the most up-to-date production rates of the ICE-D
208 database.]

209

210 *2.1. Synoptic flow of CREp*

211 The global synoptic flow of CREp can be summarized in four steps (Figure 1). First,
212 user choses the scaling procedure (scaling scheme, atmosphere, geomagnetic database).
213 Second, user enters the characteristics of the samples to be dated (nuclide
214 concentrations and uncertainties, geographical coordinates, elevation, sample thickness,
215 density, potential erosion). Third, a specific production rate is chosen among several
216 possibilities, those ranging from a global average to a single local calibration site.
217 Finally, the exposure ages of the loaded samples are calculated with this production
218 rate.



219

220

221

222

223

224 *2.2. Scaling models*

225 The CREP program includes two scaling models, the so-called "Lal modified" (Balco

226 et al., 2008) and the LSD model (Lifton et al., 2014). The Lal-Stone modified model
 227 corresponds to a time dependent version of the classical Lal-Stone scaling model that
 228 relies on nuclear emulsions, cloud chambers, and various neutron detectors for
 229 measurement of secondary cosmic-ray fluxes (Lal, 1991; Stone, 2000). In order to
 230 implement the time-dependent geomagnetic correction, the fundamental equations of
 231 Lal-Stone have been modified to use cutoff-rigidities rather than latitude as input,
 232 following Balco et al. (2008). For this, the model uses the equation linking the cutoff
 233 rigidity R_c (GV) and the latitude (Elsasser et al., 1956; Stormer, 1955):

$$234 \quad R_c = \frac{M \mu_0 c}{16 \pi \times 10^9 r^2} \cos^4 \lambda \quad (1)$$

235 where M (A.m^2) is moment of the Earth dipole field, r is the mean radius of the Earth
 236 (6.3712×10^6 m), c is the speed of light (3.0×10^8 m.s⁻¹), and μ_0 is the permeability of free
 237 space ($4\pi \times 10^{-7}$ N.A⁻²). Using the 2010 value for M ($M_0 = 7.746 \times 10^{22}$ A.m²), equation
 238 (1) reduces to (Lifton et al., 2008):

$$239 \quad R_c = 14.3 \frac{M}{M_0} \cos^4 \lambda \quad (2)$$

240 For certain periods of the past, larger values of M imply cutoff rigidities larger than 14.3
 241 GV. In that case, we assume a log-log interpolation between R_c and the nucleon flux
 242 determined by the parameters of Lal-Stone for R_c values ranging between 14.3 and 25
 243 GV (Sandstrom et al., 1962).

244 In CREp, the spatial scaling of muogenic production is done using the parameters of
 245 (Stone, 2000) but includes the empirical muogenic/spallogenic production ratios
 246 determined by (Braucher et al., 2011) (Table 1). This was motivated by several lines of
 247 evidence indicating that the parameters of (Heisinger et al., 2002a, 2002b)

248 overestimated the muogenic production (Braucher et al., 2013, 2011; Kim and Englert,
249 2004).

250 **Table 1 - Default parameters used in CREp.** The relative muogenic production rates
251 from (Braucher et al, 2011) are only used in the Lal/Stone model, since the LSD models
252 use its own muon and neutron scaling procedure. Parameters are the same for both ^3He
253 and ^{10}Be .
254

Parameters	Value	Reference
Fast muon relative production rate at sea level high latitude (%)	0.87	Braucher et al., 2011
Slow muon relative production rate at sea level high latitude (%)	0.27	Braucher et al., 2011
Λ ($\text{g}\cdot\text{cm}^{-2}$) attenuation length for spallation in rock/soil	160	Gosse and Phillips, 2001
ρ ($\text{g}\cdot\text{cm}^{-3}$) - only used if the density is not provided.	2.7	Average value of continental crustal rocks
2)	7.746 $\times 10^{22}$	Finlay et al., 2010

257

258 The recently published LSD model (Lifton et al., 2014) derives scaling factors from
259 integrals of neutron and proton fluxes, calculated using the PHITS-based Analytical
260 Radiation Model in the Atmosphere (PARMA model; Sato et al., 2008), in conjunction
261 with the most up to date neutron and proton excitation functions. In its original version,
262 the LSD model proposes to either compute scaling factors for spallation only, or to take
263 into account specific cross sections for each particle, nuclide and target element. The
264 LSD version implemented in CREp only considers this second approach and computes
265 the spatial scaling with specific cross sections for each nuclide (^{10}Be and ^3He).
266 Consequently, ^3He and ^{10}Be follow different spatial scaling laws with this LSD model
267 (see Figure 8 in (Lifton et al., 2014)).

268 LSD and Lal/Stone were the two retained models because they presently show the best
 269 ability to describe the evolution of production rates in time and space relatively to the
 270 other models based on neutron-monitor data (Section 1.2) (Borchers et al., 2016).

271 *2.3. Atmosphere models*

272 Two atmospheric models are proposed in the CREp program. First, the ERA-40
 273 atmosphere 2D model, based on a re-analysis of meteorological data over 45 years
 274 between 1957 and 2002 produced by the European Centre for Medium-Range Weather
 275 Forecasts (Uppala et al., 2005). The ERA-40 database provides a local atmospheric
 276 pressure on any location of the Earth surface. ERA-40 notably describes quite
 277 accurately the local peculiarities of the present-day pressure field. The CREp program
 278 uses the Lifton et al. (2014) implementation of this atmospheric dataset, at a spatial
 279 resolution of 125 km. This implemented version of ERA-40 is a combination of a sea
 280 level pressure and a 1000 hPa temperature grids, used to compute the pressure at any
 281 elevation.

282 ii) Alternatively, users may choose to use the U.S. Standard Atmosphere 1D model
 283 (N.O.A.A., 1976), that computes the pressure $P(z)$ at an altitude z , according to:

$$284 \quad P(z) = P_s \exp \left\{ -\frac{gM}{R} [\ln T_s - \ln(T_s - z)] \right\} \quad (3)$$

285 with sea level pressure $P_s=1013.25$ hPa, sea level temperature $T_s= 288.15$ K, and a
 286 standard lapse rate $\xi = 0.0065$ K.m⁻¹. g is the gravity acceleration, R the gas constant,
 287 and M the molar weight of air, yielding $gM/R=0.03417$ K.m⁻¹.

288 It is worth noting that this 1D model does not take into account the local peculiarities
 289 of the atmospheric pressure field and may lead to significant biases in some particular
 290 regions, such as Antarctica (Stone, 2000). CREp users should thus use this atmosphere

291 model with caution.

292

293 *2.4. Geomagnetic databases*

294 To account for the impact of the past geomagnetic activity on the production, CREP
 295 allows choosing between different geomagnetic records or to import any original
 296 Virtual Axial Dipole Moment (VADM) dataset. The origin of the data implemented in
 297 the software and their associated parameterization in the scaling models are summarized
 298 in Table 2.

299

300

301

302 **Table 2 - Geomagnetic reconstructions used in the scaling models of the CREP**
 303 **program**

304

Geomagnetic reconstruction	Reference	Period	Geomagnetic dataset
Atmospheric ¹⁰ Be-based VADM ^a	Muscheler et al. (2005)	0 - 60 ka	Muscheler et al., 2005
		60 - 2000 ka	Valet et al., 2005
LSD framework	Lifton et al. (2014)	0 - 7 ka	CALS7k.2 and CALS3k.3 (Korte and Constable, 2005 ; Korte et al., 2009) ^b
		7-18 ka	GLOPIS-75 (Laj et al., 2004)
		18 - 2000 ka	PADM2M (Ziegler et al., 2011)
Lifton 2016 VDM	Lifton (2016)	0-14 ka	Pavon-Carrasco et al., 2014
		14-75 ka	GLOPIS-75 (Laj et al., 2004)
		75-2000 ka	PADM2M (Ziegler et al., 2011)

^a VADM: Virtual Axial Dipolar Moment. All the dipolar moments are normalized to the present value of 7.746×10^{22} A.m² (Finlay et al., 2010)

^b spatialised cutoff rigidity for the LSD model (Lifton et al., 2014) and global cutoff rigidity derived from the VDM for the "Lal modified" model (Balco et al., 2008; Lal, 1991; Stone, 2000)

305

307

308 The three proposed geomagnetic databases included in CREP are: (i) the atmospheric
 309 ¹⁰Be-based VADM (Muscheler et al. 2005), ii) the geomagnetic framework initially
 310 published in the LSD model (Lifton et al., 2014) (a composite database that combines

311 the geomagnetic reconstructions of the CALS7k.2 and CALS3k.3 model for the 0 - 7 ka
312 BP period (Korte et al., 2009, 2005), the GLOPIS-75 reconstruction for the 7 to 18 ka
313 BP period and the PADM2M reconstruction (Ziegler et al., 2011) from 18 ka to 2 Ma
314 BP), and iii) the recent composite VDM/VADM record proposed by (Lifton, 2016). All
315 the original publications used to build these original geomagnetic records are given in
316 Table 2. Few adjustments have been done to include these database in CREp: the
317 Muscheler et al. (2005) and the GLOPIS-75 databases are tuned to the GICC05
318 timescale (Svensson et al., 2008) using the g2n Matlab ©function from Obrochta et al.
319 (2014). To improve the computation speed, the Muscheler et al. (2005) record has been
320 interpolated on a 50 years time step. For ages older than 60 ka, this reconstruction has
321 been extended with the SINT-2000 record with a 1 kyr time step. The (Lifton, 2016)
322 composite VDM/VADM has a varying time step but the average value for the last 200
323 ka is 200 yr. The LSD framework presents a time step of 100 yr until 50 ka and 1 kyr
324 beyond.

325 If the LSD scaling model is selected with the LSD geomagnetic framework, the CREp
326 calculator uses the LSD Matlab© code of Lifton et al. (2014) in its original form. The
327 "Lal modified" model and the LSD model each use different geomagnetic inputs for the
328 0-7 ka period: while the "Lal modified" model always uses the M/M_0 ratio (the VDM or
329 VADM normalized to the value in 2010), the LSD model only uses it beyond 7 ka BP.
330 Between 0 and 7 ka BP, the LSD model directly uses globally gridded cutoff rigidities
331 from CALS7k.2 and CALS3k.3. Therefore, if the users select the LSD model with the
332 Lifton's (2016) VDM/VADM or the atmospheric ^{10}Be VADM (Muscheler et al. 2005)
333 (or another VDM database), cut-off rigidities are first derived from the M/M_0 ratios over

334 the whole time span. For this calculation, the program uses the equation 2 proposed by
335 Lifton et al. (2014).

336 Conversely, when using the "Lal modified" model with the LSD geomagnetic
337 framework, global M/M_0 values derived from CALS7k.2 and CALS3k.3 are used over
338 the 0-7 ka BP period, leading to a loss of information about the higher order local
339 influences on the geomagnetic field.

340

341 *2.5. Sample thickness and erosion rate correction*

342 CREp corrects the depth attenuation calculating the depth normalisation factor f_E . f_E is
343 computed by integrating the average production over the sample thickness, using a
344 single exponential spallation attenuation equation (Balco et al., 2008):

$$345 \quad f_E = \frac{\Lambda}{\rho \times E} \left[1 - e^{-\frac{\rho \times E}{\Lambda}} \right] \quad (4)$$

346 E being the sample thickness (cm), Λ the spallation attenuation length (g.cm^{-2}), ρ (g.cm^{-3})
347 the density. ρ and E must be assigned by the users. Although Λ theoretically varies
348 with latitude and altitude (e.g. Marrero et al., 2016), CREp uses a default constant value
349 of 160 g.cm^{-2} (Gosse and Phillips, 2001) (Table 1). Given the limited range of these Λ
350 variations, this simplification is certainly not a source of inaccuracy in the present case.

351 It is also important to note that, in the current version of CREp, this thickness correction
352 does not account for deep muogenic production (although muons are considered at the
353 surface). In its present version, CREp is thus only suited to compute surface exposure
354 ages of samples having a reasonable thickness (typically less than 20 cm thick). For
355 thicker samples, an additional muonic correction should be included.

356 If the erosion of the sample is known and included by the user, CREp also corrects for

357 its effect by using the classical equation (6) published in (Lal, 1991), i.e. assuming
358 erosion has been constant over the exposure time.

359

360 *2.6. Shielding and topographic correction*

361 Several tools, such as the first CRONUS calculator (Balco et al., 2008)
362 (<http://hess.ess.washington.edu/>) offer simple and efficient means for computing the
363 shielding and topographic correction. Thus, CREp does not include a tool to compute
364 shielding factors (see Dunne et al., 1999 for details). It is necessary to enter this
365 previously computed correction in the input data.

366

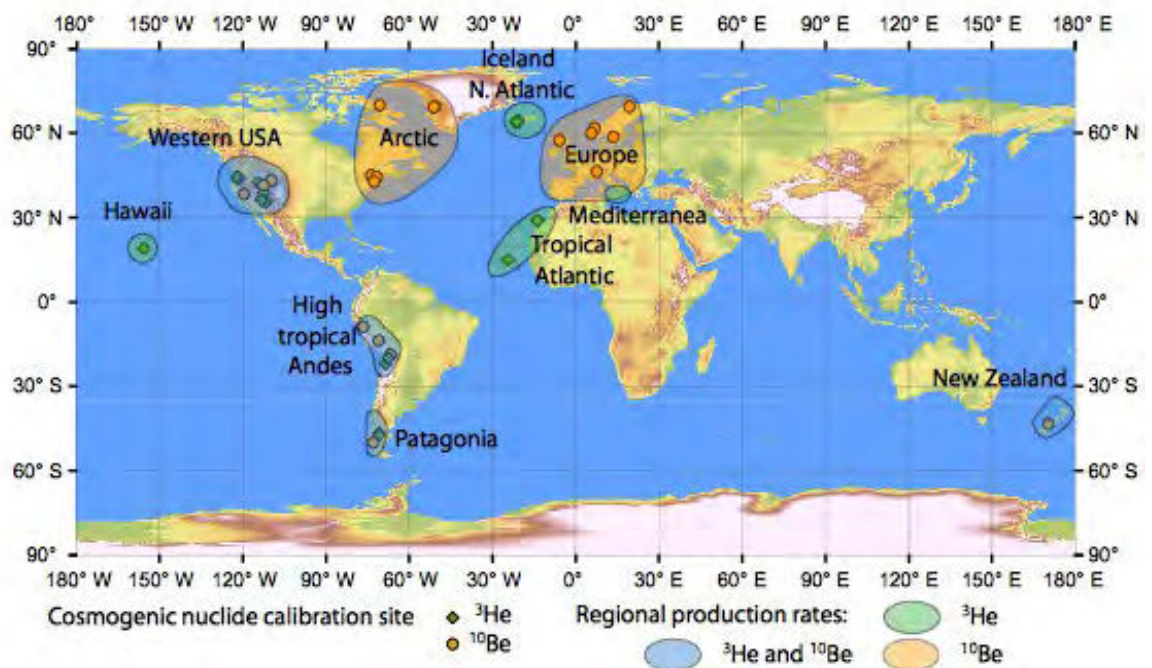
367 *2.7. Production rates*

368 The CREp program proposes different possibilities to select the SLHL production rate
369 involved in the computation of exposure ages. Users may either choose i) a worldwide
370 mean production rate, ii) a regional value, iii) a single local value, which can be chosen
371 among the existing dataset or imported by the user, or iv) any average from several
372 calibration sites selected by the user (Fig. 1).

373 All the production rates proposed in CREp are derived from the most complete
374 database of published calibration sites (ICE-D, see sections 3 and 4 below).

375 3. The ICE-D production rate calibration database

376 The CREp program makes use of an online database of production rate calibration data
 377 (<http://calibration.ice-d.org>) that we have developed as part of the ICE-D (Informal
 378 Cosmogenic-nuclide Exposure-age Database) project at <http://ice-d.org>. Figure 2 is a
 379 map displaying the global distribution of the ^3He and ^{10}Be calibration sites of the
 380 literature that are included in ICE-D.



382 **Figure 2 - Global map showing the distribution of the calibration sites for ^3He and**
 383 **^{10}Be production rates that are loaded from ICE-D to the CREp program. Contours**
 384 **of the "regions" defined in the present version of CREp are also drawn.**
 385

386

387 3.1. Motivation for creating ICE-D

388 Existing compilations of production rate calibration data (Balco et al., 2008; Borchers
 389 et al., 2016; Delunel et al., 2016; Heyman, 2014) have been distributed as spreadsheet
 390 files, typically as supplementary files to published journal articles. These files are (i)

391 incomplete, because they were developed at different times, and, in addition, each one
392 lacks some of the published production rate calibration data that were available at the
393 time it was published; (ii) inconsistent and in most cases known to contain errors and/or
394 omissions; and (iii) in general, limited to only the minimal set of numeric data necessary
395 to compute an apparent production rate from each nuclide concentration measurement.
396 Also, in some cases they are technically not available without a journal subscription,
397 although this is not a significant obstacle for most researchers.

398 This approach is weak for several reasons. First, researchers interested in working with
399 a comprehensive and up-to-date set of production rate calibration data must compile it
400 themselves from a variety of sources; this requires duplicative and redundant effort, and
401 also makes it very likely that compilations maintained by different researchers are
402 mutually inconsistent. Second, these compilations do not include supplementary
403 information, such as field photos or ancillary geochemical data, that would help
404 researchers evaluate the quality or reliability of various data sets. Third, it is difficult for
405 researchers to share efforts in this regard because each one maintains a spreadsheet that
406 is formatted to suit their preferred calculation methods or code.

407 The aim of the ICE-D database project is to improve this existing situation by
408 providing a single online database of all known production rate calibration data that has
409 the following properties. First, it should be updated often and checked for accuracy.
410 Second, it should contain only direct field observations or laboratory measurements,
411 excluding any interpreted or model-dependent parameters whose values might not be
412 generally agreed upon, or that might be calculated in a different way in future. Third, it
413 should be able to store not only the minimal numerical data needed to compute an
414 apparent production rate from a measured nuclide concentration, but also ancillary

415 information such as photos or field notes that would help researchers to evaluate site
416 suitability and data quality. Fourth, it should follow a client-server model such that the
417 raw data are maintained by a single server that can supply it to a wide variety of clients.
418 Our overall goal is that any interpretive calculations related to cosmogenic-nuclide
419 production rate calculations will always be able to address the current state of the
420 database, rather than addressing static, locally stored data sets that might be obsolete or
421 mutually inconsistent. Furthermore, additions, corrections, or improvements to the
422 existing data set can simply be added to one database rather than incurring redundant
423 efforts by many researchers. Here we describe our strategy for accomplishing these
424 goals.

425

426 *3.2. ICE-D is designed to be accurate and complete*

427 To achieve this goal, we have incorporated data from all published production rate
428 calibration studies for ^{10}Be and ^3He that are known to us at present, with the exception
429 of few studies that have been shown to be affected by significant flaws or inaccuracies
430 (Kubik et al., 1998; Kurz et al., 1990). We relied on the original publications as well as
431 any subsequent, published or unpublished, re-evaluation or re-measurement of
432 observations in the original paper. For example, various researchers involved in the
433 CRONUS-Earth or CRONUS-EU projects, as part of those projects, re-evaluated or re-
434 measured samples from previously described calibration sites (e.g. Phillips et al., 2016).
435 In some cases, we corrected errors known to exist in original publications, such as few
436 standardization issues for ^{10}Be (Balco et al., 2008; Nishiizumi et al., 2007). When
437 necessary, we also included radiogenic ^4He corrections in the case of ^3He (Blard and
438 Farley, 2008). In other cases, we added supporting data, documentation, or photographs

439 that were not published, but were available to us via other sources. In some cases we
440 have recalculated independent age constraints that were based on out-of-date
441 radiocarbon calibrations, using IntCal13 (Reimer et al., 2013). It is certainly possible
442 that errors or omissions that we are not aware of remain in the database. In order to
443 facilitate locating and correcting these errors, we provide through the ICE-D project a
444 web interface, separate and distinct from the CREp online calculator, that is indexed
445 geographically and by publication. This interface (<http://calibration.ice-d.org>) allows
446 direct examination of all data in the database. Thus, even though, as discussed above,
447 some elements of the data set are not traceable to publications, all elements can be
448 publicly examined for purposes of quality control. Any errors or omissions should be
449 brought to our attention (specifically, that of authors G. Balco and P.-H. Blard) so that
450 they can be corrected.

451

452 *3.3. Direct observations only*

453 We aim to record only direct observations and measurements in the database itself.
454 Interpretive or model-dependent decisions or assumptions -- for example, which
455 samples to include in a calibration data set, or how best to compute snow cover
456 corrections -- are not hard-coded into the database. These should instead be
457 incorporated into client software (such as CREp) that uses the database. For example,
458 we have not renormalized ^{10}Be measurements to a common standard, but instead have
459 recorded concentrations as they were originally measured along with information about
460 the standardization that was used. Another example relates to thickness and shielding
461 corrections. Where source papers reported correction factors that combined information
462 about, for example, sample thickness, geometric shielding, and/or cover by snow or

463 vegetation, we have decomposed these into separate observations. These are direct
464 observations, in contrast to model-dependent attenuation factors, which might be
465 recalculated in a different way in future. On the other hand, an example of an area
466 where we were not able to strictly achieve this goal relates to topographic/geometric
467 shielding factors. Although we recorded direct measurements of surface and horizon
468 geometry (e.g., azimuth/elevation pairs recorded in the field) where they were available
469 to us, this information is not available, and likely not recoverable, for the majority of
470 published data. Thus, in most cases we have reported a derived topographic/geometric
471 shielding factor rather than direct geometric observations. Fortunately, this correction is
472 significantly less than 2% for the majority of the calibration samples and thus does not
473 represent a significant source of inaccuracy/uncertainty.

474

475 *3.4. Ancillary information*

476 When possible, we incorporated field and analytical information in excess of the
477 minimum set of numerical data needed to compute an apparent production rate from a
478 nuclide concentration measurement. This includes information such as photographs,
479 lithological information, field notes, dates of sample collection, names of researchers
480 responsible for sample collection or analysis and other information or background data
481 that could potentially be useful in data evaluation or scaling scheme development. In
482 most such cases, we had this information because one of us was directly involved in
483 sample collection or analysis; in some other cases, this information could be gleaned
484 from publications. Thus, although this aspect of the database is incomplete at present, it
485 is designed to incorporate a wide array of background information ancillary to the actual
486 published data but potentially useful for future production rate calibration research.

487

488 *3.5. Client-server architecture*

489 Our aim here is to make the information in the database widely available to any
490 software that aims to do calculations related to production rate calibration or surface
491 exposure dating. To achieve this, we use an industry-standard model for client-server
492 database design that is commonly used in website back ends and data management
493 systems, and is interoperable with nearly all currently available computational and data-
494 management software. The database itself occupies a MySQL server that is currently
495 hosted by the Google Cloud SQL service (<http://cloud.google.com/sql>). As this is a
496 standard database format, however, it is not fundamentally linked to any particular
497 hosting service, and any equivalent service could be used. The structure and
498 organization of the database can be examined via the browsing interface at
499 <http://calibration.ice-d.org>. The database is accessible (subject to reasonable security
500 restrictions) to any client software capable of making a SQL query, which includes
501 essentially all modern programming languages as well as commonly used desktop
502 calculation environments such as MATLAB, Mathematica, iPython, or R. The online
503 version of the CREp calculator as well as the web server at <http://calibration.ice-d.org>
504 are two examples of such client software.

505 **4. Implementation of the ICE-D production rates in CREp**

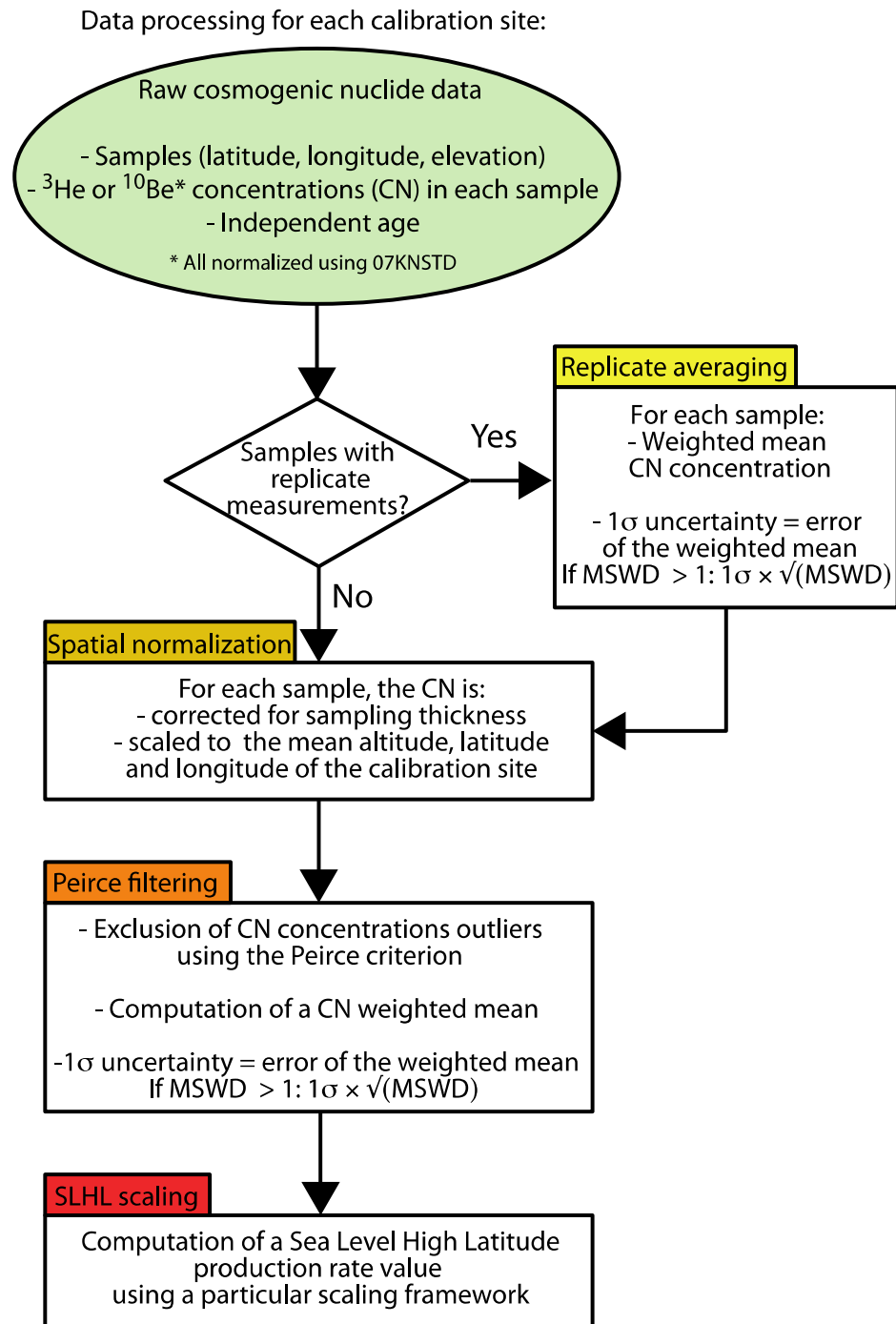
506 The CREp website client daily access to the content of the ICE-D calibration database
507 to read the calibration data, such as any modification of the ICE-D database is almost
508 instantaneously incorporated in CREp.

509 CREp incorporates these ^3He and ^{10}Be calibration data to compute local, regional and
510 global production rates. Note that CREp only includes in its dataset the calibration sites
511 having multiple surface samples. Additionally, CREp only includes landforms whose
512 age is constrained by at least 2 bracketing independent ages, or that are directly dated
513 (e.g. Ar-Ar or K-Ar-dated lava flows, or ^{14}C from wood material in a landslide); sites
514 having only one limiting (maximum or minimum) age are excluded. These default
515 arbitrary choices can however be easily overcome: for this, users have to use the "Load
516 your own calibration data" function of CREp.

517

518 *4.1. Calculation of a production rate from each calibration site*

519 CREp calculates a production rate from each calibration site applying the following
520 flow chart (Fig. 3):



521

522 **Figure 3 - Flow chart showing the raw data processing to compute a SLHL**

523

production rate from each calibration site

524

525 - Multiple aliquots averaging: If several ^3He or ^{10}Be laboratory measurements are
526 reported for a single sample, an error-weighted-mean concentration and its associated
527 error weighted uncertainty are computed from those measurements. The mean squared
528 weighted deviation (MSWD, also known as the reduced χ^2) is also calculated to test the
529 data distribution. If $\text{MSWD} > 1$, the error-weighted mean is corrected for this
530 overdispersion by multiplying the uncertainty by $\sqrt{\text{MSWD}}$ (Douglass et al., 2006;
531 York, 1966).

532 - Spatial normalization: For each sample, the cosmogenic nuclide concentration is then
533 corrected for sampling thickness (normalized to the surface, i.e. null thickness),
534 topographic shielding and scaled to a mean altitude, latitude and longitude
535 representative of each calibration site. In order to be internally consistent, this local
536 normalization scaling uses the scaling procedure (scheme, atmosphere model,
537 geomagnetic database) corresponding to the choice of the user. Note that the spatial
538 range of all the ICE-D calibration samples is narrow, implying that this correction is
539 rather limited (less than 5%) between the different samples. This normalization is very
540 useful for analyzing the sample distribution on each site and detecting outliers
541 (that could be affected by inheritance or erosion).

542 - Outlier removal and weighted-mean computation: For each calibration site having
543 more than 2 samples, the distribution of the sample concentrations is evaluated applying
544 the criterion of Peirce (Peirce, 1852; Ross, 2003). This filtering is motivated to exclude
545 samples that are affected by erosion or inheritance (or an undetected analytical bias).
546 Then, a weighted mean concentration is computed for each calibration site, and the
547 associated one-sigma uncertainty is the standard error of the weighted mean σ_w . This is
548 justified since these surface samples are similar to multiple measurements of the same

549 physical property, i.e. the cosmogenic nuclide concentration of a supposedly
550 synchronous geomorphological surface. Note that, in the case of sites having MSWD
551 larger than 1, σ_w is multiplied by $\sqrt{(\text{MSWD})}$ to account for this overdispersion
552 (Douglass et al., 2006; York, 1966).

553 The individual P_3 's calculated in this way range from 81 ± 5 to 185 ± 12 $\text{at.g}^{-1}.\text{yr}^{-1}$, for
554 global averages of 116 ± 17 to 123 ± 11 $\text{at.g}^{-1}.\text{yr}^{-1}$ (uncertainties attached to the global
555 means are weighted standard deviations), depending on the scaling framework used
556 (Table 4). Similarly, P_{10} 's range from 3.27 ± 0.09 to 5.06 ± 0.30 $\text{at.g}^{-1}.\text{yr}^{-1}$, for global
557 averages of 3.98 ± 0.23 to 4.16 ± 0.20 $\text{at.g}^{-1}.\text{yr}^{-1}$ (uncertainty attached to the global means
558 are weighted standard deviations), depending on the scaling framework used (Table 5).

559

560 *4.2. Arbitrary combination of any calibration sites*

561 CREp allows selecting any arbitrary combination of production rates from the
562 calibration data available in ICE-D. This option is proposed for flexibility and
563 transparency, to permit users testing different combination of production rates, and the
564 impact of this choice on the computed exposure ages. For this, users simply have to
565 select the sites by clicking on the displayed online map (<http://crep.cirp.cnr-nancy.fr/#/production-rate>)
566 (Fig. iv in Appendix 2). If more than one site is selected,
567 CREp computes the weighted mean of the selected production rates and the MSWD.
568 The uncertainty associated with this selection of production rates is evaluated by taking
569 the largest value between the error of the weighted mean and the weighted mean
570 standard deviation. It is worth noting that this selection function does not perform any
571 outlier exclusion since it is designed to allow the use of any arbitrary combination of
572 calibration data.

573

574 *4.3. Calculation of regional production rates*

575 Several studies (e.g. Balco et al., 2009; Martin et al., 2015; Stroeven et al., 2015)
576 proposed the use of "regionally averaged" production rate. This approach aims to
577 overcome several caveats, such as the relative inability of scaling schemes to account
578 for local peculiarities in certain regions (due for example from atmospheric or
579 geomagnetic anomalies that have not been adequately modeled). Moreover, regionally
580 averaged rates have the advantage to be statistically more robust than single local
581 calibration sites, and *may* be more likely to account for unrecognized
582 geologic/geomorphic inaccuracies (e.g. erosion, partial shielding, inaccurate dating)
583 associated with particular sites.

584 CREp offers the possibility to use this approach, by selecting pre-computed regional
585 production rates yielded by the average of several local calibration sites. To obtain these
586 average regional rates, CREp applies the following procedure: if the region has only 2
587 calibration sites, the weighted average of the 2 sites and its associated error are
588 computed.

589 If the region includes 3 or more calibration sites, these site-specific SLHL production
590 rates are filtered applying the Peirce criterion (Peirce, 1852; Ross, 2003). For each
591 regional dataset, CREp then computes the weighted mean, the weighted standard
592 deviation as well as the error of the weighted mean. The largest of these uncertainties is
593 then used as the error of the regional dataset.

594 The limits of these regions were determined by taking into account the spatial
595 distribution of the present-day calibration dataset. Since several lithologies are not
596 suited for both ^{10}Be and ^3He , some regions are nuclides specific (e.g. basaltic terrains of

597 Iceland and Hawaii are only defined for ^3He). The boundaries of these regions will
598 probably evolve in the future, with the addition of new calibration data.

599

600 *4.4. Calculation of global mean production rates*

601 The present version of CREp computes a global weighted average and the associated
602 standard deviation taking into account all the existing site-specific production rates,
603 without excluding any statistical outlier. This choice is motivated by the fact that a
604 global average is supposed to represent the global scatter of the dataset, which may
605 result from any source of variability (analytical, geological, inability of scaling scheme
606 to adequately correct for spatial and temporal scaling). Also, rejection criteria are
607 generally based on the assumption that the data are independent and normally
608 distributed. Given the remaining different sources of error (scaling, geology), it is
609 plausible that the actual distribution is not normal and that some inaccuracies are
610 scaling dependent. Moreover, given the large size of the existing dataset (31 calibration
611 sites for ^{10}Be and 23 sites for ^3He), the exclusion of outliers should not have a big effect.

612 **5. Discussion - production rates and uncertainties**

613 *5.1. Comparison with previous estimates*

614 The SLHL production rates compiled in CREp from the global ICE-D database have
615 values that are comparable with recent compilation (Borchers et al., 2016; Delunel et
616 al., 2016; Heyman, 2014; Marrero et al., 2016). A detailed comparison of the resulting
617 values is useless, however, since there are some differences in the data treatment and in
618 the scaling framework used. Since the CREp-ICE-D tool proposes the largest existing
619 calibration dataset, we think that it is worth focusing on the efficiency of the different
620 scaling frameworks by looking at the statistical dispersion of the computed SLHL rates.

621

622 *5.2. Dispersion of the world calibration database*

623 The efficiencies of 12 different scaling procedures (2 scaling schemes, 2 different
624 atmospheric models and 3 geomagnetic databases) have been evaluated by calculating
625 several statistical parameters. They were computed by taking into account all the
626 individual SLHL production rates derived from the ICE-D global database, which
627 represent 31 calibration sites for ^{10}Be and 23 sites for ^3He .

628 Table 3 summarizes the 12 different scaling procedures that are tested here to scale the
629 global P_3 and P_{10} calibration datasets of ICE-D.

630

631 **Table 3 - Description of the 12 standard scaling combinations available in CREp.**

632 **The Lal/Stone time dependent model has been described in successive incremental**
633 **studies (Balco et al., 2008; Lal, 1991; Stone, 2000). LSD is the model proposed by**
634 **(Lifton et al., 2014). The standard atmosphere model is from (N.O.A.A., 1976),**
635 **while the ERA40 atmosphere model is described in (Uppala et al., 2005). The**

636 "Atmospheric¹⁰BeVDM" combines the geomagnetic reconstruction of (Muscheler
 637 et al., 2005) with the one of (Valet et al., 2005). The VDM called "LSD framework"
 638 is described in (Lifton et al., 2014) while the "Lifton 2016 VDM" is described in
 639 (Lifton, 2016).

Scaling shortname	Scaling scheme	Atmosphere model	Geomagnetic database
LAL-STD-Musch	Lal/Stone time dependent	Standard	Atmospheric ¹⁰ Be VDM
LAL-STD-Lift	Lal/Stone time dependent	Standard	Lifton 2016 VDM
LAL-STD-L	Lal/Stone time dependent	Standard	LSD framework
LAL-ERA-Musch	Lal/Stone time dependent	ERA40	Atmospheric ¹⁰ Be VDM
LAL-ERA-Lift	Lal/Stone time dependent	ERA40	Lifton 2016 VDM
LAL-ERA-L	Lal/Stone time dependent	ERA40	LSD framework
LSD-STD-Musch	LSD	Standard	Atmospheric ¹⁰ Be VDM
LSD-STD-Lift	LSD	Standard	Lifton 2016 VDM
LSD-STD-L	LSD	Standard	LSD framework
LSD-ERA-Musch	LSD	ERA40	Atmospheric ¹⁰ Be VDM
LSD-ERA-Lift	LSD	ERA40	Lifton 2016 VDM
LSD-ERA-L	LSD	ERA40	LSD framework

640

641

642 Table 4 and 5 displays all the P_3 (n=23) and P_{10} (n=31) computed from the 12 different
 643 scaling procedures. Table 6 presents the regional P_3 and P_{10} values as well as the
 644 calibration sites included in each region.

645

646 **Table 4 - Global SLHL P₃ dataset computed with 12 scaling procedures (n = 23).** Data from (Ackert et al., 2003; Amidon and Farley, 2011; P. Blard et al., 2006; Blard et al., 2005, 2013; Cerling and Craig, 1994; Delunel et al., 2016; Dunai and Wijbrans, 2000; Fenton and Niedermann, 2014; Fenton et al., 2013; Foeken et al., 2012; Goehring et al., 2010; Licciardi et al., 1999; Poreda and Cerling, 1992).

647

648

Site name	Reference	Latitude (°)	Longitude (°)	Altitude (masl)	Age (years)	To	LAL-STD-Musch	LAL-STD-Lit	LAL-STD-L	LAL-ERA-Musch	LAL-ERA-Lit	LAL-ERA-L	LSD-STD-Musch	LSD-STD-Lit	LSD-STD-L	LSD-ERA-Musch	LSD-ERA-Lit	LSD-ERA-L
ROPINTU	Ackert et al., 2003	-47.07	-70.90	903	67800	3000	139 ± 7	138 ± 7	134 ± 7	134 ± 7	131 ± 7	131 ± 7	137 ± 7	137 ± 7	133 ± 7	132 ± 7	132 ± 7	132 ± 7
CERRO HIGH	Ackert et al., 2003	-46.70	-70.75	530	107600	2800	138 ± 4	137 ± 4	138 ± 4	134 ± 4	134 ± 4	134 ± 4	138 ± 4	138 ± 4	134 ± 4	138 ± 4	138 ± 4	138 ± 4
LAKE	Blard et al., 2006	-47.15	-70.75	530	107600	2800	138 ± 4	137 ± 4	138 ± 4	134 ± 4	134 ± 4	134 ± 4	138 ± 4	138 ± 4	134 ± 4	138 ± 4	138 ± 4	138 ± 4
SAN PEDRO	Delunel et al., 2016	-21.93	-68.51	3390	107000	11600	121 ± 13	119 ± 13	126 ± 14	119 ± 13	119 ± 13	119 ± 13	110 ± 12	110 ± 12	103 ± 11	127 ± 14	120 ± 13	121 ± 12
TUNUPA	Blard et al., 2013a	-19.89	-67.62	3814	15200	540	128 ± 5	122 ± 5	137 ± 5	133 ± 5	133 ± 5	133 ± 5	120 ± 5	115 ± 4	110 ± 4	132 ± 5	127 ± 5	121 ± 5
FOGO	Foeken et al., 2012	14.89	-24.48	222	129500	7000	89 ± 5	84 ± 5	90 ± 5	85 ± 5	81 ± 5	81 ± 5	101 ± 6	96 ± 6	91 ± 6	102 ± 6	97 ± 6	93 ± 6
KAUNA	Blard et al., 2006	19.06	-155.55	60	82900	90	151 ± 10	145 ± 10	136 ± 9	153 ± 10	147 ± 10	138 ± 9	181 ± 12	169 ± 11	161 ± 11	185 ± 12	172 ± 11	164 ± 11
ATALAYA	Dunai and Wijbrans, 2000	28.92	-13.83	35	281060	9500	102 ± 4	98 ± 4	106 ± 4	102 ± 4	100 ± 4	100 ± 4	122 ± 5	114 ± 4	112 ± 4	127 ± 5	118 ± 5	116 ± 4
TAHLICHE	Dunai and Wijbrans, 2000	29.01	-13.54	197	152060	13000	102 ± 9	99 ± 9	105 ± 9	102 ± 9	102 ± 9	102 ± 9	120 ± 11	114 ± 10	110 ± 10	125 ± 11	118 ± 11	115 ± 10
SP	Fenton et al., 2013; Fenton and Niedermann, 2014	35.60	-111.63	1831	72000	2000	106 ± 5	105 ± 5	99 ± 4	112 ± 5	110 ± 5	110 ± 5	108 ± 5	105 ± 5	97 ± 4	112 ± 5	111 ± 5	103 ± 5
UNIBARTEN	Fenton et al., 2013; Fenton and Niedermann, 2014	36.33	-113.83	1831	72000	2000	106 ± 5	105 ± 5	99 ± 4	112 ± 5	110 ± 5	110 ± 5	108 ± 5	105 ± 5	97 ± 4	112 ± 5	111 ± 5	103 ± 5
UPBARTEN	Fenton et al., 2013; Fenton and Niedermann, 2014	36.24	-113.49	1768	93000	5000	101 ± 6	100 ± 6	113 ± 7	107 ± 6	107 ± 6	107 ± 6	107 ± 6	104 ± 6	110 ± 7	110 ± 7	104 ± 6	104 ± 6
NAVE	Blard et al., 2006; Blard et al., 2006; Cerling and Craig, 1992;	37.85	-14.84	820	33060	2000	111 ± 12	108 ± 12	114 ± 12	111 ± 12	109 ± 12	109 ± 12	117 ± 13	115 ± 13	111 ± 12	120 ± 13	117 ± 13	114 ± 12
TABERNACLE	Goehring et al., 2010	38.93	-112.52	1458	18200	300	116 ± 2	116 ± 2	115 ± 2	121 ± 2	121 ± 2	121 ± 2	117 ± 2	117 ± 2	114 ± 2	122 ± 2	122 ± 2	120 ± 2
SNAKE	Amidon and Farley, 2011	42.64	-114.16	1039	18300	300	142 ± 6	142 ± 6	141 ± 6	147 ± 6	146 ± 6	146 ± 6	144 ± 6	144 ± 6	142 ± 6	148 ± 6	147 ± 6	147 ± 6
BUTTE	Licciardi et al., 1999	43.95	-121.38	1282	7057	90	115 ± 4	112 ± 4	115 ± 4	115 ± 4	115 ± 4	115 ± 4	114 ± 4	114 ± 4	108 ± 3	117 ± 4	113 ± 4	111 ± 4
BELKNAP	Licciardi et al., 1999	44.24	-121.86	1524	2759	90	111 ± 6	105 ± 5	113 ± 6	108 ± 6	107 ± 6	107 ± 6	107 ± 6	100 ± 5	103 ± 5	110 ± 6	103 ± 5	106 ± 6
YAPOAH	Licciardi et al., 1999; Cerling and Craig, 1994	44.27	-121.79	1562	2500	400	111 ± 18	105 ± 17	104 ± 17	114 ± 18	109 ± 17	109 ± 17	107 ± 17	102 ± 16	102 ± 16	103 ± 16	104 ± 17	104 ± 17
LEITIA	Licciardi et al., 1999	63.86	-114.79	268	5210	110	137 ± 6	136 ± 6	139 ± 6	130 ± 5	130 ± 5	130 ± 5	133 ± 5	133 ± 5	132 ± 5	134 ± 5	134 ± 5	124 ± 5
BURFELL	Licciardi et al., 2006	63.98	-121.47	268	5210	110	137 ± 6	136 ± 6	139 ± 6	130 ± 5	130 ± 5	130 ± 5	133 ± 5	133 ± 5	132 ± 5	134 ± 5	134 ± 5	124 ± 5
DINGVA	Licciardi et al., 2006	64.09	-21.74	35	8060	120	137 ± 4	137 ± 4	137 ± 4	128 ± 4	128 ± 4	128 ± 4	128 ± 4	128 ± 4	128 ± 4	128 ± 4	119 ± 3	119 ± 3
LAMBA	Licciardi et al., 2006	64.16	-21.04	124	10390	80	138 ± 5	138 ± 5	129 ± 4	129 ± 4	129 ± 4	129 ± 4	129 ± 4	129 ± 4	129 ± 4	121 ± 4	121 ± 4	121 ± 4
		64.37	-20.55	452	4040	250	128 ± 10	128 ± 10	119 ± 9	119 ± 9	119 ± 9	119 ± 9	122 ± 10	122 ± 10	122 ± 10	114 ± 9	114 ± 9	114 ± 9

649

650

651

652

653

654

655

656

657

658

659

660

Table 5 - Global SLHL P₁₀ dataset computed with 12 scaling procedures (n = 31). Data from (Balco et al., 2009; Borchers et al., 2016; Briner et al., 2012, 2006; Claude et al., 2014; Farber et al., 2005; Fenton et al., 2011; Goehring et al., 2012; Kaplan et al., 2011; Kelly et al., 2015; Lifton et al., 2015; Martin et al., 1989; Nishiizumi et al., 1989; Phillips et al., 2010; Putnam et al., 2010; Young et al., 2013)

Site name	Reference	Latitude (°)	Longitude (°)	Altitude (masl)	Age (years)	σ	LAL-STD-Musch	LAL-STD-L	LAL-ERA-Musch	LAL-ERA-L	LSD-STD-Musch	LSD-STD-L	LSD-ERA-Musch	LSD-ERA-L
BANDERA	Kaplan et al., 2011	-50.20	-72.70	220	12825	480	4.25 ± 0.16	4.02 ± 0.16	4.02 ± 0.16	4.02 ± 0.16	4.26 ± 0.17	4.26 ± 0.17	4.08 ± 0.16	4.05 ± 0.16
BST	Puham et al., 2010	-44.04	170.12	841.8	18200	200	4.06 ± 0.06	4.02 ± 0.06	4.02 ± 0.06	4.01 ± 0.06	4.04 ± 0.06	4.04 ± 0.06	4.14 ± 0.06	4.1 ± 0.06
MACAULAY	Puham et al., 2010	-43.58	170.61	1028	9834	50	4.12 ± 0.04	3.98 ± 0.04	3.98 ± 0.04	4.03 ± 0.04	4.15 ± 0.04	4.15 ± 0.04	4.19 ± 0.04	4.11 ± 0.04
CHILDE	Phillips et al., 2010	-18.85	-70.69	1410	12300	100	3.91 ± 0.16	3.78 ± 0.17	3.95 ± 0.17	4.04 ± 0.16	3.73 ± 0.17	3.73 ± 0.17	4.05 ± 0.16	4.11 ± 0.16
HUANCANEZA	Kohler et al., 2015; Phillips et al., 2016	-13.95	-70.69	4888	4888	0	4.05 ± 0.11	3.65 ± 0.11	3.65 ± 0.11	4.01 ± 0.18	3.95 ± 0.18	3.95 ± 0.18	4.35 ± 0.23	4.11 ± 0.18
BRECOON	Farber et al., 2005	-9.65	-77.36	4045	13000	100	4.18 ± 0.12	4.05 ± 0.11	4.51 ± 0.13	4.37 ± 0.12	4.26 ± 0.12	4.41 ± 0.11	4.63 ± 0.13	4.35 ± 0.12
BABOON	Borchers et al., 2016	37.17	-118.62	3385	13300	250	3.8 ± 0.15	3.72 ± 0.14	3.66 ± 0.14	3.83 ± 0.15	3.72 ± 0.14	3.84 ± 0.14	3.72 ± 0.14	3.73 ± 0.14
STARR	Borchers et al., 2016; Nishiizumi et al., 1989; Balco et al., 2008	37.42	-118.77	3556	19750	500	4.13 ± 0.32	4.07 ± 0.31	4.03 ± 0.31	4.37 ± 0.34	3.97 ± 0.3	3.91 ± 0.3	3.81 ± 0.29	4.22 ± 0.32
GREENS	Borchers et al., 2016; Nishiizumi et al., 1989; Balco et al., 2008	37.98	-119.30	3175	19750	500	3.72 ± 0.41	3.65 ± 0.4	3.62 ± 0.4	3.92 ± 0.43	3.81 ± 0.39	3.67 ± 0.38	3.82 ± 0.42	3.76 ± 0.41
PPHYS	Lifton et al., 2015; Borchers et al., 2016	41.26	-122.48	1603	18300	300	4.05 ± 0.07	4.08 ± 0.07	4.05 ± 0.07	4.27 ± 0.07	4.07 ± 0.07	4.12 ± 0.07	4.33 ± 0.07	4.25 ± 0.07
GLASH	Balco et al., 2009	43.01	-72.33	182	15145	300	4.05 ± 0.11	4.03 ± 0.11	4.01 ± 0.11	4.13 ± 0.11	4.11 ± 0.11	4.27 ± 0.11	4.41 ± 0.12	4.35 ± 0.11
TITCOMB	Gesse et al., 1995; Borchers et al., 2016; Balco et al., 2008	44.29	-109.64	3231	12100	700	4.86 ± 0.29	4.79 ± 0.28	4.72 ± 0.28	5.06 ± 0.3	4.89 ± 0.29	4.92 ± 0.29	4.44 ± 0.26	4.55 ± 0.27
SLAM	Balco et al., 2009; Borchers et al., 2016	44.31	-71.76	37	13900	250	4.04 ± 0.12	4.01 ± 0.12	3.99 ± 0.12	4.08 ± 0.12	4.05 ± 0.12	4.19 ± 0.12	4.26 ± 0.12	4.24 ± 0.12
BEECH	Balco et al., 2009; Borchers et al., 2016	44.31	-71.58	412	13900	250	4.18 ± 0.09	4.15 ± 0.09	4.12 ± 0.09	4.22 ± 0.09	4.16 ± 0.09	4.32 ± 0.09	4.31 ± 0.09	4.43 ± 0.11
CHILDE	Phillips et al., 2010	46.92	-71.85	1410	13320	113	4.02 ± 0.11	3.99 ± 0.11	3.97 ± 0.11	4.11 ± 0.12	4.08 ± 0.11	4.04 ± 0.11	4.18 ± 0.12	4.14 ± 0.11
KYPASS	Chardle et al., 2014	46.92	-71.85	782	13320	113	4.02 ± 0.11	3.99 ± 0.11	3.97 ± 0.11	4.11 ± 0.12	4.08 ± 0.11	4.04 ± 0.11	4.18 ± 0.12	4.14 ± 0.11
GLASH	Borchers et al., 2016	57.22	-5.72	310	11700	300	4.58 ± 0.26	4.58 ± 0.26	4.48 ± 0.26	4.48 ± 0.26	4.48 ± 0.26	4.44 ± 0.25	4.44 ± 0.25	4.34 ± 0.25
FEAR	Borchers et al., 2016	57.24	-5.97	336	11700	300	4.35 ± 0.13	4.35 ± 0.13	4.25 ± 0.13	4.25 ± 0.13	4.25 ± 0.13	4.21 ± 0.12	4.21 ± 0.12	4.12 ± 0.12
ARR	Borchers et al., 2016	57.42	-5.85	135	11700	300	4.38 ± 0.12	4.38 ± 0.12	4.29 ± 0.11	4.29 ± 0.11	4.29 ± 0.11	4.19 ± 0.11	4.22 ± 0.11	4.12 ± 0.11
MCD	Borchers et al., 2016	57.49	-5.45	515	11700	300	4.33 ± 0.12	4.33 ± 0.12	4.22 ± 0.11	4.21 ± 0.11	4.21 ± 0.11	4.22 ± 0.11	4.21 ± 0.11	4.08 ± 0.11
BLG	Borchers et al., 2015	58.53	13.88	120	11477	110	4.38 ± 0.18	4.38 ± 0.18	4.38 ± 0.18	4.38 ± 0.18	4.38 ± 0.18	4.16 ± 0.17	4.16 ± 0.17	4.13 ± 0.17
BILL	Stroeven et al., 2015	58.53	13.88	120	11477	110	4.38 ± 0.18	4.38 ± 0.18	4.38 ± 0.18	4.38 ± 0.18	4.38 ± 0.18	4.16 ± 0.17	4.16 ± 0.17	4.13 ± 0.17
BILL1	Stroeven et al., 2015	58.53	13.76	95	10680	351	4.2 ± 0.3	4.2 ± 0.3	4.17 ± 0.3	4.17 ± 0.3	3.96 ± 0.28	3.98 ± 0.28	3.97 ± 0.28	3.95 ± 0.28
HALSNOY	Goehring et al., 2012	59.80	5.80	84	10680	100	4.53 ± 0.08	4.54 ± 0.08	4.45 ± 0.08	4.46 ± 0.08	4.46 ± 0.08	4.27 ± 0.08	4.26 ± 0.08	4.21 ± 0.07
OLDEDALEN	Goehring et al., 2012	61.67	6.81	135	6010	110	4.36 ± 0.14	4.36 ± 0.14	4.36 ± 0.14	4.36 ± 0.14	4.13 ± 0.14	4.12 ± 0.14	4.11 ± 0.14	4.02 ± 0.13
GROTLANDSURA	Fenton et al., 2011	68.91	17.53	53	1424	108	3.66 ± 0.1	3.69 ± 0.1	3.5 ± 0.1	3.5 ± 0.1	3.4 ± 0.1	3.4 ± 0.1	3.27 ± 0.09	3.27 ± 0.09
RUSSNES	Fenton et al., 2011	69.21	19.47	105	10842	77	4.04 ± 0.14	4.04 ± 0.14	3.85 ± 0.13	3.85 ± 0.13	3.77 ± 0.13	3.77 ± 0.13	3.71 ± 0.13	3.62 ± 0.12
MARRAIT	Young et al., 2013	69.28	-50.76	350	9175	45	4.32 ± 0.05	4.32 ± 0.05	4.11 ± 0.05	4.11 ± 0.05	4.11 ± 0.05	4.11 ± 0.05	3.91 ± 0.05	3.91 ± 0.05
CLYDE	Briner et al., 2006; Balco et al., 2008; Young et al., 2013	69.83	-70.50	67	8193	50	4.3 ± 0.1	4.3 ± 0.1	4.22 ± 0.1	4.22 ± 0.1	3.98 ± 0.09	3.98 ± 0.09	3.92 ± 0.09	3.92 ± 0.09

662

663

664

665

666

Table 6 - Regional SLHL P_3 and P_{10} as defined in CREp computed with 12 scaling procedures

Region	LAL-STD-Musch			LAL-STD-Lift			LAL-ERA-Musch			LAL-ERA-Lift			LAL-ERA-L			LSD-STD-Musch			LSD-STD-Lift			LSD-STD-L			LSD-ERA-Musch			LSD-ERA-Lift			LSD-ERA-L		
³He production rate																																	
Iceland	138 ± 3	138 ± 3	138 ± 3	129 ± 2	129 ± 2	129 ± 2	129 ± 2	129 ± 2	129 ± 2	129 ± 2	129 ± 2	129 ± 2	128 ± 3	128 ± 3	128 ± 3	128 ± 3	128 ± 3	128 ± 3	128 ± 3	128 ± 3	128 ± 3	128 ± 3	128 ± 3	128 ± 3	120 ± 3	120 ± 3	120 ± 3	120 ± 3	120 ± 3	120 ± 3	120 ± 3	120 ± 3	120 ± 3
North Atlantic	94 ± 8	94 ± 8	94 ± 8	101 ± 9	101 ± 9	101 ± 9	96 ± 10	96 ± 10	96 ± 10	94 ± 11	94 ± 11	94 ± 11	115 ± 12	115 ± 12	115 ± 12	108 ± 10	108 ± 10	108 ± 10	108 ± 10	108 ± 10	108 ± 10	108 ± 10	108 ± 10	108 ± 10	111 ± 12	111 ± 12	111 ± 12	111 ± 12	111 ± 12	111 ± 12	111 ± 12	111 ± 12	111 ± 12
Tropical Atlantic	125 ± 4	122 ± 4	119 ± 6	136 ± 5	136 ± 5	136 ± 5	132 ± 5	132 ± 5	132 ± 5	130 ± 6	130 ± 6	130 ± 6	119 ± 4	119 ± 4	119 ± 4	115 ± 4	115 ± 4	115 ± 4	115 ± 4	115 ± 4	115 ± 4	115 ± 4	115 ± 4	115 ± 4	126 ± 5	126 ± 5	126 ± 5	126 ± 5	126 ± 5	126 ± 5	126 ± 5	126 ± 5	126 ± 5
North Africa	139 ± 3	139 ± 3	137 ± 3	135 ± 3	135 ± 3	135 ± 3	135 ± 3	135 ± 3	135 ± 3	133 ± 3	133 ± 3	133 ± 3	140 ± 3	140 ± 3	140 ± 3	139 ± 3	139 ± 3	139 ± 3	139 ± 3	139 ± 3	139 ± 3	139 ± 3	139 ± 3	139 ± 3	136 ± 3	136 ± 3	136 ± 3	136 ± 3	136 ± 3	136 ± 3	136 ± 3	136 ± 3	136 ± 3
High Tropical Andes	151 ± 10	145 ± 10	136 ± 9	153 ± 10	153 ± 10	153 ± 10	147 ± 10	147 ± 10	147 ± 10	138 ± 9	138 ± 9	138 ± 9	181 ± 12	181 ± 12	181 ± 12	169 ± 11	169 ± 11	169 ± 11	169 ± 11	169 ± 11	169 ± 11	169 ± 11	169 ± 11	169 ± 11	172 ± 11	172 ± 11	172 ± 11	172 ± 11	172 ± 11	172 ± 11	172 ± 11	172 ± 11	172 ± 11
Patagonia	113 ± 7	111 ± 7	109 ± 8	118 ± 7	118 ± 7	118 ± 7	115 ± 7	115 ± 7	115 ± 7	113 ± 8	113 ± 8	113 ± 8	113 ± 6	113 ± 6	113 ± 6	111 ± 7	111 ± 7	111 ± 7	111 ± 7	111 ± 7	111 ± 7	111 ± 7	111 ± 7	111 ± 7	115 ± 8	115 ± 8	115 ± 8	115 ± 8	115 ± 8	115 ± 8	115 ± 8	115 ± 8	115 ± 8
Hawaii	111 ± 12	109 ± 12	106 ± 12	114 ± 12	114 ± 12	114 ± 12	111 ± 12	111 ± 12	111 ± 12	109 ± 12	109 ± 12	109 ± 12	117 ± 13	117 ± 13	117 ± 13	115 ± 13	115 ± 13	115 ± 13	115 ± 13	115 ± 13	115 ± 13	115 ± 13	115 ± 13	115 ± 13	117 ± 13	117 ± 13	117 ± 13	117 ± 13	117 ± 13	117 ± 13	117 ± 13	117 ± 13	117 ± 13
Central Pacific	4.02 ± 0.2	3.91 ± 0.17	3.81 ± 0.16	4.37 ± 0.19	4.37 ± 0.19	4.37 ± 0.19	4.25 ± 0.16	4.25 ± 0.16	4.25 ± 0.16	4.14 ± 0.14	4.14 ± 0.14	4.14 ± 0.14	4.13 ± 0.17	4.13 ± 0.17	4.13 ± 0.17	3.91 ± 0.13	3.91 ± 0.13	3.91 ± 0.13	3.91 ± 0.13	3.91 ± 0.13	3.91 ± 0.13	3.91 ± 0.13	3.91 ± 0.13	3.91 ± 0.13	4.27 ± 0.12	4.27 ± 0.12	4.27 ± 0.12	4.27 ± 0.12	4.27 ± 0.12	4.27 ± 0.12	4.27 ± 0.12	4.27 ± 0.12	4.27 ± 0.12
Western USA	4.25 ± 0.17	4.24 ± 0.16	4.23 ± 0.16	4.05 ± 0.16	4.05 ± 0.16	4.05 ± 0.16	4.03 ± 0.16	4.03 ± 0.16	4.03 ± 0.16	4.02 ± 0.16	4.02 ± 0.16	4.02 ± 0.16	4.28 ± 0.17	4.28 ± 0.17	4.28 ± 0.17	4.26 ± 0.17	4.26 ± 0.17	4.26 ± 0.17	4.26 ± 0.17	4.26 ± 0.17	4.26 ± 0.17	4.26 ± 0.17	4.26 ± 0.17	4.26 ± 0.17	4.05 ± 0.16	4.05 ± 0.16	4.05 ± 0.16	4.05 ± 0.16	4.05 ± 0.16	4.05 ± 0.16	4.05 ± 0.16	4.05 ± 0.16	4.05 ± 0.16
Europe	4.1 ± 0.04	4.06 ± 0.03	3.99 ± 0.03	4.06 ± 0.04	4.06 ± 0.04	4.06 ± 0.04	4.02 ± 0.03	4.02 ± 0.03	4.02 ± 0.03	3.96 ± 0.03	3.96 ± 0.03	3.96 ± 0.03	4.21 ± 0.03	4.21 ± 0.03	4.21 ± 0.03	4.15 ± 0.03	4.15 ± 0.03	4.15 ± 0.03	4.15 ± 0.03	4.15 ± 0.03	4.15 ± 0.03	4.15 ± 0.03	4.15 ± 0.03	4.15 ± 0.03	4.11 ± 0.03	4.11 ± 0.03	4.11 ± 0.03	4.11 ± 0.03	4.11 ± 0.03	4.11 ± 0.03	4.11 ± 0.03	4.11 ± 0.03	4.11 ± 0.03
Arctic - NE America	4.04 ± 0.14	4 ± 0.17	3.96 ± 0.18	4.21 ± 0.13	4.21 ± 0.13	4.21 ± 0.13	4.17 ± 0.15	4.17 ± 0.15	4.17 ± 0.15	4.14 ± 0.16	4.14 ± 0.16	4.14 ± 0.16	4.06 ± 0.22	4.06 ± 0.22	4.06 ± 0.22	4.02 ± 0.23	4.02 ± 0.23	4.02 ± 0.23	4.02 ± 0.23	4.02 ± 0.23	4.02 ± 0.23	4.02 ± 0.23	4.02 ± 0.23	4.02 ± 0.23	4.21 ± 0.21	4.21 ± 0.21	4.21 ± 0.21	4.21 ± 0.21	4.21 ± 0.21	4.21 ± 0.21	4.21 ± 0.21	4.21 ± 0.21	4.21 ± 0.21
	4.32 ± 0.2	4.31 ± 0.21	4.31 ± 0.21	4.25 ± 0.18	4.25 ± 0.18	4.25 ± 0.18	4.25 ± 0.18	4.25 ± 0.18	4.25 ± 0.18	4.25 ± 0.19	4.25 ± 0.19	4.25 ± 0.19	4.16 ± 0.15	4.16 ± 0.15	4.16 ± 0.15	4.15 ± 0.15	4.15 ± 0.15	4.15 ± 0.15	4.15 ± 0.15	4.15 ± 0.15	4.15 ± 0.15	4.15 ± 0.15	4.15 ± 0.15	4.15 ± 0.15	4.09 ± 0.17	4.09 ± 0.17	4.09 ± 0.17	4.09 ± 0.17	4.09 ± 0.17	4.09 ± 0.17	4.09 ± 0.17	4.09 ± 0.17	4.09 ± 0.17
	4.24 ± 0.12	4.23 ± 0.14	4.22 ± 0.14	4.14 ± 0.06	4.14 ± 0.06	4.14 ± 0.06	4.13 ± 0.05	4.13 ± 0.05	4.13 ± 0.05	4.12 ± 0.06	4.12 ± 0.06	4.12 ± 0.06	4.14 ± 0.16	4.14 ± 0.16	4.14 ± 0.16	4.12 ± 0.14	4.12 ± 0.14	4.12 ± 0.14	4.12 ± 0.14	4.12 ± 0.14	4.12 ± 0.14	4.12 ± 0.14	4.12 ± 0.14	4.12 ± 0.14	4.03 ± 0.21	4.03 ± 0.21	4.03 ± 0.21	4.03 ± 0.21	4.03 ± 0.21	4.03 ± 0.21	4.03 ± 0.21	4.03 ± 0.21	4.03 ± 0.21

667

668

669

670

671

672 Table 7 shows the worldwide average P_3 and P_{10} computed from the calibration data
 673 of ICE-D as well as the associated statistical parameters.

674

675 **Table 7 - Global mean and statistical parameters for SLHL P_3 (n=23) and P_{10}**
 676 **(n=31) as defined in CREp computed with 12 scaling procedures**

677

678

	LAL-STD- Musch	LAL-STD- Lift	LAL-STD- L	LAL- ERA- Musch	LAL- ERA- Lift	LAL- ERA-L	LSD- STD- Musch	LSD-STD- Lift	LSD- STD-L	LSD- ERA- Musch	LSD- ERA-Lift	LSD- ERA-L
³He production rate												
Arithmetic mean	121	118	116	122	119	117	123	119	117	124	121	118
Weighted mean	121	118	116	122	120	118	121	119	117	123	121	119
Error of the WM	3	3	4	3	3	3	3	3	3	2	2	2
Weighted STDEV	15	16	17	13	14	14	13	14	14	11	12	12
Relative Wed STDEV	12.6%	13.8%	14.8%	10.2%	11.4%	12.2%	10.5%	11.5%	12.4%	8.9%	10%	10%
STDEV	17	18	19	15	16	16	18	18	18	17	17	16
MSWD	10.2	12.3	13.9	6.8	8.4	9.5	7.2	8.5	9.7	5.2	5.9	6.5
¹⁰Be production rate												
Arithmetic mean	4.16	4.13	4.11	4.18	4.15	4.13	4.09	4.04	3.99	4.12	4.07	4.02
Weighted mean	4.16	4.13	4.10	4.13	4.10	4.07	4.13	4.09	4.00	4.10	4.06	3.98
Error of the WM	0.04	0.04	0.04	0.04	0.04	0.04	0.04	0.04	0.04	0.05	0.04	0.04
Weighted STDEV	0.20	0.22	0.23	0.19	0.19	0.20	0.19	0.19	0.22	0.25	0.23	0.23
Relative Wed STDEV	4.9%	5.2%	5.7%	4.7%	4.7%	4.9%	4.7%	4.6%	5.5%	6.2%	5.6%	5.8%
STDEV	0.27	0.29	0.30	0.26	0.26	0.26	0.24	0.24	0.28	0.28	0.25	0.24
MSWD	3.96	4.51	5.36	3.60	3.66	3.87	3.63	3.50	4.77	6.33	5.20	5.39

679

680

681

682

683

684

685

686

687

688

689

690

691

692

693

694

695 For the global dataset, computed statistical parameters are the MSWD, the
696 weighted standard deviation and the standard deviation. MSWD is a good indicator
697 of the over-dispersion relative to the uncertainties attached to each calibration site
698 (Douglass et al., 2006; York, 1966). We thus use this as a first order indicator of the
699 scaling ability to take into account the spatial and temporal variability of the cosmic-
700 ray flux: the lower MSWD, the better the scaling procedure is.

701 In the case of the ^3He calibration database, MSWDs range from 5.2 to 13.9, with
702 corresponding relative weighted standard deviation of 9% and 15%, respectively
703 (Table 7). It is worth noting that the LSD model has lower MSWDs than the
704 Lal/Stone model (mean value of 7 vs 10, respectively) and thus seems to perform a
705 better scaling. Similarly, the ERA40 atmosphere yields lower dispersion than the
706 STD atmosphere.

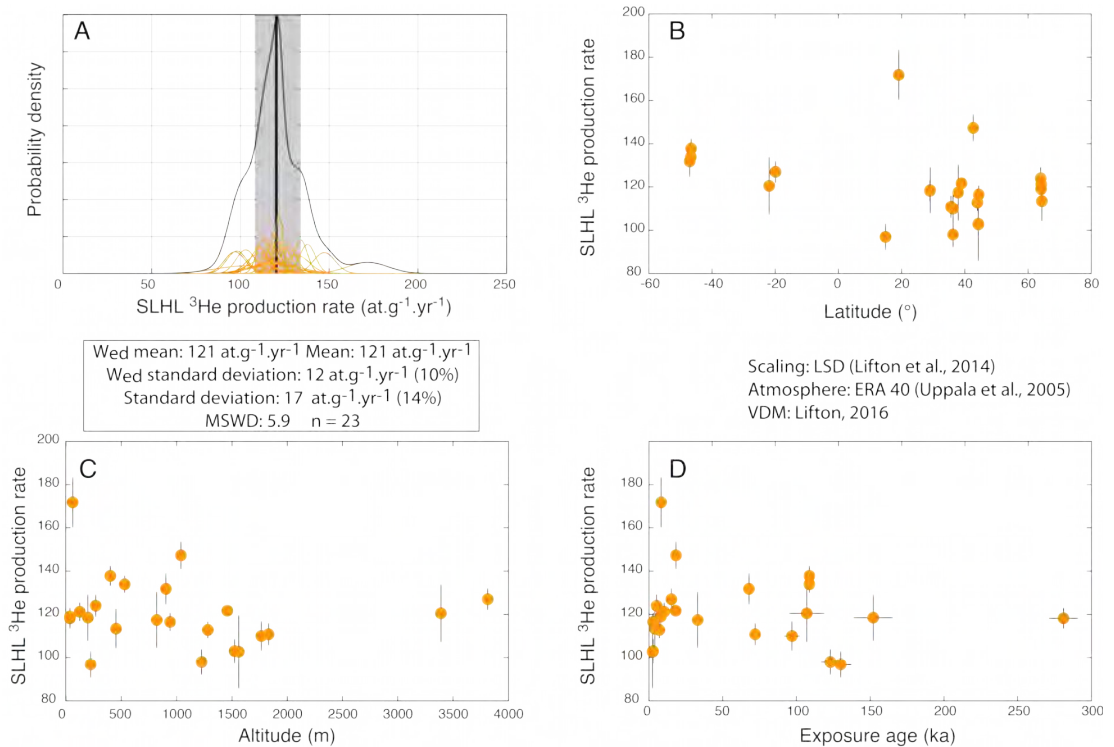
707 In the case of ^{10}Be , MSWD are lower than for ^3He : they range from 3.5 to 6.3, for
708 respective standard deviation of 4.6% and 6.2%. Contrary to what is observed with
709 the ^3He database, the mean MSWDs of LSD and Lal/Stone are not significantly
710 different (4.8 and 4.2, respectively) (Table 7). Surprisingly, the ERA40 atmosphere
711 provides a better scaling than the STD atmosphere only when it is combined with the
712 Lal/Stone model. Given the size of the dataset, this statement should however be
713 considered with caution. For both ^3He and ^{10}Be , the impact of the geomagnetic time-
714 correction is quite limited and imperceptible (Fig. 4 and 5, Table 7), although the
715 Atmospheric ^{10}Be VDM (Muscheler et al., 2005) and the Lifton VDM 2016 (Lifton,
716 2016) seems to provide slightly lower dispersions than the LSD geomagnetic

717 framework (Lifton et al., 2014).

718

719

720

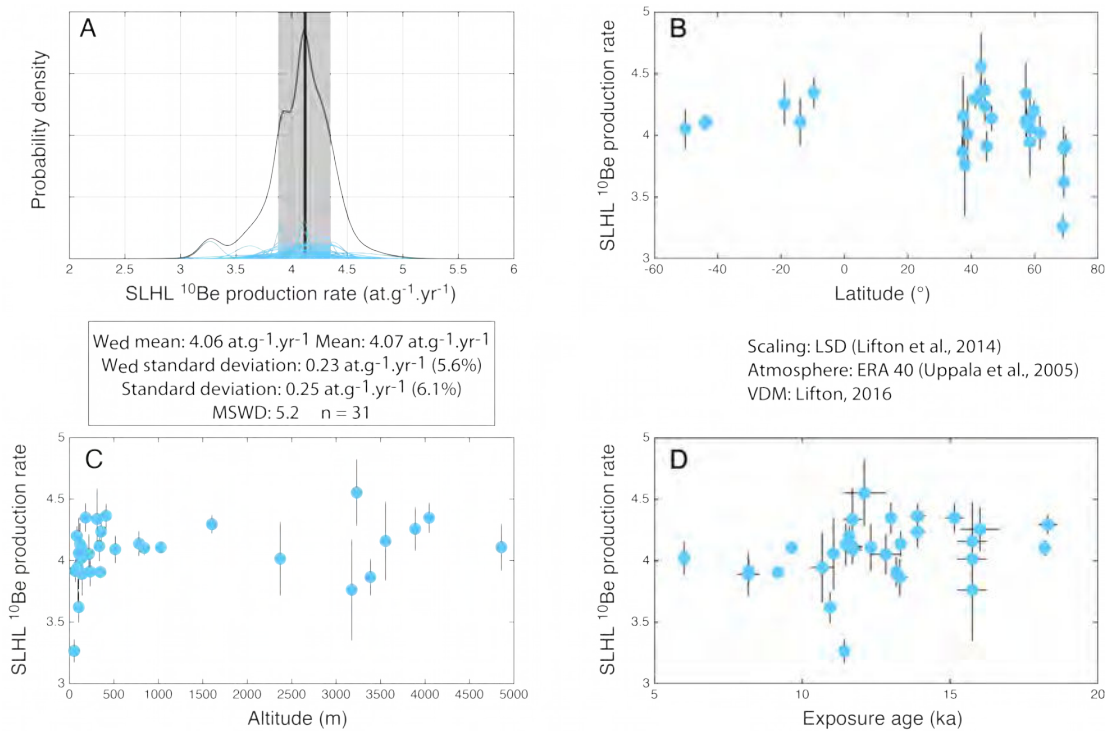


721

722 **Figure 4 - A) Probability density plot of SLHL ^3He production rates from the**
 723 **ICE-D database. Plots of the global SLHL P_3 calibration dataset against B)**
 724 **latitude, C) altitude and D) exposure age. These SLHL PR data are computed**
 725 **using the LSD-ERA-Lift scaling procedure.**
 726

727 In order to evaluate possible weakness of these scaling procedures, we also tested
 728 potential correlation between the SLHL production rates of the database and the
 729 spatial position of the sites (latitude, longitude, altitude) (Fig. 4 and 5). These plots
 730 do not indicate any significant correlation between these spatial parameters and the
 731 calibrated production rates (R^2 are lower than 0.14 in any case), supporting the idea
 732 that these 12 scaling procedures are not affected by any first order flaw; they can be

733 considered as able to describe the main characteristics of the spatial variability of the
 734 cosmic ray flux on Earth, and notably the local peculiarities of the atmospheric
 735 pressure field or the non-dipole components of the geomagnetic field. However,
 736 since large region of the world do not content any calibration site this statement may
 737 potentially be revised in the future, when new sites will be added in Asia and Africa
 738 (Fig. 2).



739

740 **Figure 5 - A) Probability density plot of SLHL ^{10}Be production rates from the**
 741 **ICE-D database. Plots of the global SLHL P_3 calibration dataset against B)**
 742 **latitude, C) altitude and D) exposure age. These SLHL PR data are computed**
 743 **using the LSD-ERA-Lift scaling procedure.**

744

745

746 Additionally, there is no significant trend between the scaled P_3 and P_{10} and the age
 747 of the calibration surfaces, suggesting that the geomagnetic correction is not affected
 748 by any major inaccuracy.

749

750

751 5.3 - *Uncertainties and justification for choosing a global, a regional or a local*
752 *production rate*

753

754 When a global production rate is selected, the dispersions of the global calibration
755 datasets (evaluated by the weighted standard deviation) will yield exposure ages with
756 minimum external 1σ uncertainty of 5% for ^{10}Be and 10% in the case of ^3He .
757 Although this represents good progress compared to the previous global compilation
758 (Balco et al. 2008 obtained 9% for ^{10}Be), these uncertainties may remain quite high
759 for certain applications, notably to perform high precision glacial chronologies.
760 However, if the dated samples are relatively close to a well-calibrated region, it
761 seems reasonable to prefer using a local or a regional production rate. This strategy
762 has often been used since it minimizes potential scaling inaccuracies (e.g. Blard et
763 al., 2014; Kaplan et al., 2011; Putnam et al., 2013), although it leaves open the
764 potential for unrecognized regional or site-specific systematic geologic uncertainties,
765 and the valid extent of the region in time and space is typically poorly defined. In this
766 regard, it would also be preferable to select a calibration dataset whose exposure age
767 is comparable to the age of the surface to be dated. In order to help users in choosing
768 calibration sites having the most appropriate exposure ages, the selection map of
769 CREp includes a function that allows filtering the age range of the calibration
770 dataset.

771 On the other hand, if the sample to be dated is located more than 1000 km away
772 from any calibration site, a warning sentence is displayed on the CREp interface to
773 suggest choosing a global average. This is the case of Asia and Africa, continents

774 where there is up to now no calibration data. Anyway, CREp users are free to use
775 their best judgement and test and use the scaling and production rate they consider
776 most appropriate.

777 **6 - Conclusion**

778 The CREp program is an online Octave/Matlab© program (crep.crpq.cnrs-nancy.fr)
779 that allows rapid and easy exposure age calculation for ^{10}Be and ^3He over the late
780 Pleistocene. It offers a flexible parameterization of the scaling scheme and is linked
781 to an online database, ICE-D, that includes the most recent calibration studies and
782 developments in cosmic ray exposure ages. The Octave/Matlab© source code of
783 CREp is available and makes it easily amenable to further developments.

784 Further improvements could include the addition of ^{21}Ne and ^{26}Al . New
785 geomagnetic and atmospheric database with improved accuracy will probably be
786 added in the future. In this regard, a great improvement would be to add in CREp a
787 time variable atmospheric pressure field, that could be for example derived from
788 global circulation models (e.g. Staiger et al., 2007).

789 Since we designed the online calculator CREp and the ICE-D database to be
790 constantly upgraded, to include the last updates of cosmogenic nuclide systematics,
791 we are very welcome to receive future readers' suggestions. Readers are notably
792 invited to write P.-H. Blard (blard@crpq.cnrs-nancy.fr) and G. Balco
793 (balcs@berkeley.edu) to report any new production rate calibration study that would
794 have not been included in ICE-D.

795

796 **Acknowledgments**

797 This study was mainly financed by l'Agence Nationale de la Recherche by the
798 Grant ANR GALAC (PI Pierre-Henri Blard, ANR-11-JS56-011-01).

799 **Appendix 1. Definition of the statistical parameters**800 **Given a set of N x_i measurements with their respective uncertainties σ_i :**

801

802 **- MSWD: Mean Squared Weighted Deviation (or reduced Chi²)**

803
$$MSWD = \frac{1}{N-1} \sum_{i=1}^N w_i (x_i - x_{\text{mean}})^2$$

804 with $w_i = 1/\sigma_i^2$, N the number of variable and x_{mean} the arithmetic mean of the dataset.805 * if $MSWD > 1$, the dataset is over-dispersed regarding the individual analytical
806 uncertainties, suggesting the existence of unrecognized external sources of
807 uncertainty.808 * if $MSWD < 1$, the dataset is over-dispersed regarding the analytical uncertainty,
809 suggesting that uncertainties are overestimated.810 **- Weighted-mean x_m**

811
$$x_m = \frac{\sum_{i=1}^N w_i x_i}{\sum_{i=1}^N w_i}$$

812 **- Error of the weighted-mean σ_w**

813
$$\sigma_w = \frac{1}{\sqrt{\sum_{i=1}^N w_i}}$$

814 **- Weighted standard deviation Wed_STD**

815
$$Wed_STD = \sqrt{\frac{N \sum_{i=1}^N w_i (x_i - x_m)^2}{(N-1) \sum_{i=1}^N w_i}}$$

816

817

818 **Appendix 2. Tutorial of the CREp online calculator**

819

820 *1. Step1: Initial parameterization*

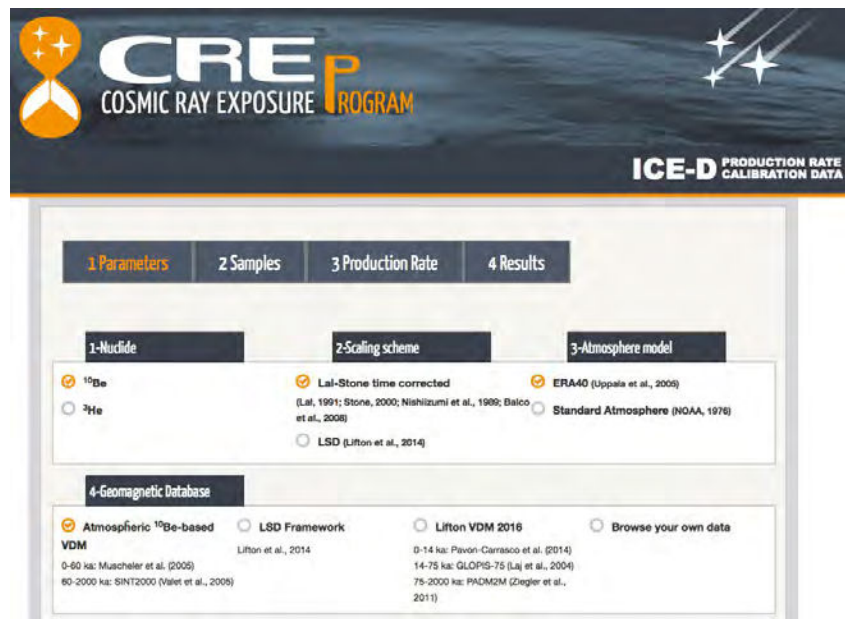
821 The parameterization commands are presented in Figure i.

822 The initial parameterization is done thanks to radio buttons, making this choice
823 quick and easy. Four items have to be set by the users (Figure 1, see Section 2 for
824 detailed presentation):

- 825 ▪ Nuclide: ^{10}Be or ^3He
- 826 ▪ Scaling scheme: Lal-Stone time corrected (Balco et al., 2008; Lal, 1991; Stone,
827 2000) or LSD (Lifton et al., 2014).
- 828 ▪ Atmosphere model: ERA-40 (Uppala et al., 2005) or the U.S. standard atmosphere
829 (National Oceanic and Atmospheric Administration, 1976).
- 830 ▪ Geomagnetic database: Muscheler et al. (2005), Lifton (2016) or the LSD
831 geomagnetic framework (Lifton et al., 2014).

832 Users may also input their own Virtual Dipole Moment database in the programme
833 by clicking to "Browse your own data". The input Virtual Dipole moment data
834 should be presented in two columns. The right column should contain the ages in kyr
835 and the second one the Virtual Dipole Moment values in 10^{22} A.m^2 . Hence, the
836 present value of $7.746 \times 10^{22} \text{ A.m}^2$ (Finlay et al., 2010) should be input 7.746.

837 When the geomagnetic reconstruction is selected or correctly imported, it is plotted
838 on the interface. Once the parameters have been selected, users need to push the
839 "Next" button. The scaling parameterization is then locked.



840

841

Figure i. Step 1: choice of the scaling parameters

842

843

2. Step2: Upload of the samples characteristics of SLHL production rate

844

This step consists in importing the cosmogenic nuclides data and the characteristics of the samples to be dated (Figure ii). The input data file must be in the format of an Excel (c) spreadsheet (xls or xlsx). A template can be downloaded using the "Download template" button.

845

846

847

848

The uploaded table must include the following data (similar information is also available by clicking the "Instructions for Sample File" button):

849

850

851 Column 1: Sample name

852

853 Column 2: Latitude (Decimal degrees). Range from -90 to 90°. Negative value for
854 Southern Hemisphere.

855

856 Column 3: Longitude (Decimal degrees). Range from -180 to 180°. Negative value
857 for Western Hemisphere.

858

859 Column 4: Altitude (masl)

860

861 Column 5: Cosmogenic nuclide concentration (at.g⁻¹). IMPORTANT: For ¹⁰Be, use
 862 the 07KNSTD standardization (Nishiizumi et al., 2007). If the ¹⁰Be concentrations
 863 are computed using another standardization, convert them to 07KNSTD before
 864 loading your data in CREp (see
 865 http://hess.ess.washington.edu/math/docs/al_be_v22/al_be_docs.html for more
 866 details).

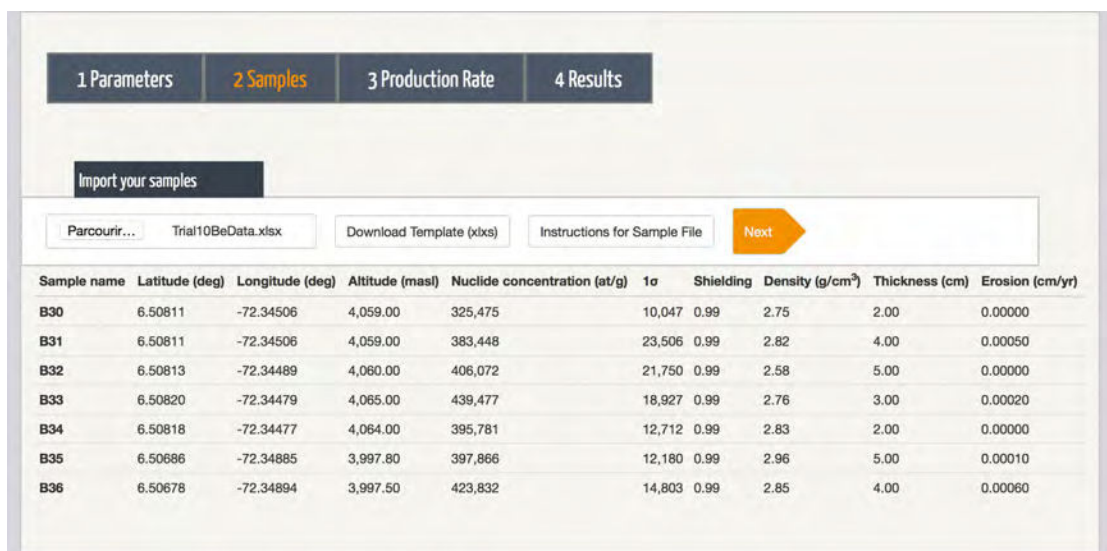
867
 868 Column 6: Analytical 1-sigma uncertainty (at.g⁻¹)

869
 870 Column 7: Shielding correction (dimensionless). Range from 0 to 1.

871
 872 Column 8: Sample density (g.cm⁻³).

873
 874 Column 9: Sample thickness (cm).

875
 876 Column 10: Erosion (cm.yr⁻¹).
 877



Sample name	Latitude (deg)	Longitude (deg)	Altitude (masl)	Nuclide concentration (at/g)	1σ	Shielding	Density (g/cm ³)	Thickness (cm)	Erosion (cm/yr)
B30	6.50811	-72.34506	4,059.00	325,475	10,047	0.99	2.75	2.00	0.00000
B31	6.50811	-72.34506	4,059.00	383,448	23,506	0.99	2.82	4.00	0.00050
B32	6.50813	-72.34489	4,060.00	406,072	21,750	0.99	2.58	5.00	0.00000
B33	6.50820	-72.34479	4,065.00	439,477	18,927	0.99	2.76	3.00	0.00020
B34	6.50818	-72.34477	4,064.00	395,781	12,712	0.99	2.83	2.00	0.00000
B35	6.50686	-72.34885	3,997.80	397,866	12,180	0.99	2.96	5.00	0.00010
B36	6.50678	-72.34894	3,997.50	423,832	14,803	0.99	2.85	4.00	0.00060

878

879 *Figure ii. Step 2. Importation of the samples characteristics*

880

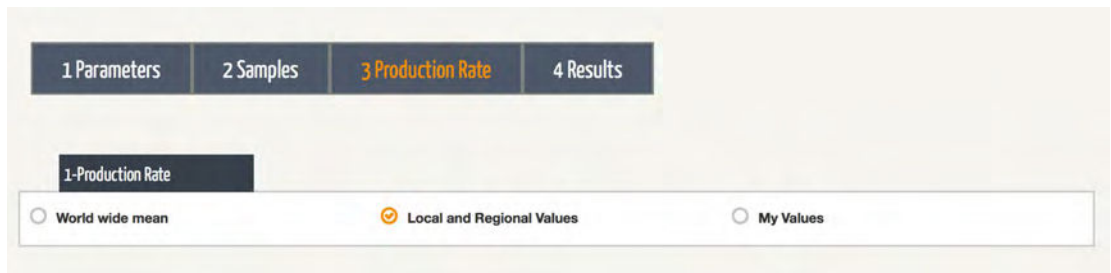
881 Once the sample characteristics are loaded, users have to press the "Next" button.

882

883 *3. Step3: Selection of SLHL production rate*

884 Users may choose i) a world wide mean, ii) a local or a regional rate, or iii) enter
 885 their own calibration data (Fig. iii). For this choice, users just have to check the

886 relevant button.



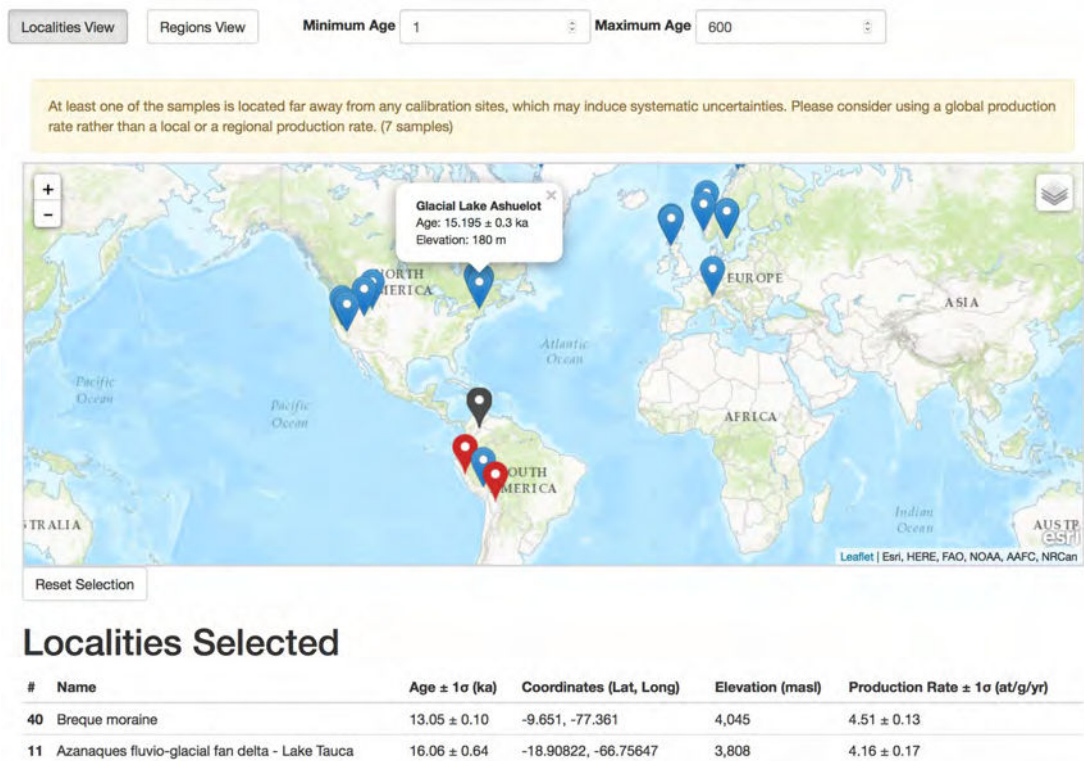
887

888 Fig. iii - Selection of the type of production rate

889

890 If the option "Local and Regional Values" is checked, a selection map is displayed,

891 showing all the calibration sites currently available in ICE-D (Fig. iv).



892

893

894 Fig. iv - CREP interface map for selecting local or regional calibration sites

895

896

897 Users may choose one or more single calibration sites by clicking on the
898 corresponding tag. The selected sites appear in red. If more than one site is selected,
899 CREp computes a weighted mean and its associated uncertainty.

900 Alternatively, the "Region View" button may be activated. In this case, users may
901 choose one of the pre-calculated regional average production rates.

902 If users choose to import their own SLHL production rate, they can either load
903 directly a SLHL production rate value (Note, however, that, in that case, user must
904 ensure that this value is computed with the appropriate scaling scheme and
905 parameters), or input data from a calibration surface to compute a new SLHL
906 production rate. The input fields are (Fig. v):

907 - Nuclide concentrations with the one-sigma uncertainty in $\text{at}\cdot\text{g}^{-1}$. For dataset with
908 multiple exposure samples, outlier selection, thickness correction, altitude scaling
909 and calculation of a global average need to be computed before entering this average
910 concentration value.

911 - Independent age with its one-sigma uncertainty in kyr.

912 - Geographic location: latitude and longitude in decimal degrees (negative values for
913 Southern and Western location).

914 - Altitude in masl.

915 - Erosion rate in $\text{cm}\cdot\text{yr}^{-1}$.

916 Once these data are entered, users have to click on the "Calculate PR" button and
917 the computed SLHL then appears in a window called "Display your Production Rate
918 ($\text{at}/\text{g}/\text{yr}$)".

919

Age (ka)	1σ(ka)
18.2	0.2
Conc (at/g)	1σ(at/g)
288000	21000
Latitude	Longitude
5.15	2.16
Altitude (masl)	Erosion Rate (cm/year)
2846	0

Scaling Fact.	SLHL	1σ
3.994970742	3.98	0.29

920

921 *Fig. v - CREp interface for computing user's own production rates*

922

923 Whatever the options, the value of the currently selected production rate is always

924 displayed in a window located at the bottom of the page (Fig. vi).

925

926 *Fig. vi. Display of the currently selected SLHL production rate and corresponding*927 *scaling framework*

928

929 Finally, once the user is happy with the PR selection, he has to click the "Calculate"

930 button.

931

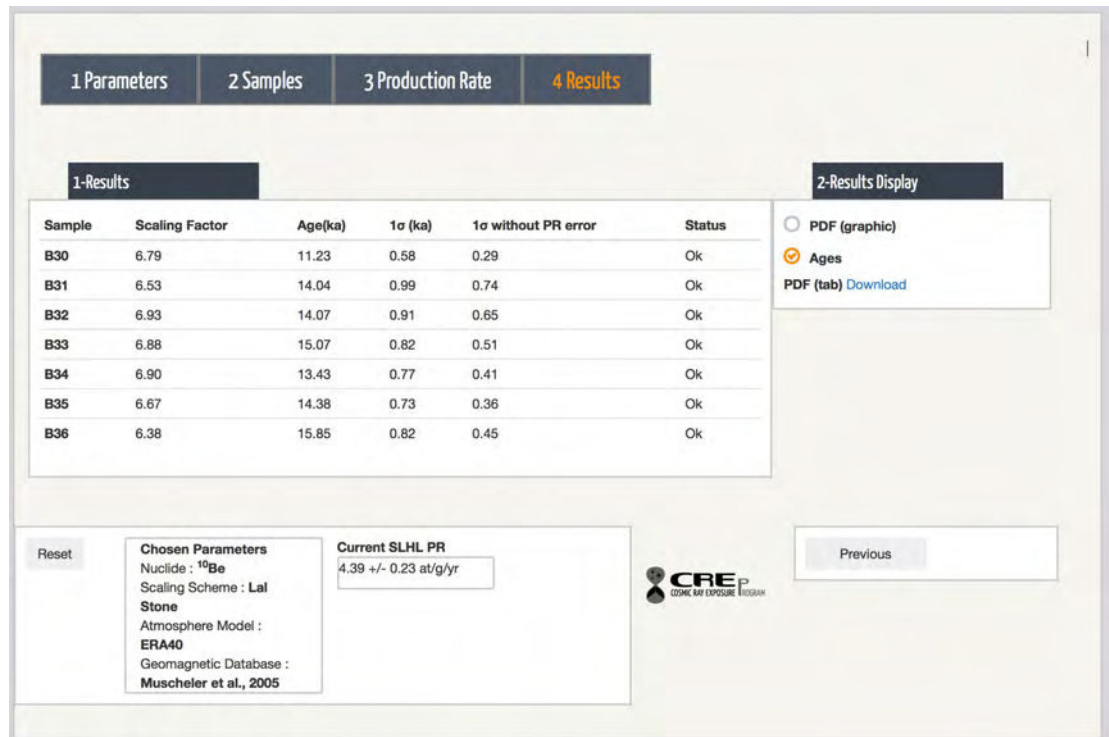
932 *4. Step 4: Results display and export*

933 The computed ages appear by default in the form of a Table that can be exported as

934 a .xlsx file by clicking on the relevant button (Fig. vii). Note that two types of

935 uncertainties are provided along with the ages: with and without the error arising

936 from the production rate. In the second case (1σ without PR error), only analytical
 937 errors are included. These uncertainties should be used to test the statistical
 938 dispersion of objects belonging to the same surface.



939

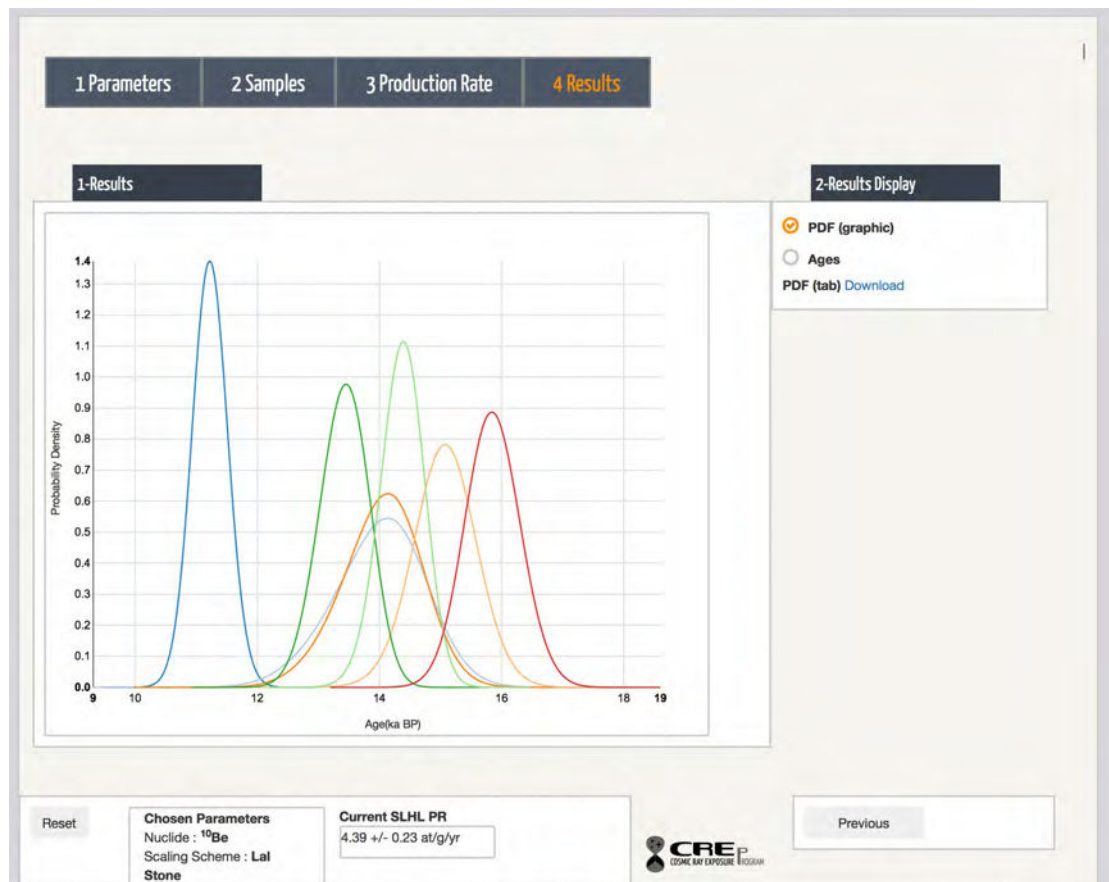
940

Fig. vii. Results display in the form of a table

941

942

943



944

945

Fig. viii. Results display in the form of a probability density plot

946

947

5. Note on input data

948

Input data for the CREP program are Excel © spreadsheet in .xls or .xlsx format.

949

Make sure there is only one page in the file or that your data are on the first page.

950

Numeric values should form a rectangular block without empty cells in it. Be aware

951

that the number format impact the value read by the CREP program: the program

952

considers the number of significant figures that is displayed, and not the double

953

precision value. This may lead to a loss of precision. For example, if the scientific

954

format with only one digit is used to display a nuclide concentration of 525 600 at.g⁻

955

¹, the CREP value will round this value to 530 000 at.g⁻¹. The documents have to be

956

placed inside the CREP folder. Two types of data may be input: the characteristics of

957 the samples to be dated and the Virtual Axial Dipole Moment values. Only the prior
958 is mandatory.

959

960 *6. Proper credit to previous publications*

961 It is important to give proper credit to the researchers that produced the original
962 calibration data as well as the used scaling schemes. Thus, CREp automatically
963 generates a relevant publication list that should be quoted, taking into account the
964 references corresponding to the used scaling procedure and the calibration dataset.
965 For example, if a worldwide average production rate is selected, then CREp yields
966 the full list of the papers that are included in this compilation.

967 **Appendix 3. Tutorial of the CREp Matlab (c) program**

968 The stand alone Matlab version of CREp is designed in a similar fashion than the
969 online calculator (crep.cprg.cnrs-nancy.fr), with these 2 exceptions: i) in the Matlab
970 version of CREp, the samples characteristics are loaded after the choice of the
971 production rate and ii) in the Matlab version, the PR selection is done from a list, the
972 interactive map is not available.

973

974 *1. Installation of the CREp program on the user's computer*

975 The CREp program has been developed on Mac © with the Matlab 2012b version.
976 It works on PC with version as old as Matlab 2011. To start using the CREp
977 program, users should follow the steps below.

- 978 ■ Download the CREp folder. It contains the CREp program, along with the CREp
979 graphical user interface file, a functions folder and a constants folder. Two trial xls
980 files are proposed to test geomagnetic data importation and exposure age calculation.
- 981 ■ Launch Matlab © and make the CREp folder your current directory.
- 982 ■ In the Matlab *Current Folder* window, right-click on the CREp7.m file and select
983 *Run*. The CREp program window will open. If elements are overlapping, or if the
984 window is too small, resize it.

985

986 *2. Step1: Initial parameterization*

987 The parameterization commands are presented in Figure i.

988 The initial parameterization is done thanks to radio buttons, making this choice
989 quick and easy. Four items have to be set by the users (Figure 1, see Section 2 for
990 detailed presentation):

- 991 ■ Nuclide: ^{10}Be or ^3He

- 992 ▪ Scaling scheme: Lal-Stone time corrected (Balco et al., 2008; Lal, 1991; Stone,
 993 2000) or LSD (Lifton et al., 2014).
 994 ▪ Atmosphere model: ERA-40 (Uppala et al., 2005) or the U.S. standard atmosphere
 995 (National Oceanic and Atmospheric Administration, 1976).
 996 ▪ Geomagnetic database: Muscheler et al. (2005), Lifton (2016) or the LSD
 997 geomagnetic framework (Lifton et al., 2014).

998 Users may also input their own Virtual Dipole Moment database in the programme
 999 by clicking to "Browse your own data". The imported data have to be placed in the
 1000 CREp folder and require a specific format described in Section 3.3. When the
 1001 geomagnetic reconstruction is selected or correctly imported, it is plotted on the
 1002 interface.

1003 Once the parameters have been selected, users need to push the "Next" button. The
 1004 scaling parameterization is then locked.



1005

1006

1007

Figure i. Step 1: choice of the parameters

1008

1009

1010

3. Step2: Selection of SLHL production rate

1011

This interface is presented on Figure ii.

1012

After the selection of the parameters, the CREp program computes a reference

1013

SLHL production rate. This reference production rate may come from the calibration

1014

dataset provided with the CREp program, but users may as well use their own

1015

calibration data. This choice is done using the first radio button panel (Figure ii).

1016

If the users decide to use the production rates proposed in the program, they have

1017

several possibilities: either a worldwide average value can be chosen, either a

1018

regional value, either a variable number of calibration can be selected and used to

1019

calculate a weighted average. A specific interface box permits to perform this

1020

selection (Figure ii). The online version CREp also permits to perform this selection

1021

from an interactive map. When the calibration dataset is selected, the user have to

1022

press the "Display PR" button and a SLHL production rate value then appears with

1023

the associated one-sigma uncertainty and scaling factor.

The screenshot shows the CREp7 software interface with the following components:

- Navigation:** Three buttons at the top: '1 - Parameters', '2 - Production Rate' (highlighted in red), and '3 - Ages'.
- 1 - Production rate:** Radio buttons for 'World wide mean', 'Local and Regional Values' (selected), and 'My Values'.
- 2 - Where ? (10Be):** A list of locations: North Atlantic, Northern Europe, North America, High Tropical Andes, Patagonia - Southern Cone, and Oceania. 'Northern Europe' is selected.
- Available Production Rates:** A dropdown menu showing 'Goehring et al., 2012 - Oldedalen rock avalanche, W. Norway'. Below it is a table:

Ref.	Goehring et al., 2012
Site	Oldedalen rock avalanche, W. Norway
Mineral	Quartz
Age(ka)	6.07
Is(ka)	0.11
C(at/g)	3.13e+04
- 3 - Display your Production Rate (at/g/yr):** A table with columns 'Scaling Factor', 'SLHL Prod Rate', and '1s Uncert'. The values are 1.1884, 4.3464, and 0.1128 respectively. To the right are buttons for 'weighted mean' and 'Clear'.
- 4 - Display PR:** A red button.
- 5 - Load for calculation:** A red button.
- Navigation:** 'Previous' and 'Next' buttons.
- Reset:** A button on the left.
- Chosen Parameters:**
 - Nuclide : 10Be
 - Scaling scheme : Lal-Stone time corrected
 - Atmosphere model : ERA40 (Uppala et al., 2005)
 - Geomagnetic database : Muscheler et al., 2005
- Current SLHL PR:** A red box displaying '4.06 +/- 0.09 at/g/yr'.
- Footer:** A blue link 'Resize window if elements overlap'.

1024
1025
1026
1027

Figure ii. Selection of a calibration dataset and calculation of SLHL production rate

1028 At that point, users can compute other production rates for the same scaling scheme
1029 in order to compare them. By doing so, the first production rate will not be lost, and
1030 the computed production rates will accumulate in the related window. When two or
1031 more production rates are computed, users can choose to compute a weighted mean
1032 out of them by pressing the "weighted mean" button. To erase these selected
1033 production rates selection, one may click on the "Clear" button.

1034 Importantly, it is necessary to push the "Load for calculation" button to export the
1035 selected production rate and load this for calculating the ages. The selected value will

1036 appear in red in the "Current SLHL PR" box located in the bottom right corner.

1037 Then, the "Next" button become active and can be pushed to move to the next step.

1038 If users choose to import their own SLHL production rate, they can either load
1039 directly a SLHL production rate value, or input several data from a calibration
1040 surface to compute a new SLHL production rate. The input fields are:

1041 - Nuclide concentrations with the one-sigma uncertainty in at.g^{-1} . For dataset with
1042 multiple exposure samples, outlier selection, thickness correction, altitude scaling
1043 and calculation of a global average need to be computed before entering this average
1044 concentration value.

1045 - Independent age with its one-sigma uncertainty in kyr.

1046 - Geographic location: latitude and longitude in decimal degrees (negative values for
1047 Southern and Western location).

1048 - Altitude in masl.

1049 - Erosion rate in cm.yr^{-1} .

1050

1051 The last field filled has to be validated using Tab or Enter to enable the "Display
1052 PR" button. If the inputs do not have the required format, they will not be accepted.

1053 When all fields are correctly filled, the "Display PR" has to be pushed to enable the
1054 production rate calculation.

1055 An alternative possibility is to enter directly a SLHL production rate along with its
1056 uncertainty. Note, however, that, in that case, user must ensure that this value is
1057 computed with the appropriate scaling scheme and parameters.

1058 Once again, it is necessary to finally push the "Load for calculation" button to
1059 export the selected production rate and load this for calculating the ages. The

1060 selected value will appear in red in the "Current SLHL PR" box located in the bottom
1061 right corner. The "Next" button become active and can then be pushed to move to the
1062 next step.

1063

1064 *4. Step 3: Data importation and exposure age calculation*

1065 This last step consists in importing the cosmogenic nuclides data and the
1066 characteristics of the samples to be dated. The input data file must be in the format of
1067 an Excel (c) spreadsheet (xls or xlsx) and has to be placed in the CREp folder. The
1068 spreadsheet must include the following data (Users may use the available spreadsheet
1069 called "Trial10BeData.xlsx" as a template):

1070 Column 1: Sample name

1071

1072 Column 2: Latitude (Decimal degrees). Range from -90 to 90°. Negative value for
1073 Southern Hemisphere.

1074

1075 Column 3: Longitude (Decimal degrees). Range from -180 to 180°. Negative value
1076 for Western Hemisphere.

1077

1078 Column 4: Altitude (masl)

1079

1080 Column 5: Cosmogenic nuclide concentration (at.g⁻¹). IMPORTANT: For ¹⁰Be, use
1081 the 07KNSTD standardization (Nishiizumi et al., 2007). If the ¹⁰Be concentrations are
1082 computed using another standardization, convert them to 07KNSTD before loading
1083 your data in CREp (see
1084 http://hess.ess.washington.edu/math/docs/al_be_v22/al_be_docs.html for more
1085 details).

1086

1087 Column 6: Analytical 1-sigma uncertainty (at.g⁻¹)

1088

1089 Column 7: Shielding correction (dimensionless). Range from 0 to 1.

1090

1091 Column 8: Sample density (g.cm⁻³).

1092

1093 Column 9: Sample thickness (cm).

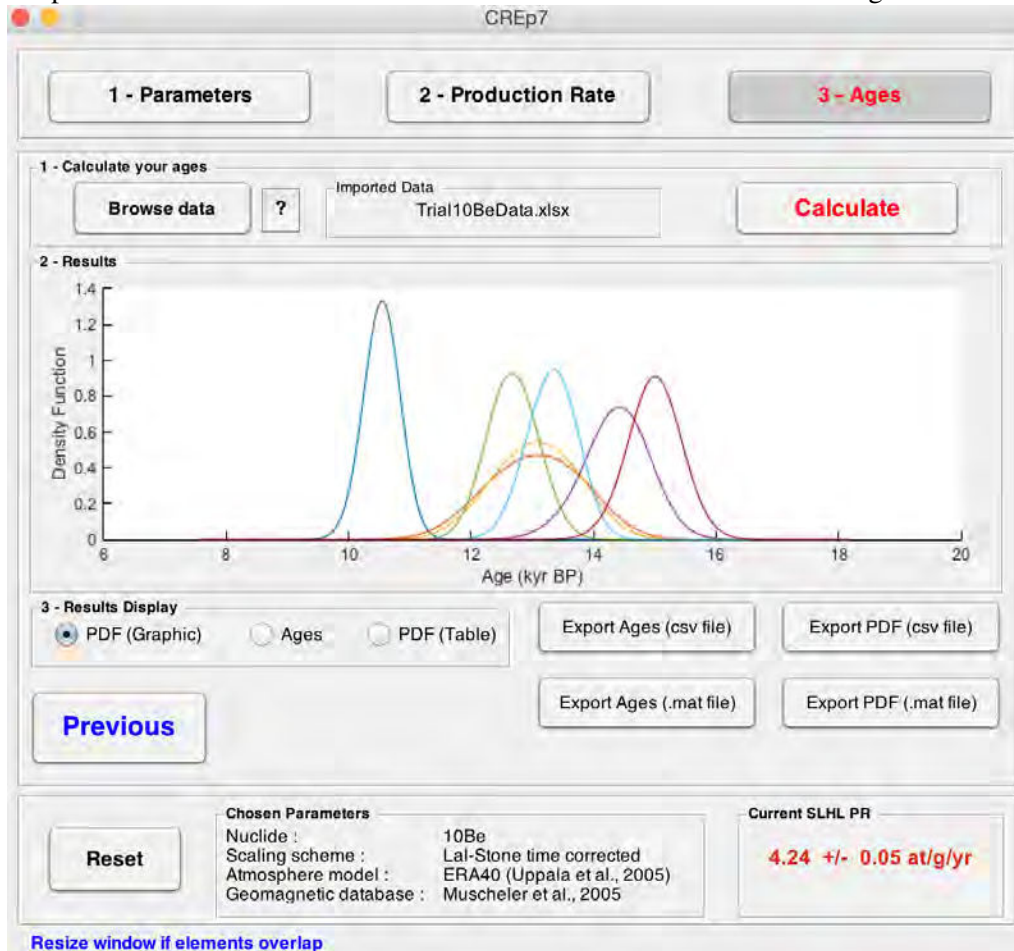
1094

1095 Column 10: Erosion (cm.yr⁻¹).

1096

1097 If the importation is successful, the name of the imported file appears in the

1098 "Imported Data" box and the "Calculate" button is enabled as shown in Figure iii.



1099
1100 *Figure iii. The CREp program when the age calculation is over. The SLHL*
1101 *production rate and the calculation parameters are indicated in the bottom band.*
1102 *The "Trial10BeData" was successfully imported, the "Calculate" button, was*
1103 *clicked. The "PDF (Graphic)" mode is selected for result display. The exports*
1104 *buttons can be clicked to save the results.*

1105
1106 Clicking on the "Calculate" button launch the calculation procedure. This step may
1107 last several seconds or minutes, depending on the number of calculable ages
1108 provided in the input data file. The calculation for one age should not exceed 3
1109 seconds, except if the user imported a very high-resolution geomagnetic
1110 reconstruction (time step smaller than 50 yr). A wait bar informs the users of the
1111 calculation progress.

1112 5. Results display

1113 Results can be displayed in three different ways thanks to the radio button panel
1114 "Results Display" that appears after the calculation. With the "PDF (Graphic)" mode,
1115 users can display a graph with the different probability density functions (PDF)
1116 associated with each age. With the "Ages" mode, a table presents the ages and
1117 associated uncertainties. The "PDF (Table)" mode provides a table that contains the
1118 numerical values of each density functions. By default, the CREp program shows the
1119 density function graph.

1120 Results presented with the "PDF" (Probability Density Function) modes and those
1121 of the "Ages" mode are not presented with the same uncertainties. The uncertainties
1122 of the "PDF" results include the analytical uncertainties only, while the "Ages" table
1123 provides both the analytical uncertainties and the total uncertainties. Total
1124 uncertainties include both the analytical uncertainties and the production rate
1125 uncertainties. They correspond to the most conservative ages of the samples. Thus
1126 these results are useful to investigate the dispersion of the different ages obtained for
1127 the same object. For example, they should be used to test the potential impact of
1128 erosion or inheritance on a pool of ages from the same moraine.

1129 It is important to note that the ability of the CREp program to compute an exposure
1130 age depends on the time steps used in the program and of the length of the
1131 geomagnetic reconstruction relatively to the age of the sample. Therefore, a sample
1132 can be too young for the program or too old for the geomagnetic database. To
1133 visualise potential problems with too young or too old ages, users may select the
1134 "Age" result display mode. The displayed table contains a "Status" column. If the
1135 status is "OK", the age calculation performed successfully and a probability density
1136 function is available for the sample. If a different status is posted, it is impossible for

1137 the program to provide a density function and three situations may be covered:

1138 - The status is "*Sample too old for geomagnetic database*". The database covers a too

1139 narrow time span. The program cannot calculate the geomagnetic time correction and

1140 no age will be proposed for the sample.

1141 - The status is "*Sample too young to provide probability density function*". Given the

1142 time steps used by the program, the time correction is conducted without using

1143 probability density function.

1144 - The status is "*Sample too old or too young to provide probability density function*".

1145 Given the time steps used by the program, the time correction is conducted without

1146 using probability density function. Another possibility is that the age of the sample is

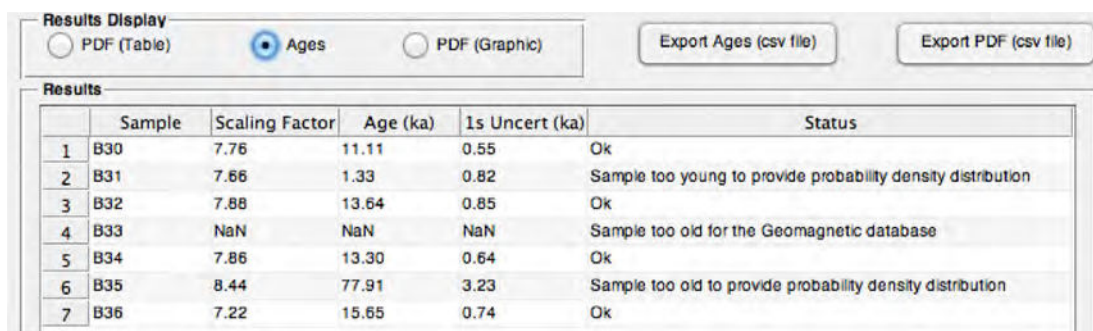
1147 approximately the oldest age of the geomagnetic reconstruction, the time correction

1148 is conducted without using probability density function. These two classes of ages

1149 that do not include probability density functions are indicative ages and should not be

1150 used to discuss and establish the age of a geological object.

1151 The result interface and the different possible status are presented in Figure iv.



	Sample	Scaling Factor	Age (ka)	1s Uncert (ka)	Status
1	B30	7.76	11.11	0.55	Ok
2	B31	7.66	1.33	0.82	Sample too young to provide probability density distribution
3	B32	7.88	13.64	0.85	Ok
4	B33	NaN	NaN	NaN	Sample too old for the Geomagnetic database
5	B34	7.86	13.30	0.64	Ok
6	B35	8.44	77.91	3.23	Sample too old to provide probability density distribution
7	B36	7.22	15.65	0.74	Ok

1152
1153

1154 *Figure iv. Results display. A. Results plotted with the "PDF" display mode. B.*

1155 *Results plotted with the "Age" display mode, with various status for the calculated*

1156 *ages.*

1157

1158 The numeric results displayed can be copied and past into a spreadsheet document

1159 but it is also possible to directly export them into spreadsheet format by clicking on

1160 the "Export" buttons above the "Results" box. Users can export directly the ages
1161 and/or the probability density functions of the ages.

1162

1163

1164

1165 *6. Results export*

1166 The CREp program allows the exportation of the computed data thanks to the
1167 "Export" buttons. Depending on the Matlab version and the platform (Mac/PC) of the
1168 users, the exportation may produce a Excel © document (.xls or .xlsx) or a
1169 standard .csv document. For a larger compatibility between the different Matlab ©
1170 version and platforms, the exported data are merely blocks of numerical values
1171 without text indications.

1172 When the "Ages" table is exported, the data block produced contains 3 columns and
1173 one line per dated sample. The first line gives the scaling factor, the second one the
1174 Age and the third, the one-sigma uncertainty associated with the age. The ages are
1175 calculated in the order of appearance of the input spreadsheet so this block can be
1176 copied and pasted on the right of the input datablock and the ages will match the
1177 good samples. If no age was calculated for this sample (see Section 5), the
1178 corresponding fields will indicate "NaN".

1179 When the PDF table is exported, the first column of the data block is a time vector
1180 on which all the calculated PDF are defined on a seven-sigmas interval. Each other
1181 column corresponds to the age PDF of a sample. Only samples with the "OK" status
1182 have a PDF vector in the data block. To identify each PDF, users just have to remove
1183 samples with an alternative status from the sample list. The name order in the

1184 resulting list will correspond to the PDF order of the table.

1185 **Acknowledgments**

1186 This work was funded by the INSU EVE-LEFE program and the ANR Jeunes
 1187 Chercheurs GALAC project “ANR-11-JS56-011-01”. G. Balco's contribution to this
 1188 work was supported in part by the Ann and Gordon Getty Foundation. J. Charreau,
 1189 R. Pik, D. Bourlès, J.-F. Ritz, M. Ferry, V. Jomelli, D. Brunstein provided very
 1190 useful advices about the design of CREp. R. Braucher and J. Amalberti are thanked
 1191 for useful discussions about muonic production scaling and Matlab GUI ©,
 1192 respectively.

1193

1194 **References**

- 1195 Ackert, R.P., Singer, B.S., Guillou, H., Kaplan, M.R., Kurz, M.D., 2003. Long-term cosmogenic ³He
 1196 production rates from ⁴⁰Ar/³⁹Ar and K–Ar dated Patagonian lava flows at 47°S. *Earth Planet. Sci.*
 1197 *Lett.* 210, 119–136. doi:10.1016/S0012-821X(03)00134-1
- 1198 Amidon, W.H., Farley, K.A., 2011. Cosmogenic ³He production rates in apatite, zircon and pyroxene
 1199 inferred from Bonneville flood erosional surfaces. *Quat. Geochronol.* 6, 10–21.
 1200 doi:10.1016/j.quageo.2010.03.005
- 1201 Balco, G., Briner, J., Finkel, R.C., Rayburn, J.A., Ridge, J.C., Schaefer, J.M., 2009. Regional beryllium-10
 1202 production rate calibration for late-glacial northeastern North America. *Quat. Geochronol.* 4, 93–107.
 1203 doi:10.1016/j.quageo.2008.09.001
- 1204 Balco, G., Stone, J.O., Lifton, N. a., Dunai, T.J., 2008. A complete and easily accessible means of
 1205 calculating surface exposure ages or erosion rates from ¹⁰Be and ²⁶Al measurements. *Quat.*
 1206 *Geochronol.* 3, 174–195. doi:10.1016/j.quageo.2007.12.001
- 1207 Barrows, T.T., Hope, G.S., Prentice, M.L., Fifield, L.K., Tims, S.G., 2011. Late Pleistocene glaciation of the
 1208 Mt Giluwe volcano, Papua New Guinea. *Quat. Sci. Rev.* 30, 2676–2689.
 1209 doi:10.1016/j.quascirev.2011.05.022
- 1210 Blard, P.-H., Bourlès, D., Lavé, J., Pik, R., 2006. Applications of ancient cosmic-ray exposures: Theory,
 1211 techniques and limitations. *Quat. Geochronol.* 1, 59–73. doi:10.1016/j.quageo.2006.06.003
- 1212 Blard, P.-H., Farley, K.A., 2008. The influence of radiogenic ⁴He on cosmogenic ³He determinations in
 1213 volcanic olivine and pyroxene. *Earth Planet. Sci. Lett.* 276, 20–29. doi:10.1016/j.epsl.2008.09.003
- 1214 Blard, P.-H., Lavé, J., Pik, R., Wagnon, P., Bourlès, D., 2007. Persistence of full glacial conditions in the
 1215 central Pacific until 15,000 years ago. *Nature* 449, 591–4. doi:10.1038/nature06142
- 1216 Blard, P.-H., Lavé, J., Sylvestre, F., Placzek, C.J., Claude, C., Galy, V., Condom, T., Tibari, B., 2013.
 1217 Cosmogenic ³ He production rate in the high tropical Andes (3800 m, 20 S): implications for the local
 1218 last glacial maximum. *Earth Planet. Sci. Lett.* 377, 260–275.
- 1219 Blard, P.-H., Sylvestre, F., Tripathi, a. K., Claude, C., Causse, C., Coudrain, a., Condom, T., Seidel, J.-L.,
 1220 Vimeux, F., Moreau, C., Dumoulin, J.-P., Lavé, J., 2011. Lake highstands on the Altiplano (Tropical
 1221 Andes) contemporaneous with Heinrich 1 and the Younger Dryas: new insights from ¹⁴C, U–Th
 1222 dating and $\delta^{18}\text{O}$ of carbonates. *Quat. Sci. Rev.* 30, 3973–3989. doi:10.1016/j.quascirev.2011.11.001

- 1223 Blard, P.H., Lave, J., Farley, K.A., Ramirez, V., Jimenez, N., Martin, L.C.P., Charreau, J., Tibari, B.,
1224 Fornari, M., 2014. Progressive glacial retreat in the Southern Altiplano (Uturuncu volcano, 22°S)
1225 between 65 and 14ka constrained by cosmogenic ³He dating. *Quat. Res. (United States)* 82, 209–221.
1226 doi:10.1016/j.yqres.2014.02.002
- 1227 Blard, P.H., Lave, J., Pik, R., Quidelleur, X., Bourles, D., Kieffer, G., 2005. Fossil cosmogenic He record
1228 from K–Ar dated basaltic flows of Mount Etna volcano (Sicily, 38°N): Evaluation of a new
1229 paleoaltimeter. *Earth Planet. Sci. Lett.* 236, 613–631. doi:10.1016/j.epsl.2005.05.028
- 1230 Blard, P.H., Pik, R., Lave, J., Bourles, D., Burnard, P., Yokochi, R., Marty, B., Trusdell, F., 2006.
1231 Cosmogenic ³He production rates revisited from evidences of grain size dependent release of matrix-
1232 sited helium. *Earth Planet. Sci. Lett.* 247, 222–234. doi:10.1016/j.epsl.2006.05.012
- 1233 Borchers, B., Marrero, S., Balco, G., Caffee, M., Goehring, B., Lifton, N., Nishiizumi, K., Phillips, F.,
1234 Schaefer, J., Stone, J., 2016. Geological calibration of spallation production rates in the CRONUS-
1235 Earth project. *Quat. Geochronol.* 31, 188–198. doi:10.1016/j.quageo.2015.01.009
- 1236 Braucher, R., Bourlès, D., Merchel, S., Vidal Romani, J., Fernandez-Mosquera, D., Marti, K., Léanni, L.,
1237 Chauvet, F., Arnold, M., Aumaître, G., Keddadouche, K., 2013. Determination of muon attenuation
1238 lengths in depth profiles from in situ produced cosmogenic nuclides. *Nucl. Instruments Methods Phys.*
1239 *Res. Sect. B Beam Interact. with Mater. Atoms* 294, 484–490. doi:10.1016/j.nimb.2012.05.023
- 1240 Braucher, R., Merchel, S., Borgomano, J., Bourlès, D.L., 2011. Production of cosmogenic radionuclides at
1241 great depth: A multi element approach. *Earth Planet. Sci. Lett.* 309, 1–9.
1242 doi:10.1016/j.epsl.2011.06.036
- 1243 Briner, J.P., Overeem, I., Miller, G., Finkel, R., 2006. The deglaciation of Clyde Inlet, northeastern Baffin
1244 Island, Arctic Canada. *J. Quat. Sci.* 22, 223–232.
- 1245 Briner, J.P., Young, N.E., Goehring, B.M., Schaefer, J.M., 2012. Constraining Holocene ¹⁰Be production
1246 rates in Greenland. *J. Quat. Sci.* 27, 2–6. doi:10.1002/jqs.1562
- 1247 Brown, E.T., Stallard, R.F., Larsen, M.C., Raisbeck, G.M., Yiu, F., 1995. Denudation rates determined
1248 from the accumulation of in situ produced ¹⁰Be in the Luquillo experimental forest, Puerto-Rico.
1249 *Earth Planet. Sci. Lett.* 129, 193–202.
- 1250 Cerling, T., Craig, H., 1994. Cosmogenic ³He production rates from 39° N to 46° N latitude, western USA
1251 and France. *Geochim. Cosmochim. Acta* 58, 249–255.
- 1252 Claude, A., Ivy-Ochs, S., Kober, F., Antognini, M., Salcher, B., Kubik, P.W., 2014. The Chironico landslide
1253 (Valle Leventina, southern Swiss Alps): age and evolution. *Swiss J. Geosci.* 107, 273–291.
1254 doi:10.1007/s00015-014-0170-z
- 1255 Delunel, R., Blard, P.-H., Martin, L.C.P., Nomade, S., Schlunegger, F., 2016. Long term low latitude and
1256 high elevation cosmogenic ³He production rate inferred from a 107ka-old lava flow in northern Chile;
1257 22°S-3400ma.s.l. *Geochim. Cosmochim. Acta* 184, 71–87. doi:10.1016/j.gca.2016.04.023
- 1258 Desilets, D., Zreda, M., 2003. Spatial and temporal distribution of secondary cosmic-ray nucleon intensities
1259 and applications to in situ cosmogenic dating. *Earth Planet. Sci. Lett.* 206, 21–42. doi:10.1016/S0012-
1260 821X(02)01088-9
- 1261 Desilets, D., Zreda, M., Prabu, T., 2006. Extended scaling factors for in situ cosmogenic nuclides: New
1262 measurements at low latitude. *Earth Planet. Sci. Lett.* 246, 265–276. doi:10.1016/j.epsl.2006.03.051
- 1263 Douglass, D.C., Singer, B.S., Kaplan, M.R., Mickelson, D.M., Caffee, M.W., 2006. Cosmogenic nuclide
1264 surface exposure dating of boulders on last-glacial and late-glacial moraines, Lago Buenos Aires,
1265 Argentina: Interpretive strategies and paleoclimate implications. *Quat. Geochronol.* 1, 43–58.
1266 doi:10.1016/j.quageo.2006.06.001
- 1267 Dunai, T., 2001. Influence of secular variation of the geomagnetic field on production rates of in situ
1268 produced cosmogenic nuclides. *Earth Planet. Sci. Lett.* 193, 197–212. doi:10.1016/S0012-
1269 821X(01)00503-9
- 1270 Dunai, T.J., Wijbrans, J.R., 2000. Long-term cosmogenic ³He production rates (152 ka - 1.35 Ma) from
1271 ⁴⁰Ar/³⁹Ar dated basalt flows at 29°N latitude. *Earth Planet. Sci. Lett.* 176.
- 1272 Dunne, J., Elmore, D., Muzikar, P., 1999. Scaling factors for the rates of production of cosmogenic nuclides
1273 for geometric shielding and attenuation at depth on sloped surfaces. *Geomorphology* 27, 3–11.

- 1274 doi:10.1016/S0169-555X(98)00086-5
- 1275 Elsasser, W.M., Ney, E.P., Wenckler, I.R., 1956. Cosmic ray intensity and geomagnetism. *Nature* 178,
1276 1226–1227.
- 1277 Farber, D.L., Hancock, G.S., Finkel, R.C., Rodbell, D.T., 2005. The age and extent of tropical alpine
1278 glaciation in the Cordillera Blanca, Peru. *J. Quat. Sci.* 20, 759–776. doi:10.1002/jqs.994
- 1279 Fenton, C.R., Hermanns, R.L., Blikra, L.H., Kubik, P.W., Bryant, C., Niedermann, S., Meixner, A.,
1280 Goethals, M.M., 2011. Regional ^{10}Be production rate calibration for the past 12ka deduced from the
1281 radiocarbon-dated Grøtlandsura and Russenes rock avalanches at 69° N, Norway. *Quat. Geochronol.*
1282 6, 437–452. doi:10.1016/j.quageo.2011.04.005
- 1283 Fenton, C.R., Mark, D.F., Barfod, D.N., Niedermann, S., Goethals, M.M., Stuart, F.M., 2013. $^{40}\text{Ar}/^{39}\text{Ar}$
1284 dating of the SP and Bar Ten lava flows AZ, USA: Laying the foundation for the SPICE cosmogenic
1285 nuclide production-rate calibration project. *Quat. Geochronol.* 18, 158–172.
1286 doi:10.1016/j.quageo.2013.01.007
- 1287 Fenton, C.R., Niedermann, S., 2014. Surface exposure dating of young basalts (1-200ka) in the San
1288 Francisco volcanic field (Arizona, USA) using cosmogenic ^3He and ^{21}Ne . *Quat. Geochronol.* 19, 87–
1289 105. doi:10.1016/j.quageo.2012.10.003
- 1290 Finlay, C.C., Maus, S., Beggan, C.D., Bondar, T.N., Chambodut, a., Chernova, T. a., Chulliat, a.,
1291 Golovkov, V.P., Hamilton, B., Hamoudi, M., Holme, R., Hulot, G., Kuang, W., Langlais, B., Lesur,
1292 V., Lowes, F.J., Lühr, H., Macmillan, S., Manda, M., McLean, S., Manoj, C., Menvielle, M.,
1293 Michaelis, I., Olsen, N., Rauberg, J., Rother, M., Sabaka, T.J., Tangborn, a., Tøffner-Clausen, L.,
1294 Thébaud, E., Thomson, a. W.P., Wardinski, I., Wei, Z., Zvereva, T.I., 2010. International
1295 Geomagnetic Reference Field: the eleventh generation. *Geophys. J. Int.* 183, 1216–1230.
1296 doi:10.1111/j.1365-246X.2010.04804.x
- 1297 Foeken, J.P.T., Stuart, F.M., Mark, D.F., 2012. Long-term low latitude cosmogenic ^3He production rate
1298 determined from a 126ka basalt from Fogo, Cape Verdes. *Earth Planet. Sci. Lett.* 359-360, 14–25.
1299 doi:10.1016/j.epsl.2012.10.005
- 1300 Goehring, B.M., Kurz, M.D., Balco, G., Schaefer, J.M., Licciardi, J., Lifton, N., 2010. A reevaluation of in
1301 situ cosmogenic ^3He production rates. *Quat. Geochronol.* 5, 410–418.
1302 doi:10.1016/j.quageo.2010.03.001
- 1303 Goehring, B.M., Lohne, Ø.S., Mangerud, J., Svendsen, J.I., Gyllencreutz, R., Schaefer, J., Finkel, R., 2012.
1304 Late glacial and holocene ^{10}Be production rates for western Norway. *J. Quat. Sci.* 27, 89–96.
1305 doi:10.1002/jqs.1517
- 1306 Gosse, J.C., Klein, J., Lawn, B., Middleton, R., Evenson, E.B., 1995. Beryllium-10 dating of the duration
1307 and retreat of the last pinedale glacial sequence. *Science* 268, 1329–33.
1308 doi:10.1126/science.268.5215.1329
- 1309 Gosse, J.C., Phillips, F.M., 2001. Terrestrial in situ cosmogenic nuclides: theory and application. *Quat. Sci.*
1310 *Rev.* 20, 1475–1560. doi:10.1016/S0277-3791(00)00171-2
- 1311 Guyodo, Y., Valet, J., 1999. Global changes in intensity of the Earth's magnetic field during the past 800
1312 kyr. *Nature* 399, 249–252. doi:10.1038/20420
- 1313 Heisinger, B., Lal, D., Jull, A.J.T., Kubik, P., Ivy-Ochs, S., Knie, K., Nolte, E., 2002a. Production of
1314 selected cosmogenic radionuclides by muons: 2. Capture of negative muons. *Earth Planet. Sci. Lett.*
1315 200, 357–369.
- 1316 Heisinger, B., Lal, D., Jull, A.J.T., Kubik, P., Ivy-Ochs, S., Neumaier, S., Knie, K., Lazarev, V., Nolte, E.,
1317 2002b. Production of selected cosmogenic radionuclides by muons; 1. Fast muons. *Earth Planet. Sci.*
1318 *Lett.* 200, 345–355.
- 1319 Heyman, J., 2014. Paleoglaciation of the tibetan plateau and surrounding mountains based on exposure ages
1320 and ELA depression estimates. *Quat. Sci. Rev.* 91, 30–41. doi:10.1016/j.quascirev.2014.03.018
- 1321 Jomelli, V., Favier, V., Vuille, M., Braucher, R., Martin, L., Blard, P.-H., Colose, C., Brunstein, D., He, F.,
1322 Khodri, M., Bourlès, D.L., Leanni, L., Rinterknecht, V., Grancher, D., Francou, B., Ceballos, J.L.,
1323 Fonseca, H., Liu, Z., Otto-Bliesner, B.L., 2014. A major advance of tropical Andean glaciers during
1324 the Antarctic cold reversal. *Nature*. doi:10.1038/nature13546

- 1325 Kaplan, M.R., Strelin, J. a., Schaefer, J.M., Denton, G.H., Finkel, R.C., Schwartz, R., Putnam, A.E.,
 1326 Vandergoes, M.J., Goehring, B.M., Travis, S.G., 2011. In-situ cosmogenic ^{10}Be production rate at
 1327 Lago Argentino, Patagonia: Implications for late-glacial climate chronology. *Earth Planet. Sci. Lett.*
 1328 309, 21–32. doi:10.1016/j.epsl.2011.06.018
- 1329 Kelly, M.A., Lowell, T. V., Applegate, P.J., Phillips, F.M., Schaefer, J.M., Smith, C.A., Kim, H., Leonard,
 1330 K.C., Hudson, A.M., 2015. A locally calibrated, late glacial ^{10}Be production rate from a low-latitude,
 1331 high-altitude site in the Peruvian Andes. *Quat. Geochronol.* 26, 70–85.
 1332 doi:10.1016/j.quageo.2013.10.007
- 1333 Kim, K.J., Englert, P.A.J., 2004. Profiles of in situ ^{10}Be and ^{26}Al at great depths at the Macraes Flat, East
 1334 Otago, New Zealand. *Earth Planet. Sci. Lett.* 223, 113–126. doi:10.1016/j.epsl.2004.04.006
- 1335 Korte, M., Donadini, F., Constable, C.G., 2009. Geomagnetic field for 0-3 ka: 2. A new series of time-
 1336 varying global models. *Geochemistry, Geophys. Geosystems* 10, n/a–n/a.
 1337 doi:10.1029/2008GC002297
- 1338 Korte, M., Genevey, a., Constable, C.G., Frank, U., Schnepp, E., 2005. Continuous geomagnetic field
 1339 models for the past 7 millennia: 1. A new global data compilation. *Geochemistry, Geophys.*
 1340 *Geosystems* 6, n/a–n/a. doi:10.1029/2004GC000800
- 1341 Kubik, P.W., Ivy-Ochs, S., Masarik, J., Frank, M., Schlüchter, C., 1998. ^{10}Be and ^{26}Al production rates
 1342 deduced from an instantaneous event within the dendro-calibration curve, the landslide of Köfels, Ötz
 1343 Valley, Austria. *Earth Planet. Sci. Lett.* 161, 231–241. doi:10.1016/S0012-821X(98)00153-8
- 1344 Kurz, M., Colodner, D., Trull, T.W., Moore, R.B., O'Brien, K., 1990. Cosmic ray exposure dating with in
 1345 situ produced cosmogenic ^3He : results from young Hawaiian lava flows. *Earth Planet. Sci. Lett.* 97,
 1346 177–189.
- 1347 Laj, C., Kissel, C., Beer, J., 2004. High Resolution Global Paleointensity Stack Since 75 kyr (GLOPIS-75)
 1348 Calibrated to Absolute Values. *Timescales Paleomagn. F., Geophysical Monograph Series* 145, 255–
 1349 265. doi:10.1029/145GM19
- 1350 Lal, D., 1991. Cosmic ray labeling of erosion surfaces: in situ nuclide production rates and erosion models.
 1351 *Earth Planet. Sci. Lett.* 104, 424–439. doi:10.1016/0012-821X(91)90220-C
- 1352 Licciardi, J., Kurz, M., Clark, P., Brook, E., 1999. Calibration of cosmogenic ^3He production rates from
 1353 Holocene lava flows in Oregon, USA, and effects of the Earth's magnetic field. *Earth Planet. Sci.*
 1354 *Lett.* 172, 261–271. doi:10.1016/S0012-821X(99)00204-6
- 1355 Licciardi, J.M., Schaefer, J.M., Taggart, J.R., Lund, D.C., 2009. Holocene glacier fluctuations in the
 1356 Peruvian Andes indicate northern climate linkages. *Science* 325, 1677–9.
 1357 doi:10.1126/science.1175010
- 1358 Lifton, N., 2016. Implications of two Holocene time-dependent geomagnetic models for cosmogenic
 1359 nuclide production rate scaling. *Earth Planet. Sci. Lett.* 433, 257–268. doi:10.1016/j.epsl.2015.11.006
- 1360 Lifton, N. a., Bieber, J.W., Clem, J.M., Duldig, M.L., Evenson, P., Humble, J.E., Pyle, R., 2005. Addressing
 1361 solar modulation and long-term uncertainties in scaling secondary cosmic rays for in situ cosmogenic
 1362 nuclide applications. *Earth Planet. Sci. Lett.* 239, 140–161. doi:10.1016/j.epsl.2005.07.001
- 1363 Lifton, N., Caffee, M., Finkel, R., Marrero, S., Nishiizumi, K., Phillips, F.M., Goehring, B., Gosse, J.,
 1364 Stone, J., Schaefer, J., Theriault, B., Jull, A.J.T., Fifield, K., 2015. In situ cosmogenic nuclide
 1365 production rate calibration for the CRONUS-Earth project from lake Bonneville, Utah, shoreline
 1366 features. *Quat. Geochronol.* 26, 56–69. doi:10.1016/j.quageo.2014.11.002
- 1367 Lifton, N., Sato, T., Dunai, T.J., 2014. Scaling in situ cosmogenic nuclide production rates using analytical
 1368 approximations to atmospheric cosmic-ray fluxes. *Earth Planet. Sci. Lett.* 386, 149–160.
 1369 doi:10.1016/j.epsl.2013.10.052
- 1370 Lifton, N., Smart, D.F., Shea, M.A., 2008. Scaling time-integrated in situ cosmogenic nuclide production
 1371 rates using a continuous geomagnetic model. *Earth Planet. Sci. Lett.* 268, 190–201.
- 1372 Lupker, M., Blard, P.H., Lavé, J., France-Lanord, C., Leanni, L., Puchol, N., Charreau, J., Bourlès, D.,
 1373 2012. ^{10}Be -derived Himalayan denudation rates and sediment budgets in the Ganga basin. *Earth*
 1374 *Planet. Sci. Lett.* 333-334, 146–156. doi:10.1016/j.epsl.2012.04.020
- 1375 Ma, X., Li, Y., Bourgeois, M., Caffee, M., Elmore, D., Granger, D., Muzikar, P., Smith, P., 2007. WebCN:

- 1376 A web-based computation tool for in situ-produced cosmogenic nuclides. *Nucl. Instruments Methods*
1377 *Phys. Res. Sect. B Beam Interact. with Mater. Atoms* 259, 646–652. doi:10.1016/j.nimb.2007.01.303
- 1378 Marrero, S.M., Phillips, F.M., Borchers, B., Lifton, N., Aumer, R., Balco, G., 2016. Cosmogenic nuclide
1379 systematics and the CRONUScal program. *Quat. Geochronol.* 31, 160–187.
1380 doi:10.1016/j.quageo.2015.09.005
- 1381 Martin, L.C.P., Blard, P.-H., Lavé, J., Braucher, R., Lupker, M., Condom, T., Charreau, J., Mariotti, V.,
1382 Davy, E., 2015. In situ cosmogenic ^{10}Be production rate in the High Tropical Andes. *Quat.*
1383 *Geochronol.* 30, 54–68. doi:10.1016/j.quageo.2015.06.012
- 1384 Muscheler, R., Beer, J., Kubik, P.W., Synal, H. -a., 2005. Geomagnetic field intensity during the last 60,000
1385 years based on ^{10}Be and ^{36}Cl from the Summit ice cores and ^{14}C . *Quat. Sci. Rev.* 24, 1849–1860.
1386 doi:10.1016/j.quascirev.2005.01.012
- 1387 N.O.A.A., 1976. U.S. Standard Atmosphere. US Gov. Print. Off.
- 1388 Nishiizumi, K., Imamura, M., Caffee, M.W., Southon, J.R., Finkel, R.C., McAninch, J., 2007. Absolute
1389 calibration of ^{10}Be AMS standards. *Nucl. Instruments Methods Phys. Res. Sect. B Beam Interact.*
1390 *with Mater. Atoms* 258, 403–413. doi:10.1016/j.nimb.2007.01.297
- 1391 Nishiizumi, K., Winterer, E.L., Kohl, C.P., Klein, J., Middleton, R., Lal, D., Arnold, J.R., 1989. Cosmic ray
1392 production rates of ^{10}Be and ^{26}Al in quartz from glacially polished rocks. *J. Geophys. Res.* 94,
1393 17907. doi:10.1029/JB094iB12p17907
- 1394 Obrochta, S.P., Yokoyama, Y., Morén, J., Crowley, T.J., 2014. Conversion of GISP2-based sediment core
1395 age models to the GICC05 extended chronology. *Quat. Geochronol.* 20, 1–7.
1396 doi:10.1016/j.quageo.2013.09.001
- 1397 Palumbo, L., Benedetti, L., Bourlès, D., Cinque, A., Finkel, R., 2004. Slip history of the Magnola fault
1398 (Apennines, Central Italy) from ^{36}Cl surface exposure dating: Evidence for strong earthquakes over
1399 the Holocene. *Earth Planet. Sci. Lett.* 225, 163–176. doi:10.1016/j.epsl.2004.06.012
- 1400 Peirce, B., 1852. Criterion for the rejection of doubtful observations. *Astron. J.* 2.
- 1401 Phillips, F.M., Kelly, M.A., Hudson, A.M., Stone, J.O.H., Schaefer, J., Marrero, S.M., Fifield, L.K., Finkel,
1402 R., Lowell, T., 2016. CRONUS-Earth calibration samples from the Huancané II moraines, Quelccaya
1403 Ice Cap, Peru. *Quat. Geochronol.* 31, 220–236. doi:10.1016/j.quageo.2015.10.005
- 1404 Phillips, F.M., Stone, W.D., Fabryka-Martin, J.T., 2001. An improvement approach to calculating low-
1405 energy cosmic-ray neutron fluxes near the land/atmosphere interface. *Chem. Geol.* 175, 689–701.
1406 doi:10.1016/S0009-2541(00)00329-6
- 1407 Poreda, R.J., Cerling, T.E., 1992. Cosmogenic neon in recent lavas from the Western United States.
1408 *Geophys. Res. Lett.* 19, 1863–1866.
- 1409 Putnam, A.E., Schaefer, J.M., Barrell, D.J.A., Vandergoes, M., Denton, G.H., Kaplan, M.R., Finkel, R.C.,
1410 Schwartz, R., Goehring, B.M., Kelley, S.E., 2010. In situ cosmogenic ^{10}Be production-rate
1411 calibration from the Southern Alps, New Zealand. *Quat. Geochronol.* 5, 392–409.
1412 doi:10.1016/j.quageo.2009.12.001
- 1413 Putnam, A.E., Schaefer, J.M., Denton, G.H., Barrell, D.J.A., Andersen, B.G., Koffman, T.N.B., Rowan, A.
1414 V., Finkel, R.C., Rood, D.H., Schwartz, R., Vandergoes, M.J., Plummer, M.A., Brocklehurst, S.H.,
1415 Kelley, S.E., Ladig, K.L., 2013. Warming and glacier recession in the Rakaia valley, Southern Alps of
1416 New Zealand, during Heinrich Stadial 1. *Earth Planet. Sci. Lett.* 382, 98–110.
1417 doi:10.1016/j.epsl.2013.09.005
- 1418 Reimer, P., Bard, E., Bayliss, A., Beck, J., Blackwell, P., Ramsey, C., Buck, C., Cheng, H., Edwards, R.,
1419 Friedrich, M., Grootes, P., Guilderson, T., Haflidason, H., Hajdas, I., Hatte, C., Heaton, T., Hoffmann,
1420 D., Hogg, A., Hughen, K., Kaiser, K., Kromer, B., Manning, S., Niu, M., Reimer, R., Richards, D.,
1421 Scott, E., Southon, J., Staff, R., Turney, C., van der Plicht, J., 2013. IntCal13 and Marine13
1422 Radiocarbon Age Calibration Curves 0–50,000 Years cal BP. *Radiocarbon* 55, 1869–1887.
1423 doi:10.2458/azu_js_rc.55.16947
- 1424 Riebe, C.S., Kirchner, J.W., Granger, D.E., Finkel, R.C., 2000. Erosional equilibrium and disequilibrium in
1425 the Sierra Nevada, inferred from cosmogenic ^{26}Al and ^{10}Be in alluvial sediment. *Geology* 28, 803–
1426 806. doi:10.1130/0091-7613(2000)28<803:EEADIT>2.0.CO;2

- 1427 Ritz, J.F., Bourlès, D.L., Philip, H., Raisbeck, G.M., Yiou, F., Enkhtuvshin, B., 1995. Slip rates along active
1428 faults estimated with cosmic-ray– exposure dates: Application to the Bogd fault, Gobi-Alta,
1429 Mongolia. *Geology* 23, 1019–1022. doi:10.1130/0091-7613(1995)023<1019
- 1430 Ross, S., 2003. Peirce’s criterion for the elimination of suspect experimental data. *J. Eng. Technol.* 20.
- 1431 Sandstrom, A.E., Pomerantz, M.A., Gronkvist, B.O., 1962. Latitude effect and atmospheric attenuation of
1432 the cosmic ray nucleon component. *Tellus* 14, 356–362.
- 1433 Sato, T., Yasuda, H., Niita, K., Endo, A., Sihver, L., 2008. Development of PARMA: PHITS-based
1434 analytical radiation model in the atmosphere. *Radiat. Res.* 170, 244–59. doi:10.1667/RR1094.1
- 1435 Schimmelpfennig, I., Williams, A., Pik, R., Burnard, P., Niedermann, S., Finkel, R., Schneider, B.,
1436 Benedetti, L., 2011. Inter-comparison of cosmogenic in-situ ³He, ²¹Ne and ³⁶Cl at low latitude along
1437 an altitude transect on the SE slope of Kilimanjaro volcano (3°S, Tanzania). *Quat. Geochronol.* 6,
1438 425–436. doi:10.1016/j.quageo.2011.05.002
- 1439 Smith, J. a, Seltzer, G.O., Farber, D.L., Rodbell, D.T., Finkel, R.C., 2005. Early local last glacial maximum
1440 in the tropical Andes. *Science* 308, 678–81. doi:10.1126/science.1107075
- 1441 Staiger, J., Gosse, J., Toracinta, R., Oglesby, B., Fastook, J., Johnson, J. V., 2007. Atmospheric scaling of
1442 cosmogenic nuclide production: Climate effect. *J. Geophys. Res. Solid Earth* 112, 1–8.
1443 doi:10.1029/2005JB003811
- 1444 Stone, J.O., 2000. Air pressure and cosmogenic isotope production. *J. Geophys. Res.* 105, 23753.
1445 doi:10.1029/2000JB900181
- 1446 Stormer, C., 1955. *The Polar Aurora*. Oxford University Press.
- 1447 Stroeven, A.P., Heyman, J., Fabel, D., Björck, S., Caffee, M.W., Fredin, O., Harbor, J.M., 2015. A new
1448 Scandinavian reference ¹⁰Be production rate. *Quat. Geochronol.* doi:10.1016/j.quageo.2015.06.011
- 1449 Svensson, a., Andersen, K.K., Bigler, M., Clausen, H.B., Dahl-Jensen, D., Davies, S.M., Johnsen, S.J.,
1450 Muscheler, R., Parrenin, F., Rasmussen, S.O., Rothlisberger, R., Seierstad, I., Steffensen, J.P.,
1451 Vinther, B.M., 2008. A 60 000 year Greenland stratigraphic ice core chronology 47–57.
1452 doi:10.5194/cpd-3-1235-2007
- 1453 Uppala, S.M., K? llberg, P.W., Simmons, a. J., Andrae, U., Bechtold, V.D.C., Fiorino, M., Gibson, J.K.,
1454 Haseler, J., Hernandez, a., Kelly, G. a., Li, X., Onogi, K., Saarinen, S., Sokka, N., Allan, R.P.,
1455 Andersson, E., Arpe, K., Balmaseda, M. a., Beljaars, a. C.M., Berg, L. Van De, Bidlot, J., Bormann,
1456 N., Caires, S., Chevallier, F., Dethof, a., Dragosavac, M., Fisher, M., Fuentes, M., Hagemann, S.,
1457 Hólm, E., Hoskins, B.J., Isaksen, L., Janssen, P. a. E.M., Jenne, R., McNally, a. P., Mahfouf, J.-F.,
1458 Morcrette, J.-J., Rayner, N. a., Saunders, R.W., Simon, P., Sterl, a., Trenberth, K.E., Untch, a.,
1459 Vasiljevic, D., Viterbo, P., Woollen, J., 2005. The ERA-40 re-analysis. *Q. J. R. Meteorol. Soc.* 131,
1460 2961–3012. doi:10.1256/qj.04.176
- 1461 Valet, J.-P., Meynadier, L., Guyodo, Y., 2005. Geomagnetic dipole strength and reversal rate over the past
1462 two million years. *Nature* 435, 802–805.
- 1463 Vermeesch, P., 2007. CosmoCalc: An Excel add-in for cosmogenic nuclide calculations. *Geochemistry,*
1464 *Geophys. Geosystems* 8, 1–14. doi:10.1029/2006GC001530
- 1465 Wittmann, H., von Blanckenburg, F., 2009. Cosmogenic nuclide budgeting of floodplain sediment transfer.
1466 *Geomorphology* 109, 246–256. doi:10.1016/j.geomorph.2009.03.006
- 1467 Yang, S., Odah, H., Shaw, J., 2000. Variations in the geomagnetic dipole moment over the last 12 000
1468 years. *Geophys. J. Int.* 1982, 158–162. doi:10.1046/j.1365-246x.2000.00011.x
- 1469 York, D., 1966. Least-squares fitting of a straight line. *Can. J. Phys.* 44, 1079–1086.
- 1470 Young, N.E., Schaefer, J.M., Briner, J.P., Goehring, B.M., 2013. A ¹⁰Be production-rate calibration for the
1471 Arctic. *J. Quat. Sci.* 28, 515–526. doi:10.1002/jqs.2642
- 1472 Ziegler, L.B., Constable, C.G., Johnson, C.L., Tauxe, L., 2011. PADM2M: a penalized maximum likelihood
1473 model of the 0-2 Ma palaeomagnetic axial dipole moment. *Geophys. J. Int.* 184, 1069–1089.
1474 doi:10.1111/j.1365-246X.2010.04905.x
- 1475 Zweck, C., Zreda, M., Anderson, K.M., Bradley, E., 2012. The theoretical basis of ACE, an Age Calculation
1476 Engine for cosmogenic nuclides. *Chem. Geol.* 291, 199–205. doi:10.1016/j.chemgeo.2011.10.005

Chapitre 6

Présentation de 4 chronologies glaciaires couplées à des inversions de températures

Les chapitres 6 et 7 profitent des développements méthodologiques des chapitres 4 et 5 pour déterminer des âges de moraines et de roches moutonnées dans différentes vallées de l'Altiplano. Ces âges sont ensuite utilisés pour des interprétations paléoclimatiques.

Dans le chapitre 6 les datations sont utilisées pour créer des reconstitutions temporelles des extensions glaciaires, des lignes d'équilibre associées puis des températures et des précipitations pendant la dernière déglaciation. Les investigations sont menées pour 4 sites : la vallée du Zongo, le Nevado Sajama, le Cerro Tunupa, et le Cerro Luxar (localisés en Figure 1 du manuscrit). Ces résultats prolongent les études de [Blard et al. \(2009, 2013\)](#) au Tunupa, et [Jomelli et al. \(2011\)](#) et [Smith et al. \(2005\)](#) au Zongo.

Dans cette approche chronologique, la méthode d'inversion couplant glacier et lac utilisée dans cette thèse est appliquée indépendamment à chaque site, et ce sans chercher à produire une cohérence spatiale des résultats. Pour chaque site, l'inversion s'appuie sur l'âge de chaque moraine. Pour un âge de moraine, l'archive glaciaire fournit une extension glaciaire associable à une ligne d'équilibre et l'archive lacustre fournit le niveau du paléolac du bassin sud (le Tauca, le Coipasa, ou bien un état intermédiaire). A ces contraintes glaciologiques et hydrologiques, les modèles de glaciers et de lac associent des refroidissements et des augmentations de pluviométrie par rapport au présent. En croisant ces résultats on détermine un seul refroidissement et une seule augmentation de la pluviométrie correspondant à l'âge de la moraine. Cette méthode est appliquée, pour chaque site, à toutes les moraines pour lesquelles un âge est déterminé, ce qui permet donc de créer une reconstruction des précipitations et des températures par site.

Relativement aux explications en préambule de cette thèse, quelques précisions peuvent s'avérer nécessaires vis à vis des résultats d'âges présentés dans les chapitres 6 et 7. Dans le cadre de la datation des morphologies glaciaires, l'utilisateur souhaite dater l'âge d'abandon des morphologies glaciaires par le glacier. Plusieurs cas de figure peuvent faire en sorte que l'âge mesuré ne corresponde pas au temps passé depuis cet abandon :

- Si le bloc morainique (ou la roche moutonnée) échantillonné a une histoire d'exposition antérieure au transport glaciaire. Auquel cas la concentration mesurée ne correspond pas au temps passé depuis l'abandon de la moraine par le glacier. Cette concentration correspond à un âge plus vieux difficilement interprétable. Dans ce cas, on dit que l'échantillon présente un héritage. Cet héritage correspond à la concentration en isotope cosmogénique déjà présente au moment de l'abandon de la moraine par le glacier. Elle est responsable de la surestimation de l'âge d'exposition vis à vis du processus étudié.
- Si le bloc échantillonné a subi de l'érosion. Dans ce cas, la surface prélevée pour la datation

a été (pendant une durée et sur une épaisseur inconnues) écrantée du rayonnement cosmique par du matériel rocheux sus-jacent, ensuite évacué par l'érosion. L'âge établi à partir de la concentration en isotopes cosmogéniques sous-estime alors l'âge depuis l'abandon par le glacier. L'érosion correspond donc à la quantité d'isotopes cosmogéniques trop faible pour établir un âge juste.

- De la même manière que pour l'érosion, des enregistrements incomplets du rayonnement cosmique peuvent être causés par une déflation de la matrice du till glaciaire qui met à jour des petits blocs précédemment écrantés, mais aussi par un couvert neigeux prolongé, une végétation dense, ou encore une rotation du bloc échantillonné. Une bonne pratique consiste donc à échantillonner les blocs morainiques les plus hauts possible. En effet, ceux-ci sont moins enclins à avoir été enfouis dans la matrice du till puis ramenés à la surface.

Afin de pouvoir identifier ces phénomènes, il est donc indispensable d'échantillonner plusieurs blocs sur une même moraine pour pouvoir la dater et espérer identifier un âge modal et des âges marginaux. Au cours de ces travaux de thèse, l'érosion et les processus apparentés d'écrantage et d'enregistrements incomplets du rayonnement cosmique ont été très peu observés. En revanche, l'héritage s'est avéré souvent problématique. Le cas le plus représentatif de ce problème est celui de la vallée de Chiar Khota pour laquelle nous avons réalisé une vingtaine de datation dont aucune interprétation n'a été tirée à ce jour. Ces résultats sont présentés en Annexes de ce manuscrit.

Dans les autres cas présentés dans les chapitres 6 et 7, la dispersion des résultats due à l'héritage a nécessité de faire l'hypothèse que certains âges étaient "hérités" et donc surestimés. Il a parfois également été nécessaire de recourir à des méthodes bayésiennes de calcul d'âges. Celles-ci permettent d'utiliser les relations stratigraphiques entre les morphologies glaciaires pour apporter de nouvelles contraintes temporelles et identifier l'âge le plus vraisemblable pour l'objets daté.

En lien avec ce constat, je souhaitais préciser que les manuscrits présentés dans les chapitres 6 et 7 ont été rédigés dans les derniers temps de cette thèse afin de présenter les dernières interprétations climatiques réalisées. De ce fait, plusieurs points de la méthodologie et des résultats nécessiteront d'avantage de développements. C'est particulièrement le cas pour la méthodologie appliquée aux résultats d'âges dispersés qui est en cours d'élaboration. Les traitements proposés pour l'instant seront à terme remplacés par une approche appliquée systématiquement à chaque site.

Concernant les inversions climatiques, toutes les incertitudes n'ont pas encore été propagées et des tests de sensibilité doivent encore être faits. Plusieurs points de la méthodologie sont encore en développement, notamment concernant l'incidence des incertitudes d'âges sur les inversions et la variabilité des résultats d'inversions correspondant à une même période. J'ai souhaité considérer que ces lacunes ont une importance mineure relativement à la portée des résultats présentés. Ces améliorations futures apporteront probablement d'avantage de robustesse à la démarche mais elles ne devraient pas modifier de manière significative les principaux résultats et conclusions.

Les nouvelles données présentées dans le chapitre 6 ne sont pas toutes de mon fait. J'ai précisé ma contribution aux différents travaux présentés dans cette thèse dans une annexe en langue anglaise appelée *Personal Contribution*.

Cette étude est présentée en langue anglaise sous la forme d'un manuscrit d'article en vue d'une soumission prochaine auprès d'une revue scientifique.

1 **Late-glacial temperature reconstruction on the Bolivian Altiplano**
 2 **inferred from palaeo-glaciers and palaeo-lakes**

3
 4
 5 L. C. P. Martin^{a*}, P. -H. Blard^{a*}, J. Lavé^a, M. Premaillon^a, V. Jomelli^b, D. Brunstein^b, M.
 6 Lupker^c, J. Charreau^a, V. Mariotti^a, T. Condom^d, B. Tibari^a, ASTER Team^{e#}, E. Davy^a.

7
 8
 9 a. CRPG, UMR7358 CNRS - Université de Lorraine, 54500 Vandoeuvre-lès-Nancy, France

10 b. Université Paris 1 Panthéon-Sorbonne, CNRS Laboratoire de Géographie Physique,
 11 92195 Meudon, France.

12 c. ETH, Inst. f. Geochemie und Petrologie, Clausiusstrasse 25, 8092 Zurich, Switzerland
 13 ETH, Geological Institute, Sonneggstrasse 5, 8092 Zurich, Switzerland

14 d. IRD, LTHE, UMR 5564, CNRS, Univ. Grenoble Alpes, G-INP, 38000 Grenoble, France

15 e. Aix-Marseille Université, CNRS-IRD-Collège de France, UM 34 CEREGE, Technopôle
 16 de l'Arbois, BP80, 13545 Aix-en-Provence, France

17
 18 # M. Arnold, G. Aumaître, D. L. Bourlès, K. Keddadouche

19
 20
 21 * Corresponding authors:

22
 23 CRPG

24 15 rue Notre Dame des Pauvres

25 54501 Vandoeuvre-lès-Nancy

26 FRANCE

27
 28 Email: leom@crpg.cnrs-nancy.fr; blard@crpg.cnrs-nancy.fr

29
 30
 31 13 500 words

32 7 Tables

33 18 Figures

34 2 Appendices

35
 36
 37
 38
 39
 40 **Keywords:** Moraine Dating, Exposure Ages, Equilibrium Line Altitude, Lake Tauca, palaeo-
 41 shorlines, lake and glacier modelling, continental palaeo-temperature reconstruction, regional
 42 climate variability.

43 **Highlights**

44 - Cosmic Ray Exposure ages determination for Late-glacial Moraines on the Bolivian
45 Altiplano.

46 - Computation of the corresponding Equilibrium Line Altitudes (ELA).

47 - New shorelines datings added to the Altiplano late-glacial palaeo-lake dataset.

48 - Continental palaeo-temperature reconstruction inferred from palaeo-glacier and palaeo-lake
49 cross modelling.

50

51 **Abstract**

52 The global climate oscillations of the late-glacial period (LGM to Holocene) involve
53 major reorganisations of the continental climate systems (Blard et al., 2009; Wang et al.,
54 2004) which are for now on poorly understood. Over the Altiplano (High Tropical Andes,
55 Bolivia), the second half of the Heinrich 1 Stadial (16.5-14.5 ka) and the Younger Dryas
56 (12.9-11.7 ka) are coeval with major hydrologic reorganisations and the waxing and waning
57 of the giant palaeo-lakes Tauca and Coipasa. Mountain glacier ice dynamics is driven by the
58 local climatic forcings, making palaeo-glaciers a suitable archive to investigate the spatio-
59 temporal variability of the past climate (Jomelli et al., 2014; Smith et al., 2005).

60 We present new Cosmic Ray Exposure (CRE) ages that extend the existing datasets in
61 the Zongo Valley (16.2°S - 68.1°W) (Jomelli et al., 2011; Smith et al., 2005) and Cerro
62 Tunupa (19.8°S - 67.6°W) (Blard et al., 2009) and provide new chronologies on Nevado
63 Sajama (18.1°S - 68.9°W) and Cerro Luxar (21.0°S - 68.0°W). We also report new shoreline
64 ¹⁴C ages from bioherm calcite on Isla Incahuasi (20.2°S - 67.6°W) indicating that the Coipasa
65 highstand reached 3720 masl, 15 m higher than previously reported (Blard et al., 2011;
66 Placzek et al., 2006; Sylvestre et al., 1999).

67 We took advantage of this new set of results to calculate the Equilibrium Line Altitude
68 (ELA) associated with each moraine using the AAR method with a value of 0.55 - 0.65
69 derived from observations on present glaciers of the High Tropical Andes (Soruco et al.,
70 2009). These ELAs along with present climate observations are used in an inverse method
71 that combines simple precipitation and temperature modelling of the palaeo-glaciers and
72 palaeo-lakes (following Blard et al., 2009) to derive temperature reconstructions for the 4
73 sites over the late-glacial period.

74 The 13 moraines studied in the Zongo valley constraint the complete late-glacial
75 period. The valley experiences a Local Late Glacial Maximum (LLGM) around 17 ka
76 followed by a quasi stillstand until 13.5 ka. On this period, the ELAs rises from 4540 to 4640
77 m and the Δ Temperature (vs. Present) from -4.3 to -3.7 °C. The 13.5 to 10 ka period is
78 marked by a massive retreat with Younger Dryas and Early Holocenes ELAs around 4800
79 masl and associated $\Delta T \approx 2.5$ -3°C.

80 Nevado Sajama, Cerro Tunupa and Cerro Luxar exhibit a broadly common behaviour,
81 different from the Zongo valley. The record a LLGM around 16 ka at the onset of the Tauca
82 highstand followed by a retreat either on the second half of the highstand (Sajama, Luxar) or
83 during the regression (Tunupa). Cerro Luxar undergoes a massive retreat with no later
84 stabilisation. Nevado Sajama and Cerro Tunupa both exhibit upstream moraine stabilisations
85 around 12-13 ka. Over the whole period Sajama and Luxar ELAs rises from 4740 to more
86 than 4800 masl. The Tunupa ELAs rise from 4450 to 4680 masl. The ΔT reconstruction
87 shows important scatter between the sites for the Tauca highstand (-6.5 to -3.5°C vs. Present)
88 likely to be caused by anomalies in the spatial rainfall pattern. The most robust ΔT is around -
89 4 to -4.5°C.

90 The spatial repartition of these anomalies along with the Tauca moraine locations
91 reported here in other studies support the idea that the major hydrologic changes during HS1

92 were driven by enhanced moist transport from wetter central Brazil through strengthening and
93 southward expansion of the easterlies. The ΔT reconstructions exhibit an overall linear
94 warming trend, which indicates that precipitations are the main driver of the spatial variability
95 in the late glacial ice extents over the Altiplano.

96

97 **1. Introduction**

98 Recent modelling studies shed light on the global mechanisms involved in the abrupt
99 oscillations of the Earth climate during the late Pleistocene. They precised the key role of the
100 Atlantic Meridional Overturning Circulation in this variability and its sensibility to changes of
101 the wind fields and atmospheric carbon dioxide concentration (CO_2) (Zhang et al., 2014;
102 Banderas et al., 2015). These works brought precious insights to the global scale
103 understanding of the Last Glacial Maximum (LGM) to Holocene climate variability. Yet the
104 concomitant reorganization patterns of continental climate systems at a regional scale are for
105 now poorly documented. Such investigations require spatially resolved past climate
106 observations to precise the expression of a global event at a smaller scale. Particularly, few
107 attempts have been made to propose spatial reconstructions of the temperatures in the High
108 Tropical Andes and the Bolivian Altiplano for the late-glacial period.

109 However, the Altiplano can be regarded from present and palaeo-climatic observations
110 as a key region to provide a deeper understanding of the South American climate. Present
111 observations show that the Altiplano is under the climatic influence of the South American
112 Summer Monsoon (SASM), which brings most of the annual rainfall during its mature phase,
113 in the austral summer (DJF) (see Vera et al., 2006 and Zhou and Lau, 1998 for detailed timing
114 of the SASM). A weakening of the dry westerlies in relation with subtropical jets modulations
115 and a concomitant southward expansion of the tropical easterlies affects the wind regime.
116 This modification promotes the transport of the humidity accumulated over central and

117 southern Brazil towards the Altiplano (Garreaud et al., 2003, 2009; Vuille and Keimig, 2004;
118 Vuille, 1999; Zhou and Lau, 1998). The Pacific Sea Surface Temperatures (SST) and the El
119 Niño Southern Oscillations (ENSO) are also important source of interannual precipitation and
120 temperature variability of the region, El Niño episodes being associated to warm and dry
121 anomalies and negative glacier mass balance in the Cordillera Blanca (Peru), with inverse
122 relationship during La Niña events (Vuille et al., 2008b, 2000). Palaeo-climatic observations
123 have shown that the palaeo-glaciers of the Altiplano responded to multiple global climate
124 forcings during the late-glacial period as they both recorded stillstand coeval with North and
125 South Hemisphere coolings (Jomelli et al., 2014). North Atlantic cooling are also associated
126 with major hydrologic modifications such as the transgression and highstand of important
127 palaeo-lakes in the southern part of the Altiplano basin (Blard et al., 2011; Placzek et al.,
128 2006; Sylvestre et al., 1999). This sensitivity to larger scale events is likely to be connected to
129 major change in the monsoon dynamics as proposed in South America (Stríkis et al., 2015)
130 and Asia (Han et al., 2015; Pausata et al., 2011; Sirocko et al., 1996; Zorzi et al., 2015), and
131 modulation of the ENSO regime (Kanner et al., 2013; Palmer and Pearson, 2003; Placzek et
132 al., 2006) as both Pacific and North Atlantic forcings may imprint the past variations of the
133 climate in central Andes (Vuille et al., 2012).

134 Numerous studies have provided local timing for glaciers dynamics in the tropical
135 Andes for the LGM and late-glacial period (Carcaillet et al., 2013; Farber et al., 2005; Shakun
136 et al., 2015; Smith et al., 2005; Ward et al., 2015; Zech et al., 2009). Jomelli et al. (2014) used
137 an exhaustive recalculation of published moraine ages to compare the Northern and Southern
138 climatic forcings recorded by glaciers. Yet, establishing a direct link between glacial
139 dynamics of an individual glacier and global climate dynamics is complex. That kind of study
140 was conducted on present glacier and has shown to require either abundant statistical
141 investigation (Vuille et al., 2008) or detailed mesoscale modelling (Mölg and Kaser, 2011) to

142 unravel the "scale mismatch" between the local climatic conditions of the glacier dynamics
143 and the large-scale atmospheric dynamics. Such detailed analyses are not possible for palaeo-
144 glacier studies, where available data are rather scarce. A possible solution to overcome this
145 issue is attempting to inverse mountain glaciers past extensions into synthetic climatic
146 variables. This approach may be challenging considering the few data available for that kind
147 of studies, yet successful inversions have already been reported (Blard et al., 2009; Kull and
148 Grosjean, 2000; Kull et al., 2003; Malone et al., 2015; Placzek et al., 2013) and started to
149 provide a palaeo- climatic variable dataset for the region. Adding new point to this dataset
150 should end in providing deeper comprehension of the climate dynamics during this period.

151 We present new glacial chronologies from four sites of the Bolivian Altiplano: the
152 Cerro Luxar (21.0°S - 68.0°W), the Zongo valley (16.3°S - 68.1°W), the Cerro Tunupa
153 (19.8°S - 67.6°W) and the Nevado Sajama (18.1°S 68.9°W). These chronologies are based on
154 Cosmic Ray Exposure dating (CRE) from an exceptional suite of recessive moraines. These
155 new data permitted to refine existing chronologies of Smith et al. (2005), Jomelli et al. (2011)
156 and Blard et al. (2009). In both sites, glaciers recorded stillstand episodes synchronous with
157 cold events of such as the Henrich 1 event, the Younger Dryas and the Antarctic Cold
158 Reversal.

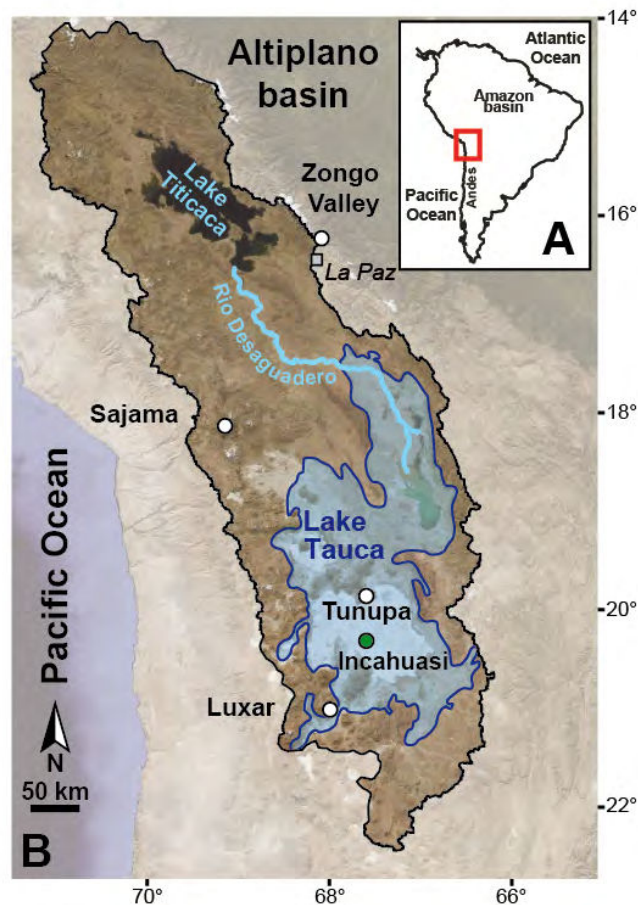
159 Since the nearby Altiplano basin recorded lake level variations over the same period,
160 we were able to apply a joint modelling of glaciers Equilibrium Line Altitude (ELA) and lake
161 budget. This method permits to derive a temporal evolution of temperature and precipitation
162 for the four sites.

163

164 **2. Geological Settings**

165 **2.1. The Altiplano basin and the palaeo-lake records**

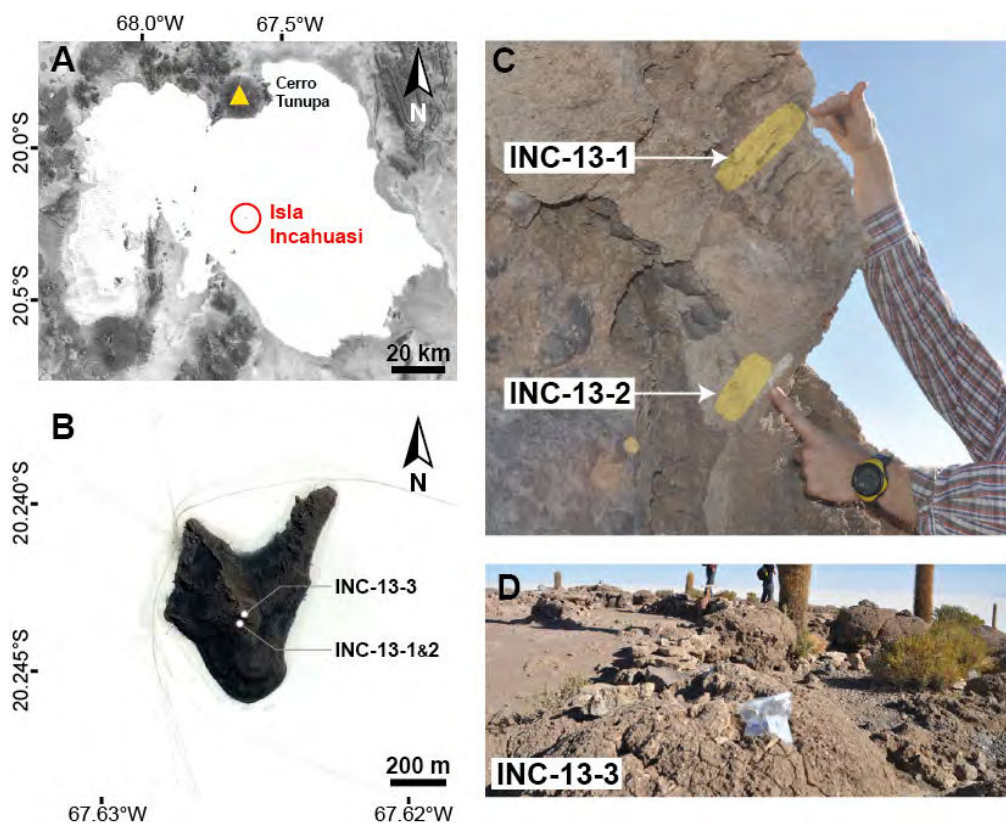
166 The Altiplano is a wide intermontane plateau, covering an area of 196 000 km² and
167 delimited by the eastern and the western Andes cordilleras (Fig. 1). Latitudinally, it spans
168 from 15.5°S (Peru) to 22.5°S (Bolivia), and it ranges in elevation from 3658 masl on the Salar
169 de Uyuni to 6542 masl at Sajama volcano. Precipitations over the Altiplano are mainly
170 provided by the SASM through a westward moist influx from central Brazil and Amazonian
171 Bolivia (Section 1). The orographic effect of the Eastern Cordillera modulates this transport
172 and creates an important precipitation gradient over the Altiplano. The annual rainfall
173 presently range from 800 mm on the edge of the Lake Titicaca to 60 mm in the vicinity of the
174 Laguna Colorada in the South West of the country (Vuille et al., 2008a). The Altiplano is an
175 endorheic basin, composed of a succession of four sub-basins located one below the other.
176 The Titicaca watershed lies in the North of the Altiplano. It is the highest (lake altitude: 3812
177 masl) and the wettest watershed. The Poopo watershed is located southeast from it. Both
178 basins are in connexion via the Rio Desaguadero (Figure 1) who fills the Poopo basin. The
179 overflowing threshold from the Titicaca Lake is around 3810 masl. The Poopo Lake occupied
180 the bottom of the Poopo watershed until December 2015 but the lake is now almost vanished.
181 The Coipasa watershed is southwest from the Poopo one, with a threshold around 3703 masl
182 between them. The Uyunui basin is south from de Coipasa basin, with a threshold around
183 3672 masl. Channels between the different basins show that they were hydrologically
184 connected during wetter periods. During the Tauca highstand, the lake extended over the three
185 southernmost basins.



186
 187 *Figure 1. Location of the different sites presented in this study. The white dots indicate glacial*
 188 *valleys and the green dot, shoreline deposits. The blue shape indicates the extent of the*
 189 *Palaeo-lake Tauca. The black line delimitate the Altiplano endorheic basin. (background:*
 190 *SPOT Imagery).*

191
 192 These 3 southernmost basins of the Altiplano are today dry, but were covered by large
 193 palaeo-lakes during the wettest periods of the Quaternary (Placzek et al., 2006; Sylvestre et
 194 al., 1999). Of the several lake episodes that have occurred during the last 120 ka, the Lake
 195 Tauca episode was the widest and deepest (~120 m deep) (Placzek et al., 2006). U-Th and ^{14}C
 196 dating of the shorelines constrain the timing of the Tauca cycle, i.e. the transgression (18-16
 197 ka BP) and regression phases (14.5-13.5 ka) (Blard et al., 2013a). During its highstand (16-15
 198 ka BP), the level of the lake reached a maximum altitude of 3770 masl and covered a surface
 199 of 55 000 km². The Coipasa Lake cycle is characterized by a transgression from 13.3 to 13.0
 200 ka, a highstand from 13.0 to 11.8 ka and a regression from 11.8 to 10.2 ka (Blard et al., 2011;
 201 Placzek et al., 2006; Sylvestre et al., 1999).

202 To expand the existing age dataset, we sampled 2 new bioherms on Isla Incahuasi
 203 (20.24°S - 67.62°W), a rocky hill located in the centre of the Salar de Uyuni (Figure 2). The
 204 first bioherm lies 5 m below the top of the hill (3715 masl). Dislocations in the calcareous
 205 crust revealed a radial cross section of its cortical structure. We took advantage of this
 206 exposure and sampled the outermost cortex (INC-13-1), which presents a fine radial
 207 branching structure; and a more inner region of the bioherm (INC-13-2), exhibiting a massive
 208 algal facies with no visible laminations. The second bioherm is located on the top of the hill
 209 (3720 masl). We sampled its outermost cortex (INC-13-3).



210
 211 *Figure 2. Bioherm samples of Isla Incahuasi. A - Location of Isla Incahuasi on the Salar de*
 212 *Uyuni. B - Location of the bioherms on Isla Incahuasi. C - The INC-13-1 and INC-13-2*
 213 *samples are different part of the same bioherm. The yellow shaded areas indicated the*
 214 *portions of the bioherm that have been sampled. D - The INC-13-3 sample on the top of the*
 215 *hill.*

216

217

218

219 **2.2. Moraines Setting**

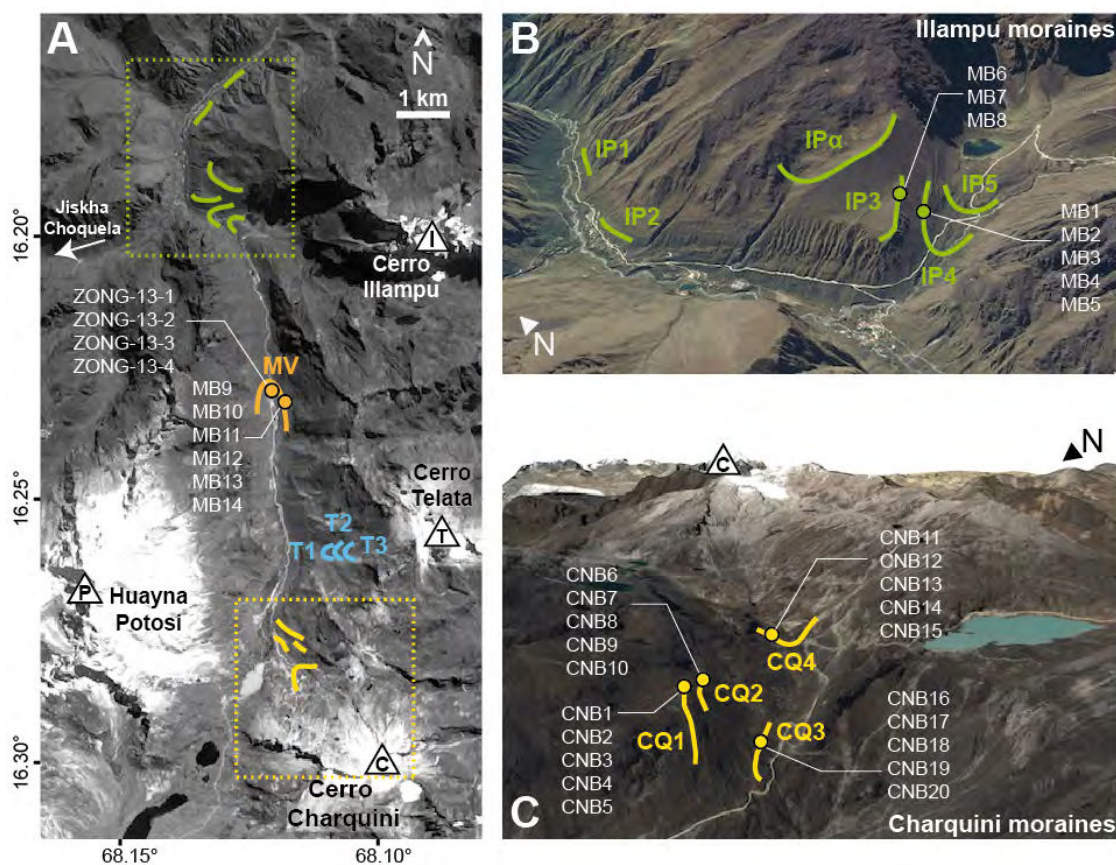
220 The different sites presented in this study are shown on Figure 1. They span from 16.3
221 to 21.0°S.

222 *2.2.1. Zongo Valley (16.2°S - 68.1°W)*

223 The Zongo valley is located in the Cordillera Real in the northern part of the Bolivian
224 Altiplano (Figure 1). It's a northward flowing valley, which drains a mountainous area of
225 about 150 km² and culminates at the Huayna Potosi (6088 masl). Present glaciated areas
226 present a small extent. The Huayna Potosi presently bears a retreating slope glacier on its
227 South face which has been monitored by the IRD-GREAT ICE team from 1991 to 2012
228 (Rabatel et al., 2013; Soruco et al., 2009). The other summits only bears small glacier or snow
229 covers. Yet, the valley exhibits geomorphic evidence of intense past glacial activity. Several
230 moraines and Roches Moutonnées can be encountered in this U-shaped valley. This part of
231 the Cordillera Real massif is mainly made of granitic rocks. Their mineral compositions
232 present quartz, feldspath and mica. The glacial geomorphic features of the Zongo Valley are
233 thus eligible to Cosmic Ray Exposure (CRE) dating by measuring ¹⁰Be in the quartz. Such
234 investigations have already been conducted by Smith et al. (2005) and Jomelli et al. (2011).
235 We sampled new moraine boulders and gathered all results together to come up with a global
236 vision of the late-glacial deglaciation in the valley (Figure 3).

237 The different moraines are classified into four groups. The Illampu group (green
238 moraines on Figure 3) includes the five most distal moraines sampled in the Zongo valley
239 (IP1 to 5) and a perched frontal moraine left by a small glacier of local origin
240 (IP α). The IP1 to 5 moraines are LGM moraines studied in Smith et al. (2005) and we only
241 resampled IP3 and IP4. Downstream from this group of moraines, glacial morphologies
242 vanish and the U shape of the valley is gradually replaced by a V - shape, indicating a
243 transition from glacial to fluvial erosion regime (Kirkbride and Matthews, 1997;

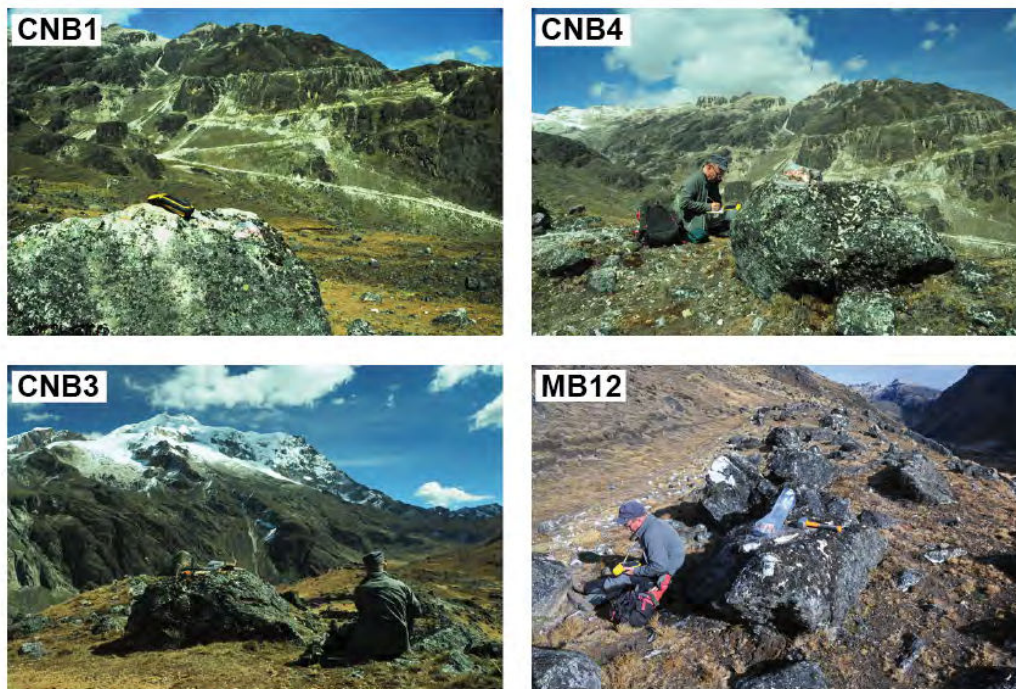
244 Montgomery, 2002) and thus the former extent of past glacial activities. IP1 to 3 are lateral
 245 moraines and IP4 and 5 are frontal. Due to their distal position in the valley, the former ice
 246 tongues associated with moraines IP1 to 5 resulted from the convergence of 5 ice streams
 247 flowing down from the Huayna Potosi, the Charquini, The Telata, the Illampu and the Jiskha
 248 Choquela (Figure 3.A). The MV frontal moraine lies upstream, in a portion of the Zongo
 249 valley flows straight North. The MV ice tongue was associated with the convergences of ice
 250 flows from the Huayna Potosi, Cerro Charquini and Cerro Telata.



251
 252 *Figure 3. Sampled moraines in the Zongo Valley. A - Overview of the moraine groups. B -*
 253 *Zoom on the Illampu moraines. C - Zoom on the Charquini moraines. Indicated samples are*
 254 *new samples for this study. Other samples from the IP moraines group (green) are from Smith*
 255 *et al. (2005), and samples from T moraines group (blue) are from Jomelli et al. (2011).*
 256

257 The T1 to T3 moraines are associated with ice flows donstream from Cerro Telata.
 258 These sets of terminal moraines have been dated to the Pleistocene - Holocene transition in
 259 Jomelli et al. (2011). The CQ1 to 4 moraines are a group of 3 lateral (CQ1 to 3) and one

260 frontal moraines (IP4). While the ice tongue associated with CQ1 must have resulted from the
 261 convergence of the ice streams from the Huayna Potosi and the Charquini, CQ2 to 4 moraines
 262 are only associated with downstream ice flows from Cerro Charquini. From IP1 to CQ4, this
 263 glacial records span over 15 km along the valley thalweg and over 1200 m in vertical range.
 264 For this study, 38 samples have been collected on 7 moraines for quartz extraction and in situ
 265 ^{10}Be measurement. Examples of collected samples are shown on Figure 4.

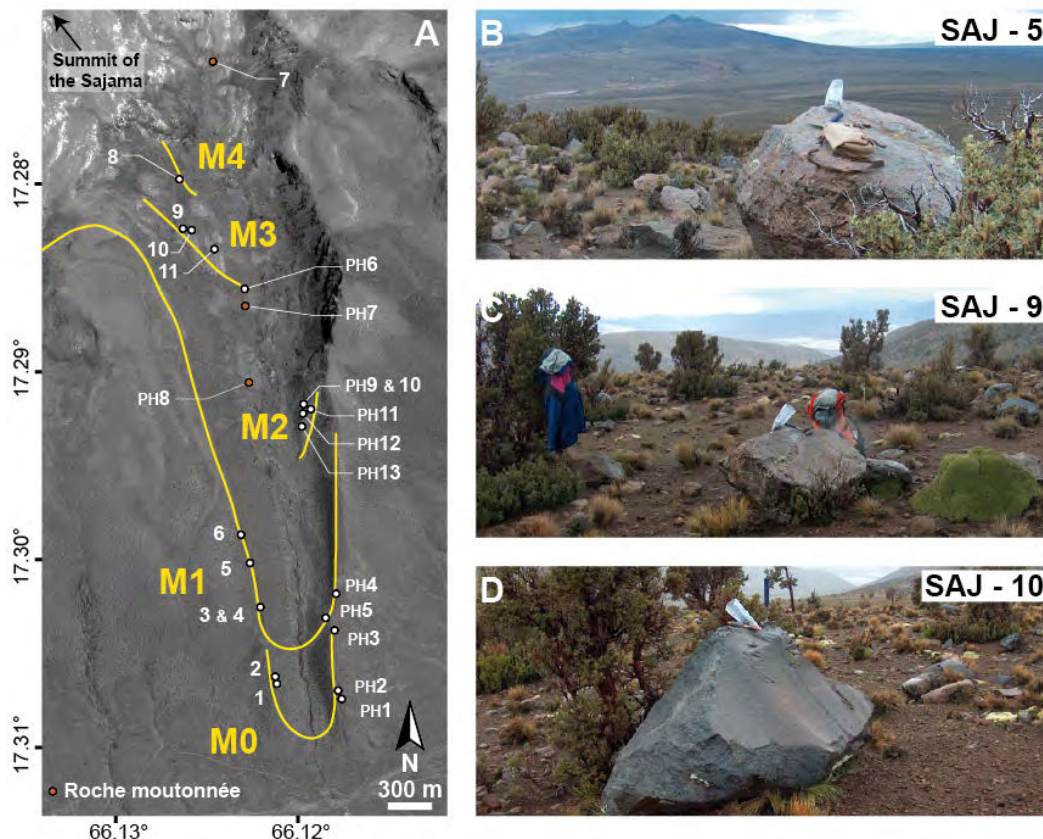


266
 267 *Figure 4. Example of sampled boulders in the Zongo Valley. The presented samples belong to*
 268 *the CQ1 (CNB1 to 4) and the MV (MB) moraines (Figure A.1.).*
 269

270 2.2.2. Nevado Sajama (18.1°S - 68.9°W)

271 Nevado Sajama is an andesitic and rhyodacitic stratovolcano located on the western
 272 part of the central Altiplano. Reaching 6542 masl, it is the summit of Bolivia. The Sajama
 273 presently bears a small ice cap and a permanent snow cover of reduced extension. Yet, past
 274 glacial activities carved numerous glacial valleys on the flanks of the volcano radiating from
 275 the summit. We collected 27 samples on 4 moraines and 3 roches moutonnées in the main

276 southward valley of the Sajama where a former glacier left a prominent moraine and smaller
 277 cordons (Figure 5).



278
 279 *Figure 5. Sampled moraines and sample locations on Nevado Sajama. A - Global map of the*
 280 *valley with the detailed sampling on each moraine. White dots indicate morainic boulder*
 281 *samples, orange dots, roche moutonnées samples. Solid yellow lines show the moraines in the*
 282 *main scope of this study. The full name of each sample is obtained in adding SAJ to the*
 283 *indicated name. B to D - Example of samples.*

284
 285 The frontal M0 moraine delimitates the maximal ice extent in the valley. M1 to 4 are
 286 recessional moraines deposited subsequently. All these moraines lie in the bottom part of the
 287 valley, oriented towards the South West. The terminus of the M1 moraine is located 700 m
 288 upstream the one of M0 (horizontal distance). It is more sharp-crested than M0 and was built
 289 laterally on top of M0 lateral moraines. The M2 to M3 recessional moraines are associated to
 290 probably short still-stand as they exhibit a poorly developed till deposit. Additionally, M3
 291 indicates and ice stream flowing from the right bank of the valley associated with a reduced
 292 accumulation area up stream (Figure 5). Two roches moutonnées were sampled between M2

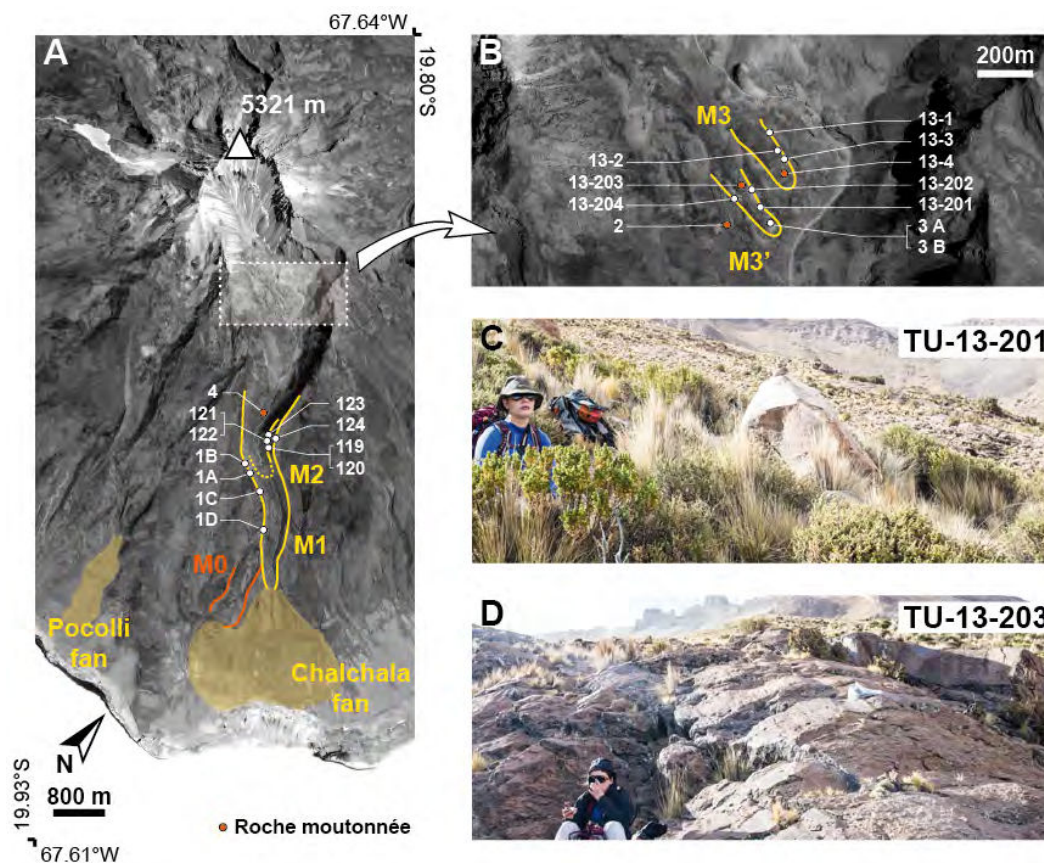
293 and M3 (SAJ-PH7 &8) and one upstream, above M4 (SAJ-7). This glacial record spans over
294 5 km in horizontal distance and covers a 300 m vertical range. The andesitic composition of
295 the samples leads us to establish CRE ages based on the in situ cosmogenic ^3He concentration
296 in the pyroxenes. CRE ages have already been reported by Smith et al. (2009) on eastward
297 valleys of the Sajama. Using ^{36}Cl CRE ages, they identify lateglacial and Holocene moraines.
298 For the lateglacial period, the results exhibit an important scatter, which prevents from
299 proposing a precise chronology.

300 *2.2.3 Cerro Tunupa (19.8°S - 67.6°W)*

301 Cerro Tunupa is an andesitic stratovolcano located in the center of the southern
302 Altiplano. It culminates at 5321 masl above the northern edge of the Salar de Uyuni. The
303 Cerro Tunupa does not presently bear permanent ice cover, yet its southern flanks exhibit
304 numerous glacial geomorphic features. The Chalchala valley is the main glacial valley that
305 extends radially from the glacial cirque below the summit towards the South East.
306 Downstream, the glacial carving gradually disappears and the valley widens on the Chalchala
307 glacial fan (Figure 6). In this valley, (Blard et al., 2013, 2009) sampled 3 moraines reported as
308 M1, M2 and M3 on the Figure 6 along with the Chalchala fan. The M0 moraine is a pre LGM
309 moraine outlet cross cut by the M1 moraine. The M1 moraine indicates the Last Local Glacial
310 Maximum contemporaneous with the Lake Tauca highstand (Blard et al., 2009). The M2 and
311 M3 moraines are recessional moraines. This recession was dated to 14.5 ka in the same study.
312 As shown on Figure 6, the lateral part of M2 was sampled but the evidence of its frontal part
313 remains unclear. The M3 moraines correspond to small ice tongues that stood as the
314 downstream digitations of a small extent cirque glacier. Complete description of the
315 Chalchala moraines can be found in Blard et al. (2009). The samples of the Calchala valley
316 span over 400 m vertically and 4 km horizontally. The Pocolli valley is a smaller valley
317 flowing southward, 1.5 km West of the Chalchala valley. The glacial fan that ends the Pocolli

318 valley was sampled in Blard et al. (2013) for a ^3He production rate determination. The age of
 319 the fan was established at 15.2 ka.

320 In this study we complete the sampling of the M3 - M3' moraine group. We sampled 2
 321 new roches moutonnées and 6 new morainic boulders. These samples were collected for CRE
 322 ages determination based on in situ ^3He concentration in the pyroxenes.



323
 324 *Figure 6. Sampled moraines and sample localisations on Cerro Tunupa. A - Localisation of*
 325 *the moraines and samples in a general map of the main glacial valley. White dots indicate*
 326 *morainic boulder samples, orange dots, roche moutonnées samples. Solid yellow lines show*
 327 *the moraines in the main scope of this study. B - Zoomed localisation of the upstream samples*
 328 *associated with the M3 moraine. C - The TU-13-201 morainic boulder. D - the TU-13-203*
 329 *roche moutonnée. The full name of each sample is obtained in adding TU to the indicated*
 330 *name (except for the indicated TUN samples). New samples from this study are labelled 13-X,*
 331 *other samples have been presented in Blard et al. (2009 and 2013).*
 332
 333

334

335

2.2.4. Cerro Luxar (21.0°S - 68.0°W)

336

337

Cerro Luxar is an andesitic stratovolcano located in the South West of the Altiplano.

338

Located 70 km south of the Salar de Uyuni, it belongs to a wide volcanic province spanning

339

from the western Cordillera to the center of the Altiplano. Nowadays, Cerro Luxar does not

340

have a permanent ice cover but numerous glacial geomorphic features can be found in the

341

valleys carved on its flank, indicating intense past glacial activity. We sampled 3 moraines

342

and 2 roches moutonnées in an eastward flowing glacial valley of Cerro Luxar (Figure 7). The

343

M1 moraine is the terminal moraine that indicates the last maximal extent of the ice tongue. It

344

is a sharp-crested moraine, which delimitates a narrow and sinuous ice tongue. The M2 and

345

M3 moraines are recessional moraines located upstream in the valley. As they both left a

346

smaller imprint in the landscape, they were sampled on their most expressed bank, the left

347

bank for M2 and the right bank for M3. The sampled roches moutonnées are located upstream

348

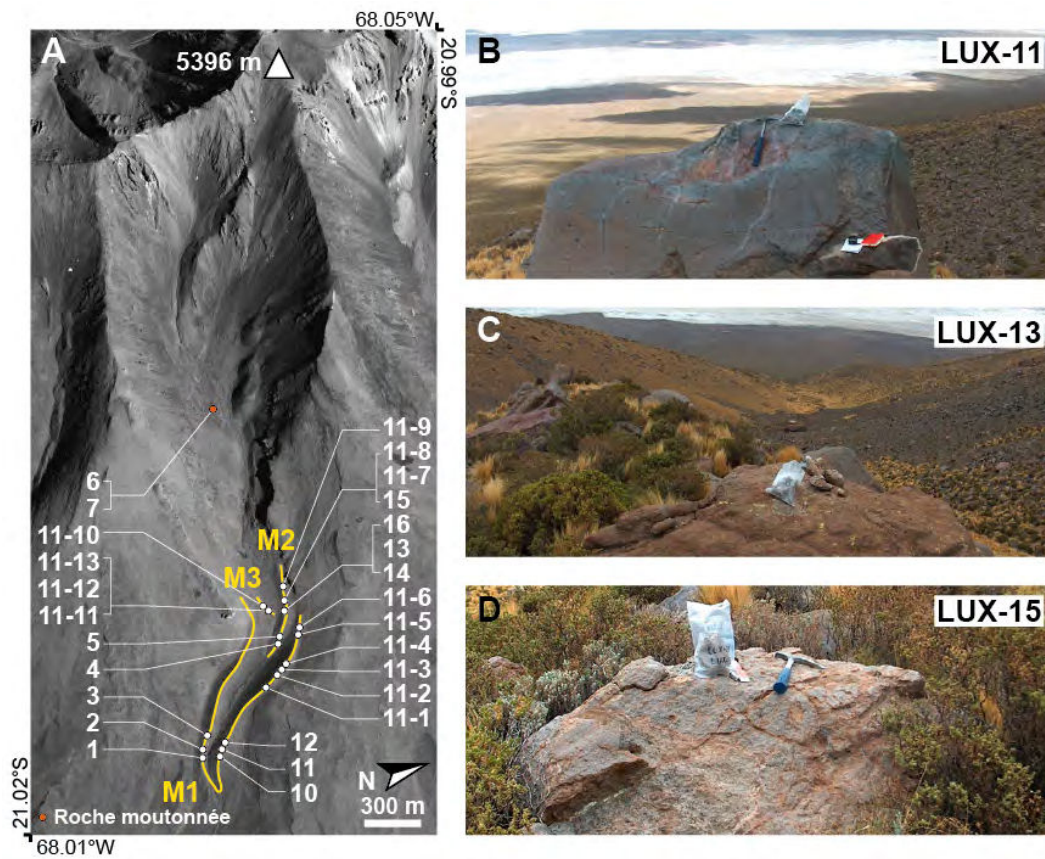
of the 3 moraines, in the glacial cirque. These 27 samples span over 1.2 km horizontally and

349

450m vertically. Due to their andesitic composition, they were collected for in situ ^3He

350

concentration measurement in the pyroxenes.



351
 352
 353
 354
 355
 356

Figure 7. Sampled moraines and sample locations Cerro Luxar. A - Global map of the valley with the detailed sampling on each moraine. White dots indicate morainic boulder samples, orange dots, roche moutonnées samples. Solid yellow lines show the moraines in the main scope of this study. The full name of each sample is obtained in adding LUX to the indicated name. B to D - Example of samples.

357 **3. Methods**

358 **3.1. CRE dating methods**

359 *3.1.1. Sampling methods*

360 The sampling was done using a hammer and a chisel. We favoured large angular
361 boulders to avoid boulders that may have been recently brought to the surface by deflation of
362 the diamict matrix. The surfaces of the boulders were sampled over a maximum of 6 cm.
363 Many boulder tops presented flat or slightly sloping surfaces, with a generally smooth and
364 clean aspect and without any evidence for exfoliation or physical weathering. This suggests
365 that they have experienced only negligible denudation (i.e. less than a few mm) since their
366 deposition.

367

368 *3.1.2. In situ ¹⁰Be concentration measurement*

369 The samples were then processed at CRPG (Nancy, France) for measurement of their
370 in situ produced cosmogenic ¹⁰Be concentration in the quartz mineral fraction. Samples were
371 first crushed and then sieved under water to collect the 200-800 µm fraction. The quartz was
372 concentrated from this fraction by magnetic and electrostatic separation and then isolated
373 through selective dissolution in an H₂SiF₆-HCl concentrated solution. Once pure quartz had
374 been obtained, 30% of the mass of each sample was dissolved during three successive HF
375 leaching steps in order to remove any atmospheric ¹⁰Be contamination from the quartz. We
376 then added 150 to 300 mg of an in-house ⁹Be carrier (⁹Be concentration: 2020 ppm) to the
377 samples and dissolved them completely in concentrated HF. To extract the beryllium, samples
378 underwent three alkaline fractionated precipitations alternated with two separations on ionic-
379 exchange columns and a final dehydration at 700°C.

380 The resulting BeO was mixed with niobium powder, introduced into a copper cathode,
381 pressed and then finally measured at the French national AMS facility ASTER (CEREGE,

382 Aix-en-Provence, France). During each analytical session, the measured $^{10}\text{Be}/^9\text{Be}$ ratios were
383 normalized to the $^{10}\text{Be}/^9\text{Be}$ ratio of the SRM 4325 NIST reference material ($^{10}\text{Be}/^9\text{Be}$: $2.79 \pm$
384 0.03×10^{-11} , Nishiizumi et al. (2007)). During the three analytical sessions, the blank values
385 were $2.7 \pm 1.7 \times 10^{-15}$, $1.5 \pm 0.4 \times 10^{-15}$ and 3.9×10^{-15} , respectively. These yielded maximum
386 blank corrections of the sample $^{10}\text{Be}/^9\text{Be}$ ratios of 6%, 3% and 3%, respectively.

387

388 *3.1.3. In situ ^3He concentration measurements*

389 The samples were processed and measured at the CRPG. They were first crushed and
390 sieved under water to collect the 180 - 800 μm fraction. We concentrated heavy minerals
391 through density separation in sodium polytungstate solutions ($d \approx 3.1$) and then rinsed them
392 with deionised water. Black and green pyroxenes were observed and identified on scanning
393 electron microscope and then hand picked separately under binocular magnifier. We selected
394 monomineral grains without any adhering lava and packed them into stain capsules. The
395 prepared pyroxene aliquots weighed between 11.4 and 57.2 mg.

396 The total ^3He concentration of the samples was measured on a SFT mass spectrometer
397 following the procedure described in Mabry et al. (2012), Schimmelpfennig et al. (2011) and
398 Zimmermann et al. (2012). Pyroxenes aliquots were fused in a vacuum furnace during 15 min
399 at 1400 to 1500 $^{\circ}\text{C}$. The extracted gas was purified using activated carbons, getters and a
400 cryogenic pump and the ^3He and ^4He were analysed in the spectrometer. Furnace blank
401 induced a mean correction of $4 \pm 3\%$ (with a maximal value of 12%). The SFT sensitivity was
402 calibrated using the HESJ standard (Matsuda et al., 2002) as described in Blard et al. (2013)
403 and fit to a numerical model that allowed us to predict sensitivities corresponding precisely to
404 the sample measurements. Mean 1σ reproducibilities for ^3He and ^4He were respectively
405 $2.0 \pm 0.6\%$ and $1.9 \pm 2.3\%$ with respective maximum values of 3.1 and 7.0%. Analytical
406 sessions included concentration measurements of the CRONUS-P pyroxene standard aliquots

407 measurements which yielded a mean concentration of $4.92 \pm 0.16 \times 10^9$ at.g⁻¹ in agreement
408 with the $5.02 \pm 0.06 \times 10^9$ at.g⁻¹ standard reference (Blard et al., 2014, at 1 σ).

409 Blard et al. (2013, 2014) measured magmatic ³He concentrations on pyroxenes from
410 Cerro Tunupa and Cerro Uturuncu doing vacuo step-crushing. They showed that magmatic
411 ³He concentrations ranged 2 to 3 order of magnitude below cosmogenic ³He concentrations in
412 the volcanic formations of the Altiplano. In view of these results, we decided not to do vacuo
413 step-crushing measurements and considered an 8.50×10^4 at.g⁻¹ magmatic ³He concentrations
414 for all the new samples. This synthetic value was derived from the measurements of Blard et
415 al. (2013, 2014).

416 Nucleogenic ³He concentrations were calculated from major and trace element
417 compositions of each sample as in Blard et al. (2013) (measurements performed by the
418 SARM-CNRS). We both calculated (U-Th-Sm)/⁴He eruption ages and nucleogenic ³He
419 production rates (following Andrews and Kay (1982) and Andrews (1983)) to derive ³He
420 nucleogenic concentrations.

421 For each sample, the cosmogenic ³He concentration was finally obtained by
422 subtracting the magmatic and nucleogenic components to the total ³He concentration.

423

424 *3.1.4. Cosmogenic ages computation*

425 The Sea Level High Latitude (SLHL) production rate used to calculate the ¹⁰Be CRE
426 ages is a weighted mean of the production rates of Blard et al. (2013a), Kelly et al. (2013) and
427 Martin et al. (2015). All these studies have been performed in the High Tropical Andes in
428 close location of the dated sites (particularly for the Blard et al. (2013a) and the Martin et al.
429 (2015) production rates). This value can be regarded as a synthetic local value, being both
430 robust and able to limit the age dependence on scaling procedures.

431 In the same way, ^3He CRE ages were calculated using a weighted mean of the
 432 production rates of Blard et al. (2013b) and Delunel et al. (In Prep).

433 The age computation relied on the *Lal modified* time dependant scaling scheme (Balco
 434 et al., 2008; Lal, 1991; Stone, 2000) used with the ERA-40 spatialized atmosphere (Uppala et
 435 al., 2005) and the Muscheler et al. (2005) Virtual Dipolar Moment (VDM) reconstruction.
 436 Borchers et al. (2015) showed that the Lal modified model and the LSD model (Lifton et al.,
 437 2014) were the most performant model presently available to reduce discrepancies between
 438 the different calibration studies at the SLHL conditions. With the same type of approach
 439 Martin et al. (2015) showed that the *Lal modified* scheme showed slightly better performance
 440 in the High Tropical Andes, especially when combined with the ERA-40 atmosphere and the
 441 Muscheler et al. (2005) VDM reconstruction. All the ages were also computed using the LSD
 442 model with the ERA-40 atmosphere and its composite geomagnetic framework to provide
 443 comparison between the scaling procedures (to be done).

444

445 *3.1.5 Bayesian Age calculation*

446 Stratigraphic relations between moraines and roches moutonnées bring additional time
 447 constraints on the object they bracket. These can be formulated in term of Bayesian
 448 conditions (conditional probability) to either refine or produce age probability densities
 449 associated with moraines (Parnell et al., 2011). We use the approach described in Blard et al.
 450 (2013b) and Martin et al. (2015) on some of the studied moraines to precise their ages. For an
 451 object with a probability density function (PDF) f_{object} , if stratigraphic observations enable the
 452 identification of an older object and a younger object respectively associated with the $f_{\text{OlderObject}}$
 453 and $f_{\text{YoungerObject}}$ functions, a new PDF may be recalculated for the dated object as presented in
 454 the Equation 1.

$$\text{for } t \in \mathbb{R}, \quad f_{Object}^*(t) = f_{Object}(t) \times \int_t^{\infty} f_{OlderObject}(\tau) d\tau \times \int_0^t f_{YoungerObject}(\tau) d\tau \quad (1)$$

455

456 If no measurements are available for the object of interest, or if scatter is too
 457 important, a PDF can be derived for the bracketed object by replacing f_{Object} by 1. This
 458 approach is used to improve the age dataset obtained in this study.

459

460 **3.2. Equilibrium Line Altitude calculation methods**

461 At the Equilibrium Line Altitude (ELA), the annual mass balance of the glacier is null.
 462 Because the ELA is an integrative signal of the climatic conditions driving the glacial
 463 dynamics (Ohmura et al., 1992), palaeo-ELA have been extensively studied over the past 40
 464 years to propose climate reconstructions (Loibl et al., 2014; Porter, 2001, 1975; Stauch and
 465 Lehmkuhl, 2010; Sissons and Sutherland, 1976). Several methods have been reported and
 466 compared to infer the palaeo-ELAs from the geomorphic features of the glacial valleys (Benn
 467 and Lehmkuhl, 2000; Benn et al., 2005; Meierding, 1982). These methods rely on different
 468 observations such as glacial cirque altitude, the maximum elevation of the lateral moraines,
 469 the terminus altitude or the hypsometry of the valley and requires variable amount of
 470 knowledge about the past glacial extent. The climatic inversions presented in this study
 471 (Section 3.3) rely on the determination of the ELA associated with each dated moraine. The
 472 AAR method present several advantage for our study. It enables ELA determination for
 473 several glacier stillstand in the same valley, whereas this can be a challenging issue when
 474 relying on the cirque altitude or the maximum altitude of the lateral moraines. In these later
 475 methods, the required information for every stillstand is often unavailable. The AAR method
 476 does not require any balance ratio or index; it is thus less precise than the Balance Ratio (BR)
 477 method or the Area Altitude Balance Ratio (Osmaston, 2005). Yet this method makes implicit
 478 reference to the glacier mass balance what makes it more reliable than the widely used Toe to

479 Summit Altitude Method (TSAM) and Toe to Headwall Altitude Ratio (Benn and Lehmkühl,
480 2000; Osmaston, 2005). This method has been reported to bring appropriate ELA values in
481 different cases of mountain glacier (Benn and Lehmkühl, 2000; Porter, 2001; Torsnes et al.,
482 1993).

483 ELA determination with the AAR methods relies on the use of an appropriate AAR
484 parameter. This ratio is likely to vary depending on the location of the glacier. It has been
485 determined on present glacier in different locations and globally range between 0.5 and 0.8
486 (see Benn and Lehmkühl (2000) and Benn et al. (2005) for review) but no mean value has
487 been reported for the High Tropical Andes Glaciers. For this study we summed the glacier
488 monitoring observations conducted on the Antizana (Equador, 0.5°S - 78.1°W) and the Zongo
489 glaciers (Figure 1) by the GLACIOCLIM-IRD National Observation Service from 1991 to
490 2010 (1995 - 2010 for Antizana glacier) to come up with a mean AAR value for both glaciers
491 (Rabatel et al., 2013; Soruco et al., 2009). We derive an AAR value of 0.58 for the Zongo
492 glacier and a 0.61 value for the Antizana. These glaciers are small extent glaciers and we used
493 this AAR value on large extent valley palaeo-glaciers. We discuss the possible issues with
494 this situation in Section 5.3. For the rest of the study, we chose to consider a 0.55-0.65 AAR
495 range to address the uncertainty associated with the palaeo-ELA determination. This range
496 encompasses the 2 observed values and its width either corresponds to or exceeds those
497 commonly reported in ELA focused studies (Benn et al., 2005 for review). The hypsometry
498 data required for the AAR method were derived from the SRTM 1 Arc-Second Global digital
499 elevation models from NASA-USGS.

500

501

502

503

504 **3.3. Climatic inversion methods**

505 *3.3.1 Glacial extent and climatic conditions*

506 The climate controls the glaciers dynamics through accumulation (precipitations) and
507 ablation processes (mainly melting, sublimation). This has lead glaciers, and more precisely
508 the past glacial extent indicated by moraine records, to be used has tracers of the past climate
509 changes. Sagredo and Lowell (2012) proposed a complete climatic contextual setting of the
510 glaciers of the Andes. They proposed to classify glaciers in different groups characterized by
511 common climate settings. The glaciers records presented in this study set in two close groups
512 characterized by cold and homogenous temperature over the year and scarce precipitation
513 input grouped during the Austral summer (Section 1). The main difference between the two
514 groups lies in the annual rainfall, higher in the group including the Zongo valley than in the
515 one including the three other sites. The glaciers cirques lie above the 0°C isotherm during an
516 important part of the year but volcanoes such as the Cerro Tunupa and Cerro Luxar do not
517 bear permanent ice cover. The context has lead to described these glaciers as "precipitation-
518 limited" (Ammann et al., 2001; Kull et al., 2008).

519 Various methods have been proposed to infer past climatic conditions from moraine
520 records (Seltzer, 1994). A simple approach consist in assuming no change in the precipitation
521 regime and convert an ELA variation into a temperature variation with a lapse rate value
522 (Eaves et al., 2016). Yet the strong hypothesis made over the precipitations need to be
523 assessed in the studied place. In the case of the Altiplano glaciers, the massive hydrologic
524 reorganisation undergone during the late-glacial period make this method irrelevant as it
525 would imply to investigate the wax and wane of giant palaeo-lakes without considering the
526 possibility of rainfall changes.

527 Other approaches lie in ablation computation coupled with ice flow modelling. Two
528 different models are generally exploited to describe ablation: the temperature index models

529 and the energy balance models. The temperature index methods assume empirical relationship
530 between are temperature and melt rates. They have been widely used because they require
531 light calculation and easily available data (see Hock (2003) for presentation and review). A
532 common example these methods is the Positive Day Degree (PDD) that links the melt rate
533 with the daily average temperature . Degree-day models have been used in various different
534 climatic conditions with successful results and they perform best in low elevation mid-latitude
535 wet regions (Hock, 2003; Sicart et al., 2008). Yet, they are improper to reproduce daily melt
536 for High Andes glaciers because of the low dependency of melt energy on the air temperature,
537 supplanted by the net short-wave radiations (Sicart et al., 2008). On longer timescale, this is
538 compensated by the integrative nature of temperature relatively to radiative melting processes
539 but the method remains inappropriate to take into account sublimation which represent a non
540 negligible part of the ablation process over the Altiplano (Wagnon et al., 2001). Energy
541 balance models describe more precisely the physical processes of the ablation. They require a
542 greater amount of data and calculation and have thus mostly been applied to present glacier
543 (Greuell and Smeets, 2001; Mölg and Hardy, 2004; Sicart et al., 2011; Wagnon et al., 1999).
544 Yet, recent efforts have been done to reduce the number of input parameters and variables and
545 simplify the calculation (Giesen and Oerlemans, 2012; Rupper and Roe, 2008), providing
546 appropriate tools for palaeo-glaciers studies. Malone et al. (2015) successfully coupled a 1D
547 ice flow model with an energy balance model to constrain the climatic conditions associated
548 with Little Ice Age (LIA) and Younger Dryas ice extents on the Huancané outlet glacier of
549 Quelccaya Ice Cap (13.9°S - 70.9°W, Peru). Yet, their model was unable to jointly unravel
550 the precipitation and temperature associated with the past glacial extents and they relied on
551 precipitation value inferred from ice core data to propose palaeo-temperatures.

552 Another approach to infer palaeo-climatic conditions is to use empirical relations
553 between the ELA and the present climate derived from statistical analysis on modern glaciers.

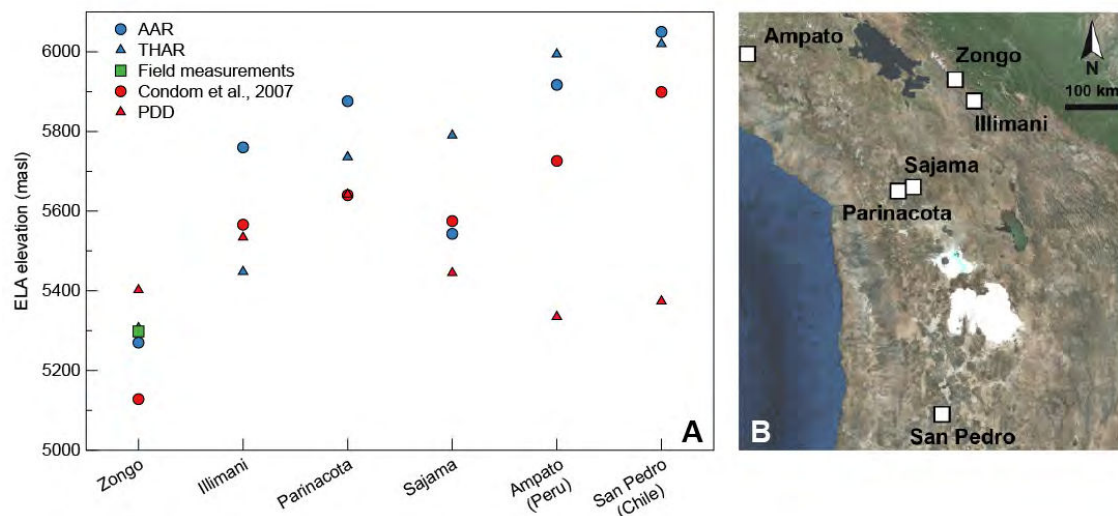
554 These relations consider that the ELA position depends primarily on mean temperature and
555 precipitation values. The enhanced accumulation concomitant with ELA lowering is
556 associated with temperature decrease and precipitation increase. The opposite trend is
557 associated with ELA rising (Condom et al., 2007; Kuhn, 1989; Ohmura et al., 1992; Seltzer,
558 1994). Condom et al. (2007) extended the work of Fox (1993) to derive the following
559 equation 2 for the Andes :

$$560 \quad ELA = 3427 - 1148 \times \log_{10}(P) + \frac{T(z)}{LR} + z \quad (2)$$

561 In this equation ELA is the elevation of the ELA in masl, P is the annual rainfall in
562 mm, T is the mean annual Temperature in °C, LR is the atmospheric lapse rate in °C.m⁻¹ and z
563 is the altitude of the temperature measurement in masl. They showed that this equation
564 performed well for Altiplano glaciers such as the Zongo glacier.

565 We decided to rely on this approach for our study for different reasons: (i) Equation 2
566 propose a direct link between the ELA and the climatic variable to investigate, (ii) it is easy to
567 use, both in term of data availability and calculation (iii) it performs well for Bolivian
568 glaciers. Prémaillon (2014) compared the ability of the Equation 2 and the PDD method to
569 reproduce the present ELA on 6 present glaciers of the High Tropical Andes (determined with
570 the THAR and AAR methods). Figure 8 shows the results of the comparison.

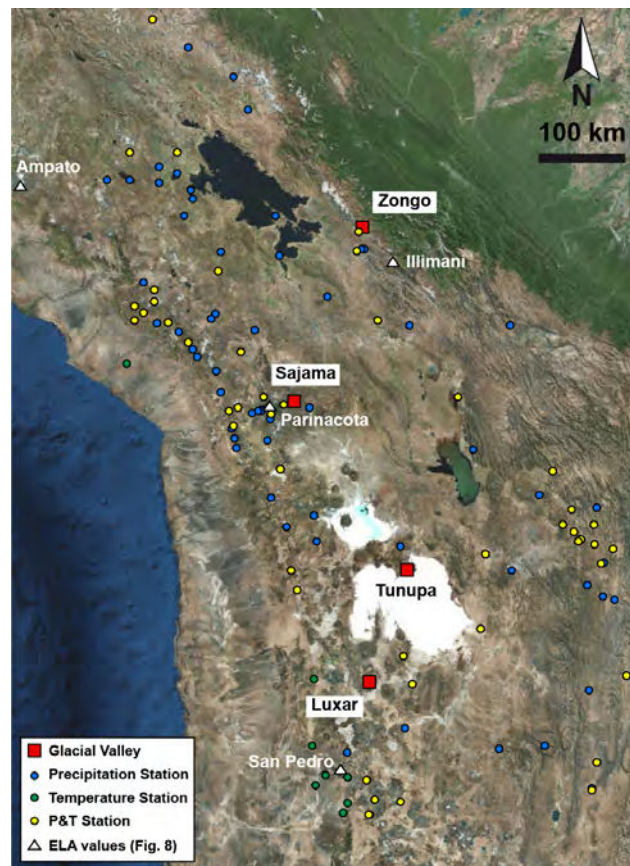
571



572
 573 *Figure 8. Comparison between the PDD and the Condom et al. 2007 method to reproduce the*
 574 *ELA of 6 High Andes Tropical glaciers (determined from THAR and AAR) from Prémaillon*
 575 *(2014). A - Results. The blue dots are topographic measurements and stand as observations.*
 576 *The green dot for the Zongo comes from glaciological measurements (GLACIOCLIM, see*
 577 *Section 3.2). The PDD and Condom et al. (2007) methods infer ELAs from climate data. We*
 578 *compare their ability to match the topographic measurements. Site locations are on Figure 9.*
 579 *B - sites localisation.*

580
 581 For the Zongo, Illimani, Parinacota and Sajama glaciers, both PDD and Equation 2
 582 (Condom et al., 2007) methods give appropriate results. For the Ampato (15.8°S - 71.9°W,
 583 Peru) and the San Pedro (21.9°S - 68.4°W, Chile), the PDD method produce inaccurate value
 584 underestimating the ELA by more than 600m whereas the Equation 2 method produces a 200
 585 m underestimation. These glaciers experience arid conditions with annual rainfall close to 300
 586 mm at the Ampato and 100 mm at San Pedro. These results show that the Condom et al.
 587 (2007) approach is more suitable for our study that focus on palaeoglacier located dry regions
 588 of the Altiplano (Cerro Tunupa, Cerro Luxar).

589 In order to use the Equation 2 models, present mean annual temperature and annual
 590 rainfall have been determined for the 4 locations from monthly data stations reported in Vuille
 591 et al., (2008a). These data concern 57 stations for the temperature and 102 for the
 592 precipitation, spread from 14 to 23°S over the Cordilleras and the Altiplano. They cover a
 593 period of observations from 1948 to 2001 for precipitation and 2007 for temperatures, with
 594 numerous missing measurements. Their locations are presented in Figure 9.



595
596 *Figure 9. Location of the temperature and precipitation stations relatively to the glacial*
597 *valleys.*

598
599 Various averaging methods were tested to derive the site values. They are presented in
600 the appendix. The final synthetic values are presented in Table 1. For the precipitations, the
601 dispersion between the averaging methods ranges between 1% at the Zongo Valley and 6% at
602 the Luxar. For the temperature, the dispersion ranges between 0.11°C at the Tunupa and
603 0.61°C at the Luxar. We used a 6.5°C/km lapse rate to bring all the temperatures to 3780 masl
604 and also for model computation.

Sites	Zongo	Sajama	Tunupa	Luxar
Mean annual Rainfall (mm)	529 ± 7	320 ± 6	201 ± 10	145 ± 9
Mean annual temperature normalized to 3780 masl ^a (°C)	8.65 ± 0.14	8.32 ± 0.59	6.46 ± 0.11	7.64 ± 0.61

^a Normalization calculated for a lapse rate of 6.5°C/km

605
606 *Table 1. Present annual rainfall and mean temperature at the studied sites.*
607

608 Using the method of Condom et al., 2007 to interpret an ELA in term of annual
609 temperature and precipitation only provides a precipitation-temperature space solution.
610 Additional constraints are required to derive unique precipitation and temperature values. To
611 do so we coupled glacier and lake modelling as in Blard et al. (2009) and Placzek et al.
612 (2013).

613 *3.3.1 Lake model*

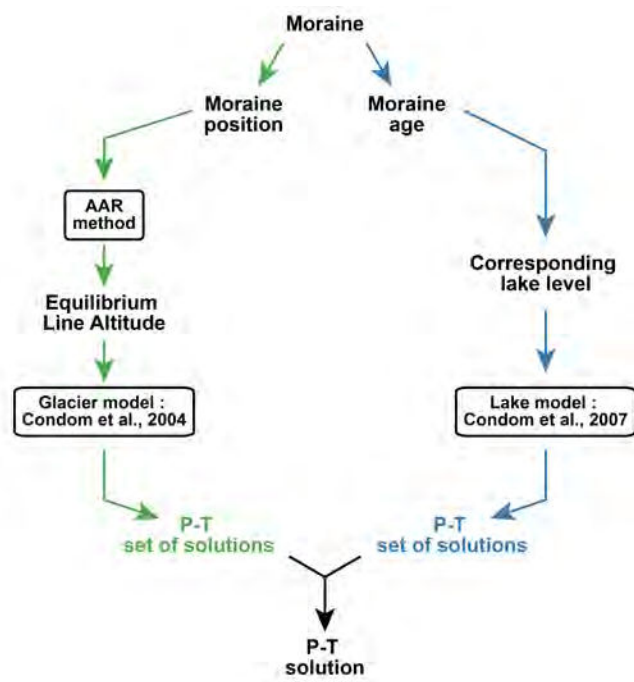
614 Following Blard et al. (2009), we modelled the palaeo-lakes of the Altiplano using a
615 model derived from the one of Condom et al. (2004). As for the glacier model, the same
616 problematic of data availability and ease of calculation lead us to use a simple model that has
617 proven to perform adequately for the Altiplano. This model divides the Altiplano basin into
618 lake pixels and soil watershed pixels. All soil pixels are represented as a reservoir with an
619 overflow level *CapaS*. When the precipitations fill the reservoir above the *CapaS* level, the
620 water runs directly to the lake. The flow path of the water from the watershed pixel to the lake
621 is not taken into account. As in Blard et al. (2009), the equation used to calculate evaporation
622 is derived from the generalized equation of Xu and Singh (2000) that relies on an energy
623 balance budget. The model is run at a quarterly time resolution and at a spatial resolution of 5
624 km. The temperature and precipitation input are derived from the New et al. (2002) dataset.
625 The elevation is based on the 1 arc second SRTM Digital Elevation Model from NASA-
626 USGS. The *CapaS* version was calibrated on the Titicaca watershed for the present period.

627 Amendments have been done on the original version of Condom et al. (2004) to take
628 into account 2 points. The first point is the management of the eventual snow stock. The
629 second point is the fill level of the Poopo and Coipasa lakes and the hydrologic connexion of
630 the different sub-basins of the Altiplano with the southern bottom basin for which the
631 hydrologic budget is computed. The solutions implemented to take into account these 2
632 difficulties are detailed in the Appendix A.

633 For different global cooling levels over the Altiplano basin, the lake model is run so as
634 to find the associated global precipitation increase that provide a null global hydrologic
635 balance. This condition is verified during the Tauca highstand and the Coipasa highstand
636 (Section 2.1). For other periods we considered that the deviation from the balance associated
637 with a transgression or a regression is negligible on an annual time scale. We assume uniform
638 temperature cooling and precipitation increase precipitation. We discuss these assumptions in
639 Section 5.

640 *3.3.2 Lake and glacier cross modelling*

641 For a given late-glacial moraine called M, CRE dating give us a build-up age. With
642 this age we read the level of the southern basin palaeo-lake on the shoreline age dataset we
643 updated (Section 4.1). We infer a palaeo-lake extent from this level and compute its
644 hydrologic balance for different levels of cooling. We obtain a set of Precipitation-
645 Temperature pairs that allow this null balance. The Condom et al. (2007) equation gives us a
646 similar set of Precipitation-Temperature pairs for the palaeo-glacier associated with the M
647 moraine. The intersection of the 2 computed Precipitation-Temperature curves enable the
648 determination of the climatic conditions associated with the M glacial extent. This approach is
649 summarized in Figure 10.



650
651
652
653

Figure 10. Workflow for palaeo-climatic interpretations in this study.

654

655 **4. Results**656 **4.1. Dating results**657 *4.1.1. Incahuasi shoreline results*

658 The age results from the Incahuasi shoreline deposits are presented in Table 2.

Sample	Material	Latitude Dec°	Longitude Dec°	Elevation masl	Mass mg	$\delta^{13}\text{C}$ ‰ vs PDB	Modern C %	^{14}C age ^a yr	Calendar age (1 σ) ^b ka BP
INC-13-1	Bioherm, white massive algal carbonate (external part)	-20.2435	-67.6255	3715	0.35	2.28	23.8 ± 0.2	11550 ± 50	13.44 ± 0.05
INC-13-2	Bioherm, cream-coloured carbonate (internal part)				0.37	1.53	19.2 ± 0.2	13240 ± 60	15.97 ± 0.11
INC-13-3-A	Bioherm, white massive algal carbonate	-20.2432	-67.6254	3720	0.62	2.65	26.2 ± 0.1	10745 ± 45	12.75 ± 0.03
INC-13-3-B					0.69	3.49	27.9 ± 0.2	10270 ± 45	12.09 ± 0.10

^a Uncalibrated ages^b Present refers to 2010. Calibration performed with IntCal13, OxCal 4.2 (Ramsey, 2009; Reimer, 2013)

659

660 *Table 2. Age results from the Incahuasi Shoreline deposits.*

661

662

663

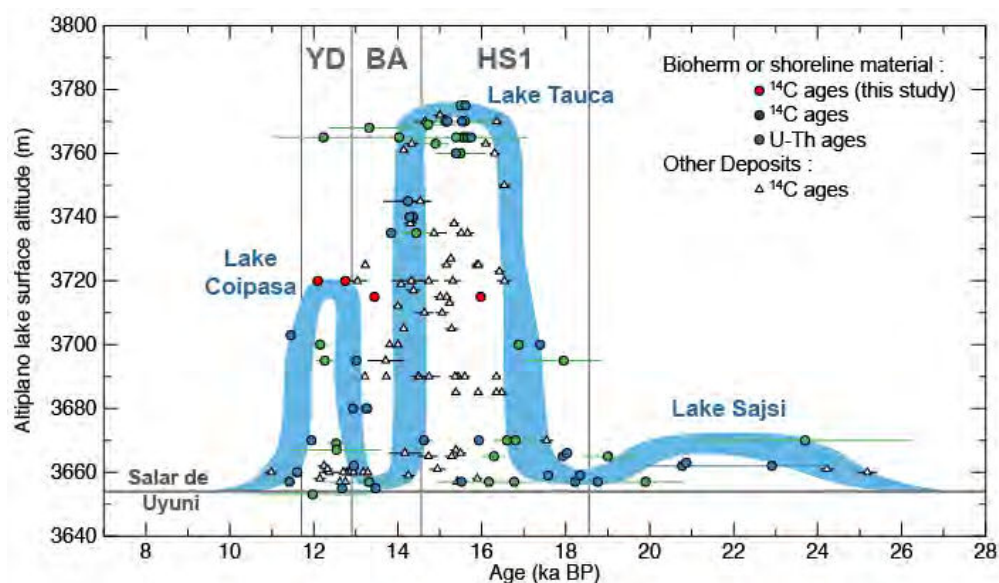
664

665

666

667

Calibrated ages were obtained using IntCal13 - OxCal 4.2 (Ramsey, 2009; Reimer, 2013). The 4 calibrated ages span from the Tauca to Coipasa highstand, with both INC-13-3 ages precisely coeval with the Coipasa highstand. Along with their GPS elevation, these new data points were used to update the former lake level dataset summarized in Blard et al., 2011 in Figure 11. We re-calibrated the former dataset with IntCal13 - OxCal 4.2.



668
 669 *Figure 11. Palaeo-lake chronology of the southern Altiplano. The blue curve has been*
 670 *updated from Blard et al., 2011 to fit a 15m higher Coipasa highstand indicated by our new*
 671 *data (red points). Other data (Blue, Green and white points) are from (Blard et al., 2011;*
 672 *Placzek et al., 2006; Sylvestre et al., 1999).*

673
 674 The new dated shoreline deposits indicate that the Coipasa highstand stood broadly 15
 675 m higher than previously reported (Blard et al., 2011; Placzek et al., 2006). Both INC-13-1
 676 and INC-13-2 yield an age that does not fit the blue curve. They are both 1 ka too old to fit the
 677 Tauca transgression and regression. As they come from the same bioherm, a contamination
 678 with modern carbon can be suspected.

679

680 4.1.2. Zongo Valley

681 The CRE age results from the Zongo valley are presented in the Table 3 and Figure
 682 12. For each moraine, we computed a normalised sum of the sample PDF age. We then
 683 determined the characteristics (median and 1σ -range) of the so computed moraine PDF to
 684 assign them an age. The IP1, IP2 and MV moraines exhibit extreme scatter, making it hard to
 685 identify a precise timing in the late-glacial period. The MB4 sample from the IP4 moraine
 686 yielded an age 2 times higher than the other samples (36.9 ka compared to 16.6 ka). It was
 687 considered as an outlier and rejected for the median and error computation. On other

688 moraines, boulder ages present sufficient consistence to derive moraine ages associated with a
689 1 ka or smaller error bar (1σ). These ages are stratigraphically consistent and span from 17.2
690 to 9.9 ka, covering the late-glacial period and the Pleistocene to Holocene transition. The
691 Illampu moraines yield ages between 17 and 13.5 ka. The Charquini moraines range between
692 11.6 and 10.3 ka and the Telata between 10.6 and 9.9 ka.

693 We used Bayesian calculation (Section 3.1.5) to constraint the age of the MV moraine.
694 It is stratigraphically bracketed by IP5 and CQ1. We used this relation to apply a Bayesian
695 filter on the initial MV PDF function (white filled on Figure 12). We considered IP5 as an
696 older object than MV and CQ1 as a younger object. The computed PDF for MV yields an age
697 of 12.55 ± 0.80 ka.

Moraine	Source	Sample	Latitude Dec°	Longitude Dec°	Altitude masl	¹⁰ Be (1σ) 10 ⁷ at.g ⁻¹	Thickness cm	Thick. Corr. ^a -	Shielding ^b -	Scaling Factor ^c -	Age (1σ) ^d ka
IP1	Smith et al., 2005	ZONG-03-06	-16.1310	-68.1697	3417	3.57 ± 0.14	1	0.99	0.87	6.1	16.77 ± 0.68
		ZONG-03-07	-16.1314	-68.1697	3408	3.47 ± 0.15	4	0.97	0.89	6.0	16.50 ± 0.70
		ZONG-03-08	-16.1310	-68.1693	3399	1.15 ± 0.05	3	0.98	0.85	5.4	6.33 ± 0.26
		ZONG-03-09	-16.1310	-68.1693	3393	3.33 ± 0.09	3	0.98	0.89	6.0	15.89 ± 0.49
		ZONG-03-10	-16.1309	-68.1692	3391	1.31 ± 0.05	3	0.98	0.89	5.5	6.82 ± 0.25
		ZONG-03-11	-16.1310	-68.1691	3383	0.69 ± 0.04	3	0.98	0.89	5.2	3.77 ± 0.26
		ZONG-03-12	-16.1309	-68.1692	3386	2.51 ± 0.07	2	0.98	0.89	5.8	12.23 ± 0.46
IP2	Smith et al., 2005	ZONG-03-01	-16.1366	-68.1755	3489	4.73 ± 0.24	1	0.99	0.95	6.5	19.23 ± 0.89
		ZONG-03-02	-16.1366	-68.1755	3500	4.15 ± 0.12	3	0.98	0.95	6.4	17.37 ± 0.58
		ZONG-03-03	-16.1367	-68.1757	3503	3.27 ± 0.12	2	0.98	0.95	6.2	14.03 ± 0.55
		ZONG-03-04	-16.1367	-68.1757	3503	1.97 ± 0.09	1	0.99	0.95	6.0	8.65 ± 0.42
		ZONG-03-05	-16.1368	-68.1757	3505	3.54 ± 0.14	1	0.99	0.95	6.2	14.91 ± 0.57
IP3	This Study	MB6	-16.1915	-68.1330	3870	5.02 ± 0.19	1	0.99	0.97	7.7	16.81 ± 0.66
		MB7	-16.1918	-68.1326	3886	5.02 ± 0.16	1	0.99	0.97	7.7	16.71 ± 0.60
		MB8	-16.1918	-68.1325	3887	4.69 ± 0.25	3	0.98	0.97	7.7	15.86 ± 0.79
	Smith et al., 2005	ZONG-00-06	-16.1333	-68.1919	3895	4.76 ± 0.21	5	0.96	0.98	7.7	16.19 ± 0.70
		ZONG-00-07	-16.1333	-68.1919	3895	5.14 ± 0.21	5	0.96	0.95	7.8	17.74 ± 0.74
		ZONG-00-08	-16.1333	-68.1919	3895	4.71 ± 0.16	5	0.96	0.98	7.7	16.03 ± 0.57
		ZONG-00-09	-16.1333	-68.1919	3895	4.30 ± 0.15	5	0.96	0.98	7.6	14.86 ± 0.53
IP4	This Study	MB1	-16.1932	-68.1328	3768	4.65 ± 0.42	2	0.98	0.97	7.3	16.57 ± 1.32
		MB2	-16.1933	-68.1320	3784	4.66 ± 0.22	2	0.98	0.96	7.3	16.55 ± 0.75
		MB4	-16.1933	-68.1317	3790	11.05 ± 0.92	0.5	1.00	0.96	7.7	36.87 ± 2.75
IP5	Smith et al., 2005	ZONG-00-01	-16.1308	-68.1962	3806	3.56 ± 0.18	5	0.96	0.95	7.2	13.47 ± 0.72
		ZONG-00-02	-16.1308	-68.1962	3806	3.75 ± 0.22	5	0.96	0.95	7.2	14.14 ± 0.81
		ZONG-00-03	-16.1308	-68.1962	3806	3.33 ± 0.23	5	0.96	0.95	7.2	12.57 ± 0.92
		ZONG-00-04	-16.1308	-68.1962	3806	3.57 ± 0.16	5	0.96	0.95	7.2	13.48 ± 0.67
		ZONG-00-05	-16.1308	-68.1962	3806	3.71 ± 0.14	5	0.96	0.95	7.2	13.99 ± 0.58
MV	This Study	MB9	-16.2321	-68.1179	4255	5.38 ± 0.29	3	0.98	0.97	9.1	15.50 ± 0.76
		MB10	-16.2322	-68.1178	4256	5.16 ± 0.16	3	0.98	0.97	9.0	14.96 ± 0.49
		MB11	-16.2329	-68.1177	4264	4.38 ± 0.16	1	0.99	0.97	8.9	12.63 ± 0.56
		MB12	-16.2330	-68.1177	4265	7.82 ± 0.38	2	0.98	0.97	9.6	20.96 ± 1.00
		MB13	-16.2330	-68.1177	4265	3.79 ± 0.24	2	0.98	0.97	8.8	11.07 ± 0.65
		MB14	-16.2330	-68.1177	4265	5.16 ± 0.26	3	0.98	0.97	9.0	14.82 ± 0.67
		Zong-13-01	-16.2302	-68.1199	4183	2.97 ± 0.11	2	0.99	0.97	8.3	9.13 ± 0.39
		Zong-13-02	-16.2301	-68.1201	4177	2.90 ± 0.11	2	0.99	0.97	8.3	8.95 ± 0.38
		Zong-13-03	-16.2281	-68.1225	4180	2.08 ± 0.10	0.5	1.00	0.97	8.0	6.60 ± 0.30
		Zong-13-04	-16.2300	-68.1200	4191	3.43 ± 0.15	1	0.99	0.97	8.4	10.37 ± 0.47
IP alpha	Smith et al., 2005	ZONG-00-10	-16.1301	-68.1902	4105	5.28 ± 0.21	5	0.96	0.99	8.5	16.08 ± 0.64
		ZONG-00-11	-16.1301	-68.1902	4105	4.66 ± 0.22	5	0.96	0.99	8.3	14.51 ± 0.64
		ZONG-00-12	-16.1301	-68.1902	4105	4.72 ± 0.16	5	0.96	0.99	8.3	14.65 ± 0.50
CQ1	This Study	CNB1	-16.2751	-68.1158	4630	4.99 ± 0.31	2	0.99	0.99	10.5	11.98 ± 0.76
		CNB2	-16.2751	-68.1158	4631	4.74 ± 0.16	3	0.98	0.99	10.5	11.56 ± 0.43
		CNB3	-16.2750	-68.1160	4630	4.85 ± 0.16	2	0.98	0.99	10.5	11.69 ± 0.44
		CNB4	-16.2750	-68.1162	4628	4.56 ± 0.19	3	0.98	0.99	10.4	11.22 ± 0.47
		CNB5	-16.2750	-68.1159	4629	4.76 ± 0.19	2	0.98	0.99	10.5	11.55 ± 0.48
CQ3	This Study	CNB16	-16.2749	-68.1192	4486	3.77 ± 0.13	1	0.99	0.97	9.6	9.99 ± 0.40
		CNB17	-16.2748	-68.1193	4488	4.15 ± 0.15	1	0.99	0.97	9.7	10.90 ± 0.42
		CNB18	-16.2748	-68.1191	4493	4.03 ± 0.13	1	0.99	0.97	9.7	10.60 ± 0.38
		CNB19	-16.2748	-68.1190	4492	4.11 ± 0.25	1	0.99	0.97	9.7	10.79 ± 0.63
		CNB20	-16.2748	-68.1192	4489	3.71 ± 0.14	2	0.99	0.98	9.6	9.82 ± 0.42
CQ4	This Study	CNB11	-16.2814	-68.1148	4585	3.94 ± 0.13	2	0.98	0.95	10.1	10.24 ± 0.39
		CNB13	-16.2748	-68.1190	4492	3.96 ± 0.17	3	0.98	0.97	9.7	10.63 ± 0.46
		CNB15	-16.2814	-68.1144	4594	3.88 ± 0.13	2	0.98	0.96	10.1	10.00 ± 0.38

^a Calculated with a density of 2.7 g.cm⁻³ and an attenuation length of 160 g.cm⁻²

^b Calculated using the CRONUS shielding application

^c Global scaling factor that accounts for the geomagnetic correction

^d SLHL PR: 4.08 ± 0.11 at.g⁻¹.yr⁻¹ (Kelly et al. (2013), Blard et al. (2013b) and Martin et al. (2015) - Scaling scheme: Lal modified - Atmosphere: ERA40 - VDM: Muscheler et al. (2005))

698
699
700

Table 3. Zongo valley CRE age results. Part 1.

Moraine	Source	Sample	Latitude Dec°	Longitude Dec°	Altitude masl	¹⁰ Be (1σ) 10 ⁷ at.g ⁻¹	Thickness cm	Thick. Corr. ^a	Shielding ^b	Scaling Factor ^c	Age (1σ) ^d ka
T1	Jomelli et al., 2011	B1	-16.2601	-68.1132	4529	4.87 ± 0.42	4	0.97	0.99	10.0	12.52 ± 1.09
		B2	-16.2610	-68.1123	4609	5.02 ± 0.43	4	0.97	0.98	10.4	12.50 ± 1.08
		B3	-16.2580	-68.1136	4434	3.49 ± 0.20	3	0.98	0.96	9.4	9.74 ± 0.57
		B4	-16.2611	-68.1123	4698	3.36 ± 0.34	3	0.98	0.99	10.5	8.16 ± 0.77
		B5	-16.2606	-68.1121	4581	3.32 ± 0.18	4	0.97	0.97	10.0	8.67 ± 0.50
		B6	-16.2586	-68.1136	4475	4.74 ± 0.19	4	0.97	0.98	9.8	12.58 ± 0.59
		B7	-16.2597	-68.1118	4536	4.46 ± 0.27	3	0.97	0.98	10.0	11.52 ± 0.68
		B8	-16.2605	-68.1119	4580	4.23 ± 0.14	4	0.97	0.98	10.1	10.85 ± 0.40
		B9	-16.2574	-68.1098	4605	3.94 ± 0.43	4	0.97	0.98	10.2	10.05 ± 1.02
		B10	-16.2605	-68.1118	4575	3.85 ± 0.48	4	0.97	0.99	10.0	9.91 ± 1.17
		B11	-16.2578	-68.1122	4503	3.29 ± 0.45	4	0.97	0.94	9.7	9.24 ± 1.20
		B12	-16.2599	-68.1121	4534	4.25 ± 0.12	4	0.97	1.00	9.9	10.92 ± 0.36
		B13	-16.2576	-68.1110	4559	0.60 ± 0.35	4	0.96	0.97	9.1	1.73 ± 1.00
		B14	-16.2573	-68.1093	4624	2.92 ± 0.79	4	0.96	0.97	10.1	7.67 ± 1.83
		B15	-16.2597	-68.1119	4479	4.41 ± 0.13	3	0.97	0.98	9.8	11.62 ± 0.41
T2	Jomelli et al., 2011	B16	-16.2575	-68.1093	4619	4.52 ± 0.21	4	0.97	0.99	10.4	11.21 ± 0.52
		B17	-16.2601	-68.1109	4601	4.38 ± 0.12	4	0.97	0.98	10.3	11.08 ± 0.36
		B18	-16.2601	-68.1109	4553	4.27 ± 0.64	4	0.97	0.98	10.0	11.07 ± 1.53
		B19	-16.2601	-68.1115	4553	4.37 ± 0.24	4	0.97	0.98	10.1	11.27 ± 0.59
		B20	-16.2601	-68.1109	4584	4.44 ± 0.14	3	0.97	0.98	10.2	11.27 ± 0.40
		B21	-16.2580	-68.1097	4579	4.05 ± 0.15	4	0.96	0.98	10.1	10.43 ± 0.42
		B22	-16.2602	-68.1105	4540	4.59 ± 0.13	3	0.97	0.98	10.1	11.79 ± 0.40
		B23	-16.2600	-68.1102	4561	3.89 ± 0.19	4	0.97	0.97	10.0	10.17 ± 0.51
		B24	-16.2602	-68.1101	4562	3.84 ± 0.34	4	0.96	0.98	10.0	10.07 ± 0.85
		B25	-16.2578	-68.1090	4608	4.02 ± 0.29	4	0.96	0.99	10.2	10.22 ± 0.71
		B26	-16.2601	-68.1099	4547	4.45 ± 0.10	4	0.97	0.98	10.1	11.48 ± 0.34
		B27	-16.2578	-68.1086	4619	4.03 ± 0.51	4	0.97	0.98	10.2	10.15 ± 1.18
		B28	-16.2594	-68.1097	4562	3.52 ± 0.40	4	0.97	0.97	9.9	9.23 ± 1.01
		B29	-16.2594	-68.1097	4562	3.48 ± 0.25	3	0.97	0.97	9.9	9.09 ± 0.65
		B30	-16.2576	-68.1084	4630	4.53 ± 0.21	4	0.96	0.98	10.4	11.31 ± 0.53
		B31	-16.2606	-68.1081	4605	3.53 ± 0.45	4	0.97	0.98	10.1	9.05 ± 1.11
		B32	-16.2593	-68.1092	4551	4.31 ± 0.16	4	0.97	0.98	10.0	11.11 ± 0.44
		B33	-16.2599	-68.1090	4548	4.14 ± 0.49	4	0.97	0.98	10.0	10.72 ± 1.16
		T3	Jomelli et al., 2011	B34	-16.2599	-68.1090	4548	4.58 ± 0.34	4	0.97	0.98
B35	-16.2575			-68.1076	4632	3.86 ± 0.40	4	0.97	0.98	10.3	9.78 ± 0.98
B36	-16.2594			-68.1124	4706	4.16 ± 0.16	4	0.97	0.97	10.6	10.29 ± 0.42
B37	-16.2598			-68.1071	4612	3.23 ± 0.24	4	0.97	0.98	10.1	8.29 ± 0.60
B38	-16.2597			-68.1069	4640	3.65 ± 0.20	3	0.98	0.98	10.3	9.17 ± 0.53
B39	-16.2596			-68.1070	4734	4.16 ± 0.15	3	0.98	0.98	10.7	10.01 ± 0.40
B40	-16.2594			-68.1070	4642	3.92 ± 0.15	3	0.98	0.98	10.3	9.78 ± 0.42
B41	-16.2598			-68.1068	4639	3.59 ± 0.35	3	0.98	0.99	10.2	8.97 ± 0.84
B42	-16.2579			-68.1064	4630	3.97 ± 0.15	3	0.97	0.97	10.3	10.05 ± 0.41
B43	-16.2592			-68.1069	4642	4.08 ± 0.15	3	0.98	0.98	10.3	10.17 ± 0.42
B44	-16.2600			-68.1061	4647	4.02 ± 0.17	3	0.98	0.99	10.3	9.96 ± 0.46
B45	-16.2592			-68.1069	4641	4.42 ± 0.15	3	0.98	0.98	10.4	10.92 ± 0.41
B46	-16.2591			-68.1066	4607	2.75 ± 0.20	4	0.97	0.98	9.9	7.20 ± 0.45
B47	-16.2574			-68.1061	4646	3.95 ± 0.39	4	0.97	0.98	10.3	9.87 ± 0.94
B48	-16.2577			-68.1060	4640	4.08 ± 0.42	3	0.97	0.98	10.3	10.16 ± 0.97
B49	-16.2577			-68.1060	4641	4.17 ± 0.27	4	0.97	0.97	10.4	10.57 ± 0.65
B50	-16.2595			-68.1054	4648	3.65 ± 0.20	3	0.98	0.97	10.3	9.18 ± 0.53
B51	-16.2599			-68.1050	4655	3.78 ± 0.13	3	0.98	0.98	10.3	9.40 ± 0.39
B52	-16.2592			-68.1054	4652	4.04 ± 0.14	3	0.98	0.97	10.4	10.07 ± 0.40
B53	-16.2594			-68.1044	4668	3.63 ± 0.13	3	0.98	0.98	10.4	8.96 ± 0.37
B54	-16.2586			-68.1047	4671	4.24 ± 0.15	3	0.98	0.99	10.5	10.33 ± 0.40
B55	-16.2592			-68.1045	4667	4.24 ± 0.15	3	0.98	0.98	10.5	10.42 ± 0.40
B56	-16.2586			-68.1048	4669	4.34 ± 0.15	3	0.98	0.99	10.5	10.57 ± 0.41
B57	-16.2594			-68.1041	4666	4.33 ± 0.15	3	0.98	0.97	10.5	10.68 ± 0.40
B58	-16.2571			-68.1016	4703	0.31 ± 0.04	3	0.98	0.99	10.0	0.78 ± 0.11
B59	-16.2572			-68.1016	4734	0.09 ± 0.01	3	0.98	0.98	10.8	0.20 ± 0.03

^a Calculated with a density of 2.7 g.cm⁻³ and an attenuation length of 160 g.cm⁻²

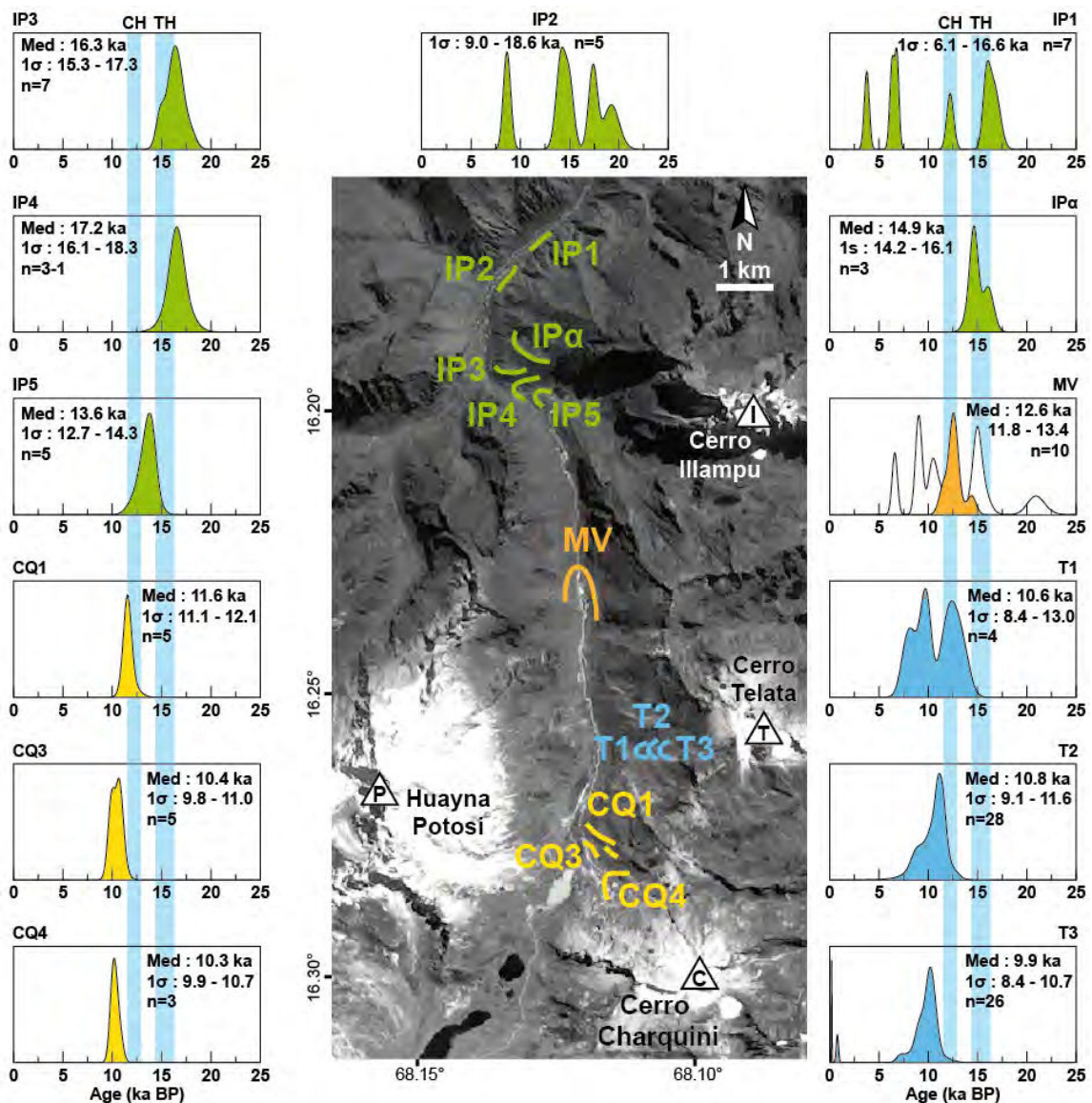
^b Calculated using the CRONUS shielding application

^c Global scaling factor that accounts for the geomagnetic correction

^d SLHL PR: 4.08 ± 0.11 at.g⁻¹.yr⁻¹ (Kelly et al. (2013), Blard et al. (2013b) and Martin et al. (2015) - Scaling scheme: Lal modified - Atmosphere: ERA40 - VDM: Muscheler et al. (2005)

701
702
703

Table 3. Zongo valley CRE age results. Part 2.



704
 705 *Figure 12. Moraine CRE ages in the Zongo Valley. An age probability density function (PDF)*
 706 *is indicated for each moraine with respect to the map colours. For each PDF, the median age*
 707 *is indicated with the 1σ range. Boulders ages contributing to the moraine PDF beyond 25 ka*
 708 *are not represented. For the IP1 and 2 moraines, the scatter is too important to propose a*
 709 *relevant central value and the central 1 σ is indicated. The n value indicates the number of*
 710 *samples. When n=A-B, A is the total number of boulders dated on the moraine and B is the*
 711 *number of boulders considered as outliers. For the MV moraine, the white filled PDF is the*
 712 *initial PDF including all the boulder ages. The orange filled PDF is the final PDF after*
 713 *applying the two following Bayesian conditions: IP5 is older than MV and CQ1 is younger*
 714 *than MV. The TH and CH blue bars indicate respectively the Tauca and Coipasa highstands*
 715

716

717

718

719 *4.1.3. Nevado Sajama*

720 The CRE age results from the Nevado Sajama are presented in the Table 4 and Figure
721 13. The M0 and M2 moraines exhibit an important scatter. The M1 PDF is composed of one
722 main peak corresponding to 4 boulder ages and 2 older minor peaks each associated with one
723 boulder age. We attributed these 2 minor peaks to pre-glacial ^3He accumulation (i.e.
724 inheritance) and considered them as outliers. The age PDF computed with the 4 remaining
725 samples was used to derive the 15.1 ± 1.1 ka age of M1. We considered M1 being younger
726 than M0 as a Bayesian condition to improve the wide spread of the M0 PDF. The resulting
727 PDF (yellow on Figure 13) yielded an age of 16.1 ± 1.5 ka.

728 The 4 boulders of M3 yielded clustered ages; the resulting PDF indicates an age of
729 15.0 ± 0.8 ka. The M2 ages exhibited an important scatter. We applied a Bayesian filter on
730 M2 considering its age bracketed by M1 and M3 to derive the final PDF (yellow on Figure
731 13) that yielded an age of 15.1 ± 0.8 ka. The M4 age is only based on one boulder (SAJ-8).
732 Yet the 11.8 ± 0.7 ka age obtained is coherent with the upper SAJ-7 roche moutonnée of 10.8
733 ± 0.5 ka.

734 The age of the SAJPH-8 roches moutonnées (15.1 ± 0.7 ka) is in good agreement with
735 the moraine ages whereas SAJPH-7 yields inconsistent ages with the global chronology and
736 must have been affected by erosion or indeterminable shielding.

737

Glacial Feature	Sample	Latitude Dec°	Longitude Dec°	Altitude masl	Pyroxene Color	Li ppm	Eruption age ^a Ma	Pn at.g ⁻¹ .yr ⁻¹	³ He _n 10 ⁷ at.g ⁻¹	³ He _e (10) ^b 10 ⁷ at.g ⁻¹	Thickness cm	Thick. Corr. ^c	Shielding ^d	Scaling Factor ^e	Age (1σ) ^f ka
M0	SAJ 1	-18.1817	-68.8494	4400	Black	68	4.9	0.17	8.55	2.06 ± 0.09	2.0	0.98	1.0	10.03	15.65 ± 0.69
	SAJ 2	-18.1813	-68.8496	4407	Black	21	3.5	0.06	2.04	1.90 ± 0.14	1.0	0.99	1.0	9.90	14.57 ± 0.97
	SAJ PH 1	-18.1823	-68.8451	4422	Black	15	3.5	0.05	1.77	1.77 ± 0.20	1.0	0.99	1.0	9.87	13.55 ± 1.47
	SAJ PH 2	-18.1820	-68.8452	4436	Black	28	3.8	0.10	3.69	1.83 ± 0.09	1.5	0.99	1.0	9.95	13.97 ± 0.75
	SAJ PH 3	-18.1779	-68.8458	4498	Black	51	4.4	0.17	7.37	2.47 ± 0.12	2.0	0.98	1.0	10.71	17.63 ± 0.88
M1	SAJ 3	-18.1761	-68.8505	4532	Black	67	0.2	2.10	4.16	2.14 ± 0.11	1.5	0.99	1.0	10.61	15.37 ± 0.77
	SAJ 3-R	-18.1761	-68.8505	4532	Green	47	0.2	1.48	3.22	2.15 ± 0.14	1.5	0.99	1.0	10.62	15.43 ± 0.91
	SAJ 4	-18.1761	-68.8505	4532	Black	54	0.2	0.82	1.78	1.86 ± 0.09	2.0	0.98	1.0	10.37	13.72 ± 0.77
	SAJ 5	-18.1734	-68.8510	4570	Black	115	0.3	1.88	5.37	2.26 ± 0.11	1.0	0.99	1.0	10.86	15.78 ± 0.78
	SAJ 6	-18.1717	-68.8516	4580	Black	53	0.3	0.90	2.31	2.13 ± 0.10	3.0	0.97	1.0	10.81	15.16 ± 0.70
M2	SAJ PH 4	-18.1755	-68.8456	4527	Black	43	4.1	0.14	5.58	4.42 ± 0.18	1.0	0.99	1.0	11.44	29.22 ± 1.56
	SAJ PH 5	-18.1771	-68.8464	4480	Black	148	2.9	0.46	13.19	2.75 ± 0.12	2.0	0.98	1.0	10.83	19.37 ± 0.86
	SAJ PH 9	-18.1632	-68.8474	4584	Black	52	5.6	0.17	9.72	3.90 ± 0.14	0.5	1.00	1.0	11.48	25.63 ± 1.09
	SAJ PH 10	-18.1632	-68.8474	4584	Black	89	0.6	0.20	1.15	3.44 ± 0.17	1.0	0.99	1.0	11.61	22.42 ± 1.39
	SAJ PH 11	-18.1632	-68.8477	4578	Black	43	4.6	0.15	6.91	2.02 ± 0.07	0.5	1.00	1.0	10.65	14.30 ± 0.59
M3	SAJ PH 12	-18.1637	-68.8476	4569	Black	99	5.5	0.32	17.50	2.23 ± 0.10	3.0	0.97	1.0	10.85	15.84 ± 0.71
	SAJ PH 13	-18.1643	-68.8478	4565	Black	27	3.8	0.08	2.88	2.56 ± 0.12	1.5	0.99	1.0	11.03	17.63 ± 0.84
	SAJ PH 8	-18.1617	-68.8510	4545	Black	65	7.6	0.20	15.54	2.10 ± 0.10	2.0	0.98	1.0	10.63	15.11 ± 0.69
	SAJ PH 7	-18.1565	-68.8514	4593	Black	33	7.2	0.09	6.48	1.61 ± 0.09	3.0	0.97	1.0	10.61	11.70 ± 0.68
	SAJ 9	-18.1518	-68.8553	4662	Black	126	0.2	2.05	3.94	2.24 ± 0.12	1.5	0.99	1.0	11.21	15.22 ± 0.78
M4	SAJ 10	-18.1518	-68.8550	4660	Black	68	0.4	1.88	8.27	2.27 ± 0.14	1.0	0.99	1.0	11.22	15.35 ± 0.89
	SAJ 10-R	-18.1518	-68.8550	4660	Green	24	0.5	0.66	3.45	2.15 ± 0.12	1.0	0.99	1.0	11.10	14.68 ± 0.80
	SAJ 11	-18.1532	-68.8534	4640	Black	36	0.4	0.19	0.82	2.25 ± 0.15	1.5	0.99	1.0	11.12	15.36 ± 0.93
	SAJ 11-R	-18.1532	-68.8534	4640	Green	8	0.5	0.04	0.21	2.26 ± 0.15	1.5	0.99	1.0	11.14	15.41 ± 0.95
	SAJ PH 6	-18.1555	-68.8516	4604	Black & Green	22	0.4	0.13	0.56	2.06 ± 0.10	0.5	1.00	1.0	10.78	14.38 ± 0.70
R. Mout.	SAJ 8	-18.1485	-68.8552	4670	Black & Green	25	0.2	0.31	0.71	1.70 ± 0.09	1.5	0.99	1.0	10.98	11.78 ± 0.69
	SAJ 7	-18.1413	-68.8535	4706	Black	16	5.1	0.07	3.65	1.57 ± 0.06	1.0	0.99	1.0	11.01	10.79 ± 0.46

R replicate. For the sample from this study, replicates have been used to compare ³He concentrations from black and green pyroxenes

^a (U-Th-Sm)/⁴He age

^b He_e = He_{tot} - He_n - He_m (we considered He_m = 8.5 × 10⁴ at.g⁻¹ for all samples)

^c Calculated with a density of 2.7 g.cm⁻³ and an attenuation length of 160 g.cm⁻²

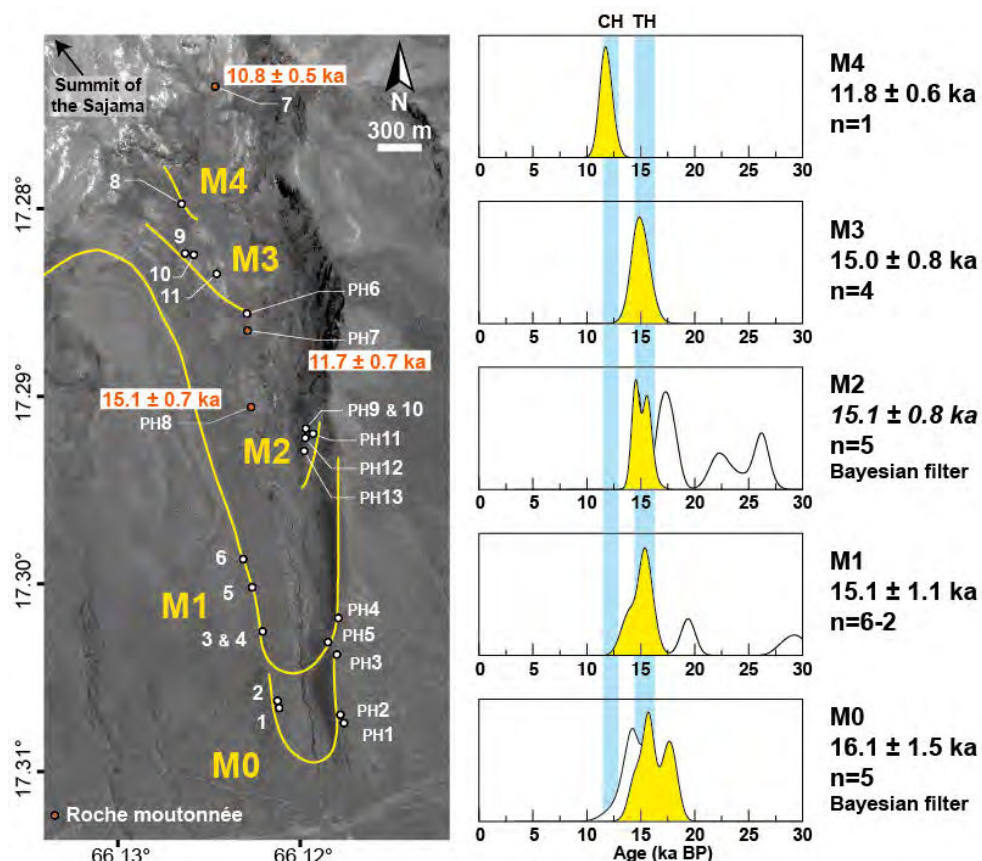
^d Shielding is negligible

^e Global scaling factor that accounts for the geomagnetic correction

^f SIHL PR. 136.2 ± 4.5 at.g⁻¹.yr⁻¹ (Blard et al. (2013a) and Delunel et al. (In Prep)) - Scaling scheme: Lal modified - Atmosphere: ERA40 - VDM: Muscheler et al. (2005)

738

739 *Table 4. Nevado Sajama CRE age results.*



740
 741 *Figure 13. CRE ages on the Nevado Sajama. Uncertainties are given at 1σ. An age*
 742 *probability density function (PDF) is indicated for each moraine. Boulders ages contributing*
 743 *to the moraine PDF beyond 30 ka are not represented. Roche moutonnées ages are reported*
 744 *on the map in orange. For each PDF, the median age is reported. The n value indicates the*
 745 *number of samples. When n=A-B, A is the total number of boulders dated on the moraine and*
 746 *B is the number of boulders considered as outliers. Portions of PDF corresponding to outlier*
 747 *ages are filled in white and not in yellow. For the M0 and the M2 moraine, the white filled*
 748 *PDF is the initial PDF including all the boulder ages. The yellow filled PDF is the final PDF*
 749 *after applying the Bayesian conditions considering a time bracketing by the underlying*
 750 *and/or overlying moraines. The TH and CH blue bars indicate respectively the Tauca and*
 751 *Coipasa highstands*

752
 753

754 4.1.4. Cerro Tunupa

755 The CRE age results from the Cerro Tunupa are presented in the Table 5 and Figure
 756 14. The age PDF of the M1 moraine, exhibit a major peak with five boulder ages clustered
 757 around 16 ka and one outlier yielding an age superior to 20 ka. This outlier was excluded
 758 from age calculation. The combination of the four remaining boulders yields an age of $16.2 \pm$
 759 0.7 ka, coeval with the Tauca transgression. For the M2 moraine, one outliers lying at 10.7 ka

760 is discarded and the remaining boulders yield clustered ages and provide a moraine age of
761 14.5 ± 0.7 ka. The M3 moraines group exhibits a more important scatter. Considering it is
762 younger than M2, we discarded 4 boulders yielding ages superior to 15.5 ka. The 7 remaining
763 boulders provided an age of 13.1 ± 1.0 ka. Three roches moutonnées yield ages clustered
764 around 15.5 ka and 2 around 21.5 ka.
765

Glacial Feature	Sample	Reference	Latitude Dec°	Longitude Dec°	Altitude masl	Pyroxene Color	Li ppm	Eruption age ^a Ma	Pn at.g ⁻¹ .yr ⁻¹	³ He _n 10 ⁴ at.g ⁻¹	³ He _c (1σ) ^b 10 ⁴ at.g ⁻¹	Thickness cm	Thick. Corr. ^c	Shielding ^d	Scaling Factor ^e	Age (1σ) ^f Ka
M1	TU-124		-19.8586	-67.6138	4292	-	-	-	-	-	1.99 ± 0.08	2.2	0.98	1.00	9.7	15.65 ± 0.68
	TU-1A		-19.8643	-67.6128	4260	-	-	-	-	-	2.02 ± 0.06	3.3	0.97	1.00	9.7	16.17 ± 0.61
	TU-1B	Blard et al., 2009	-19.8638	-67.6144	4290	-	-	-	-	-	2.21 ± 0.07	2.2	0.98	1.00	9.9	17.11 ± 0.68
	TU-1Cf		-19.8652	-67.6099	4206	-	-	-	-	-	2.96 ± 0.13	3.3	0.97	1.00	9.9	23.07 ± 1.42
	TU-1D		-19.8691	-67.6054	4083	-	-	-	-	-	1.83 ± 0.06	5.5	0.95	1.00	8.9	16.22 ± 0.65
R. Mout.	TU-4	Blard et al., 2009	-19.8570	-67.6180	4260	-	-	-	-	-	1.89 ± 0.07	2.2	0.98	0.98	9.6	15.46 ± 0.63
	TU-119		-19.8599	-67.6138	4250	-	-	-	-	-	1.83 ± 0.06	0.5	1.00	1.00	9.4	14.66 ± 0.56
	TU-120		-19.8599	-67.6138	4250	-	-	-	-	-	1.79 ± 0.06	0.5	1.00	1.00	9.4	14.41 ± 0.57
M2	TU-121		-19.8590	-67.6147	4267	-	-	-	-	-	1.87 ± 0.13	0.5	1.00	1.00	9.5	14.84 ± 0.94
	TU-121 - R	Blard et al., 2009	-19.8590	-67.6147	4267	-	-	-	-	-	1.96 ± 0.09	0.5	1.00	1.00	9.6	15.41 ± 0.71
	TU-122		-19.8590	-67.6147	4267	-	-	-	-	-	1.74 ± 0.10	0.5	1.00	1.00	9.4	13.98 ± 0.83
	TU-123		-19.8588	-67.6149	4275	-	-	-	-	-	1.31 ± 0.05	0.5	1.00	1.00	9.2	10.71 ± 0.47
	TU-2	Blard et al., 2009	-19.8455	-67.6272	4450	-	-	-	-	-	2.08 ± 0.06	3.3	0.97	0.98	10.5	15.68 ± 0.57
M3	TU-3A		-19.8446	-67.6259	4415	-	-	-	-	-	1.57 ± 0.06	2.2	0.98	0.98	10.0	12.24 ± 0.60
	TU-3A - R	Blard et al., 2009	-19.8446	-67.6259	4415	-	-	-	-	-	1.63 ± 0.07	2.2	0.98	0.98	10.0	12.71 ± 0.68
	TU-3B		-19.8446	-67.6259	4415	-	-	-	-	-	1.81 ± 0.05	2.2	0.98	0.98	10.1	14.08 ± 0.53
	TU-13-201		-19.8443	-67.6268	4432	Black	51	0.57	0.4736	2.71E+05	1.86 ± 0.11	1.7	0.99	1.00	10.1	13.96 ± 0.82
	TU-13-201 - R		-19.8443	-67.6268	4432	Green	45	1.72	0.4179	7.18E+05	1.65 ± 0.07	1.7	0.99	1.00	10.1	12.43 ± 0.67
	TU-13-202		-19.8441	-67.6275	4457	Green	50	2.06	0.3340	6.88E+05	2.36 ± 0.09	5.0	0.96	1.00	10.7	17.30 ± 0.75
	TU-13-204		-19.8447	-67.6276	4456	Black	51	0.84	0.4651	3.92E+05	1.76 ± 0.10	5.0	0.96	1.00	10.2	13.49 ± 0.84
	TU-13-204 - R	This Study	-19.8447	-67.6276	4456	Green	48	1.70	0.4378	7.43E+05	1.65 ± 0.07	2.2	0.98	1.00	10.2	12.37 ± 0.63
	TU-13-01		-19.8424	-67.6286	4502	Black	61	1.27	0.2345	2.98E+05	2.15 ± 0.12	3.9	0.97	1.00	10.7	15.58 ± 0.83
	TU-13-02		-19.8426	-67.6278	4480	Black	54	1.49	0.2092	3.11E+05	2.36 ± 0.12	2.2	0.98	1.00	10.8	16.80 ± 0.89
TU-13-03		-19.8426	-67.6275	4467	Black	48	1.49	0.1773	2.65E+05	3.23 ± 0.17	4.5	0.96	1.00	11.2	22.45 ± 1.46	
Roches	TU-13-04		-19.8430	-67.6271	4461	Black	87	1.20	0.3297	3.96E+05	3.19 ± 0.17	2.8	0.98	1.00	11.2	21.92 ± 1.32
	TU-13-203	This Study	-19.8442	-67.6278	4462	Black	66	1.38	0.2545	3.51E+05	2.04 ± 0.10	5.0	0.96	1.00	10.5	15.27 ± 0.71

R replicate. For the sample from this study, replicates have been used to compare ³He concentrations from black and green pyroxenes

^a (U-Th-Sm)/He age

^b He_c = He_{tot} - He_n - He_m (we considered He_m = 8.5 × 10⁴ at.g⁻¹ for all samples)

^c Calculated with a density of 2.7 g.cm⁻³ and an attenuation length of 160 g.cm⁻²

^d Shielding from Blard et al. (2009) calculated with the CRONUS application, shielding for samples from this study is negligible

^e Global scaling factor that accounts for the geomagnetic correction

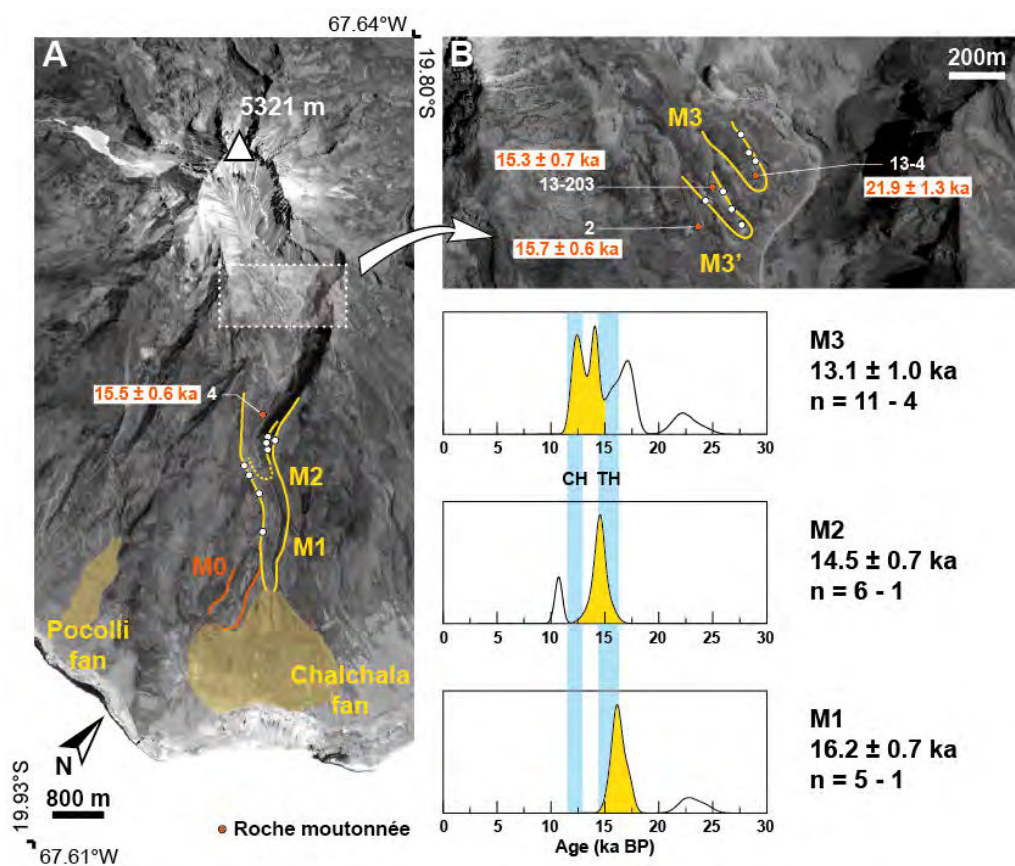
^f SLHL PR: 136.2 ± 4.5 at.g⁻¹.yr⁻¹ (Blard et al. (2013a) and Delunel et al. (In Prep)) - Scaling scheme: Lal modified - Atmosphere: ERA40 - VDM: Muscheler et al. (2005)

Table 5. Cerro Timupa CRE Age results

766

767

768



769

770 Figure 14. CRE ages on the Cerro Tunupa. Uncertainties are given at 1σ . An age probability
 771 density function (PDF) is indicated for each moraine. Boulders ages contributing to the
 772 moraine PDF beyond 30 ka are not represented. Roche moutonnées ages are reported on the
 773 map in orange. For each PDF, the median age is reported. The n value indicates the number
 774 of samples. When $n=A-B$, A is the total number of boulders dated on the moraine and B is the
 775 number of boulders considered as outliers. Portions of PDF corresponding to outlier ages
 776 are filled in white and not in yellow.
 777

778 4.1.5. Cerro Luxar

779 The CRE age results from the Cerro Luxar are presented in the Table 6 and Figure 15.
 780 Boulder ages exhibit an important scatter on all moraines toward old ages; what lead us to
 781 suspect an important inherited ^3He component in the results. Several assumptions are made to
 782 end with moraine ages. For the M1 moraine, the 10 boulder ages form a major peak with 4
 783 clustered ages around 16 ka and 6 minor peaks, each corresponding to one boulder age and
 784 spreading until 150 ka (not represented beyond 30 ka). We consider these 6 boulders as
 785 outliers, presenting a non-negligible inherited ^3He component. With the four remaining

786 samples, we derive an age of 16.1 ± 0.9 ka. For the M2 moraines, four boulders yielding ages
787 from 16.9 to 26.2 ka were considered as outliers. The 2 remaining boulder ages are consistent
788 and provide a moraine age of 15.4 ± 0.7 ka. The 2 boulder ages of M3 lies around 20 ka and
789 are neither consistent with the former ages nor with the upper roche moutonnées, clustered
790 around 14.8 ka. We discarded the two boulder ages obtained for M3 and produced a Bayesian
791 age PDF considering that M3 is younger than M2 and older than the roches moutonnées (See
792 section 3.1.5).
793

Glacial Feature	Sample	Latitude Dec°	Longitude Dec°	Altitude masl	Pyroxene Color	Li ⁺ ppm	Eruption age ^a Ma	Pr ^a at.g ⁻¹ .yr ⁻¹	³ He _{at} ^b 10 ⁶ at.g ⁻¹	³ He _c ^c 10 ⁶ at.g ⁻¹	Thickness cm	Thick. Corr. ^d	Shielding	Scaling Factor ^e	Age (1σ) ^f ka
	LUX-1	-21.0096	-68.0129	4230	-	-	-	-	3.18	7.22 ± 0.18	1.0	0.99	1.00	10.8	50.75 ± 2.72
	LUX-2	-21.0094	-68.0132	4236	-	-	-	-	3.18	4.46 ± 0.17	4.0	0.97	1.00	10.3	33.72 ± 1.69
	LUX-3	-21.0091	-68.0139	4263	-	-	-	-	3.18	9.39 ± 0.34	1.5	0.99	1.00	10.9	65.40 ± 3.20
	LUX-10	-21.0085	-68.0128	4228	-	-	-	-	3.18	3.26 ± 0.11	2.0	0.98	1.00	10.1	24.61 ± 1.24
	LUX-11	-21.0084	-68.0131	4244	-	-	-	-	3.18	2.19 ± 0.08	1.5	0.99	1.00	9.9	16.90 ± 0.71
M1	LUX-12	-21.0080	-68.0135	4265	-	-	-	-	3.18	21.66 ± 0.54	1.5	0.99	1.00	10.9	150.59 ± 7.09
	LUX-11-1	-21.0054	-68.0158	4384	-	-	-	-	3.18	2.15 ± 0.09	2.0	0.98	1.00	10.4	15.78 ± 0.69
	LUX-11-2	-21.0047	-68.0164	4418	-	-	-	-	3.18	2.04 ± 0.07	2.0	0.98	1.00	10.4	14.96 ± 0.58
	LUX-11-3	-21.0043	-68.0167	4429	-	-	-	-	3.18	2.31 ± 0.06	2.0	0.98	1.00	10.7	16.45 ± 0.61
	LUX-11-4	-21.0039	-68.0170	4440	-	-	-	-	3.18	3.03 ± 0.09	2.0	0.98	1.00	11.2	20.59 ± 0.79
	LUX-4	-21.0044	-68.0177	4320	-	-	-	-	3.18	1.94 ± 0.10	3.0	0.98	1.00	10.0	14.97 ± 0.73
	LUX-5	-21.0043	-68.0180	4383	-	-	-	-	3.18	2.42 ± 0.11	4.0	0.97	1.00	10.6	17.72 ± 0.84
M2	LUX-13	-21.0039	-68.0194	4420	-	-	-	-	3.18	3.83 ± 0.15	2.0	0.98	1.00	11.2	26.17 ± 1.09
	LUX-14	-21.0039	-68.0194	4420	-	-	-	-	3.18	2.48 ± 0.10	1.5	0.99	1.00	10.8	17.52 ± 0.77
	LUX-15	-21.0036	-68.0200	4431	-	-	-	-	3.18	2.18 ± 0.09	3.0	0.98	1.00	10.6	15.79 ± 0.68
	LUX-16	-21.0038	-68.0195	4415	-	-	-	-	3.18	2.31 ± 0.09	5.0	0.96	1.00	10.7	16.93 ± 0.74
M3	LUX-11-12	-21.0042	-68.0194	4450	-	-	-	-	3.18	2.91 ± 0.20	3.0	0.98	0.95	11.3	20.77 ± 1.36
	LUX-11-13	-21.0042	-68.0194	4454	-	-	-	-	3.18	2.69 ± 0.12	3.0	0.98	0.99	11.1	18.91 ± 0.88
Roches	LUX-6	-21.0044	-68.0312	4676	-	-	-	-	3.18	2.19 ± 0.12	5.0	0.96	0.98	11.7	14.97 ± 0.77
Moutonnées	LUX-7	-21.0044	-68.0312	4676	-	-	-	-	3.18	2.15 ± 0.11	5.0	0.96	0.98	11.7	14.75 ± 0.73

^a Measurements to be done

^b Average value from Tunupa, Uturuncu and Sajama volcano, to be replaced when the missing measurements are done

^c He_c = He_{at} - He_{in} (we considered He_{in} = 8.5 × 10⁶ at.g⁻¹ for all samples)

^d Calculated with a density of 2.7 g.cm⁻³ and an attenuation length of 160 g.cm⁻²

^e Global scaling factor that accounts for the geomagnetic correction

^f SLHL PR: 136.2 ± 4.5 at.g⁻¹.yr⁻¹ (Blard et al. (2013a) and Delunel et al. (in Prep)) - Scaling scheme: Lal modified - Atmosphere: ERA40 - VDM: Muscheler et al. (2005)

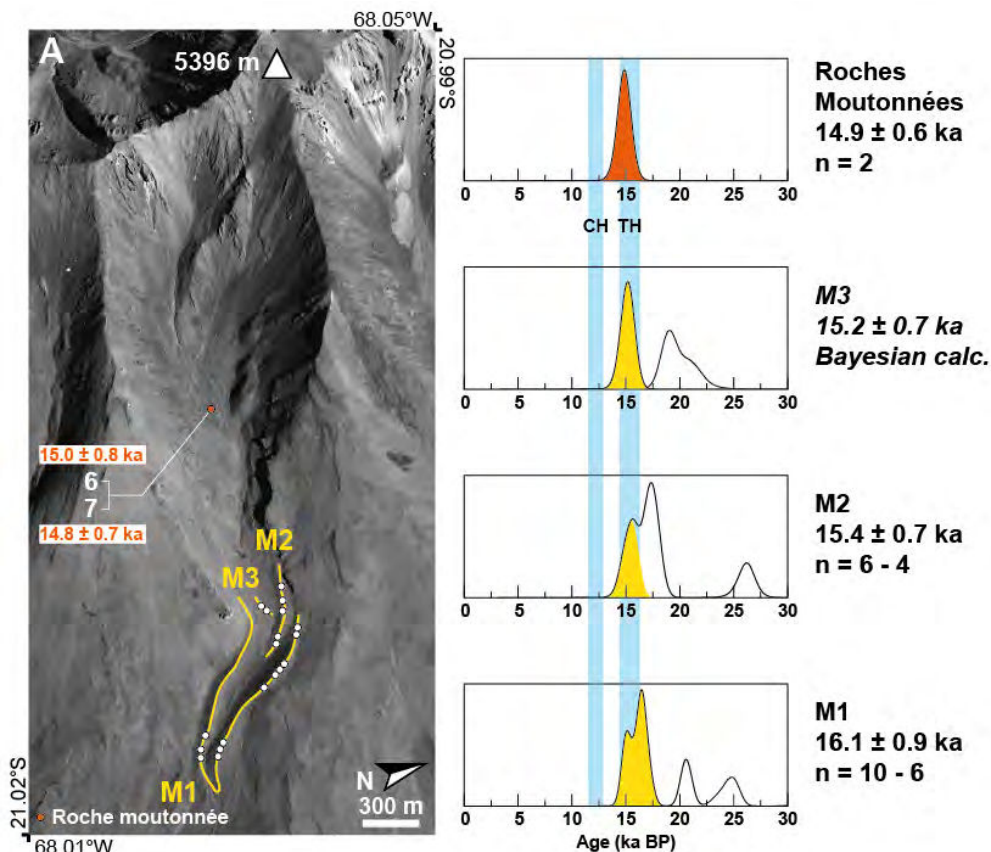
Table 6. Cerro Luxar CRE age results.

794

795

796

797



798
799
800
801
802
803
804
805
806

Figure 15. CRE ages on the Cerro Luxar. Uncertainties are given at 1σ . An age probability density function (PDF) is indicated for each moraine. Boulders ages contributing to the moraine PDF beyond 30 ka are not represented. Roche moutonnées ages are reported on the map in orange. For each PDF, the median age is reported. The n value indicates the number of samples. When $n=A-B$, A is the total number of boulders dated on the moraine and B is the number of boulders considered as outliers. Portions of PDF corresponding to outlier ages are filled in white and not in yellow.

807

4.2. ELA results

808

The ELA computed for each moraine are summarized in Table 7 and Figure 16, which also provide a global context for these results. All late-glacial ELA range between 4400 and 4950 masl. The Zongo Valley experience the most important ELA rise with a difference of 500 m between the Local Last Glacial Maximum (LLGM) moraines and the Pleistocene - Holocene moraine. The Tunupa ELA follows the Zongo pattern but the glacial record does not extend as far towards present. The Sajama and Luxar ELAs range higher (4700 - 4900) m and the moraine record is more centred on the late HS1 period. HS1 - Tauca highstand ELA

814

815 exhibit an important scatter (4400 - 4900 m). ELA coeval with the younger dryas are more
 816 clustered around 4800 - 4900 m.

Site	Moraine	Glacier	Age ^a ka BP	ELA ^b masl	Cooling vs. Present ^{c&d} °C	Rainfall vs. Present ^{d&e} Past / Present
Zongo	IP3	Zongo	16.3 ± 1.0	4542 ± 53	4.35 ± 1.56	1.61 ± 0.58
	IP4		17.2 ± 1.1	4592 ± 48	4.07 ± 1.59	1.61 ± 0.61
	IP5		13.6 ± 0.8	4640 ± 45	3.70 ± 1.56	1.63 ± 0.61
	MV		12.6 ± 0.8	4705 ± 37	3.27 ± 0.93	1.55 ± 0.33
	CQ1		11.6 ± 0.5	4781 ± 33	2.68 ± 0.87	1.59 ± 0.31
	T1	Telata	10.6 ± 2.3	4794 ± 23	2.27 ± 1.09	1.80 ± 0.50
	T2		10.8 ± 1.3	4831 ± 25	2.49 ± 0.96	1.55 ± 0.37
	T3		9.9 ± 1.2	4838 ± 23	2.69 ± 0.69	1.41 ± 0.23
	CQ3	Charquini	10.4 ± 0.6	4807 ± 22	2.93 ± 0.69	1.39 ± 0.23
	CQ4		10.3 ± 0.4	4880 ± 27	2.40 ± 0.67	1.41 ± 0.21
Sajama	M0	-	16.1 ± 1.5	4712 ± 32	4.51 ± 1.53	1.61 ± 0.55
	M1	-	15.1 ± 1.1	4724 ± 30	4.55 ± 1.56	1.58 ± 0.57
	M2	-	15.1 ± 0.8	4761 ± 28	4.10 ± 1.50	1.64 ± 0.54
	M3	-	15.0 ± 0.8	4842 ± 27	3.43 ± 1.41	1.70 ± 0.53
	M4	-	11.8 ± 0.6	4914 ± 24	3.15 ± 1.10	1.56 ± 0.33
Tunupa	M1	-	16.2 ± 0.7	4446 ± 40	6.13 ± 1.38	1.50 ± 0.49
	M2	-	14.5 ± 0.7	4494 ± 35	5.78 ± 1.37	1.52 ± 0.51
	M3	-	13.1 ± 1.0	4673 ± 26	4.52 ± 1.41	1.57 ± 0.57
Luxar	M1	-	16.1 ± 0.9	4765 ± 37	6.36 ± 1.45	1.47 ± 0.47
	M2	-	15.4 ± 0.7	4800 ± 33	5.04 ± 0.85	1.94 ± 0.11
	M3	-	15.2 ± 0.7	4812 ± 36	6.02 ± 1.48	1.50 ± 0.50

^a See calculation details in Section 4.2

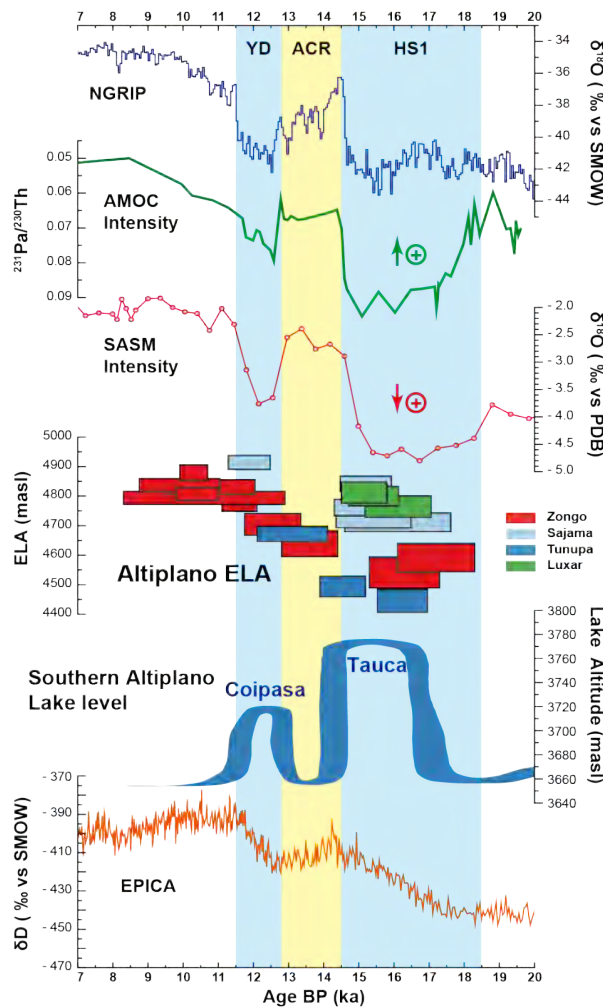
^b AAR = 0.55 to 0.65, derived from observations on High Andes tropical glacier (Section 3.2)

^c Absolute temperature difference with present

^d Uncertainty over the ELA and the actual climate conditions have been propagated

^e Ratio between the computed rainfall relative to the moraine age and the actual rainfall

817
 818 *Table 7. ELA and Temperature results associated with the moraine CRE ages for the 4 sites.*
 819 *For the Zongo valley, we neither computed ELA and cooling vs. Present for IP1 and IP2, as*
 820 *we were unable to derive a CRE age for these moraines (Section 4.1.2), nor for IPα, which is*
 821 *an outsider in the palaeo-glacial system (Section 2.2.1).*



822
 823 *Figure 16. Late-glacial Altiplano ELA compared to other late-glacial proxies for the 7 - 20*
 824 *ka. NGRIP: $\delta^{18}\text{O}$ (‰ vs. SMOW) from North Greenland ice core (Andersen et al., 2004).*
 825 *Santiago Cave: $\delta^{18}\text{O}$ (‰ vs. PDB) from Santiago Cave speleothem carbonates (Ecuador*
 826 *(Mosblech et al., 2012). Botuvera Cave: $\delta^{18}\text{O}$ (‰ vs. PDB) from Botuvera Cave speleothem*
 827 *carbonates (SE Brazil) (Wang et al., 2007). Pacific SST: Alkenone sea-surface temperature*
 828 *of the East Pacific (oceanic core TR163-22; 0°3'N, 92°23'W) (Dubois et al., 2009). Altiplano*
 829 *ELA: PaleaoELA computed in this study for the 4 sites of interest. EPICA: δD (‰ vs. SMOW)*
 830 *from EPICA Dome C ice core (Jouzel et al., 2007)*

831

832

4.3. Climatic inversion Results

833

The palaeo-climatic inversion method described in Section 3.3 enables the

834

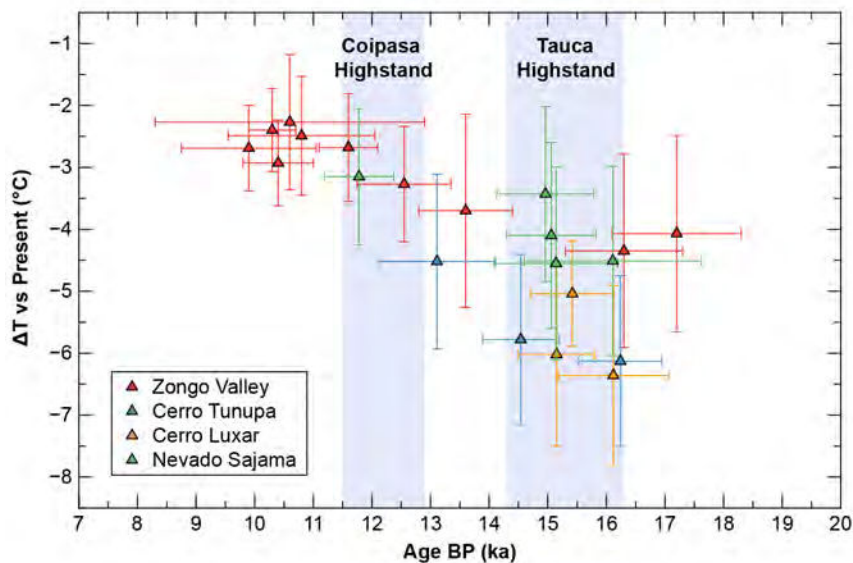
determination of both temperature and precipitation conditions associated with a moraine

835

stillstand. Both results are presented in the last 2 columns of Table 7. The temperature results

836

are also reported on Figure 17.



837
 838 *Figure 17. Late-glacial temperature reconstruction inferred from palaeo-glacier and palaeo-*
 839 *lake cross modelling. Results are expressed as temperature variation vs. present day mean*
 840 *annual temperature.*

841
 842 Temperate shifts (compared to present day conditions) range for the late-glacial period
 843 from 7 to 2 °C. The global dataset exhibit a monotonic warming trend from the LGM to the
 844 Holocene. The uncertainties associated with these results does not enable to precise second
 845 order temperature oscillations. An important spread is observed during the Tauca highstand.
 846 Cerro Luxar and Cerro Tunupa experience the most intense cooling, around - 6 °C whereas
 847 Zongo and Sajama values range between 4.5 and 3.5 °C. During the Coipasa highstand,
 848 temperature lies around - 3°C below the present values. The Pleistocene to Holocene
 849 transition shows a $\approx 2.5^{\circ}\text{C}$ cooling.

850 Because the precipitation results bear important uncertainties they are not subject to
 851 extensive investigations. For a given site, all precipitation factors presented here, that account
 852 for uniform precipitation increase over the Altiplano compared to Present, are compatible
 853 within the error bars. Between different sites, only 2 result sets are significantly different: the
 854 Luxar M2 factor (1.94 ± 0.11 , Tauca Highstand) and the grouped formed by T3 CQ3 and
 855 CQ4 in the Zongo Valley (1.40 ± 0.20 , Holocene onset). This difference points toward a
 856 decrease in the rainfall between the Tauca Highstand and the onset of the Holocene but this

857 trend cannot be regarded as robust. Because of the low significance of the precipitation results
858 they are not further discussed.
859

860 **5. Discussion**

861 **5.1. Glacial chronologies**

862 *5.1.1. Zongo Valley*

863 For the Zongo valley, we expanded Smith et al. (2005) and Jomelli et al. (2011)'s
864 dataset. We add no further chronological insight on the Telata records (Jomelli et al., 2011),
865 in the rest of the valley our new datings complete and extend those of Smith et al. (2005) and
866 enable to precise the glacial history as follow.

867 The IP1 and 2 moraines occupy the most downstream position in the valley, and are
868 therefore the oldest of the moraines studied here. Their ages are spreading from LGM to
869 Holocene (20 - 10 ka) whereas the upstream moraines record a late-glacial retreat starting at
870 17 ka. The erosion of the sampled boulder surface is most likely to explain such a spread. No
871 precise age can be derived for IP1 and 2 but the geomorphic relations with IP3 and IP4
872 indicates that they are 17 ka or older.

873 The IP3 to IP5 group yields rather solid results. Both IP3 and 5 present an important
874 number of clustered ages (respectively 7 and 5) and give internally and externally (with the
875 rest of the valley) consistent ages. IP4 only relies on 2 samples but yield and close from IP3
876 and older than IP5. IP5 and 4 indicates a late Local Last Glacial Maximum (LLGM) around
877 17ka. Climatic conditions enabled a long still stand of the ice tongue until 13.5 ka as IP5 is
878 3.5 ka younger than IP5 and 4 but lies only 400 m upstream (horizontal distance) from IP4.

879 A rapid retreat is observed from IP5 to CQ4 with a 10 km upward movement of the
880 glacier in a 3-3.5 ka time interval. IP5 is coeval with the Antarctic Cold Reversal episode
881 (14.5-12.9 ka) and CQ1 with the Younger Dryas (12.8 - 11.5 ka). The CQ3 and 4 and the
882 Telata moraines are concomitant with the Pleistocene to Holocene transition.

883

884

885 *5.1.2. Nevado Sajama*

886 Nevado Sajama records a late LLGM around 16.1 ka coeval with the Tauca
887 transgression. The glacier present a 1ka still stand during most of the Tauca highstand from
888 16.1 to 15.1 ka. Changes in the climatic conditions induce a rapid retreat of the ice tongue
889 recorded by the M1 to M3 succession which all yield an age of 15 ka. A short retreat is
890 observed between the Tauca highstand and the Younger Dryas with the transition from M3 to
891 M4. After the Younger Dryas, a rapid deglaciation is indicated by the Saj-7 roche moutonnée.
892 We confirm the presence of lateglacial moraines on the Sajama as exposed by Smith et al.
893 (2009), yet the important scatter of the ages they reported prevent further comparison with our
894 results.

895

896 *5.1.3. Cerro Tunupa*

897 As already reported by Blard et al. (2009), the Tunupa records a LLGM around 16.2
898 ka, with a progressive retreat after the Tauca highstand marked by M2 (14.5 ka) and M3 (13.1
899 ka).

900

901 *5.1.4. Cerro Luxar*

902 Cerro Luxar also records a late LLGM coeval with the Tauca Transgression. A
903 progressive retreat is observed during the highstand from M1 to M2 and later From M2 to
904 M3. After the highstand, a rapid deglaciation is shown by the upper roche moutonnées.

905

906 *5.1.5. Overview*

907 The Sajama, Tunupa and Luxar present similar glacial chronologies. They record a
908 LLGM around 16ka coeval with the onset of the Tauca highstand. They undergo a retreat over
909 the end of the highstand either before the end (Cerro Luxar) of after it (Cerro Tunupa). On

910 Cerro Luxar, a massive retreat immediately follows the highstand. On the Sajama, the ice
911 tongue maintains at higher levels during the Younger Dryas before a new retreat. The location
912 of the Tunupa in the centre of the Tauca Lake is likely to have maintained locally wetter
913 conditions until the regression.

914 The Zongo valley does not exhibit the same pattern with a 1 ka older LLGM and the
915 persistence of a climatic conditions close to the LLGM until 13.5ka. A rapid and massive
916 retreat is then observed with high-perched Younger Dryas to Holocene moraines.

917

918 **5.2. ELA calculation**

919 Two possible weakness of the ELA calculation can be considered. The first is due to
920 the glacier and valley orientation. In the Southern Hemisphere, glaciers located on south faces
921 or flowing in southward valleys expand lower than those in northward valleys because they
922 receive less solar radiations. Our calibration relied on the present Zongo glacier which is
923 oriented South-East and East and the Antizana, which lies at a latitude of 0.5°S. Our palaeo-
924 glacier were South to Southeast oriented except for the Zongo valley palaeo-glacier, which
925 was oriented North. The palaeo-ELA in the Zongo valley are thus likely to be overestimated.

926 The second one lies in the fact that our calibration data come from small extent
927 glaciers. The palaeo-glaciers presented in this study were large extent valley glaciers with a
928 different hypsometry. The AAR value we considered is likely to be inappropriate for the
929 kilometric ice tongues reported in the Zongo Valley.

930 To address these issues, an important AAR range representing 10% of the total
931 hypsometry was used for the ELA calculation. As this 0.1 range only results in 30 to 50 m
932 error bars on the ELA values, we are therefore rather confident that the AAR method brought
933 solid constraints on the palaeo-ELAs.

934

935 **5.3. Climatic inversion discussions**

936 *5.3.1. Spatially uniform precipitation changes*

937 A strong assumption of our approach is to consider global precipitations to compute
938 our hydrological budget for the Altiplano. Yet, important spatial precipitation anomalies are
939 likely to be induced by precipitation recycling over the palaeo-lakes and modifications in the
940 location of moist inputs (Blard et al., 2009; Hostetler et al., 1994). Cerro Tunupa and Cerro
941 Luxar exhibit more intense coolings than the Zongo and Sajama in our reconstruction. These
942 2 first sites are located closer from the palaeo-lakes. During the Tauca highstand, Cerro Luxar
943 was at the edge of the lake and Cerro Tunupa was in the middle of the lake, surrounded by
944 water. This spatial distribution of our temperature reconstruction support the idea that both
945 sites benefited from this precipitation recycling. In the precipitation - temperature models
946 we use, both a temperature decrease and a precipitation increase influence the glacier ELA
947 and the lake hydrologic budget in the same way. Thus not considering a positive precipitation
948 anomaly over Cerro Luxar and Tunupa may lead to an overestimation of the cooling level.
949 The Zongo Valley belongs to an presently wetter part of the Altiplano and was located 100
950 km further away from the northern edge of the Tauca Lake. It is thus less likely to have
951 experienced local precipitation anomalies. On this point, the Sajama founds itself in an
952 intermediate situation. Its glacial chronology is globally consistent with the Luxar and Tunupa
953 but it was located 100 km away from the Tauca lake and exhibits ΔT results of the same
954 magnitude as the Zongo Valley. It is thus likely to have undergone the same regional climatic
955 reorganisation as the 2 southern palaeo-glaciers without the recycling influence of the lake.
956 On this basis, the Zongo valley and Sajama ΔT results can be regarded as more robust than
957 those of the Tunupa and Luxar.

958

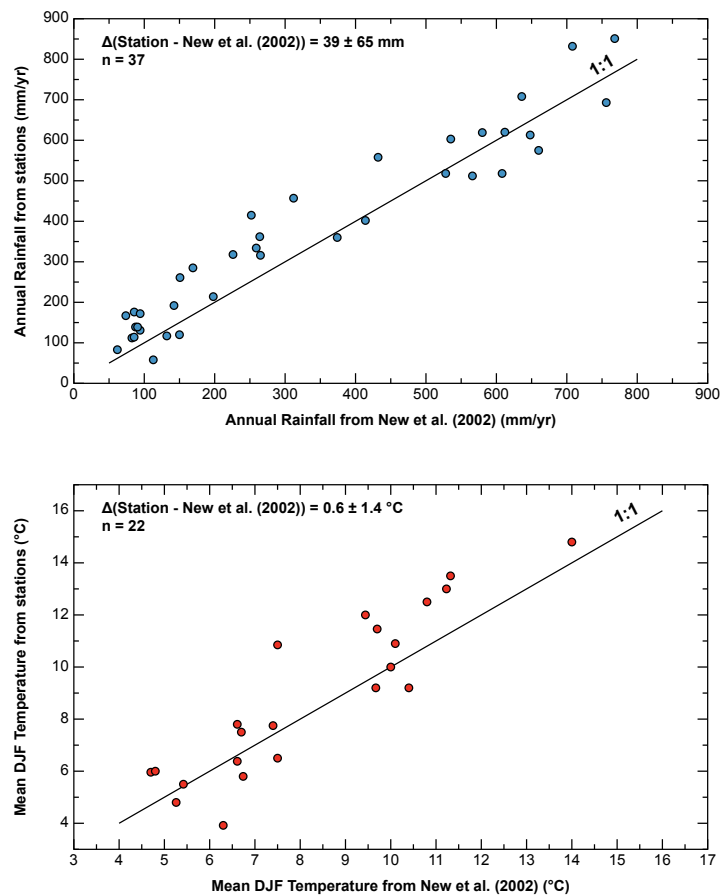
959 *5.3.2. Uncertainties on the ΔT results*

960 The uncertainty of the ΔT results should be propagated from (i) the variability related
961 to the present mean temperature and annual rainfall at the 8 sites used in the glacier model,
962 (ii) the uncertainty associated with the ELA, (iii) the uncertainty on the input temperature and
963 precipitation grid used in the Lake model. For now on, the 2 first points have been addressed
964 but we only tried the temperature and precipitation grids of New et al. (2002). Mourre et al.
965 (2015) compared 3 different types of rainfall gridded datasets: a station based dataset (kriging
966 interpolation), an atmospheric model output and TRMM grid (satellite measurement). They
967 show that the 3 datasets correctly represent the rainfall pattern at the annual scale. This result
968 is a good omen concerning the precipitation variability resulting from the lake model input.
969 They also precise that the main weakness of krigged products is the localization of rainfall
970 maxima. The New et al. (2002) dataset we used belongs to the same type of dataset. The
971 localisation of precipitation maxima is of little importance for our study as we run calculation
972 for the whole Altiplano basin and do not need spatial precision for the precipitation location.

973

974 5.3.3 *Two datasets for the present climate*

975 Our approach relies on the determination of temperature and precipitation shift for
976 different time intervals of the Late-glacial period compared to the present. This present datum
977 is not represented by the same dataset in the glacier and lake model. For the glacier model we
978 used interpolation from station data and for the lake model, we rely on the New et al. (2002)
979 dataset (re-interpolated at a 5 km resolution). A bias is expectable if these 2 datasets are not
980 consistent. To address this issue, we compared the annual rainfall and the mean DJF
981 temperature observed at the stations and their corresponding values on the New et al. (2002)
982 dataset for respectively 37 and 22 stations (Figure 18).



983

984

985 *Figure 18. Comparison of the Annual Rainfall and DJF Temperature from station data and*
 986 *the New et al. (2002) dataset. The New et al. (2002) dataset has been re-interpolated on a 5*
 987 *km grid for this study. One dot indicates the observation at one station and its corresponding*
 988 *value on the New et al. (2002) dataset. The black line indicates the 1:1 slope.*
 989

990 The New et al. (2002) dataset underestimate the precipitation for dry stations (Annual
 991 rainfall < 300 mm) of about 80-100 mm, inducing up to a 100% underestimation. It performs
 992 better for wetter stations with smaller anomalies centred on 0. Over the 37 observations we
 993 report, the New et al. (2002) values lies $39 \pm 65 \text{ mm}$ below the station data. The average
 994 rainfall over the Altiplano derived from the New et al. (2002) dataset is 380 mm. This bias is
 995 therefore around 10%. The New et al. (2002) dataset slightly underestimates the DJF
 996 temperatures with a mean difference of $0.6 \pm 1.4^\circ\text{C}$ for 22 observations. The underestimation
 997 is more important for hot stations (mean annual T > 9°C) where it lies around 1°C . The
 998 average DJF temperature for the Altiplano derived from the New et al. (2002) is 8.9°C . The 2

999 datasets are therefore globally consistent and the discrepancies observed are not likely to be
1000 inaccuracy sources for our results. Yet, tests can be done to (i) fit the New et al. (2002) data to
1001 the station data, (ii) try different temperature and rain inputs.

1002

1003 5.3.4. Comparison with other glacial chronology

1004 We compared our new CRE results with the late-glacial records from the Altiplano
1005 based on the review of Ward et al. (2015). For the Zongo valley, we compare the present
1006 chronology (merging Jomelli et al. (2011), Smith et al. (2005) and our new results) with
1007 others from the Cordillera Real. The 17 ka moraine stabilization is consistent with the datings
1008 on the Nevado Illimani (Smith et al., 2011) and in Laguna Milluni (Smith et al., 2005) lying
1009 just a few kilometres South from the Zongo Valley. The 13.5 ka moraine is coherent with
1010 moraine ages in Valle San Francisco (Zech et al., 2007). The Younger Dryas and early
1011 Holocene moraines are also in good agreement with the Illimani and the Milluni ages and also
1012 with Huancané moraines in the North of the basin (Kelly et al., 2013). This overview shows
1013 that the Cordillera Real exhibit a globally consistent response to the late-glacial climate
1014 forcings.

1015 The global pattern observed on Nevado Sajama, Cerro Tunupa (results merged with
1016 Blard et al. (2009)) and Cerro Luxar characterized by glacial stillstands coeval with the Tauca
1017 highstand presents similarities with Cerro Uturuncu (Blard et al., 2014) on the Altiplano.
1018 Furthermore, a major glacial advance is recorded on the flank of Cerro Azanaques at the onset
1019 of the highstand with the build up of a massive glacial fan-delta on the eastern edge of the
1020 lake (Clapperton et al., 1997; Clayton and Clapperton, 1995). On the eastern cordillera, the
1021 glaciers from Cochabamba and Tres Lagunas record a major stabilization around 15-16 ka
1022 (Zech et al., 2009, 2007). These signals indicate climatic conditions suitable for glacial
1023 stillstand both over southern Altiplano and the eastern Andes around 15 ka

1024 *5.3.5. Palaeo-climatic implications*

1025 The new CRE ages and temperature inversion reported here bring new insight on the
1026 timing and magnitude of the deglaciation over the Altiplano. They enable to identify 2
1027 different types of late-glacial climate forcings. In the Northern Altiplano, climatic conditions
1028 remain close from the LLGM until 13.5 ka and then drive a massive retreat until the early
1029 Holocene. The associated temperature shift (vs. Present) evolves linearly from $\approx -4.5^{\circ}\text{C}$
1030 around 17 ka and $\approx -2.5^{\circ}\text{C}$ around 10 ka.

1031 In the middle and southern Altiplano, climate forcings induce a LLGM around 16 ka.
1032 The wide spread of our temperature reconstruction for this period points the importance of the
1033 spatial rainfall anomalies associated with this climate anomaly. Our computed coolings are
1034 consistent with those previously reported for the Tunupa ($\approx -6^{\circ}\text{C}$, Blard et al., 2009; Placzek et
1035 al., 2013) and the Sajama ($\approx -4-4.5^{\circ}\text{C}$, Placzek et al., 2013). Yet, the Samaja temperature
1036 results being close to the Zongo, it can be expected that the Tauca cooling did not result
1037 cooler than $\approx -4-4.5^{\circ}\text{C}$ and that spatial precipitation anomalies lead to an overestimation of the
1038 cooling for the Cerro Tunupa and Luxar. Rainfall spatial distribution is thus likely to play a
1039 key role in the spatial variability of the ice fluctuations.

1040 Both Eastern Cordillera and Southern Altiplano glacier recorded glacial Stadials
1041 around 15-16 ka. This spatial pattern along with the precipitation anomaly suspected over
1042 Cerro Luxar and Tunupa points toward an enhanced easterly moist transport crossing the
1043 eastern cordillera towards the southern Altiplano. Such a transport could be promoted by a
1044 strengthening and southward expansion of the easterlies, consistently with present
1045 observations during wet periods (Vuille, 1999). This would be compatible with 2 synoptic
1046 climate change reported during HS1 (and a fortiori during the Tauca highstand): (i) massive
1047 moist inputs over central Brazil reported by Stríkis et al. (2015) as "mega SACZ events"
1048 (relatively to the activity of the South Atlantic Convergence Zone), (ii) southward shift of the

1049 westerly winds belt (Montade et al., 2015) which are present inhibitors of the easterly moist
1050 transport over Altiplano during dry periods (Garreaud et al., 2003; Vuille, 1999).

1051 **6. Conclusion**

1052 We conducted CRE datings in the Zongo Valley (^{10}Be on quartz), Nevado Sajama,
1053 Cerro Tunupa and Cerro Luxar (^3He on Pyroxenes). We expanded the results of Smith et al.
1054 (2005) and Jomelli et al. (2011) in the Zongo Valley and Blard et al. (2009) on Cerro Tunupa.
1055 No CRE dating had been reported before on Cerro Luxar and Nevado Sajama. To bring new
1056 insight on the late-glacial climatic conditions over the Altiplano, we couple these glacial
1057 chronologies with simple Precipitation-Temperature modelling for both palaeo-glaciers and
1058 palaeo-lakes in the way of Blard et al. (2009).

1059 In the Zongo Valley a late LLGM is recorded around 17 ka associated with a ΔT vs.
1060 Present around $4-4.5^\circ\text{C}$. The glacial extent is globally maintained until 13.5 ka and followed
1061 by a massive retreat until the early Holocene. A linear temperature increase is observed
1062 during this period with $\Delta T \approx 2.5^\circ\text{C}$ at the end of the Younger Dryas.

1063 Nevado Sajama, Cerro Tunupa and Luxar records LLGMs synchronous with the
1064 Tauca Lake highstand followed by different retreat timings. A first abrupt retreat is observed
1065 on the Sajama during the second half of the highstand, followed by an upstream stillstand
1066 until the end of the Coipsasa highstand. On Cerro Luxar, the end of the highstand is marked
1067 by a massive retreat. On Cerro Tunupa, a progressive retreat is initiated during the
1068 transgression and an upstream stillstand is observed before or during the Coipasa highstand.
1069 An important spread between the ΔT reconstructions is observed during the Tauca highstand,
1070 most likely to reflect spatial precipitation anomalies. The most likely $\Delta T \approx 4-4.5^\circ\text{C}$ is
1071 proposed for the Tauca highstand. The spatial repartition of these anomalies and of the Tauca
1072 moraines reported here in other studies support the idea that the major hydrologic changes
1073 during HS1 were driven by enhanced moist transport from wetter central Brazil through
1074 strengthening and southward expansion of the easterlies. The ΔT reconstructions suggests that

1075 precipitations are the main driver of the spatial variability in the late glacial ice dynamics for
1076 the Altiplano.
1077

1078 **Appendix**

1079 **A.1. Determination of the present day P-T conditions at the glacial sites**

1080 We considered the 4 to 10 closer stations from the sites and computed a weighted
1081 mean of the Annual rainfall and mean annual temperature. When a station cluster was
1082 overweighting a particular location in the vicinity of a site, an average value was derived from
1083 the cluster to confer him a normal weight in the mean calculation. The weights included either
1084 the inverse of the distance to the site or the inverse square of the distance. For each of the 2
1085 distance weightings, we applied 4 different averaging methods. In the method 1 the mean is
1086 also weighted considering the variability observed at each station and the number of
1087 observations. In method 2 we only consider distance weighting. In method 3, the distance and
1088 the number of observation are considered only. In method 4 the distance and the variability
1089 are considered only. The 8 different methods (2 x 4) mainly yielded close values.

1090

1091 **A.2. Lake model amendments and functioning**

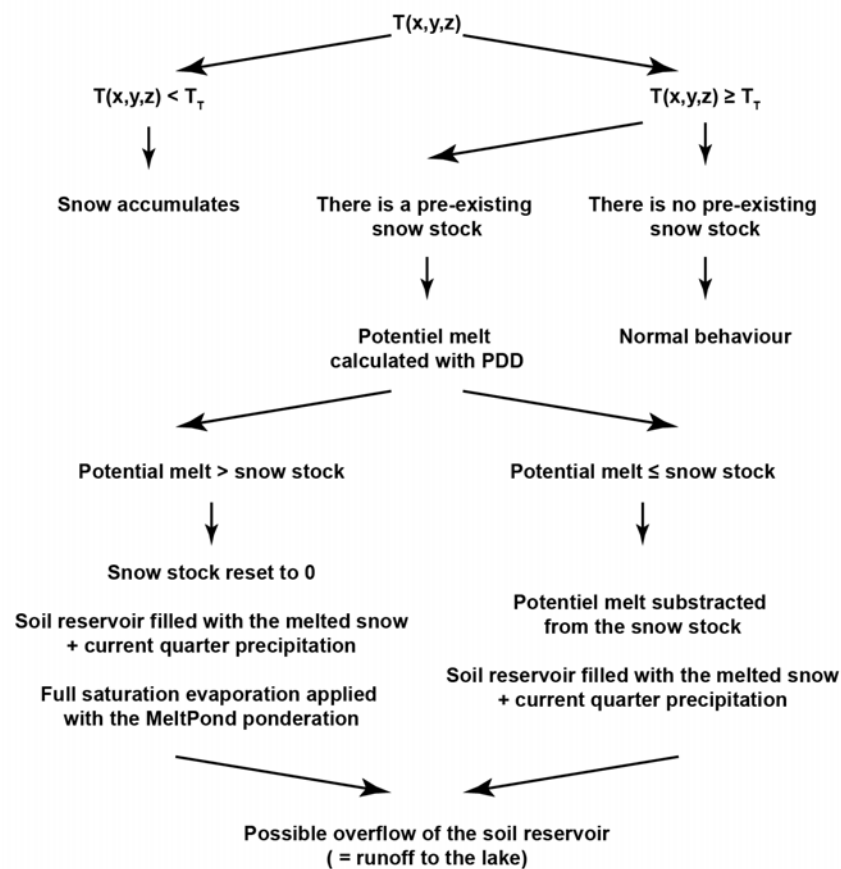
1092 *A.2.1. Management of the snow stock*

1093 The lake model was implemented so as to calculate an annual lake balance grid and
1094 watershed balance grid for a given Δ Temperature and Δ Precipitation versus present (ΔT and
1095 ΔP). These grids were initialised over a period of 5 years to erase the random initial state.

1096 As this model is run to test an important range of cooling level over the Altiplano from
1097 the present situation (from 0 to 10°C cooling), significant areas may experience snow
1098 precipitation instead of rain. To take into account the temporal or permanent snow
1099 accumulation, we considered for each watershed pixels a snow stock. We linked the melting
1100 of this stock to a PDD value of 6 mm.°C⁻¹.day⁻¹ (consistently with the review of Hock (2003)
1101 and the value of Blard et al. (2009)) and considered the evolution of the underlying soil
1102 reservoir level according to the workflow presented in Figure A.1. This method relies on the

1103 use of a temperature threshold to determine whether precipitation is snow or rain. Then, the
 1104 PDD melting is used to increase or decrease the snow stock of each pixel. For locations
 1105 appearing to be in perpetual snow accumulation after the 5 years run, the annual increase of
 1106 the snow stock is directly added to the run off. This way we consider that melting completely
 1107 compensate accumulation for steady state glaciers.

For a given quarter and at a given location (x,y) and elevation z:



1108
 1109 *Figure A.1. Snow management workflow in the lake model. $T(p)$ indicates the temperature for*
 1110 *a given pixel at a given quarter. T_T is the temperature threshold that delimitates snow from*
 1111 *rain precipitations. MeltPond is defined as $(1 - \text{Snow Stock} / \text{Potential melt})$ to account for the*
 1112 *progressive melt of the snow cover that shields the soil evaporation during the quarter.*
 1113 *Normal behaviour indicates the default precipitation workflow of the model.*

1114

1115

A.2.2. Hydrologic connexion between the Altiplano sub-basins

1116

1117

Our shoreline archive makes that we rely on hydrologic budget related with the level

1118 of the southern basin lake for our climatic inversions. Yet during the Late-glacial period the

1119 hydrologic connexion between all the 4 basins of the Altiplano is not proven. It was then

1120 necessary to determine the basins connected with the southern basin for a given ΔT and ΔP
1121 shift (vs. Present), so as to compute the relevant hydrologic budget.

1122 To do so, we used the annual lake balance grid and watershed balance grid on each
1123 sub-basin sequentially to evaluate the connexion between one basin and its downstream
1124 counterpart. First we compute the Titicaca overflow toward the Poopo basin. Then we
1125 compute annual hydrologic budgets for the Poopo basin, allowing lake level adjustment from
1126 one year to another until reaching a steady state. If this steady state corresponds to an
1127 overflow towards the Coipasa basin, we determine the corresponding input for the Coipasa.
1128 We apply the same approach to the Coipasa basin to see if it overflows in the Uyuni basin.
1129 We ends up identifying the basins hydrologically connected with the southern basin for which
1130 we know the lake level from the shoreline datings. We compute the hydrological budget for
1131 the identified basins and find the ΔT and ΔP (vs. Present) that zeros it.

1132

1133 **Acknowledgments**

1134 This work was funded by the INSU EVE-LEFE program and the ANR Jeunes
1135 Chercheurs GALAC project “ANR-11-JS56-011-01”. We greatly appreciated the logistical
1136 support of the IRD of La Paz (Bolivia) during our field trips conducted between 2010 and
1137 2013. We are much indebted to C. Hautefeuille and B. Barry for their contribution on the
1138 Luxar datings. P. Burnard and L. Zimmerman are warmly thanked for essential help with the
1139 SFT mass spectrometer and related device during analytic sessions. The same feelings are
1140 addressed to F. Gallo and M. Protin for vital support on ^{10}Be separative chemistry and L.
1141 Tissandier and Y. Marrocchi for much-needed help with the SEM and mineral analysis. We
1142 are grateful to the SARM-CNRS for high quality chemical analysis. R. Joussemet and the
1143 STEVAL crew (GeoRessources, Nancy) are acknowledged for their technical support for
1144 sample crushing and mineral separation.

1145 The ASTER French national AMS facility (CEREGE, Aix-en-Provence) is supported
 1146 by the INSU/CNRS, the ANR through the “Equipements d’Excellence” program, IRD and
 1147 CEA.

1148 The field measurements of mass balance and ELA on the glaciers in Bolivia and
 1149 Ecuador were provided by the Andean part of the *Service National d’Observation*
 1150 GLACIOCLIM funded by the French IRD (*Institut de Recherche pour le Développement*), the
 1151 *Universidad Mayor de San Andres* (UMSA, IGEMA, IHH) in Bolivia and the *Instituto*
 1152 *Nacional de Meteorología e Hidrología* (INAMHI) in Ecuador.

1153

1154 Bibliography

- 1155 Ammann, C., Jenny, B., Kammer, K., Messerli, B., 2001. Late quaternary glacier response to humidity changes
 1156 in the arid Andes of Chile (18-29°S). *Palaeogeogr. Palaeoclimatol. Palaeoecol.* 172, 313–326.
 1157 doi:10.1016/S0031-0182(01)00306-6
- 1158 Andersen, K.K., Azuma, N., Barnola, J.-M., Bigler, M., Biscaye, P., Caillon, N., Chappellaz, J., Clausen, H.B.,
 1159 Dahl-Jensen, D., Fischer, H., Flückiger, J., Fritzsche, D., Fujii, Y., Goto-Azuma, K., Grønbold, K.,
 1160 Gundestrup, N.S., Hansson, M., Huber, C., Hvidberg, C.S., Johnsen, S.J., Jonsell, U., Jouzel, J., Kipfstuhl,
 1161 S., Landais, a., Leuenberger, M., Lorrain, R., Masson-Delmotte, V., Miller, H., Motoyama, H., Narita, H.,
 1162 Popp, T., Rasmussen, S.O., Raynaud, D., Rothlisberger, R., Ruth, U., Samyn, D., Schwander, J., Shoji, H.,
 1163 Siggard-Andersen, M.-L., Steffensen, J.P., Stocker, T., Sveinbjörnsdóttir, a E., Svensson, a, Takata, M.,
 1164 Tison, J.-L., Thorsteinsson, T., Watanabe, O., Wilhelms, F., White, J.W.C., 2004. High-resolution record
 1165 of Northern Hemisphere climate extending into the last interglacial period. *Nature* 431, 147–51.
 1166 doi:10.1038/nature02805
- 1167 Andrews, J., Kay, R., 1982. Natural production of tritium in permeable rocks. *Nature*. doi:10.1038/298361a
- 1168 Andrews, J.N., 1983. The isotopic composition of radiogenic helium and its use to study groundwater. *Water*
 1169 *Rock* 49, 17–21.
- 1170 Balco, G., Stone, J.O., Lifton, N. a., Dunai, T.J., 2008. A complete and easily accessible means of calculating
 1171 surface exposure ages or erosion rates from ¹⁰Be and ²⁶Al measurements. *Quat. Geochronol.* 3, 174–195.
 1172 doi:10.1016/j.quageo.2007.12.001
- 1173 Benn, D.I., Lehmkuhl, F., 2000. Mass balance and equilibrium-line altitudes of glaciers in high-mountain
 1174 environments. *Quat. Int.* 65-66, 15–29. doi:10.1016/S1040-6182(99)00034-8
- 1175 Benn, D.I., Owen, L.A., Osmaston, H.A., Seltzer, G.O., Porter, S.C., Mark, B., 2005. Reconstruction of
 1176 equilibrium-line altitudes for tropical and sub-tropical glaciers. *Quat. Int.* 138-139, 8–21.
 1177 doi:10.1016/j.quaint.2005.02.003
- 1178 Blard, P.-H., Braucher, R., Lavé, J., Bourlès, D., 2013a. Cosmogenic ¹⁰Be production rate calibrated against
 1179 ³He in the high Tropical Andes (3800–4900 m, 20–22° S). *Earth Planet. Sci. Lett.* 382, 140–149.
 1180 doi:10.1016/j.epsl.2013.09.010
- 1181 Blard, P.-H., Lavé, J., Farley, K. a., Fornari, M., Jiménez, N., Ramirez, V., 2009. Late local glacial maximum in
 1182 the Central Altiplano triggered by cold and locally-wet conditions during the paleolake Tauca episode (17–
 1183 15ka, Heinrich 1). *Quat. Sci. Rev.* 28, 3414–3427. doi:10.1016/j.quascirev.2009.09.025
- 1184 Blard, P.-H., Lave, J., Farley, K. a., Ramirez, V., Jimenez, N., Martin, L.C.P., Charreau, J., Tibari, B., Fornari,
 1185 M., 2014. Progressive glacial retreat in the Southern Altiplano (Uturuncu volcano, 22°S) between 65 and
 1186 14ka constrained by cosmogenic ³He dating. *Quat. Res.* 82, 209–221. doi:10.1016/j.yqres.2014.02.002
- 1187 Blard, P.-H., Lavé, J., Sylvestre, F., Placzek, C.J., Claude, C., Galy, V., Condom, T., Tibari, B., 2013b.
 1188 Cosmogenic ³He production rate in the high tropical Andes (3800 m, 20°S): Implications for the local last
 1189 glacial maximum. *Earth Planet. Sci. Lett.* 377-378, 260–275. doi:10.1016/j.epsl.2013.07.006
- 1190 Blard, P.-H., Sylvestre, F., Tripathi, a. K., Claude, C., Causse, C., Coudrain, a., Condom, T., Seidel, J.-L.,

- 1191 Vimeux, F., Moreau, C., Dumoulin, J.-P., Lavé, J., 2011. Lake highstands on the Altiplano (Tropical
1192 Andes) contemporaneous with Heinrich 1 and the Younger Dryas: new insights from ^{14}C , U–Th dating
1193 and $\delta^{18}\text{O}$ of carbonates. *Quat. Sci. Rev.* 30, 3973–3989. doi:10.1016/j.quascirev.2011.11.001
- 1194 Blard, P.H., Balco, G., Burnard, P.G., Farley, K.A., Fenton, C.R., Friedrich, R., Jull, A.J.T., Niedermann, S., Pik,
1195 R., Schaefer, J.M., Scott, E.M., Shuster, D.L., Stuart, F.M., Stute, M., Tibari, B., Winckler, G.,
1196 Zimmermann, L., 2014. An inter-laboratory comparison of cosmogenic ^3He and radiogenic ^4He in the
1197 CRONUS-P pyroxene standard. *Quat. Geochronol.* 26, 11–19. doi:10.1016/j.quageo.2014.08.004
- 1198 Borchers, B., Marrero, S., Balco, G., Caffee, M., Goehring, B., Lifton, N., Nishiizumi, K., Phillips, F., Schaefer,
1199 J., Stone, J., 2015. Geological calibration of spallation production rates in the CRONUS-Earth project.
1200 *Quat. Geochronol.* 1–11. doi:10.1016/j.quageo.2015.01.009
- 1201 Carcaillet, J., Angel, I., Carrillo, E., Audemard, F. a., Beck, C., 2013. Timing of the last deglaciation in the
1202 Sierra Nevada of the Mérida Andes, Venezuela. *Quat. Res.* 80, 482–494. doi:10.1016/j.yqres.2013.08.001
- 1203 Clapperton, C., Clayton, J., Benn, D., 1997. LATE QUATERNARY GLACIER ADVANCES AND
1204 PALAEO LAKE HIGHSTANDS IN THE BOLIVIAN ALTIPLANO. *Quat. ...* 6182, 49–59.
- 1205 Clayton, J.D., Clapperton, C.M., 1995. The last glacial cycle and palaeolake synchrony in the southern volivian
1206 altiplano: cerro azanaques case study.
- 1207 Condom, T., Coudrain, A., Dezetter, A., Brunstein, D., Delclaux, F., Jean-Emmanuel, S., 2004. Transient
1208 modelling of lacustrine regressions: two case studies from the Andean Altiplano. *Hydrol. Process.* 18,
1209 2395–2408. doi:10.1002/hyp.1470
- 1210 Condom, T., Coudrain, A., Sicart, J.E., Théry, S., 2007. Computation of the space and time evolution of
1211 equilibrium-line altitudes on Andean glaciers (10°N – 55°S). *Glob. Planet. Change* 59, 189–202.
1212 doi:10.1016/j.gloplacha.2006.11.021
- 1213 Dubois, N., Kienast, M., Normandeau, C., Herbert, T.D., 2009. Eastern equatorial Pacific cold tongue during the
1214 Last Glacial Maximum as seen from alkenone paleothermometry. *Paleoceanography* 24, 1–12.
1215 doi:10.1029/2009PA001781
- 1216 Eaves, S.R., N. Mackintosh, A., Winckler, G., Schaefer, J.M., Alloway, B. V., Townsend, D.B., 2016. A
1217 cosmogenic ^3He chronology of late Quaternary glacier fluctuations in North Island, New Zealand (39°S).
1218 *Quat. Sci. Rev.* 132, 40–56. doi:10.1016/j.quascirev.2015.11.004
- 1219 Farber, D.L., Hancock, G.S., Finkel, R.C., Rodbell, D.T., 2005. The age and extent of tropical alpine glaciation
1220 in the Cordillera Blanca, Peru. *J. Quat. Sci.* 20, 759–776. doi:10.1002/jqs.994
- 1221 Fox, A.N., 1993. Snowline altitude and climate at present and during the Last Pleistocene Glacial Maximum in
1222 the Central Andes (5° – 28°S). Cornell University.
- 1223 Garreaud, R., Vuille, M., Clement, A.C., 2003. The climate of the Altiplano: observed current conditions and
1224 mechanisms of past changes. *Palaeogeogr. Palaeoclimatol. Palaeoecol.* 194, 5–22. doi:10.1016/S0031-
1225 0182(03)00269-4
- 1226 Garreaud, R.D., Vuille, M., Compagnucci, R., Marengo, J., 2009. Present-day South American climate.
1227 *Palaeogeogr. Palaeoclimatol. Palaeoecol.* 281, 180–195. doi:10.1016/j.palaeo.2007.10.032
- 1228 Giesen, R.H., Oerlemans, J., 2012. Global application of a surface mass balance model using gridded climate
1229 data. *Cryosph. Discuss.* 6, 1445–1490. doi:10.5194/tcd-6-1445-2012
- 1230 Greuell, W., Smeets, P., 2001. Variations with elevation in the surface energy balance on the Pasterze (Austria).
1231 *J. Geophys. Res.* 106, 31717. doi:10.1029/2001JD900127
- 1232 Han, Z., Li, X., Yi, S., Stevens, T., Chen, Y., Wang, X., Lu, H., 2015. Extreme monsoon aridity episodes
1233 recorded in South China during Heinrich Events. *Palaeogeogr. Palaeoclimatol. Palaeoecol.* 440, 467–474.
1234 doi:10.1016/j.palaeo.2015.09.037
- 1235 Hock, R., 2003. Temperature index melt modelling in mountain areas. *J. Hydrol.* 282, 104–115.
1236 doi:10.1016/S0022-1694(03)00257-9
- 1237 Hostetler, S.W., Giorgi, F., Bates, G.T., Bartlein, P.J., 1994. Lake-Atmosphere Feedbacks Associated with
1238 Paleolakes Bonneville and Lahontan. *Science* (80- .). 263, 665–668. doi:10.1126/science.263.5147.665
- 1239 Jomelli, V., Favier, V., Vuille, M., Braucher, R., Martin, L., Blard, P.-H., Colose, C., Brunstein, D., He, F.,
1240 Khodri, M., Bourlès, D.L., Leanni, L., Rinterknecht, V., Grancher, D., Francou, B., Ceballos, J.L.,
1241 Fonseca, H., Liu, Z., Otto-Bliesner, B.L., 2014. A major advance of tropical Andean glaciers during the
1242 Antarctic cold reversal. *Nature*. doi:10.1038/nature13546
- 1243 Jomelli, V., Khodri, M., Favier, V., Brunstein, D., Ledru, M.-P., Wagon, P., Blard, P.-H., Sicart, J.-E.,
1244 Braucher, R., Grancher, D., Bourlès, D.L., Braconnot, P., Vuille, M., 2011. Irregular tropical glacier retreat
1245 over the Holocene epoch driven by progressive warming. *Nature* 474, 196–9. doi:10.1038/nature10150
- 1246 Jouzel, J., Masson-Delmotte, V., Cattani, O., Dreyfus, G., Falourd, S., Hoffmann, G., Minster, B., Nouet, J.,
1247 Barnola, J.M., Chappellaz, J., Fischer, H., Gallet, J.C., Johnsen, S., Leuenberger, M., Loulergue, L.,
1248 Luethi, D., Oerter, H., Parrenin, F., Raisbeck, G., Raynaud, D., Schilt, A., Schwander, J., Selmo, E.,
1249 Souchez, R., Spahni, R., Stauffer, B., Steffensen, J.P., Stenni, B., Stocker, T.F., Tison, J.L., Werner, M.,
1250 Wolff, E.W., 2007. Orbital and Millennial Antarctic Climate Variability over the Past 800,000 Years.

- 1251 Science (80-.). 317, 793–796. doi:10.1126/science.1141038
- 1252 Kanner, L.C., Burns, S.J., Cheng, H., Edwards, R.L., Vuille, M., 2013. High-resolution variability of the South
1253 American summer monsoon over the last seven millennia: Insights from a speleothem record from the
1254 central Peruvian Andes. *Quat. Sci. Rev.* 75, 1–10. doi:10.1016/j.quascirev.2013.05.008
- 1255 Kelly, M. a., Lowell, T. V., Applegate, P.J., Phillips, F.M., Schaefer, J.M., Smith, C. a., Kim, H., Leonard, K.C.,
1256 Hudson, A.M., 2013. A locally calibrated, late glacial ^{10}Be production rate from a low-latitude, high-
1257 altitude site in the Peruvian Andes. *Quat. Geochronol.* 1–16. doi:10.1016/j.quageo.2013.10.007
- 1258 Kirkbride, M., Matthews, D., 1997. The role of fluvial and glacial erosion in landscape evolution: The Ben Ohau
1259 Range, New Zealand. *Earth Surf. Process. Landforms* 22, 317–327. doi:10.1002/(SICI)1096-
1260 9837(199703)22:3<317::AID-ESP760>3.0.CO;2-I
- 1261 Kuhn, M., 1989. *Glacier Fluctuations and Climatic Change: Proceedings of the Symposium on Glacier
1262 Fluctuations and Climatic Change, held in Amsterdam, 1--5 June 1987*, in: Oerlemans, J. (Ed.), . Springer
1263 Netherlands, Dordrecht, pp. 407–417. doi:10.1007/978-94-015-7823-3_26
- 1264 Kull, C., Grosjean, M., 2000. Late pleistocene climate conditions in the north Chilean Andes drawn from a
1265 climate-glacier model. *J. Glaciol.* doi:10.3189/172756500781832611
- 1266 Kull, C., Hänni, F., Grosjean, M., Veit, H., 2003. Evidence of an LGM cooling in NW-Argentina (22°S) derived
1267 from a glacier climate model. *Quat. Int.* 108, 3–11. doi:10.1016/S1040-6182(02)00190-8
- 1268 Kull, C., Imhof, S., Grosjean, M., Zech, R., Veit, H., 2008. Late Pleistocene glaciation in the Central Andes:
1269 Temperature versus humidity control - A case study from the eastern Bolivian Andes (17°S) and regional
1270 synthesis. *Glob. Planet. Change* 60, 148–164. doi:10.1016/j.gloplacha.2007.03.011
- 1271 Lal, D., 1991. Cosmic ray labeling of erosion surfaces: in situ nuclide production rates and erosion models. *Earth
1272 Planet. Sci. Lett.* 104, 424–439. doi:10.1016/0012-821X(91)90220-C
- 1273 Lifton, N., Sato, T., Dunai, T.J., 2014. Scaling in situ cosmogenic nuclide production rates using analytical
1274 approximations to atmospheric cosmic-ray fluxes. *Earth Planet. Sci. Lett.* 386, 149–160.
1275 doi:10.1016/j.epsl.2013.10.052
- 1276 Loibl, D., Lehmkuhl, F., Griebinger, J., 2014. Reconstructing glacier retreat since the Little Ice Age in SE Tibet
1277 by glacier mapping and equilibrium line altitude calculation. *Geomorphology* 214, 22–39.
1278 doi:10.1016/j.geomorph.2014.03.018
- 1279 Mabry, J., Burnard, P., Blard, P.-H., Zimmermann, L., 2012. Mapping changes in helium sensitivity and peak
1280 shape for varying parameters of a Nier-type noble gas ion source. *J. Anal. At. Spectrom.* 27, 1012.
1281 doi:10.1039/c2ja10339g
- 1282 Malone, A.G.O., Pierrehumbert, R.T., Lowell, T. V., Kelly, M.A., Stroup, J.S., 2015. Constraints on southern
1283 hemisphere tropical climate change during the Little Ice Age and Younger Dryas based on glacier
1284 modeling of the Quelccaya Ice Cap, Peru. *Quat. Sci. Rev.* 125, 106–116.
1285 doi:10.1016/j.quascirev.2015.08.001
- 1286 Martin, L., Blard, P.-H., Lave, J., Braucher, R., Lupker, M., Condom, T., Charreau, J., Mariotti, V., Bourlès, D.,
1287 Arnold, M., G. Keddadouche, K.A., Davy, E., 2015. In situ cosmogenic ^{10}Be production rate in the High
1288 Tropical Andes. *Quat. Geochronol.* 30, 54–68. doi:10.1016/j.quageo.2015.06.012
- 1289 Matsuda, J., Matsumoto, T., Sumino, H., Nagao, K., Yamamoto, J., Miura, Y., Kaneoka, I., Takahata, N., Sano,
1290 Y., 2002. The $^3\text{He}/^4\text{He}$ ratio of new internal He Standard of Japan (HESJ). *Geochem. J.* 36, 191–195.
1291 doi:10.2343/geochemj.36.191
- 1292 Meierding, T.C., 1982. Late Pleistocene Glacial Equilibrium-Line Front Range: A Comparison Altitudes in the
1293 Colorado of Methods. *Quat. Res.* 18, 289–310.
- 1294 Mölg, T., Hardy, D.R., 2004. Ablation and associated energy balance of a horizontal glacier surface on
1295 Kilimanjaro. *J. Geophys. Res. D Atmos.* 109, 1–13. doi:10.1029/2003JD004338
- 1296 Mölg, T., Kaser, G., 2011. A new approach to resolving climate-cryosphere relations: Downscaling climate
1297 dynamics to glacier-scale mass and energy balance without statistical scale linking. *J. Geophys. Res.*
1298 *Atmos.* 116, 1–13. doi:10.1029/2011JD015669
- 1299 Montade, V., Kageyama, M., Combourieu-Nebout, N., Ledru, M.P., Michel, E., Siani, G., Kissel, C., 2015.
1300 Teleconnection between the intertropical convergence zone and southern westerly winds throughout the
1301 last deglaciation. *Geology* 43, 735–738. doi:10.1130/G36745.1
- 1302 Montgomery, D.R., 2002. Valley formation by fluvial and glacial erosion. *Geology* 30, 1047–1050.
1303 doi:10.1130/0091-7613(2002)030<1047:VFBFAG>2.0.CO;2
- 1304 Mosblech, N.A.S., Bush, M.B., Gosling, W.D., Hodell, D., Thomas, L., van Calsteren, P., Correa-Metrio, A.,
1305 Valencia, B.G., Curtis, J., van Woesik, R., 2012. North Atlantic forcing of Amazonian precipitation during
1306 the last ice age. *Nat. Geosci.* 5, 817–820. doi:10.1038/ngeo1588
- 1307 Mourre, L., Condom, T., Junquas, C., Lebel, T., Sicart, J.E., Figueroa, R., Cochachin, A., 2015. Spatio-temporal
1308 assessment of WRF, TRMM and in situ precipitation data in a tropical mountain environment (Cordillera
1309 Blanca, Peru). *Hydrol. Earth Syst. Sci. Discuss.* 12, 6635–6681. doi:10.5194/hessd-12-6635-2015
- 1310 Muscheler, R., Beer, J., Kubik, P.W., Synal, H. -a., 2005. Geomagnetic field intensity during the last 60,000

- 1311 years based on ^{10}Be and ^{36}Cl from the Summit ice cores and ^{14}C . *Quat. Sci. Rev.* 24, 1849–1860.
 1312 doi:10.1016/j.quascirev.2005.01.012
- 1313 New, M., Lister, D., Hulme, M., Makin, I., 2002. A high-resolution data set of surface climate over global land
 1314 areas. *Clim. Res.* 21, 1–25. doi:10.3354/cr021001
- 1315 Nishiizumi, K., Imamura, M., Caffee, M.W., Southon, J.R., Finkel, R.C., McAninch, J., 2007. Absolute
 1316 calibration of ^{10}Be AMS standards. *Nucl. Instruments Methods Phys. Res. Sect. B Beam Interact. with*
 1317 *Mater. Atoms* 258, 403–413. doi:10.1016/j.nimb.2007.01.297
- 1318 Ohmura, A., Kasser, P., Funk, M., 1992. Climate at the equilibrium line of glaciers.
 1319 Osmaston, H., 2005. Estimates of glacier equilibrium line altitudes by the Area x Altitude, the Area x Altitude
 1320 Balance Ratio and the Area x Altitude Balance Index methods and their validation. *Quat. Int.* 138–139, 22–
 1321 31. doi:10.1016/j.quaint.2005.02.004
- 1322 Palmer, M.R., Pearson, P.N., 2003. A 23,000-Year Record of Surface Water pH and $\text{pH}_{\text{chem}}\{\text{CO}_2\}$ in the
 1323 Western Equatorial Pacific Ocean. *Science* (80-.). 300, 480–482.
- 1324 Parnell, A.C., Buck, C.E., Doan, T.K., 2011. A review of statistical chronology models for high-resolution,
 1325 proxy-based Holocene palaeoenvironmental reconstruction. *Quat. Sci. Rev.* 30, 2948–2960.
 1326 doi:10.1016/j.quascirev.2011.07.024
- 1327 Pausata, F.S.R., Battisti, D.S., Nisancioglu, K.H., Bitz, C.M., 2011. Chinese stalagmite $\delta^{18}\text{O}$ controlled by
 1328 changes in the Indian monsoon during a simulated Heinrich event. *Nat. Geosci.* 4, 474–480.
 1329 doi:10.1038/ngeo1169
- 1330 Placzek, C., Quade, J., Patchett, P.J., 2006. Geochronology and stratigraphy of late Pleistocene lake cycles on
 1331 the southern Bolivian Altiplano: Implications for causes of tropical climate change. *Geol. Soc. Am. Bull.*
 1332 118, 515–532. doi:10.1130/B25770.1
- 1333 Placzek, C.J., Quade, J., Patchett, P.J., 2013. A 130ka reconstruction of rainfall on the Bolivian Altiplano. *Earth*
 1334 *Planet. Sci. Lett.* 363, 97–108. doi:10.1016/j.epsl.2012.12.017
- 1335 Porter, S.C., 1975. Equilibrium-line altitudes of late Quaternary glaciers in the Southern Alps, New Zealand.
 1336 *Quat. Res.* 5, 27–47. doi:10.1016/0033-5894(75)90047-2
- 1337 Porter, S.C., 2001. Snowline depression in the tropics during the last glaciation. *Quat. Sci. Rev.* 20, 1067–1091.
 1338 doi:10.1016/S0277-3791(00)00178-5
- 1339 Prémaillon, M., 2014. Conditions paléo-climatiques de l'Altiplano durant la phase humide Tauca. Université de
 1340 Lorraine - ENSG.
- 1341 Rabatel, A., Francou, B., Soruco, A., Gomez, J., Cerecés, B., Ceballos, J.L., Basantes, R., Vuille, M., Sicart,
 1342 J.E., Huggel, C., Scheel, M., Lejeune, Y., Arnaud, Y., Collet, M., Condom, T., Consoli, G., Favier, V.,
 1343 Jomelli, V., Galarraga, R., Ginot, P., Maisincho, L., Mendoza, J., Murgoz, M., Ramirez, E., Ribstein,
 1344 P., Suarez, W., Villacis, M., Wagnon, P., 2013. Current state of glaciers in the tropical Andes: A multi-
 1345 century perspective on glacier evolution and climate change. *Cryosphere* 7, 81–102. doi:10.5194/tc-7-81-
 1346 2013
- 1347 Ramsey, C.B., 2009. BAYESIAN ANALYSIS OF RADIOCARBON DATES Christopher Bronk Ramsey.
 1348 *Radiocarbon* 51, 337–360. doi:10.2458/azu_js_rc.v51i1.3494
- 1349 Reimer, P., 2013. IntCal13 and Marine13 Radiocarbon Age Calibration Curves 0–50,000 Years cal BP.
 1350 *Radiocarbon* 55, 1869–1887. doi:10.2458/azu_js_rc.55.16947
- 1351 Rupper, S., Roe, G., 2008. Glacier changes and regional climate: A mass and energy balance approach. *J. Clim.*
 1352 21, 5384–5401. doi:10.1175/2008JCLI2219.1
- 1353 Sagredo, E.A., Lowell, T.V., 2012. Climatology of Andean glaciers: A framework to understand glacier
 1354 response to climate change. *Glob. Planet. Change* 86–87, 101–109. doi:10.1016/j.gloplacha.2012.02.010
- 1355 Schimmelpfennig, I., Williams, A., Pik, R., Burnard, P., Niedermann, S., Finkel, R., Schneider, B., Benedetti, L.,
 1356 2011. Inter-comparison of cosmogenic in-situ ^3He , ^{21}Ne and ^{36}Cl at low latitude along an altitude
 1357 transect on the SE slope of Kilimanjaro volcano (3°S, Tanzania). *Quat. Geochronol.* 6, 425–436.
 1358 doi:10.1016/j.quageo.2011.05.002
- 1359 Seltzer, G.O., 1994. Climatic Interpretation of Alpine Snowline Variations on Millennial Time Scales. *Quat.*
 1360 *Res.* 41, 154–159. doi:10.1006/qres.1994.1017
- 1361 Shakun, J.D., Clark, P.U., Marcott, S.A., Brook, E.J., Lifton, N.A., Caffee, M., Shakun, W.R., 2015.
 1362 Cosmogenic dating of Late Pleistocene glaciation, southern tropical Andes, Peru. *J. Quat. Sci.* 30, 841–
 1363 847. doi:10.1002/jqs.2822
- 1364 Sicart, J.E., Hock, R., Ribstein, P., Litt, M., Ramirez, E., 2011. Analysis of seasonal variations in mass balance
 1365 and meltwater discharge of the tropical Zongo Glacier by application of a distributed energy balance
 1366 model. *J. Geophys. Res. Atmos.* 116, 1–18. doi:10.1029/2010JD015105
- 1367 Sicart, J.E., Hock, R., Six, D., 2008. Glacier melt, air temperature, and energy balance in different climates: The
 1368 Bolivian Tropics, the French Alps, and northern Sweden. *J. Geophys. Res. Atmos.* 113, 1–11.
 1369 doi:10.1029/2008JD010406
- 1370 Sirocko, F., Garbe-Schonberg, D., McIntyre, A., Molfino, B., 1996. Teleconnections Between the Subtropical

- 1371 Monsoons and High-Latitude Climates During the Last Deglaciation. *Science* (80-). 272, 526–529.
 1372 doi:10.1126/science.272.5261.526
- 1373 Smith, C. a., Lowell, T. V., Owen, L. a., Caffee, M.W., 2011. Late Quaternary glacial chronology on Nevado
 1374 Illimani, Bolivia, and the implications for paleoclimatic reconstructions across the Andes. *Quat. Res.* 75,
 1375 1–10. doi:10.1016/j.yqres.2010.07.001
- 1376 Smith, C., Lowell, T., Caffee, M., 2009. Lateglacial and Holocene cosmogenic surface exposure age glacial
 1377 chronology and geomorphological evidence for the presence of cold-based glaciers at Nevado Sajama ,
 1378 Bolivia. *J. Quat. ...* 24, 360–372. doi:10.1002/jqs
- 1379 Smith, J. a, Seltzer, G.O., Farber, D.L., Rodbell, D.T., Finkel, R.C., 2005. Early local last glacial maximum in
 1380 the tropical Andes. *Science* 308, 678–81. doi:10.1126/science.1107075
- 1381 Soruco, A., Vincent, C., Francou, B., Ribstein, P., Berger, T., Sicart, J.E., Wagnon, P., Arnaud, Y., Favier, V.,
 1382 Lejeune, Y., 2009. Mass balance of Glacier Zongo, Bolivia, between 1956 and 2006, using glaciological,
 1383 hydrological and geodetic methods. *Ann. Glaciol.* 50, 1–8. doi:10.3189/172756409787769799
- 1384 Stauch, G., Lehmkühl, F., 2010. Quaternary glaciations in the Verkhoyansk Mountains, Northeast Siberia. *Quat.*
 1385 *Res.* 74, 145–155. doi:10.1016/j.yqres.2010.04.003
- 1386 Stone, J.O., 2000. Air pressure and cosmogenic isotope production. *J. Geophys. Res.* 105, 23753.
 1387 doi:10.1029/2000JB900181
- 1388 Strikis, N.M., Chiessi, C.M., Cruz, F.W., Vuille, M., Cheng, H., Barreto, E.A.S., Mollenhauer, G., Kasten, S.,
 1389 Karmann, I., Edwards, R.L., Bernal, J.P., Sales, R., 2015. Timing and structure of Mega-SACZ events
 1390 during Heinrich Stadial 1. *Geophys. Res. Lett.* 1–8. doi:10.1002/2015GL064048.Received
- 1391 Sylvestre, F., Servant, M., Servant-Vildary, S., Causse, C., Fournier, M., Ybert, J.-P., 1999. Lake-Level
 1392 Chronology on the Southern Bolivian Altiplano (18°–23°S) during Late-Glacial Time and the Early
 1393 Holocene. *Quat. Res.* 51, 54–66. doi:10.1006/qres.1998.2017
- 1394 Torsnes, I., Rye, N., Nesje, a, 1993. and Little Ice Age equilibrium-line altitudes on outlet valley glaciers from
 1395 Jostedalbreen, western Norway: an evaluation of different approaches to their calculation. *Arct. Alp. Res.*
 1396 25, 106–116.
- 1397 Uppala, S.M., KÅllberg, P.W., Simmons, a J., Andrae, U., Bechtold, V.D.C., Fiorino, M., Gibson, J.K.,
 1398 Haseler, J., Hernandez, a, Kelly, G. a., Li, X., Onogi, K., Saarinen, S., Sokka, N., Allan, R.P., Andersson,
 1399 E., Arpe, K., Balmaseda, M. a., Beljaars, a. C.M., Berg, L. Van De, Bidlot, J., Bormann, N., Cairns, S.,
 1400 Chevallier, F., Dethof, a., Dragosavac, M., Fisher, M., Fuentes, M., Hagemann, S., Hólm, E., Hoskins,
 1401 B.J., Isaksen, L., Janssen, P. a. E.M., Jenne, R., McNally, a. P., Mahfouf, J.-F., Morcrette, J.-J., Rayner, N.
 1402 a., Saunders, R.W., Simon, P., Sterl, a., Trenberth, K.E., Untch, a., Vasiljevic, D., Viterbo, P., Woollen,
 1403 J., 2005. The ERA-40 re-analysis. *Q. J. R. Meteorol. Soc.* 131, 2961–3012. doi:10.1256/qj.04.176
- 1404 Vera, C., Higgins, W., Amador, J., Ambrizzi, T., Garreaud, R., Gochis, D., Gutzler, D., Lettenmaier, D.,
 1405 Marengo, J., Mechoso, C.R., Nogues-Paegle, J., Silva Dias, P.L., Zhang, C., 2006. Toward a unified view
 1406 of the American monsoon systems. *J. Clim.* 19, 4977–5000. doi:10.1175/JCLI3896.1
- 1407 Vuille, M., 1999. Atmospheric circulation over the Bolivian Altiplano during dry and wet periods and extreme
 1408 phases of the southern oscillation. *Int. J. Climatol.* 19, 1579–1600. doi:10.1002/(SICI)1097-
 1409 0088(19991130)19:14<1579::AID-JOC441>3.0.CO;2-N
- 1410 Vuille, M., Bradley, R.S., Keimig, F., 2000. Interannual climate variability in the Central Andes and its relation
 1411 to tropical Pacific and Atlantic forcing. *J. Geophys. Res.* 105, 12447. doi:10.1029/2000JD900134
- 1412 Vuille, M., Burns, S.J., Taylor, B.L., Cruz, F.W., Bird, B.W., Abbott, M.B., Kanner, L.C., Cheng, H., Novello,
 1413 V.F., 2012. A review of the South American monsoon history as recorded in stable isotopic proxies over
 1414 the past two millennia. *Clim. Past* 8, 1309–1321. doi:10.5194/cp-8-1309-2012
- 1415 Vuille, M., Francou, B., Wagnon, P., Juen, I., Kaser, G., Mark, B.G., Bradley, R.S., 2008a. Climate change and
 1416 tropical Andean glaciers: Past, present and future. *Earth-Science Rev.* 89, 79–96.
 1417 doi:10.1016/j.earscirev.2008.04.002
- 1418 Vuille, M., Kaser, G., Juen, I., 2008b. Glacier mass balance variability in the Cordillera Blanca, Peru and its
 1419 relationship with climate and the large-scale circulation. *Glob. Planet. Change* 62, 14–28.
 1420 doi:10.1016/j.gloplacha.2007.11.003
- 1421 Vuille, M., Keimig, F., 2004. Interannual variability of summertime convective cloudiness and precipitation in
 1422 the central Andes derived from ISCCP-B3 data. *J. Clim.* 17, 3334–3348. doi:10.1175/1520-
 1423 0442(2004)017<3334:IVOSCC>2.0.CO;2
- 1424 Wagnon, P., Ribstein, P., Francou, B., Pouyaud, B., 1999. Annual cycle of energy balance of Zongo Glacier,
 1425 Cordillera Real, Bolivia. *J. Geophys. Res. Atmos.* 104, 3907–3923. doi:10.1029/1998JD200011
- 1426 Wagnon, P., Ribstein, P., Francou, B., Sicart, J.E., 2001. Anomalous heat and mass budget of Glacier Zongo ,
 1427 Bolivia , during the 1997 / 98 El Ni · o year. *October* 47, 21–28.
- 1428 Wang, X., Auler, A.S., Edwards, R.L., Cheng, H., Cristalli, P.S., Smart, P.L., Richards, D. a. Shen, C.-C., 2004.
 1429 Wet periods in northeastern Brazil over the past 210 kyr linked to distant climate anomalies. *Nature* 432,
 1430 740–3. doi:10.1038/nature03067

- 1431 Wang, X., Auler, A.S., Edwards, R.L., Cheng, H., Ito, E., Wang, Y., Kong, X., Solheid, M., 2007. Millennial-
1432 scale precipitation changes in southern Brazil over the past 90,000 years. *Geophys. Res. Lett.* 34, 1–5.
1433 doi:10.1029/2007GL031149
- 1434 Ward, D.J., Cesta, J.M., Galewsky, J., Sagredo, E., 2015. Late pleistocene glaciations of the arid subtropical
1435 Andes and new results from the Chajnantor Plateau, northern Chile. *Quat. Sci. Rev.* 128, 98–116.
1436 doi:10.1016/j.quascirev.2015.09.022
- 1437 Xu, C.Y., Singh, V.P., 2000. Evaluation and generalization of radiation-based methods for calculating
1438 evaporation. *Hydrol. Process.* 14, 339–349. doi:10.1002/(SICI)1099-1085(20000215)14:2<339::AID-
1439 HYP928>3.0.CO;2-O
- 1440 Zech, J., Zech, R., Kubik, P.W., Veit, H., 2009. Glacier and climate reconstruction at Tres Lagunas, NW
1441 Argentina, based on ¹⁰Be surface exposure dating and lake sediment analyses. *Palaeogeogr.*
1442 *Palaeoclimatol. Palaeoecol.* 284, 180–190. doi:10.1016/j.palaeo.2009.09.023
- 1443 Zech, R., Kull, C., Kubik, P.W., Veit, H., 2007. LGM and Late Glacial glacier advances in the Cordillera Real
1444 and Cochabamba (Bolivia) deduced from ¹⁰Be surface exposure dating. *Clim. Past Discuss.* 3, 623–635.
1445 doi:10.5194/cpd-3-839-2007
- 1446 Zhou, J., Lau, K.M., 1998. Does a monsoon climate exist over South America? *J. Clim.* 11, 1020–1040.
1447 doi:10.1175/1520-0442(1998)011<1020:DAMCEO>2.0.CO;2
- 1448 Zimmermann, L., Blard, P.H., Burnard, P., Medynski, S., Pik, R., Puchol, N., 2012. A New Single Vacuum
1449 Furnace Design for Cosmogenic ³He Dating. *Geostand. Geoanalytical Res.* 36, 121–129.
1450 doi:10.1111/j.1751-908X.2011.00145.x
- 1451 Zorzi, C., Sanchez Goñi, M.F., Anupama, K., Prasad, S., Hanquiez, V., Johnson, J., Giosan, L., 2015. Indian
1452 monsoon variations during three contrasting climatic periods: The Holocene, Heinrich Stadial 2 and the
1453 last interglacial-glacial transition. *Quat. Sci. Rev.* 125, 50–60. doi:10.1016/j.quascirev.2015.06.009
- 1454

Chapitre 7

Reconstitution du champ des précipitations pendant le Haut niveau Tauca

Dans le chapitre 7, les âges d'exposition sont utilisés, non plus pour faire des reconstitutions temporelles, mais pour identifier des moraines synchrones. Une telle approche permet de créer une "photographie" des extensions glaciaires à différents endroits de l'Altiplano, à un moment précis de la dernière déglaciation : pendant le haut niveau du lac Tauca. Sont concernés 8 sites pour lesquels nous pouvons identifier une ligne d'équilibre synchrone de ce haut niveau lacustre : la vallée du Zongo, le Sajama, le Tunupa, le Luxar, le Pikacho, le Tambo, Azanaques et l'Uturuncu.

L'approche croisée lac-glacier est ensuite utilisée de manière à traduire la variabilité spatiale des lignes d'équilibre pendant le haut niveau du Tauca en variabilité des précipitations afin de produire une carte des précipitations pendant ce haut niveau. Pour ce faire, une hypothèse forte de la démarche consiste à considérer que le stade Tauca est caractérisé par un unique refroidissement (par rapport au Présent) pour tout l'Altiplano. A partir de cette hypothèse et du modèle de glacier, la variabilité des lignes d'équilibre pour les 8 sites étudiés est convertie en 8 différentes valeurs de pluviométrie extrapolées ensuite en carte des précipitations. Comme cette démarche peut être menée pour n'importe quelle valeur de refroidissement, le modèle de lac est utilisé pour identifier le cas pour lequel le bilan hydrologique annuel du Lac Tauca est à l'équilibre. On définit ainsi la carte des précipitations caractéristiques du Tauca.

Cette étude permet ainsi de comparer la variabilité spatiale des précipitations entre le haut niveau Tauca et l'Actuel. Elle amène ainsi un résultat pertinent pour étudier les apports d'humidité sur l'Altiplano et les régimes de vents qui leur sont associés pendant la période. De telles informations apportent un éclairage nouveau sur les modulations du fonctionnement de la mousson sud américaine pendant cette période.

De même que pour le chapitre 6, le lecteur est renvoyé à l'Annexe *Personal Contribution* pour voir ma contribution aux travaux présentés dans ce chapitre. Ce manuscrit d'article sera également sujet modifications. Des propagations d'erreur et des tests de sensibilité doivent encore être menés pour asseoir les résultats.

Cette étude est présentée en langue anglaise sous la forme d'un manuscrit d'article en vue d'une soumission prochaine à une revue scientifique.

1 **Precipitation field reconstruction during the Lake Tauca highstand**
2 **on the Altiplano inferred from palaeo-glaciers and palaeo-lakes**
3
4

5 L. C. P. Martin^{a*}, P. -H. Blard^{a*}, J. Lavé^a, M. Premaillon^a, V. Jomelli^b, D. Brunstein^b, M.
6 Lupker^c, J. Charreau^a, V. Mariotti^a, T. Condom^d, B. Tibari^a, ASTER Team^{e#}, E. Davy^a.
7
8

9 a. CRPG, UMR7358 CNRS - Université de Lorraine, 54500 Vandoeuvre-lès-Nancy, France

10 b. Université Paris 1 Panthéon-Sorbonne, CNRS Laboratoire de Géographie Physique,
11 92195 Meudon, France.

12 c. ETH, Inst. f. Geochemie und Petrologie, Clausiusstrasse 25, 8092 Zurich, Switzerland
13 ETH, Geological Institute, Sonneggstrasse 5, 8092 Zurich, Switzerland

14 d. IRD, LTHE, UMR 5564, CNRS, Univ. Grenoble Alpes, G-INP, 38000 Grenoble, France

15 e. Aix-Marseille Université, CNRS-IRD-Collège de France, UM 34 CEREGE, Technopôle
16 de l'Arbois, BP80, 13545 Aix-en-Provence, France
17

18 # M. Arnold, G. Aumaître, D. L. Bourlès, K. Keddadouche
19
20

21 * Corresponding authors:
22

23 CRPG

24 15 rue Notre Dame des Pauvres

25 54501 Vandoeuvre-lès-Nancy

26 FRANCE
27

28 Email: leom@crpg.cnrs-nancy.fr; blard@crpg.cnrs-nancy.fr
29
30
31

32 7731 words

33 5 Tables

34 10 Figures
35
36
37
38

39 **Keywords:** Moraine dating, Exposure ages, Equilibrium Line Altitude, Lake Tauca, palaeo-
40 shorelines, lake and glacier modelling, precipitation field reconstruction, regional climate
41 variability.
42

43 **Highlights**

44 - New lateglacial cosmic ray exposure ages reported from Cerro Azanaques (18.9°S -
45 66.7°W), Cerro Tambo (19.9°S - 66.6°W) and Cerro Pikacho (19.9°S - 68.3°W) (Bolivian
46 Altiplano).

47 - Identification of 8 moraine stages coeval with the Tauca Lake Highstand across the
48 Altiplano.

49 - Computation of the corresponding Equilibrium Line Altitudes (ELA).

50 - Reconstruction of the palaeo-precipitation field during the Lake Tauca Highstand inferred
51 from coupled palaeo-glacier and palaeo-lake cross modelling.

52 - Results show massive easterly moist input over North and Central Altiplano likely to be
53 resulting from a strengthening and southward expansion of the easterly winds.

54

55 **Abstract**

56 Global climatic events such as Heinrich Stadials (HS) are linked with major
57 reorganisations of the continental systems (Wang et al., 2004) that are for now on poorly
58 understood. Over the Altiplano (High Tropical Andes, Bolivia) the second half of HS1 (16.5 -
59 14.5 ka) is coeval with the transgression and Highstand of the Tauca Lake - a giant palaeo-
60 lake ($\approx 50\,000\text{ km}^2$) now vanished in the South of the Altiplano (Servant and Fontes, 1978).
61 This region is presently very arid (annual rainfall between 50 and 300 mm.yr⁻¹) and this
62 contrast indicates drastically different precipitation regime during this period compared with
63 today (Blard et al., 2009; Placzek et al., 2013) in link with global scale modification of the
64 South American Summer Monsoon (SASM) (Cruz et al., 2005).

65 We present new cosmic ray exposure (CRE) datings of glacial features from Cerro
66 Azanaques (18.9°S - 66.7°W), Cerro Tambo (19.9°S - 66.6°W) and Cerro Pikacho (19.9°S -
67 68.3°W). We combine these results with other studies to identify 8 moraines coeval with the

68 Tauca Highstand in different glacial valleys spread across the Altiplano. ELAs are calculated
69 for each moraine using the AAR method with a value of 0.55 - 0.65 derived from
70 observations on present glaciers of the High Tropical Andes (Soruco et al., 2009). These
71 palaeo-ELAs range between 4500 and 5300 m.

72 These ELAs along with present climate observations are used in an inverse method
73 that combines simple precipitation and temperature modelling of the palaeo-glaciers and
74 palaeo-lake Tauca (following Blard et al., 2009) to derive an annual rainfall grid for the
75 Altiplano during the Highstand. This reconstitution brings quantitative constraints on the
76 rainfall regime of the Tauca highstand: mean precipitation was ≈ 2 times higher than present-
77 day values. Moreover, this rainfall repartition indicates important precipitations in the North
78 and along the Eastern cordilleras (1200 to 1800 mm.yr⁻¹) whereas the south-western part of
79 the Altiplano remains relatively dry (≈ 300 mm.yr⁻¹). This probably results from major easterly
80 moist input above the eastern cordillera as far as 19°S. Consistently with present observations
81 (Garreaud et al., 2003; Vuille, 1999) and reconstruction of the evolution of the South Atlantic
82 Convergence Zone (SACZ) (Strikis et al., 2015) and the westerly winds belt (Montade et al.,
83 2015) during HS1, we propose that this enhanced moist transport results from a strengthening
84 and southward expansion of the easterly wind belt.

85

86 **1. Introduction**

87 The Heinrich Stadials (HS) are key components of the global climate variability over
88 the late Pleistocene (Barker et al., 2015; Bond et al., 1992; Broecker, 1994; Heinrich, 1988).
89 Recent studies shed light on the global oceanic and cryospheric mechanisms involved in those
90 major cooling events (Banderas et al., 2014; Zhang et al., 2014), yet the reorganizations
91 undergone by the continental climate systems during those periods remain unclear.

92 The South American Summer Monsoon (SASM) plays a prominent role in the modern
93 South American climate as it provides most of the precipitations to the continent (Carvalho et
94 al., 2012). Important synchronisms between the Heinrich Stadials and the South American
95 climate have already been reported. Oxygen isotopes record from Brazilian speleothem have
96 shown that the atmospheric circulation over subtropical Brazil react in pace with the Heinrich
97 Stadials (Cruz et al., 2005; Stríkis et al., 2015; Wang et al., 2004). On the South of the
98 Bolivian Altiplano (20°W - 68°S), the last Heinrich Stadial (HS1, 18.5-14.5 ka following
99 Barker et al. (2009)) was coeval with the transgression and highstand on the palaeo-lake
100 Tauca, the widest and the deepest lake episode of the endorheic basin of the Altiplano over
101 the last 120 ka (Blard et al., 2011; Placzek et al., 2006; Servant and Fontes, 1978; Sylvestre et
102 al., 1999).

103 This region presently receives between 100 and 400 mm of annual rainfall mostly
104 during the austral summer (DJF), which corresponds to the mature phase of the SASM. In this
105 period, a strong convective activity over central Brazil is linked with the development of the
106 South Atlantic Convergence Zone (SACZ), a southeastward precipitation band that develops
107 from the southern Amazonia toward southeastern Brazil and that can extend laterally over the
108 Altiplano Plateau. In the same time, the Bolivian High (BH) - a upper troposphere high-
109 pressure cell - forms over the Altiplano, (Chen et al., 1999; Zhou and Lau, 1998). The activity
110 of the BH along with modulation of the subtropical jets are in connection with the emerging

111 of mid and upper level easterly winds over the central Andes and the weakening or the dryer
112 westerlies. This modification of the wind regime promotes moist transport from central and
113 southeastern Brazil over the Altiplano (Garreaud et al., 2003, 2009; Vuille and Keimig, 2004;
114 Vuille, 1999; Zhou and Lau, 1998). Another important influence on the climate of the
115 Altiplano arises from the Pacific Ocean. The Pacific Sea Surface Temperatures and the El
116 Niño Southern Oscillations are source of interannual precipitation and temperature variability
117 of the region, El Niño episodes being associated with warm and dry anomalies, with inverse
118 relationship for La Niña events (Vuille et al., 2000).

119 The drastically more humid conditions that existed over the Altiplano during the Lake
120 Tauca highstand (and the end of HS1) have already been investigated in Blard et al. (2011,
121 2009) and Placzek et al. (2013). By coupling lake budget and glaciers models these studies
122 proposed a global temperature shift between 5 and 7°C a global annual rainfall increase
123 between 200 and 300% for the Altiplano during this period. However, they were unable to
124 propose spatial information about the repartition of the precipitation during this period. This
125 spatial parameter is crucial to track the source of humidity and to understand the connection
126 of Altiplano climate with the global South American dynamics. Indeed, spatial information
127 about precipitation may bring major insights on the sensitivity of the Altiplano climate to
128 larger scale events such as changes in the monsoon dynamics as they have been reported in
129 South America (Stríkis et al., 2015) and Asia (Han et al., 2015; Pausata et al., 2011; Sirocko
130 et al., 1996; Zorzi et al., 2015), and modulation of the ENSO regime (Kanner et al., 2013;
131 Palmer and Pearson, 2003; Placzek et al., 2006). Indeed, both Pacific and North Atlantic
132 forcings are likely to imprint the past variations of the climate in central Andes (Vuille et al.,
133 2012).

134 In this study, we gather new cosmic ray exposure (CRE) ages along with already
135 published ages to identify a set of 8 moraines spread over the Bolivian Altiplano that indicate

136 a glacial stillstand during the Lake Tauca Highstand. The Equilibrium Line Altitude
137 associated with each moraine is calculated and then used in the Precipitation-Temperature
138 glacier model of Condom et al. (2007). The lake budget of the Altiplano during the Tauca
139 phase is modelled using the Condom et al. (2004) model. Combining glacier and lake outputs
140 from these models, we are able to derive a precipitation field over the Altiplano during the
141 Lake Tauca Highstand. This spatial reconstruction is then compared to other palaeo-climate
142 proxies and discussed in terms of moisture influx during the Heinrich Stadial 1 event.

143

144 **2. Geological Settings**

145

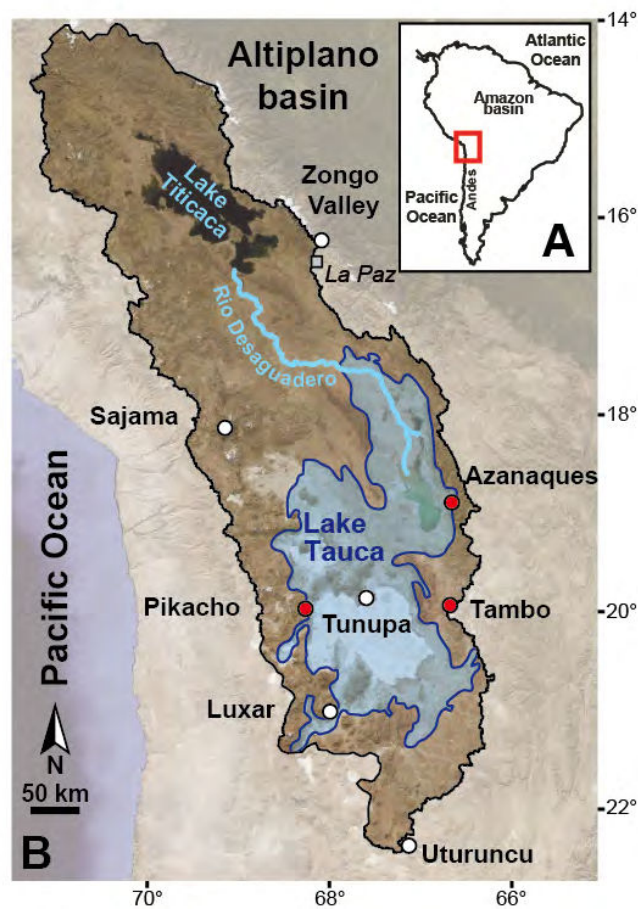
146 **2.1. The Altiplano basin and the palaeo-lake records**

147 The Altiplano basin and the Palaeo-lake shorelines from the lateglacial period are
148 presented in the precedent manuscript and will not be further developed here.

149

150 **2.2. Moraines Setting**

151 The different glacial valleys presented in this study are shown on Figure 1. They span
152 from 16.3 to 22.3°S in latitude and 66.6 to 68.9°W in longitude, most of them are located in
153 the vicinity of the palaeo-lake Tauca.



154

155 *Figure 1. Localisation of the different sites in the scope of this study. A - Localisation of the*
 156 *Altiplano in South America. B - Site localisations over the Altiplano. Red dots indicate the site*
 157 *for which we are presenting new CRE ages. White dots indicate sites with CRE ages from*
 158 *other studies. The blue shape indicates the extent of the Palaeo-lake Tauca. The black line*
 159 *delimitate the Altiplano endorheic basin.*

160

161

162

2.2.1 Documented palaeo-glacier valleys from the literature

163

164 A number of studies have characterized glacier advances in the Altiplano region. They
 165 are further exploited here to constrain the equilibrium line altitude (ELA) of the palaeo-
 166 glacier during the Tauca Highstand.

166

167

168

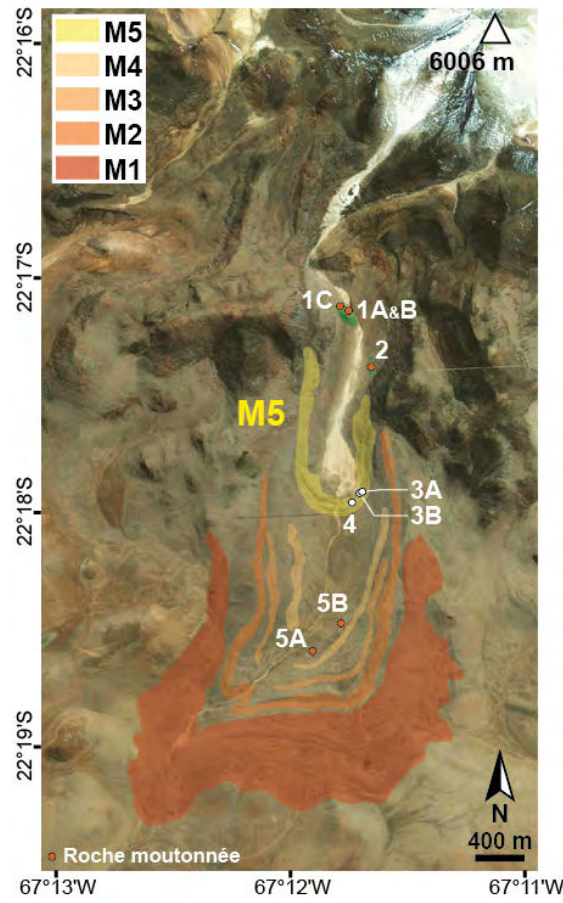
169

The Zongo valley (16.2°S - 68.1°W) is located in Cordillera Real, in the North of the
 Altiplano (Figure 1). The numerous glacial features of this granitic valley have already been
 dated using ^{10}Be cosmic ray exposure ages (CRE ages) (Jomelli et al., 2011; Smith et al.,
 2005; Martin et al. (Precedent Manuscript)). These datings enable to identify 13 moraines

170 spanning from 17 ka to 10 ka. The moraines reported as IP4 and IP5 in Martin et al.
171 (Precedent Manuscript) are of particular interest in this study (Table 5).

172 The Nevado Sajama (18.1°S - 68.9°W), the Cerro Tunupa (19.8°S - 67.6°W) and the
173 Cerro Luxar (21.0°S - 68.0°W) are andesitic strato-volcanoes located respectively in the
174 centre, the South and the South - East of the Altiplano (Figure 1). The glacial features
175 encountered in valleys located on their flanks have been dated by Blard et al. (2013, 2009)
176 and Martin et al. (Precedent Manuscript) for Cerro Tunupa, and Martin et al. (Precedent
177 Manuscript) for the the Sajama and the Luxar. All these sites record a local last glacial
178 maximum (LLGM) at the onset of the Tauca Highstand.

179 Cerro Uturuncu (22.2°S - 67.2°W) is a dacitic stratovolcano located at the
180 southernmost limit of the Altiplano basin (Figure 1). It rises at 6006 masl and does not bear a
181 permanent ice cover. The flanks of the volcano present abundant glacial geomorphic features.
182 Blard et al. (2014) dated 5 moraines and 2 groups of roches moutonnées in a southward
183 flowing valley using ³He CRE ages (Figure 2). There are no new samples reported in the
184 present study but the cosmogenic data in Blard et al. (2014) are used here to constrain the age
185 of the M5 moraine (Table 1). Direct datings on M5 boulders are reported but also ages on 2
186 sets of roches moutonnées (Upper and Lower Roches moutonnées) that stratigraphically
187 bracket the M5 moraine. The data processing used to constraint the age of M5 is described in
188 Section 3.1. For a complete description of the glacial features see Blard et al. (2014) (*enclosed*
189 *in the appendix of this thesis manuscript*).



190
 191
 192
 193
 194
 195
 196
 197

Figure 2. The moraines studied in Blard et al. (2014) on Cerro Uturuncu. The Yellow M5 moraine is of particular interest for this study. We only indicate the samples we rely on to propose an age for the M5 moraine. White dots stand for morainic bloc samples and orange dots for outcropping bedrock sample. Figure adapted from Blard et al. (2014).

Geomorphic Object	Sample name	Latitude <i>dec °</i>	Longitude <i>dec °</i>	Altitude <i>masl</i>	³ He ^a (1σ) <i>10⁷ at.g⁻¹</i>	Topographique Shielding <i>-</i>	Thickness ^b <i>cm</i>	CRE age ^{c,d} <i>ka</i>	Role in M5 Age determination
Upper Roche moutonnées	UTU-1A	-22.2854	-67.1961	5097	2.73 ± 0.08	0.98	5	15.21 ± 0.55	Younger Object
	UTU-1A	-22.2854	-67.1961	5097	2.78 ± 0.09	0.98	5	15.43 ± 0.58	
	UTU-1B	-22.2854	-67.1961	5094	2.76 ± 0.07	0.98	4	15.25 ± 0.52	
	UTU-1C	-22.2852	-67.1967	5111	2.51 ± 0.07	0.98	3	13.92 ± 0.54	
	UTU-1C	-22.2852	-67.1967	5111	2.53 ± 0.26	0.98	3	14.02 ± 1.34	
	UTU-2	-22.2898	-67.1946	5004	3.46 ± 0.07	0.98	3	18.88 ± 0.61	
M5 moraine	UTU-2	-22.2898	-67.1946	5004	3.37 ± 0.10	0.98	3	18.48 ± 0.68	Dated Object
	UTU-3A	-22.2984	-67.1951	4885	2.14 ± 0.10	1.00	5	13.09 ± 0.74	
	UTU-3A	-22.2984	-67.1951	4885	2.23 ± 0.06	1.00	5	13.63 ± 0.55	
	UTU-3B	-22.2986	-67.1953	4896	11.43 ± 0.12	1.00	5	60.55 ± 2.10	
	UTU-4	-22.2993	-67.1956	4880	2.60 ± 0.07	1.00	5	15.51 ± 0.54	
Lower Roches moutonnées	UTU-4	-22.2993	-67.1956	4880	2.67 ± 0.14	1.00	5	15.85 ± 0.81	Older Object
	UTU-5A	-22.3077	-67.1963	4825	2.94 ± 0.09	1.00	5	17.57 ± 0.68	
	UTU-5B	-22.3099	-67.1985	4820	2.83 ± 0.08	1.00	5	17.03 ± 0.65	
	UTU-5B	-22.3099	-67.1985	4820	2.91 ± 0.19	1.00	5	17.45 ± 1.09	

^a Cosmogenic ³He concentrations reported in Blard et al., 2014 after nucleogenic and magmatic corrections

^b The thickness correction was calculated using a density of 2.7 g.cm⁻³ and an attenuation length of 160 g.cm⁻²

^c Calculated using a weighted mean of the production rates of Blard et al., 2013a and Delunel et al., *In Prep*

^d Age computation was conducted using the Lm scaling with the ERA-40 atmosphere and the Muscheler et al. (2005) VDM

198
199
200
201

Table 1. Data from Blard et al. (2014) used to constraint the age of the M5 moraine on Cerro Uturuncu.

202

2.2.2. Cerro Azanaques (18.9°S - 66.7°W)

203

Located at mid-latitude on the eastern Altiplano, Cerro Azanaques culminates at 5140

204

masl on the eastern flank of the Poopo basin. Cerro Azanaques is the summit of a wide

205

granodiorite massif that formed during the upper Oligocene/lower Miocene (Clayton and

206

Clapperton (1995); K-Ar age of 23.7 ± 1.6 Ma, GEOBOL, 1994). Though not glaciated today,

207

Cerro Azanaques presents clear geomorphic and sedimentological evidence for intense glacial

208

activity during the Quaternary.

209

Five glacial advances on Cerro Azanaques were mapped and described in Clapperton

210

et al., (1997), Clayton and Clapperton (1997, 1995) . In this study, only two of these are

211

considered. The first advance built the highest and most massive lateral moraines, which can

212

reach up to 100 m in height (M1 moraines on Figure 3). The second advance built up smaller

213

lateral moraines (the M2 moraines) as well as a distal fan-shaped deposit composed of

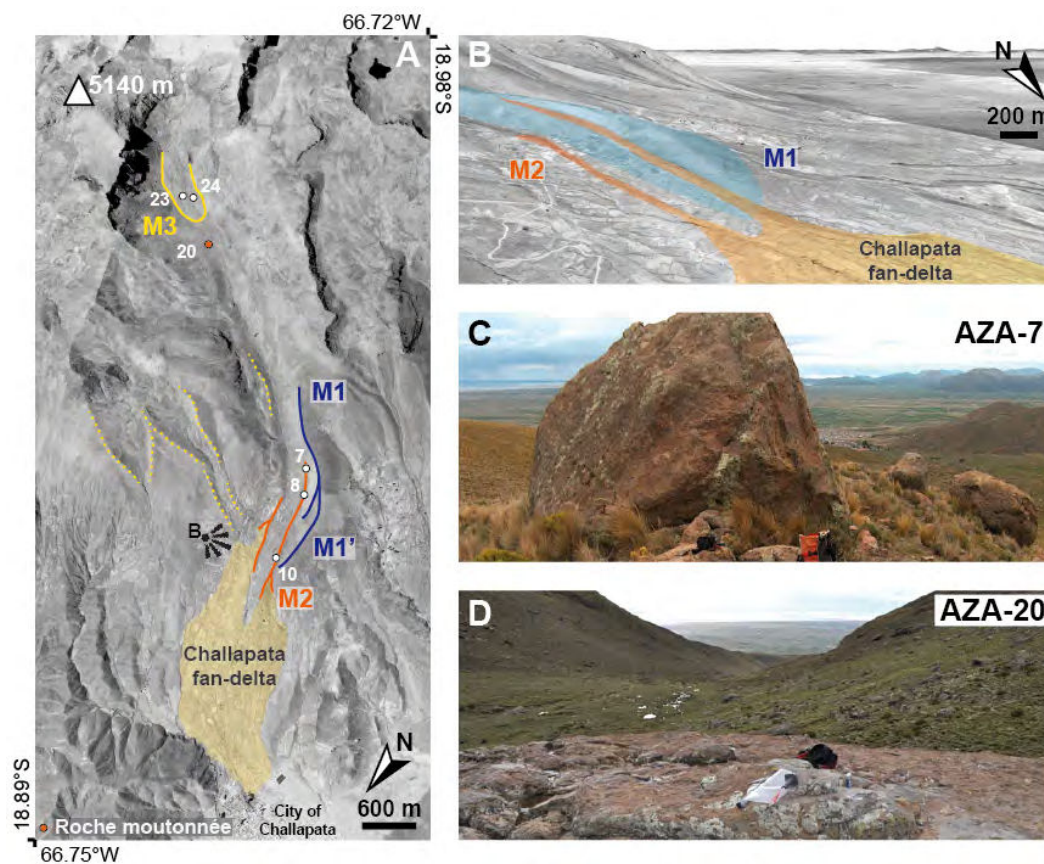
214

diamicton and containing large blocks up to 5 m in size. This landform evolves into coarse

215 fluvio- glacial deposits further downstream, at the outlet of the Quebrada Lijunimayu (the
216 Challapata fan-delta on the Figure 3).

217 The concomitant build up of the M2 moraines and the fan delta described in Clayton
218 and Clapperton (1995) is based on the continuity between the moraine and the fan. At the
219 outlet of the quebrada, the M1 moraines end but the M2 moraines extend and evolve
220 downstream. Their ridges widen gradually, connecting in the axis of the valley and spreading
221 laterally on the open slopes that converge towards the Poopo Lake (Figure 3.B). Combining
222 ^{14}C ages on peat and sedimentological observation along the Challapata fan-delta, Clapperton
223 et al. (1997) and Clayton and Clapperton (1995) reported that the fan-delta build up was
224 coeval with the Lake Tauca Highstand. Martin et al. (2015) extended these observations and
225 used Bayesian age constrains from the Tauca Highstand dataset (Blard et al., 2011; Placzek et
226 al., 2006; Sylvestre et al., 1999) to infer an age of 16.07 ± 0.64 ka BP for the fan-delta. We
227 collected 3 samples on M2 for this study. The AZA-7 to 10 samples are located between 4240
228 and 4015 masl.

229 A roche moutonnée was sampled upstream from these moraines (AZA-20). In the
230 upper part of the valley, below the glacial cirque, we sampled the M3 moraine, an upstream
231 ground moraine (Figure 3). These samples presented an acidic composition with a noticeable
232 proportion of quartz. They were collected to establish CRE ages based on ^{10}Be concentration
233 in quartz. These upstream samples lie between 4540 and 4600 masl.



234
 235 *Figure 3. Sampled moraines and sample locations on Cerro Azanaques. A - Global map of*
 236 *the valley with the detailed sampling on each moraine. White dots indicate morainic boulder*
 237 *samples, orange dots, roche moutonnées samples. Solid lines show the moraines in the main*
 238 *scope of this study. Dashed lines indicate other noticeable moraines associated with the ice*
 239 *flow from Cerro Azanaques. The viewpoint sign indicates the point of view proposed on*
 240 *image B. The full name of each sample is obtained in adding AZA to the indicated name. B -*
 241 *The gradual evolution of the M2 moraines into the Challapata fan-delta observed from the*
 242 *viewpoint indicated in A. C and D - Example of samples.*

243

244

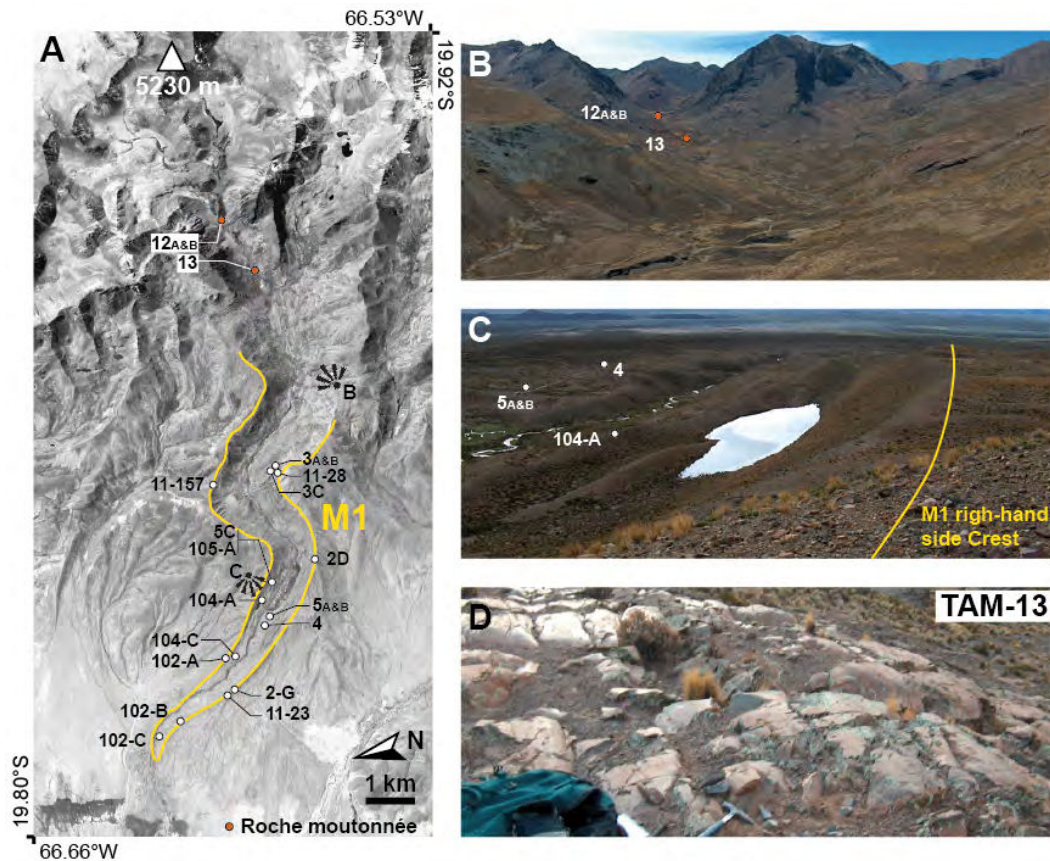
2.2.3. Cerro Tambo (19.9°S - 66.6°W)

245

246

247 Cerro Tambo is located on the western edge of the eastern cordillera in the South of
 248 the Altiplano basin (Figure 1). It belongs to a North-South massif of sedimentary and
 249 metasedimentary rocks with small extent granitic areas. The sampled valley (Figure 4) is
 250 dominated by fine-grained siliciclastic facies with the presence of quartzite, pelites, and
 251 sandstones. Presently, Cerro Tambo does not bear any ice cover. Yet, its westward flowing
 252 valleys exhibit an intense glacial carving. The low cohesion lithology of the massif fostered
 this glacial shaping and the moraines on its flanks offer a detailed record of the former ice

253 tongue positions and outwash areas (Figure 4). The main glacier tongue built impressive 300
 254 m high moraine M1 that ends up in its downstream part in a wide nearly flat fan-shaped
 255 moraine indicating small extent glacier avulsion.



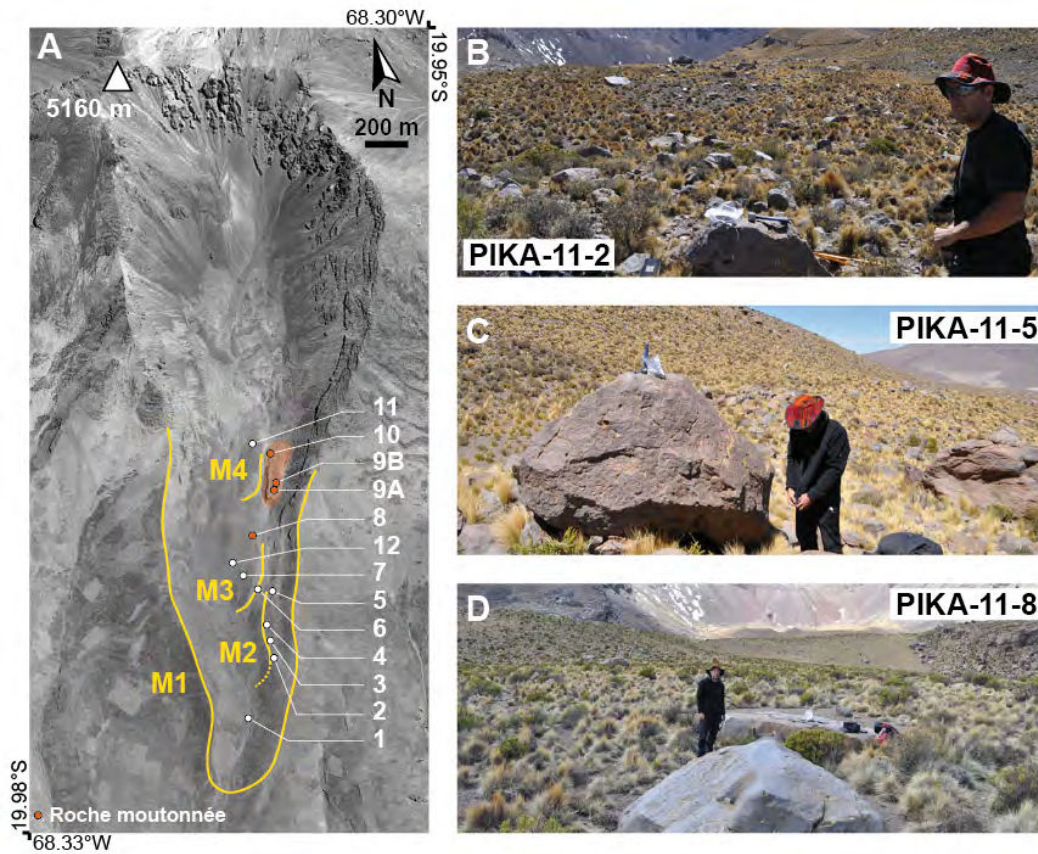
256
 257 *Figure 4. Cerro Tambo glacial valley. White dots indicate morainic boulder samples, orange*
 258 *dots, roche moutonnées samples. The yellow line shows the sampled moraine. The full name*
 259 *of each sample is obtained in adding TAM to the indicated name. B to D - Example of*
 260 *samples.*

261
 262 Recessional moraines are visible inside the extent of the main valley. To constrain the
 263 age of the M1 moraine, 15 morainic boulders were sampled in and 2 roche moutonnées were
 264 sampled in the northern upstream part of the valley (blue on Figure 4). The morainic samples
 265 range from 4100 to 4450 masl and the bedrock samples from 4530 to 4460 masl. They present
 266 either a siliciclastic (greywacke) or a granitic petrology and were collected for CRE ages
 267 determination based on ^{10}Be concentrations in the quartz.

268

269 2.2.4 Cerro Pikacho (19.9°S - 68.3°W)

270 Cerro Pikacho is an andesitic volcano located on the northwestern edge of the Salar de
271 Uyuni (Figure 1). It rises to 5160 masl and presents no permanent ice cover. Figure 5 shows
272 the glacial features of the main southward flowing valley of the volcano. The M1 moraines
273 was deposited during the maximum extent reached by the palaeo-glacier in this valley. They
274 are massive sharp-crested moraines with a maximal elevation difference of 40 m between the
275 moraine crest and the central axis of the valley. M2, M3 and M4 are small recessional
276 moraines. They have a very weak topographic expression, particularly on the right-hand side
277 of the valley. They incompletely fill the valley width and were associated with minor ice
278 flows. Outcropping bedrock was sampled upstream from the M3 moraine and on the left-hand
279 side of the M4 moraine. The collected samples range from 4290 and 4500 masl. Their
280 andesitic compositions lead us to rely on ³He concentration in the pyroxenes for CRE age
281 determination.



282
 283
 284
 285
 286
 287
 288
 289
 290

Figure 5. Cerro Pikacho glacial valley. A - Global map of the valley with the sampling details. White dots indicate morainic and erratic boulder samples, orange dots, roche moutonnées samples. Solid yellow lines show the moraines in the main scope of this study. The orange shaded area indicates the extent of the outcropping bedrock. The full name of each sample is obtained in adding PIKA-11 to the indicated name. B to D - Example of sampled boulders.

291 **3. Methods**

292 **3.1. CRE dating methods**

293 We followed the same methodology as Martin et al. (Precedent Manuscript) for the
294 CRE datings. For the ^{10}Be production rate, we averaged the values of Kelly et al. (2013),
295 Blard et al. (2013a) and Martin et al. (2015). For the ^3He production rate we did the same
296 with the Blard et al. (2013b) and the Delunel et al. (In Prep) values. We used the Lal-Stone
297 scaling model (Lal, 1991; Stone, 2000), with the ERA-40 atmosphere model (Uppala et al.,
298 2005) and the Muscheler et al. (2005) geomagnetic reconstruction.

299 **3.2. Equilibrium Line Altitude (ELA) calculation methods**

300 We followed the same methodology as Martin et al. (Precedent Manuscript) for the
301 ELA calculation. We relied on the AAR method with a range of 0.55 to 0.66 for the AAR
302 coefficient derived from present-day observations on monitored glaciers (Soruco et al., 2009).

303 **3.3. Climatic inversion methods**

304 *3.3.1. Glacier and lake modelling*

305

306 As Martin et al. (Precedent Manuscript) we took advantage of the combined use of the
307 Condom et al. (2007) glacier model and Condom et al., (2004) lake model.

308 Present mean annual temperature and annual rainfall have been determined for all the
309 glacier locations from monthly data records reported in Vuille et al., (2008a). These data
310 comes from 57 stations for temperature and 102 for precipitation, spread from 14 to 23°S over
311 the Cordilleras and the Altiplano (Figure 6). They cover a period of observations from 1948 to
312 2001 for precipitation and 2007 for temperatures, with numerous missing measurements.

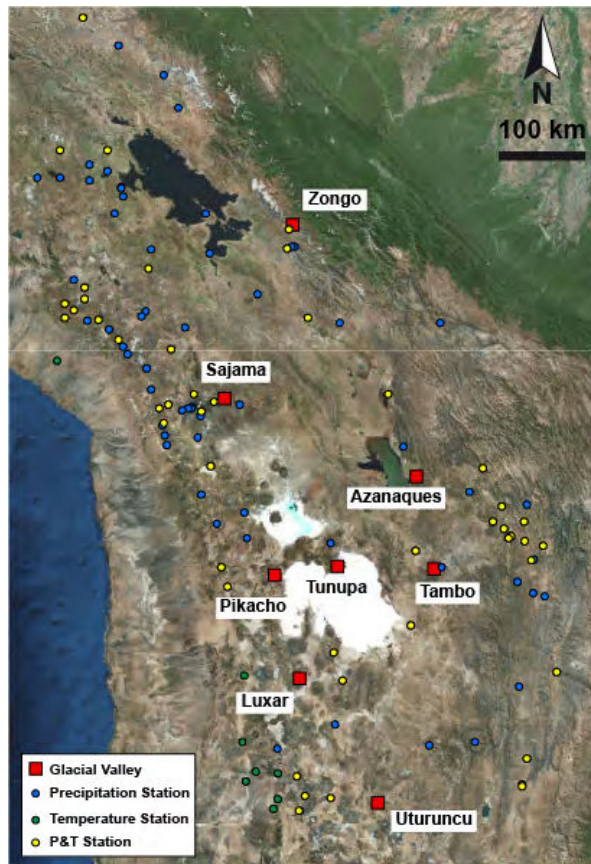


Figure 6. Location of the climate stations relatively to the glacial valleys.

313
314
315

316 Annual rainfall and mean temperature (Table 2) were derived from these station data
317 for the 8 sites of this study with the same methodology as Martin et al. (Precedent
318 Manuscript). The uncertainties presented in Table 2 only take into account the dispersion
319 between the different interpolation methods.

Sites	Zongo	Sajama	Tunupa	Luxar	Azanaques	Tambo	Pikacho	Uturuncu
Mean annual Rainfall (mm)	529 ± 7	320 ± 6	201 ± 10	145 ± 9	394 ± 22	255 ± 9	148 ± 7	119 ± 18
Mean annual temperature normalized to 3780 masl ^a (°C)	8.65 ± 0.14	8.32 ± 0.59	6.46 ± 0.11	7.64 ± 0.61	8.91 ± 0.05	7.56 ± 0.13	5.80 ± 0.51	7.67 ± 0.35

^a Normalization calculated for a lapse rate of 6.5°C/km

320
321
322

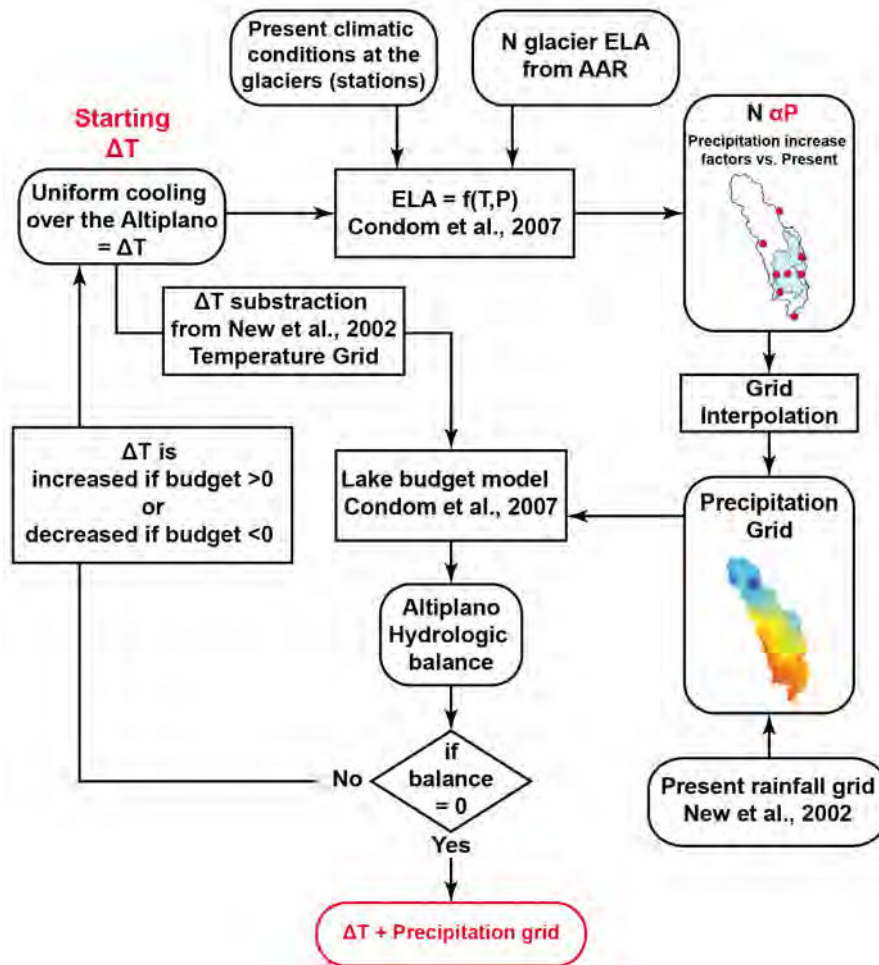
Table 2. Present mean annual rainfall and temperature at the studied sites.

323 An important dispersion is observed for the annual rainfall at Cerro Azanaques (18%)
324 and to a lesser extent for the temperatures at Sajama Luxar and Pikacho (respectively 7%, 8%
325 and 7%). These dispersions will be accounted in the result uncertainties (See Section 5).

326

327 *3.3.2 Determination of the precipitation field during the Tauca Highstand*

328 To determine a precipitation field during the Tauca Highstand, we assume the same
329 ΔT cooling at different palaeo-glaciers during the Tauca Highstand. First, we compute the
330 ELAs and use the Condom et al. (2007) equation for the past glacial extents coeval with the
331 Highstand. For each moraine, this permits to define a set of Precipitation-Temperature pairs
332 determined by the ELA position. For the given ΔT cooling, we collect the Precipitation
333 change associated with each of the sites. We derive precipitation grid from these values
334 spread over the Altiplano and compute the hydrological budget of the basin with our modified
335 version of the Condom et al. (2004) lake model. We then look for the ΔT cooling for which
336 we have a null hydrologic balance. This condition enables to identify the precipitation field
337 representative of the Tauca highstand. This approach is presented in Figure 7. The
338 interpolation is based on the square inverse of the distance.



339
340
341
342

Figure 7. Workflow for precipitation field reconstruction during the Tauca Highstand. Data from stations (Vuille et al., 2008a) are located on Figure 6.

343 **4. Results**

344 **4.1. Dating results**

345 Age results for the Cerro Tambo, Azanaques, Pikacho and Uturncu are presented in
346 Table 3, Table 4 and Figure 8. The ages reported in this study are median ages associated with
347 the probability density function (PDF) of the moraine along with the 1σ error bar (taken as the
348 half of the 1σ interval around the median).

349 On Cerro Tambo, the M1 boulder ages spread from 10 to 17 ka. Yet the 2 upstream
350 roche moutonnées TAM-12 and TAM-13 yield a common deglaciation signal around 14.5 ka.
351 Considering their upstream position and younger age, we applied a Bayesian filter on the M1
352 PDF to constrain the age of M1 (Figure 8). We considered a conditional probability stating
353 that M1 moraine is stratigraphically older than the roches moutonnées. The final PDF for M1
354 gives a median age of 16.5 ± 1.2 ka.

355 On Cerro Azanaques, the 3 boulder ages of M2 exhibit an important scattering. They
356 spread from 16.9 to 32.8 ka. The upstream ages of M3 and AZA-20 (Roche Moutonnée) are
357 also scattered ranging from 14.5 to 17.6 ka.

358 An important dispersion characterises the Pikacho boulder ages. PIKA-11-1 gives an
359 age of 33.7 ka for M1. M2 spreads for 13.1 to 19.5 ka. For M3, 2 out of 3 boulders give
360 consistent ages, including consistent age replicates between green and black pyroxenes for
361 PIKA-11-7. We considered PIKA-11-12 as an outlier and excluded it. We computed a median
362 age of 14.5 ± 1.1 ka for the M3 moraine. PIKA-11-11 yield and age of 26.4 ka and the roches
363 moutonnées spread from 14.1 to 2.5 ka.

364 On Cerro Uturncu the Bayesian constraints brought by the Upper and Lower roches
365 moutonnées on M5 (see Section 2.2.5. and 3.1) allowed deriving an age of 15.6 ± 0.5 ka.

366 Our dating results illustrate the fact that the Tauca phase was characterized by glacier

367 advances at all our studied sites. This readvance correspond to M1, M2 and the fan-delta and
368 finally probably M3 at Tambo, Azanaques and Pikacho respectively.

369 Our results confirm former results (Smith et al., 2005; Blard et al., 2009; Martin et al.,
370 Precedent Manuscript) obtained all over the Altiplano showing regional glaciomorphic
371 signature of the Tauca phase.

372 Moraines M1, M2 and M5 were found to chronologically correspond to this advance
373 at Sajama, Luxar and Uturuncu. For the Zongo and the Tunupa, we inferred the Tauca ice
374 extent using respectively IP4 - IP5 and M1 - M2 (Table 5).

375 The elevations of these moraines are further considered to calculate palaeo-ELAs and
376 reconstruct palaeo-climate.

Site	Glacial Feature	Sample	Latitude Dec°	Longitude Dec°	Altitude masl	¹⁰ Be (1σ) 10 ⁷ at.g ⁻¹	Thickness cm	Thick. Corr. ^a	Shielding ^b	Scaling Factor ^c	Age (1σ) ^d ka
Cerro Tambo	M1	TAM-2G	-19.8490	-66.6387	4180	5.08 ± 0.20	3.0	0.97	1.00	9.06	14.16 ± 0.57
		TAM-5A	-19.8584	-66.6279	4225	5.24 ± 0.18	3.0	0.97	1.00	9.27	14.27 ± 0.52
		TAM 2D	-19.8688	-66.6199	4364	3.89 ± 0.12	3.0	0.97	1.00	9.58	10.25 ± 0.35
		TAM 3A	-19.8666	-66.6017	4450	5.71 ± 0.19	3.0	0.97	1.00	10.26	14.06 ± 0.52
		TAM 3B	-19.8667	-66.6017	4452	4.82 ± 0.35	3.0	0.97	1.00	10.20	11.91 ± 0.84
		TAM 3C	-19.8661	-66.6020	4442	5.13 ± 0.19	3.0	0.97	1.00	10.18	12.71 ± 0.57
		TAM 4	-19.8565	-66.6293	4220	5.35 ± 0.22	3.0	0.97	1.00	9.28	14.56 ± 0.58
		TAM 5B	-19.8583	-66.6277	4225	4.73 ± 0.15	3.0	0.97	1.00	9.21	12.96 ± 0.52
		TAM 5C	-19.8598	-66.6231	4220	6.44 ± 0.18	3.0	0.97	1.00	9.58	16.99 ± 0.56
		TAM-102-A	-19.8483	-66.6332	4205	5.69 ± 0.18	1.5	0.99	1.00	9.32	15.24 ± 0.51
		TAM-102-B	-19.8377	-66.6422	4131	5.14 ± 0.26	2.0	0.98	1.00	8.89	14.48 ± 0.68
		TAM-102-C	-19.8337	-66.6440	4105	6.29 ± 0.31	2.0	0.98	1.00	9.09	17.35 ± 0.82
		TAM-104-A	-19.8575	-66.6249	4235	3.94 ± 0.18	3.0	0.97	1.00	9.11	10.91 ± 0.48
		TAM-104-B	-19.8502	-66.6335	4169	4.46 ± 0.17	3.0	0.97	1.00	8.97	12.56 ± 0.56
		TAM-104-C	-19.8501	-66.6338	4168	6.14 ± 0.34	3.0	0.97	1.00	9.31	16.64 ± 0.87
		TAM-105-A	-19.8599	-66.6230	4240	3.66 ± 0.28	3.0	0.97	1.00	9.04	10.22 ± 0.72
		TAM 11-23	-19.8479	-66.6392	4159	6.26 ± 0.12	1.5	0.99	1.00	9.29	16.81 ± 0.46
		TAM-11-157	-19.8555	-66.6012	4452	3.88 ± 0.27	4.0	0.97	1.00	9.93	9.95 ± 0.67
		TAM-11-28	-19.8666	-66.6028	4440	5.41 ± 0.32	3.0	0.97	1.00	10.17	13.42 ± 0.83
		Cerro Azanaques	Roches Moutonnées	TAM-12A	-19.8700	-66.5547	4535	5.66 ± 0.16	5.0	0.96	0.97
TAM-12B	-19.8700			-66.5547	4535	5.82 ± 0.18	5.0	0.96	0.97	10.72	14.43 ± 0.48
TAM-13	-19.8733			-66.5650	4456	5.92 ± 0.14	5.0	0.96	0.99	10.41	14.83 ± 0.42
Cerro Azanaques	M2	AZA-7	-18.9360	-66.7402	4240	6.34 ± 0.27	3.0	0.98	1.00	9.5	16.86 ± 0.72
		AZA-8	-18.9334	-66.7419	4200	10.34 ± 0.42	4.0	0.97	1.00	9.81	26.92 ± 1.06
		AZA-10	-18.9255	-66.7442	4015	11.60 ± 0.41	2.0	0.98	1.00	8.91	32.76 ± 1.57
	Roche Moutonnée	AZA-20	-18.9465	-66.7169	4541	6.32 ± 0.20	3.5	0.97	1.00	10.67	15.03 ± 0.5
	M3	AZA-23	-18.9486	-66.7116	4593	6.29 ± 0.22	2.0	0.98	1.00	10.83	14.53 ± 0.52
		AZA-24	-18.9494	-66.7119	4606	7.94 ± 0.25	2.0	0.98	1.00	11.32	17.57 ± 0.61

^a Calculated with a density of 2.7 g.cm⁻³ and an attenuation length of 160 g.cm⁻²

^b Calculated using the CRONUS shielding application

^c Global scaling factor that accounts for the geomagnetic correction

^d SLHL PR: 4.08 ± 0.11 at.g⁻¹.yr⁻¹ (Kelly et al. (2013), Blard et al. (2013b) and Martin et al. (2015) - Scaling scheme: Lal modified - Atmosphere: ERA40 - VDM: Muscheler et al. (2005)

377
378
379

Table 3. CRE age results for ¹⁰Be datings on Cerro Tambo and Cerro Azanaques

Site	Glacial Feature	Sample	Reference	Latitude Dec°	Longitude Dec°	Altitude masl	Pyroxene Color	Li ⁶ ppm	Eruption age ^b Ma	Pn at.g. ⁻¹ .yr ⁻¹	³ He _n 10 ⁴ at.g. ⁻¹	³ He _n (1σ) ^c 10 ⁴ at.g. ⁻¹	Thickness cm	Thick. Corr. ^d	Shielding ^e	Scaling Factor ^f	Age (1σ) ^g ka	
Cerro Pikacho	M1	PIKA-11-01	This Study	-19.9751	-68.3150	4289	Black	54	5.35	0.4124	0.22	4.52 ± 0.16	4.0	0.97	1.00	10.41	33.72 ± 1.62	
		PIKA-11-02		-19.9720	-68.3130	4370	Black	76	6.57	0.5470	0.36	2.46 ± 0.10	6.0	0.95	1.00	10.50	18.52 ± 0.82	
		PIKA-11-03		-19.9712	-68.3127	4377	Brown	51	4.82	0.3615	0.17	3.53 ± 0.09	3.0	0.97	1.00	10.74	25.31 ± 0.98	
		PIKA-11-04		-19.9708	-68.3126	4388	Black	45	4.02	0.3467	0.14	2.28 ± 0.13	2.5	0.98	1.00	10.42	16.81 ± 0.93	
		PIKA-11-05		-19.9699	-68.3121	4405	Black	89	8.53	0.7081	0.60	2.65 ± 0.10	3.0	0.97	1.00	10.74	19.04 ± 0.80	
Cerro Pikacho	M3	PIKA-11-06	This Study	-19.9694	-68.3126	4403	Black	35	7.59	0.2681	0.20	2.00 ± 0.12	3.0	0.97	1.00	10.25	15.01 ± 0.83	
		PIKA-11-07		-19.9686	-68.3127	4411	Black	71	9.55	0.4080	0.39	1.91 ± 0.09	2.2	0.98	1.00	10.18	14.39 ± 0.69	
		PIKA-11-07 - R		-19.9686	-68.3127	4411	Green	17	10.04	0.0960	0.10	1.73 ± 0.08	2.2	0.98	1.00	10.09	13.09 ± 0.76	
		PIKA-11-12		-19.9680	-68.3133	4465	Green	16	8.70	0.0961	0.08	2.85 ± 0.13	1.0	0.99	1.00	11.10	19.47 ± 0.91	
Cerro Uturuncu	M4	PIKA-11-09A	Blard et al. (2014)	-19.9654	-68.3107	4480	Black	63	8.03	0.4609	0.37	2.77 ± 0.09	3.0	0.97	1.00	11.13	19.16 ± 0.75	
		PIKA-11-09B		-19.9653	-68.3106	4482	Black	68	7.84	0.4965	0.39	2.46 ± 0.10	2.2	0.98	1.00	10.91	17.22 ± 0.79	
		PIKA-11-09B - R		-19.9653	-68.3106	4482	Green	30	12.22	0.2190	0.27	1.93 ± 0.09	2.2	0.98	1.00	10.48	14.12 ± 0.73	
		PIKA-11-10		-19.9638	-68.3104	4499	Green	27	8.05	0.1983	0.16	3.44 ± 0.07	2.0	0.98	1.00	11.50	22.82 ± 1.00	
		PIKA-11-08		-19.9670	-68.3122	4445	Black	31	6.81	0.2428	0.17	3.41 ± 0.12	3.0	0.97	1.00	11.16	23.51 ± 1.30	
Cerro Uturuncu	M5	PIKA-11-11	Blard et al. (2014)	-19.9633	-68.3110	4491	Black	86	6.54	0.4856	0.32	3.92 ± 0.11	2.8	0.98	1.00	11.44	26.35 ± 0.92	
		UTU-5A		-22.3077	-67.1963	4825	-	-	-	-	-	-	2.94 ± 0.09	5.5	0.95	1.00	13.16	17.57 ± 0.68
		UTU-5B		-22.3099	-67.1985	4820	-	-	-	-	-	-	2.83 ± 0.08	5.5	0.95	1.00	13.07	17.03 ± 0.65
		UTU-5B - R		-22.3099	-67.1985	4820	-	-	-	-	-	-	2.91 ± 0.19	5.5	0.95	1.00	13.12	17.45 ± 1.09
		UTU-3A		-22.2984	-67.1951	4885	-	-	-	-	-	-	2.14 ± 0.10	5.5	0.95	1.00	12.86	13.09 ± 0.74
		UTU-3A - R		-22.2984	-67.1951	4885	-	-	-	-	-	-	2.23 ± 0.06	5.5	0.95	1.00	12.87	13.63 ± 0.55
		UTU-3B		-22.2986	-67.1953	4896	-	-	-	-	-	-	11.43 ± 0.12	5.5	0.95	1.00	14.85	60.55 ± 2.10
		UTU-4		-22.2993	-67.1956	4880	-	-	-	-	-	-	2.60 ± 0.07	5.5	0.95	1.00	13.18	15.51 ± 0.54
		UTU-4 - R		-22.2993	-67.1956	4880	-	-	-	-	-	-	2.67 ± 0.14	5.5	0.95	1.00	13.25	15.85 ± 0.81
		UTU-1A		-22.2854	-67.1961	5097	-	-	-	-	-	-	2.73 ± 0.08	5.5	0.95	0.98	14.41	15.21 ± 0.55
Cerro Uturuncu	Upper Roches Moutonnées	UTU-1A - R	-22.2854	-67.1961	5097	-	-	-	-	-	-	2.78 ± 0.09	5.5	0.95	0.98	14.46	15.43 ± 0.58	
		UTU-1B	-22.2854	-67.1961	5094	-	-	-	-	-	-	2.76 ± 0.07	4.5	0.96	0.98	14.39	15.25 ± 0.52	
		UTU-1C	-22.2852	-67.1967	5111	-	-	-	-	-	-	2.51 ± 0.07	3.3	0.97	0.98	14.21	13.92 ± 0.54	
		UTU-1C - R	-22.2852	-67.1967	5111	-	-	-	-	-	-	2.53 ± 0.26	3.3	0.97	0.98	14.22	14.02 ± 1.34	
		UTU-2	-22.2898	-67.1946	5004	-	-	-	-	-	-	3.46 ± 0.07	3.3	0.97	0.98	14.44	18.88 ± 0.61	
		UTU-2 - R	-22.2898	-67.1946	5004	-	-	-	-	-	-	3.37 ± 0.10	3.3	0.97	0.98	14.37	18.48 ± 0.68	

R replicate. For the sample from this study, replicates have been used to compare ³He concentrations from black and green pyroxenes

^a Pyroxene concentrations

^b (U-Th-Sm)/⁴He age determined from pyroxenes

^c He_n = He_{tot} - He_n (we considered He_n = 8.5 × 10⁴ at.g.⁻¹ for all samples)

^d Calculated with a density of 2.7 g.cm⁻³ and an attenuation length of 160 g.cm⁻²

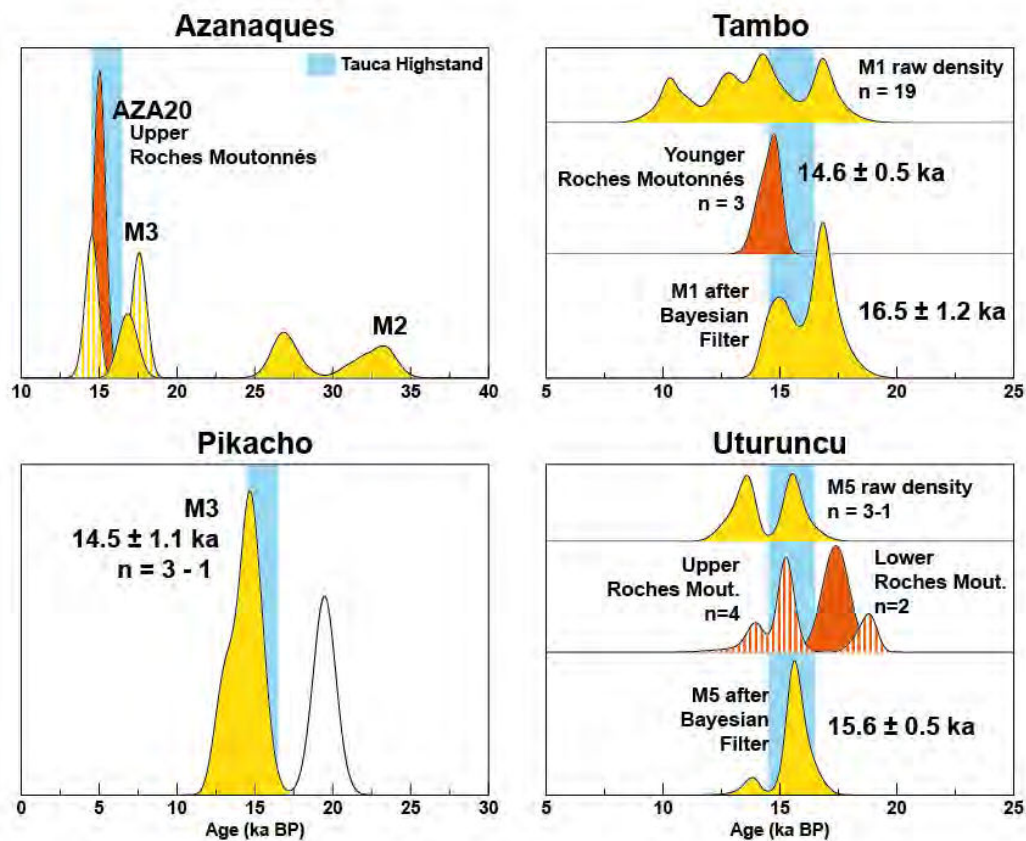
^e Shielding from Blard et al. (2014) calculated with the CRONUS application, shielding for samples from this study is negligible

^f Global scaling factor that accounts for the geomagnetic correction

^g SJHL PR: 136.2 ± 4.5 at.g.⁻¹.yr⁻¹ (Blard et al. (2013a) and Delunel et al. (2005))

^h Scaling scheme: Lal modified - Atmosphere: ERA40 - VDM: Muscheler et al. (2005)

Table 4. ³He CRE age results on Cerro Pikacho and Cerro Uturuncu



382
 383 *Figure 8. Moraine age computation and identification of glacial extents coeval with the*
 384 *Tauca Highstand at the four sites. Median ages associated with the PDF are indicated with*
 385 *uncertainties of 1σ . We do not derive a precise CRE age for Azanaques M2 moraine (see*
 386 *results description). One outlier was identified on Cerro Pikacho. We used a Bayesian*
 387 *approach to constraint the ages of M1 at Cerro Tambo and M5 at Cerro Uturuncu. At Cerro*
 388 *Tambo, the M1 PDF was filtered considering the upstream roches moutonnées being younger*
 389 *than M1. At Cerro Tambo the M5 PDF was bracketed by the Upper and Lower roches*
 390 *moutonnées ages.*

391

392

393

4.2. ELA results

394

395 At each site for which Taica moraine has been identified, ELA has been calculated
 396 (Table 5). When the site presented 2 moraine ages bracketing the Tauca Highstand with no
 397 age in between, we calculated a mean ELA between the 2 moraines. This was the case for the
 398 Zongo and Tunupa valley (see Table 5). The error bars associated with the computed ELA
 399 include the 0.55 - 0.65 AAR range described in Section 3.2. For mean ELA (Zongo, Tunupa),
 400 we considered an error bar associated with the mean of the same magnitude as the 2
 bracketing ELAs.

401 Tauca Highstand ELA mainly range between 4500 and 4600 masl for 5 out of 8 sites.
 402 The Sajama and Luxar ELA are slightly above this trend (respectively 4724 and 4800 masl).
 403 The Uturuncu yields the highest value around 5300 m, 800 m higher that the smaller value
 404 observed on the Tunupa (4470 masl).

Site	Moraine	Age ^a (ka BP)	ELA ^b (masl)	Tauca rainfall ^{e&f} Amplification factor -	Tauca Highstand ^g Annual rainfall mm.a ⁻¹
Zongo	IP4	17.2 ± 1.1	4592 ± 48	1.66 ± 0.12	877 ± 65
	IP5	13.6 ± 0.8	4640 ± 45		
	Mean		4611 ± 48		
Sajama	M1	15.1 ± 1.1	4724 ± 30	1.98 ± 0.23	632 ± 73
Tunupa	M1	16.2 ± 0.7	4446 ± 40	2.94 ± 0.23	592 ± 46
	M2	14.5 ± 0.7	4494 ± 35		
	Mean		4470 ± 40		
Luxar	M2	15.4 ± 0.7	4800 ± 33	3.07 ± 0.58	446 ± 85
Uturuncu	M5	15.6 ± 0.5	5274 ± 21	1.47 ± 0.27	175 ± 32
Pikacho	M3	14.5 ± 1.1	4595 ± 27	2.54 ± 0.18	376 ± 26
Tambo	M1	16.5 ± 1.2	4643 ± 57	2.32 ± 0.24	591 ± 62
Azanaques	M2	16.1 ± 0.6 ^c & 16.9 ± 0.7 ^d	4589 ± 33	2.52 ± 0.13	992 ± 49

^a See calculation details in Section 4.2

^b AAR = 0.55 to 0.65, derived from observations on High Andes tropical glacier (Section 3.2)

^c Age based on sedimentological continuity with the Challapata fan-delta (Martin et al., 2015)

^d CRE age of sample AZA-7

^e Annual rainfall ratio (Tauca/Actual)

^f The uncertainty on the actual climate variables (Table 2) has been propagated, but not the ELA uncertainty (work in progress)

^g Actual annual rainfall (Table 2) × Amplification factor

405
 406 *Table 5. ELA of the glacial extents coeval with the Tauca Highstand and associated*
 407 *Precipitation results. For Zongo and Tunupa we derived mean ELA associated with 2*
 408 *moraines bracketing the Tauca Highstand.*

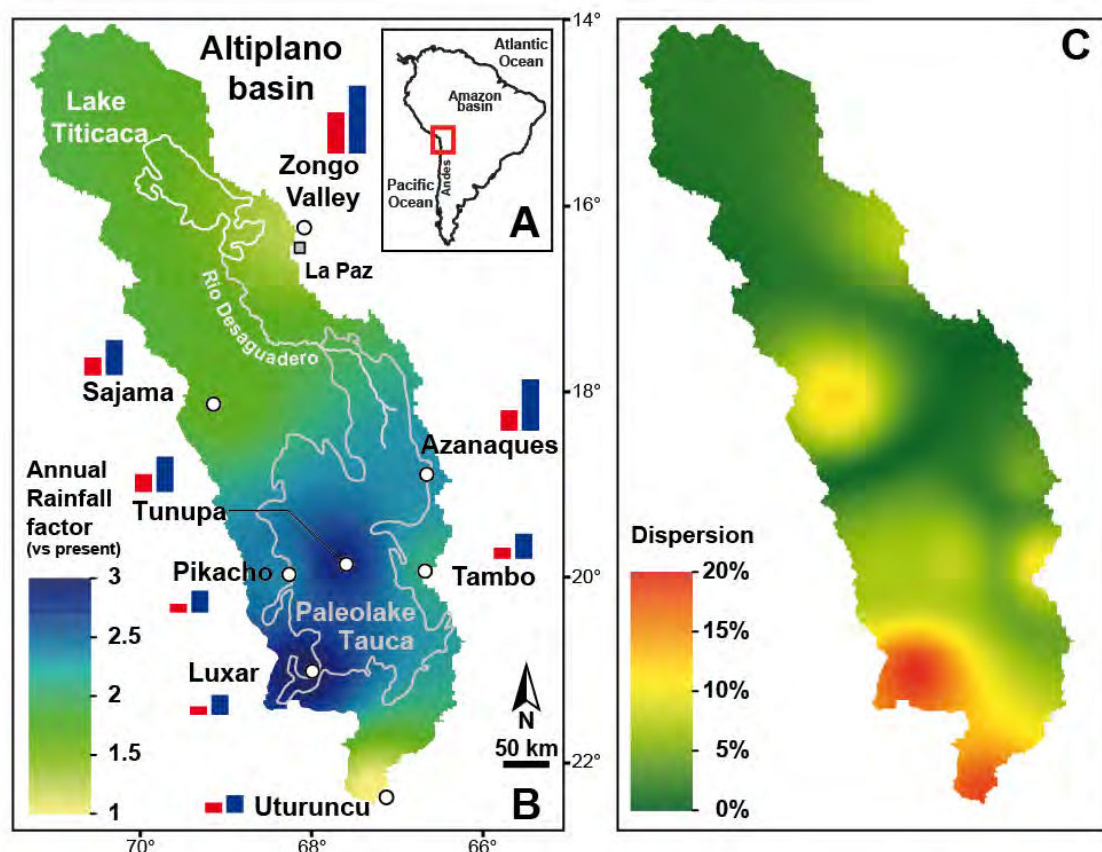
409
 410

4.3. Annual Precipitation results for the Tauca Highstand

412 The algorithm presented in Figure 7, lead us to explore different uniform ΔT coolings
 413 over the Altiplano. We came up with a null hydrologic balance for the Altiplano with a ΔT
 414 cooling of -3.3 ± 0.2 °C vs. Present. The rainfall amplification factors (Tauca vs. present) for
 415 our 8 sites and the precipitation grid associated with these values are presented in Table 5,
 416 Figure 9 and Figure 10. The rainfall amplification for the 8 glacial sites lies between 1.8 and
 417 3.4 (Table 5). The smallest amplification is observed for the Uturuncu in the extreme South of

418 the basin. The 2 northernmost sites, Zongo and Sajama, yield moderate ratios (1.8 and 2.).
419 The sites surrounding the Lake Tauca show the most important rainfall increase, ranging from
420 2.5 to 3.4. These amplifications are also presented on Figure 9 by the red and blue
421 precipitation histograms.

422 These 8 rainfall factors were used to derive an amplification matrix for the whole
423 Altiplano basin presented on Figure 9. We observe the strongest ratios in the southwestern
424 Altiplano and over the Lake Tauca. These high values are associated with a North to South
425 progressive increase from the northern Altiplano to the Cerro Luxar and an abrupt decrease
426 from the south of the Lake Tauca to the extreme southern edge of the Altiplano and the
427 Uturuncu volcano. The standard deviation associated to these amplification factors (Figure
428 9C) ranges between 0 and 0.2 for most of the map, corresponding to a $\approx 10\%$ dispersion but
429 climb to 0.7 in the South West of the Altiplano where it corresponds to more than 20% of
430 dispersion. These values reflect both dispersion on present climate knowledge, as well
431 uncertainty on lapse rate.

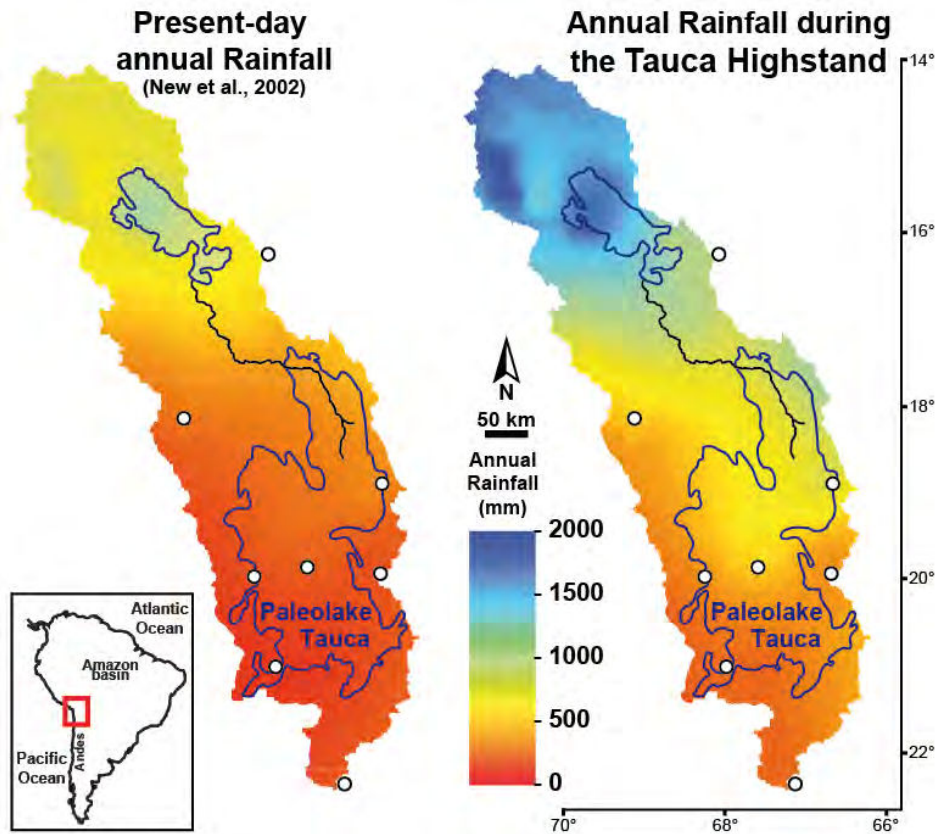


432
 433 *Figure 9. Annual rainfall amplification factor during the Tauca Highstand compared to*
 434 *present. A - General localisation of the Altiplano in South America. Blue bars indicate the*
 435 *rainfall during the Tauca Highstand. The vertical scale for the bar length is consistent*
 436 *between the different sites. B - Amplification factors map. C - Standard deviation associated*
 437 *with the Annual Rainfall factor accounting for the spread among the different present climate*
 438 *variables. White and grey contours indicate the Titicaca and Tauca edges and the Rio*
 439 *Desaguadero. White dots indicate the studied sites. Red bars indicate the present amount of*
 440 *annual rainfall.*

441
 442

443 We applied this amplification grid to the present precipitation grid derived from the
 444 data of New et al. (2002) to compute an annual rainfall grid during the Tauca Highstand
 445 (Figure 10). The grid shows an important North - South gradient with abundant precipitation
 446 over the Titicaca Lake watershed. An East-West gradient is also observed in the South of the
 447 basin. The Southwestern part of the Altiplano, along the present Chilean border, is the driest
 448 zone with 100 to 300 mm of annual rainfall. Abundant rainfall is observed over the Poopo
 449 Lake watershed, in continuity with the Northern Altiplano, delimiting an eastern precipitation

450 band. This band gradually fades going southward and the South East of the Altiplano, which is
 451 relatively dry with around 500-600 mm of annual rainfall.



452
 453 *Figure 10. Annual rainfall over the Altiplano during the Tauca Highstand compared with*
 454 *Present. Blue contours indicate the Titicaca and Tauca edges and the Rio Desaguadero.*
 455 *White dots indicate the studied sites.*
 456

457 **5. Discussion**

458 **5.1. Identification and measurement of Tauca Highstand ELA**

459 The palaeo-climatic inference presented in this study relies on the determination of
460 ELAs coeval with the Tauca highstand. Therefore, the robustness of the time constraints on
461 the Tauca moraines is a prerequisite to the rest of the study. In the Zongo valley (Figure 12 of
462 Martin et al. (Precedent Manuscript)), the Tauca Highstand ELA identification relies on the
463 ages of IP4 and IP5. IP4 age is only based on 2 boulder ages, yet it is bracketed by IP3 and
464 IP5, which can both be regarded as robust. IP3 relies on 7 boulder ages and IP5 on 5 with no
465 outliers and tightly clustered ages for IP5. Furthermore, the 3 moraines lies close from each
466 other, there is only a 100 m elevation difference between IP3 and IP5 and an 50 m difference
467 between IP4 and IP5, making them compatible in the error bars. Thus whatever the glacial
468 dynamics was from IP4 to IP5, the average value we peaked remains coherent with both
469 moraines. We are therefore confident that the final Tauca Highstand ELA value for the Zongo
470 valley is robust.

471 The M1 moraine age on Nevado Sajama relies on 4 ages and the identification of 2
472 outliers (Figure 13 of Martin et al. (Precedent Manuscript)). The distribution observed for M1
473 correspond to CRE inheritance dispersion CRE results with a main peak where a majority of
474 samples group, and several secondary peaks all associated to a single boulder age with no
475 overlapping between these outliers. Considering the consistency of this age with the rest of
476 the valley, we are confident with our outlier detection and consider the M1 age trustworthy.

477 The situation is similar for the Tunupa ages of M1 and M2 (Figure 14 of Martin et al.
478 (Precedent Manuscript)). The outlier detection present no ambiguity with 5 and 4 clustered
479 boulder ages giving coherent moraine ages and one outlier yielding an inconsistent age. The
480 glacial dynamic can be discuss to precise if the ice extent remained the one indicated by M1
481 during the whole Tauca highstand or if a progressive retreat between the M1 and M2

482 happened, but here again the difference between the 2 ELAs is of 50m making them
483 compatible in the error bars. The mean value we retained suits both ice extents.

484 Cerro Luxar chronology is less robust and presents an important inheritance trend
485 (Figure 15 of Martin et al. (Precedent Manuscript)). Yet the M1 age of 16.1 ± 0.9 ka still
486 relies on 4 relatively clustered boulder ages ($1\sigma = 0.9$ ka) after unambiguous identification of
487 outliers. The upstream roches moutonnées ages are also well clustered with an age of $14.9 \pm$
488 0.6 ka. Therefore the M2 age relies only on 2 boulders ages but is closely bracketed by two
489 objects with more robust ages. Eventually, the glacial features of Cerro Luxar span over a
490 small elevation range and the 3 ELAs computed in Martin et al. (In Prep) for M1, M2 and M3
491 are all compatible within the error bars.

492 On Cerro Uturunco (Figure 2 and 8, Table 4), the CRE age chronology between the
493 Lower roches moutonnées (Lower RM), M5 and the Upper roches moutonnées (Upper RM) is
494 consistent with their stratigraphical succession. The Bayesian bracketing lessens the 13.5 ka
495 peak - which is younger than the Upper RM - to the benefits of the 15.7 ka peak and leads to
496 an age centered on the Tauca highstand.

497 An important inheritance trend is also observed on Cerro Pikacho (Figure 5 and 8,
498 Table 4), with several boulder ages and roche moutonnées ages beyond 20 ka leading to an
499 important spread of the ages. The age of M3 relies on 2 boulder ages and the identification of
500 1 outlier. The overall CRE age chronology of the valley does not exhibit a global consistency.
501 Yet the glacial valley of Cerro Pikacho present a small extent and the different ELA
502 associated with M1, M2 and M3 yield close values. The M1 ELA value is 4532 ± 29 m, 60 m
503 below the M3 ELA. Therefore, the overall observation that lateglacial ice extents on Cerro
504 Pikacho lie around M3 or between M1 and M3 brings sufficient constraints on the ELA
505 position for this period.

506 On Cerro Tambo (Figure 4 and 8, Table 3) the initial spread observed on the M1 CRE
507 ages benefits from the deglaciation signal of the upstream roches moutonnées clustered round
508 14.6 ka. This spread suggests that the moraines in the Tambo valley are probably exposed to
509 surface deflation and that the small boulders (usually < 1m high) on that area lead to
510 underestimation of the moraine ages. The Bayesian constraints brought by these roche
511 moutonnées lessen this erosion-biased component of the M1 distribution and lead to age
512 centred on the Tauca Lake Highstand.

513 The CRE age results on Cerro Azanaques (Figure 3 and 8, Table 3) bring weak
514 arguments to assess the timing of M2. Two boulders out of 3 yield ages superior to 25 ka. Yet
515 AZA-7 gives an age compatible with the age of the Challapata Fan-delta of 16.1 ± 0.6 ka
516 (Martin et al., 2015). This age is also compatible with the upstream results for M3 and AZA-
517 20 (Roche moutonnées) who indicate a glacial retreat around 14.5-15 ka. These results are
518 consistent with the sedimentological continuity between M2 and the fan-delta reported in
519 Section 2.2.2 and supports a synchronous build up of the 2 objects. Therefore, the M2
520 moraine can be considered as a good indicator of the ice extent during the Tauca Highstand.

521 The ELA calculation from the moraine geometry can be subjected to the same
522 discussion as Martin et al. (Precedent Manuscript). The main sources of bias in the calculation
523 may arise from the fact that (i) the AAR value was determined from small extent actual
524 glaciers and are used on kilometric valley glaciers, (ii) the orientation of the ice tongue
525 influence the ELA position and we conducted the same calculation for northward and
526 southward flowing glacier. We attempted to account for these sources of bias in considering
527 an important 0.1 range of AAR values which ended up in generating 50 m wide error bars.

528

529 **5.2. Precipitation grid and climatic implications**

530 The results presented in this article are recent works that includes methodological
531 simplifications. Therefore, we discuss our results in the light of the hypothesis we made.

532 5.2.1. Different climatic input in the glacier and lake model

533 The difference between the climate input in the glacier and lake model can be
534 discussed in the same way as in Martin et al. (Precedent Manuscript). The difference between
535 the 2 datasets mainly concern the low precipitations, underestimated by the New et al., 2002
536 data.

537 5.2.2 A unique ΔT cooling for the whole Altiplano

538 Our approach to reconstruct the precipitation field relies on the strong assumption that
539 all the glacial valleys experienced the same cooling compared to present during the Tauca
540 Highstand. A motivation for this assumption is that the Altiplano is located in low latitude
541 where the low seasonality and spatial variability of the incident solar radiation create small
542 horizontal temperature gradients as exhibited by the actual data. Yet several phenomena can
543 biased this situation. Indeed, the Tunupa and Pikacho yield the 2 lowest mean annual
544 temperature of the 8 sites. As they both lie on the edge of the Salar de Uyuni, we can assume
545 that this is due to the strong albedo of the salt crust, which led to a smaller regional absorption
546 of the incident short waves. During the Tauca highstand, this situation was reversed because a
547 lake has a smaller albedo than land. The presence of the lake may also have induced a positive
548 thermal anomaly. Not accounting for these differences leads to underestimate the precipitation
549 increase at the Tunupa and Pikacho.

550

551 5.2.3. Uncertainties on the precipitation grid

552 The uncertainty of the precipitation grid results from (i) the variability associated with
553 the present mean temperature and annual rainfall at the 8 sites used in the glacier model, (ii)

554 the uncertainty associated with the ELA computed with the AAR method, (iii) the uncertainty
555 associated with the $ELA = f(P,T)$ relation , (iv) the uncertainty on the input temperature and
556 precipitation grid used in the Lake model, (v) the uncertainties on the evaporation on the land
557 and lake. For now, the uncertainty of the ELAs has not been propagated yet and the only
558 temperature and precipitation grids that have been used are those of New et al. (2002). The
559 ELA uncertainties lie around 1% and we do not expect them to increase the final error bars in
560 great proportions. Mourre et al. (2015) compared 3 different types of rainfall gridded datasets:
561 a station based dataset (kriging interpolation), an atmospheric model output and TRMM grid
562 (satellite measurement). They show that the 3 datasets correctly represent the rainfall pattern
563 at the annual scale. This result is a good omen concerning the precipitation variability
564 resulting from the lake model inputs. The uncertainties on the present climate create around
565 10% of uncertainty on the precipitation results with maximum values around 20% in the south
566 west of the Altiplano. This magnitude is acceptable for our conclusion. Even a global 20%
567 uncertainty would not change the global pattern of precipitation reported for the Tauca
568 Highstand as the final precipitation range from 100 to more than 1500 mm per year.

569

570 *5.2.4 Interpolation method*

571 The interpolation method used to produce a rainfall amplification factor for the whole
572 basin from the 8 values obtained at the glacial sites is for now based on the inverse square of
573 the distances. Different and more sophisticated methods exist such as the kriging. The
574 influence of the interpolation method on the final result will be tested in further works.

575

576 *5.2.5. Precipitation and Temperature conditions for the Tauca Highstand*

577 As morainic records offer so far a low temporal resolution, our study constrains us to
578 derive constant precipitation and temperature conditions for the whole Tauca Highstand,

579 which corresponds to a 1 ka period. The relevance of this approach can be challenged
580 considering that major precipitation proxies such as the speleothem often present a 80 to 90
581 years resolution (Cheng et al., 2013; Mosblech et al., 2012). The variability of SASM
582 monsoon activity exhibited by the speleothem records from Lapa Sem Fim Cave and Paixão
583 Cave lead Strikis et al. (2015) to attribute a three-fold structure to HS1 over South America.
584 The Earlier stage of HS1 spans from 16.1 to 14.7 ka and is a globally wet period coeval with
585 the Tauca Highstand. The global consistency of the SASM activity during this period is hence
586 a positive point for our approach.

587 The cooling values of 3.3 ± 0.2 °C vs. Present we report is lower than the values
588 reported for the same period in Martin et al. (Precedent Manuscript) that range between 6.5
589 and 3.5°C and those of Blard et al. (2009) of 6 and 7°C. The values of Martin et al. (Precedent
590 Manuscript) and the 7°C value of Blard et al. (2009) were determined considering a uniform
591 increase of the precipitation over the Altiplano from the present conditions. The important
592 North-South precipitation gradient observed today induces a dominant contribution of the
593 Northern Altiplano in the lake budget when a uniform increase is considered. Thus, the
594 precipitation input for the lake increases quickly with the value of the uniform increase. As a
595 consequence, small values for these increases satisfy the lake budget. When coupled with the
596 glacier model, the strong gradient of the precipitation-temperature relation makes that the low
597 increase of the precipitations is compensated with an important decrease of the temperature.
598 Blard et al. (2009) also tested the possibility of a non-uniform precipitation increase that still
599 yields a 6°C cooling. We propose a two-fold explanation for this situation. First, Blard et al.
600 (2009) relied on a Positive Degree Day model to evaluate the climatic dependence of the ice
601 extent rather than the Condom et al. (2007). The gradient difference of the Precipitation-
602 Temperature relation between these two methods is likely to induce the observed difference.
603 To a lesser extent, another difference lies in the fact that we did not use the same approach to

604 derive the present climatic conditions. While we find the same annual rainfall value of 200
605 mm. We get a mean annual temperature 2.3°C cooler (8.8°C for Blard et al. (2009) when
606 scaled at 3780 m with a 6.5°C.km⁻¹). This difference must have contributed to this difference
607 also.

608

609 *5.2.6. Climatic implications*

610 Our precipitation field reconstruction during the Tauca Highstand indicates an Eastern
611 precipitation band that reaches the South of the Poopo Lake basin. Such precipitation band is
612 not observed in the present precipitation regime over the Altiplano (Figure 10). This pattern
613 indicates that the precipitation increase during this period was accompanied with a
614 modification of the moist transport toward the basin. This repartition indicates moist input
615 located further South compared with present, with enhanced moist transport across the eastern
616 Andes.

617 The South West of the basin remains relatively dry, indicating no major rain input
618 from the Pacific for this period. Though less humid than in the North, the South East of the
619 basin also reflects moist contribution from the East of the basin.

620 These interpretations are consistent with the SAMS reorganisation expected for the
621 period. The southward shifts of the ITCZ during Heinrich Stadials reported by proxies
622 (Peterson et al., 2000) and climate modelling (Zhang and Delworth, 2005) are likely to
623 provide important moisture level farther South than today, over central Brazil. Similarly,
624 Strikis et al. (2015) indentified Mega-SACZ events coeval with the Tauca highstand. These
625 events are described as periods of major convective activity of the SACZ responsible for
626 massive amounts of moisture over central and southern Brazil. This moisture could be later
627 transported over the Altiplano. This transport would be linked with a strengthening and

628 southward expansion of the easterly belt that would create the high annual rainfall observed
629 over the Poopo lake watershed.

630 Presently, westerly winds prevent moist transport from the east over the Altiplano
631 during dry periods; and positive easterly anomalies are linked with increased moist transport
632 (Vuille, 1999). Therefore, the spatial pattern we propose for the easterlies is also in good
633 agreement with the southward shift of the southern westerly winds reported by Montade et al.
634 (2015) during decrease of the AMOC intensity such as HS1 (McManus et al., 2004). A
635 southward shift of the southern westerly winds would promote easterly moist transport over
636 the Altiplano from central Brazil.

637

638 **6. Conclusion**

639 We identify 8 moraines from 8 different sites of the Altiplano coeval with the Lake
640 Tauca Highstand. These observations are either derived from other studies (Clayton and
641 Clapperton, 1997; Blard et al., 2014, Martin et al., in prep) or presented as new results. ELA
642 are computed out of these moraines and used in a Lake and Glacier modelling approach that
643 enables us to derive a precipitation field over the Altiplano for the Tauca Highstand.

644 We report new CRE ages from Cerro Tambo, Cerro Pikacho and Cerro Azanaques. In
645 Cerro Tambo, we observe a LLGM around 16.5 ka and a rapid glacial retreat during the
646 transgression of the Lake around 14.6 ka. Cerro Pikacho and Azanaques yield scattered data.
647 We identify moraine stabilization around 14.5 ka on Cerro Pikacho. On Cerro Azanaques
648 results converge with sedimentological observations of a global LLGM at the onset of the
649 Highstand followed by a rapid and massive retreat around 14.5-15 ka.

650 We used the AAR method calibrated on present High Andes tropical glacier (AAR =
651 0.55 - 0.65) to calculate the ELA for those 8 moraines. Tauca Highstand ELAs mainly lies
652 around 4500 - 4600 m, with 3 higher values ranging from 4700 to 5300 masl. We used these
653 ELA in a simple Precipitation - Temperature modelling approach that combine glacier and

654 lake modelling to derive a precipitation field over the Altiplano during the Tauca phase. The
655 Tauca Highstand precipitation field is characterized by (i) abundant rainfall in its northern
656 part (1500-1800 mm.yr⁻¹) and a North to South precipitation gradient, (ii) An eastern
657 precipitation band (1200 mm.yr⁻¹) that extent from the Titicaca to the Poopo watershed and
658 fades in the south-eastern basin, (iii) an East to West precipitation gradient, with a dry South-
659 western Altiplano (200 mm.yr⁻¹).

660 These results indicate major easterly moist input during the Tauca Highstand most
661 likely resulting from a strengthening and southward expansion of the easterly winds,
662 promoting moist transport from central Brazil over the eastern Andes. This view is consistent
663 with the consistent climate and with observations on the evolution of the SACZ and the
664 Westerly winds belt during HS1.

665

666 **Acknowledgments**

667 This work was funded by the INSU EVE-LEFE program and the ANR Jeunes
668 Chercheurs GALAC project “ANR-11-JS56-011-01”. We greatly appreciated the logistical
669 support of the IRD of La Paz (Bolivia) during our field trips conducted between 2010 and
670 2013. P. Burnard and L. Zimmerman are warmly thanked for essential help with the SFT
671 mass spectrometer and related device during analytic sessions. The same feelings are
672 addressed to F. Gallo and M. Protin for vital support on ¹⁰Be separative chemistry and L.
673 Tissandier and Y. Marrocchi for much-needed help with the SEM and mineral analysis. We
674 are grateful to the SARM-CNRS for high quality chemical analysis. R. Joussemet and the
675 STEVAL crew (GeoRessources, Nancy) are acknowledged for their technical support for
676 sample crushing and mineral separation.

677 The ASTER French national AMS facility (CEREGE, Aix-en-Provence) is supported
678 by the INSU/CNRS, the ANR through the “Equipements d’Excellence” program, IRD and

679 CEA. The field measurements of mass balance and ELA on the glaciers in Bolivia and
 680 Ecuador were provided by the Andean part of the *Service National d'Observation*
 681 GLACIOCLIM funded by the French IRD (*Institut de Recherche pour le Développement*), the
 682 *Universidad Mayor de San Andres* (UMSA, IGEMA, IHH) in Bolivia and the *Instituto*
 683 *Nacional de Meteorología e Hidrología* (INAMHI) in Ecuador.

684

685 **Bibliography**

- 686 Banderas, R., Alvarez-Solas, J., Robinson, A., Montoya, M., 2014. An interhemispheric mechanism for glacial
 687 abrupt climate change. *Clim. Dyn.* 2897–2908. doi:10.1007/s00382-014-2211-8
 688 Barker, S., Chen, J., Gong, X., Jonkers, L., Knorr, G., Thornalley, D., 2015. Icebergs not the trigger for North
 689 Atlantic cold events. *Nature* 520, 333–336. doi:10.1038/nature14330
 690 Barker, S., Diz, P., Vautravers, M.J., Pike, J., Knorr, G., Hall, I.R., Broecker, W.S., 2009. Interhemispheric
 691 Atlantic seesaw response during the last deglaciation. *Nature* 457, 1097–1102. doi:10.1038/nature07770
 692 Blard, P.-H., Braucher, R., Lavé, J., Bourlès, D., 2013a. Cosmogenic ¹⁰Be production rate calibrated against
 693 ³He in the high Tropical Andes (3800–4900 m, 20–22° S). *Earth Planet. Sci. Lett.* 382, 140–149.
 694 doi:10.1016/j.epsl.2013.09.010
 695 Blard, P.-H., Lavé, J., Farley, K. a., Fornari, M., Jiménez, N., Ramirez, V., 2009. Late local glacial maximum in
 696 the Central Altiplano triggered by cold and locally-wet conditions during the paleolake Tauca episode (17–
 697 15ka, Heinrich 1). *Quat. Sci. Rev.* 28, 3414–3427. doi:10.1016/j.quascirev.2009.09.025
 698 Blard, P.-H., Lave, J., Farley, K. a., Ramirez, V., Jimenez, N., Martin, L.C.P., Charreau, J., Tibari, B., Fornari,
 699 M., 2014. Progressive glacial retreat in the Southern Altiplano (Uturuncu volcano, 22°S) between 65 and
 700 14ka constrained by cosmogenic ³He dating. *Quat. Res.* 82, 209–221. doi:10.1016/j.yqres.2014.02.002
 701 Blard, P.-H., Lavé, J., Sylvestre, F., Placzek, C.J., Claude, C., Galy, V., Condom, T., Tibari, B., 2013b.
 702 Cosmogenic ³He production rate in the high tropical Andes (3800 m, 20°S): Implications for the local last
 703 glacial maximum. *Earth Planet. Sci. Lett.* 377–378, 260–275. doi:10.1016/j.epsl.2013.07.006
 704 Blard, P.-H., Sylvestre, F., Tripathi, a. K., Claude, C., Causse, C., Coudrain, a., Condom, T., Seidel, J.-L.,
 705 Vimeux, F., Moreau, C., Dumoulin, J.-P., Lavé, J., 2011. Lake highstands on the Altiplano (Tropical
 706 Andes) contemporaneous with Heinrich 1 and the Younger Dryas: new insights from ¹⁴C, U–Th dating
 707 and δ¹⁸O of carbonates. *Quat. Sci. Rev.* 30, 3973–3989. doi:10.1016/j.quascirev.2011.11.001
 708 Bond, G., Heinrich, H., Broecker, W., Labeyrie, L., McManus, J., Andrews, J., Huon, S., Jantschik, R., Clasen,
 709 S., Simet, C., Tedesco, K., Klas, M., Bonani, G., Ivy, S., 1992. Evidence for massive discharges of
 710 icebergs into the North Atlantic ocean during the last glacial period. *Nature* 360, 245–249.
 711 doi:10.1038/360245a0
 712 Broecker, W.S., 1994. Massive iceberg discharges as triggers for global climate change. *Nature*.
 713 doi:10.1038/372421a0
 714 Carvalho, L.M. V, Jones, C., Posadas, A.N.D., Quiroz, R., Bookhagen, B., Liebmann, B., 2012. Precipitation
 715 characteristics of the South American monsoon system derived from multiple datasets. *J. Clim.* 25, 4600–
 716 4620. doi:10.1175/JCLI-D-11-00335.1
 717 Chen, T.-C., Weng, S.-P., Schubert, S., 1999. Maintenance of Austral Summertime Upper-Tropospheric
 718 Circulation over Tropical South America: The Bolivian High–Nordeste Low System. *J. Atmos. Sci.* 56,
 719 2081–2100. doi:10.1175/1520-0469(1999)056<2081:MOASUT>2.0.CO;2
 720 Cheng, H., Sinha, A., Cruz, F.W., Wang, X., Edwards, R.L., D’Horta, F.M., Ribas, C.C., Vuille, M., Stott, L.D.,
 721 Auler, A.S., 2013. Climate change patterns in Amazonia and biodiversity. *Nat. Commun.* 4, 1411.
 722 doi:10.1038/ncomms2415
 723 Clapperton, C., Clayton, J., Benn, D., 1997. LATE QUATERNARY GLACIER ADVANCES AND
 724 PALAEO LAKE HIGHSTANDS IN THE BOLIVIAN ALTIPLANO. *Quat. ...* 6182, 49–59.
 725 Clayton, J.D., Clapperton, C.M., 1995. The last glacial cycle and palaeolake synchrony in the southern volivian
 726 altiplano: cerro azanaques case study.
 727 Clayton, J.D., Clapperton, C.M., 1997. Broad synchrony of a Late-glacial glacier advance and the highstand of
 728 palaeolake Tauca in the Bolivian Altiplano. *J. Quat. Sci.* 12, 169–182. doi:10.1002/(SICI)1099-
 729 1417(199705/06)12:3<169::AID-JQS304>3.0.CO;2-S

- 730 Condom, T., Coudrain, A., Dezetter, A., Brunstein, D., Delclaux, F., Jean-Emmanuel, S., 2004. Transient
731 modelling of lacustrine regressions: two case studies from the Andean Altiplano. *Hydrol. Process.* 18,
732 2395–2408. doi:10.1002/hyp.1470
- 733 Condom, T., Coudrain, A., Sicart, J.E., Théry, S., 2007. Computation of the space and time evolution of
734 equilibrium-line altitudes on Andean glaciers (10°N–55°S). *Glob. Planet. Change* 59, 189–202.
735 doi:10.1016/j.gloplacha.2006.11.021
- 736 Cruz, F.W., Burns, S.J., Karmann, I., Sharp, W.D., Vuille, M., Cardoso, A.O., Ferrari, J.A., Silva Dias, P.L.,
737 Viana, O., 2005. Insolation-driven changes in atmospheric circulation over the past 116,000 years in
738 subtropical Brazil. *Nature* 434, 63–66. doi:10.1038/nature03365
- 739 Garreaud, R., Vuille, M., Clement, A.C., 2003. The climate of the Altiplano: observed current conditions and
740 mechanisms of past changes. *Palaeogeogr. Palaeoclimatol. Palaeoecol.* 194, 5–22. doi:10.1016/S0031-
741 0182(03)00269-4
- 742 Garreaud, R.D., Vuille, M., Compagnucci, R., Marengo, J., 2009. Present-day South American climate.
743 *Palaeogeogr. Palaeoclimatol. Palaeoecol.* 281, 180–195. doi:10.1016/j.palaeo.2007.10.032
- 744 GEOBOL, 1994. Mapas Tematicos de Recursos Minerales de Bolivia.
- 745 Han, Z., Li, X., Yi, S., Stevens, T., Chen, Y., Wang, X., Lu, H., 2015. Extreme monsoon aridity episodes
746 recorded in South China during Heinrich Events. *Palaeogeogr. Palaeoclimatol. Palaeoecol.* 440, 467–474.
747 doi:10.1016/j.palaeo.2015.09.037
- 748 Heinrich, H., 1988. Origin and consequences of cyclic ice rafting in the Northeast Atlantic Ocean during the past
749 130,000 years. *Quat. Res.* 29, 142–152. doi:10.1016/0033-5894(88)90057-9
- 750 Jomelli, V., Khodri, M., Favier, V., Brunstein, D., Ledru, M.-P., Wagnon, P., Blard, P.-H., Sicart, J.-E.,
751 Braucher, R., Grancher, D., Bourlès, D.L., Braconnot, P., Vuille, M., 2011. Irregular tropical glacier retreat
752 over the Holocene epoch driven by progressive warming. *Nature* 474, 196–9. doi:10.1038/nature10150
- 753 Kanner, L.C., Burns, S.J., Cheng, H., Edwards, R.L., Vuille, M., 2013. High-resolution variability of the South
754 American summer monsoon over the last seven millennia: Insights from a speleothem record from the
755 central Peruvian Andes. *Quat. Sci. Rev.* 75, 1–10. doi:10.1016/j.quascirev.2013.05.008
- 756 Kelly, M. a., Lowell, T. V., Applegate, P.J., Phillips, F.M., Schaefer, J.M., Smith, C. a., Kim, H., Leonard, K.C.,
757 Hudson, A.M., 2013. A locally calibrated, late glacial ^{10}Be production rate from a low-latitude, high-
758 altitude site in the Peruvian Andes. *Quat. Geochronol.* 1–16. doi:10.1016/j.quageo.2013.10.007
- 759 Lal, D., 1991. Cosmic ray labeling of erosion surfaces: in situ nuclide production rates and erosion models. *Earth
760 Planet. Sci. Lett.* 104, 424–439. doi:10.1016/0012-821X(91)90220-C
- 761 Martin, L., Blard, P.-H., Lave, J., Braucher, R., Lupker, M., Condom, T., Charreau, J., Mariotti, V., Bourlès, D.,
762 Arnold, M., G. Keddadouche, K.A., Davy, E., 2015. In situ cosmogenic ^{10}Be production rate in the High
763 Tropical Andes. *Quat. Geochronol.* 30, 54–68. doi:10.1016/j.quageo.2015.06.012
- 764 McManus, J.F., Francois, R., Gherardi, J.-M., Keigwin, L.D., Brown-Leger, S., 2004. Collapse and rapid
765 resumption of Atlantic meridional circulation linked to deglacial climate changes. *Nature* 428, 834–837.
766 doi:10.1038/nature02494
- 767 Montade, V., Kageyama, M., Combourieu-Nebout, N., Ledru, M.P., Michel, E., Siani, G., Kissel, C., 2015.
768 Teleconnection between the intertropical convergence zone and southern westerly winds throughout the
769 last deglaciation. *Geology* 43, 735–738. doi:10.1130/G36745.1
- 770 Mosblech, N.A.S., Bush, M.B., Gosling, W.D., Hodell, D., Thomas, L., van Calsteren, P., Correa-Metrio, A.,
771 Valencia, B.G., Curtis, J., van Woesik, R., 2012. North Atlantic forcing of Amazonian precipitation during
772 the last ice age. *Nat. Geosci.* 5, 817–820. doi:10.1038/ngeo1588
- 773 Murre, L., Condom, T., Junquas, C., Lebel, T., Sicart, J.E., Figueroa, R., Cochachin, A., 2015. Spatio-temporal
774 assessment of WRF, TRMM and in situ precipitation data in a tropical mountain environment (Cordillera
775 Blanca, Peru). *Hydrol. Earth Syst. Sci. Discuss.* 12, 6635–6681. doi:10.5194/hessd-12-6635-2015
- 776 Muscheler, R., Beer, J., Kubik, P.W., Synal, H. -a., 2005. Geomagnetic field intensity during the last 60,000
777 years based on ^{10}Be and ^{36}Cl from the Summit ice cores and 14C. *Quat. Sci. Rev.* 24, 1849–1860.
778 doi:10.1016/j.quascirev.2005.01.012
- 779 New, M., Lister, D., Hulme, M., Makin, I., 2002. A high-resolution data set of surface climate over global land
780 areas. *Clim. Res.* 21, 1–25. doi:10.3354/cr021001
- 781 Palmer, M.R., Pearson, P.N., 2003. A 23,000-Year Record of Surface Water pH and $\text{P}\{\text{chem}\}_{\text{CO}_2}$ in the
782 Western Equatorial Pacific Ocean. *Science* (80-.). 300, 480–482.
- 783 Pausata, F.S.R., Battisti, D.S., Nisancioglu, K.H., Bitz, C.M., 2011. Chinese stalagmite $\delta^{18}\text{O}$ controlled by
784 changes in the Indian monsoon during a simulated Heinrich event. *Nat. Geosci.* 4, 474–480.
785 doi:10.1038/ngeo1169
- 786 Peterson, L.C., 2000. Rapid Changes in the Hydrologic Cycle of the Tropical Atlantic During the Last Glacial.
787 *Science* (80-.). 290, 1947–1951. doi:10.1126/science.290.5498.1947
- 788 Placzek, C., Quade, J., Patchett, P.J., 2006. Geochronology and stratigraphy of late Pleistocene lake cycles on
789 the southern Bolivian Altiplano: Implications for causes of tropical climate change. *Geol. Soc. Am. Bull.*

- 790 118, 515–532. doi:10.1130/B25770.1
- 791 Placzek, C.J., Quade, J., Patchett, P.J., 2013. A 130ka reconstruction of rainfall on the Bolivian Altiplano. *Earth*
- 792 *Planet. Sci. Lett.* 363, 97–108. doi:10.1016/j.epsl.2012.12.017
- 793 Servant, M., Fontes, J.-C., 1978. Les lacs quaternaires des hauts plateaux des Andes boliviennes - premières
- 794 interprétations paléoclimatiques. *Cah. O.R.S.T.O.M., Série Géologie X*, 9–23.
- 795 Sirocko, F., Garbe-Schonberg, D., McIntyre, A., Molfino, B., 1996. Teleconnections Between the Subtropical
- 796 Monsoons and High-Latitude Climates During the Last Deglaciation. *Science* (80-). 272, 526–529.
- 797 doi:10.1126/science.272.5261.526
- 798 Smith, J. a., Seltzer, G.O., Farber, D.L., Rodbell, D.T., Finkel, R.C., 2005. Early local last glacial maximum in
- 799 the tropical Andes. *Science* 308, 678–81. doi:10.1126/science.1107075
- 800 Soruco, A., Vincent, C., Francou, B., Ribstein, P., Berger, T., Sicart, J.E., Wagnon, P., Arnaud, Y., Favier, V.,
- 801 Lejeune, Y., 2009. Mass balance of Glaciar Zongo, Bolivia, between 1956 and 2006, using glaciological,
- 802 hydrological and geodetic methods. *Ann. Glaciol.* 50, 1–8. doi:10.3189/172756409787769799
- 803 Stone, J.O., 2000. Air pressure and cosmogenic isotope production. *J. Geophys. Res.* 105, 23753.
- 804 doi:10.1029/2000JB900181
- 805 Strikis, N.M., Chiessi, C.M., Cruz, F.W., Vuille, M., Cheng, H., Barreto, E.A.S., Mollenhauer, G., Kasten, S.,
- 806 Karmann, I., Edwards, R.L., Bernal, J.P., Sales, R., 2015. Timing and structure of Mega-SACZ events
- 807 during Heinrich Stadial 1. *Geophys. Res. Lett.* 1–8. doi:10.1002/2015GL064048.Received
- 808 Sylvestre, F., Servant, M., Servant-Vildary, S., Causse, C., Fournier, M., Ybert, J.-P., 1999. Lake-Level
- 809 Chronology on the Southern Bolivian Altiplano (18°–23°S) during Late-Glacial Time and the Early
- 810 Holocene. *Quat. Res.* 51, 54–66. doi:10.1006/qres.1998.2017
- 811 Uppala, S.M., KÅllberg, P.W., Simmons, a. J., Andrae, U., Bechtold, V.D.C., Fiorino, M., Gibson, J.K.,
- 812 Haseler, J., Hernandez, a., Kelly, G. a., Li, X., Onogi, K., Saarinen, S., Sokka, N., Allan, R.P., Andersson,
- 813 E., Arpe, K., Balmaseda, M. a., Beljaars, a. C.M., Berg, L. Van De, Bidlot, J., Bormann, N., Caires, S.,
- 814 Chevallier, F., Dethof, a., Dragosavac, M., Fisher, M., Fuentes, M., Hagemann, S., Hólm, E., Hoskins,
- 815 B.J., Isaksen, I., Janssen, P. a. E.M., Jenne, R., McNally, a. P., Mahfouf, J.-F., Morcrette, J.-J., Rayner, N.
- 816 a., Saunders, R.W., Simon, P., Sterl, a., Trenberth, K.E., Untch, a., Vasiljevic, D., Viterbo, P., Woollen,
- 817 J., 2005. The ERA-40 re-analysis. *Q. J. R. Meteorol. Soc.* 131, 2961–3012. doi:10.1256/qj.04.176
- 818 Vuille, M., 1999. Atmospheric circulation over the Bolivian Altiplano during dry and wet periods and extreme
- 819 phases of the southern oscillation. *Int. J. Climatol.* 19, 1579–1600. doi:10.1002/(SICI)1097-
- 820 0088(19991130)19:14<1579::AID-JOC441>3.0.CO;2-N
- 821 Vuille, M., Bradley, R.S., Keimig, F., 2000. Interannual climate variability in the Central Andes and its relation
- 822 to tropical Pacific and Atlantic forcing. *J. Geophys. Res.* 105, 12447. doi:10.1029/2000JD900134
- 823 Vuille, M., Burns, S.J., Taylor, B.L., Cruz, F.W., Bird, B.W., Abbott, M.B., Kanner, L.C., Cheng, H., Novello,
- 824 V.F., 2012. A review of the South American monsoon history as recorded in stable isotopic proxies over
- 825 the past two millennia. *Clim. Past* 8, 1309–1321. doi:10.5194/cp-8-1309-2012
- 826 Vuille, M., Francou, B., Wagnon, P., Juen, I., Kaser, G., Mark, B.G., Bradley, R.S., 2008. Climate change and
- 827 tropical Andean glaciers: Past, present and future. *Earth-Science Rev.* 89, 79–96.
- 828 doi:10.1016/j.earscirev.2008.04.002
- 829 Vuille, M., Keimig, F., 2004. Interannual variability of summertime convective cloudiness and precipitation in
- 830 the central Andes derived from ISCCP-B3 data. *J. Clim.* 17, 3334–3348. doi:10.1175/1520-
- 831 0442(2004)017<3334:IVOSCC>2.0.CO;2
- 832 Wang, X., Auler, A.S., Edwards, R.L., Cheng, H., Cristalli, P.S., Smart, P.L., Richards, D. a., Shen, C.-C., 2004.
- 833 Wet periods in northeastern Brazil over the past 210 kyr linked to distant climate anomalies. *Nature* 432,
- 834 740–3. doi:10.1038/nature03067
- 835 Zhang, R., Delworth, T.L., 2005. Simulated tropical response to a substantial weakening of the Atlantic
- 836 thermohaline circulation. *J. Clim.* 18, 1853–1860. doi:10.1175/JCLI3460.1
- 837 Zhang, X., Lohmann, G., Knorr, G., Purcell, C., 2014. Abrupt glacial climate shifts controlled by ice sheet
- 838 changes. *Nature* 512, 290–294. doi:10.1038/nature13592
- 839 Zhou, J., Lau, K.M., 1998. Does a monsoon climate exist over South America? *J. Clim.* 11, 1020–1040.
- 840 doi:10.1175/1520-0442(1998)011<1020:DAMCEO>2.0.CO;2
- 841 Zorzi, C., Sanchez Goñi, M.F., Anupama, K., Prasad, S., Hanquiez, V., Johnson, J., Giosan, L., 2015. Indian
- 842 monsoon variations during three contrasting climatic periods: The Holocene, Heinrich Stadial 2 and the
- 843 last interglacial-glacial transition. *Quat. Sci. Rev.* 125, 50–60. doi:10.1016/j.quascirev.2015.06.009
- 844

Chapitre 8

Conclusions et Perspectives

Ces travaux de thèse sur la paléoclimatologie de l'Altiplano comprennent donc deux volets différents mais complémentaires. Le premier, qui regroupe les chapitres 4 et 5, présente des développements méthodologiques pour les datations par âges d'exposition. Le second, à travers les chapitres 6 et 7, présente des études paléoclimatologiques.

Si, comme le disait Blondin, le monde se divise en 2 catégories, celui de la paléoclimatologie se partage souvent entre la production de données et la modélisation. Pour ceux qui produisent les données (ceux qui creusent?), la datation est la pierre angulaire de toute observation. Toutes les archives climatiques ne sont pas égales devant la datation. En les plaçant toutes de gauche à droite sur un axe indiquant les difficultés de datations croissantes, on pourrait probablement commencer à gauche par le comptage des couches de glaces dans les carottes jeunes ou des cernes de bois des dendrochronologues. Les barres d'erreur associées aux âges constituent un bon indicateur de la databilité des différentes archives. Les glaciologues du Groenland préfèrent d'ailleurs exprimer les âges "b2k" (avant l'an 2000) que BP (Before Present). Les datations de spéléothèmes atteignent également des précisions très élevées avec des barres d'erreurs pouvant atteindre quelques dizaines d'années (Stríkis et al., 2015). Nul doute que la réalisation d'un tel diagramme amènerait à de nombreux débats et discussions étant donné que chacun est confronté à des problématiques complexes de datation. Malgré cela, je maintiens que la datation des moraines par âge d'exposition occuperait une position plutôt à droite dans ce diagramme.

C'est probablement cette position "plutôt à droite" qui a fait que ces travaux de thèse incluent le développement d'outils visant à perfectionner le calcul d'âges d'exposition. Levier d'Archimède du calcul des âges d'exposition, le taux de production des isotopes cosmogéniques est donc le premier sujet d'étude de cette thèse. Les lithologies rencontrées sur l'Altiplano sont variées et nous ont amené à utiliser des âges d'exposition se basant sur le ^3He dans les pyroxènes pour les lithologies basiques rencontrées dans le sud de l'Altiplano du Sajama à l'Uturuncu, mais également le ^{10}Be dans les quartz pour les lithologies granitiques et granodioritiques du Zongo et d'Azanaques ou celles silicoclastiques du Tambo. L'étude du fan-delta de Challapata sur les flancs de Cerro Azanaques a permis d'établir un nouveau taux de production ^{10}Be de $4.07 \pm 0.18 \text{ at.g}^{-1}.\text{a}^{-1}$ (valeur SLHL pour le scaling reposant sur (i) le modèle de Lal-Stone dépendant du temps, (ii) l'atmosphère spatialisée ERA-40, (iii) la reconstruction géomagnétique de Muscheler et al. (2005)). Ce taux est venu s'ajouter à ceux de Kelly et al. (2013) et Blard et al. (2013). Ce groupe montre une bonne cohérence des 3 valeurs et on peut raisonnablement penser que le taux de production du ^{10}Be dans les hautes Andes tropicales est maintenant bien établi pour les objets de la période tardiglaciaire. Ce constat a été utile à ces travaux de thèse car il fournit une base robuste au calcul d'âges nécessaire aux interprétations climatiques.

Les amendements successifs apportés à ce qui n'était initialement qu'une série de ligne Matlab© ont abouti au calculateur en ligne CREp présenté dans le chapitre 5. Ce projet est une autre contribution au calcul d'âges d'exposition. La possibilité de choisir un taux de production local à partir de la base de données en ligne est inédite. Elle constitue à ce jour la meilleure solution au problème central de la dépendance aux modèles de mise à l'échelle que j'ai évoqué dans les chapitres 4 et 5. D'autre part, ce programme permet également en quelques clics d'appréhender

l'influence des choix qui sont faits pour paramétrer la mise à l'échelle des taux de production. Tant qu'il ne sera pas possible de prouver qu'il existe une procédure de mise à l'échelle qui surpasse toutes les autres du point de vue de la justesse, la solution de la boîte noire (encore en vogue actuellement) ne sera pas satisfaisante. Elle réduit artificiellement la variabilité sur les âges calculés. Il faut concéder qu'une procédure commune de calcul a l'avantage de rendre les âges d'expositions comparables entre eux. Cependant, pour comparer des âges d'expositions avec des résultats provenant d'une autre méthode de datation, il est important pour l'utilisateur de pouvoir évaluer le "niveau de consensus" qui existe entre les différents modèles relativement aux âges qu'il calcule. Le programme CREp propose donc une avancée méthodologique dans le sens de la responsabilisation de l'utilisateur vis-à-vis du calcul. Une responsabilisation qui ne s'accompagne pas pour autant d'une complexification puisque le programme a été développé dans le but d'être simple à utiliser et "user friendly" vis-à-vis des formats de données et de l'interactivité des différentes interfaces.

Dans *La République*, I, 352d, 353b, Platon explique que le Souverain Bien (quête ultime du bonheur antique) d'un être ou d'une chose (et a fortiori d'un programme informatique) est de réaliser ce pour quoi il est fait, d'accomplir sa fonction propre. Or, les travaux qui viennent d'être évoqués constituent une amélioration de la boîte-à-outils paléo-glacio-climatique. Ils ont avant tout comme fonction propre de permettre de calculer des âges d'exposition. C'est dans cette perspective de bonheur platonicien que s'inscrivent les chapitres 6 et 7. Ils visent donc à documenter le climat andin tardiglaciaire pour lequel nous avons présenté les enjeux dans l'introduction de ce manuscrit et des manuscrits d'articles des chapitres en question.

Le chapitre 6 présente notamment 4 chronologies de retrait glaciaire établies dans la vallée du Zongo, au Nevado Sajama, Cerro Tunupa et Cerro Luxar. Dans un premier temps, l'interprétation des âges obtenus fait émerger 2 tendances dans le comportement des glaciers de l'Altiplano pour la période tardiglaciaire. Au Nord de l'Altiplano, le Zongo, forme un groupe à lui seul, mais non des moindres puisqu'il propose une chronologie glaciaire d'une densité sans équivalent dans les Andes tropicales pour l'instant. Ce site enregistre un Dernier Maximum Glaciaire Local (LLGM en anglais) vers 17 ka, il est associé à une ligne d'équilibre voisine de 4550 m d'altitude. Cette extension maximale est suivie d'une très faible retraite jusqu'à 13.5 ka, indiquant un maintien de conditions climatiques proches du LLGM jusqu'à ce moment. S'en suit une retraite massive réalisée en moins de 2000 ans. Les lignes d'équilibre de la transition Pleistocène-Holocène viennent alors se percher à 4800 m. Le deuxième groupe comprend les 3 autres sites. Pour eux, le LLGM a lieu à 16 ka BP, à l'initiation du haut niveau lacustre Tauca. S'en suit une régression soit pendant la deuxième moitié du Tauca (Sajama, Luxar), soit pendant sa régression (Tunupa). Durant cette période, les lignes d'équilibre passent de 4750 à plus de 4800 m au Sajama et au Luxar et de 4450 m à 4500 m au Tunupa. Pour ce dernier, et pour le Sajama, cette retraite est suivie d'une stabilisation postérieure des langues glaciaires vers 13-12 ka en global synchronisme avec le haut niveau du Coipasa. Elle est en revanche définitive pour le Luxar dont l'hypsométrie et la faible extension ne permettent pas au glacier de résister à la remontée de la ligne d'équilibre enregistrée. A la différence des glaciers du Nord, la dynamique des glaciers du Sud de l'Altiplano semble donc en bonne cohérence avec la dynamique lacustre. Ces tendances identifiées sont en accord avec les premières observations de Clayton and Clapperton (1995), ainsi qu'avec les âges d'exposition déjà publiés dans la région (Blard et al., 2014; Kelly et al., 2012; Smith et al., 2011, 2005; Zech et al., 2009, 2007b,a) et présentés de manière synoptique dans la synthèse de Ward et al. (2015).

Afin d'exploiter le plus complètement possible l'archive climatique que constitue ces morphologies glaciaires, nous avons appliqué la méthode d'inversion climatique couplant la modélisation glaciaire et lacustre présentée en Introduction et détaillée dans le chapitre 6. Cette méthode nous a permis d'associer à chaque extension glaciaire un refroidissement et une augmentation des précipitations par rapport au Présent. Les résultats produits par cette approche possèdent d'importantes barres d'erreur, à tel point que les reconstitutions de précipitations ne permettent pas d'identifier de tendances claires. En revanche, les reconstructions de températures ont permis de proposer que les LLGM à 17 et 16 ka étaient associés à des refroidissements voisins de 4-4.5 °C par rapport au présent. Les températures remontent ensuite jusqu'à un refroidissement voisin de 2.5-3°C pour le Dryas Récent et le début de l'Holocène. Les reconstitutions des températures montrent une forte disparité pour la période Tauca que nous proposons de lier avec une variabilité spatiale du champ des précipitations. Cette observation, jointe à celle du synchronisme glacier observé par nos soins dans le

sud de l'Altiplano et par Zech et al. (2009, 2007b) sont des premiers éléments d'interprétations qui semblent indiquer que cette période était marquée par un transport accru de l'humidité depuis l'Est possiblement en lien avec une modification des vents d'Est qui se seraient intensifiés et déployés plus au Sud qu'à l'accoutumée pendant l'été austral.

Ces premières observations témoignant possiblement d'une modification de la mousson sud américaine pendant le stade Tauca sont approfondies dans le chapitre 7. Dans ce dernier chapitre, le couplage glacier-lac n'est plus utilisé pour reconstruire des évolutions temporelles des précipitations et des températures, mais pour investiguer la variabilité spatiale des précipitations au stade Tauca. Pour se faire, les précédentes chronologies ainsi que de nouvelles données sur Cerro Tambo, Cerro Pichacho, Cerro Azanaques et les données de Blard et al. (2014) sont utilisées pour identifier 8 extensions glaciaires dans 8 sites différents synchrones du haut niveau Tauca. Ensuite, l'inversion climatique se fait en supposant un refroidissement uniforme pour tout l'Altiplano durant cette période. Cette hypothèse permet de traduire la variabilité spatiale des lignes d'équilibre des glaciers en variabilité de la pluviométrie et de calculer des cartes de pluviométrie pendant le Tauca. Le modèle de Lac est finalement utilisé pour identifier la carte de pluviométrie qui produit un bilan hydrologique nul pour le lac. La carte ainsi produite montre un Altiplano ≈ 2.2 fois plus humide que l'Actuel. Dans le Nord du bassin, assez humide aujourd'hui, les précipitations sont multipliées par ≈ 1.8 , dans le Sud du bassin, les zones aujourd'hui très arides voient les précipitations annuelles se multiplier par ≈ 3 au Tunupa et même ≈ 3.4 au Luxar. Comparativement à aujourd'hui, la carte des précipitations montre toujours un gradient Nord Sud très fort, mais à celui-ci vient se coupler un gradient Est Ouest. En effet, l'inversion fait apparaître une bande pluvieuse de 100 km de large qui s'étend vers le Sud en longeant la cordillère Orientale jusqu'à 19° de latitude Sud.

Ces résultats confirment nos premières propositions, ils mettent clairement en avant un transport accru de l'humidité pendant la phase Tauca via l'Est. Cette observation présente une bonne cohérence avec des observations faites sur le climat actuel et sur le climat de la période Tauca.

- Actuellement, les périodes plus humides enregistrées sur l'Altiplano sont associées à un renforcement des vents d'Est transportant l'humidité du bassin Amazonien. Les périodes plus arides sont liées à une prédominance des vents d'Ouest plus secs qui inhibent ce transport (Garreaud et al., 2003; Vuille, 1999).
- La période Tauca est caractérisée par (i) une humidité accrue sur le Brésil Central et Sud du une activité renforcée de la Zone de Convergence Sud Atlantique (Stríkis et al., 2015), (ii) un déplacement vers le sud des westerlies (Montade et al., 2015).

Toutes ces informations nous amènent donc à conclure que pendant la période Tauca, l'expression de la mousson Sud américaine sur l'Altiplano a été modulée par une expansion et un renforcement des vents d'Est qui ont permis un transport accru de l'humidité abondante localisée dans le Brésil Central et Sud.

Les 2 différents types d'utilisation de la méthode d'inversion glacier-lac présentés dans les chapitres 6 et 7 nous montrent ses limites vis à vis de la localisation de l'information paléoclimatique. Des hypothèses sont systématiquement faites pour l'un ou l'autre des fonctionnements. Dans le chapitre 6, on extrapole un changement régional (sur tout le bassin) à partir d'un seul site, on perd donc la variabilité spatiale. Dans le chapitre 7, on étudie la variabilité spatiale des précipitations mais en faisant une croix sur celle des températures. Cette limitation a plusieurs conséquences. Dans l'approche temporelle du chapitre 6, l'exploitation de différents sites produit des valeurs de refroidissement et d'augmentation des précipitations par rapport au présent (ΔPT vs. Présent) différentes d'un site à l'autre pour des périodes qui se superposent parfois. On en arrive donc à considérer qu'à un moment donné t , le bassin de l'Altiplano connaît à la fois un ΔT global de -3.5°C et de -4.2°C . De plus, compte tenu du gradient actuel de précipitations, les augmentations globales des précipitations sont limitées par la contribution du Nord, beaucoup plus arrosé, qui écrase la potentielle contribution du Sud. Dans le chapitre 7, la variabilité de la répartition des lignes d'équilibre est considérée comme étant à 100% le fait de la variabilité spatiale des précipitations. Si le refroidissement n'a pas été uniforme, la variabilité spatiale des précipitations a pu être différente.

De même, la prise en compte des incertitudes sur l'âge modifie les résultats des inversions. Dans l'approche temporelle, si un âge est à cheval sur le haut niveau Tauca et une période de bas niveau lacustre (ce qui est très souvent le cas), la propagation des erreurs d'âge fait que le ΔPT vs. Présent

est calculé pour le plus haut et le plus bas niveau du paléolac. Ce traitement combiné à la contribution massive du Nord dans le bilan hydrique dès lors que l'on envisage une augmentation globale des précipitations, fait que les ΔP du chapitre 6 sont très inférieurs à ceux calculés dans le chapitre 7. En effet, dans ce chapitre, nous identifions des moraines synchrones du Taucá. Une fois qu'elles sont considérées comme telles, le calcul ne prend plus en compte le fait que la barre d'erreur associée à l'âge de ses moraines peut empiéter en dehors du haut niveau lacustre.

Pour remédier à ces difficultés, plusieurs solutions peuvent être mises en place. Pour la barre d'erreur des âges, une première solution peut être de mesurer de nouveaux âges sur les moraines pour mieux les contraindre. Pour les autres problèmes, il faut réussir à mettre en place une méthode qui résout localement les ΔP vs. Présent. Pour cela, plusieurs possibilités complémentaires peuvent être envisagées :

- Dater des petits lacs à proximité des glaciers pour lesquels le bilan hydrologique aura des implications locales uniquement. En utilisant la méthode glacier-lac dans une telle configuration, on résout localement les précipitations et les températures et si la démarche est généralisable à chaque site, on a à la fois la variabilité spatiale et temporelle des 2 variables climatiques.
- Améliorer le modèle de glacier de manière à ce qu'à lui seul il permette de résoudre les précipitations et les températures localement. Ce projet a été envisagé pendant un moment au cours de cette thèse mais n'a pas été entamé par manque de temps. Il faudrait pour cela utiliser un code d'écoulement de la glace suffisamment performant pour discriminer les flux de glace différents associés à différentes hauteurs de la langue glaciaire (hauteurs qui seraient extrapolées depuis les morphologies glaciaires). Pour le modèle d'ablation, compte tenu des difficultés rencontrées par les modèles type PDD dans les Andes, un modèle type bilan d'énergie simplifié serait probablement plus souhaitable. Il introduirait un terme de sublimation (perte de chaleur latente) qui serait souhaitable compte tenu de l'importance actuelle de l'ablation sur les glaciers boliviens (Wagon et al., 2001). Il faudrait pour cela essayer d'utiliser le modèle utilisé par Malone et al. (2015) ou celui proposé par Rupper and Roe (2008). Un tel chantier est ambitieux mais peut s'avérer particulièrement intéressant et fructueux.

Un des principaux résultats de ces travaux de thèse porte donc sur l'importance de la modification des régimes de vents dans les perturbations climatiques majeures observées sur l'Altiplano. Il semble que l'intensité et la position des vents jouent un rôle majeur dans les réorganisations climatiques globales observées à la fin du Pléistocène (Denton et al., 2010; Toggweiler, 2009). De même que nous l'avons rapporté, les modifications des circulations atmosphériques dans l'hémisphère Sud sont souvent observées comme des conséquences des modifications globales du climat initiées dans l'hémisphère Nord et liées à la croissance des calottes et à des ralentissements de la circulation thermohaline.

De tels événements caractéristiques d'un refroidissement dans l'hémisphère Nord ont pour conséquence une déflexion vers le Sud de la zone de convergence intertropicale (Peterson, 2000; Zhang and Delworth, 2005) et une perturbation des systèmes de mousson (Han et al., 2015; Pausata et al., 2011; Sirocko et al., 1996; Wang et al., 2007). On observe également des réorganisations encore plus au sud avec une déflexion des westerlies de l'hémisphère Sud vers le Sud (Montade et al., 2015) et des épisodes froids rapides au sud du Chili synchrone de ceux de l'hémisphère Nord pour lesquels une connexion atmosphérique est la plus probable (Moreno et al., 2001).

Une explication de cette connectivité atmosphérique Nord-Sud est expliquée par Chiang et al. (2014). Il propose que les déflexions de la zone de convergence intertropicale s'accompagnent de modifications du parcours des Jet streams sub-tropicaux (notamment l'affaiblissement du phénomène de partage du jet Sud Pacifique) qui aboutit aux perturbations rapportées sur les westerlies. Une telle explication est d'ailleurs cohérente avec les observations actuelles sur les rôles de la fusion et de la séparation des jets dans l'initiation et la fin de la mousson sud américaine (Zhou and Lau, 1998). Il existe donc un ensemble d'observations et de mécanismes cohérents qui permettent de considérer les variations de régimes de vents et de circulations atmosphériques telles qu'observées dans cette thèse, comme une conséquence, en bout de chaîne des modifications globales du climat initiées dans l'Atlantique Nord.

Dans une autre perspective, certaines théories placent les modifications de la position et de la vitesse des vents parmi les initiateurs des changements climatiques dans l'hémisphère Nord mais aussi dans

l'hémisphère Sud. Dans l'hémisphère Nord, Wunsch (2006) développe l'idée que (i) les vents sont les principaux moteurs des circulations océaniques globales comme les gyres océaniques, (ii) la hauteur et l'étendue des calottes arctiques influencent la position des westerlies de l'hémisphère Nord. Il propose donc que les variations des westerlies soient le levier par lequel les changements de la taille des calottes de l'Hémisphère Nord entraînent des modifications globales du climat, des circulations océaniques et des différentes réorganisations observées sur le Globe. Il assoit cette hypothèse en constatant que la stabilité climatique de l'Holocène s'est installée quand les calottes de l'hémisphère Nord ont régressé (disparition des calottes Laurentide et Fennoscandienne). Ce lien possible entre hauteur de la calotte, répartition des vents et changements globaux a d'ailleurs été observé dans des travaux de modélisation (Zhang et al., 2014).

Dans l'Hémisphère Sud, Toggweiler (2009) propose qu'un déplacement vers le Sud des westerlies induise un effet de ventilation de l'Océan Sud responsable d'un relargage de dioxyde de carbone. Ce relargage amène à un réchauffement, qui renforce le déplacement des westerlies et l'effet de ventilation. Ce feedback positif entre les vents et le dioxyde de carbone serait l'effet "boule de neige" qui initie une oscillation climatique globale. Des travaux de modélisation (Banderas et al., 2014) ont mis en évidence l'influence de ces deux variables sur l'Océan Sud et leur rôle dans le comportement oscillatoire de l'activité de la circulation thermohaline. De tels mécanismes montrent également une bonne cohérence avec des réinterprétations des données de carottes de glace (Buizert and Schmittner, 2015). Ces résultats mettent en lumière un contrôle de la dynamique des événements de Dansgaard-Oeschger par le climat antarctique, les circulations dans l'Océan Sud et la position des westerlies Sud.

Il y a donc deux positionnements au sein de la chaîne d'évènements affectant la machine climatique au cours des oscillations de la fin du Pléistocène pour les modifications du régime des vents dans l'Hémisphère Sud :

- Une position en bout de chaîne pour laquelle les vents dans l'hémisphère Sud répondent à une cascade de perturbations océaniques et atmosphériques initiées dans l'Atlantique Nord et propagées via les phénomènes atmosphériques globaux (zone de convergence intertropicale, jet streams)
- Une position en amont de la chaîne, parmi les processus initiateurs, avec l'augmentation du dioxyde de carbone. Deux phénomènes qui attribuerait à l'Océan Sud un rôle de contrôle du comportement de la circulation thermohaline.

Une telle diversité des théories est peut être due au manque d'un proxy précis des changements des vents et à une connaissance encore insuffisante des paléoclimats et des mécanismes à l'œuvre lors de ces changements globaux. Elle montre que des pièces du puzzle sont encore à apporter. Elle témoigne également de la richesse et de la complexité fascinante des rouages de la machine climatique.

Chapitre 9

Annexes

Sommaire

9.1	Personal Contribution	248
9.1.1	Sampling	248
9.1.2	Sample preparation and measurements	248
9.1.3	Other contribution	248
9.1.4	Co-authorship	248
9.2	Agés d'exposition à Chiar-Khota	249
9.3	Collaborations	252
9.3.1	Blard et al. (2014)	252
9.3.2	Jomelli et al. (2014)	267
9.3.3	Delunel et al. (2016)	286
9.3.4	Zumaque et al. (Submitted)	305

9.1 Personal Contribution

As this manuscript gathers works of many people, I considered useful to precise my contribution to the different effort that permitted the redaction of this thesis.

9.1.1 Sampling

The new results presented in the different chapters of the manuscript come from different sampling campaigns. I only took part of the 2013 field trip. The corresponding samples can easily be identified as their names all include the index 13. During this trip, we completed the sampling of the Zongo Valley, the Cerro Tunupa, the Azanaques fan-delta, and sampled the bioherms on Isla Incahuasi (Chapter 6).

The 2013 sampling campaign was realized with Pierre-Henri Blard (referred farther as PHB), Véronique Mariotti, Maarten Lupker and Abdul Castillo. The former missions involved Jérôme Lavé, Julien Charreau, Thomas Condom, Nestor Jimenez, Victor Ramirez, Vincent Jomelli and Daniel Brunstein.

9.1.2 Sample preparation and measurements

I prepared the new Zongo valley samples, except those of the CQ3 and CQ4 moraines. I also prepared the Sajama, Pikacho, Chiar Khota and the Tunupa (TU-13-X only) samples. For Azanaques, I prepared those for which the Table 2 of the chapter 4 indicates CRPG as preparation lab. I measured all the ^3He samples I prepared. This was done at the CRPG Noble Gas Lab. The complementary chemical analyses for ^3He corrections were performed by the SARM at the CRPG. The ASTER Team (at the CEREGE) measured the ^{10}Be samples.

The preparation of the other samples involved PHB, Jérôme Lavé, Vincent Jomelli, Daniel Brunstein, Camille Hautefeuille, Benjy Barry, Gabino Fabrizio Delgado Madera, Elsa Mondon, Eva Leriche et Yoann Jacquin.

9.1.3 Other contribution

I developed the CREp program, but not the web developing, performed by Vivien Laurent. I transformed my code accordingly to his indications, so as the web interface and Octave could communicate via special data format. PHB, Greg Balco and Nat Lifton did the online production rate database. The CREp website was designed by Eric Mory.

I calculated the different exposure ages, did the Azanaques calibration study, the different moraines cartography, the ELA calculations, the climatic inversions. For the Lake model, I brought several amendments to the version of PHB, which was used in [Blard et al. \(2009\)](#). I wrote the articles in chapter 4, 6 and 7 and benefited of the corrections from PHB and Jérôme Lavé (and other writers for the chapter 4). The chapter 5 was co-written by PHB and me.

9.1.4 Co-authorship

For the article where I appear as co-author (enclosed in the Appendix), my contributions are :

- Blard et al. (2014) : CRE age calculations.
- Jomelli et al. (2014) : compilation of the CRE age data in the tropical Andes (along with PHB), homogenous re-calculation of these ages with up to date production rates.
- Delunel et al. (Submitted) : Production rate calculations for the San Pedro ^3He production rate. Homogenous global recalculation of all published ^3He production rates used for the discussion. Writing of a few paragraphs and contribution to subsequent corrections for reviews.
- Zumaque et al. (Submitted) : Help on the development of the paleomagnetic calculations in the program.

9.2 Ages d'exposition à Chiar-Khota

Afin de pouvoir proposer davantage de contraintes paléoclimatiques sur l'Altiplano, des âges d'exposition ont été établis dans une vallée du volcan Chiar-Khota. C'est un stratovolcan andésitique situé à une dizaine de km au Sud du bassin de l'Altiplano (Figure 9.1). Il culmine à 5800 m, son sommet présente des endroits d'enneigement persistant mais pas de glacier. En revanche, ses flancs portent les reliques d'une activité glaciaire passée intense. Dix huit blocs morainiques ont été échantillonnés dans une vallée orientée Nord pour déterminer leur concentration en ^3He dans les pyroxènes. Trois moraines ont été échantillonnées en commençant par M1 qui indique le maximum de l'extension glaciaire (Figure 9.2). Deux roches moutonnées (CHK-11-09 et 10) ont également été échantillonnées en amont de la vallée.

Les résultats des datations se sont avérés très décevants. Les âges présentent une forte dispersion vers des âges vieux caractéristique du biais du à l'héritage (Figure CK3). Cette situation est probablement due au fait que la vallée est orientée Nord, ce qui correspond donc à un adret dans l'hémisphère Sud. La fonte induite par les radiations solaire a probablement limité la croissance de la langue glaciaire et par la même son pouvoir érosif. L'abrasion lors des avancées récentes n'a ainsi pas permis de "remettre à zéro" les concentrations en ^3He des morphologies glaciaires. J'ai souhaité présenter ces résultats dans ce manuscrit à titre informatif. (Tableau 9.1).

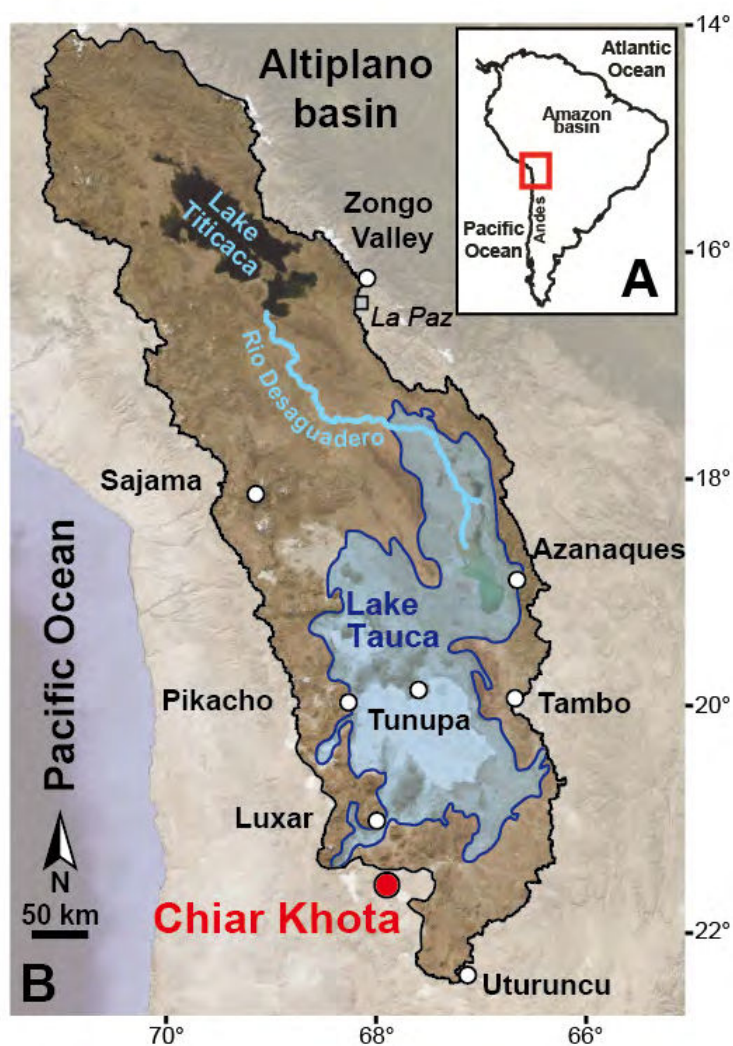


FIGURE 9.1 : Localisation du volcan Chiar-Khota.

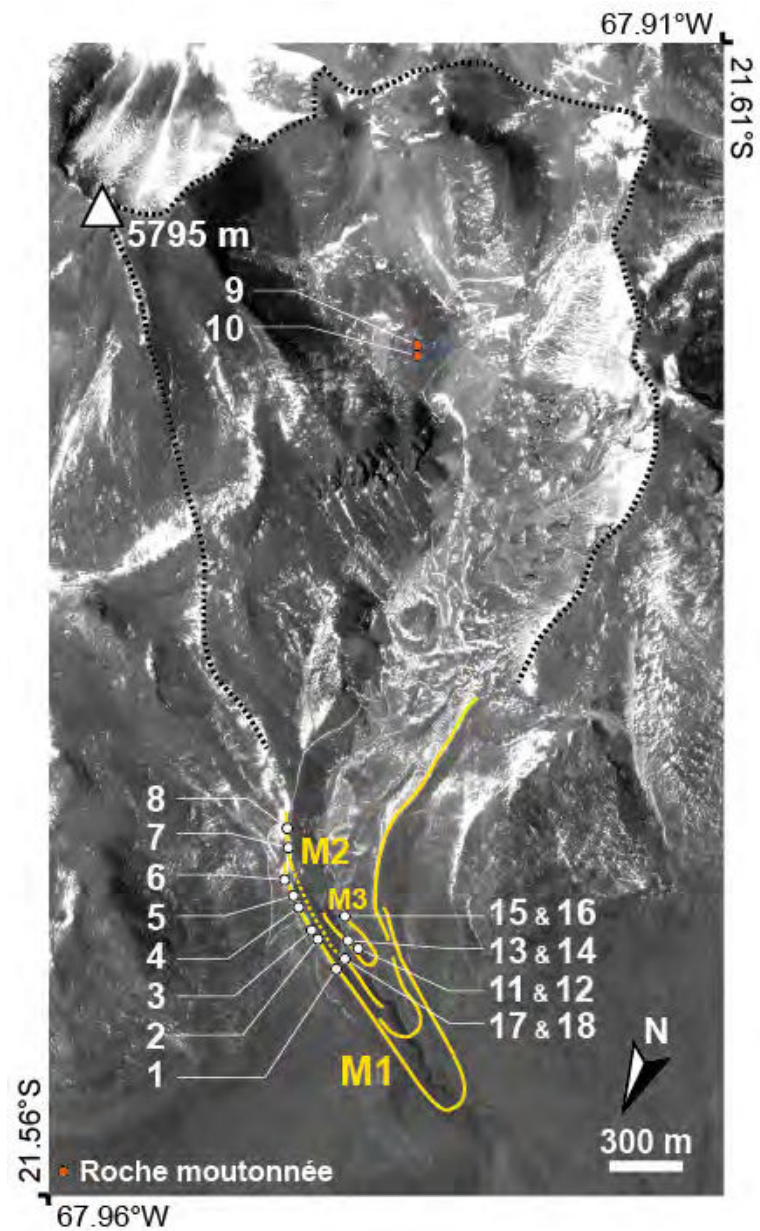


FIGURE 9.2 : Localisation des moraines et des échantillons à Chiar-Khota. Les lignes jaunes indiquent les moraines, les pointillés noirs, la limite du bassin versant.

Glacial Feature	Sample	Latitude Dec°	Longitude Dec°	Altitude masl	Pyroxene Color	Li ^a ppm	Eruption age ^b Ma	Pn ^a at.g ⁻¹ .yr ⁻¹	³ He _n ^b 10 ⁵ at.g ⁻¹	³ He _c (1σ) ^c 10 ⁷ at.g ⁻¹	Thickness cm	Thick. Corr. ^d	Shielding	Scaling Factor ^e	Age (1σ) ^f ka
	CHK-11-01	-21.5768	-67.9698	4755	Green	56	1.0	1.0136	10.25	3.47 ± 0.15	3.3	0.97	1.00	13.07	20.49 ± 0.94
	CHK-11-02	-21.5779	-67.9686	4794	Green	54	0.7	0.9965	7.14	15.22 ± 0.43	1.1	0.99	1.00	13.82	83.49 ± 4.09
	CHK-11-03	-21.5780	-67.9685	4797	Green	63	0.9	1.1197	9.94	11.67 ± 0.31	2.2	0.98	1.00	14.08	63.41 ± 2.75
M1	CHK-11-04	-21.5789	-67.9676	4815	Black	96	0.7	1.8097	12.97	9.04 ± 0.14	2.2	0.98	1.00	14.53	47.60 ± 2.35
	CHK-11-04-R	-21.5789	-67.9676	4815	Green	21	0.8	0.3958	3.23	7.81 ± 0.24	1.1	0.99	1.00	14.37	41.17 ± 1.07
	CHK-11-05	-21.5792	-67.9673	4828	Black	56	1.7	1.1553	20.08	4.25 ± 0.13	1.0	0.99	1.00	13.52	23.83 ± 1.25
	CHK-11-06	-21.5798	-67.9668	4841	Green	51	0.5	1.1455	5.57	4.94 ± 0.17	2.8	0.98	1.00	13.83	27.44 ± 1.14
	CHK-11-07	-21.5810	-67.9665	4856	Black	135	1.8	2.7904	51.56	3.56 ± 0.12	2.8	0.98	1.00	13.62	20.12 ± 0.80
	CHK-11-07-R	-21.5810	-67.9665	4856	Green	59	1.9	1.2195	23.00	3.26 ± 0.11	2.8	0.98	1.00	13.39	18.71 ± 0.73
M2	CHK-11-08	-21.5818	-67.9663	4898	Black	89	1.3	1.8786	24.28	22.75 ± 0.50	1.5	0.99	1.00	14.96	115.66 ± 4.02
	CHK-11-17	-21.5773	-67.9701	4735	Green	17	0.4	0.3152	1.34	14.17 ± 0.48	3.3	0.97	1.00	13.49	81.13 ± 4.30
	CHK-11-18	-21.5773	-67.9701	4730	Green	50	1.0	0.9739	10.10	3.13 ± 0.11	2.0	0.98	1.00	12.68	18.84 ± 0.74
	CHK-11-11	-21.5780	-67.9703	4736	Black	167	1.8	3.3068	61.17	23.57 ± 0.49	3.5	0.97	1.00	13.96	130.53 ± 5.33
	CHK-11-13	-21.5781	-67.9700	4737	Black	92	2.1	1.8317	38.30	4.58 ± 0.15	1.0	0.99	1.00	13.09	26.51 ± 0.99
M3	CHK-11-14	-21.5781	-67.9700	4737	Green	93	0.4	1.9307	7.49	3.20 ± 0.13	2.8	0.98	1.00	12.79	19.25 ± 0.84
	CHK-11-15	-21.5790	-67.9695	4759	Black	35	1.2	0.7153	8.84	2.46 ± 0.10	1.0	0.99	1.00	12.32	15.15 ± 0.65
	CHK-11-16	-21.5790	-67.9695	4760	Black	103	2.6	1.8710	49.57	8.75 ± 0.23	1.5	0.99	1.00	14.25	46.71 ± 2.46
Roches	CHK-11-09	-21.6003	-67.9658	5335	Green	67	1.3	1.4406	18.82	12.64 ± 0.33	5.5	0.95	1.00	17.63	56.39 ± 2.38
Moutonnées	CHK-11-10	-21.6002	-67.9658	5332	Black	45	2.2	0.9153	20.36	5.75 ± 0.17	5.5	0.95	1.00	16.98	26.66 ± 0.96
	CHK-11-10-R	-21.6002	-67.9658	5332	Green	73	1.1	1.4848	16.78	8.58 ± 0.20	5.5	0.95	1.00	17.32	38.98 ± 1.13

R replicate. Replicates have been used to compare ³He concentrations from black and green pyroxenes

^a (U-Th-Sm)/⁴He age

^b He_c = He_{tot} - He_n - He_m (we considered He_m = 8.5 × 10⁴ at.g⁻¹ for all samples)

^c Calculated with a density of 2.7 g.cm⁻³ and an attenuation length of 160 g.cm⁻²

^d Shielding for samples from this study is negligible

^e Global scaling factor that accounts for the geomagnetic correction

^f SLHL PR: 136.2 ± 4.5 at.g⁻¹.yr⁻¹ (Bard et al. (2013a) and Delunel et al. (In Prep)) - Scaling scheme: Lal modified - Atmosphere: ERA40 - VDM: Muscheler et al. (2005)

TABLE 9.1 : Résultats d'âges d'exposition pour le volcan Chiar-Khota.

9.3 Collaborations

9.3.1 Déglaciation à Cerro Uturuncu

Ces travaux de thèse m'ont permis de collaborer à l'étude des glaciations du volcan Cerro Uturuncu dont la localisation et certains résultats sont présentés dans le chapitre 4 (Blard et al., 2014). Cette étude montre que l'Uturuncu a enregistré un Dernier Maximum Glaciaire local (DMG local) à 65 ka, c'est à dire bien avant le DMG global autour de 20 ka. Le glacier de l'Uturuncu est par la suite resté proche de cette extension maximale, comme indiqué par des stabilisations notables à 40, 35 et 17 ka. S'en suit une récession jusqu'à une nouvelle stabilisation synchrone du lac Tauca qui est utilisée dans le chapitre 7.

J'ai contribué à cette étude en calculant les âges d'exposition présentés.

Cette étude a fait l'objet d'une publication dans la revue Quaternary Research.



Contents lists available at ScienceDirect

Quaternary Research

journal homepage: www.elsevier.com/locate/yqres

Progressive glacial retreat in the Southern Altiplano (Uturuncu volcano, 22°S) between 65 and 14 ka constrained by cosmogenic ^3He dating

Pierre-Henri Blard ^{a,*}, Jérôme Lave ^a, Kenneth A. Farley ^b, Victor Ramirez ^c, Nestor Jimenez ^c, Léo C.P. Martin ^a, Julien Charreau ^a, Bouchaïb Tibari ^a, Michel Fornari ^d

^a CRPG, UMR7358, CNRS, Université de Lorraine, Vandoeuvre les Nancy, France

^b Division of Geological and Planetary Sciences, California Institute of Technology, Pasadena, CA, USA

^c Universidad Mayor de San Andrés, La Paz, Bolivia

^d IRD, Université de Nice, France

ARTICLE INFO

Article history:

Received 2 July 2013

Available online 20 March 2014

Keywords:

Altiplano

Uturuncu

Glaciations

Moraines

Cosmogenic ^3He

Equilibrium line altitude

Local last glacial maximum

Lake Tauca

ABSTRACT

This work presents the first reconstruction of late Pleistocene glacier fluctuations on Uturuncu volcano, in the Southern Tropical Andes. Cosmogenic ^3He dating of glacial landforms provides constraints on ancient glacier position between 65 and 14 ka. Despite important scatter in the exposure ages on the oldest moraines, probably resulting from pre-exposure, these ^3He data constrain the timing of the moraine deposits and subsequent glacier recessions: the Uturuncu glacier may have reached its maximum extent much before the global LGM, maybe as early as 65 ka, with an equilibrium line altitude (ELA) at 5280 m. Then, the glacier remained close to its maximum position, with a main stillstand identified around 40 ka, and another one between 35 and 17 ka, followed by a limited recession at 17 ka. Then, another glacial stillstand is identified upstream during the late glacial period, probably between 16 and 14 ka, with an ELA standing at 5350 m. This stillstand is synchronous with the paleolake Tauca highstand. This result indicates that this regionally wet and cold episode, during the Heinrich 1 event, also impacted the Southern Altiplano. The ELA rose above 5450 m after 14 ka, synchronously with the Bolling–Allerod.

© 2014 University of Washington. Published by Elsevier Inc. All rights reserved.

Introduction

The reconstruction of past fluctuations of mountain glaciers is a sensitive and useful means to constrain paleoclimatic evolution of high-altitude alpine regions where other paleoclimatic records are scarce (e.g. Gosse et al., 1995; Smith et al., 2005b; Schaefer et al., 2006; Blard et al., 2007; Licciardi et al., 2009). Indeed, alpine glaciers are very sensitive to both local and regional changes of atmospheric variables, mainly temperature and precipitation (Ohmura et al., 1992; Oerlemans, 2005). They also have the interesting ability to rapidly (in 25 to 100 years) adjust their mass balance to the local climate (Oerlemans, 2005).

It is particularly important to study the Quaternary evolution of mountain glaciers in the Tropical Andes (Rodbell et al., 2009). First, it is a key region that may potentially have a role in global climate through positive feedbacks (Leduc et al., 2007; Rodbell et al., 2009). Second, during the late Pleistocene, the Altiplano closed watershed recorded several well-dated lake-level fluctuations (Sylvestre et al., 1999; Placzek et al., 2006; Blard et al., 2011; Placzek et al., 2011). This is of major interest because coupling the chronology of

paleolake and paleoglaciers is a powerful method to reconstruct past precipitation and temperatures (Blard et al., 2009). Third is the relatively low precipitation in the Altiplano region (average is lower than $300 \text{ mm} \cdot \text{yr}^{-1}$). This characteristic increases the likelihood of preservation of cosmogenic inheritance due to pre-exposure, but it also induces low erosion rates and very good preservation of glacial landscapes.

Consequently, exposure dating methods based on cosmogenic nuclides appear to be well suited and applicable in this region, even for moraines older than 100 ka (Smith et al., 2005a; Blard et al., 2009).

Several glacial chronologies based on cosmogenic dating have been proposed in different locations of the Central Tropical Andes area (Fig. 1) (Smith et al., 2005b; Zech et al., 2006, 2007; Blard et al., 2009; Bromley et al., 2009; Smith et al., 2009; Zech et al., 2009, 2010; Smith et al., 2010; Blard et al., 2013a). However, many areas remain unstudied, and this lack of data makes it difficult to establish a robust and integrated scenario of the deglaciation of this region. Many of the undated glaciated locations were developed on andesitic volcano summits where the petrology lacks quartz, which does not permit the use of the standard ^{10}Be dating method. However, these relatively young lavas ($<5 \text{ Ma}$) (Villeneuve et al., 2002) contain pyroxene, a mineral that is well suited for cosmogenic ^3He ($^3\text{He}_c$) dating (Ackert et al., 2003; Blard et al., 2005, 2009; Bromley et al., 2009).

In this study we present the first glacial chronology from Uturuncu volcano (Southern Altiplano, 22.27°S, 67.19°W) based on cosmogenic

* Corresponding author at: CRPG, 15 rue Notre Dame des Pauvres, 54501 Vandoeuvre lès Nancy, France.

E-mail address: blard@crpg.cnrs-nancy.fr (P.-H. Blard).

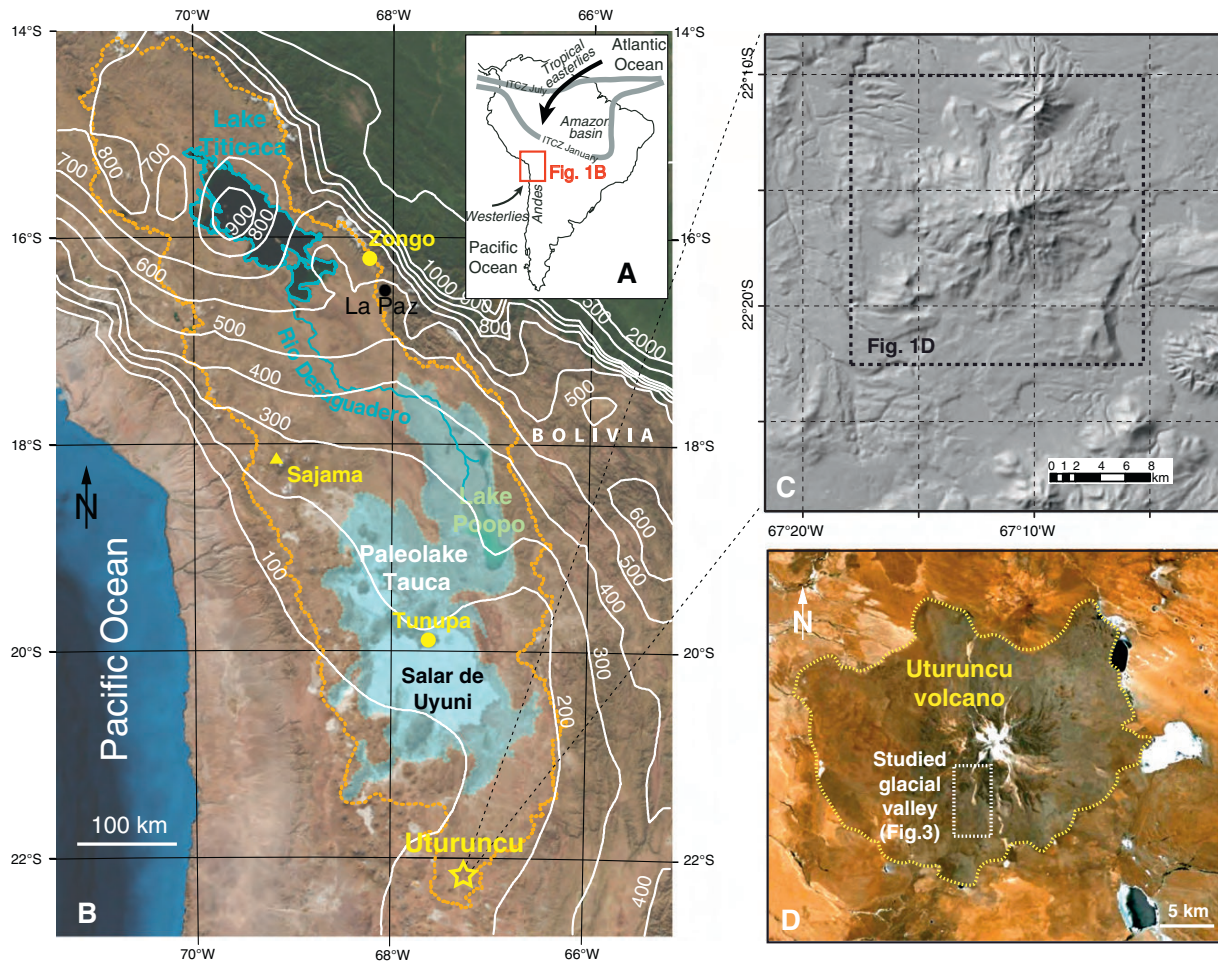


Figure 1. A) Map of South America. B) Landsat picture of the Altiplano region. White lines represent isoprecipitation curves (precipitation in mm/yr). Orange line is the limit of the Altiplano endorheic watershed. Lake Tauca extent is shown at 15.5 ka, corresponding to a lake surface elevation of 3770 m (Blard et al., 2011). C) Shaded topography of the Uturuncu volcano. D) Satellite photograph of the Uturuncu volcano. Panel C is from Aster DEM. Panel D is from Google Earth.

^3He exposure dating of moraines and striated bedrock (roches moutonnées). As these ages are calculated using the locally calibrated $^3\text{He}_c$ production rate (Blard et al., 2013a), the absolute uncertainty of these exposure ages may be lower than 5%. This glacial record is then compared with glacier chronologies obtained elsewhere on the Altiplano (Smith et al., 2005b; Blard et al., 2009; Zech et al., 2009), as well as with paleolake fluctuations observed in the endorheic Altiplano watershed (Placzek et al., 2006; Blard et al., 2011). Finally, we discuss the broader paleoclimatic implications of the Uturuncu paleoglaciers record. Some of the Uturuncu boulder samples, being rich in quartz, have also been used to calibrate the production ratio of ^3He in pyroxene against ^{10}Be in quartz. These results are presented in a companion paper (Blard et al., 2013b).

Regional and geological settings

Climate of the Southern Altiplano Lipez

Uturuncu volcano (22.27°S, 67.19°W) is located in the Lipez area, in the most southern part of the Bolivian Altiplano (Fig. 1). Present-day temperature and precipitation records are scarce in the southernmost part of Altiplano, but the few available records (Ammann et al., 2001; Blard et al., 2011) indicate very dry condition, with precipitation lower than $100 \text{ mm} \cdot \text{yr}^{-1}$ (New et al., 2002). Indeed, the main source of

moisture on the Altiplano originates from the Amazonian basin. This air transport toward the southwest creates a strong decreasing precipitation gradient over the Altiplano (Fig. 1) and, therefore, dry conditions in the Lipez area (Garreaud et al., 2009).

The 0°C annual isotherm is located at 5000 m (Ammann et al., 2001; Kull et al., 2008), but there are no glaciers today at the top of Uturuncu and surrounding summits (Fig. 2). This indicates that the present equilibrium line altitude (ELA) is above the summit of Uturuncu (6006 m). This is caused by a very low snow input. This mass balance configuration is characteristic of glaciers that are so-called “precipitation-limited” (Ammann et al., 2001; Kull et al., 2008): even small changes in precipitation will induce a significant ELA shift.

Geology of Uturuncu volcano

The geology of Uturuncu volcano has been thoroughly described by Sparks et al. (2008), who reported a suite of petrographic and geochemical observations along with $^{39}\text{Ar}/^{40}\text{Ar}$ ages. These authors describe Uturuncu as a dormant stratovolcano (more than 2000 m tall, 85 km^3) built by a succession of dacitic lava domes and flows. This volcanic material is mainly porphyritic dacite (SiO_2 64–68%), rich enough in pyroxene to yield a sufficient abundance of phenocrysts for cosmogenic ^3He dating. 50 mg of pyroxene is necessary to yield an analytical uncertainty



Figure 2. View of Uturuncu volcano. Photograph taken from the NW.

lower than 5%. ^{39}Ar – ^{40}Ar dating indicates that the main eruption events occurred between 271 and 890 ka (Sparks et al., 2008).

Geomorphic mapping and sampling of the Uturuncu southern glacial valley

The studied paleoglacial valley is situated on the southern flank of the volcano. Detailed geomorphologic mapping and identification of glacial features were based on field observations and aerial photo analysis (Figs. 3 and 4). This former glacial valley is characterized by very limited incision: the elevation difference between the bottom and the shoulders of the U-shaped valley is less than 100 m. Such limited glacier incision probably arises from very low ice flux as a consequence of weak snow accumulation. In the southern distal part of the valley, five successive frontal and lateral moraines have been identified (M1 to M5) (Figs. 3 and 4). M1 is the most distal moraine and ranges from 4800 to 4850 m elevation. The stratigraphic relationships indicate that M2 to M5 are recessional moraines.

The M1 moraine is characterized by a very wide and flat frontal depositional zone with two small internal crests. Its smooth geometry corresponds to a suite of imbricate moraine loops with topographic expression altered and smoothed by surface processes, or, alternatively, by a posterior glacier readvance.

The M2 moraine, representing the proximal northern part of this flat and smooth surface, displays clear and prominent ~10 m wide and 2–4 m high frontal and lateral ridges. These observations indicate that the M2 frontal moraine postdates M1 and that the glacier at that time was slightly overriding or coalescing the older M1 moraine. The M3 and M4 moraines are imbricate recessional glacial deposits with poorly expressed topography and morphology. Finally, moraine M5 represents the youngest episode of moraine construction with a clear arcuate shape and a 2–4 m high ridge. All these moraines are characterized by smooth crests, with a maximum of 5 m in height. On these ridges, large boulders (>1 m in size) are ideal targets for cosmogenic exposure dating. Indeed, large boulders are generally less impacted by the deflation of moraine surface. However, selecting large boulders does not prevent the possibility of cosmogenic inheritance due to previous exposure.

A total of 15 boulders and 6 roches moutonnées were sampled for cosmogenic ^3He dating (Table 1).

Eight boulders (UTU-7A, B, C, UTU-8A, B, C, D and UTU-9A) were sampled on moraine M1 and 4 boulders (UTU-6A, B, C, D) were collected on moraine M2 (Fig. 3, Table 1). To limit the impact of soil deflation, we focused our sampling on the larger boulders located at the top of the moraine ridges (Fig. 4). The typical height above the ground of the sampled boulder is more than 1 m (Fig. 5).

Upslope, two large whaleback-shaped roches moutonnées are visible, a few decameters north from the M4 moraine, at about 4820 m elevation (Fig. 3). These glacial features, developed on highly

fractured lava flows, clearly show well-preserved glacial striations parallel to the main slope of the valley. Two samples (UTU-5A, B) were collected from the top of these striated bedrock surfaces (Fig. 3, Table 1), at about 4820 m elevation. Samples were collected at the lower part of these roches moutonnées, where evidence of plucking suggests that at least ~50 cm of rock was removed during the last glacier advance. Although this is not enough to totally warrant pre-exposure, this precaution reduces the contribution of a potential cosmogenic inheritance.

Three boulders (UTU 3A, B and UTU-4) were sampled on the smooth M5 moraine ridge at 4990 m elevation (Figs. 3–5, Table 1).

Finally, the most upslope area of the valley displays large outcrops of striated bedrock from which we collected 4 samples (UTU-1A, B, C and UTU-2). UTU-2 is located on the eastern flank of the valley at 5004 m elevation on a large and relatively prominent roche moutonnée, while the 3 UTU-1 samples were collected further upslope (at about 5100 m elevation) on a highly fractured, plucked and striated bedrock area. Those striated rocks were exposed during the final deglaciation of the valley (Fig. 3, Table 1).

Cosmogenic ^3He dating

The cosmogenic method allows determination of the exposure age t of a geological sample that has been exposed to cosmic rays. This requires both a precise determination of the cosmogenic ^3He concentration ($^3\text{He}_c$) in the rock sample, as well as an independent, accurate and precise knowledge of the local production rate (P_3):

$$t = ^3\text{He}_c / P_3. \quad (1)$$

Cosmogenic ^3He and correction of the non-cosmogenic ^3He components

The in situ cosmogenic ^3He concentration needs to be measured in a mineral that is helium-retentive, such as pyroxene. ^3He being a stable isotope, it may originate from different sources in a pyroxene. A complete budget of the ^3He component of a lava phenocryst is thus necessary to calculate the cosmogenic ^3He ($^3\text{He}_c$) (Farley et al., 2006):

$$^3\text{He}_c = ^3\text{He}_{\text{total}} - ^3\text{He}_m - ^3\text{He}_n \quad (2)$$

where $^3\text{He}_{\text{total}}$ ($\text{at} \cdot \text{g}^{-1}$) is the total ^3He extracted by fusing the phenocrysts, $^3\text{He}_m$ ($\text{at} \cdot \text{g}^{-1}$) is the inherited (magmatic) component, and $^3\text{He}_n$ ($\text{at} \cdot \text{g}^{-1}$) is the nucleogenic component.

The $^3\text{He}_n$ has been accumulating in the pyroxene since the eruption of the lava flow and can be estimated as follows:

$$^3\text{He}_n = \int_0^{T_c} P_n \cdot dt \quad (3)$$

where P_n ($\text{at} \cdot \text{g}^{-1} \cdot \text{yr}^{-1}$) is the nucleogenic production rate of ^3He and T_c (yr) is the helium closure age of the mineral.

For each sample, we estimated P_n by applying the equations of Andrews and Kay (1982) and Andrews (1985) and using the Li concentration measured in the pyroxenes (Table 1) as well as the major and minor elements measured in the whole rock (Supplementary Table). These data are essential to evaluate the neutron flux.

Given the helium closure temperature of pyroxenes (Trull and Kurz, 1993), the $(\text{U}-\text{Th})/^4\text{He}$ age of the pyroxene phenocrysts, T_c , can be considered as similar to the eruption age of the lavas. The eruption was dated using the $(\text{U}-\text{Th})/^4\text{He}$ method, measuring the radiogenic ^4He ($^4\text{He}^*$) content of the phenocrysts, and the concentrations of U and Th in both the lavas and the phenocrysts. Indeed, radiogenic ^4He is mainly produced by the radioactive decay of ^{238}U , ^{235}U and

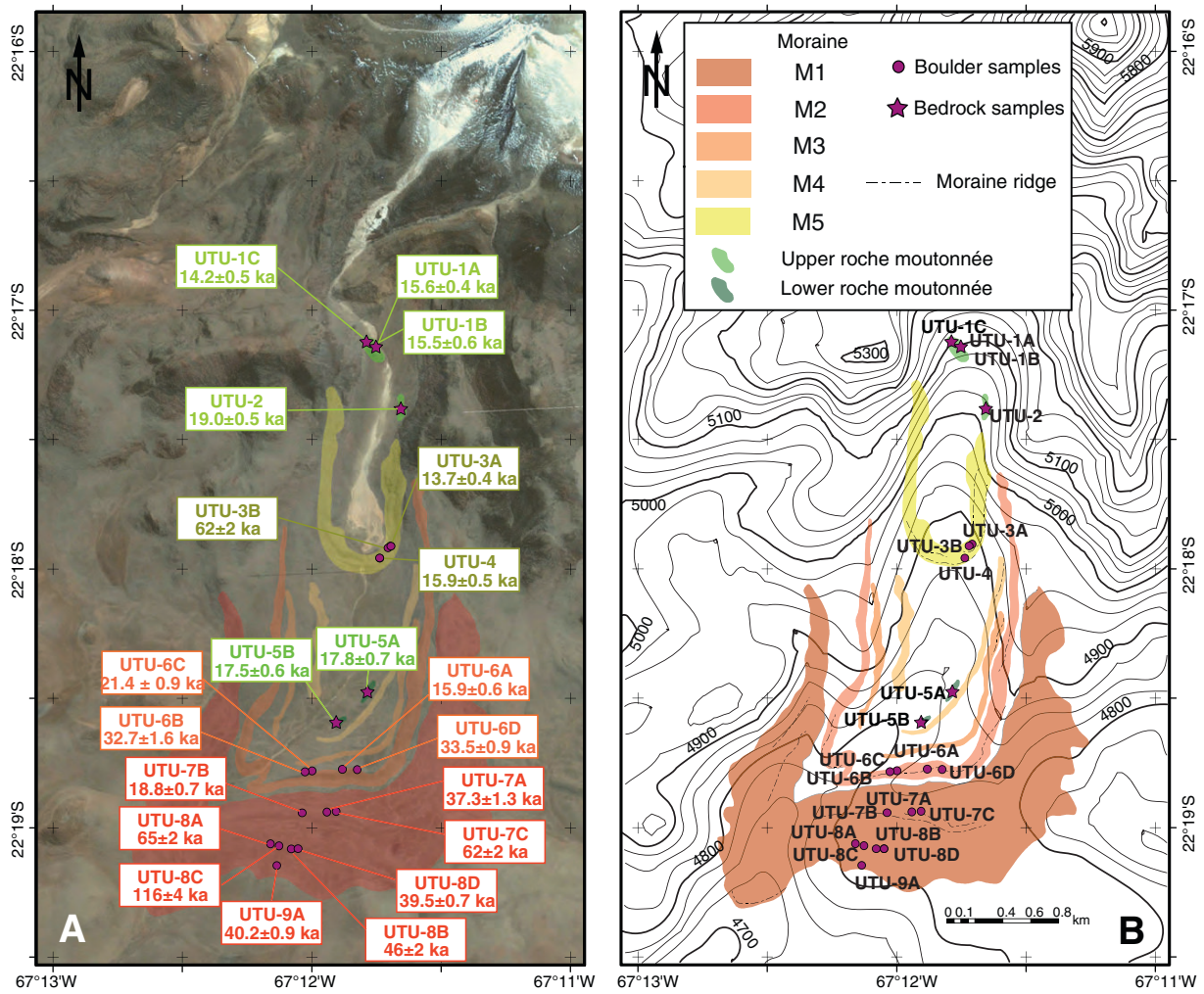


Figure 3. Map of the studied moraines, southern valley of Uturuncu volcano. Cosmogenic ³He ages are shown in panel A.

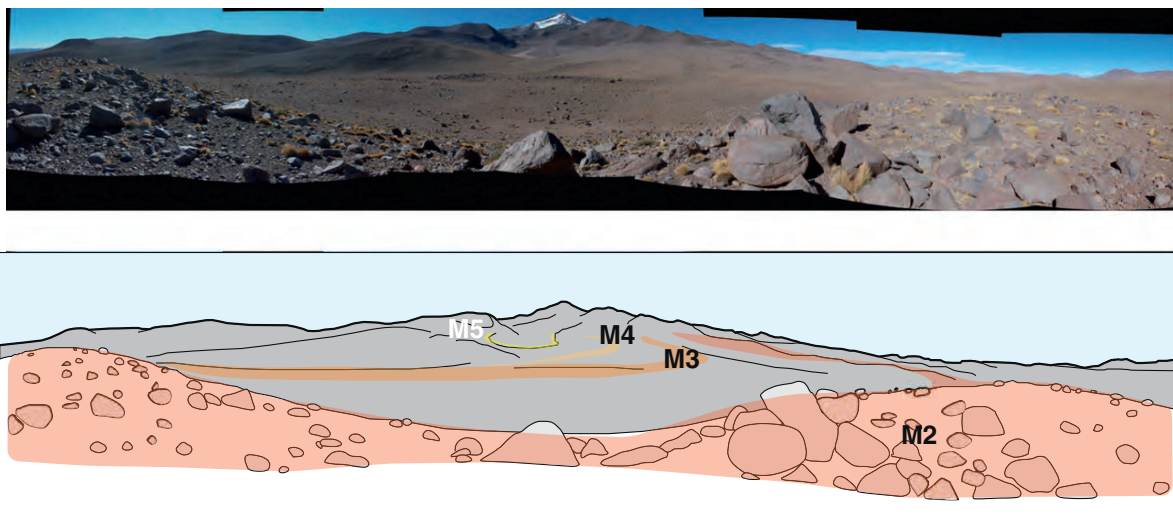


Figure 4. Panoramic view of the valley from the Uturuncu M2 moraine (toward the North).

^{232}Th . However, a proper estimate of the $^4\text{He}^*$ content needs also to include a correction of the magmatic ^4He component ($^4\text{He}_m$):

$$^4\text{He}^* = ^4\text{He}_{\text{total}} - ^4\text{He}_m. \quad (4)$$

The radiogenic $^4\text{He}^*$ production rate was calculated applying the equations described in Blard and Farley (2008) and Farley et al. (2006).

Sample treatment, measurements and helium results

All helium data are given in Tables 1, 2 and 3. We first isolated pure pyroxene phenocrysts by crushing the sampled rocks and applying successive physical separation techniques (magnet, heavy liquid). For each sample, we selected the most appropriate size fraction (typically from 0.2 to 1 mm, Table 1). The purity of each pyroxene sample was checked with a microscope. The pyroxene major-element composition was determined on each sample using an electronic microprobe (Supplementary Table).

^3He and ^4He analyses were performed in two different noble gas laboratories, Caltech and CRPG (Nancy), using three different mass spectrometers (Helix SFT and MAP at Caltech and Helix SFT at CRPG). The analytical procedures (gas extraction, purification, mass spectrometer measurement) were similar to those previously described (Farley et al., 2006; Blard et al., 2009; Zimmermann et al., 2012; Blard et al., 2013a). ^3He and ^4He blank corrections represent on average less than 1% and 4%, respectively, of the total helium released from the samples. Typical total uncertainties during an analytical session were 2% and 2.9% for ^4He and ^3He , respectively. Replicates measured in two different laboratories agree within uncertainties, indicating that CRPG and Caltech are correctly intercalibrated. Moreover, absolute comparison is obtained by measuring the ^3He concentration of the CRONUS-P pyroxene material during these analytical sessions: $4.85 \pm 0.06 \times 10^9 \text{ at} \cdot \text{g}^{-1}$ ($n = 8$) at Caltech and $4.93 \pm 0.04 \times 10^9 \text{ at} \cdot \text{g}^{-1}$ ($n = 8$) at CRPG.

The $^3\text{He}_m$ component can be estimated by prolonged vacuum crushing of the phenocrysts (Hilton et al., 1993; Scarsi, 2000; Blard et al., 2008). However, this technique may also cause partial loss of the matrix-sited helium components, i.e., $^3\text{He}_c$ and $^4\text{He}^*$ (Hilton et al., 1993; Scarsi, 2000; Yokochi et al., 2005; Blard et al., 2006). This estimate can thus be considered a maximum correction. A complementary approach is direct fusion of small phenocrysts (<500 μm diameter), which generally bear less fluid inclusions, and hence less magmatic helium than larger ones (Williams et al., 2005; Amidon et al., 2008; Blard et al., 2009). We applied both approaches in the present study, performing at CRPG a prolonged crushing (6 min, i.e. about 300 strokes) of 3 different samples (UTU-1B, UTU-3B, UTU-5A) ranging in size between 0.2 and 0.5 mm. The average $^3\text{He}_m$ concentration measured by this technique is $6 \pm 6 \times 10^4 \text{ at} \cdot \text{g}^{-1}$ (Table 2). For all the samples, this ^3He correction represents less than 1% of the total ^3He measured by fusing the phenocrysts. These primordial helium corrections are thus almost negligible, and induce an uncertainty on $^3\text{He}_c$ of less than 1%. Moreover, the measured $^3\text{He}_{\text{total}}$ concentrations obtained here by fusing pyroxene aliquots of different sizes show that the interaliquot variability is limited and lower than the total analytical uncertainty (Table 1). This strongly suggests that the magmatic ^3He correction is accurate and does not represent a significant source of uncertainty.

Similar to $^3\text{He}_m$, the amount of magmatic ^4He was constrained by vacuum crushing of the pyroxene samples UTU-1B, UTU-3B and UTU-5 during 6 min. The measured $^4\text{He}_m$ concentration is $8 \pm 6 \times 10^{10} \text{ at} \cdot \text{g}^{-1}$ (Table 2). This $^4\text{He}_m$ correction ranges between 0.3 and 16.4% of the total ^4He extracted by fusion. This induces an uncertainty lower than 12% on the estimated $^4\text{He}^*$. U–Th concentrations were measured in the pyroxenes and the surrounding lava by ICPMS, at SARM (CRPG). U and Th were not measured on the same aliquots as those used for $^4\text{He}^*$ determinations, which may be a significant source of uncertainty. Indeed, some samples exhibit a significant interaliquot

variability in (U–Th)/ $^4\text{He}^*$ age, which can be much larger than the propagated total uncertainty (Table 3).

These (U–Th)/ $^4\text{He}^*$ ages range between 0.09 ± 0.01 Ma (UTU-8A and UTU-7C) and 1.02 ± 0.1 Ma (UTU-2), for an average of ~ 0.4 Ma. Such ages are in good agreement with the previously reported K–Ar ages between 0.27 and 0.89 Ma (Sparks et al., 2008).

Lithium (Li) was measured in each pyroxene sample, with concentrations ranging between 15 and 28 ppm. The calculated P_n is from 0.19 to $0.45 \text{ at} \cdot \text{g} \cdot \text{yr}^{-1}$ (Table 1). Combined with the (U–Th)/ $^4\text{He}^*$ ages, these values imply that the $^3\text{He}_n$ concentration ranges from 0.4 to $2.9 \times 10^5 \text{ at} \cdot \text{g}^{-1}$ (Table 1). This correction represents between 0.1 and 1% of the total ^3He measured by fusing the pyroxene phenocrysts. Similar to the magmatic ^3He , this nucleogenic component has thus a minor impact on the $^3\text{He}_c$ ages.

$^3\text{He}_c$ production rate and exposure age calculation

Measured $^3\text{He}_c$ concentrations are corrected for sampling thickness. This correction ranges between 3 and 5% (Table 1). Topographic shielding estimated using the model of Dunne et al. (1999) is lower than 2% (Table 1). Snow cover is assumed negligible.

All exposure ages were then calculated using the cosmogenic ^3He production rate that was calibrated on the Altiplano, in the Tunupa volcano Pocolli fan (Blard et al., 2013a). The $^3\text{He}_c$ production rate obtained at this site (19.89°S, 67.62°W) is 999 ± 38 (1σ) $\text{at} \cdot \text{g}^{-1} \cdot \text{yr}^{-1}$, at 3800 m. This corresponds to a sea level high latitude rate of $121 \pm 5 \text{ at} \cdot \text{g}^{-1} \cdot \text{yr}^{-1}$ using the time-dependent scaling of Lal (1991) and Stone (2000). All Uturnuncu rates were derived from this locally calibrated production rate using the scaling model of Lal (1991) and Stone (2000), including a time-dependent correction based on the model of Nishiizumi et al. (1989) and the virtual dipole magnetic moment database of Muscheler et al. (2005). Existing scaling models yield significant scatter in the high tropics (Balco et al., 2008). However, the Tunupa calibration site is located only 200 km from Uturnuncu, at an elevation of 3800 m, slightly lower than the elevation range of the Uturnuncu glacial landforms, between 4800 and 5000 m. The divergence of the different scaling schemes over such a limited elevation range is therefore small, and the choice of the scaling scheme has only a limited impact on the uncertainty of the cosmogenic ^3He ages.

Some studies suggest that the capture of cosmogenic thermal neutrons by Li may exert a significant influence on the ^3He production rate in pyroxenes (Dunai et al., 2007; Amidon and Farley, 2011). However, as our dataset obtained on the Tunupa andesites did not show a detectable correlation between the cosmogenic ^3He and the Li concentration of co-genetic pyroxenes (Blard et al., 2013a), we decided not to make any Li-correction and used the local production rate determined from the pyroxene of the Tunupa calibration site.

It is important to correct for temporal variations of the production rate due to geomagnetic field fluctuations (Dunai, 2001; Masarik et al., 2001). Indeed, this correction is at a maximum in the tropics, a region where the cutoff rigidity is large (Dunai, 2001). We used here a version of the Stone (2000) scaling factor that incorporates the time dependent fluctuations of the Earth's magnetic field using the model of Nishiizumi et al. (1989) and the geomagnetic virtual dipole moment database (VDM) of Muscheler et al. (2005). This choice is justified by the recent work of Menabreaz et al. (2012), who demonstrated that atmospheric ^{10}Be records are the best VDM proxy.

At Uturnuncu (22°S, 4800 m), this time-dependent geomagnetic correction is minimal (<5%) for ages ranging between 14 and 18 ka, but it reaches up to 10% for ages older than 50 ka (Fig. 6). In order to evaluate the potential uncertainty attached to such a systematic correction, we compared two different time-dependent models (Nishiizumi et al., 1989; Dunai, 2001) and three different virtual-dipole-moment databases (Guyodo and Valet, 1999; Carcaillet et al., 2004; Muscheler et al., 2005). The six resulting correction curves are

Table 1
Samples characteristics and cosmogenic ^3He ages.

Sample	Object	Boulder height (cm)	Altitude (m)	Latitude (°S)	Longitude (°W)	Sampling thickness (cm)	Depth correction	Topographic shielding	Laboratory – mass spectrometer	Size (mm)	Mass (mg)	$^4\text{He}_t$ (10^{12} at \cdot g $^{-1}$)	$^3\text{He}_t$ (10^7 at \cdot g $^{-1}$)	Li (ppm)	P_n (at \cdot g $^{-1}$ yr $^{-1}$)	(U-Th)/ ^4He eruption age (Ma)	$^3\text{He}_n$ (10^7 at \cdot g $^{-1}$)	$^3\text{He}_c$ (10^7 at \cdot g $^{-1}$)	Exposure age (ka) ^a
<i>Uturuncu southern flank</i>																			
Upper "roches moutonnées"																			
UTU-1A	Striated bedrock	–	5097	22.28539	67.19605	5	0.95	0.98	Caltech – SFT	0.2–0.3	28.9	15.9 ± 0.2	2.76 ± 0.08	24	0.33	0.96 ± 0.1	2.7	2.73 ± 0.08	–
UTU-1A	Striated bedrock	–	5097	22.28539	67.19605	5	0.95	0.98	CRPG – SFT	0.3–0.5	31.5	10.8 ± 0.1	2.81 ± 0.09	24	0.33	0.66 ± 0.07	2.7	2.78 ± 0.09	15.6 ± 0.4
UTU-1B	Striated bedrock	–	5094	22.28539	67.19605	4	0.96	0.98	CRPG – SFT	0.2–0.4	87.4	23.7 ± 0.2	2.78 ± 0.07	19	0.28	0.59 ± 0.1	1.6	2.76 ± 0.07	15.5 ± 0.6
UTU-1C	Striated bedrock	–	5111	22.28522	67.19668	3	0.97	0.98	Caltech – MAP	0.3–0.6	46.2	9.0 ± 0.1	2.53 ± 0.07	23	0.33	0.40 ± 0.04	1.6	2.51 ± 0.07	–
UTU-1C	Striated bedrock	–	5111	22.28522	67.19668	3	0.97	0.98	Caltech – SFT	0.3–0.6	19.7	13.2 ± 0.1	2.55 ± 0.26	23	0.33	0.58 ± 0.1	1.6	2.53 ± 0.26	14.2 ± 0.5
UTU-2	Striated bedrock	–	5004	22.28978	67.19463	3	0.97	0.98	Caltech – SFT	0.2–0.3	75.9	13.8 ± 0.1	3.49 ± 0.07	20	0.29	1.02 ± 0.1	2.9	3.46 ± 0.07	–
UTU-2	Striated bedrock	–	5004	22.28978	67.19463	3	0.97	0.98	Caltech – MAP	0.3–0.5	34.8	1.62 ± 0.03	3.41 ± 0.1	20	0.29	1.02 ± 0.1	2.9	3.37 ± 0.1	19.0 ± 0.5
Recessional moraine M5																			
UTU-3A	Boulder	100	4885	22.29843	67.19512	5	0.95	1	Caltech – MAP	0.3–0.5	35.0	9.91 ± 0.21	2.2 ± 0.1	21	0.33	0.54 ± 0.06	1.6	2.13 ± 0.1	–
UTU-3A	Boulder	100	4885	22.29843	67.19512	5	0.95	1	Caltech – MAP	0.3–0.6	22.8	7.48 ± 0.08	2.24 ± 0.06	21	0.33	0.41 ± 0.04	1.3	2.23 ± 0.06	13.7 ± 0.4
UTU-3B	Boulder	140	4896	22.29856	67.19532	5	0.95	1	Caltech – SFT	0.4–1	46.5	3.67 ± 0.04	11.44 ± 0.12	24	0.34	0.15 ± 0.02	0.5	11.43 ± 0.12	61.5 ± 2.1
UTU-4	Boulder	140	4880	22.29933	67.19558	5	0.95	1	Caltech – MAP	0.3–0.5	43.5	3.94 ± 0.03	2.61 ± 0.07	25	0.33	0.33 ± 0.03	0.8	2.6 ± 0.07	–
UTU-4	Boulder	140	4880	22.29933	67.19558	5	0.95	1	CRPG – SFT	0.2–0.6	16.1	1.43 ± 0.1	2.68 ± 0.14	25	0.33	0.12 ± 0.02	0.8	2.67 ± 0.14	15.9 ± 0.5
Lower "roches moutonnées"																			
UTU-5A	Striated bedrock	–	4825	22.30772	67.19631	5	0.95	1	Caltech – MAP	0.3–0.5	28.6	1.96 ± 0.04	2.95 ± 0.09	19	0.31	0.12 ± 0.01	0.4	2.94 ± 0.09	17.8 ± 0.7
UTU-5B	Striated bedrock	–	4820	22.30991	67.19849	5	0.95	1	Caltech – MAP	0.3–0.6	31.9	3.48 ± 0.04	2.85 ± 0.08	23	0.37	0.17 ± 0.02	0.8	2.83 ± 0.08	–
UTU-5B	Striated bedrock	–	4820	22.30991	67.19849	5	0.95	1	CRPG – SFT	0.3–0.5	28.0	4.85 ± 0.04	2.93 ± 0.19	23	0.37	0.24 ± 0.02	0.8	2.91 ± 0.19	17.5 ± 0.6
Moraine M2																			
UTU-6A	Boulder	150	4827	22.31302	67.19997	4	0.96	1	Caltech – MAP	0.2–0.5	20.2	2.76 ± 0.03	2.61 ± 0.07	21	0.36	0.41 ± 0.04	1.5	2.59 ± 0.07	15.9 ± 0.6
UTU-6B	Boulder	200	4829	22.31308	67.20042	3	0.97	1	Caltech – MAP	0.2–0.5	37.2	0.63 ± 0.04	5.73 ± 0.15	28	0.40	0.16 ± 0.03	0.6	5.72 ± 0.15	32.7 ± 1.6
UTU-6C	Boulder	150	4832	22.31292	67.19801	4	0.96	1	Caltech – MAP	0.3–0.6	36.0	3.24 ± 0.03	3.71 ± 0.1	15	0.22	0.22 ± 0.02	0.5	3.7 ± 0.1	21.4 ± 0.9
UTU-6D	Boulder	70	4830	22.31294	67.19704	4	0.96	1	Caltech – MAP	0.3–0.6	36.5	0.62 ± 0.01	5.49 ± 0.15	27	0.41	0.15 ± 0.02	0.6	5.48 ± 0.15	–
UTU-6D	Boulder	70	4830	22.31294	67.19704	4	0.96	1	Caltech – MAP	0.3–0.5	31.6	1.09 ± 0.02	6.0 ± 0.2	27	0.41	0.27 ± 0.03	0.6	5.94 ± 0.24	–
UTU-6D	Boulder	70	4830	22.31294	67.19704	4	0.96	1	CRPG – SFT	0.2–0.3	35.2	1.35 ± 0.03	6 ± 0.14	27	0.41	0.26 ± 0.03	0.6	5.99 ± 0.14	33.5 ± 0.9
Terminal moraine M1																			
UTU-7A	Boulder	120	4818	22.31573	67.20060	4	0.96	1	Caltech – SFT	0.4–1	34.3	8.08 ± 0.08	6.5 ± 0.11	15	0.19	0.91 ± 0.09	1.7	6.48 ± 0.11	37.3 ± 1.3
UTU-7B	Boulder	100	4817	22.31567	67.19900	4	0.96	1	Caltech – SFT	0.4–1	51.3	2.41 ± 0.02	3.15 ± 0.08	27	0.45	0.14 ± 0.01	0.6	3.14 ± 0.08	18.8 ± 0.7
UTU-7C	Boulder	120	4817	22.31563	67.19840	4	0.96	1	Caltech – MAP	0.2–0.5	40.4	0.41 ± 0.03	11.4 ± 0.3	27	0.42	0.09 ± 0.02	0.6	11.41 ± 0.28	–
UTU-7C	Boulder	120	4817	22.31563	67.19840	4	0.96	1	CRPG – SFT	0.2–0.5	59.7	0.72 ± 0.02	10.9 ± 0.2	27	0.42	0.17 ± 0.02	0.6	10.91 ± 0.23	61.5 ± 1.6
UTU-8A	Boulder	250	4812	22.31786	67.20209	4	0.96	1	Caltech – SFT	0.4–1	35.5	0.62 ± 0.01	11.9 ± 0.1	26	0.41	0.09 ± 0.01	0.4	11.85 ± 0.12	64.9 ± 2.1
UTU-8B	Boulder	120	4812	22.31806	67.20131	4	0.96	1	Caltech – SFT	0.4–1	31.5	3.09 ± 0.03	8.6 ± 0.1	18	0.28	0.29 ± 0.03	0.8	8.61 ± 0.11	46.4 ± 2.2
UTU-8C	Boulder	100	4813	22.31807	67.20078	2	0.98	1	Caltech – SFT	0.4–1	27.3	1.59 ± 0.02	23.5 ± 0.2	16	0.23	0.48 ± 0.05	1.1	23.52 ± 0.24	116 ± 4
UTU-8D	Boulder	120	4813	22.31807	67.20078	4	0.96	1	Caltech – MAP	0.2–0.5	36.4	0.65 ± 0.04	7.1 ± 0.2	25	0.40	0.14 ± 0.02	0.9	7.1 ± 0.18	–
UTU-8D	Boulder	120	4813	22.31807	67.20078	4	0.96	1	Caltech – MAP	0.3–0.5	79.5	1.00 ± 0.02	6.8 ± 0.2	25	0.40	0.23 ± 0.03	0.8	6.8 ± 0.25	–
UTU-8D	Boulder	120	4813	22.31807	67.20078	4	0.96	1	CRPG – SFT	0.2–0.3	78.7	1.12 ± 0.02	6.96 ± 0.15	25	0.40	0.2 ± 0.02	0.9	6.95 ± 0.15	39.5 ± 0.7
UTU-9A	Boulder	50	4800	22.31983	67.20222	4	0.96	1	Caltech – SFT	0.4–1	50.4	0.78 ± 0.01	7.2 ± 0.1	22	0.32	0.16 ± 0.02	0.5	7.15 ± 0.09	40.2 ± 0.9

⁴He_t and ³He_t: total ⁴He and ³He extracted by melting.

P_n : production rate of nucleogenic ³He.

³He_n: nucleogenic ³He.

³He_c: cosmogenic ³He.

^a Weighted means are computed for samples with replicates.

plotted vs. time in Figure 6. This comparison shows that the agreement between these models is quite good (<10%) over certain periods of time, such as 0–20 ka. However, differences in these production rate corrections may reach up to 15% for other periods, for example between 40 and 60 ka. These discrepancies are mainly due to differences in the virtual dipole moment database, while the model has a smaller impact on the correction. It is beyond the scope of this study to decide which geomagnetic database is the most accurate. However, 15% should be considered as an upper limit of the uncertainty attached to this time-dependent correction. In the following, the provided age uncertainties do not include the uncertainty attached to the geomagnetic correction.

Results: cosmogenic ^3He ages

The cosmogenic $^3\text{He}_c$ ages of terminal moraine M1 (4810 m) are characterized by a large scatter, ranging between 18.8 ± 0.7 and 116 ± 4 ka. Excluding these two extreme ages, however, six boulders of M1 have ages between 37.3 ± 1.3 and 65 ± 2 ka.

The 4 ages from moraine M2 (4830 m) range from 15.9 ± 0.6 to 33.5 ± 0.9 ka. Two boulders (UTU-6B and UTU-6D) agree very well (~ 33 ka), but the scatter of the 4 ages of M2 prevents precise establishment of the age of deposition. It is important to note that this time range is younger than all but one of the $^3\text{He}_c$ ages of M1, which is in agreement with the stratigraphic order.

Lower roches moutonnées UTU-5A and UTU-5B (4820 m) have $^3\text{He}_c$ ages of 17.8 ± 0.7 and 17.5 ± 0.6 ka, respectively.

The 3 boulders of moraine M5 (4890 m) have $^3\text{He}_c$ ages of 13.7 ± 0.4 , 15.9 ± 0.5 and 62 ± 2 ka.

Finally, the upper roches moutonnées (5000–5100 m) yielded $^3\text{He}_c$ ages between 14.2 ± 0.5 and 19.0 ± 0.5 ka, with two samples (UTU-1A and 1B) clustering at $\sim 15.5 \pm 0.5$ ka.

Discussion

Interpretation of the glacial $^3\text{He}_c$ chronology: inheritance vs. erosion

This cosmogenic ^3He dataset provides the first absolute chronology for past-glaciation on Uturunco volcano. These exposure ages constrain the Late Pleistocene glacier fluctuations between 65 and 14 ka.

This dataset is characterized by a large scatter of the exposure ages obtained from each single moraine. This makes it difficult to establish a firm interpretation of the glacial chronology. However, after removal of the most probable outliers, each set has a relatively well-defined clustering. In summary, of the 15 boulders, 3 samples can be considered as outliers (UTU-3B, UTU-7B, UTU-8C), and, of the 6 roches moutonnées, only 1 sample (UTU-2) can be considered as an outlier.

From the method we applied here (vacuum crushing, determination of the $^3\text{He}_n$ by measuring the Li and the (U-Th)/ $^4\text{He}^*$ ages) we can firmly exclude that such dispersion arises from the magmatic or the nucleogenic ^3He components. Hence, we can conclude that this scatter is not analytical and more likely arises from geomorphological processes: pre-exposure of boulders (i.e. inheritance) or post-depositional mechanisms (i.e. erosion, exhumation or boulder rotation). The former may cause an overestimate of the actual exposure age, while the latter induces an underestimate of the true age.

Several studies have aimed at evaluating whether pre-exposure or erosion has the main impact on the accuracy of cosmogenic exposure ages. By analyzing a large dataset of boulder exposure ages from Tibet and Northern Hemisphere paleo-ice sheets, Heyman et al. (2011) have concluded that, for glacial boulders older than a few thousand years, post-depositional moraine degradation is the most important process leading to scatter in cosmogenic ages. If applicable to our samples, this would imply that the $^3\text{He}_c$ exposure ages of each glacial deposit should be considered as minimum ages.

However, the geomorphological and climatic contexts of the Uturunco site are quite different from those of the dataset analyzed by

Heyman et al. (2011). Several observations tend to suggest that Heyman et al.'s (2011) conclusion does not apply in the case of the Uturunco glacial sequence. First, the youngest ages obtained on each moraine are in stratigraphic order, within error bars (Figs. 3 and 7). For example, in the case of moraine M5, the two youngest dates among the three dated boulders are in agreement with the stratigraphic order defined by the bracketing roches moutonnées, i.e. a deposition age between 17 and 14 ka. Preferential post-depositional erosion or exhumation of moraine boulders would have disturbed such order. Second, for all the moraines, there is no correlation between boulder heights and observed $^3\text{He}_c$ exposure ages. This suggests that soil deflation was probably limited on the Uturunco moraines (Blard et al., 2007).

In contrast with Heyman et al.'s (2011) conclusion, we infer that, in this case, inheritance (pre-exposure) is the dominant process causing the spread of ages. First, the width and depth of the investigated glacial U-valley are small, which indicates that the paleo-glaciers of the Uturunco were characterized by a small ice flow. This observation is consistent with the present-day limited precipitation occurring in the Lipez area ($<100 \text{ mm}\cdot\text{yr}^{-1}$). A major consequence of a low ice flow is a limited eroding power of the glacier, which makes it more probable that the transported and deposited boulders had been previously exposed for a long period of time. Second, the $^3\text{He}_c$ ages obtained from roches moutonnées are much more clustered than the boulder ages determined on each moraine crest (Fig. 7). All the roches moutonnées but UTU-2 are located in the thalweg of the glacial valley, where the incision depth of the bedrock is maximum. At such a location, the probability of finding a surface with no prior exposure is higher. Additionally, there is no evidence for post-depositional erosion of the striated rocks on prominent roches moutonnées. On the contrary, moraine boulders have higher probability to have been exposed to cosmic rays before they have been carried and deposited by the glacier. Third, all the age distributions from each glacial object, except moraine M2, have a mode that does not coincide with the oldest age (Fig. 7). Indeed, several moraines (M1, M5) and the two roches moutonnées sites are characterized by $^3\text{He}_c$ modes that are similar or close to the younger age of the distribution. Although our dataset is too small to draw definitive conclusions, such distribution is quite similar to those that are characteristic of a pre-exposure signature (Applegate et al., 2010).

Finally, several previous cosmogenic dating studies carried out in the Andes have also concluded that the scatter of their dataset most probably resulted from the impact of pre-exposure inheritance rather than post-depositional erosion (Smith et al., 2005b; Blard et al., 2009). Aridity indeed increases the likelihood of cosmogenic nuclide inheritance (Owen et al., 2003), while it is not a problem in other contexts where the glacial flow is high (Shulmeister et al., 2010; Putnam et al., 2012).

Besides these classical explanations (inheritance and erosion) for the age scatter, an alternative and complementary mechanism may be proposed for the M1 surface. Indeed, the blocks on top of M1 could have been actively moved and rotated during the glacial stillstand that built M2.

Glacier chronology

Although these observations suggest that inheritance is the most likely process explaining the age distribution, we cannot rule out the possibility that erosion also played a role.

We thus adopt a conservative approach to establish the following chronology. For this, we consider the whole distribution of the exposure ages and discuss both the respective influence of inheritance and erosion.

For each of the glacier positions, we also calculated the corresponding equilibrium line altitude (ELA) by using the terminus-to-head altitude ratio (THAR) method and a ratio of 0.4, which is the median value reported in the review of Benn et al. (2005). Although this quite

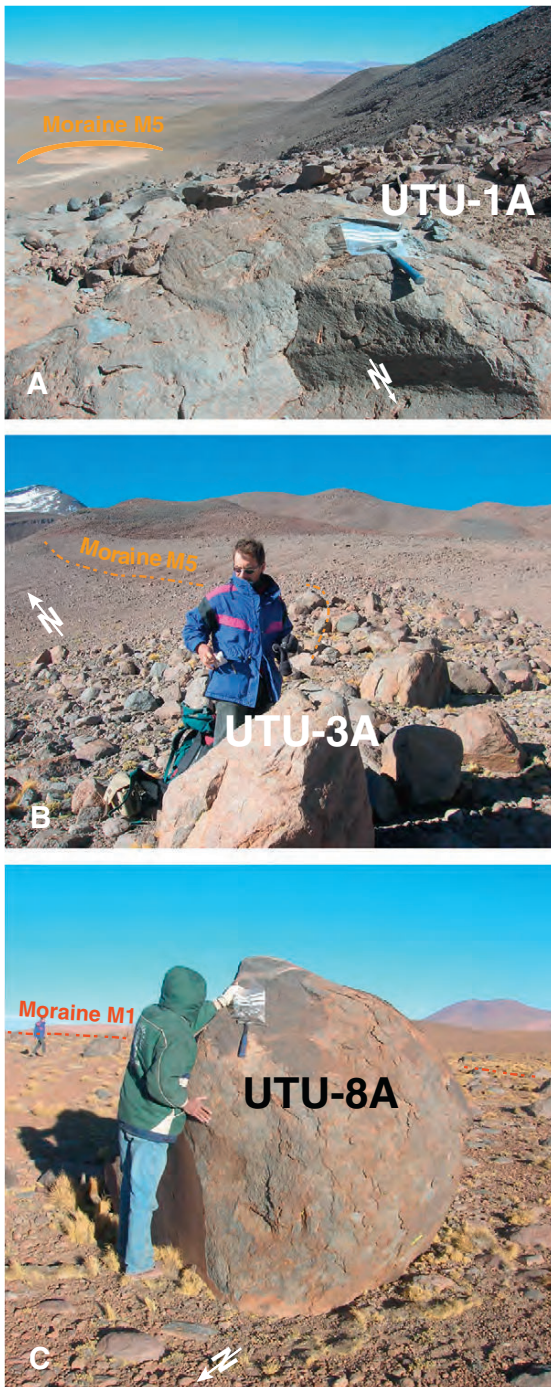


Figure 5. A) Photo of striated roche moutonnée UTU-1A, B) photo of boulder sample UTU-3A from moraine M5, C) photo of boulder sample UTU-8A from moraine M1.

crude method may suffer from uncertainties, it allows us evaluate quite firmly the relative ELA change (Benn et al., 2005) (Table 4).

The following relative chronology and interpretations then follow:

- The most distal moraine M1 was probably emplaced between 65 and 37 ka. Indeed, the mode of these M1 exposure ages is about 40 ka, and six of the eight ages range between 37 and 65 ka (Fig. 7). This time range can be considered as the most probable

- period for the stillstand that led to the deposition of the M1 loops, with a glacial front at about 4800 m elevation and an ELA at 5250 m.
- The range of the exposure ages on M2 (17–34 ka) suggests that this moraine could have emplaced any time during this period.
- Then, the well-clustered ages from lower *roches moutonnées* UTU-5A and UTU-5B firmly establish that the glacial front receded about 1 km at ~17 ka, and reached 4900 m elevation (75 m upward shift), where moraine M5 started to be deposited.
- Although the $^3\text{He}_c$ ages of moraine M5 are not well clustered, the most rational interpretation of these exposure ages is that this recessional moraine was emplaced between 16 and 14 ka. The front of the glacier tongue remained at about 4900 m during this relatively brief late glacial stillstand episode, with a corresponding ELA at 5350 m.
- Finally, the $^3\text{He}_c$ exposure ages obtained from the upper *roches moutonnées* UTU-1A, UTU-1B and UTU-1C, indicate that the deglaciation of this valley occurred just after 15 ka and, was probably accomplished at 14 ka. After 14 ka, the ice front thus rose above 5100 m, the ELA above 5450 m, and they never returned to lower elevations.

Comparison with regional and global paleoclimatic records

Evidence for an early local LGM in the South Lipez

The lowest moraine of the Uturuncu glacial sequence is characterized by $^3\text{He}_c$ exposure ages ranging between 65 and 37 ka. This observation provides new evidence that the last glacial maximum in the Andes may have occurred before the global last glacial maximum. Several other glacial chronologies in the Altiplano also reported local LGM being much older than the canonical age (about 21 ka) of the global LGM: Zech et al. (2009) reported a ^{10}Be chronology indicating that the local LGM occurred between 50 and 100 ka in the Tres Lagunas site (NW Argentina), 200 km south of Uturuncu volcano. Similarly, 700 km North of Uturuncu, the ^{10}Be glacial chronology of Smith et al. (2005b) provides additional evidence that the local LGM in the Zongo and Milluni valleys occurred before 30 ka (Cordillera Real, Bolivia).

The Uturuncu glacier chronology thus provides new clues that several alpine glaciers of the Tropical Andes may have reached their maximum extents well before the global LGM (Fig. 8).

However, it is intriguing to note that the glaciers located in the center of the Altiplano did not follow this pattern. Indeed, there are several lines of evidence that paleo-glaciers in the vicinity of the Salar de Uyuni reached their maximum extent between 17 and 15 ka (Clapperton et al., 1997; Clayton and Clapperton, 1997; Blard et al., 2009). Given that the glaciers located at the northern and southern edges of the Altiplano are characterized by early local LGMs (older than 30 ka), it may seem odd that glaciers of the central Altiplano reached their maximum extent 3 to 5 ka after the global LGM. Blard et al. (2009) proposed that this contrasting spatial and temporal behavior arises from the spatial distribution of precipitation on the Altiplano during the giant paleolake Tauca episode, between 17 and 15 ka.

Southern signature of the Lake Tauca episode

Our new $^3\text{He}_c$ ages suggest that the Uturuncu moraine M5 (16–14 ka) is, within uncertainties, synchronous with the Lake Tauca highstand (Sylvestre et al., 1999; Placzek et al., 2006; Blard et al., 2011) (Fig. 8). The giant paleolake Tauca was draining the entire Altiplano and reached a maximum depth of 120 m and a surface area of 50,000 km² between 15.5 and 15 ka, at the end of the Heinrich 1 event (Blard et al., 2011). M5 can thus be considered the “Tauca moraine”, which is a glacial stadial that has been reported at different places across the Altiplano (Clapperton et al., 1997; Clayton and Clapperton, 1997; Blard et al., 2009, 2013a). In the center of the Altiplano, the “Tauca moraine” is very close to, or corresponds with, the terminal moraine (Clapperton et al., 1997; Clayton and Clapperton, 1997; Blard et al., 2009).

Table 2
Vacuum crushing helium data from the Uturuncu pyroxenes.

Sample	Mineral	Size (mm)	Mass (g)	Crushing time (min)/strikes	^4He (10^{10} at·g $^{-1}$)	^3He (10^4 at·g $^{-1}$)	$^3\text{He}/^4\text{He}$ (Ra)
UTU-1B	Pyroxene	0.2–0.4	0.332	1/60	3.7 ± 0.2	4 ± 1	0.8 ± 0.2
				5/300	10.9 ± 0.3	8.1 ± 1.6	0.5 ± 0.1
				Total	14.6 ± 0.3	12.1 ± 1.9	
UTU-3B	Pyroxene	0.3–0.5	0.267	1/60	1.01 ± 0.14	2.4 ± 0.6	1.7 ± 0.5
				5/300	0.93 ± 0.13	2.6 ± 0.7	1.5 ± 0.4
				Total	1.9 ± 0.2	4.2 ± 0.7	
UTU-5A	Pyroxene	0.3–0.5	0.191	1/60	4.8 ± 0.5	0.3 ± 0.6	0.05 ± 0.1
				5/300	3.4 ± 0.4	0.6 ± 1.7	0.1 ± 0.4
				Total	8.2 ± 0.7	0.9 ± 1.9	
Average of 3 samples ($\pm 1\sigma$)					8 ± 6	6 ± 6	

The Lake Tauca highstand was the result of a significant regional precipitation increase (about 80%) (Blodgett et al., 1997; Blard et al., 2009). Additionally, it is plausible that, during this period, the

presence of the lake induced a local amplification of the precipitation intensity in the Lake Tauca surroundings, as a result of recycling effects of evaporated lake water (Blard et al., 2009). Such a positive

Table 3
(U–Th)/ ^4He eruption ages of the sampled Uturuncu rocks.

Sample	Type	U (ppm)	Th (ppm)	Mass (mg)	Sphere equivalent radius (mm)	P_d (10^6 at·g $^{-1}$ ·yr $^{-1}$)	$^4\text{He}^*$ (10^{12} at·g $^{-1}$)	Eruption age (Ma)
UTU-1A	Pyroxene 0.2–0.3 mm	1.26	14.9	28.9	130	16.6	15.9 ± 0.17	0.96 ± 0.1
UTU-1A	Pyroxene 0.3–0.5 mm	1.26	14.9	31.50	210	16.2	10.7 ± 0.09	0.66 ± 0.07
UTU-1A	Groundmass	3.74	15.8					
UTU-1B	Pyroxene 0.4–1 mm	1.15	14.3	51.3	403	15.2	8.97 ± 0.11	0.59 ± 0.1
UTU-1B	Groundmass	4.09	16.5					
UTU-1C	Pyroxene 0.3–0.59 mm	1.93	20.8	46.2	242	22.58	8.95 ± 0.11	0.40 ± 0.04
UTU-1C	Pyroxene 0.3–0.6 mm	1.93	20.8	19.70	246	22.57	13.1 ± 0.15	0.58 ± 0.1
UTU-1C	Groundmass	4.07	16.4					
UTU-2	Pyroxene 0.3–0.6 mm	1.13	10.9	75.90	130	12.94	13.7 ± 0.15	1.02 ± 0.1
UTU-2	Groundmass	3.68	16.3					
UTU-3A	Pyroxene 0.3–0.5 mm	1.35	16.9	34.96	210	18.26	9.8 ± 0.22	0.54 ± 0.06
UTU-3A	Pyroxene 0.3–0.59 mm	1.35	16.9	22.75	242	18.2	7.4 ± 0.1	0.41 ± 0.04
UTU-3A	Groundmass	4.52	18.6					
UTU-3B	Pyroxene 0.4–1 mm	1.36	24.8	46.50	403	23.63	3.6 ± 0.07	0.15 ± 0.02
UTU-3B	Groundmass	3.51	17.3					
UTU-4	Pyroxene 0.3–0.5 mm	0.49	11.6	43.52	210	11.53	3.9 ± 0.07	0.33 ± 0.03
UTU-4	Pyroxene 0.19–0.59 mm	0.49	11.6	16.10	236	11.42	1.3 ± 0.12	0.12 ± 0.02
UTU-4	Groundmass	3.44	16.6					
UTU-5A	Pyroxene 0.3–0.5 mm	0.73	16.6	28.59	210	16.12	1.9 ± 0.07	0.12 ± 0.01
UTU-5A	Groundmass	3.90	19.7					
UTU-5B	Pyroxene 0.3–0.59 mm	1.19	19.6	31.90	242	19.53	3.4 ± 0.07	0.17 ± 0.02
UTU-5B	Pyroxene 0.3–0.5 mm	1.19	19.6	28.00	210	19.60	4.8 ± 0.07	0.24 ± 0.02
UTU-5B	Groundmass	3.89	19.0					
UTU-6A	Pyroxene 0.19–0.5 mm	0.40	4.5	20.20	201	6.56	2.7 ± 0.07	0.41 ± 0.04
UTU-6A	Groundmass	4.10	20.0					
UTU-6B	Pyroxene 0.19–0.5 mm	0.29	0.9	37.20	201	3.46	0.54 ± 0.07	0.16 ± 0.03
UTU-6B	Groundmass	3.85	17.7					
UTU-6C	Pyroxene 0.3–0.59 mm	0.99	13.1	36.00	242	14.14	3.2 ± 0.07	0.22 ± 0.02
UTU-6C	Groundmass	3.74	17.7					
UTU-6D	Pyroxene 0.3–0.59 mm	0.33	1.11	36.50	242	3.51	0.54 ± 0.06	0.15 ± 0.02
UTU-6D	Pyroxene 0.3–0.5 mm	0.33	1.11	31.56	210	3.75	1 ± 0.07	0.27 ± 0.03
UTU-6D	Pyroxene 0.2–0.3 mm	0.33	1.11	35.20	130	4.88	1.27 ± 0.07	0.26 ± 0.03
UTU-6D	Groundmass	4.14	18.5					
UTU-7A	Pyroxene 0.4–1 mm	0.61	8.1	34.30	403	8.80	8 ± 0.1	0.91 ± 0.09
UTU-7A	Groundmass	3.37	16.6					
UTU-7B	Pyroxene 0.4–1 mm	0.91	16.9	51.30	403	16.49	2.32 ± 0.07	0.14 ± 0.01
UTU-7B	Groundmass	3.98	20.6					
UTU-7C	Pyroxene 0.19–0.5 mm	0.26	1.2	40.40	201	3.76	0.33 ± 0.07	0.09 ± 0.02
UTU-7C	Pyroxene 0.2–0.5 mm	0.26	1.2	59.70	201	3.76	0.64 ± 0.067	0.17 ± 0.02
UTU-7C	Groundmass	4.04	19.7					
UTU-8A	Pyroxene 0.4–1 mm	0.64	3.6	35.50	403	5.74	0.54 ± 0.06	0.09 ± 0.01
UTU-8A	Groundmass	4.18	20.1					
UTU-8B	Pyroxene 0.4–1 mm	0.59	10.0	31.50	403	10.27	3.01 ± 0.07	0.29 ± 0.03
UTU-8B	Groundmass	3.82	19.4					
UTU-8C	Pyroxene 0.4–1 mm	0.31	1.6	27.30	403	3.15	1.51 ± 0.07	0.48 ± 0.05
UTU-8C	Groundmass	3.82	18.3					
UTU-8D	Pyroxene 0.19–0.5 mm	0.35	1.2	36.40	201	4.14	0.56 ± 0.075	0.14 ± 0.02
UTU-8D	Pyroxene 0.3–0.5 mm	0.35	1.2	79.54	210	4.05	0.91 ± 0.07	0.23 ± 0.03
UTU-8D	Pyroxene 0.2–0.3 mm	0.35	1.2	78.70	130	5.25	1.04 ± 0.07	0.2 ± 0.02
UTU-8D	Groundmass	4.30	20.3					
UTU-9A	Pyroxene 0.4–1 mm	0.58	2.2	50.40	403	4.43	0.7 ± 0.06	0.16 ± 0.02
UTU-9A	Groundmass	3.86	18.5					

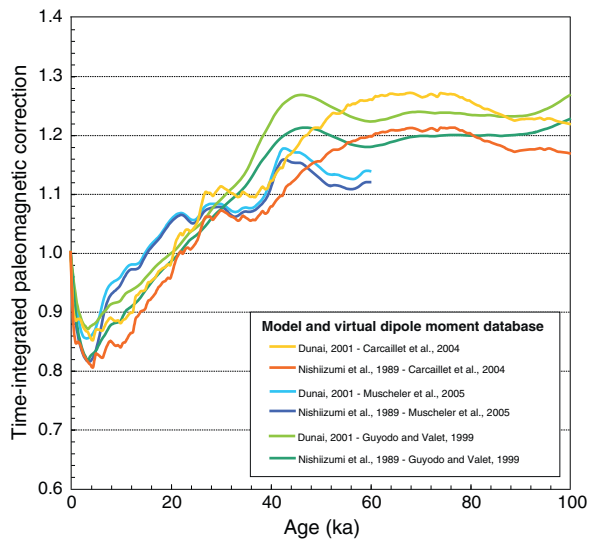


Figure 6. Time integrated correction of the cosmogenic ^3He production rate due to the Earth magnetic field variations at 4800 m and 22°S . Two time-dependent correction models (Nishizumi et al., 1989; Dunai, 2001) and three virtual dipole moment (VDM) databases (Guyodo and Valet, 1999; Carcaillet et al., 2004; Muscheler et al., 2005) are shown for comparison.

precipitation anomaly could have triggered an important downward shift of the ELA in the vicinity of the lake, while this effect may have been attenuated several hundreds of km further from the lake (Kull et al., 2008; Blard et al., 2009). Support for this scenario comes from the spatial variability of the paleoELA drop: indeed, the ELA corresponding to the Tauca moraine is about 4450 m at Tunupa volcano, in the very center of Lake Tauca, while it is about 5350 m at the Uturuncu site. The spatial gradient of temperature is not sufficient to explain such an ELA difference (Ammann et al., 2001). This ELA difference of 900 m was most probably the result of focused rainfall over the center of the paleolake Tauca.

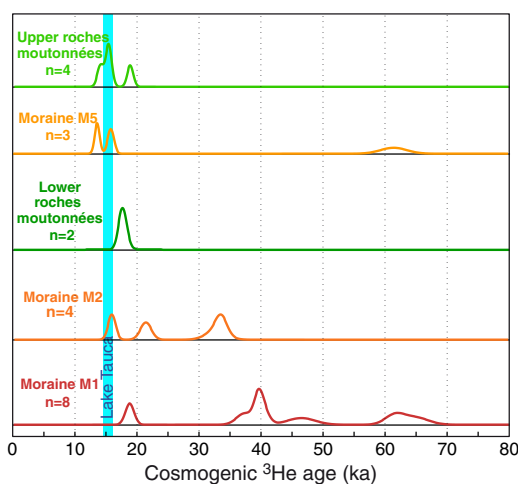


Figure 7. Probability density plot of the $^3\text{He}_c$ ages of the Uturuncu moraines. These exposure ages are computed using a locally calibrated ^3He production rate (Blard et al., 2013b), the scaling model of Stone (2000), the time-dependent correction of Nishizumi et al. (1989) and the VDM database of Muscheler et al. (2005).

Table 4

ELA vs time for Uturuncu and Tunupa volcanos.

Moraine	Altitude of terminus (m)	ELA ^a (m)	Age (ka)
Uturuncu			
M1	4800	5280	65–37
M2	4820	5292	34–17
Lower RM	4830	5298	17
M5	4900	5340	16–14
Upper RM	5100	5460	15–14
Tunupa			
M1	3850	4390	20–15
M2	3950	4450	16–14
Lower RM	4240	4624	15.5
Upper RM	4450	4750	15.5–14.5
M3	4450	4750	13.5–12

^a Calculated using the THAR method, using a ratio of 0.4.

An abrupt deglaciation after 14 ka, in accord with the Lake Tauca disappearance

Despite contrasting relative glacier extents between 30 and 15 ka, the Uturuncu glaciers and those of the center of the Altiplano behave similarly after 14 ka, when abrupt recession occurs (Fig. 8). Such timing is in accord with the disappearance of Lake Tauca between 14.5 and 14 ka (Placzek et al., 2006; Blard et al., 2011). As suggested in previous studies (Clapperton et al., 1997; Kull et al., 2008; Blard et al., 2009), it is tempting to propose that the coincident regressions of lake and glaciers between 14.5 and 14 ka results from an abrupt regional climatic change, i.e. an abrupt precipitation decrease, probably coupled with a significant temperature increase (Fig. 8). The Northern Atlantic and the Tropics were affected by warmer conditions at the end of the Heinrich 1 event, just after 15 ka (Lea et al., 2003; Andersen et al., 2004; Blard et al., 2007). This probably triggered major atmospheric changes, and notably a northward shift of the South American monsoon, leading to warmer and drier climate on the Altiplano after 14.5 ka (Chiang et al., 2003; Blard et al., 2009).

Comparison with regional and global paleoclimatic archives

The Uturuncu deglacial chronology between 30 and 14 ka corresponds to first order with the warming trend recorded by Arctic temperature proxies (Andersen et al., 2004), as well as with sea-surface temperature (SST) of the Eastern Tropical Pacific (e.g. Dubois et al., 2009) (Fig. 8). Indeed, while Antarctic air temperature started to rise earlier, around 18 ka, SST proxies indicate that the Eastern Pacific warmed significantly after 15 ka, coincident with the Arctic and the Tropical Atlantic (Andersen et al., 2004; Martrat et al., 2007) (Fig. 8). Considering a local lapse rate of about $6.5^\circ\text{C}\cdot\text{km}^{-1}$, the 2°C warming of the Tropical Pacific SST between 15 and 10 ka would be sufficient to induce an ELA rise of about 300 m, to about 5700 m, under invariant precipitation. However, given that the Uturuncu summit is now free of ice, the local present-day ELA stands above 6000 m. This probably indicates that the deglacial warming was amplified at high elevation compared to sea level, as suggested by several paleoclimatic records and modeling results (Kageyama et al., 2005; Blard et al., 2007). Additionally, a concomitant precipitation decrease may have also played a role in the case of Uturuncu. More work is required to further quantify both effects.

Conclusion

The new cosmogenic $^3\text{He}_c$ chronology from the southern valley of Uturuncu volcano (Southern Altiplano, Bolivia) indicates that glaciers reached their maximum extent between 65 and 37 ka. Then, they probably remained close to their maximum position until as late as 18 ka. The glacier thus receded slowly after 18 ka. A late glacial stillstand probably occurred between 16 and 14 ka, with an ELA

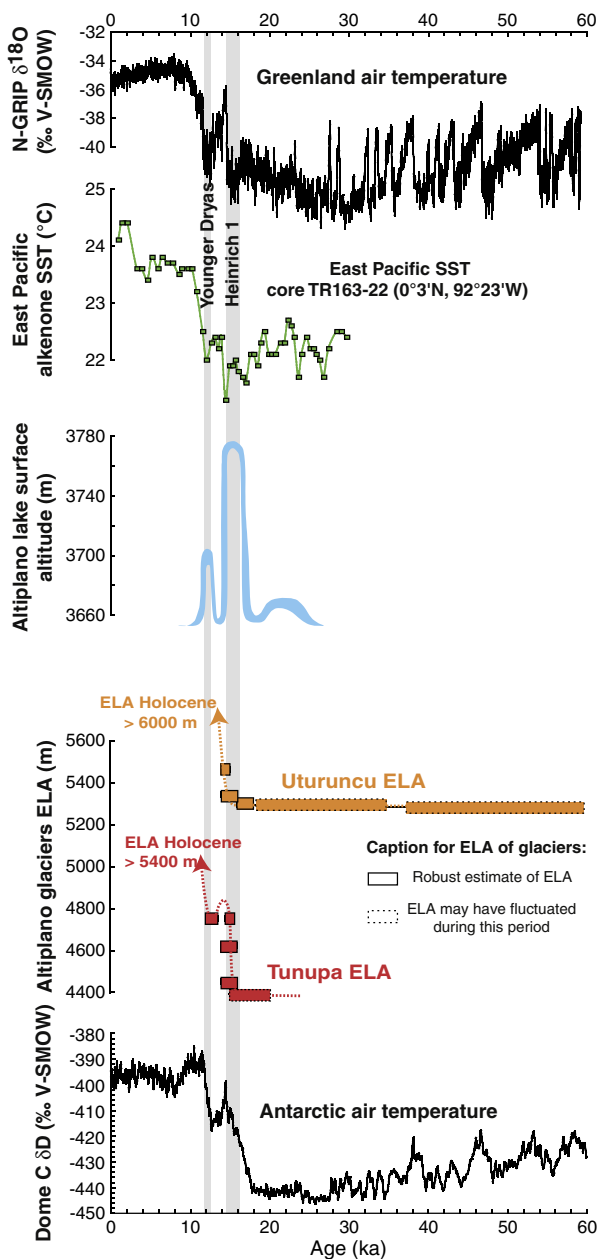


Figure 8. Comparison of the Uturuncu and Tunupa ELA time variations with other climatic proxies. A) NGRIP Greenland air temperature (Andersen et al., 2004). Age model from Lemieux-Dudon et al. (2010). B) Alkenone sea-surface temperature of the East Pacific (oceanic core TR163-22; 0°3'N, 92°23'W) (Dubois et al., 2009). Age model from Lea et al. (2006). C) Altiplano lake levels (Sylvestre et al., 1999; Placzek et al., 2006; Blard et al., 2011). D) Equilibrium line altitudes of glaciers at Tunupa (Blard et al., 2009; Blard et al., 2013a) and Uturuncu (this study). ELA are computed using the THAR method and a ratio of 0.4. E) Dome C Antarctic air temperature (EPICA, 2004). Age model from Lemieux-Dudon et al. (2010).

standing between 5300 and 5400 m. This episode is, within dating uncertainties, synchronous with the highstand of paleolake Tauca (17–15 ka) (Sylvestre et al., 1999; Placzek et al., 2006; Blard et al., 2011). This result confirms that this regionally wet and cold episode (Blard et al., 2009) also impacted the most southern part of the Altiplano. The intense rainfall accompanying the Lake Tauca episode, during the Heinrich 1 event, had a major influence on regional glaciers. Indeed, this event may have maintained the ELA in the same position for several centuries, or more. The glacial tongue then

receded above 5100 m after 14 ka, synchronous with the Bolling–Allerod warming. The glaciers of this zone thus probably reflect a mixed influence of regional temperature increase, coupled with the Late Pleistocene abrupt oscillations of precipitation, in pace with North Atlantic events.

More studies remain necessary to provide a complete picture of the spatio-temporal variability of the Altiplano glaciers. This will permit a quantitative reconstruction of the time variations of precipitation and temperature in this high altitude tropical region.

Supplementary data to this article can be found online at <http://dx.doi.org/10.1016/j.yqres.2014.02.002>.

Acknowledgments

This work was mainly funded by the INSU programs Relief de la Terre and EVE-LEFE and by the ANR Jeune Chercheur GALAC project “ANR-11-JS56-011-01”. We greatly appreciated the logistical support of the IRD de La Paz (Bolivia) during our field trip of September 2006. The SARM technicians and engineers are kindly acknowledged for their high-quality measurements of major and trace elements of rock samples. Two anonymous reviewers and associate editor David Fink made useful comments that allowed us to improve the article. This is CRPG contribution no. 2285.

References

- Ackert, R.P., Singer, B.S., Guillou, H., Kaplan, M.R., Kurz, M.D., 2003. Long-term cosmogenic ^3He production rates from $^{40}\text{Ar}/^{39}\text{Ar}$ and K–Ar dated Patagonian lava flows at 47°S. *Earth and Planetary Science Letters* 210, 119–136.
- Amidon, W.H., Farley, K.A., 2011. Cosmogenic ^3He production rates in apatite, zircon and pyroxene inferred from Bonneville flood erosional surfaces. *Quaternary Geochronology* 6, 10–21.
- Amidon, W.H., Farley, K.A., Burbank, D.W., Pratt-Sitaula, B., 2008. Anomalous cosmogenic ^3He production and elevation scaling in the high Himalaya. *Earth and Planetary Science Letters* 265, 287–301.
- Ammann, C., Jenny, B., Kammer, K., Messerli, B., 2001. Late Quaternary Glacier response to humidity changes in the arid Andes of Chile (18–29°S). *Palaeogeography, Palaeoclimatology, Palaeoecology* 172, 313–326.
- Andersen, K.K., Azuma, N., Barnola, J.M., Bigler, M., Biscaye, P., Caillon, N., Chappellaz, J., Clausen, H.B., Dahljensen, D., Fischer, H., Flückiger, J., Fritzsche, D., Fujii, Y., Goto-Azuma, K., Gronvold, K., Gundestrup, N.S., Hansson, M., Huber, C., Hvidberg, C.S., Johnsen, S.J., Jonsell, U., Jouzel, J., Kipfstuhl, S., Landais, A., Leuenberger, M., Lorrain, R., Masson-Delmotte, V., Miller, H., Motoyama, H., Narita, H., Popp, T., Rasmussen, S.O., Raynaud, D., Rothlisberger, R., Ruth, U., Samyn, D., Schwander, J., Shoji, H., Siggard-Andersen, M.L., Steffensen, J.P., Stocker, T., Sveinbjornsdottir, A.E., Svensson, A., Takata, M., Tison, J.L., Thorsteinsson, T., Watanabe, O., Wilhelms, F., White, J.W.C., 2004. High-resolution record of Northern Hemisphere climate extending into the last interglacial period. *Nature* 431, 147–151.
- Andrews, J.N., 1985. The isotopic composition of radiogenic helium and its use to study groundwater movement in confined aquifers. *Chemical Geology* 49, 339–351.
- Andrews, J.N., Kay, R.L.F., 1982. Natural production of tritium in permeable rocks. *Nature* 298, 361–363.
- Applegate, P., Urban, N., Laabs, B., Keller, K., Alley, R., 2010. Modeling the statistical distributions of cosmogenic exposure dates from moraines. *Geoscientific Model Development* 3, 293–307.
- Balco, G., Stone, J.O., Lifton, N.A., Dunai, T.J., 2008. A complete and easily accessible means of calculating surface exposure ages or erosion rates from ^{10}Be and ^{26}Al measurements. *Quaternary Geochronology* 3, 174–195.
- Benn, D.I., Owen, L.A., Osmaston, H.A., Seltzer, G.O., Porter, S.C., Mark, B.G., 2005. Reconstruction of equilibrium-line altitudes for tropical and sub-tropical glaciers. *Quaternary International* 138–139, 8–21.
- Blard, P.-H., Farley, K.A., 2008. The influence of radiogenic ^4He on cosmogenic ^3He determinations in volcanic olivine and pyroxene. *Earth and Planetary Science Letters* 276, 20–29.
- Blard, P.-H., Lave, J., Pik, R., Quidelleur, X., Bourles, D., Kieffer, G., 2005. Fossil cosmogenic ^3He record from K–Ar dated basaltic flows of Mount Etna volcano (Sicily, 38°N): evaluation of a new paleoaltimeter. *Earth and Planetary Science Letters* 236, 613–631.
- Blard, P.-H., Pik, R., Lavé, J., Bourlès, D., Burnard, P.G., Yokochi, R., Marty, B., Trusdell, F., 2006. Cosmogenic ^3He production rates revisited from evidences of grain size dependent release of matrix sited helium. *Earth and Planetary Science Letters* 247, 222–234.
- Blard, P.-H., Lave, J., Pik, R., Wagnon, P., Bourles, D., 2007. Persistence of full glacial conditions in the central Pacific until 15,000 years ago. *Nature* 449, 591–594.
- Blard, P.-H., Puchol, N., Farley, K.A., 2008. Constraints on the loss of matrix-sited helium during vacuum crushing of mafic phenocrysts. *Geochimica et Cosmochimica Acta* 72, 3788–3803.
- Blard, P.-H., Lavé, J., Farley, K.A., Fornari, M., Jiménez, N., Ramirez, V., 2009. Late local glacial maximum in the Central Altiplano triggered by cold and locally-wet conditions

- during the paleolake Tauca episode (17–15 ka, Heinrich 1). *Quaternary Science Reviews* 28, 3414–3427.
- Blard, P.-H., Sylvestre, F., Tripathi, A., Claude, C., Causse, C., Vimeux, F., Coudrain, A., Condom, T., Moreau, C., Dumoulin, J.-P., Lavé, J., 2011. Lake highstands on the Altiplano (Tropical Andes) contemporaneous with Heinrich 1 and the Younger Dryas: new insights from ^{14}C , U–Th dating and $\delta^{18}\text{O}$ of carbonates. *Quaternary Science Reviews* 30, 3973–3989.
- Blard, P.-H., Lavé, J., Sylvestre, F., Placzek, C., Claude, C., Galy, V., Condom, T., Tibari, B., 2013a. Cosmogenic ^3He production rate in the high tropical Andes (3800 m, 20°S): implications for the local last glacial maximum. *Earth and Planetary Science Letters* 377–378, 260–275.
- Blard, P.-H., Braucher, R., Lavé, J., Bourlès, D., 2013b. Cosmogenic ^{10}Be production rate calibrated against ^3He in the high Tropical Andes (3800–4900 m, 20–22°S). *Earth and Planetary Science Letters* 382, 140–149.
- Blodgett, T.A., Lenters, J.D., Isacks, B.L., 1997. Constraints on the origin of paleolake expansions in the Central Andes. *Earth Interactions* 1.
- Bromley, G.R.M., Schaefer, J.M., Winckler, G., Hall, B.L., Todd, C.E., Rademaker, K.M., 2009. Relative timing of last glacial maximum and late-glacial events in the central tropical Andes. *Quaternary Science Reviews* 28, 2514–2526.
- Carcaillat, J.T., Bourlès, D.L., Thouveny, N., 2004. Geomagnetic dipole moment and ^{10}Be production rate intercalibration from authigenic $^{10}\text{Be}/^9\text{Be}$ for the last 1.3 Ma. *Geochemistry, Geophysics, Geosystems* 5. <http://dx.doi.org/10.1029/2003GC000641>.
- Chiang, J.C.H., Biasutti, M., Battisti, D.S., 2003. Sensitivity of the Atlantic Intertropical Convergence Zone to Last Glacial Maximum boundary conditions. *Paleoceanography* 18.
- Clapperton, C.M., Clayton, J.D., Benn, D.I., Marden, C.J., Argollo, J., 1997. Late quaternary glacier advances and Palaeolake highstands in the Bolivian Altiplano. *Quaternary International* 38–9, 49–59.
- Clayton, J.D., Clapperton, C.M., 1997. Broad synchrony of a Late-glacial glacier advance and the highstand of paleolake Tauca in the Bolivian Altiplano. *Journal of Quaternary Science* 12, 169–182.
- Dubois, N., Kienast, M., Normandeau, C., Herbert, T.D., 2009. Eastern equatorial Pacific cold tongue during the Last Glacial Maximum as seen from alkenone paleothermometry. *Paleoceanography* 24 PA4207.
- Dunai, T.J., 2001. Influence of secular variation of the geomagnetic field on production rates of in situ produced cosmogenic nuclides. *Earth and Planetary Science Letters* 193, 197–212.
- Dunai, T.J., Stuart, F.M., Pik, R., Burnard, P., Gayer, E., 2007. Production of ^3He in crustal rocks by cosmogenic thermal neutrons. *Earth and Planetary Science Letters* 258, 228–236.
- Dunne, J., Elmore, D., Muzikar, P., 1999. Scaling factors for the rates of production of cosmogenic nuclides for geometric shielding and attenuation at depth on sloped surfaces. *Geomorphology* 27, 3–11.
- Epica, C., 2004. Eight glacial cycles from an Antarctic ice core. *Nature* 429, 623–628.
- Farley, K.A., Libarkin, J., Mukhopadhyay, S., Amidon, W., 2006. Cosmogenic and nucleogenic ^3He in apatite, titanite, and zircon. *Earth and Planetary Science Letters* 248, 451–461.
- Garreaud, R.D., Vuille, M., Compagnucci, R., Marengo, J., 2009. Present-day South American climate. *Palaeogeography, Palaeoclimatology, Palaeoecology* 281, 180–195.
- Gosse, J.C., Klein, J., Evenson, E.B., Lawn, B., Middleton, R., 1995. ^{10}Be dating of the duration and retreat of the Last Pinedale glacial sequence. *Science* 268, 1329–1333.
- Guyodo, Y., Valet, J.P., 1999. Global changes in intensity of the Earth's magnetic field during the past 800 kyr. *Nature* 399, 249–252.
- Heyman, J., Stroeve, A.P., Harbor, J.M., Caffee, M.W., 2011. Too young or too old: evaluating cosmogenic exposure dating based on an analysis of compiled boulder exposure ages. *Earth and Planetary Science Letters* 302, 71–80.
- Hilton, D.R., Hammerschmidt, K., Teufel, S., Friedrichsen, H., 1993. Helium isotope characteristics of Andean geothermal fluids and lavas. *Earth and Planetary Science Letters* 120, 265–282.
- Kageyama, M., Harrison, S.P., Abe-Ouchi, A., 2005. The depression of tropical snowlines at the last glacial maximum: what can we learn from climate model experiments? *Quaternary International* 138, 202–219.
- Kull, C., Imhof, S., Grosjean, M., Zech, R., Veit, H., 2008. Late Pleistocene glaciation in the Central Andes: Temperature versus humidity control — a case study from the eastern Bolivian Andes (17°S) and regional synthesis. *Global and Planetary Change* 60, 148–164.
- Lal, D., 1991. Cosmic ray labeling of erosion surfaces: in situ nuclide production rates and erosion models. *Earth and Planetary Science Letters* 104, 424–439.
- Lea, D.W., Pak, D.K., Peterson, L.C., Hughen, K.A., 2003. Synchronicity of tropical and high-latitude Atlantic temperatures over the last glacial termination. *Science* 301, 1361–1364.
- Lea, D.W., Pak, D.K., Belanger, C.L., Spero, H.J., Hall, M.A., Shackleton, N.J., 2006. Paleoclimate history of Galapagos surface waters over the last 135,000 yr. *Quaternary Science Reviews* 25, 1152–1167.
- Leduc, G., Vidal, L., Tachikawa, K., Rostek, F., Sonzogni, C., Beaufort, L., Bard, E., 2007. Moisture transport across Central America as a positive feedback on abrupt climatic changes. *Nature* 445, 908–911.
- Lemieux-Dudon, B., Blayo, E., Petit, J.-R., Waelbroeck, C., Svensson, A., Ritz, C., Barnola, J.-M., Narcisi, B.M., Parrenin, F., 2010. Consistent dating for Antarctic and Greenland ice cores. *Quaternary Science Reviews* 29, 8–20.
- Licciardi, J.M., Schaefer, J.M., Taggart, J.R., Lund, D.C., 2009. Holocene glacier fluctuations in the Peruvian Andes indicate northern climate linkages. *Science* 325, 1677–1679.
- Martrat, B., Grimalt, J.O., Shackleton, N.J., de Abreu, L., Hutterli, M.A., Stocker, T.F., 2007. Four climate cycles of recurring deep and surface water destabilizations on the Iberian margin. *Science* 317, 502–507.
- Masarik, J., Frank, M., Schafer, J.M., Wieler, R., 2001. Correction of in situ cosmogenic nuclide production rates for geomagnetic field intensity variations during the past 800,000 years. *Geochimica et Cosmochimica Acta* 65, 2995–3003.
- Menabrea, L., Bourlès, D.L., Thouveny, N., 2012. Amplitude and timing of the Laschamp geomagnetic dipole low from the global atmospheric ^{10}Be overproduction: contribution of authigenic $^{10}\text{Be}/^9\text{Be}$ ratios in west equatorial Pacific sediments. *Journal of Geophysical Research — Solid Earth* 117.
- Muscheler, R., Beer, R., Kubik, P.W., Synal, H.A., 2005. Geomagnetic field intensity during the last 60,000 years based on ^{10}Be and ^{36}Cl from the Summit ice cores and ^{14}C . *Quaternary Science Reviews* 24, 1849–1860.
- New, M., Lister, D., Hulme, M., Makin, I., 2002. A high-resolution data set of surface climate over global land areas. *Climate Research* 21, 1–25.
- Nishiizumi, K., Winterer, E.L., Kohl, C.P., Klein, J., Middleton, R., Lal, D., Arnold, J.R., 1989. Cosmic-ray production rates of ^{10}Be and ^{26}Al in quartz from glacially polished rocks. *Journal of Geophysical Research — Solid Earth and Planets* 94, 17907–17915.
- Oerlemans, J., 2005. Extracting a climate signal from 169 glacier records. *Science* 308, 675–677.
- Ohmura, A., Kasser, P., Funk, M., 1992. Climate at the equilibrium line of glaciers. *Journal of Glaciology* 38, 397–411.
- Owen, L.A., Finkel, R.C., Haizhou, M., Spencer, J.Q., Derbyshire, E., Barnard, P.L., Caffee, M.W., 2003. Timing and style of Late Quaternary glaciation in northeastern Tibet. *Geological Society of America Bulletin* 115, 1356–1364.
- Placzek, C., Quade, J., Patchett, P.J., 2006. Geochronology and stratigraphy of late Pleistocene lake cycles on the southern Bolivian Altiplano: implications for causes of tropical climate change. *Geological Society of America Bulletin* 118, 515–532.
- Placzek, C.J., Quade, J., Patchett, P.J., 2011. Isotopic tracers of paleohydrologic change in large lakes of the Bolivian Altiplano. *Quaternary Research* 75, 231–244.
- Putnam, A.E., Schaefer, J.M., Denton, G.H., Barrell, D.J.A., Finkel, R.C., Andersen, B.G., Schwartz, R., Chinn, T.J.H., Doughty, A.M., 2012. Regional climate control of glaciers in New Zealand and Europe during the pre-industrial Holocene. *Nature Geoscience* 5, 627–630.
- Rodbell, D.T., Smith, J.A., Mark, B.G., 2009. Glaciation in the Andes during the Lateglacial and Holocene. *Quaternary Science Reviews* 28, 2165–2212.
- Scarsi, P., 2000. Fractional extraction of helium by crushing of olivine and clinopyroxene phenocrysts: effects on the $^3\text{He}/^4\text{He}$ measured ratio. *Geochimica et Cosmochimica Acta* 64, 3751–3762.
- Schaefer, J.M., Denton, G.H., Barrell, D.J.A., Ivy-Ochs, S., Kubik, P.W., Andersen, B.G., Phillips, F.M., Lowell, T.V., Schluchter, C., 2006. Near-synchronous interhemispheric termination of the last glacial maximum in mid-latitudes. *Science* 312, 1510–1513.
- Shulmeister, J., Fink, D., Hyatt, O.M., Thackray, G.D., Rother, H., 2010. Cosmogenic ^{10}Be and ^{26}Al exposure ages of moraines in the Rakaia Valley, New Zealand and the nature of the last termination in New Zealand glacial systems. *Earth and Planetary Science Letters* 297, 558–566.
- Smith, J.A., Finkel, R.C., Farber, D.L., Rodbell, D.T., Seltzer, G.O., 2005a. Moraine preservation and boulder erosion in the tropical Andes: interpreting old surface exposure ages in glaciated valleys. *Journal of Quaternary Science* 20, 735–758.
- Smith, J.A., Seltzer, G.O., Farber, D.L., Rodbell, D.T., Finkel, R.C., 2005b. Early local last glacial maximum in the tropical Andes. *Science* 308, 678–681.
- Smith, C., Lowell, T., Caffee, M., 2009. Lateglacial and Holocene cosmogenic surface exposure age glacial chronology and geomorphological evidence for the presence of cold-based glaciers at Nevado Sajama, Bolivia. *Journal of Quaternary Science* 24, 360–372.
- Smith, C.A., Lowell, T.V., Owens, L.A., Caffee, M.W., 2010. Late Quaternary glacial chronology on Nevado Illimani, Bolivia, and the implications for paleoclimatic reconstructions across the Andes. *Quaternary Research*. <http://dx.doi.org/10.1016/j.yqres.2010.07.001>.
- Sparks, R.S.J., Folkes, C.B., Humphreys, M.C.S., Barford, D.N., Clavero, J., Sunagua, M.C., McNutt, S.R., Pritchard, M.E., 2008. Uturuncu volcano, Bolivia: volcanic unrest due to mid-crustal magma intrusion. *American Journal of Science* 308, 727–769.
- Stone, J.O., 2000. Air pressure and cosmogenic isotope production. *Journal of Geophysical Research — Solid Earth* 105, 23753–23759.
- Sylvestre, F., Servant, M., Servant-Vildary, S., Causse, C., Fournier, M., Ybert, J.P., 1999. Lake-level chronology on the southern Bolivian Altiplano (18°–23°S) during late-glacial time and the early Holocene. *Quaternary Research* 51, 54–66.
- Trull, T.W., Kurz, M.D., 1993. Experimental measurements of ^3He and ^4He mobility in olivine and clinopyroxene at magmatic temperatures. *Geochimica et Cosmochimica Acta* 57, 1313–1324.
- Villeneuve, M.E., Pérez de Arce, C., Uribe-Zeballos, H., Zappettini, E., Hickson, C.J., Stasiuk, M.V., 2002. Geochronological compilation for the border region between Argentina, Bolivia, Chile and Peru (14°S–28°S). In: Makepeace, A.J., Stasiuk, M.V., Krauth, O.R., Hickson, C.J., Cocking, R.B., Ellerbeck, D.M. (Eds.), *Proyecto Multinacional Andino*. (Multinational Andean Project GeoData CD-ROM). Publicación Geológica Multinacional/Multinational Geological Publication, Hull, Canada.
- Williams, A.J., Stuart, F.M., Day, S.J., Phillips, W.M., 2005. Using pyroxene microphenocrysts to determine cosmogenic ^3He concentrations in old volcanic rocks: an example of landscape development in central Gran Canaria. *Quaternary Science Reviews* 24, 211–222.
- Yokochi, R., Marty, B., Pik, R., Burnard, P., 2005. High $^3\text{He}/^4\text{He}$ ratios in peridotite xenoliths from SW Japan revisited: evidence for cosmogenic ^3He released by vacuum crushing. *Geochemistry, Geophysics, Geosystems* 6. <http://dx.doi.org/10.1029/2004GC000836>.
- Zech, R., Kull, C., Veit, H., 2006. Late Quaternary glacial history in the Encierro Valley, northern Chile (29° S), deduced from ^{10}Be surface exposure dating. *Palaeogeography, Palaeoclimatology, Palaeoecology* 234, 277–286.

- Zech, R., Kull, C., Kubik, P.W., Veit, H., 2007. LGM and Late Glacial glacier advances in the Cordillera Real and Cochabamba (Bolivia) deduced from ^{10}Be surface exposure dating. *Climate of the Past* 3, 623–635.
- Zech, J., Zech, R., Kubik, P.W., Veit, H., 2009. Glacier and climate reconstruction at Tres Lagunas, NW Argentina, based on ^{10}Be surface exposure dating and lake sediment analyses. *Palaeogeography, Palaeoclimatology, Palaeoecology* 284, 180–190.
- Zech, J., Zech, R., May, J.H., P.W., K., Veit, H., 2010. Lateglacial and early Holocene glaciation in the tropical Andes caused by La Nina-like conditions. *Palaeogeography, Palaeoclimatology, Palaeoecology* 293, 248–254.
- Zimmermann, L., Blard, P.H., Burnard, P.G., Medynski, S., Pik, R., Puchol, N., 2012. A new single vacuum furnace design for cosmogenic ^3He dating. *Geostandard and Geoanalytical Research*. <http://dx.doi.org/10.1111/j.1751-908X.2011.00145.x>.

9.3.2 Forçages interhémisphériques dans les Hautes Andes Tropicales

Au cours de cette thèse j'ai collaboré à une étude de synthèse sur les enregistrements morainiques dans les Andes tropicales de [Jomelli et al. \(2014\)](#). Cette étude présente de nouveaux âges d'exposition en Colombie sur le Ritacuba qui permettent de mettre en évidence une stabilisation glaciaire majeure entre 13.5 et 14 ka. Le propos principal de cette étude est ensuite de proposer une synthèse des âges publiés dans les Andes tropicales afin de comparer les enregistrements synchrones de l'Antarctic Cold Reversal et du Dryas Récent. L'étude montre que l'Antarctic Cold Reversal est d'avantage exprimé que le Younger Dryas.

J'ai contribué à cette étude en travaillant avec Pierre-Henri Blard à la compilation des données existantes et en recalculant tous les âges d'expositions de manière homogène avec les taux de productions les plus appropriés pour la région (Blard et al., 2013a, 2013b).

Cette étude a fait l'objet d'une publication dans la revue Nature.

LETTER

doi:10.1038/nature13546

A major advance of tropical Andean glaciers during the Antarctic cold reversal

V. Jomelli¹, V. Favier², M. Vuille³, R. Braucher⁴, L. Martin⁵, P.-H. Blard⁵, C. Colose³, D. Brunstein¹, F. He⁶, M. Khodri⁷, D. L. Bourlès⁴, L. Leanni⁴, V. Rinterknecht⁸, D. Grancher¹, B. Francou⁹, J. L. Ceballos¹⁰, H. Fonseca¹¹, Z. Liu¹² & B. L. Otto-Bliesner¹³

The Younger Dryas stadial, a cold event spanning 12,800 to 11,500 years ago, during the last deglaciation, is thought to coincide with the last major glacial re-advance in the tropical Andes¹. This interpretation relies mainly on cosmic-ray exposure dating of glacial deposits. Recent studies, however, have established new production rates²⁻⁴ for cosmogenic ¹⁰Be and ³He, which make it necessary to update all chronologies in this region^{1,5-15} and revise our understanding of cryospheric responses to climate variability. Here we present a new ¹⁰Be moraine chronology in Colombia showing that glaciers in the northern tropical Andes expanded to a larger extent during the Antarctic cold reversal (14,500 to 12,900 years ago) than during the Younger Dryas. On the basis of a homogenized chronology of all ¹⁰Be and ³He moraine ages across the tropical Andes, we show that this behaviour was common to the northern and southern tropical Andes. Transient simulations with a coupled global climate model suggest that the common glacier behaviour was the result of Atlantic meridional overturning circulation variability superimposed on a deglacial increase in the atmospheric carbon dioxide concentration. During the Antarctic cold reversal, glaciers advanced primarily in response to cold sea surface temperatures over much of the Southern Hemisphere. During the Younger Dryas, however, northern tropical Andes glaciers retreated owing to abrupt regional warming in response to reduced precipitation and land-surface feedbacks triggered by a weakened Atlantic meridional overturning circulation. Conversely, glacier retreat during the Younger Dryas in the southern tropical Andes occurred as a result of progressive warming, probably influenced by an increase in atmospheric carbon dioxide. Considered with evidence from mid-latitude Andean glaciers¹⁶, our results argue for a common glacier response to cold conditions in the Antarctic cold reversal exceeding that of the Younger Dryas.

The general warming trend during deglaciation was interrupted by cooler conditions in the Southern Hemisphere during the Atlantic cold reversal (ACR). Conversely, temperature records from Greenland reveal warm conditions during the ACR (termed the Bölling-Allerød interstadial in the Northern Hemisphere), followed by the cold Younger Dryas event. The response of tropical Andean glaciers to these rapid and non-linear climate changes remains puzzling. A recent review of published data¹ suggests that tropical Andean glaciers recorded a Younger Dryas signal, a view supported by several ¹⁰Be chronologies^{5,8,13,15}. However, the dating accuracy of these glacier fluctuations is questionable because ¹⁰Be chronologies are affected by large uncertainties (>10%) associated with the cosmogenic production rates. This prevents unambiguous attributions of glacier response to the ACR and Younger Dryas events. Indeed, at least three scaling schemes using different sea-level, high-latitude ¹⁰Be production rates were considered in establishing these

chronologies. More importantly, recent calibration studies for the first time established local production rates for cosmogenic ³He and ¹⁰Be in the high tropical Andes²⁻⁴. These new developments imply that all previously published moraine ages need to be reconsidered and that the mechanisms leading to glacial advance during the ACR and Younger Dryas events warrant further investigation.

Here we present a new chronology of eight prominent moraines of the Ritacuba Negro glacier (Colombia, Sierra Nevada del Cocuy) deposited during the 'late glacial', that is, the later stages of the last deglaciation. Forty-six ¹⁰Be cosmic-ray exposure (CRE) ages were obtained from boulders collected on the moraines and roches moutonnées (Fig. 1 and Methods). Analytic uncertainties on the entire set of CRE ages averaged $6 \pm 6\%$. The Ritacuba Negro glacier chronology was compared with a recalculated data set comprising 246 published ¹⁰Be and ¹²³He ages (Supplementary Information) obtained from 47 moraines^{1,5-15} sampled on one glacier in the northern tropical Andes (NTA) and 19 glaciers in the southern tropical Andes (STA) over the last 15 kyr. The recalculated data set was standardized using the recently revised local production rate² of 3.95 ± 0.18 atoms $\text{g}^{-1} \text{yr}^{-1}$ with a time-dependent scaling and a specific Andes atmosphere model (Methods). It is important to stress that the production rate used here was calibrated at locations that are comparable in elevation and latitude ranges to the dated moraines. To assess the impact of the different scaling parameters, we report the ages using four different scaling models (Methods).

When used in combination, the new and published ages allow investigation of the following key questions, at the regional scale of the tropical Andes. (1) When did the maximum glacial extents occur over the last 15 kyr in the NTA and the STA, respectively? (2) Did the tropical Andean glaciers show a synchronous behaviour? (3) What climatic mechanisms were driving the observed glacier fluctuations?

The maximum glacial extent of Ritacuba Negro glacier during the late glacial is indicated by the outer and frontal termination moraine M18, located at 3,975 m above sea level, and dates to 13.9 ± 0.3 ¹⁰Be kyr ago ($n = 5$) (Fig. 1; ages expressed in these units are calculated from the measured ¹⁰Be concentrations). Upslope, four boulders on moraine M17 are internally consistent and yield a mean CRE age of 14.0 ± 0.3 ¹⁰Be kyr. Seven samples collected on the large moraine M16 yield a mean CRE age of 13.4 ± 0.3 ¹⁰Be kyr. These three moraines indicate several advances or stillstands during the ACR. Upslope from M16, a very large accumulation is composed of three small moraines: M15 formed 11.8 ± 0.2 ¹⁰Be kyr ago ($n = 4$), at the very end of the Younger Dryas, and M14 and M13 yield respective mean CRE ages of 11.3 ± 0.1 ¹⁰Be kyr ($n = 9$) and 11.0 ± 0.4 ¹⁰Be kyr ($n = 4$). Two samples on a roche moutonnée confirm the chronology with a mean age of 11.1 ± 0.2 ¹⁰Be kyr. M12, which is roughly 350 m upslope from M13, dates to 1.2 ± 0.1 ¹⁰Be kyr

¹Université Paris 1 Panthéon-Sorbonne, CNRS Laboratoire de Géographie Physique, 92195 Meudon, France. ²Université Grenoble Alpes, LGGE, UMR 5183, F-38041 Grenoble, France. ³Department of Atmospheric and Environmental Sciences, University at Albany, Albany, New York 12222, USA. ⁴Aix-Marseille Université, CNRS-IRD-Collège de France, CEREGE UM34, 13545 Aix-en-Provence, France. ⁵CNRS, Centre de Recherches Pétrographiques et Géochimiques, UMR 7358, Université de Lorraine, BP 20, Vandœuvre-lès-Nancy 54501, France. ⁶Center for Climatic Research, Nelson Institute for Environmental Studies, University of Wisconsin-Madison, Madison, Wisconsin 53706, USA. ⁷IRD-Laboratoire d'Océanographie et du Climat: Expérimentation et Approche numérique, Université Pierre et Marie Curie, F-75252 Paris Cedex 05, France. ⁸School of Geography and Geosciences Irvine Building, University of St Andrews, St Andrews KY16 9AL, UK. ⁹Institut de Recherche pour le Développement, CP 9214, La Paz, Bolivia. ¹⁰Institute for Hydrology, Meteorology and Environmental Studies, Bogota, 07603, Colombia. ¹¹Escuela de Ingeniería Geológica, UPTC Sede Seccional Sogamoso, Sogamoso, 152211, Colombia. ¹²Center for Climatic Research and Department of Atmospheric and Oceanic Sciences, University of Wisconsin-Madison, Madison, Wisconsin 53706, USA. ¹³Climate and Global Dynamics Division, National Center for Atmospheric Research, Boulder, Colorado 80305, USA.

RESEARCH LETTER

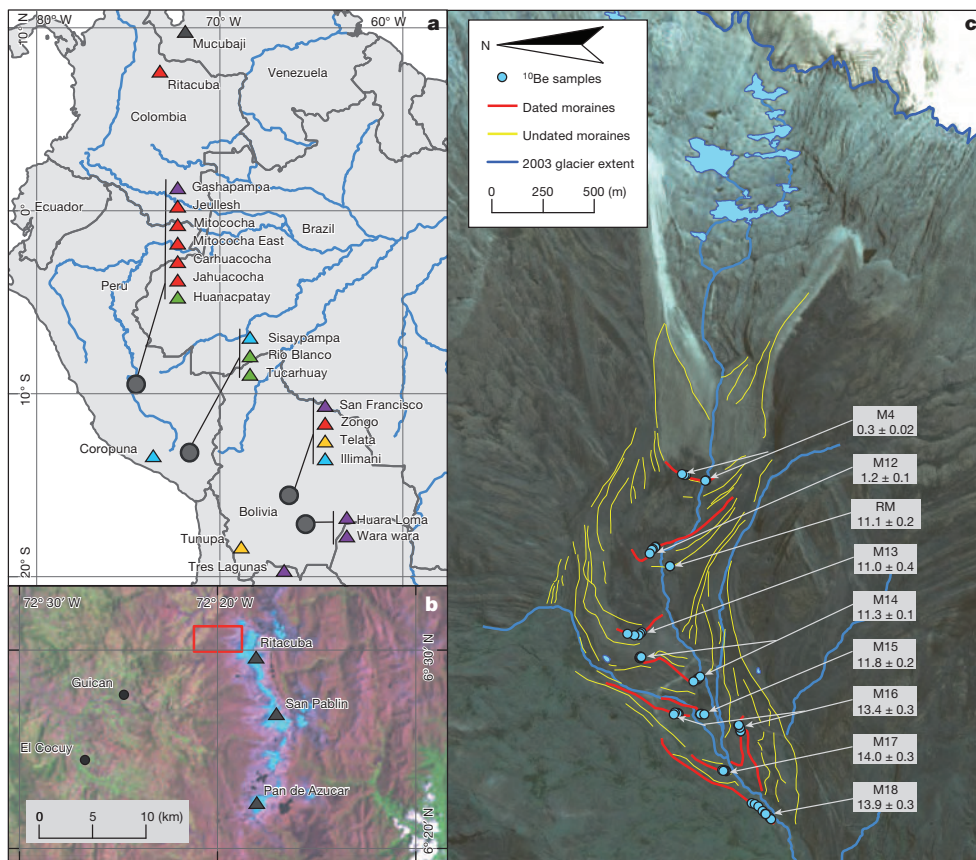


Figure 1 | The Ritacuba Negro glacier and studied sites. **a**, Location of the homogenized ^{10}Be and ^3He moraine record sites covering the northern and southern tropical Andes, with the largest glacial advance dated to during the ACR or possibly before (considering uncertainties) in purple; those during the ACR in red; those during the ACR or the Younger Dryas (considering uncertainties) in orange; those during the Younger Dryas in blue; those during the Holocene in green; and rejected chronology in black (Methods). **b**, Location of the northern tropical Ritacuba Negro glacial valley in the Cordillera de

Cocuy (red square), with filled triangles indicating summits. **c**, Map of the Ritacuba Negro glacier, showing dated and undated moraines (prefix M indicates a main moraine as discussed in the text and RM means roche moutonnée; units, ^{10}Be kyr; Supplementary Information and Methods), the location of ^{10}Be samples (blue dots), the snout of the Ritacuba Negro glacier in 2003 (thick blue line). The uncertainties associated with the ages account for analytical uncertainties only (1 s.d.).

($n = 2$). The innermost dated moraine of the Ritacuba Negro sequence is located about 2.5 km from the present frontal position of 4,660 m above sea level. Three boulders from this ridge yield a mean CRE age of 264 ± 23 ^{10}Be yr. Finally, three small, fresh moraines were formed during the twentieth century. Among the 46 samples, six were rejected as outliers on the basis of a χ^2 test reflecting cosmogenic nuclide inheritance from previous exposures and post-depositional erosion processes (two from M18, two from M16, one from M12 and one from M4; Methods).

To evaluate the wider implications of the Ritacuba Negro glacier moraine chronology, we first compare it with indirect evidence of glacier fluctuations derived from lake-level fluctuations in Venezuela¹⁷. The Venezuelan glacier chronology⁵ was not considered because of the uncertainties associated with ^{10}Be CRE ages (Methods). ACR advances (or stillstands) are evident in both records (moraine and lake sediments) at ~ 14.0 kyr ago. Minor advances (or stillstands) at the end of the Younger Dryas and during the early Holocene can also be detected in both records. However, on the basis of high titanium concentrations, ref. 17 identified a major glacial advance between ~ 12.8 and 12.1 kyr ago in their record. Such a glacial stillstand may have occurred in the Ritacuba Negro valley (Fig. 2), but, if so, it would necessarily have been smaller than both the ACR advances and the ones occurring at the end of the Younger Dryas. Indeed, there is no moraine dated to between 12.8 and 12.1 kyr ago preserved on Ritacuba Negro valley. However, the moraine M15, dated to 11.8 ± 0.2 kyr ago, could correspond to the end of the Younger Dryas.

We then compared the behaviour of the Ritacuba Negro glacier with 16 STA glacier chronologies that cover the ACR/Younger Dryas period (Figs 1 and 2 and Methods). The data show that seven glaciers have formed moraines at least once during the ACR chronozone *sensu stricto* and that seven others contain moraine deposits, whose dates, within the margin of error, overlap with the ACR period (Methods). Moraine formation implies the obliteration of any older moraines deposited by less extensive glaciation upstream, and the ACR advances correspond to the outermost front positions over the last 14.5 kyr in many locations in Peru, Bolivia and northern Argentina. Consequently, the corresponding ACR glacial stillstands are undoubtedly more extensive than those that occurred later during the Younger Dryas. This comparison thus reveals comparable behaviour between the Ritacuba Negro (NTA) and STA glaciers. Glacial advances during the Younger Dryas were recorded in several cordilleras but were generally slightly smaller than those occurring during the ACR. However, larger advances during the Younger Dryas than during the ACR are observed for three glaciers^{9,13,15} (five within the limits of dating uncertainty; Fig. 1) and may result from site-specific conditions.

Three glaciers in our data set contain only Holocene moraines (Fig. 1 and Methods), and suggest that early Holocene glacial extents are observed in the Ritacuba valley and at many STA sites. However, it is clear that mid- and late-Holocene stillstands are very rarely observed, probably because these moraines have been erased by Little Ice Age glacial advances¹⁸. Hence, a coherent retreat from the ACR extent to the present

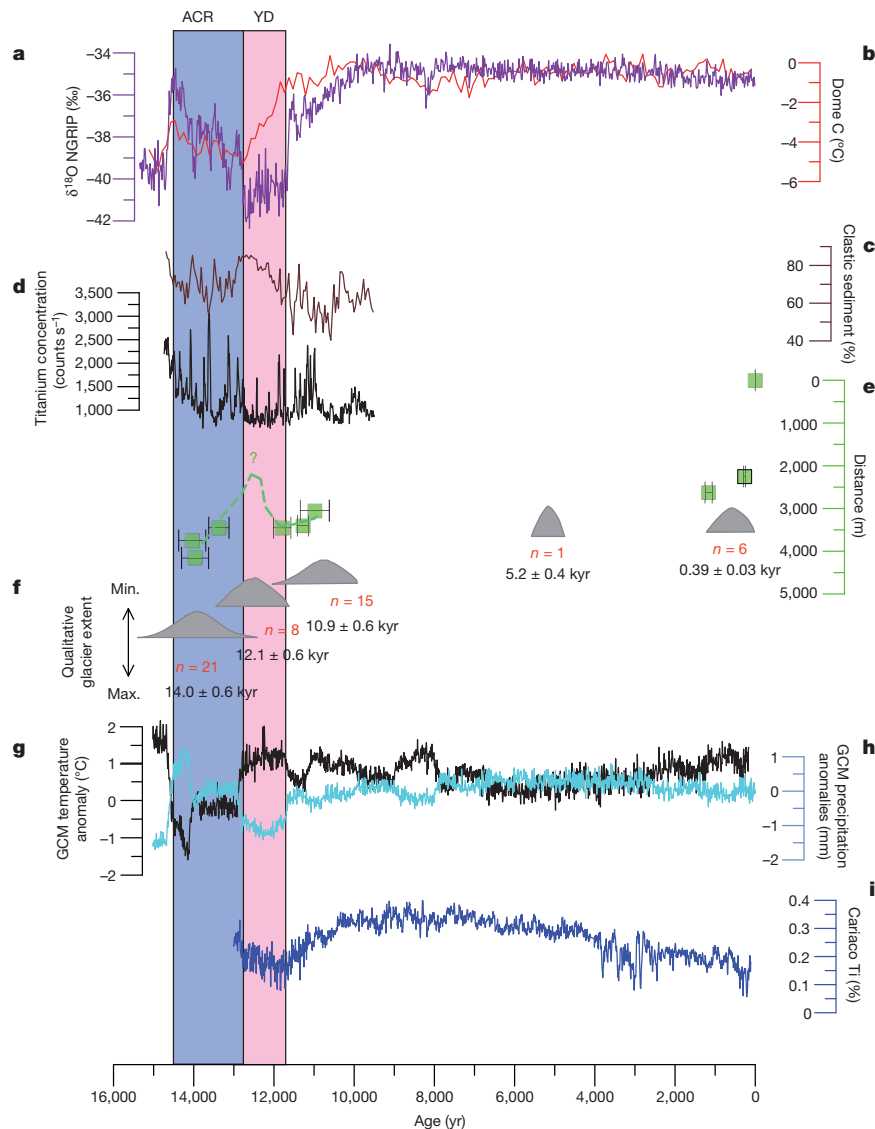


Figure 2 | Changes in the Ritacuba Negro glacier compared with proxy records. **a**, NGRIP $\delta^{18}\text{O}$ from ref. 24 (purple line). **b**, Temperature anomalies at EPICA Dome C²⁴ (red line). **c**, **d**, Clastic sediment (**c**; brown line) and titanium concentration (**d**; black line) from Los Anteojos lake¹⁷ (Venezuela). **e**, Ritacuba Negro glacier front variations relative to extent in 2010 and chronology based on the 40 new ^{10}Be ages documenting the NTA region. Error bars are moraine age uncertainty (1 s.d.). The dashed line shows the possible evolution of the front. **f**, STA moraine ages (based on 246 ^{10}Be surface exposure ages from 19 glaciers; Supplementary Information and Methods). Shaded

grey areas correspond to probability distribution functions of moraine ages. Their position on the y axis illustrates the progressive general retreat of the glaciers over time. The number of moraines <15 kyr old is shown in red, the mean age of each distribution (uncertainty, 2 s.d.) is shown in black. **g**, CCSM3 temperature anomalies in the Ritacuba region (77–69° W, 2–10° N; black line). **h**, CCSM3 precipitation anomalies in the Ritacuba region (77–69° W, 2–10° N; blue line). Anomalies are with respect to the 13.9 kyr period in the all-forcings run. **i**, Titanium concentration in Cariaco basin sediments¹⁹. YD, Younger Dryas; ACR, Antarctic cold reversal.

position, interrupted by minor stillstands or re-advances during the Younger Dryas and early Holocene epoch, is observed across the tropical Andes. Together these fluctuations reveal a common trend in glacier size evolution.

The glacier size evolution across the tropics during the ACR/Younger Dryas period is in step with other Southern Hemisphere glaciers such as those in Patagonia and New Zealand¹⁶, and strongly suggests that they mostly result from a common climate driver. The fact that the NTA and STA glacier systems, each exposed to different precipitation regimes¹⁹, display a common evolution suggests that increased temperature served as a dominant control for glacier retreat during the ACR/Younger Dryas period (Figs 2 and 3). This temperature sensitivity is consistent with modern observations which show that temperature affects glacier melt rates through a change in the rain–snow line and albedo feedbacks^{20,21}.

To explore possible mechanisms responsible for this tropical Andean glacier evolution during the ACR/Younger Dryas period, we analysed the transient simulation of the last deglaciation with the coupled global climate model²² (GCM) Community Climate System Model version 3 (CCSM3) (Methods). Two studies^{23,24} demonstrate that the GCM simulation successfully represents the antiphased hemispheric temperature response to ocean circulation changes during the last deglaciation. The transient simulation indicates a significant warming over the STA region during the deglaciation, interrupted by a minimum 14.1 kyr ago and a smaller decrease in temperature ~ 12.1 kyr ago (Fig. 3). The temperature change is in good agreement with moraine records in the STA. In the Ritacuba region, however, temperature changed rapidly between 14.1 and 11 kyr ago, with two cold episodes during the ACR and at the end of the Younger Dryas, separated by a warm period during the Younger

RESEARCH LETTER

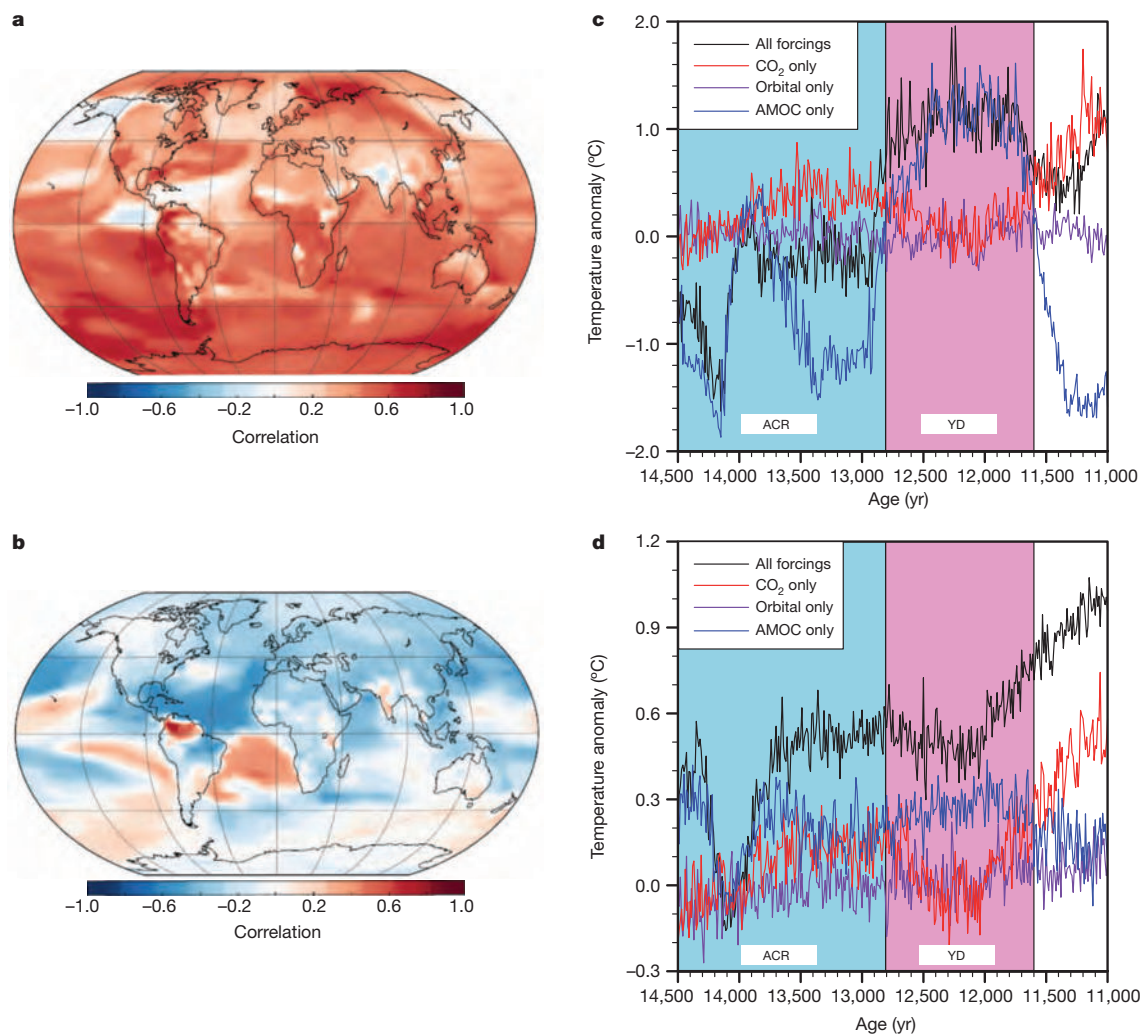


Figure 3 | Decadal temperature variations in the Ritacuba region correlated with global surface temperature. a, ACR period. b, Younger Dryas period. Statistically insignificant ($P > 0.05$) values are shown in white. c, d, Temperature evolution simulated with different CCSM3 single-forcing

and all-forcing runs in the Ritacuba region ($77\text{--}69^\circ\text{ W}$, $2\text{--}10^\circ\text{ N}$; c) and, documenting the STA region, in the Andes of Bolivia¹⁴ ($73\text{--}65^\circ\text{ W}$, $14\text{--}22^\circ\text{ S}$; d). The keys show the various forcings used. Anomalies are with respect to the decadal averages at 14.0 kyr in all-forcing runs.

Dryas (Figs 2 and 3). Again this temperature evolution is in agreement with our direct observations of glacier change in the Ritacuba region, but is inconsistent with results from ref. 17, where a cold episode is identified during the main Younger Dryas period on the basis of clastic sediments and pollen collected in a Venezuelan lake. This discrepancy may result from uncertainties in regional GCM simulations or from distinct sensitivities of the different proxies to climate forcing.

To further explore such a hypothesis and better understand this common glacier behaviour, decadal temperature and precipitation variations were correlated with global surface temperature and precipitation fields, respectively. During the ACR, a positive relationship is observed between temperature fluctuations in the Ritacuba region and temperatures over large parts of the Southern Hemisphere. Correlations are most significant at southern high latitudes and in the eastern equatorial Pacific (Fig. 3), with cold sea surface temperatures in the eastern equatorial Pacific being associated with glacier advance, in agreement with present-day observations²⁵. During the Younger Dryas, the slowdown of the Atlantic meridional overturning circulation (AMOC) that maintained cold sea surface temperatures in the northern tropical Atlantic produced a very different pattern. In the STA, temperature evolved gradually and in step with the large-scale temperature signal. In the Ritacuba

region, however, the continental temperature warmed when the cooling in the Northern Hemisphere occurred during the Younger Dryas (Supplementary Discussion). In the transient simulation, the Younger Dryas warming in the Ritacuba region results from decreased latent heat loss due to reduction of tropical forests, which is caused by the southward shift of the intertropical convergence zone²⁶ associated with the slowdown of the AMOC during the Younger Dryas (Supplementary Discussion and Extended Data Figs 4–9). Therefore, the temperature increase in the region during the Younger Dryas (Fig. 2) may at least in part be caused by decreased cloudiness and related local land–surface feedbacks such as reduced soil moisture and less evaporative cooling^{27,28}, as a result of the large-scale reorganization of precipitation over tropical South America. Other mechanisms, such as upwelling Antarctic intermediate water in the eastern tropical Pacific²⁹ may also have a role in NTA warming during the Younger Dryas. CCSM3 results from simulations²³ that isolate individual forcing components indicate that tropical glacier fluctuations during the ACR/Younger Dryas period were primarily driven by a CO_2 increase superimposed on AMOC variability. AMOC variability was responsible for the abrupt regional climate change observed in the NTA during the Younger Dryas period, whereas temperature changes in the STA carry a predominantly CO_2 -forced fingerprint (Fig. 3).

Our results clearly demonstrate that tropical Andean glaciers were impacted by the ACR, consistent with results from recent studies in southern mid latitudes¹⁶, suggesting a common temperature response to this event along the entire Andean cordillera. Regardless of our interpretation, any proposed mechanisms for drivers of deglacial climate change in the tropical Andes must account for the widespread stability of glacier ice during the ACR. Our analyses suggest AMOC variability superimposed on CO₂ forcing as the main drivers of the late deglaciation in the Andes. Finally, our results based on new cosmogenic production rates²⁻⁴ illustrate that most previous chronologies and climate interpretations from tropical glaciers since the LGM may need to be revisited.

METHODS SUMMARY

To compare chronologies from the northern and southern tropical Andes, we homogenized existing late-glacial cosmogenic ¹⁰Be and ³He ages younger than 21 kyr (Supplementary Table 1). Beryllium-10 concentrations were normalized against an assigned value of the NIST ¹⁰Be/⁹Be ratio (2.79×10^{-11}). Existing ¹⁰Be ages were recalculated using the recent Altiplano production rate of 3.95 ± 0.11 atoms g⁻¹ yr⁻¹. To test the impact of the different parameters involved in the production scaling, we recalculated the age of each moraine from 20 glaciers selected in this study using four models (Supplementary Information). We excluded all glaciers that did not document the ACR–Holocene period. In this process, moraine identification was strictly the same as those documented in cited studies. We used and excluded the same samples as in the cited studies.

We did not use a χ^2 analysis to compare the ages of the moraines because such a test was not used in most previous papers. Instead, we conducted two distinct analyses on the 20 glaciers. The first was done to assess the number of glaciers with the maximum extent belonging to the ACR chronozone, assuming that the youngest moraine (as dated) since the ACR period corresponds to the maximum extent. In this case, we distinguished five different chronozones: pre-ACR, ACR, ACR/Younger Dryas, Younger Dryas and post-Younger Dryas. Each glacier was classified in a single chronozone according to the age of the maximum extent moraine and its uncertainty. The second analysis was conducted on the moraine ages to get the distribution function with time. This time we distinguished three groups of moraines, corresponding to the ACR, Younger Dryas and Holocene chronozones, respectively. Each moraine was classified in one or two distinct chronozones according to age and the associated uncertainties.

Online Content Methods, along with any additional Extended Data display items and Source Data, are available in the online version of the paper; references unique to these sections appear only in the online paper.

Received 26 November 2013; accepted 28 May 2014.

Published online 24 August 2014.

- Rodbell, D. T., Smith, J. A. & Mark, B. G. Glaciation in the Andes during the late glacial and Holocene. *Quat. Sci. Rev.* **28**, 2165–2212 (2009).
- Blard, P. H., Braucher, R., Lavé, J. & Bourlès, D. Cosmogenic ¹⁰Be production rate calibrated against ³He in the high tropical Andes (3800–4900 m, 20–22° S). *Earth Planet. Sci. Lett.* **382**, 140–149 (2013).
- Blard, P.-H. *et al.* Cosmogenic ³He production rate in the high tropical Andes (3800 m, 20° S): implications for the local last glacial maximum. *Earth Planet. Sci. Lett.* **377–378**, 260–275 (2013).
- Kelly, M. *et al.* A locally calibrated, late glacial ¹⁰Be production rate from a low latitude, high-altitude site in the Peruvian Andes. *Quat. Geochronol.* (in the press).
- Carcaillet, J., Angel, I., Carrillo, E., Audemard, F. A. & Beck, C. Timing of the last deglaciation in the Sierra Nevada of the Merida Andes, Venezuela. *Quat. Res.* **80**, 482–494 (2013).
- Smith, J. A., Seltzer, G. O., Farber, D. L., Rodbell, D. T. & Finkel, R. C. Early local last glacial maximum in the tropical Andes. *Science* **308**, 678–681 (2005).
- Zech, R., Kull, Ch., Kubik, P. W. & Veit, H. LGM and Late Glacial glacier advances in the Cordillera Real and Cochabamba (Bolivia) deduced from ¹⁰Be surface exposure dating. *Clim. Past* **3**, 623–635 (2007).
- Glasser, N. F., Clemmens, S., Schnabel, C., Fenton, C. R. & McHargue, L. Tropical glacier fluctuations in the Cordillera Blanca, Peru between 12.5 and 7.6 ka from cosmogenic ¹⁰Be dating. *Quat. Sci. Rev.* **28**, 3448–3458 (2009).

- Licciardi, J. M., Schaefer, J. M., Taggart, J. R. & Lund, D. C. Holocene glacier fluctuations in the Peruvian Andes indicate northern climate linkages. *Science* **325**, 1677–1679 (2009).
- Hall, S. R. *et al.* Geochronology of Quaternary glaciations from the tropical Cordillera Huayhuash, Peru. *Quat. Sci. Rev.* **28**, 2991–3009 (2009).
- Zech, J., Zech, R., Kubik, P. W. & Veit, H. Glacier and climate reconstruction at Tres Lagunas, NW Argentina, based on ¹⁰Be surface exposure dating and lake sediment analyses. *Palaeogeogr. Palaeoclimatol. Palaeoecol.* **284**, 180–190 (2009).
- Smith, J. A. & Rodbell, D. T. Cross-cutting moraines reveal evidence for North Atlantic influence on glaciers in the tropical Andes. *J. Quat. Sci.* **25**, 243–248 (2010).
- Smith, C. A., Lowell, T. V., Owen, L. A. & Caffee, M. W. Late Quaternary glacial chronology on Nevado Illimani, Bolivia, and the implications for paleoclimatic reconstructions across the Andes. *Quat. Res.* **75**, 1–10 (2011).
- Jomelli, V. *et al.* Irregular tropical glacier retreat over the Holocene epoch driven by progressive warming. *Nature* **474**, 196–199 (2011).
- Bromley, G. *et al.* Glacier fluctuations in the southern Peruvian Andes during the late-glacial period, constrained with cosmogenic ³He. *J. Quat. Sci.* **26**, 37–43 (2011).
- Putnam, A. E. *et al.* Glacier advance in southern middle-latitudes during the Antarctic Cold Reversal. *Nature Geosci.* **3**, 700–704 (2010).
- Stansell, N. D. *et al.* Abrupt Younger Dryas cooling in the northern tropics recorded in lake sediments from the Venezuelan Andes. *Earth Planet. Sci. Lett.* **293**, 154–163 (2010).
- Jomelli, V. *et al.* Fluctuations of Andean tropical glaciers since the last millennium and palaeoclimatic implications: a review. *Palaeogeogr. Palaeoclimatol. Palaeoecol.* **281**, 269–282 (2009).
- Haug, G. H., Hughen, K. A., Sigman, D. M., Peterson, L. C. & Röhl, U. Southward migration of the Intertropical Convergence Zone through the Holocene. *Science* **293**, 1304–1308 (2001).
- Favier, V., Wagnon, P. & Ribstein, P. Glaciers of the outer and inner tropics: a different behaviour but a common response to climatic forcing. *Geophys. Res. Lett.* **31**, L16403 (2004).
- Favier, V., Wagnon, P., Chazarin, J.-P., Maisincho, L. & Coudrain, A. One-year measurements of surface heat budget on the ablation zone of Antizana Glacier 15, Ecuadorian Andes. *J. Geophys. Res.* **109**, D18105 (2004).
- Liu, Z. *et al.* Transient simulation of deglacial climate evolution with a new mechanism for Bolling-Allerod warming. *Science* **325**, 310–314 (2009).
- He, F. *et al.* Northern Hemisphere forcing of Southern Hemisphere climate during the last deglaciation. *Nature* **494**, 81–85 (2013).
- Shakun, J. D. *et al.* Global warming preceded by increasing carbon dioxide concentrations during the last deglaciation. *Nature* **484**, 49–54 (2012).
- Franco, B., Vuille, M., Favier, V. & Caceres, B. New evidence for an ENSO impact on low-latitude glaciers: Antizana 15, Andes of Ecuador, 0–28° S. *J. Geophys. Res.* **109**, D18106 (2004).
- Peterson, L. C., Haug, G. H., Hughen, K. A. & Röhl, U. Rapid changes in the hydrologic cycle of the tropical Atlantic during the last glacial. *Science* **290**, 1947–1951 (2000).
- Leduc, G. *et al.* Moisture transport across central America as a positive feedback on abrupt climatic changes. *Nature* **445**, 908–911 (2007).
- Davin, E. L. & de Noblet-Ducoudre, N. Climatic impact of global-scale deforestation: radiative versus nonradiative processes. *J. Clim.* **23**, 97–112 (2010).
- Pierrehumbert, R. T. Climate change and the tropical Pacific: the sleeping dragon wakes. *Proc. Natl Acad. Sci. USA* **97**, 1355–1358 (2000).

Supplementary Information is available in the online version of the paper.

Acknowledgements Financial support was provided by the French ANR El Paso programme no. 10-blan-68-01. The ¹⁰Be measurements were performed at the ASTER AMS national facility (CEREGE, Aix en Provence), which is supported by the INSU/CNRS, the French Ministry of Research and Higher Education, IRD and CEA. TRACE21 is supported by the P2C2 programme (NSF), the Abrupt Change Program (DOE), the EaSM programme (DOE) and the INCITE computing programme (DOE and NCAR). We thank M. Arnold, G. Aumaitre and K. Keddadouche for their assistance during ¹⁰Be measurements.

Author Contributions V.J., D.B., J.L.C. and H.F. conducted the field work on Ritacuba Negro glacier; F.H., Z.L. and B.O.-B. performed the GCM simulations; M.V. and C.C. provided temperature correlation maps; D.L.B., R.B., P.-H.B., L.L. and L.M. participated in producing the cosmogenic data; L.M., P.-H.B. and V.J. updated and homogenized the previously published cosmogenic ages; P.-H.B., V.R., V.J., D.G. and D.L.B. interpreted the cosmogenic ages; and V.J., V.F., M.V., F.H. and D.L.B. contributed to writing the paper.

Author Information Reprints and permissions information is available at www.nature.com/reprints. The authors declare no competing financial interests. Readers are welcome to comment on the online version of the paper. Correspondence and requests for materials should be addressed to V.J. (vincent.jomelli@igp.cnrs.fr).

RESEARCH LETTER

METHODS

The chronology of Ritacuba Negro glacier fluctuations. We report the chronology of the most complete, preserved moraine sequence from the Ritacuba Negro glacier (2.8 km² in 2010; 5,271 m above sea level; 6° 30' N, 72° 20' W), located on the western slope of the Colombian Cordillera de Cocuy. The moraines were used to estimate an earlier glacial extent and represent the minimum estimate of the fluctuations of the Ritacuba Negro glacier. The behaviour of the glacier between two successive moraine ridges is unknown. The glacier may have strongly retreated between two successive moraines observed in the field, but the front never overlapped the down-slope ridge. These moraines are composed of sandstone rock blocks. Each moraine ridge was mapped by means of a differential GPS survey in the field (accuracy, <1 m; Extended Data Fig. 1). Our interpretation of moraine records is that lateral or terminal moraine ridges are constructed at times when the glacier is in, or close to, equilibrium with the prevailing climate. The reaction of the glacier in equilibrium to a superimposed climate change is almost immediate and less than the uncertainty in the dates provided in this paper. The ages provided by ¹⁰Be of boulders on moraine ridges represent the onset of the retreat. Moraines are assumed to form by a combination of extreme cold situations superimposed on a long-term cold period; that is, very high-frequency (decade) cold periods superimposed on a long-term temperature minimum just before or at the beginning of a warming trend that causes glacial retreat. In other words, a moraine indicates that the glacier is beginning to retreat after reaching a maximum extent, and, hence, a moraine indicates a temperature minimum before the climate begins to warm.

The chronology of the Ritacuba Negro glacier fluctuations is based on 46 *in situ*-produced cosmogenic ¹⁰Be boulder exposure ages (Supplementary Table 1 and Extended Data Figs 1–3). This chronology was based on the following considerations. Moraines are potentially vulnerable to denudation, and a moraine formed during a glacial advance is preserved and observed in the field only if the glacier did not overlap it during a subsequent extensive ice advance.

Large blocks (>60 cm high) were sampled (Supplementary Table 1) on landforms with clear geomorphologic context relating directly to a former glacier margin. Ten remains of moraine crests representing indistinguishable advances were ignored. Samples were collected from near horizontal boulder top surfaces. These boulders were preferentially collected on stable parts of the moraine crest. Denudation was considered as absent for all of them (Supplementary Table 1). We used clinometer and compass to document the surrounding topographic shielding for all sample locations. We photographed all boulders (Supplementary Information) and we measured the ground-to-sample height of every boulder (Supplementary Table 1).

Cosmic-ray exposure dating is based on the quantification of the cosmogenic nuclide content accumulated in a rock exposed at the surface to cosmic rays. This high-energy cosmic radiation induces a nuclear reaction when penetrating Earth's environment. Energetic particles interact with target atoms to produce cosmogenic nuclides. In this study, *in situ*-produced ¹⁰Be was measured in the quartz mineral collected in the rock samples. Samples were crushed and sieved (250–1,000 μm); magnetic components were eliminated by means of a Frantz magnetic separator. Quartz was extracted by dissolution of unwanted minerals in mixtures of HCl and H₂SiF₆. Solutions were renewed daily until they remained clear. Potential pollution by atmospheric ¹⁰Be was removed by three successive leaching steps in HF, each step dissolving ~10% of the quartz. Before complete dissolution in HF (48%), a weighted amount (~100 mg) of a 3,025 μg g⁻¹ homemade ⁹Be spike solution³⁰ was added. Successive separation by anion and cation exchange resins (DOWEX 1X8 then 50WX8) and precipitations were performed to isolate beryllium. The final hydroxide precipitates were dried and heated at 700 °C to obtain BeO, and were finally mixed with niobium powder to prepare targets before their measurement by accelerator mass spectrometry. All measurements were performed at the French AMS National Facility, ASTER, located at CEREGE in Aix-en-Provence. The data were calibrated directly against the National Institute of Standards and Technology (NIST) standard reference material 4325 by using an assigned ¹⁰Be/⁹Be value of (2.79 ± 0.03) × 10⁻¹¹ (ref. 31).

Exposure ages were calculated using a ¹⁰Be production rate that has been locally calibrated in the high tropical Andes (20° S, 3,800 m) from a 15.3 ± 0.5 kyr-old surface^{2,3}. Using the time-dependent scaling of ref. 32 and the specific Andes atmosphere model of ref. 33, this locally calibrated rate corresponds to a sea-level, high-latitude ¹⁰Be production rate of 3.95 ± 0.18 atoms g⁻¹ yr⁻¹ (ref. 2). This locally calibrated production rate is based on 11 boulders, and 10 of them have cosmogenic concentrations that agree within analytical uncertainties. This low dispersion indicates that geological complications such as erosion or inheritance are not affecting this data set. This is not the case of the data set of ref. 33, which is characterized by a bimodal distribution. Although these data were used as a reference calibration site by ref. 9, we believe that the recent calibration studies by refs 2, 3 are thus more robust than those of ref. 33. Finally this rate is also in agreement with recently published independent production rate for southern Peru⁴.

Time-dependent correction was done according to the model of ref. 34 and using the VDM database of ref. 35. Indeed, a recent study by ref. 36 demonstrated that atmospheric ¹⁰Be records are probably the best proxy of the Earth's VDM fluctuations. Consequently, the high-resolution ¹⁰Be record measured in Greenland ice³⁵ should be considered a more reliable estimate of the Earth's VDM than the one of ref. 37, which is used in the CRONUS online calculator³⁸. This sea-level, high-latitude spallation production rate was scaled for the sampling altitudes and latitudes using the scaling factor proposed by ref. 32. To do so, a non-standard atmospheric model was used. This model takes into account the specificity of the regional atmospheric pressure according to the pressure data reported by ref. 33.

To test the impact of the scaling factors on the ages, we recalculated moraine ages using four different scaling procedures, all of them relying on the Lal/Stone polynomials³². Model 1 is time independent (no palaeomagnetic field correction). It considers the standard atmosphere (as defined in ref. 32). Model 2 is time independent (no palaeomagnetic field correction). It considers an alternative atmosphere model, specific to the tropical Andes (following ref. 33). Model 3 considers the time variations of production rates, using the palaeomagnetic record of ref. 35 and the geomagnetic correction described in ref. 34. The atmosphere model used is the one of ref. 32. Model 4 considers the time variations of production rates, using the palaeomagnetic record of ref. 35 and the geomagnetic correction described in ref. 34. The atmosphere model used is the tropical Andes model³³.

Given that the local calibration site used and the Ritacuba Negro moraines have nearly the same elevations and absolute latitudes, the differences between these four scaling models are limited (<5%), which strengthens the accuracy of our dating. In the main text and the figures, we have retained exposure ages calculated using model 4. This choice is justified because many data support the existence of time variations in production rates, as well as regional atmosphere peculiarities^{33,36}.

The calculated surface production rates were also corrected for local slope, topographic shielding due to surrounding morphologies following ref. 39, and thickness, assuming an attenuation length of 160 g cm⁻² and a rock density of 2.7 g cm⁻³. Analytical uncertainties (reported as 1 s.d.) include a conservative 0.5% uncertainty based on long-term measurements of standards, a 1 s.d. statistical error on counted ¹⁰Be events, and the uncertainty associated with the chemical and analytical blank correction (Supplementary Table 1 and Extended Data Fig. 2).

To combine and compare the different exposure ages of Ritacuba Negro glacier, the method proposed by ref. 40 was applied (Supplementary Table 1). This method is based on χ^2 analysis. To obtain enough samples (*n*) per moraine, the 0.05 critical value for χ^2 with *n* - 1 degrees of freedom is calculated and compared with the theoretical value given by a χ^2 table. If the calculated value is lower than the theoretical one, then all ¹⁰Be ages with their analytical uncertainties are used to calculate a mean exposure age; otherwise, outliers are rejected until the distribution passes the test. Then the mean exposure age with its associated analytical uncertainty is calculated using the remaining samples (Supplementary Table 1). Analytical uncertainties for the entire set of cosmic ray exposure ages averaged 6%.

The oldest moraine in Ritacuba Negro valley, M18, is dated to 13.9 ± 0.3 ¹⁰Be kyr ago on the basis of the weighted mean of five samples with their analytical standard deviation (Supplementary Table 1 and Extended Data Figs 1 and 2). Two samples, B36 and B46, dated to 15.1 ± 0.5 ¹⁰Be kyr ago and 11.4 ± 0.9 ¹⁰Be kyr ago, respectively, were considered as outliers on the basis of a χ^2 test reflecting isotope inheritance from previous exposure and/or post-depositional processes. Including these two samples would have given a mean value of 14.0 ± 0.2 ¹⁰Be kyr.

M16 is dated to 13.4 ± 0.3 ¹⁰Be kyr ago on the basis of the weighted mean of seven samples. Two samples, B30 and B33, dated to 11.4 ± 0.3 ¹⁰Be kyr ago and 15.1 ± 0.6 ¹⁰Be kyr ago, respectively, were rejected on the basis of the χ^2 test. Including these two samples would have given a mean value of 12.9 ± 0.2 ¹⁰Be kyr.

Three hundred metres upslope, a very large lobated accumulation is composed of three younger glacial moraines from M15 to M13. M15 and M14 were dated to 11.8 ± 0.2 ¹⁰Be kyr ago (*n* = 4) and 11.3 ± 0.1 ¹⁰Be kyr ago (*n* = 9), respectively. Combining samples from these two moraines would have given a mean value of 11.4 ± 0.1 ¹⁰Be kyr. M13 was dated to 10.9 ± 0.4 ¹⁰Be kyr ago (*n* = 4).

Four small, undated recessional moraines, located only a few metres from each other and intercalated between these advanced moraines (M15–13), document numerous pulses at that time and explain the very large size of this debris accumulation.

M12 was dated to 1.1 ± 0.1 ¹⁰Be kyr ago. One sample (B10), dated to 2.2 ± 0.2 ¹⁰Be kyr ago, was considered an outlier on the basis of a χ^2 test reflecting isotope inheritance from previous exposure. Including this sample would have given a mean value of 1.3 ± 0.1 ¹⁰Be kyr.

On M4, three boulders yielded ¹⁰Be ages of 253 ± 28 yr, 263 ± 40 yr and 482 ± 130 yr, resulting in a mean age of 264 ± 23 ¹⁰Be yr. A fourth boulder, dated at 1,285 ± 140 yr, was rejected. Including this sample would have given a mean value of 292 ± 22 ¹⁰Be yr.

The chronology of the Andean glaciers. To compare our Ritacuba Negro record with existing chronologies from the northern and southern Andes, we compiled

and homogenized existing late-glacial cosmogenic ^{10}Be and ^3He chronologies (ages less than 21 kyr) from published studies from Venezuela, Peru, Bolivia and northern Argentina^{15–15} (Supplementary Table 1). We proceeded to a homogenization (see below) of chronologies covering the last 14.5 kyr on the following bases. (1) Beryllium-10 concentrations were normalized against an assigned value of the NIST $^{10}\text{Be}/^9\text{Be}$ ratio (2.79×10^{-11} ; ref. 31). Recalculations were made if necessary. (2) Existing ^{10}Be ages were recalculated using the Altiplano production rate of 3.95 ± 0.11 atoms $\text{g}^{-1} \text{yr}^{-1}$ recently calibrated by ref. 2. All the required data for calculating the ^3He and ^{10}Be production rates used are available in refs 1, 2, 41. To test the impact of the different parameters involved in the production scaling, we recalculated moraine ages using the four models described above, similar to those used for the Ritacuba Negro data.

All models are shown for comparison in Supplementary Table 1, but, similarly to the Ritacuba Negro data set, we used only ages from model 4 in the figure and in the text. We then excluded all glaciers that did not document the ACR–Holocene period (for instance ref. 33) assuming that the ACR began 14.5 kyr ago.

Selected moraines for our study. Moraine identification was strictly the same as documented by other authors in their original studies. We used the same moraine notation as the authors did in their papers. When the name was missing, we arbitrary gave an alphabetic letter to each of the documented moraines, with A corresponding to the closest moraine from the present glacier front position. This classification was based on our analysis of maps or aerial photos shown in the papers.

We then calculated the age of each moraine. We used strictly the same samples as the authors did in their own analyses, except as regards moraine M3 from ref. 42 (Supplementary Table 1), for which we choose to differentiate the left side (dated to 14.1 ± 0.2 ^{10}Be kyr ago) from the right side (dated to 16.5 ± 0.2 ^{10}Be kyr ago). We excluded the same samples from our mean moraine age calculation as did the authors. To compare the different exposure ages of each glacial moraine, our results presented in Fig. 1 and Supplementary Table 1 were not based on a χ^2 analysis, because such a test was not used in most previous papers.

Standardized ages. We used standardized ages to retrieve glaciers with a maximum extent that occurred in the ACR to the Younger Dryas chronozone (see refs. 1, 5–15). Standardization shows that several data should be cautiously used. Ref. 43 published evidence for a Younger Dryas glacial advance in the Andes of northwestern Venezuela based on radiocarbon ages collected in Mucubají valley. Parts of these results were reinvestigated by ref. 5 using ^{10}Be CRE ages (Supplementary Table 1). However, the new local production rate incorporates the fact that on Los Zepa glacier the moraine previously attributed to the Younger Dryas by refs 43, 5 is actually older than the ACR period. On Mucubají glacier, moraine chronology shows that the level-7 frontal position corresponds to the ACR. However, we did not consider this chronology because of too large uncertainties and discrepancies with the stratigraphic order. Indeed levels 9–10 show evidence of glacial advance during the Younger Dryas. However, these ages are bracketed by two other ages that make the whole chronology questionable. Age at level 8 located at a lower altitude must be older than level 9 (considering the stratigraphic order) but shows a very large uncertainty and may correspond to the ACR–Holocene period. Age at level 11 located at the highest altitude corresponds to the ACR period but does not respect the stratigraphic order. This Venezuelan glacier was then rejected from our analysis because of too large uncertainties in the chronology.

Analysis on the retreat chronology. We then conducted two distinct analyses on the 20 glaciers.

The first one was done to assess the number of glaciers with a maximum extent belonging to the ACR chronozone. In this case, we distinguished five different chronozones: pre-ACR, ACR, ACR/Younger Dryas, Younger Dryas and post-Younger Dryas. Each glacier was classified in a single chronozone according to the age of the maximum-extent moraine and its uncertainty. To determine whether glaciers were sensitive to the ACR signal, we next counted the number of cases per group. We concluded that most glaciers were larger during the ACR than during the Younger Dryas (Supplementary Table 1). This information is given in Fig. 1.

The second analysis was conducted on the moraine ages to get the distribution function of moraine ages with time. We distinguished, this time, three groups of moraines corresponding to the ACR, Younger Dryas and Holocene chronozones, respectively. Each moraine was classified in one or two distinct chronozones according to age and the associated uncertainties. Depending on the uncertainty range, a moraine may be unequivocally attributed to one group, or the moraine age may overlap two periods, leading the moraine to be included in two groups. We next computed a density function (Fig. 2f) for those moraines associated with a specific chronozone.

Analysis of glaciers. We assumed that the youngest moraine (as dated) since the ACR period corresponds to the maximum extent of the 20 glaciers in this study. To assess whether the glacier reached its maximum extent in the ACR or in a more recent period, we classified the 20 glaciers according to the five groups presented earlier, on the basis that a glacier cannot belong to two different groups (Fig. 1).

The first group corresponds to glaciers with a maximum extent possibly included in the ACR or older (pre-ACR) if we account for the uncertainty range. Glacier Gashapampa, with a moraine dated to 14.4 ± 0.2 ^{10}Be kyr ago (purple triangle in Fig. 1), is an example.

A glacier was attributed to the second group (ACR) if the age of the maximum-extent moraine belongs to the chronozone *sensu stricto* (14.5–12.9 kyr). The term *sensu stricto* means here that the age of the moraine with the uncertainties is inside the chronozone. Jeullesh glacier is a good example, with the maximum extent moraine over the period considered dated to 13.9 ± 0.2 ^{10}Be kyr ago (red triangles in Fig. 1).

The third group corresponds to glaciers with a maximum that could be dated to the ACR or to the Younger Dryas period taking into account uncertainties associated with the age. Telata glacier, the oldest moraine of which is dated to 13.0 ± 0.7 ^{10}Be kyr ago (orange triangle in Fig. 1) is an example.

The fourth group corresponds to glaciers with a maximum extent during the Younger Dryas (*sensu stricto*) 12.8–11.5 kyr ago (blue triangles in Fig. 1).

The last group includes glaciers for which the oldest documented moraines are younger than 11.6 kyr (green triangles in Fig. 1).

Assuming this selection, 17 glaciers have a dated maximum extent during the pre-ACR/Younger Dryas period. Seventy per cent of the latter glaciers showed a maximum during the pre-ACR and ACR periods, and 30% during the Younger Dryas. Moraines of three other glaciers covered the Holocene only.

Analysis of moraines. Density functions in Fig. 2 show the distribution of moraine ages for three periods: the ACR, Younger Dryas and Holocene chronozones. Each density function is based on the number of moraines with ages belonging to the same chronozone (not the number of glaciers), taking into account that some moraines in this analysis were counted in two chronozones because we were not able to assess whether they were from the ACR or from the Younger Dryas, for instance when accounting for age uncertainties. For example, a moraine dated to 12.6 ± 1.0 ^{10}Be kyr ago was used to plot the density functions of the ACR and the Younger Dryas as well. This calculation differs from the analysis conducted on glaciers as follows. We took into account all moraines and not exclusively the largest maximum extent, and a moraine may be counted twice. Consequently, we did not focus on the number of moraines per period but focused here on the mean age and the shape of the distribution.

The moraine analysis shows that glaciers were reduced in size throughout the whole ACR/Little Ice Age period. This information is given by the position of the density function along a qualitative y axis, shown in grey in Fig. 2f.

A common trend in glacier size evolution. We considered glaciers to have a common glacier size evolution in the NTA and STA, on the basis of the following facts: 70% of the selected glaciers from both the NTA and the STA showed a larger advance during the ACR than the Younger Dryas; an early Holocene period characterized by moraines smaller than those characterizing the ACR/Younger Dryas period but larger than those characterizing the Little Ice Age for all glaciers; mid and late Holocene stillstands are very rarely observed (only one glacier); Little Ice Age moraines are located several hundred metres downslope from the current front position in every case.

This common trend was, however, caused by different climate drivers during the ACR/Younger Dryas period.

The coupled climate model and experimental set-up. The CGCM employed is the National Center for Atmospheric Research (NCAR) CCSM3 with a dynamic global vegetation module. CCSM3 is a global, coupled ocean/atmosphere/sea-ice/land-surface climate model without flux adjustment⁴⁴. All the simulations were performed in the version with T31_gx3v5 resolution⁴⁵. The atmospheric model is the Community Atmospheric Model 3 (CAM3) with 26 hybrid coordinate levels in the vertical and $\sim 3.75^\circ$ resolution in the horizontal. The land model uses the same resolution as the atmosphere, and each grid box includes a hierarchy of land units, soil columns and plant types. Glaciers, lakes, wetlands, urban areas and vegetated regions can be specified in the land units. The ocean model is the NCAR implementation of the Parallel Ocean Program (POP) in the vertical z-coordinate with 25 levels. The longitudinal resolution is 3.6° and the latitudinal resolution is variable, with finer resolution near the equator ($\sim 0.9^\circ$). The sea-ice model is the NCAR Community Sea Ice Model (CSIM). CSIM is a dynamic thermodynamic model that includes a subgrid-scale ice-thickness distribution. The resolution of CSIM is identical to that of POP. The preindustrial control simulation reproduces the major features of global climate, notably in the deep ocean⁴⁶. The transient simulation was started at the end of an equilibrium run at 22 kyr. The transient concentrations of the greenhouse gases (CO_2 , CH_4 and N_2O) were adopted from ref. 47. The continental ice sheets were modified approximately once per thousand years according to the ICE-5G reconstruction⁴⁸. The coastlines at LGM were also taken from the ICE-5G reconstruction and were changed twice, at 12.9 kyr and 6 kyr. The melt-water flux was constructed roughly following the observations. More detailed discussions on the setup of this simulation can be found in refs 22, 49.

RESEARCH LETTER

Discussion. To explore the relationship between glaciers in the STA region and climate forcing, we analysed the correlation field between temperature estimated from the model in the Andes of Bolivia¹⁴ and global temperature (Extended Data Fig. 4). In the STA region, a significant correlation ($P < 0.05$) with Southern Hemisphere high-latitude temperature and with the Ritacuba region is observed during the ACR period. During the Younger Dryas period, the correlation with Southern Hemisphere high-latitude temperature is weaker but still significant in the tropics. The insignificant correlation on the decadal timescale between the Ritacuba region and the Andes of Bolivia can be explained by contrasting temperature variations between the two regions during this period (Fig. 3c, d).

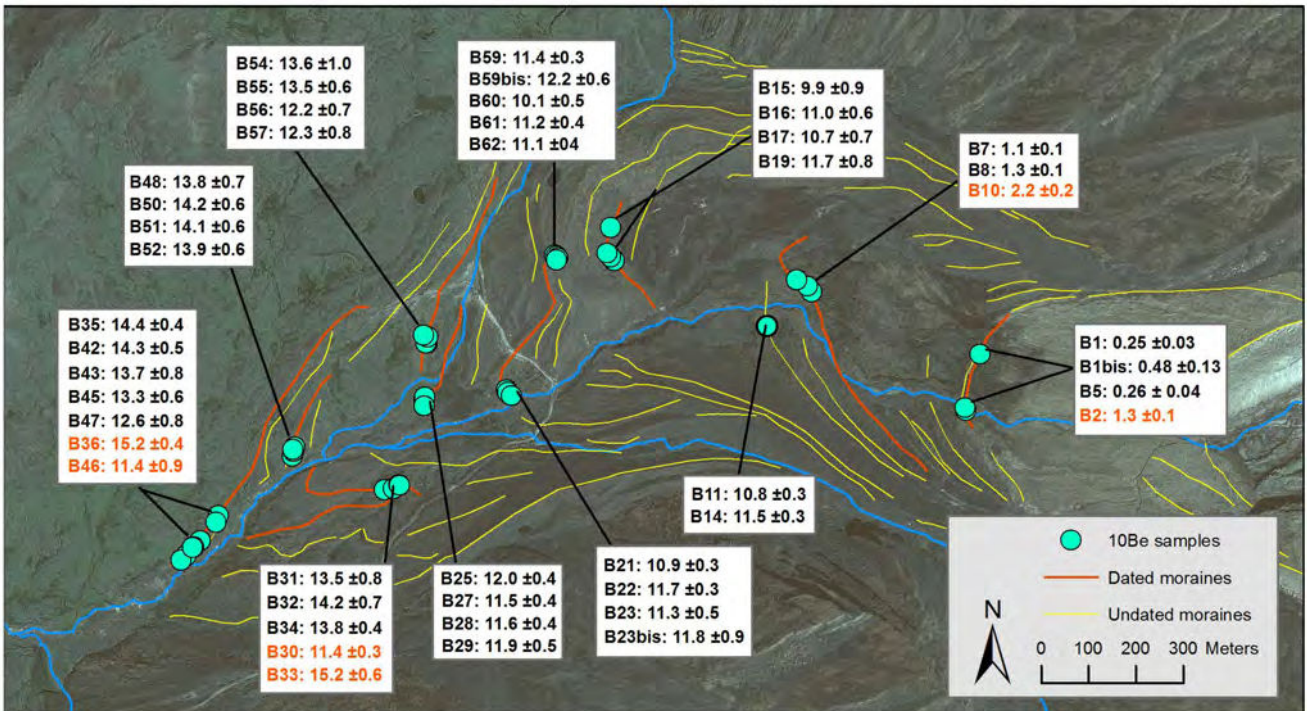
We also computed a map of the simulated precipitation difference between the ACR and the Younger Dryas (Extended Data Fig. 5). This map shows a strong decrease in precipitation over a band that stretches from the eastern equatorial Pacific to the Caribbean, including the Ritacuba region. This figure needs to be compared with the map of temperature differences (Extended Data Fig. 4). During the ACR, a global cooling is observed in agreement with the large glacial extent in the Andes. During the Younger Dryas, however, the global temperature signal resembles the typical hemispheric see-saw. A strong increase in temperature is observed over the Ritacuba region, while the North Atlantic is anomalously cold. This pattern is confirmed by the negative correlation of Ritacuba temperature with temperature along the same areas during both the ACR and the Younger Dryas (Fig. 3). This suggests that precipitation and temperature are anticorrelated on a regional scale over the continent, a phenomenon that is also visible in Fig. 2.

In addition, analysis of the transient simulation shows that NTA warming is the result of vegetation feedback. We have included the simulated changes in precipitation (Extended Data Fig. 5), tree fraction, latent heat flux and surface temperature changes during the Younger Dryas (Extended Data Figs 6–9). These figures clearly document the following mechanism for the NTA warming. The slowdown of the AMOC induces a southward shift of the intertropical convergence zone, producing a precipitation reduction in the NTA. The resulting drought conditions lead to reduced tropical forest cover, reduced evapotranspiration and latent heat release, and consequently induces warming over the NTA. The surface warming due to reduced tree cover in the tropics is a robust result in the land cover change literature^{28,30}.

Finally, ref. 51 emphasized the role of CO₂ as a major driver in glacier fluctuations. Here we show that CO₂ forcing alone cannot explain the observed change in glacier extent. Transient simulations with the coupled global climate model suggest that the common glacier behaviour was the result of AMOC variability superimposed on deglacial CO₂ rise.

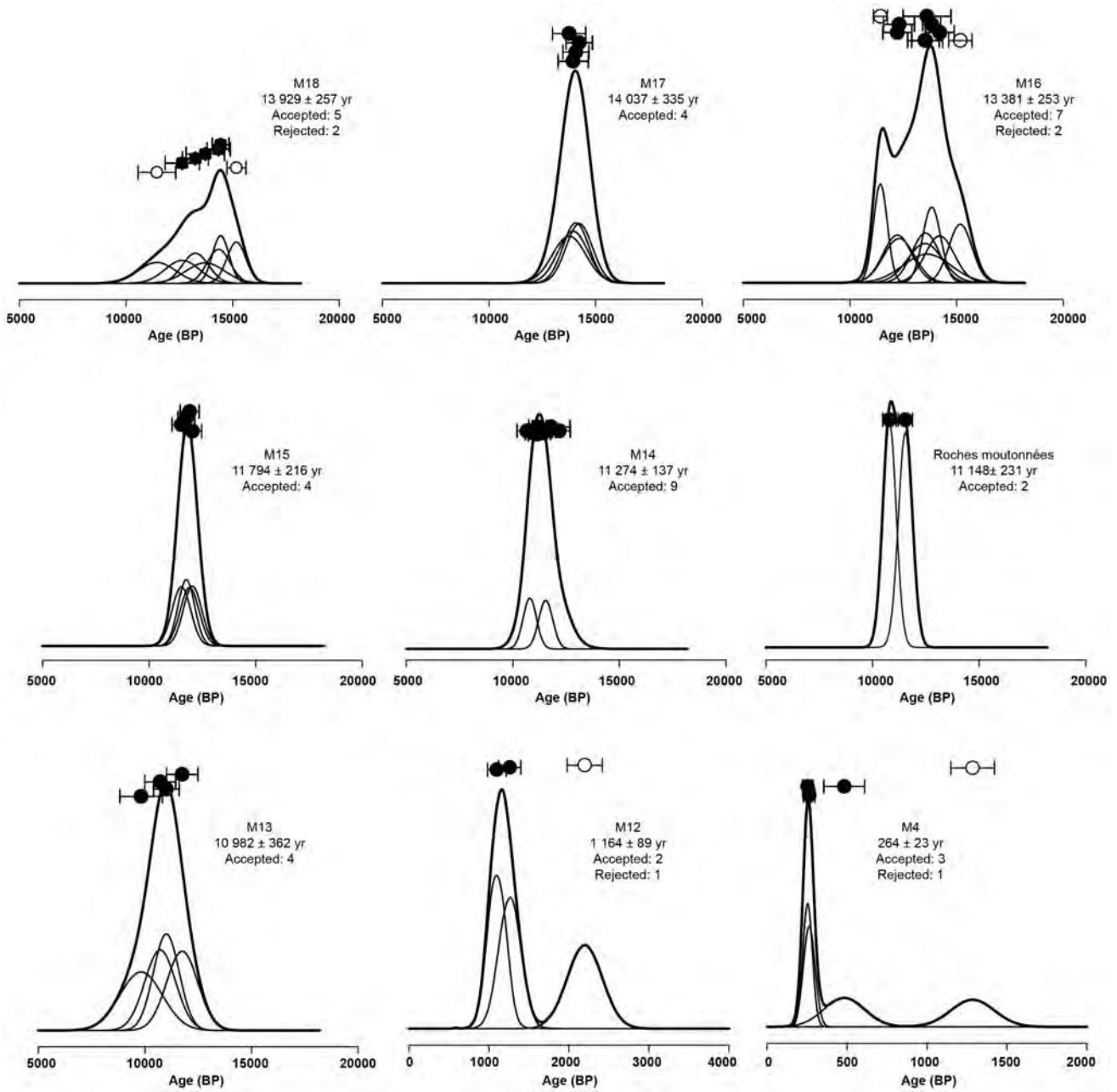
30. Merchel, S. *et al.* Towards more precise ¹⁰Be and ³⁶Cl data from measurements at the 10⁻¹⁴ level: Influence of sample preparation. *Nucl. Instrum. Methods Phys. Res. B* **266**, 4921–4926 (2008).

31. Nishiizumi, K. *et al.* Absolute calibration of ¹⁰Be AMS standards. *Nucl. Instrum. Methods Phys. Res. B* **258**, 403–413 (2007).
32. Stone, J. O. Air pressure and cosmogenic isotope production. *J. Geophys. Res.* **105**, 23753–23759 (2000).
33. Farber, D. L., Hancock, G. S., Finkel, R. C. & Rodbell, D. T. The age and extent of tropical alpine glaciation in the Cordillera Blanca, Peru. *J. Quat. Sci.* **20**, 759–776 (2005).
34. Nishiizumi, K. *et al.* Cosmic-ray production rates of ¹⁰Be and ²⁶Al in quartz from glacially polished rocks. *J. Geophys. Res.* **94**, 17907–17915 (1989).
35. Muscheler, R., Beer, R., Kubik, P. W. & Synal, H. A. Geomagnetic field intensity during the last 60,000 years based on Be-10 and Cl-36 from the Summit ice cores and C-14. *Quat. Sci. Rev.* **24**, 1849–1860 (2005).
36. Ménébréaz, L., Bourles, D. L. & Thouveny, N. Amplitude and timing of the Laschamp geomagnetic dipole low from the global atmospheric ¹⁰Be overproduction: contribution of authigenic ¹⁰Be/⁹Be ratios in west equatorial Pacific sediments. *J. Geophys. Res.* **117**, B11101 (2012).
37. Guyodo, Y. & Valet, J. P. Global changes in intensity of the Earth's magnetic field during the past 800 kyr. *Nature* **399**, 249–252 (1999).
38. Balco, G., Stone, J. O., Lifton, N. A. & Dunai, T. J. A complete and easily accessible means of calculating surface exposure ages or erosion rates from ¹⁰Be and ²⁶Al measurements. *Quat. Geo.* **3**, 174–195 (2008).
39. Dunne, J., Elmore, D. & Muzikar, P. Scaling factors for the rates of production of cosmogenic nuclides for geometric shielding and attenuation at depth on sloped surfaces. *Geomorphology* **27**, 3–11 (1999).
40. Ward, G. K. & Wilson, S. R. Procedures for comparing and combining radiocarbon age determinations: a critique. *Archaeometry* **20**, 19–31 (1978).
41. Blard, P. H. *et al.* Progressive glacial retreat in the Southern Altiplano (Uturuncu volcano, 22°S) between 65 and 14 ka constrained by cosmogenic ³He dating. *Quat. Res.* (in the press).
42. Smith, J. A. & Rodbell, D. T. Cross-cutting moraines reveal evidence for North Atlantic influence on glaciers in the tropical Andes. *J. Quat. Sci.* **25**, 243–248 (2010).
43. Mahaney, W. C. *et al.* Evidence for a Younger Dryas glacial advance in the Andes of northwestern Venezuela. *Geomorphology* **96**, 199–211 (2008).
44. Collins, W. D. *et al.* The Community Climate System Model Version 3 (CCSM3). *J. Clim.* **19**, 2122–2143 (2006).
45. Yeager, S. G., Shields, C. A., Large, W. & Hack, J. The low-resolution CCSM3. *J. Clim.* **19**, 2545–2566 (2006).
46. Otto-Bliesner, B. L. *et al.* Last glacial maximum and Holocene climate in CCSM3. *J. Clim.* **19**, 2526–2544 (2006).
47. Joos, F. & Spahni, R. Rates of change in natural and anthropogenic radiative forcing over the past 20,000 years. *Proc. Natl Acad. Sci. USA* **105**, 1425–1430 (2008).
48. Peltier, W. R. Global glacial isostasy and the surface of the ice-age. *Annu. Rev. Earth Planet. Sci.* **32**, 111–149 (2004).
49. He, F. *Simulating Transient Climate Evolution of the Last Deglaciation with CCSM3*. PhD thesis, Univ. Wisconsin-Madison (2011).
50. He, F. *et al.* Simulating global and local surface temperature changes due to Holocene anthropogenic land cover change. *Geophys. Res. Lett.* **41**, 623–631 (2014).
51. Broecker, W. *What Drives Glacier Cycles?* (Eldidgio, 2013).



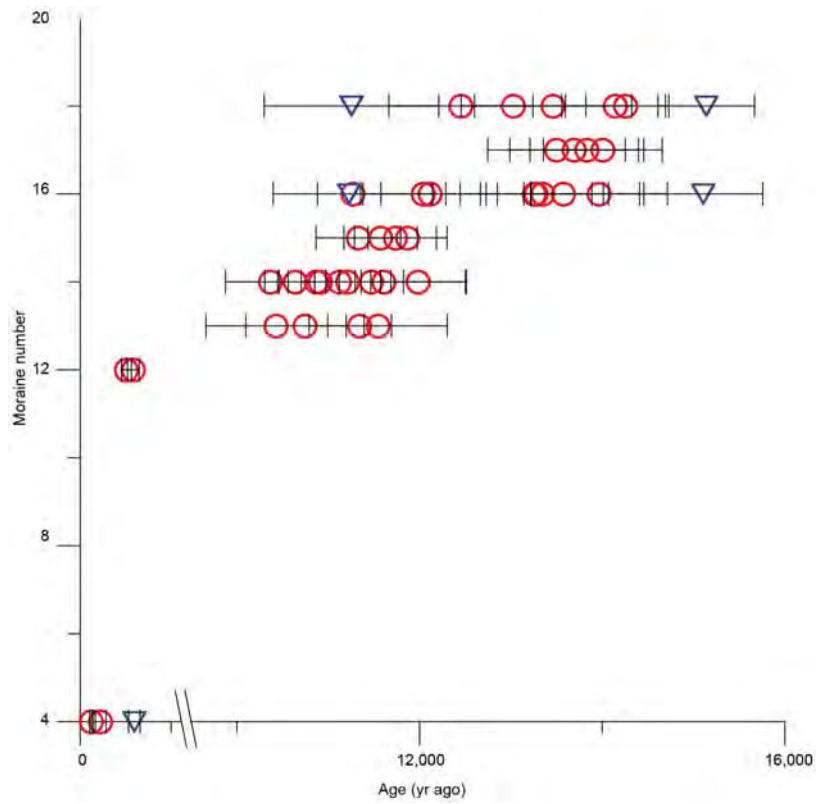
Extended Data Figure 1 | Location of the ¹⁰Be samples collected on the Ritacuba Negro glacier. Rejected samples in red. Dates are given in kyr with analytical uncertainties reported as 1 s.d. Photographs of ¹⁰Be sampled boulders are given in a separate file (Supplementary Information).

RESEARCH LETTER



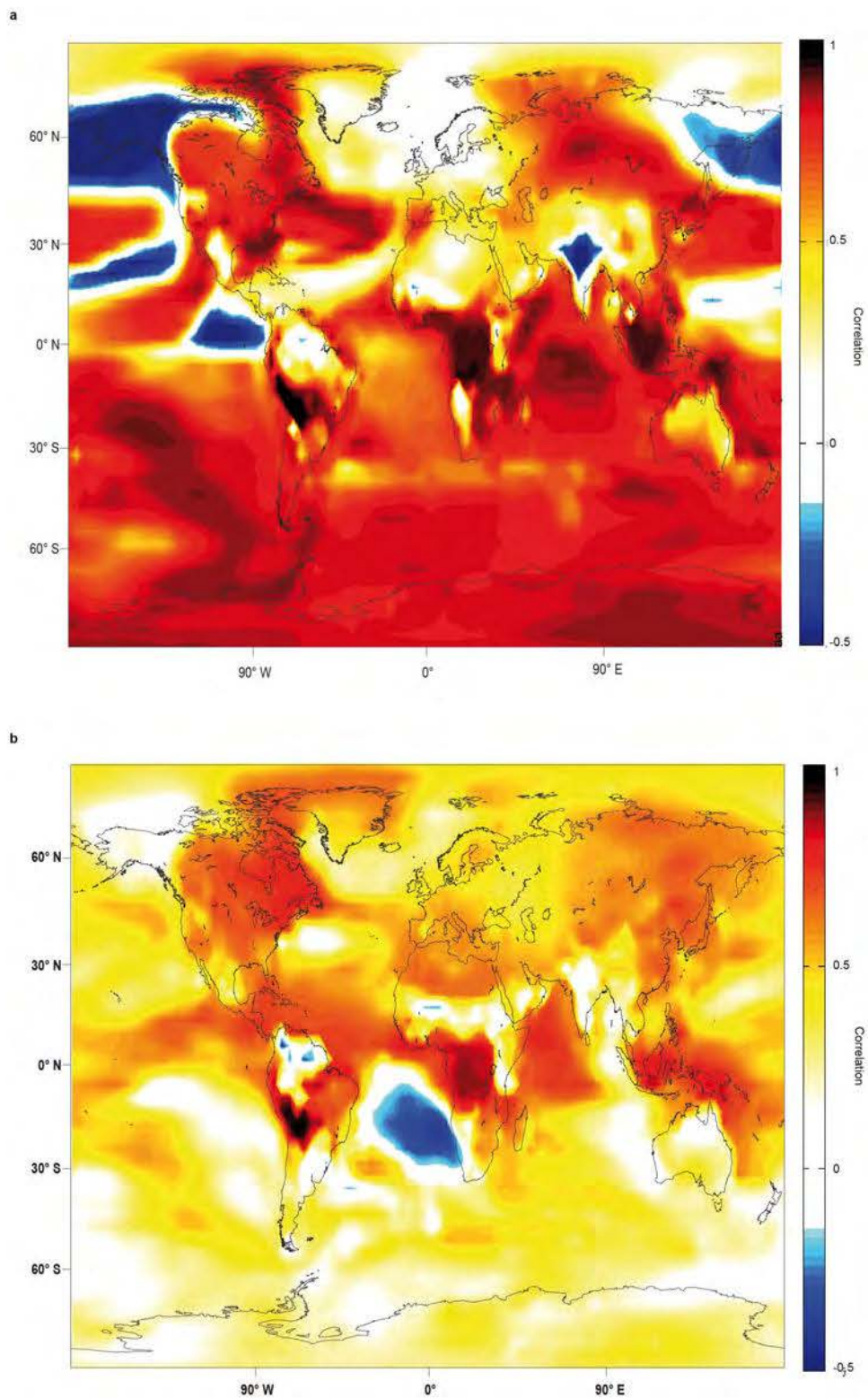
Extended Data Figure 2 | Cosmogenic ¹⁰Be surface exposure ages of moraine boulders of Ritacuba Negro glacier. Error bars on each symbol represent 1 s.d. analytical uncertainty only. Open symbols indicate outliers not included in the means. Thin black curves show relative probability distributions

of individual ages and thick black curves represent the cumulative probability distributions of age populations. Uncertainties associated with the mean ages account for analytical uncertainties only.

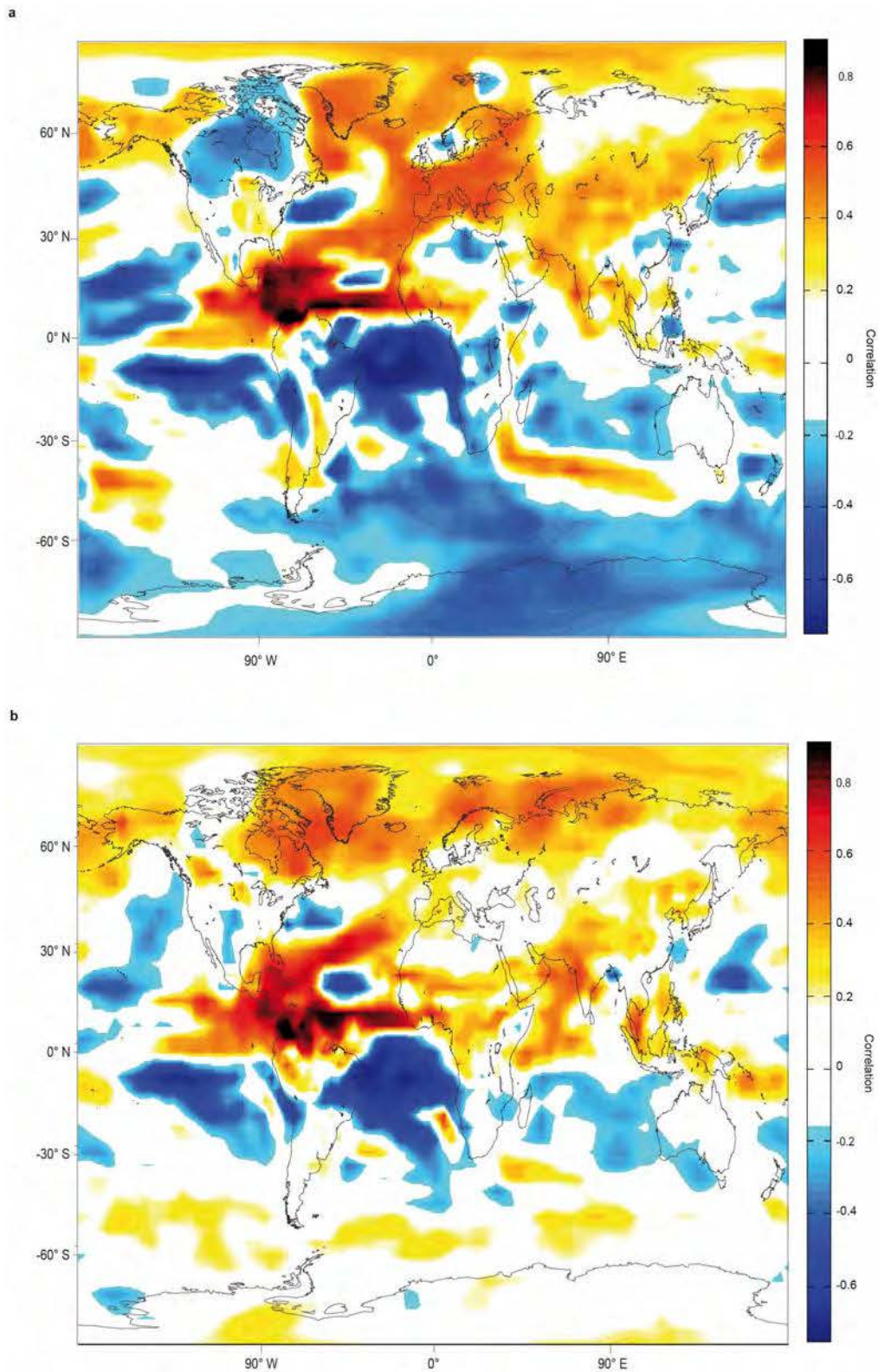


Extended Data Figure 3 | Age of the moraine versus moraine number. Error bars on each symbol represent the analytical uncertainties. Red circles indicate samples used in this study; blue triangles indicate rejected samples.

RESEARCH LETTER

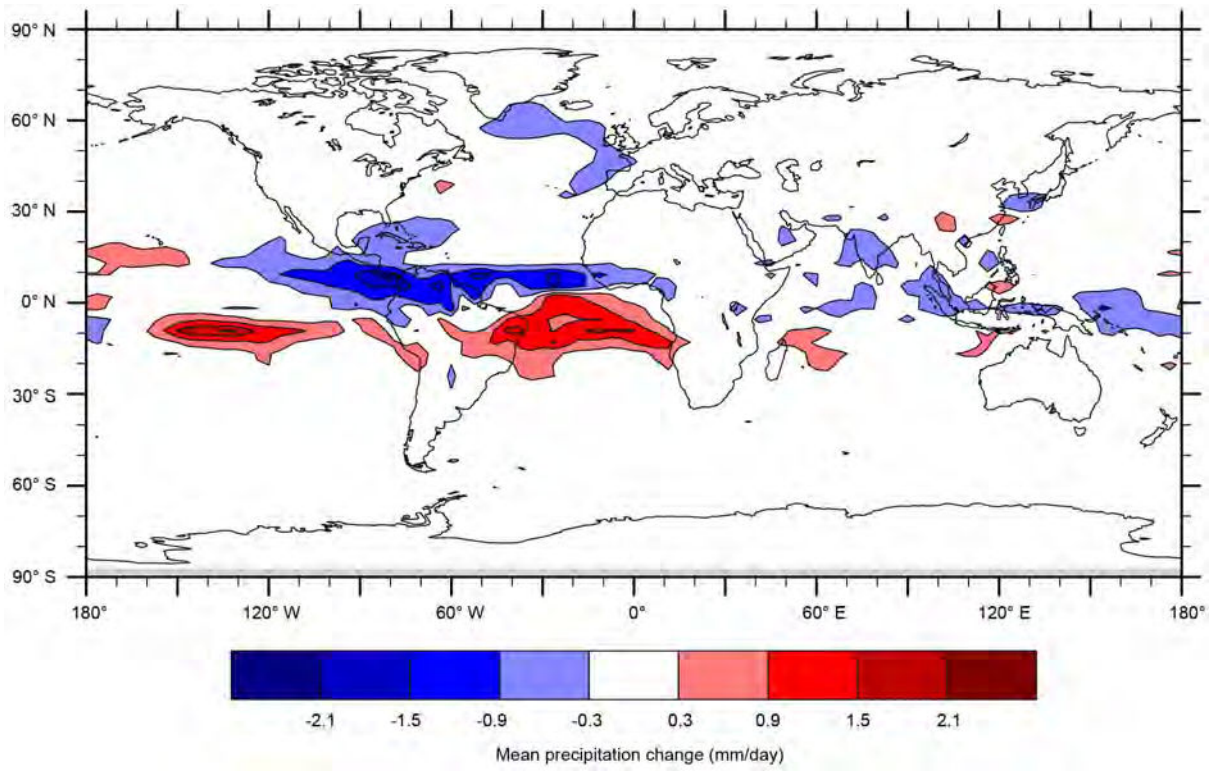


Extended Data Figure 4 | Decadal temperature variations in the Andes of Bolivia ($73\text{--}65^\circ\text{W}$, $14\text{--}22^\circ\text{S}$) correlated with global temperature. **a**, Correlations during the ACR period. **b**, Correlations during the Younger Dryas period. Statistically insignificant ($P > 0.05$) values are shown in white.

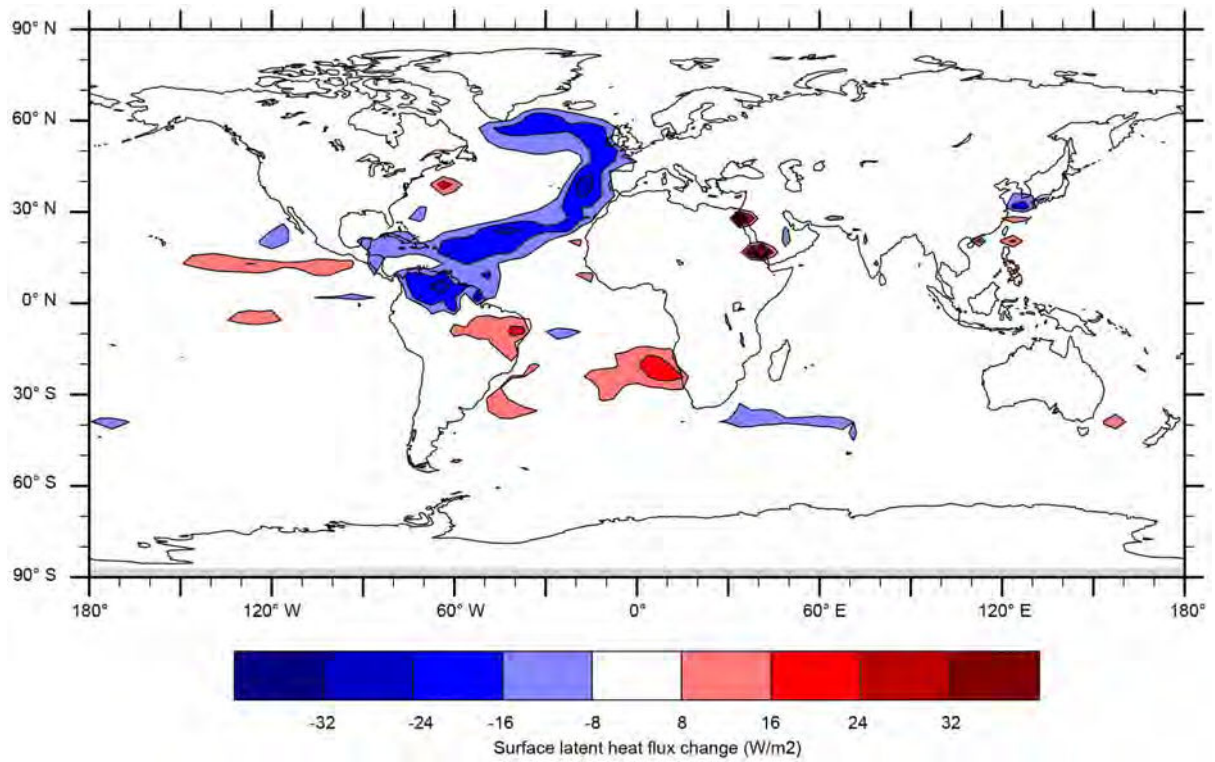


Extended Data Figure 5 | Decadal precipitation variations in the Ritacuba region (75–71° W, 2–6° N) correlated with global precipitation. a, Correlations during the ACR period. b, Correlations during the Younger Dryas period. Statistically insignificant ($P > 0.05$) values are shown in white.

RESEARCH LETTER

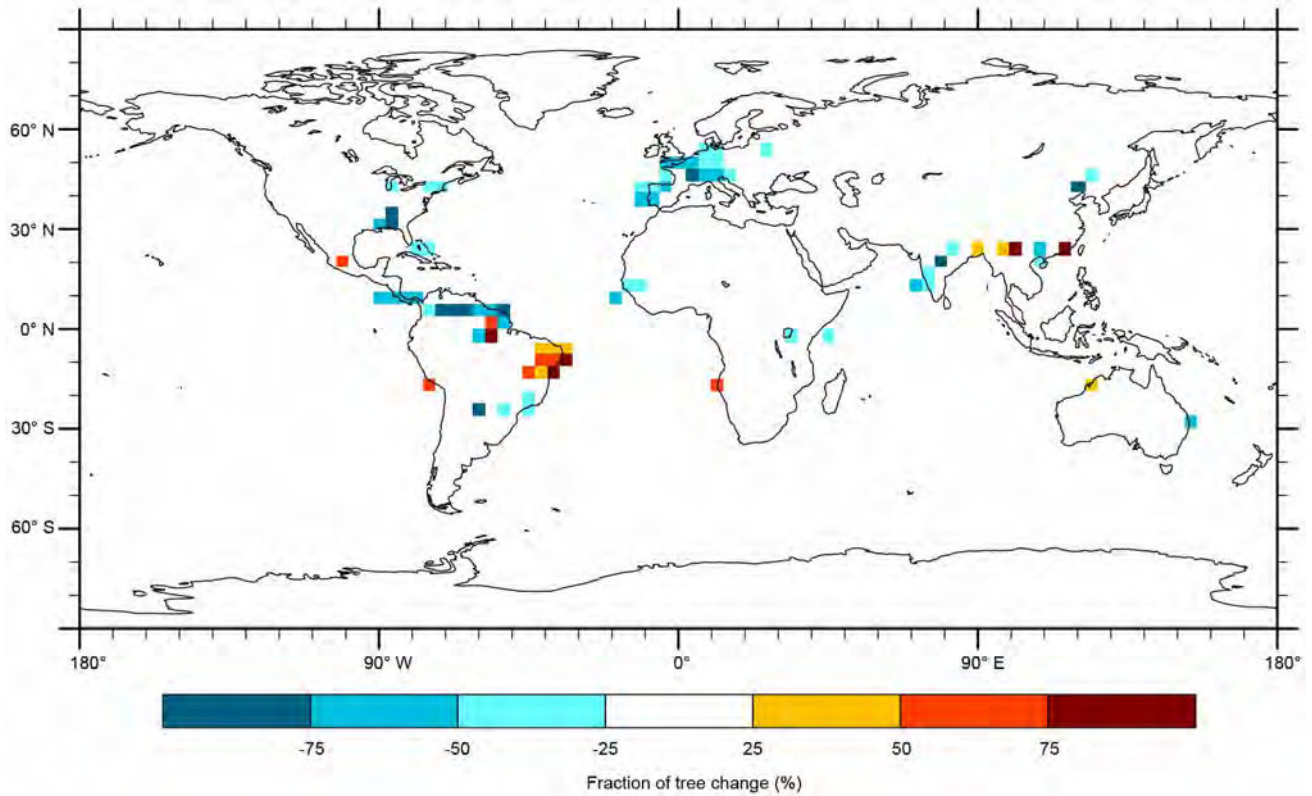


Extended Data Figure 6 | Mean precipitation change during the Younger Dryas. Data for 12.9 kyr ago minus data for 12.0 kyr ago.

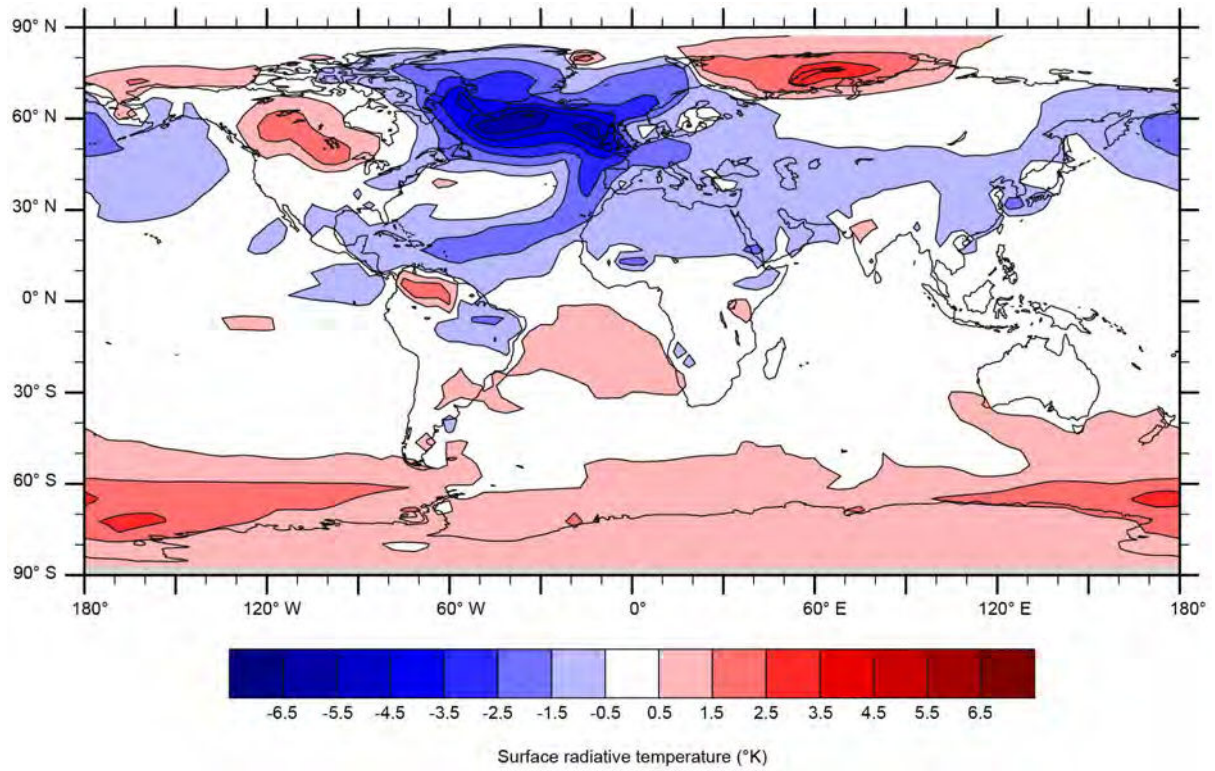


Extended Data Figure 7 | Latent heat change during the Younger Dryas. Data for 12.9 kyr ago minus data for 12.0 kyr ago.

RESEARCH LETTER



Extended Data Figure 8 | Simulated change in tree fraction during the Younger Dryas. Data for 12.9 kyr ago minus data for 12.0 kyr ago.



Extended Data Figure 9 | Surface temperature change during the Younger Dryas. Data for 12.9 kyr ago minus data for 12.0 kyr ago.

9.3.3 Calibration d'un taux de production ^3He au Nord du Chili

Mes travaux de thèse m'ont également permis de collaborer à une étude de calibration d'un taux de production ^3He sur le volcan San Pedro au Nord du Chili (Delunel et al., 2016). Ce taux est établi à partir d'une coulée de lave datée par la méthode $^{40}\text{Ar}/^{39}\text{Ar}$ à 107 ± 12 ka. La concentration en ^3He de la coulée est mesurée à $99.3 \pm 1.2 \times 10^6$ at.g $^{-1}$ et permet de calculer un taux de production local de 928 ± 101 at.g $^{-1}$.a $^{-1}$. Ramené aux conditions SLHL avec la mise à l'échelle systématiquement utilisée dans cette thèse, ce taux est de 129 ± 14 at.g $^{-1}$.a $^{-1}$. L'étude se conclue par une discussion présentant un re-calcul homogène de tous les taux de productions ^3He publiés dans le monde.

J'ai contribué à cette étude en faisant les calculs du taux de production de San Pedro et le re-calcul homogène de tous les taux de production rassemblés dans la synthèse mondiale. J'ai également écrit quelques paragraphes en lien avec les procédures de mise à l'échelle et j'ai contribué à la réponse aux reviews.

Cette étude a fait l'objet d'une publication dans la revue Quaternary Geochronology.

Available online at www.sciencedirect.com**ScienceDirect**

Geochimica et Cosmochimica Acta 184 (2016) 71–87

**Geochimica et
Cosmochimica
Acta**
www.elsevier.com/locate/gca

Long term low latitude and high elevation cosmogenic ^3He production rate inferred from a 107 ka-old lava flow in northern Chile; 22°S-3400 m a.s.l.

Romain Delunel^{a,*}, Pierre-Henri Blard^b, Léo C.P. Martin^b, Sébastien Nomade^c, Fritz Schlunegger^a

^a *Institute of Geological Sciences, University of Bern, Bern, Switzerland*

^b *CRPG, UMR 7358, CNRS, Université de Lorraine, Vandoeuvre-lès-Nancy, France*

^c *Laboratoire des Sciences du Climat et de l'Environnement, IPSL, CEA-CNRS-UVSQ et Université Paris-Saclay, Gif-sur-Yvette, France*

Received 13 November 2015; accepted in revised form 12 April 2016; Available online 19 April 2016

Abstract

Available geological calibration sites used to estimate the rate at which cosmogenic ^3He is produced at the Earth's surface are mostly clustered in medium to high latitudes. Moreover, most of them have exposure histories shorter than tens of thousands of years. This lack of sites prevents a qualitative assessment of available production models used to convert cosmogenic ^3He concentrations into exposure ages and/or denudation rates. It thus limits our ability to take into account the atmospheric, geomagnetic and solar modulation conditions that might have affected the production of cosmogenic nuclides in the past for longer exposure histories and in low latitude regions. We present the cosmogenic ^3He production rate inferred from a new geological calibration site located in northern Chile. Five samples were collected on the surface of the largest and best-preserved lava flow of the San Pedro volcano (21.934°S–68.510°W-3390 m a.s.l.), which displays pristine crease-structure features. $^{40}\text{Ar}/^{39}\text{Ar}$ dating yields a reliable plateau age of 107 ± 12 ka for the eruption of this lava flow. Eight pyroxene aliquots separated from the surface samples yield a weighted average cosmogenic ^3He concentration of 99.3 ± 1.2 Mat g^{-1} from which a local cosmogenic ^3He production rate of 928 ± 101 at $\text{g}^{-1} \text{yr}^{-1}$ is calculated. The local production rate is then scaled to a sea level high latitude (SLHL) reference position using different combinations of geographic spatialization schemes, atmosphere models and geomagnetic field reconstructions, yielding SLHL production rates between 103 ± 11 and 130 ± 14 at $\text{g}^{-1} \text{yr}^{-1}$ consistent with the most recent estimates available from the literature. Finally, we use the same scaling frameworks to re-evaluate the mean global-scale cosmogenic ^3He production rate in olivine and pyroxene minerals at 120 ± 16 at $\text{g}^{-1} \text{yr}^{-1}$ from the compilation of previously published calibration datasets.

© 2016 Elsevier Ltd. All rights reserved.

Keywords: Cosmogenic nuclides; ^3He ; Production rates; Calibration; Scaling; South America

1. INTRODUCTION

Studies relying on dating landforms and quantifying rates of Earth surface processes have greatly benefitted from the recent development of Terrestrial Cosmogenic Nuclides (TCN; see von Blanckenburg and Willenbring, 2014 and references therein for a review). Since the mid-80s (e.g. Craig and Poreda, 1986; Kurz, 1986), cosmogenic

* Corresponding author. Tel.: +41 316318773.

E-mail addresses: romain.delunel@geo.unibe.ch (R. Delunel), blard@crpg.cnrs-nancy.fr (P.-H. Blard), leom@crpg.cnrs-nancy.fr (L.C.P. Martin), sebastien.nomade@lsce.ipsl.fr (S. Nomade), fritz.schlunegger@geo.unibe.ch (F. Schlunegger).

helium-3 (^3He) has been successfully used to date geologic features in various environments and over periods of times ranging from hundreds to millions of years (e.g. Kurz et al., 1990; Licciardi et al., 1999; Schäfer et al., 1999; Evenstar et al., 2009). Cosmogenic ^3He combines high production rates (>100 at $\text{g}^{-1} \text{yr}^{-1}$ at sea level and high latitude) and low analytical detection limits (ca. 10^5 at g^{-1} in most favorable cases) with the absence of radioactive decay (i.e. ^3He is stable). Cosmogenic ^3He also has the advantage to be produced and quantitatively retained over geological timescales in mafic minerals such as olivines and pyroxenes, which offers an interesting alternative for applying surface exposure dating in volcanic terrains where quartz-bearing lithologies might not be available for ^{10}Be and ^{26}Al measurements.

The rate at which cosmogenic ^3He is produced at the Earth's surface has been estimated between 100 and 140 at $\text{g}^{-1} \text{yr}^{-1}$ (see Dunai, 2010 and reference therein) from several geological calibration datasets with independent age assignments (e.g. Cerling and Craig, 1994; Licciardi et al., 1999, 2006; Dunai and Wijbrans, 2000; Ackert et al., 2003; Blard et al., 2006; Goehring et al., 2010; Amidon and Farley, 2011; Foeken et al., 2012; Fenton et al., 2013; Blard et al., 2013a; Fenton and Niedermann, 2014). At a global scale, cosmogenic ^3He production rates at sea level and high latitude (SLHL) were estimated using the time-dependent adaptation of the Lal (1991)/Stone (2000) scaling scheme ("Lm"; Balco et al., 2008). The available calibration datasets yielded values of 119 ± 10 at $\text{g}^{-1} \text{yr}^{-1}$ for pyroxene (Goehring et al., 2010) and 116 ± 13 (Goehring et al., 2010), 122 ± 15 (Blard et al., 2013a) and ca. 117 at $\text{g}^{-1} \text{yr}^{-1}$ (Borchers et al., 2016) when ^3He concentrations of both pyroxene and olivine minerals are considered. Although the global-scale SLHL cosmogenic ^3He production rates are consistent within associated uncertainties, Phillips et al. (2016) recently emphasized that the initial datasets used in these compilations are clustered both in space (medium to high latitudes) and time (ca. 5–20 ka). According to these authors, this circumstance prevents reliable integrations of past atmospheric, geomagnetic and solar modulation conditions that might have affected the production of cosmogenic nuclides at the Earth's surface. In particular, cosmogenic ^3He calibration data are lacking at latitudes $<25^\circ$ (Blard et al., 2013a), where large temporal variations in the paleo magnetic-field intensity might have significantly affected the production of cosmogenic nuclides (e.g. Dunai and Lifton, 2014). Accordingly, improving the accuracy of time dependent corrections requires more low latitude calibration sites with exposure durations significantly longer than 20 ka.

This article presents a new calibration of the cosmogenic ^3He production rate from a site located in the hyperarid region of northern Chile (3400 m a.s.l., ca. 22°S), over a long exposure time (ca. 107 ka). The aim is to reduce the lack of long exposure calibration sites located at high elevation/low latitude. Five samples were collected for helium analyses on top of an andesitic lava flow. This surface is characterized by pristine crease-structure features, which are common on silicic volcanic flows and previously

identified as reliable targets for surface exposure dating (Anderson et al., 1994). First we document the age of a lava flow of the San Pedro volcano using $^{40}\text{Ar}/^{39}\text{Ar}$ dating techniques. We then report the results of the cosmogenic ^3He measurements from five samples (8 aliquots) from which we infer the local production rate of cosmogenic ^3He , as well as the production normalized to sea level and high latitude (SLHL), both integrated over the age of the lava flow. Finally, we combine our results with previously reported cosmogenic ^3He calibration datasets, to re-evaluate the global ^3He production rate at SLHL.

2. GEOLOGICAL SETTING AND SAMPLING

2.1. Volcanic architecture

The San Pedro volcano (6159 m a.s.l., Fig. 1) is situated in the El Loa province of northern Chile ca. 80 km north east of Calama and 100 km north of San Pedro de Atacama. While the San Pedro volcano is located on the western slope of the High Andean Cordillera and therefore does not belong to the Atacama Desert *stricto sensu*, it is characterized by a hyperarid climate, with annual precipitation <100 mm/y (Houston and Hartley, 2003). The San Pedro volcano is paired with the San Pablo volcano (6118 m a.s.l.) located 5 km further to the east. It represents one of the highest and best-preserved volcanic edifices of the Central Volcanic Zone (de Silva, 1989), one of the four active volcanic zones in the Andes (see Hora et al., 2007 and reference therein). Only few studies (Francis et al., 1974; Thorpe et al., 1976; O'Callaghan and Francis, 1986) described and identified the nature and composition of erupted materials and the history of eruption of these volcanoes. The San Pedro volcano represents a composite andesitic stratovolcano (Fig. 2) made of two east-west oriented coalescent cones that have been successively built as the volcanic belt shifted westward (O'Callaghan and Francis, 1986). The cones stand >2 km above an extensive ignimbrite plateau (Fig. 1) that has formed since the Late Miocene at ca. 10.4 Ma during the development of the Altiplano-Puna volcanic complex (de Silva, 1989). The San Pedro cones have been built due to the eruption of silicic materials ranging from basaltic andesite to potassium-rich dacite (O'Callaghan and Francis, 1986). Structural mapping and petrologic investigations (Francis et al., 1974; O'Callaghan and Francis, 1986) revealed that the San Pedro Volcano records three evolutionary steps, comprising (i) the edification and subsequent collapse of an "old cone", whose summit marks the highest peak of the volcano, (ii) the construction, c.a. 5 km to the west, of the "young cone" that has produced several large lava flows and is still marked by fumarolic activity and (iii) the formation of the South West Dome and La Poruña scoria cone, representing the last eruptive episode and associated with the emission of two large and well preserved lava flows (Fig. 1). Above 4500 m a.s.l., Francis et al. (1974) reported the presence of glacial moraines and cirques on the southern flanks of both the San Pablo and San Pedro volcanoes. Thus, the last eruptions are probably older than the last large glacial advances in the region (i.e. ca. >15 ka; Blard

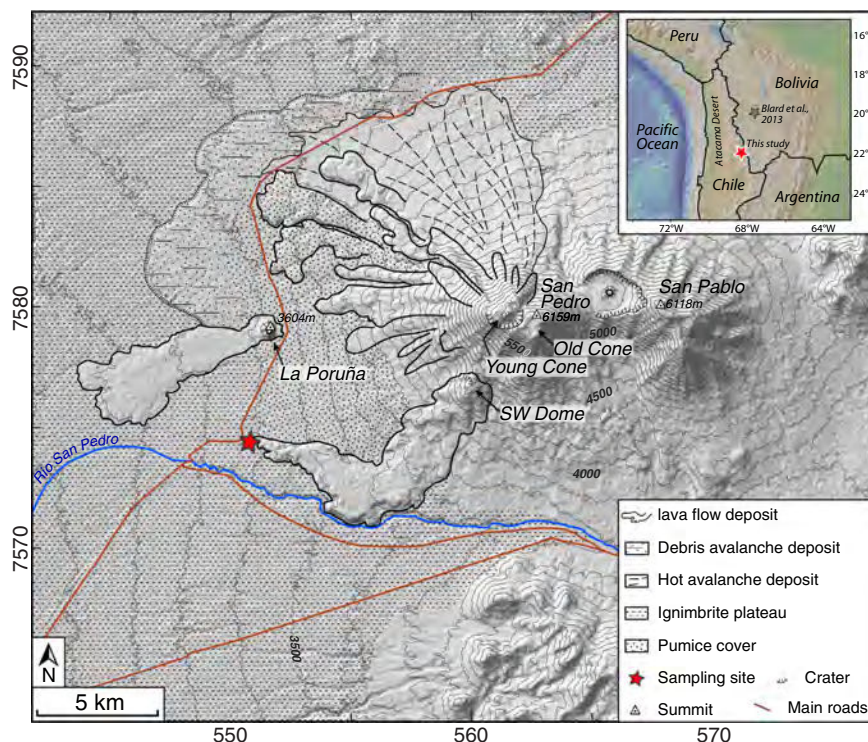


Fig. 1. Geological sketch of the San Pedro volcano showing the location of the sampling site. The map is modified after Francis et al. (1974) and O'Callaghan and Francis (1986). Hillshade model and 100-m-interval contours are based on the ASTER GDEM 30-m-resolution digital topography. False easting and northing kilometer coordinates are based on UTM zone 19S projection. Inset shows the location of the San Pedro volcano in the Central Andes, the Atacama Desert as well as the Cerro Tunupa calibration site from Blard et al. (2013a,b). (For interpretation of the references to color in this figure legend, the reader is referred to the web version of this article.)

et al., 2013a). In addition, Wörner et al. (2000) reported an exposure age of ca. 103 ka based on the cosmogenic- ^3He analysis of one sample collected on La Poruña (Fig. 1), suggesting that the lava flow emitted by the SW Dome might be at least 100 ka old, or even older.

2.2. The SW Dome of the San Pedro volcano

The lava flow emitted by the SW Dome is the largest of the San Pedro volcano. It extends towards the south west for ca. 13 km from ca. 4800 m to 3370 m a.s.l. (Fig. 1) and covers an area of ca. 20 km² with a volume estimated at 2.8 km³ (O'Callaghan and Francis, 1986). The lava flow is considered the product of a 200-m-thick early pyroxene dacite lava flow that was locally overlain by subsequent hornblende dacite flows (Fig. 1). Although most of the surface of the lava flow displays a rough blocky structure typical of low-viscosity Andean andesite/dacite flows, its distal part presents smooth stream-oriented and elongated features (Fig. 2). These features correspond to crease structures (Anderson and Fink, 1992) as inferred from the curved and striated walls situated on both sides of a main central fracture (Fig. 2). Such crease structures have been identified as typical constructional volcanic features materializing excellent landforms for surface exposure dating with in-situ produced cosmogenic nuclides (Anderson et al., 1994).

2.3. Sampling site

Samples were collected on the top of one crease structure immediately above the main lava flow front. The site is characterized by a perfectly preserved rind crust displaying stream-parallel striations (Table 1, Figs. 1 and 2). We collected 5 different samples at a few meters interval in order to capture variations in noble gas concentrations that might be related with differences in the preservation of the flow surface. All sampled surfaces showed no sign of post-eruptive erosion or burial. Seasonal snow cover is unlikely given the hyperaridity of the local climate. Samples were collected with a combination of drill-hammer, sledge-hammer and chisels in order to extract homogeneous <10-cm-thick rock cuboids. Samples' locations were recorded with a hand-GPS, and both the local surface geometry and its surrounding topography were measured with a sighting compass and inclinometer. These measurements were later used to correct for geomorphic shielding using equations from Dunne et al. (1999).

3. EXPERIMENTAL PROCEDURES

The following sections provide a description of the sample preparation and analytical experiments conducted for the determination of the eruption age of the San Pedro

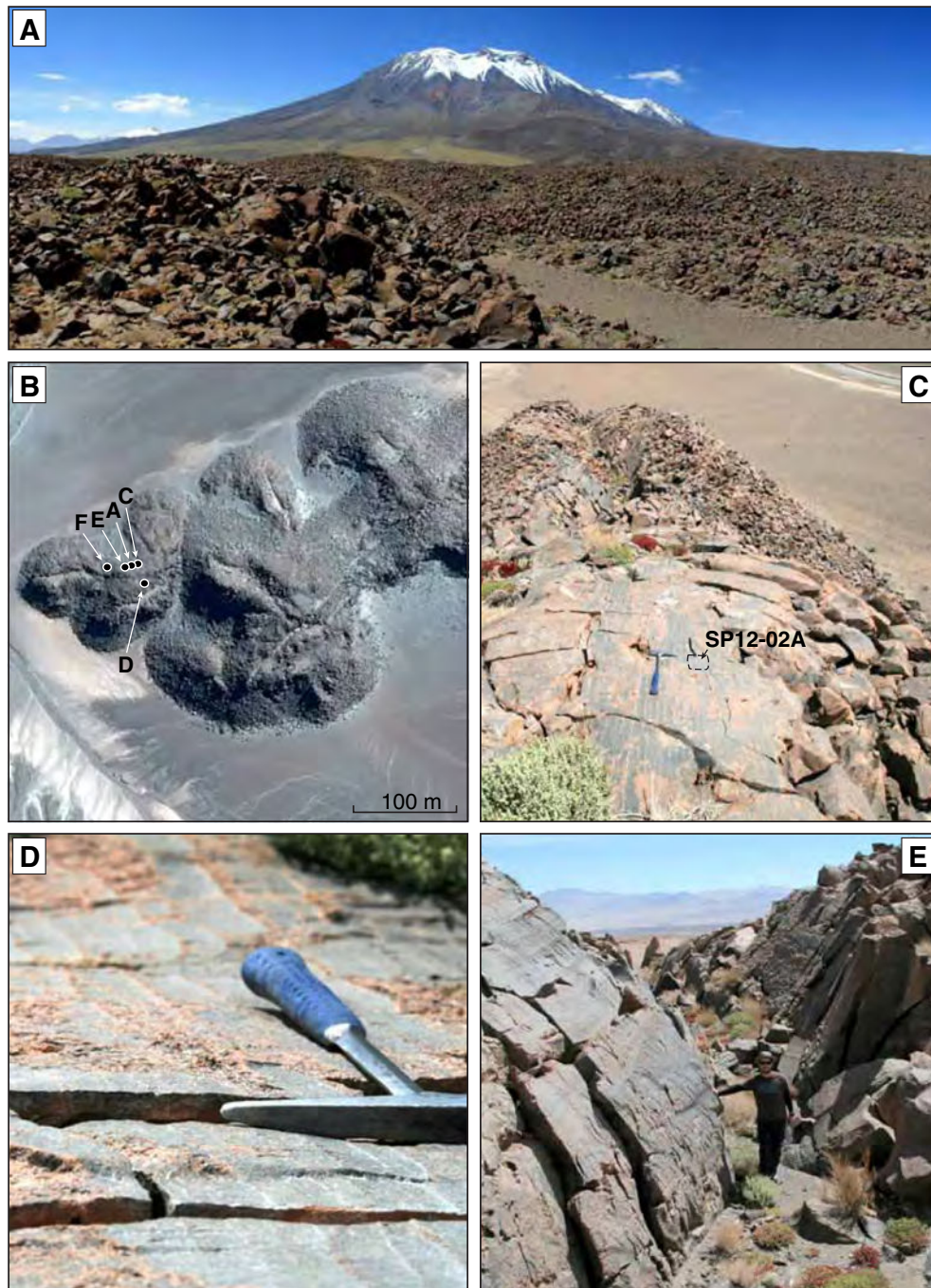


Fig. 2. Photograph collection of the sampling site. (A) General overview of the San Pedro volcano photographed from the SW lava flow at ca. 3600 m a.s.l. toward the NE. (B) Satellite image (Google Earth) showing the situation of samples (see red star in Fig. 1). Note the lobate morphology of the lava front and the stream-oriented elongated features that correspond to crease structures. For representation purposes sample labels are shortened but should be read SP12-02(letter). (C) Picture taken from the sampling site (see position of SP12-02A) looking East toward the apex of the lava; a large crease structure can be seen in the background (see close up in D). Note that the sampled surface is perfectly smooth though fractured in m-scale compartments and displays stream-parallel striations that are characteristics of pristine crease-structures surfaces. (D) Close-up of the surface sampled for SP12-02A showing ~ 5 -cm wide and few-mm high striations marked on top of the ca. 2-cm-thick rind. (E) Left half-part of the large crease structure situated at the apex of the sampled lava flow showing the general smooth and convex morphology of the rock wall as well as the subhorizontal striations and subvertical wall offsets characteristics of these features. Note the person (for scale) is located in the central valley of the crease structure. The materials forming this structure were exhumed from the central valley up. The second half of this structure can be seen on the right of the person.

Table 1
Sample characteristics.

Sample name	Latitude (°)	Longitude (°)	Elevation (m)	Atmospheric pressure (hPa) ^a	Altitude factor ^b	Sample thickness (cm)	Density (g cm ⁻³)	Thickness correction ^c	Geomorphic shielding ^d	Total correction ^e (%)
SP12-02A	-21.93434	-68.50980	3389	679.55	0.999	6	2.44	0.956	0.996	4.9
SP12-02C	-21.93431	-68.50974	3394	679.13	1.002	6	2.41	0.956	0.995	4.6
SP12-02D	-21.93440	-68.50966	3393	679.22	1.002	6	2.43	0.956	0.998	4.5
SP12-02E	-21.93435	-68.50983	3391	679.38	1.001	7	2.22	0.953	0.998	4.9
SP12-02F	-21.93437	-68.51005	3384	679.97	0.997	7.5	2.21	0.950	0.964	8.7

^a Local atmospheric pressure was calculated using the ICAO standard atmosphere equation with sea level temperature and pressure derived from the ERA-40 reanalysis dataset (Uppala et al., 2005).

^b Correction factors used to scale cosmogenic ³He concentrations to 21.934°S–68.510°W, 3390 m (679.468 hPa). Values are calculated as the ratio between the scaling factor obtained using the Lal (1991)/Stone (2000) scheme with the ERA-40 atmosphere model for the sampling position and at 21.934°S–68.510°W, 3390 m a.s.l.

^c Thickness corrections are calculated using an attenuation length of 160 g cm⁻² and the sample densities measured.

^d Total geomorphic shielding, including self-shielding by the sampled surface and the topography around the sampling site, are calculated according to Dunne et al. (1999) and an algorithm provided by G. Balco (<http://hess.ess.washington.edu/>).

^e Calculated as the product of altitude, thickness and geomorphic shielding factors.

volcano lava flow via ⁴⁰Ar/³⁹Ar dating and the quantification of the cosmogenic ³He concentrations of the collected samples.

3.1. Sample preparation

Before proceeding to the preparation of samples for ⁴⁰Ar/³⁹Ar dating and helium analyses, the rocks were sawed and 3 separates of each sample were used for estimating the lava density. In addition, the bulk rock composition of major elements was measured on one additional sample separate (Tables 1 and 2). Each sample's average density was determined by weighing several times the sample fragments in air and immersed. Bulk rock composition of collected samples was obtained from mass-spectrometry analyses conducted by Activation Laboratories Ltd. (Canada).

After measuring the sample thickness, materials for ⁴⁰Ar/³⁹Ar and helium analyses were crushed via electrodynamic disaggregation using the high-voltage pulsed power selfFrag-Lab instrument at the Institute of Geological Sciences of the University of Bern. This crushing equipment was preferred to a usual jaw crusher because of its efficiency in liberating mono-mineral phenocrysts. It also results in a lower loss of material due to mechanical fining, thereby increasing the recovery of mineral separates. Moreover, it has been shown that the electrodynamic disaggregation of rocks do not affect the noble gas content of liberated minerals (Giese et al., 2010). After crushing, the samples were sieved. The 65–125 microns fraction of the sample SP12-02A was processed in order to extract the potassium-rich groundmass for ⁴⁰Ar/³⁹Ar dating purposes. Mafic minerals such as pyroxene, amphibole and associated oxides were first removed using a magnetic separator, after which the remaining material was leached in 10% HNO₃ and rinsed several times with deionized water before small aggregates of clean groundmass were hand-picked under a binocular microscope. About 150 mg were finally used for the ⁴⁹Ar/³⁹Ar dating.

Sample preparation for helium analyses consisted of the separation of heavy minerals from the 250–500 microns fraction using bromoform (CHBr₃, 2.9 g cm⁻³) and methylene iodide (CH₂I₂, 3.3 g cm⁻³) heavy liquids. Pure separates of pyroxenes without any adhering lava or solid-inclusions were carefully handpicked under a binocular microscope. Clinopyroxene (augite, prismatic greenish grains) and orthopyroxene (enstatite, orthorhombic brownish grains) were isolated. We used color and shape as criteria for mineral separation during picking. Mineral separates were then sonicated with acetone and rinsed several times with deionized water. About 15 grains of each separate were mounted on epoxy-resin discs in order to measure the equivalent spherical radius of the phenocrysts and to determine the composition in major elements of the mineral separates. This was accomplished using the electron microprobe (JEOL-8200) of the Institute of Geological Sciences in Bern. Laser ablation (LA) ICP-MS analyses were subsequently conducted at the University of Bern on the two discs of sample SP12-02D (i.e. both the clino- and orthopyroxene separates) in order to measure the concentration of

Table 2
Major element composition of lava and pyroxene phenocrysts.

Sample name	Type	SiO ₂ (wt %)	Al ₂ O ₃ (wt %)	Fe ₂ O ₃ (wt %)	MnO (wt %)	MgO (wt %)	CaO (wt %)	Na ₂ O (wt %)	K ₂ O (wt %)	TiO ₂ (wt %)	P ₂ O ₅ (wt %)	LOI (wt %)	Total (%)
SP12-02A	Bulk rock	63.3	15.6	5.5	0.08	2.4	4.1	4.0	3.3	0.8	0.2	1.2	100
SP12-02A	Clinopyroxene	52.1	2.4	9.8	–	14.7	19.6	0.5	0.0	0.5	–	–	100
SP12-02A	Orthopyroxene	54.0	0.9	20.0	–	22.9	1.2	0.0	0.0	0.4	–	–	100
SP12-02C	Bulk rock	65.1	14.7	5.4	0.08	2.2	3.9	3.7	3.1	0.8	0.2	1.5	101
SP12-02C	Clinopyroxene	52.7	2.2	8.9	–	14.9	20.4	0.4	0.0	0.4	–	–	100
SP12-02D	Bulk rock	62.8	15.2	5.5	0.08	2.3	4.1	3.7	3.0	0.8	0.2	1.7	99
SP12-02D	Clinopyroxene	52.0	2.4	10.0	–	14.8	19.3	0.5	0.0	0.6	–	–	100
SP12-02D	Orthopyroxene	53.6	1.1	20.5	–	23.1	1.3	0.0	0.0	0.2	–	–	100
SP12-02E	Bulk rock	61.4	15.2	5.4	0.07	2.2	4.6	3.9	3.0	0.8	0.2	2.0	99
SP12-02E	Clinopyroxene	53.0	1.9	8.8	–	14.8	20.3	0.4	0.0	0.4	–	–	100
SP12-02F	Bulk rock	63.8	14.8	5.2	0.08	2.1	4.2	3.7	2.9	0.7	0.2	1.7	99
SP12-02F	Clinopyroxene	52.7	2.0	9.9	–	14.3	20.0	0.5	0.0	0.4	–	–	100
SP12-02F	Orthopyroxene	54.1	0.8	19.4	–	23.4	1.1	0.0	0.0	0.3	–	–	99

a selection of trace elements, notably U, Th, Sm, Li and Gd (Table 3). These data were later used for correcting the helium analyses for the inherited nucleogenic and radiogenic components.

3.2. ⁴⁰Ar/³⁹Ar analytical method

About 150 mg of groundmass from SP12-02A was irradiated for 1 h (IRR-95) in the OSIRIS nuclear reactor (β1 tube, CEA Saclay, France). After irradiation, ca. 40 mg of the sample was transferred into a stainless steel sample holder and then loaded into a differential vacuum Cleartran[®] window. Argon isotopes were then extracted from the groundmass by step heating using a 25 W CO₂ laser (Synrad[®]). Ar isotopes were analyzed using a VG5400 mass spectrometer equipped with a single ion counter following the protocol reported in Nomade et al. (2010). Each Ar isotope measurement consisted of 20 cycles of peak jumping over the argon isotopes. Neutron fluence (J) was monitored by co-irradiation of Alder Creek Sanidine (ACs-2, Nomade et al., 2005) placed in the same pit as the sample. J values were determined from analyses of three ACs-2 single grains. Corresponding J value was calculated using an age of 1.194 Ma (Nomade et al., 2005) and the total decay constant reported by Steiger and Jäger (1977). An ⁴⁰Ar/³⁶Ar atmospheric ratio of 298.56 was then applied (Lee et al., 2006), consistent with the value reported by Valkiers et al. (2010). Recent revisions of decay and monitor constants suggest values about 0.64% (Kuiper et al., 2008, 1.201 Ma for ACs-2) and 1.0% (Renne et al., 2011; 1.2059 Ma for ACs-2) older than used here. However, the implied difference in calibrated age is negligible for our samples (ca. 1 ka) and therefore remains identical within uncertainty with the age reported here. Procedural blanks were measured every three to four steps depending on the beam size. For a typical 10-min static blank, typical backgrounds were about (2–5) × 10^{−17} and (4–5) × 10^{−19} moles for ⁴⁰Ar and ³⁶Ar, respectively. The precision and accuracy of the mass discrimination correction was monitored by daily measurements of air argon at various pressures (Nomade et al., 2010). Nucleogenic production ratios used to correct for reactor produced Ar isotopes from K and Ca could be found in the full data table (Table A1). Data reductions were done using ArArCalc (Koppers, 2002). Plateau age and corresponding uncertainty were calculated using IsoPlot 3.0 (Ludwig, 2003).

3.3. Helium analyses

Helium analyses were carried out at the CRPG noble-gas lab in Nancy, France. ³He and ⁴He isotope concentrations were measured using the Split Flight Tube mass spectrometer designed by GV. The magmatic contribution to the measured ³He and ⁴He concentrations was estimated by a 6 min in-vacuo crushing (Kurz, 1986; Scarsi, 2000) of 97 mg of an aliquot of orthopyroxene of sample SP12-02D. These values were then used for all other samples, assuming that the magmatic contribution is the same in all pyroxenes collected on the San Pedro lava flow. Following Williams et al. (2005) and Blard et al. (2013a), this potential

Table 3
Trace element composition of lava and pyroxene phenocrysts.

Sample name	Type	Li (ppm)	B (ppm)	Cr (ppm)	Co (ppm)	Ni (ppm)	Gd (ppm)	U (ppm)	Th (ppm)	Sm (ppm)
SP12-02A	Bulk rock	18	41	90	12	20	4.7	2.6	9.9	5.6
SP12-02A	Clinopyroxene	–	–	820	–	392	–	–	–	–
SP12-02A	Orthopyroxene	–	–	184	–	174	–	–	–	–
SP12-02C	Bulk rock	16	27	70	11	20	4.0	2.5	8.5	5.0
SP12-02C	Clinopyroxene	–	–	802	–	301	–	–	–	–
SP12-02D	Bulk rock	21	33	90	12	20	4.3	2.5	9.4	5.3
SP12-02D	Clinopyroxene	24	0.7	946	–	725	7.4	<0.01	0.06	7.2
SP12-02D	Orthopyroxene	16	0.6	245	–	185	0.7	<0.01	<0.01	0.4
SP12-02E	Bulk rock	20	32	80	11	20	4.1	2.4	9.1	5.3
SP12-02E	Clinopyroxene	–	–	410	–	384	–	–	–	–
SP12-02F	Bulk rock	18	42	70	11	20	4.2	2.2	8.3	5.2
SP12-02F	Clinopyroxene	–	–	366	–	142	–	–	–	–
SP12-02F	Orthopyroxene	–	–	109	–	171	–	–	–	–

Major and trace elements in lava (bulk rock) were measured by ICP-OES and ICP-MS, respectively, in aliquots of ca. 1 g. Major element concentrations in phenocrysts represent mean values that were determined by electron-microprobe on 10–15 grains per sample. Absolute standard deviations associated with mean values are <1% in mass (1 σ). MnO and P₂O₅ analyses in phenocrysts were substituted by NiO and Cr₂O₃ (values are shown as traces and represent <0.2% in mass of the total pyroxene composition). Trace element concentrations in phenocrysts represent mean values that were determined by Laser ICP-MS on ca. 15 grains per samples. Relative standard deviations (1 σ) represent ca. <15% (Li), 40% (B, Gd and Sm) and >50% (U and Th).

magmatic contribution is negligible in these micro-phenocrysts (<1%).

Between ca. 12 and 28 mg of clino- and orthopyroxene were packed in tin foils and fused in-vacuo for 15 min at 1400 °C, within an in-house-built single vacuum furnace (Zimmermann et al., 2012). The extracted gas was purified using a succession of activated-charcoal cold traps, Ti-foam and SAES getters. Cryo-focusing of the gas at various temperatures (12 K and 70 K) thus allowed suppression of neon before helium analysis. Following the purification steps, the total ³He and ⁴He concentrations were analyzed with the SFT mass spectrometer. Re-extraction procedure were conducted on 3 aliquots by heating the furnace to 1400 °C for an additional 15 min to ensure a complete degassing of the samples. Blank signatures were systematically obtained for these tests. Typical furnace blanks were $(3.3 \pm 1.1) \times 10^4$ and $(1.8 \pm 0.4) \times 10^9$ atoms for ³He and ⁴He, respectively, which represent <3% of the total ³He concentrations and ca. 50–80% of the total ⁴He measured. We emphasize that such a large contribution by the furnace blank to the total ⁴He signal of the samples is actually not related to the quality of the blanks (i.e. blank values obtained during the experiments were consistent with long term blank values) but rather to the very low ⁴He content of the samples. The SFT sensitivity was calibrated using a known amount of helium gas standard with a ³He/⁴He ratio of 20.63 Ra (1Ra = 1.384×10^{-6} corresponds to the atmospheric ratio) (Matsuda et al., 2002). The reproducibility at the 1-sigma level on the gas standard was 1.5% for ³He and 0.3% for ⁴He over a 2-month-period overlapping with our analyses (1 week).

Potential contributions in radiogenic ⁴He due to U, Th and Sm decay were estimated following Blard and Farley (2008). The contribution due to nucleogenic ³He was

calculated following Andrews and Kay (1983) and Andrews (1985) and using (1) Li concentrations measured in both clino- and orthopyroxene separates of SP12-02D, (2) the compositions in major and trace elements measured in bulk rocks as well as (3) the eruption age of the lava inferred from the ⁴⁰Ar/³⁹Ar dating (Tables 2–4). The concentration of cosmogenic ³He in our samples (³He_c) was finally determined using the equations reported by Kurz (1986) assuming a negligible contribution from radiogenic ⁴He (Blard and Farley, 2008):

$${}^3\text{He}_c = {}^3\text{He}_t - {}^3\text{He}_n - {}^3\text{He}_m \quad (1)$$

where ³He_t is the quantity of ³He measured when fusing the sample, ³He_n is the nucleogenic component predicted from geochemical analyses of the minerals and bulk rock and ³He_m the magmatic contribution measured from the in-vacuo crushing of an aliquot of the sample. Note that we do consider here ³He_c as the product of both spallogenic (induced by high-energy neutrons) and capture reactions (induced by cosmogenic thermal neutrons, CTN). Previous studies reported by e.g. Dunai et al. (2007) and Amidon and Farley (2011) have shown that the contribution of CTN to the cosmogenic ³He concentration depends on the Li concentration of the analyzed minerals and the thermal neutrons flux that irradiates the considered surface. We emphasize, however, that the CTN contribution to the San Pedro samples is likely negligible due to the limited content in Li (<30 ppm) in both the bulk rocks and pyroxene separates (Table 3) and because of the extreme local climate aridity that strongly reduces the probability of H-rich material (e.g. snow) covering the sampled surfaces, and consequently the thermal neutrons flux (see Dunai et al., 2007). We thus anticipate a CTN contribution lower than 5% to the cosmogenic ³He concentrations inferred for

Table 4
Summary of the SP12-02A $^{40}\text{Ar}/^{39}\text{Ar}$ step heating experiment.

Incremental heating	$^{40}\text{Ar}/^{39}\text{Ar}$	$^{37}\text{Ar}/^{39}\text{Ar}$	$^{36}\text{Ar}/^{39}\text{Ar}$	^{40}Ar (%)	K/Ca	^{39}Ar (%)	Age $\pm 1\sigma$ (ka)
#1	0.1547	0.1727	0.0381	1.36	2.49	9.87	98.9 \pm 24.9
#2	0.1708	0.1384	0.0587	0.98	3.11	19.14	109.2 \pm 39.8
#3	0.1476	0.2527	0.0507	0.98	1.70	7.50	94.3 \pm 35.6
#4	0.1805	0.1416	0.0407	1.48	3.04	22.30	115.4 \pm 23.8
#5	0.1873	0.3236	0.0529	1.18	1.33	10.31	119.8 \pm 40.1
#6	0.1765	0.2447	0.0580	1.02	1.76	14.77	112.8 \pm 37.5
#7	0.1752	0.4887	0.0904	0.65	0.88	5.70	112.0 \pm 73.5
#8	0.1587	0.3469	0.0509	1.04	1.24	10.40	101.5 \pm 30.3
Total fusion	0.1712	0.2275	0.1042		1.89		109.4 \pm 13.2
Plateau	0.1674				1.40		107.0 \pm 11.6

the San Pedro samples based on observations reported by Amidon et al. (2009) and Blard et al. (2013b).

4. RESULTS

4.1. $^{40}\text{Ar}/^{39}\text{Ar}$ dating of the eruption of the San Pedro Lava flow

The eruption age of the San Pedro volcano lava flow has been estimated from the $^{40}\text{Ar}/^{39}\text{Ar}$ analyses. Results are presented in Table 4 and Fig. 3. The step-heating degassing spectrum yielded a statistically robust plateau age of 107 ± 12 ka (1σ , Mean Square Weighted Deviates, MSWD = 0.07) with 100% of the released ^{39}Ar and no rejected heating steps. The age obtained for the total fusion step is consistent with the plateau age at 109 ± 13 ka (Table 4). Alternatively, Ar data were also cast as inverse isochron age. However, this age is poorly constrained at 100 ± 52 ka, mainly because of the low radiogenic content in the sample resulting in a very limited spread on the isochron. We therefore discarded this age when calculating the production rates of cosmogenic ^3He . Instead, we applied the $^{40}\text{Ar}/^{39}\text{Ar}$ plateau age of 107 ± 12 ka for the calibration of the cosmogenic ^3He production rate, as this age yields a good reproducibility at all heating steps. This age is also consistent with the exposure age ca. 103 ka reported by Wörner et al. (2000) for the eruption of La Poruña.

4.2. Helium isotopic results and corrections applied to ^3He

Helium isotope analyses are reported in Table 5 and cosmogenic ^3He concentrations ($^3\text{He}_c$) calculated for the San Pedro volcano samples are plotted in Fig. 4. Note that helium concentrations are reported in “Mat g $^{-1}$ ” (i.e. 10^6 atoms per gram of pyroxene or ca. 3.7×10^{-14} cc STP/g) in the following sections. Total concentrations released by melting ranged between 89 ± 3 and 97 ± 3 Mat g $^{-1}$ for ^3He ($^3\text{He}_t$) and between (29 ± 14) and $(90 \pm 16) \times 10^3$ Mat g $^{-1}$ for ^4He ($^4\text{He}_t$). ^3He concentrations cluster around ca. 94 ± 2 Mat g $^{-1}$, while the ^4He data show a large scatter, which is probably due to the low amount of released gas and the significant contribution of the furnace blank correction (Table 5). In-vacuo crushing of the aliquot of sample SP12-02D yielded concentrations of (0.29 ± 0.09) Mat g $^{-1}$

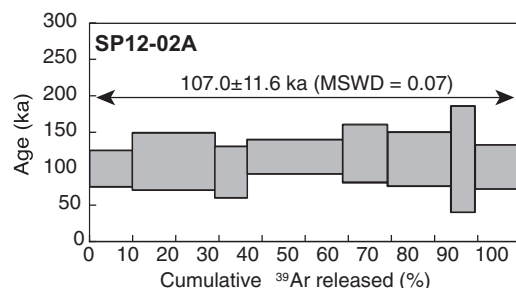


Fig. 3. $^{40}\text{Ar}/^{39}\text{Ar}$ ages obtained plotted vs. the cumulated amount of ^{39}Ar released for SP12-02A. The calculated plateau ages (ka $\pm 1\sigma$) is presented with the MSWD value ($n = 8$).

and $(17.0 \pm 0.6) \times 10^3$ Mat g $^{-1}$ for ^3He and ^4He , respectively (Table 5). The gas liberated during crushing has thus a $^3\text{He}/^4\text{He}$ isotopic ratio of 12 ± 4 Ra that is higher than the values usually reported for volcanic rocks in the Central Andes (Hilton et al., 1993; Blard et al., 2013a). This result suggests that unquantifiable amounts of cosmogenic ^3He might have been released during in-vacuo crushing, with the consequence that the magmatic correction applied to the samples must be considered as a maximum (Blard and Farley, 2008). However, the impact of this magmatic correction is most likely negligible because the ^3He released during crushing ($^3\text{He}_m$) only represents ca. 0.3% of the total ^3He released during melting ($^3\text{He}_t$, Table 5). Note that the magmatic ^3He correction applied to all the samples was realized using the ^3He concentration measured from the prolonged in-vacuo crushing experiment of the sample SP12-02D. This correction systematically represented less than 0.4% of the total ^3He extracted by fusion in all samples and thus is not a significant source of uncertainty.

Regarding ^4He , the concentration we measured during the crushing experiment $(17 \pm 0.6) \times 10^3$ Mat g $^{-1}$ represents ca. 20% of $^4\text{He}_t$ determined in the orthopyroxene aliquot of SP12-02D $(77 \pm 23) \times 10^3$ Mat g $^{-1}$ (Table 5). If we consider that this ^4He concentration measured during crushing is magmatic and representative for all samples, then 40–80% of $^4\text{He}_t$ is most likely radiogenic in other samples. Using the radiogenic production rates estimated from the minerals composition (P_{4r} : ca. 1.1 ± 0.1 Mat g $^{-1}$ yr $^{-1}$, Table 3), the calculated (U–Th–Sm)/ ^4He ages vary from 12 to 54 ka, i.e. significantly younger than the $^{40}\text{Ar}/^{39}\text{Ar}$

Table 5
Helium analyses.

Sample name	Mineral	Mass (mg)	$^3\text{He}_c$ (Mat g $^{-1}$) ^a	$^4\text{He}_r$ (10^3 Mat g $^{-1}$) ^a	$\text{P}3_n$ (at g $^{-1}$ yr $^{-1}$) ^b	$^3\text{He}_m$ (Mat g $^{-1}$) ^c	$\text{P}4_r$ (Mat g $^{-1}$ yr $^{-1}$) ^d	$^3\text{He}_c$ (Mat g $^{-1}$) ^e	$^3\text{He}_{c(s)}$ (Mat g $^{-1}$) ^f	P^3He_c (at g $^{-1}$ yr $^{-1}$) ^f
SP12-02A	Clinop.	22.9	96.0 ± 2.6	89.9 ± 15.7	0.2	0.02	1.19	95.7 ± 2.6	100.7 ± 2.7	941 ± 25 (105)
SP12-02A	Orthop.	12.2	96.6 ± 3.3	29.9 ± 29.5	0.1	0.01	1.16	96.3 ± 3.3	101.3 ± 3.4	946 ± 32 (108)
SP12-02A	Average	–	–	–	–	–	–	95.9 ± 2.0	100.9 ± 2.1	943 ± 20 (104)
SP12-02C	Clinop.	27.8	91.9 ± 2.4	71.6 ± 13.0	0.2	0.02	1.12	91.6 ± 2.4	96.1 ± 2.5	898 ± 23 (100)
SP12-02D	Clinop.	18.1	95.7 ± 2.8	35.6 ± 20.6	0.2	0.02	1.17	95.4 ± 2.8	99.9 ± 2.9	934 ± 27 (105)
SP12-02D	Orthop.	16.4	89.2 ± 2.8	76.9 ± 22.8	0.1	0.01	1.11	88.9 ± 2.8	93.0 ± 2.9	870 ± 27 (98)
SP12-02D	Average	–	–	–	–	–	–	92.2 ± 3.3	96.5 ± 3.4	902 ± 32 (103)
SP12-02E	Clinop.	25.9	93.5 ± 2.4	29.2 ± 14.4	0.2	0.02	1.13	93.2 ± 2.5	98.0 ± 2.6	916 ± 24 (102)
SP12-02F	Clinop.	25.9	93.0 ± 2.3	29.2 ± 14.4	0.1	0.02	1.04	92.7 ± 2.3	101.5 ± 2.6	949 ± 24 (106)
SP12-02F	Orthop.	23.4	92.6 ± 2.4	37.1 ± 15.4	0.1	0.01	0.98	92.3 ± 2.4	101.1 ± 2.6	945 ± 25 (106)
SP12-02F	Average	–	–	–	–	–	–	92.5 ± 1.7	101.3 ± 1.8	947 ± 17 (104)

^a ^3He and ^4He concentrations measured by fusing the sample and corrected for blanks. Typical ^3He and ^4He blanks during the measurements were $(3.3 \pm 1.1) \times 10^4$ atoms and $(1.8 \pm 0.4) \times 10^9$ atoms, respectively, or <3% of ^3He and ca. 50–80% of ^4He measured in the samples. Associated errors (1σ) include sample and blank counting statistics as well as the one-sigma reproducibility on standard analyses over a 2 months period (1.5% for ^3He and 0.3% for ^4He).

^b Nucleogenic ^3He production rates were calculated according to Andrews (1985) and Andrews and Kay (1983) using Li concentration measured in pyroxene aliquots and major and trace element compositions of lava (Table 2).

^c Total nucleogenic ^3He calculated as the product of $\text{P}3_n$ and the age of the lava based on the Ar/Ar dating.

^d Radiogenic ^4He production rate were predicted from equations described in Farley et al. (2002) and Blard and Farley (2008). Calculations are based on U, Th and Sm concentrations measured both in bulk rocks and clinopyroxene and orthopyroxene aliquots of sample SP12-02D (see Table 3) together with a measured equivalent spherical radius of 215 μm for pyroxene grains and an estimated 20- μm alpha-nuclei stopping distance.

^e Corrected for magmatic ($^3\text{He}_m$) and nucleogenic ($^3\text{He}_n$) contributions to $^3\text{He}_c$. The magmatic contribution was inferred from a 6 min in-vacuo crushing of an aliquot of sample SP12-02D that yielded concentrations of (0.29 ± 0.09) Mat g $^{-1}$ and $(17.0 \pm 0.6) \times 10^3$ Mat g $^{-1}$ for ^3He and ^4He , respectively, which represented a $^3\text{He}/^4\text{He}$ isotopic ratio of 12 ± 4 Ra. Reported errors (1σ) integrate ca. 3% uncertainty on $^3\text{He}_c$ measurements and 10% and 31% uncertainties on nucleogenic and magmatic contribution estimates, respectively.

^f Local cosmogenic ^3He production rates estimated from $^3\text{He}_c$ concentrations scaled to the surface, an open-sky topography and 21.934°S–68.510°W and 3390 m a.s.l. and the age of the lava based on the $^{40}\text{Ar}/^{39}\text{Ar}$ dating. Bracketed values correspond to external errors (1σ) and include the ca. 3% uncertainty on $^3\text{He}_c$ concentrations and 11% on the $^{40}\text{Ar}/^{39}\text{Ar}$ inferred age of the lava.

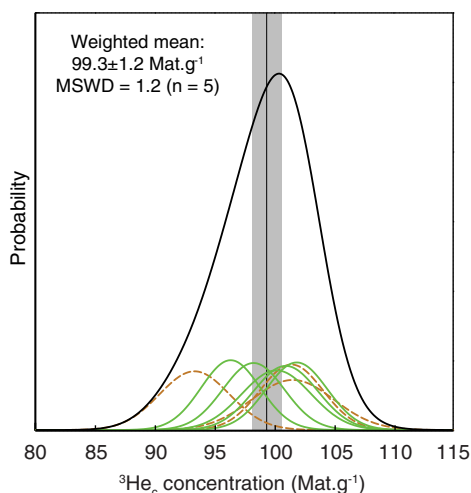


Fig. 4. Camel diagram showing the distribution of cosmogenic ^3He concentrations obtained for the San Pedro volcano samples. ^3He concentrations are corrected for magmatic and nucleogenic contributions, scaled for geomorphic shielding and sample thickness and normalized to 21.934°S – 68.510°W and 3390 m. Note that normalizing each sample's concentration to the surface, an open-sky topography and to a common coordinate allow to better identifying any potential outliers due to erosion or inheritance. Each individual cosmogenic ^3He concentration is represented as a Gaussian distribution, considering the concentration value and its 1σ -error. Green and dashed-brown curves represent clinopyroxene ($n = 5$) and orthopyroxene ($n = 3$) aliquots, respectively. Black curve represents the sum of individual curves. The weighted average concentration is calculated after averaging clinopyroxene and orthopyroxene values and is reported with its associated MSWD value. (For interpretation of the references to color in this figure legend, the reader is referred to the web version of this article.)

age of 107 ± 12 ka. Assuming no magmatic ^4He correction, these $(\text{U}+\text{Th}+\text{Sm})/^4\text{He}$ ages range from 26 to 76 ka. Such a difference with the $^{40}\text{Ar}/^{39}\text{Ar}$ age may indicate that the U, Th and Sm decay chains are out of secular equilibrium (Farley et al., 2002). In any case, given the large uncertainties related to the measurement of ^4He concentrations and to the production rate, the $(\text{U}+\text{Th}+\text{Sm})/^4\text{He}$ approach cannot be used to thoroughly constrain the age of the flow eruption. We will therefore rely on the $^{40}\text{Ar}/^{39}\text{Ar}$ age only to calibrate the cosmogenic ^3He production rate at the San Pedro volcano.

The nucleogenic ^3He ($^3\text{He}_n$) production rates range between ca. 0.1 and 0.2 at $\text{g}^{-1} \text{yr}^{-1}$ (Table 5). The Li concentrations used for this calculation are 20 ppm Li for clinopyroxene and 15 ppm Li for orthopyroxene (from LA ICP-MS analyses of sample SP12-02D, Table 3). Although these values have been used for all 5 samples, we emphasize that this simplification does not induce significant uncertainties on the nucleogenic ^3He correction as $^3\text{He}_n$ represents indeed less than 0.03% of $^3\text{He}_c$ (Table 5).

4.3. Calculation of cosmogenic ^3He concentrations

Cosmogenic ^3He ($^3\text{He}_c$) reported in Table 5 are corrected for inherited magmatic and nucleogenic components.

They range between 89 ± 3 and 96 ± 3 Mat g^{-1} . Subsequent corrections for thickness, geomorphic shielding and normalization to a geographic position of 21.934°S – 68.510°W –3390 m a.s.l. (i.e. total relative correction of ca. 4.5–8.7%, see Table 1) yield surface cosmogenic ^3He concentrations ($^3\text{He}_{c(s)}$) that range from 93 ± 3 to 102 ± 3 Mat g^{-1} , with an arithmetic mean of 99 ± 3 Mat g^{-1} .

The $^3\text{He}_{c(s)}$ concentrations obtained for clinopyroxene and orthopyroxene separates are similar within uncertainties. This is consistent with results from elemental production models (e.g. Masarik and Reedy, 1996) that do not predict any significant differences in production rate between these two pyroxene phases. Weighted average values can therefore be calculated from clinopyroxene and orthopyroxene for the same samples. The narrow distribution displayed by the data thus suggests that all sampled surfaces have experienced the same exposure history. This indicates that the surface of the San Pedro lava flow has not been affected by post-eruptive erosion or burial, consistent with our observations in the field. This also implies that the San Pedro site is suitable for calibrating the production rate of cosmogenic ^3He . In summary, the five samples finally yield a weighted average of 99.3 ± 1.2 $\text{Mat}_{(3\text{He})} \text{g}_{(\text{pyroxene})}^{-1}$ with a relative standard deviation of ca. 1% and a MSWD of 1.2 (Fig. 4).

5. DISCUSSION

5.1. Estimations of cosmogenic ^3He production rates

The production rate of cosmogenic ^3He can be estimated locally, at the geographic position of the calibration site, and/or scaled to a sea level high latitude (SLHL) reference position. Locally, the cosmogenic ^3He production rate is obtained by dividing the average cosmogenic ^3He concentration obtained for the calibration site by the age of the considered landform deduced from an independent dating technique (e.g. ^{14}C , K/Ar, $^{40}\text{Ar}/^{39}\text{Ar}$). Note that individual concentrations are first normalized to the surface, an open-sky topography and the mean geographic coordinates (latitude, longitude and elevation) in order to identify potential outliers due to erosion or inheritance (see e.g. Martin et al., 2015, and reference therein). Scaling the cosmogenic ^3He production rate to SLHL (referred to as SLHL P3 in following sections) is, however, not straightforward. The scaling procedure indeed requires the combination of a geographic spatialization model with an atmosphere model and the reconstruction of the past geomagnetic field conditions (see Balco et al., 2008; Lifton et al., 2014). Here we followed the calculation procedure outlined in Martin et al. (2015) and the scaling frameworks presented below. SLHL P3 estimates were inferred from the San Pedro samples using the time-independent Lal/Stone scaling model (Lal, 1991; Stone, 2000), noted “St”, as well as two time-dependent schemes: “Lm”, the adaptation of the Lal/Stone model (Balco et al., 2008) and “LSD”, recently developed by Lifton et al. (2014). SLHL P3 estimates were thus obtained by dividing the local production rate by a scaling factor representative for a given combination of scaling, atmosphere and geomagnetic

reconstruction models. Regarding scaling schemes, we favored the “Lm” and “LSD” time-dependent models. Indeed, recent studies (Lifton et al., 2014; Borchers et al., 2016; Phillips et al., 2016) have demonstrated that these scaling schemes yield more consistent and reliable spatial and temporal estimates of cosmogenic nuclide production rates than former neutron-monitor based models (Dunai, 2001; Desilets and Zreda, 2003; Lifton et al., 2005; Desilets et al., 2006). These “Lm” and “LSD” models thus represent the most widely used and recently available scaling schemes, respectively (see e.g. Lifton et al., 2014 and Martin et al., 2015). We then calculated SLHL P3s for “St”, “Lm” and “LSD” using the Standard atmosphere model (National Oceanic and Atmospheric Administration, 1976) and the ERA-40 reanalysis dataset (Uppala et al., 2005), which allows accounting for the regional variations in height-pressure relationship. Finally, we inferred SLHL P3s for the time-dependent “Lm” and “LSD” scaling schemes with three paleomagnetic-field reconstruction models (see details regarding the geomagnetic field reconstructions in Martin et al., 2015). The first two geomagnetic models rely on Virtual Dipole Moment values based on 1) Muscheler et al. (2005) for 0–62 ka BP and SINT-2000 (Valet et al., 2005) beyond and 2) GLOPIS-75 (Laj et al., 2004) for 0–75 ka BP and SINT-2000 beyond. The third model is based on the composite reconstruction of temporal variations in geomagnetic and solar intensity modulations implemented in the LSD model (Lifton et al., 2014).

5.2. Calibration of $^3\text{He}_c$ production rates at 21.934°S–68.510°W–3390 m a.s.l.

The local cosmogenic ^3He production rate, estimated for the San Pedro calibration site at a geographic position of 21.934°S–68.510°W and 3390 m a.s.l., is obtained by dividing the weighted average $^3\text{He}_{c(s)}$ with the eruption age of the San Pedro lava flow obtained from the $^{40}\text{Ar}/^{39}\text{Ar}$ dating. This approach yields a local production rate of 928 ± 11 at $\text{g}^{-1} \text{yr}^{-1}$, and 928 ± 101 at $\text{g}^{-1} \text{yr}^{-1}$ when propagating both the cosmogenic ^3He and $^{40}\text{Ar}/^{39}\text{Ar}$ uncertainties respectively, at the 1-sigma level (Table 5). This rate combines all production pathways of cosmogenic ^3He including spallation, thermal neutron capture and muogenic production. We note however, that the contribution of cosmogenic thermal neutrons to the production of cosmogenic ^3He at the San Pedro calibration site is likely lower than 5% and therefore negligible, based on the predictions obtained with the model reported by Amidon and Farley (2011) for pyroxenes with 15–20 ppm apparent Li and a He-closure age of ca. 100 ka.

The local cosmogenic ^3He production rate is then scaled to a sea level and high latitude (SLHL) reference position. SLHL P3s inferred from the San Pedro samples are presented in Table 6. SLHL P3s obtained from the time-independent “St” scheme with the Standard and ERA-40 atmosphere models are 132 ± 14 and 143 ± 16 at $\text{g}^{-1} \text{yr}^{-1}$, respectively. SLHL P3s estimated with the time-dependent

Table 6
SLHL ^3He production rates from the San Pedro calibration site.

Scaling scheme ^a	Atmosphere model ^b	Geomagnetic reconstruction ^c	SLHL P3 (at $\text{g}^{-1} \text{yr}^{-1}$) ^d
“St”	Standard	–	132 ± 14
	ERA-40 (1)	–	143 ± 16
“Lm”	Standard	Muscheler-SINT2000	120 ± 13
		GLOPIS75-SINT2000	118 ± 13
		LSD	109 ± 12
	ERA-40	Muscheler-SINT2000 (2)	130 ± 14
		GLOPIS75-SINT2000 (3)	128 ± 14
		LSD (4)	118 ± 14
“LSD”	Standard	Muscheler-SINT2000	116 ± 13
		GLOPIS75-SINT2000	113 ± 12
		LSD	103 ± 11
	ERA-40	Muscheler-SINT2000 (5)	127 ± 14
		GLOPIS75-SINT2000 (6)	124 ± 14
		LSD (7)	112 ± 12

^a Cosmogenic ^3He production rates are scaled to the reference sea level high latitude (SLHL) position using the calculation procedures and employed the scaling frameworks reported by Martin et al. (2015). “St” refers to Lal (1991)/Stone (2000), “Lm” to the time-dependent adaptation of the Lal/Stone scheme (see e.g. Balco et al., 2008) and “LSD” to Lifton et al. (2014).

^b The Standard atmosphere model is based on the National Oceanic and Atmospheric Administration (1976) and the ERA-40 reanalysis dataset on Uppala et al. (2005).

^c Geomagnetic models rely on Virtual Dipole Moment values based on Muscheler et al. (2005), GLOPIS-75 (Laj et al., 2004) and SINT-2000 (Valet et al., 2005). Numbers in brackets refer to scaling factor curves as labeled in Fig. 5.

^d SLHL P3 estimates are obtained by dividing the local production rate by a scaling factor inferred for a given combination of scaling, atmosphere and geomagnetic reconstruction models (see text for details). Reported errors correspond to external (total) uncertainties at 1-sigma level and comprise a ca. 1% uncertainty associated with the weighted average cosmogenic ^3He concentration and ca. 11% from the $^{40}\text{Ar}/^{39}\text{Ar}$ dating.

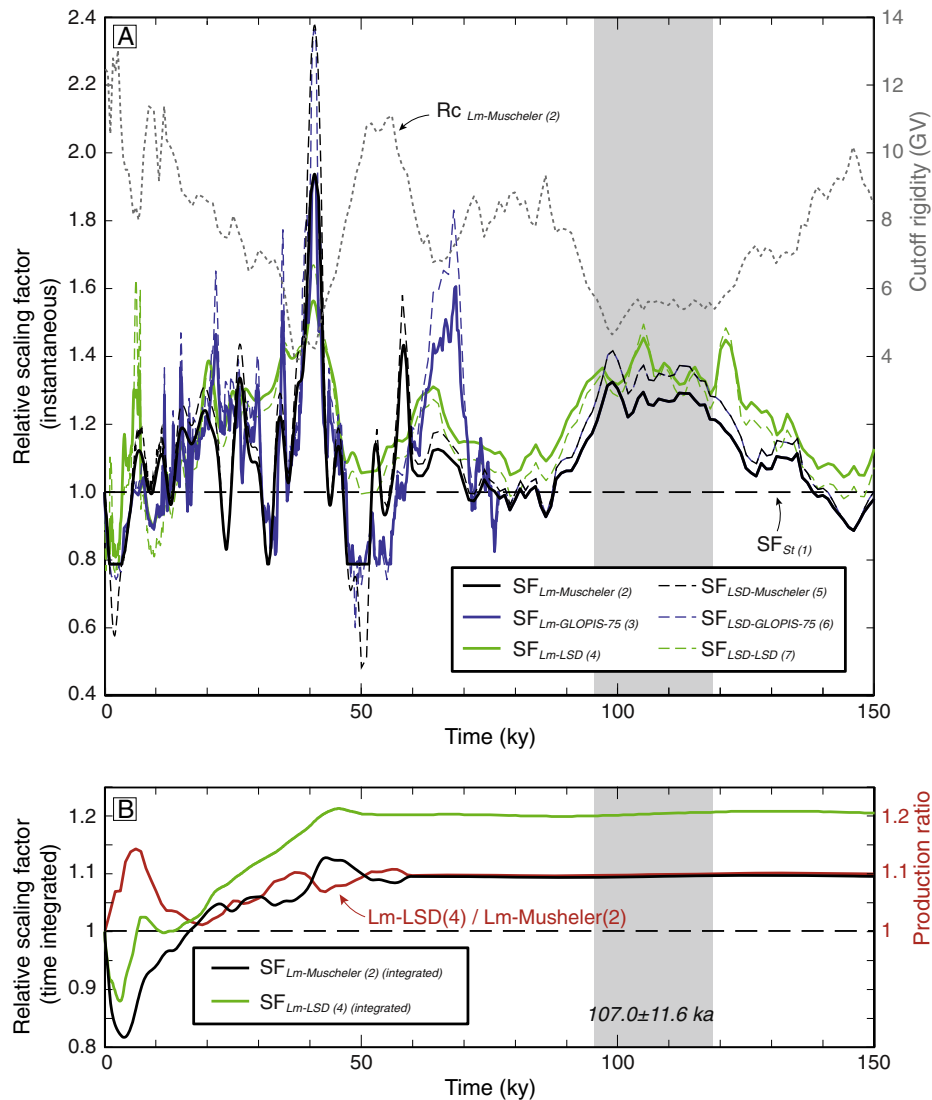


Fig. 5. (A) 150-ka-long variations of TCN scaling-factors and magnetic-field cutoff rigidity calculated for 21.934°S–68.510°W–3390 m a.s.l. using calculation procedures and scaling frameworks reported by Martin et al. (2015). All scaling factors are calculated based on the atmospheric pressure derived from the ERA-40 reanalysis dataset (Uppala et al., 2005). Numbers in brackets are the same as in Table 6 and represent predictions from different combinations of scaling schemes and geomagnetic field reconstructions. (B) Time-integrated scaling factors using the “Lm” scaling scheme and the ERA-40 atmosphere model with geomagnetic field reconstructions based on Musheler-SINT2000 (black curve) and as implemented in the “LSD” model (green curve). The red curves represent the production ratio between “Lm-LSD” and “Lm-Muscheler”. (For interpretation of the references to color in this figure legend, the reader is referred to the web version of this article.)

“Lm” and “LSD” schemes, with various combinations of atmosphere and geomagnetic models, vary from 103 ± 11 to 130 ± 14 at $\text{g}^{-1} \text{yr}^{-1}$ (Table 6). In general, the inferred values agree well with the SLHL P3 reported from global-scale compilations by Goehring et al. (2010) and more recently by Blard et al. (2013a). Moreover, SLHL P3s that we estimated using the time-dependent adaptation of the Lal/Stone scaling scheme (“Lm”) with the Musheler-SINT2000 geomagnetic reconstruction and considering both the Standard and ERA-40 atmosphere models are 120 ± 13 and 130 ± 14 at $\text{g}^{-1} \text{yr}^{-1}$, respectively. Interest-

ingly, these SLHL P3 estimates fit perfectly with the values reported by Blard et al. (2013a) from a ca. 15-ka-old calibration site located at 3800 m a.s.l. on the Bolivian Altiplano (Fig. 1).

Note that all applied time-dependent scaling frameworks predict that at the San Pedro volcano calibration site, the production of cosmogenic nuclides, including cosmogenic ^3He , has been generally higher during the last 100 to 150 ka than at present (Fig. 5). Such a situation can be explained by the persistence of a weaker geomagnetic field intensity that has induced lower cutoff rigidities,

thereby allowing more cosmic-ray particles to enter the Earth's magnetic field (see [Dunai and Lifton, 2014](#) and references therein). This effect is particularly amplified in high tropical areas integrating >50-ka exposure histories (e.g. [Balco et al., 2008](#)), since it yields relative corrections between 10% and 20% of the modern rate ([Fig. 5](#)). It thus explains why the San Pedro calibration site yields time-independent “St” scaling factors that are higher than those inferred from time-dependent schemes (“Lm” and “LSD”). [Fig. 5](#) and [Table 6](#) illustrate that geomagnetic field reconstructions relying on the Muscheler-SINT2000 and “LSD” frameworks systematically yield the highest and lowest SLHL P3s, respectively, independently of the scaling scheme and atmosphere model considered. The geomagnetic field and solar modulation reconstructions implemented in the “LSD” frameworks predict time-integrated scaling factors that are up to ca. 10% higher than with the Muscheler-SINT2000 for an exposure length >60 ka.

5.3. Re-evaluation of the global SLHL cosmogenic ^3He production rate

Cosmogenic ^3He production rates have rarely been calibrated to sea level high latitude positions using a common calculation framework that included similar scaling schemes, atmosphere model and geomagnetic field reconstructions. Here we re-evaluate the global SLHL P3 by compiling and processing available calibration datasets for both olivine and pyroxene within a common calculation framework that combines the scaling schemes, atmosphere and geomagnetic field models presented above. Twenty different calibration sites and ca. 150 cosmogenic ^3He analyses have been compiled from the literature and combined with the San Pedro samples (see [Table A2](#)). This new compilation includes the studies of [Cerling and Craig \(1994\)](#), [Licciardi et al. \(1999, 2006\)](#), [Dunai and Wijbrans \(2000\)](#), [Ackert et al. \(2003\)](#), [Blard et al. \(2006, 2013a\)](#), [Goehring et al. \(2010\)](#), [Amidon and Farley \(2011\)](#), [Foeken et al. \(2012\)](#), [Fenton et al. \(2013\)](#), and [Fenton and Niedermann \(2014\)](#). We do note that we only considered dataset originating from absolute calibration studies and therefore excluded those from cross calibrations (e.g. [Amidon et al., 2009](#)). Some of the studies included in this compilation did not address the impact of radiogenic ^4He on the measured cosmogenic ^3He concentrations. In several of these previous studies indeed, the authors overestimated the amount of ^4He that was derived from trapped magmatic gases and thus over-corrected for magmatic ^3He , thereby resulting in an underestimation of cosmogenic ^3He concentrations. To tackle this issue, the compiled data were first corrected for this radiogenic contribution, either using the reported U–Th–Sm concentrations in the phenocrysts or considering the global mean of these elements as proposed by [Blard and Farley \(2008\)](#), see [Table A2](#)). The resulting corrections increase the cosmogenic ^3He concentrations by 4% on average, as illustrated in the inset of [Fig. 6A](#). Subsequently, the cosmogenic ^3He concentrations available for each calibration site were (1) normalized to the surface, an open-sky topography and the sites' mean geographic coordinates, (2) used to calculate a weighted average

concentration and (3) inverted to SLHL P3s, following the procedure outlined in Section 3.4. SLHL P3s inferred from all possible combinations in scaling, atmosphere and geomagnetic field models cover the range 76 ± 4 – 186 ± 12 at $\text{g}^{-1} \text{yr}^{-1}$ (see [Table A2](#)). When considering each scaling framework separately, the values yield arithmetic means that range between 115 ± 19 and 122 ± 20 at $\text{g}^{-1} \text{yr}^{-1}$, therefore identical within uncertainty (1σ -level). These re-evaluated global SLHL P3s are consistent with values reported from previous compilations that also considered olivine and pyroxene minerals together (e.g. [Goehring et al., 2010](#); [Blard et al., 2013a](#); [Borchers et al., 2016](#)). We emphasize, however, that SLHL P3s estimated from the combination of the “Lm” scaling scheme with the ERA-40 atmosphere model and the geomagnetic field reconstruction based on [Muscheler et al. \(2005\)](#) and SINT2000 ([Valet et al., 2005](#)) yield the least scatter in the distribution, with a 14% relative standard deviation and an arithmetic mean of 120 ± 16 at $\text{g}^{-1} \text{yr}^{-1}$. [Fig. 6](#) represents the distribution of SLHL P3s inferred from this latter scaling framework. It does not show any correlation with elevation nor with latitude. This confirms previous observations reported by [Goehring et al. \(2010\)](#) and [Blard et al. \(2013a\)](#) that there is no anomalous production of cosmogenic ^3He at high elevations, at least in pyroxene and olivine. It is, however, important to emphasize that the estimated Mean Square Weighted Deviation is significantly higher than 1 ($\text{MSWD} = 10.4$; [Fig. 6](#)), indicating that the observed variability in the data is larger than a statistical dispersion that would result from analytical uncertainties only. In other words, the global SLHL P3 compilation unlikely represents a single population. Note that while [Fig. 6](#) only represents SLHL P3s estimated from the combination of the “Lm” scaling scheme with the ERA-40 atmosphere model and Muscheler-SINT2000 based geomagnetic field reconstruction, all other scaling frameworks present a similar picture. Part of this over-dispersion might result from calibration sites older than ca. 120 ka that systematically yield SLHL P3s lower than ca. 110 at $\text{g}^{-1} \text{yr}^{-1}$ when considering the “Lm” scaling scheme ([Fig. 6](#)). This inference, however, should be tuned down when considering the “LSD” scaling scheme, as P3s estimates do not show such temporal pattern. In any cases and for all considered scaling frameworks, the variability in SLHL P3s seems independent from the exposure age for calibration sites younger than 110 ka ([Fig. 6](#)). The observed variability in SLHL P3s might result from unrecognized erosion, variations in atmospheric pressure, inaccurate correction of the time-dependent production rate variability, and/or unaccounted excess in Li concentrations of crustally contaminated magmas (e.g. [Dunai and Wijbrans, 2000](#); [Dunai et al., 2007](#); [Staiger et al., 2007](#); [Amidon and Farley, 2011](#); [Foeken et al., 2012](#)). Excluding calibration sites older than 120 ka from the global compilation leads to slightly higher average cosmogenic ^3He production rates by ca. 2–4% and reduces the standard deviations from 14–17% to ca. 11–17%, depending on the considered scaling framework (see [Table A2](#)), but do not fundamentally change the overall picture.

In summary, SLHL P3s inferred from the combination of the “Lm” scaling scheme with the ERA-40 atmosphere

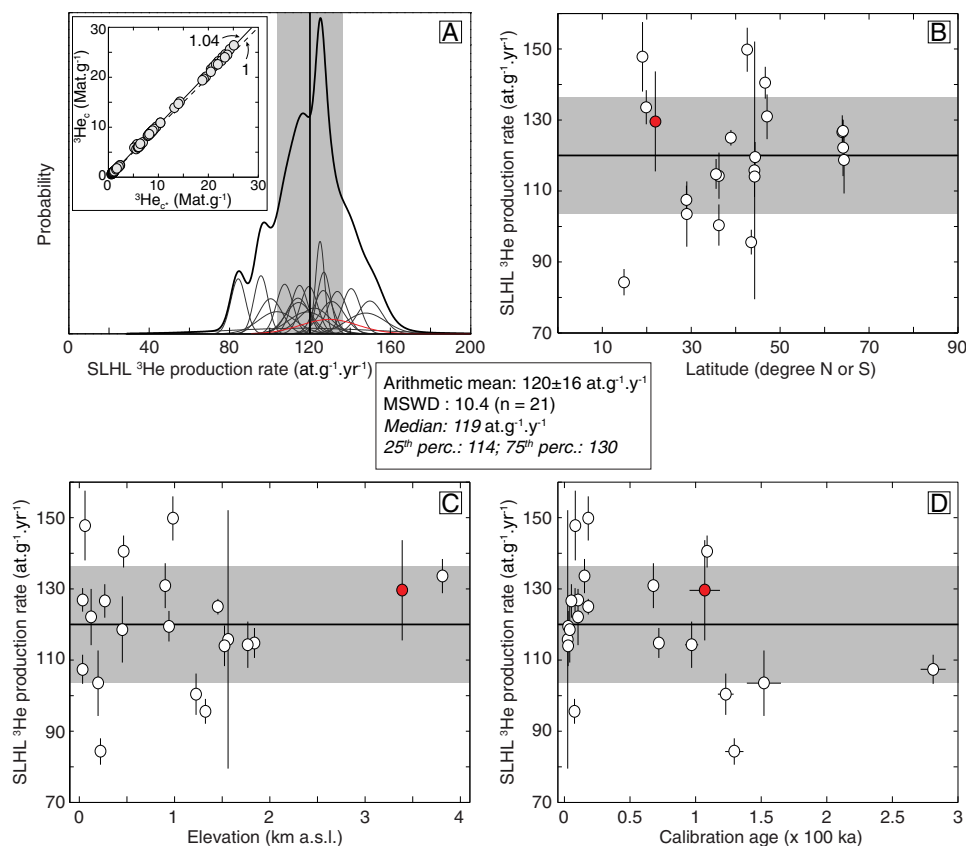


Fig. 6. Distribution of the reevaluated SLHL P3s inferred from the compilation of previous geological calibration sites as well as the San Pedro lava flow. Values represented are inferred from the combination of the “Lm” scaling scheme with the ERA-40 atmosphere model and the geomagnetic field reconstruction relying on the VDM values based on Muscheler et al. (2005) for the period 0–62 ka and SINT2000 (Vale et al., 2005) beyond. (A) Camel diagram showing the distribution of reevaluated SLHL P3s. Inset illustrates the impact of the radiogenic correction applied on cosmogenic ^3He concentrations following Blard and Farley (2008) (see text). (B)–(D) show the distribution of SLHL P3s as a function of latitude, elevation and calibration age, respectively. Note the absence of statistically significant relationships between the production rate and these parameters. Red data represents the San Pedro volcano calibration site. (For interpretation of the references to color in this figure legend, the reader is referred to the web version of this article.)

model and Muscheler-SINT2000 based geomagnetic field reconstruction yield the best constrained mean global-scale cosmogenic ^3He production rate. This scaling framework therefore represents a qualitative combination of currently available geographic spatialization schemes, atmosphere as well as geomagnetic field reconstruction models to estimate exposure ages from cosmogenic ^3He concentrations. Similar statements were also reported by Martin et al. (2015) regarding the production of in-situ ^{10}Be in the high tropical Andes.

6. CONCLUSION

We report a new geological calibration site located in northern Chile (21.934°S–68.510°W) at 3390 m a.s.l. that we used to infer the production rate of cosmogenic ^3He in pyroxenes. $^{40}\text{Ar}/^{39}\text{Ar}$ dating gives a consistent plateau age of 107 ± 12 ka. Eight mineral separates of clinopyroxene and orthopyroxene from five different surface samples yield clustered ^3He concentrations, for both pyroxene phases.

Magmatic and nucleogenic ^3He corrections are negligible (<1%) in this lava flow. The weighted average cosmogenic ^3He concentration is 99.3 ± 1.2 Mat g^{-1} , which represents the highest cosmogenic ^3He concentrations measured in natural calibration samples.

We then used this data to constrain a local cosmogenic ^3He production rate of 928 ± 101 at $\text{g}^{-1} \text{yr}^{-1}$ at 21.934°S–68.510°W and 3390 m a.s.l. After scaling to sea level and high latitudes (SLHL), cosmogenic ^3He production rate estimates vary from 103 ± 11 to 130 ± 14 at $\text{g}^{-1} \text{yr}^{-1}$, which depends on different combinations of scaling schemes, atmosphere models and geomagnetic field reconstructions.

Finally we combined the SLHL P3s inferred from the San Pedro lava flow samples with cosmogenic ^3He production rates (in both olivine and pyroxene) inferred from various calibration sites and re-evaluated the mean global SLHL P3. This compilation, where cosmogenic ^3He production rates were scaled to SLHL with two scaling schemes, two atmosphere models and three different

geomagnetic field reconstructions, yield arithmetic means for SLHL P3s that vary between 115 ± 19 and 122 ± 20 at $\text{g}^{-1} \text{yr}^{-1}$. These values are identical within uncertainty and consistent with values previously reported from similar compilation studies (e.g. Goehring et al., 2010; Blard et al., 2013a; Borchers et al., 2016). This new compilation thus illustrates that a calculation framework including the (1) time-dependent adaptation of the Lal (1991)/Stone (2000) scheme, (2) ERA-40 atmosphere model (Uppala et al., 2005), and a (3) geomagnetic field reconstruction relying on the Virtual Dipole Moment values based on Muscheler et al. (2005) and SINT-2000 (Valet et al., 2005) currently yields the best constrained mean global-scale cosmogenic ^3He production rate. Our observations also appear perfectly in line with the recent findings reported by Lifton (2016). We thus suggest that the update of the scaling framework presented here, together with the inferred mean global SLHL P3 of 120 ± 16 at $\text{g}^{-1} \text{yr}^{-1}$, should be favored when calculating exposure ages from cosmogenic ^3He concentrations.

ACKNOWLEDGMENTS

This project received financial supports by the Swiss National Science Foundation awarded to Schlunegger (grant No. 137516). Helium analyses were partially funded by the ANR GALAC grant (PI Pierre-Henri Blard, ANR-11-JS56-011-01). We thank Christine Lemp, Martin Robyr and Thomas Pettke for their support during sample preparation and geochemical analyses. We thank David L. Shuster for his careful editorial handling, as well as Will Amidon and an anonymous reviewer who provided constructive comments on the submitted manuscript.

APPENDIX A. SUPPLEMENTARY DATA

Supplementary data associated with this article can be found, in the online version, at <http://dx.doi.org/10.1016/j.gca.2016.04.023>.

REFERENCES

- Ackert R. P., Singer B. S., Guillou H., Kaplan M. R. and Kurz M. D. (2003) Long-term cosmogenic ^3He production rates from $^{40}\text{Ar}/^{39}\text{Ar}$ and K–Ar dated Patagonian lava flows at 47°S. *Earth Planet. Sci. Lett.* **210**, 119–136.
- Amidon W. H. and Farley K. A. (2011) Cosmogenic ^3He production rates in apatite, zircon and pyroxene inferred from Bonneville flood erosional surfaces. *Quat. Geochronol.* **6**, 10–21.
- Amidon W. H., Rood D. H. and Farley K. A. (2009) Cosmogenic ^3He and ^{21}Ne production rates calibrated against ^{10}Be in minerals from the Coso volcanic field. *Earth Planet. Sci. Lett.* **280**, 194–204.
- Anderson S. W. and Fink J. H. (1992) Crease structures: indicators of emplacement rates and surface stress regimes of lava flows. *Geol. Soc. Am. Bull.* **104**(5), 615–625.
- Anderson S. W., Krinsley D. H. and Fink J. H. (1994) Criteria for recognition of constructional silicic lava flow surfaces. *Earth Surf. Proc. Land.* **19**(6), 531–541.
- Andrews J. (1985) The isotopic composition of radiogenic helium and its use to study groundwater movement in confined aquifers. *Chem. Geol.* **49**, 339–351.
- Andrews J. and Kay R. (1983) The U contents and $^{234}\text{U}/^{238}\text{U}$ activity ratios of dissolved uranium in groundwaters from some Triassic sandstones in England. *Chem. Geol.* **41**, 101–117.
- Balco G., Stone J. O., Lifton N. A. and Dunai T. J. (2008) A complete and easily accessible means of calculating surface exposure ages or erosion rates from ^{10}Be and ^{26}Al measurements. *Quat. Geochronol.* **3**, 174–195.
- Blard P. H., Bourlès D., Lavé J. and Pik R. (2006) Applications of ancient cosmic-ray exposures: theory, techniques and limitations. *Quat. Geochronol.* **1**, 59–73.
- Blard P.-H. and Farley K. (2008) The influence of radiogenic ^4He on cosmogenic ^3He determinations in volcanic olivine and pyroxene. *Earth Planet. Sci. Lett.* **276**, 20–29.
- Blard P.-H., Lavé J., Sylvestre F., Placzek C., Claude C., Galy V., Condom T. and Tibari B. (2013a) Cosmogenic ^3He production rate in the high tropical Andes (3800 m, 20°S): implications for the local last glacial maximum. *Earth Planet. Sci. Lett.* **377**, 260–275.
- Blard P.-H., Braucher R., Lavé J. and Bourlès D. (2013b) Cosmogenic ^{10}Be production rate calibrated against ^3He in the high Tropical Andes (3800–4900 m, 20–22°S). *Earth Planet. Sci. Lett.* **382**, 140–149.
- Borchers B., Marrero S., Balco G., Caffee M., Goehring B., Lifton N., Nishiizumi K., Phillips F., Schaefer J. and Stone J. (2016) Geological calibration of spallation production rates in the CRONUS-Earth Project. *Quat. Geochronol.* **31**, 188–198.
- Cerling T. E. and Craig H. (1994) Cosmogenic ^3He production rates from 39°N to 46°N latitude, western USA and France. *Geochim. Cosmochim. Acta* **58**, 249–255.
- Craig H. and Poreda R. J. (1986) Cosmogenic ^3He in terrestrial rocks: the summit lavas of Maui. *Proc. Natl. Acad. Sci. U.S.A.* **83**, 1970–1974.
- Desilets D. and Zreda M. (2003) Spatial and temporal distribution of secondary cosmic-ray nucleon intensities and applications to in situ cosmogenic dating. *Earth Planet. Sci. Lett.* **206**, 21–42.
- Desilets D., Zreda M. and Prabu T. (2006) Extended scaling factors for in situ cosmogenic nuclides: new measurements at low latitude. *Earth Planet. Sci. Lett.* **246**, 265–276.
- De Silva S. (1989) Altiplano-Puna volcanic complex of the central Andes. *Geology* **17**, 1102–1106.
- Dunai T. J. (2001) Influence of secular variation of the geomagnetic field on production rates of in situ produced cosmogenic nuclides. *Earth Planet. Sci. Lett.* **193**, 197–212.
- Dunai T. J. (2010) *Cosmogenic Nuclides: Principles, Concepts and Applications in the Earth Surface Sciences*, New York.
- Dunai T. J. and Lifton N. A. (2014) The nuts and bolts of cosmogenic nuclide production. *Elements* **10**, 347–350.
- Dunai T. J. and Wijbrans J. R. (2000) Long-term cosmogenic ^3He production rates (152 ka–1.35 Ma) from $^{40}\text{Ar}/^{39}\text{Ar}$ dated basalt flows at 29°N latitude. *Earth Planet. Sci. Lett.* **176**, 147–156.
- Dunai T. J., Stuart F. M., Pik R., Burnard P. and Gayer E. (2007) Production of ^3He in crustal rocks by cosmogenic thermal neutrons. *Earth Planet. Sci. Lett.* **258**, 228–236.
- Dunne J., Elmore D. and Muzikar P. (1999) Scaling factors for the rates of production of cosmogenic nuclides for geometric shielding and attenuation at depth on sloped surfaces. *Geomorphology* **27**, 3–11.
- Evenstar L. A., Hartley A. J., Stuart F. M., Mather A. E., Rice C. M. and Chong G. (2009) Multiphase development of the Atacama Planation Surface recorded by cosmogenic ^3He exposure ages: implications for uplift and Cenozoic climate change in western South America. *Geology* **37**, 27–30.
- Farley K., Kohn B. and Pillans B. (2002) The effects of secular disequilibrium on (U–Th)/He systematics and dating of Quaternary volcanic zircon and apatite. *Earth Planet. Sci. Lett.* **201**, 117–125.

- Fenton C. R. and Niedermann S. (2014) Surface exposure dating of young basalts (1–200 ka) in the San Francisco volcanic field (Arizona, USA) using cosmogenic ^3He and ^{21}Ne . *Quat. Geochronol.* **19**, 87–105.
- Fenton C. R., Mark D. F., Barfod D. N., Niedermann S., Goethals M. M. and Stuart F. M. (2013) $^{40}\text{Ar}/^{39}\text{Ar}$ dating of the SP and Bar Ten lava flows AZ, USA: laying the foundation for the SPICE cosmogenic nuclide production-rate calibration project. *Quat. Geochronol.* **18**, 158–172.
- Foeken J. P. T., Stuart F. M. and Mark D. F. (2012) Long-term low latitude cosmogenic ^3He production rate determined from a 126 ka basalt from Fogo, Cape Verdes. *Earth Planet. Sci. Lett.* **359–360**, 14–25.
- Francis P. W., Roobol M. J., Walker G. P. L., Cobbold P. R. and Coward M. (1974) The San Pedro and San Pablo volcanoes of northern Chile and their hot avalanche deposits. *Geol. Rundsch.* **63**, 357–388.
- Giese J., Seward D., Stuart F. M., Wüthrich E., Gnos E., Kurz D., Eggenberger U. and Schreurs G. (2010) Electrodynamical disaggregation: does it affect apatite fission-track and (U–Th)/He analyses? *Geostand. Geoanal. Res.* **34**, 39–48.
- Goehring B. M., Kurz M. D., Balco G., Schaefer J. M., Licciardi J. and Lifton N. (2010) A reevaluation of in situ cosmogenic ^3He production rates. *Quat. Geochronol.* **5**, 410–418.
- Hilton D., Hammerschmidt K., Teufel S. and Friedrichsen H. (1993) Helium isotope characteristics of Andean geothermal fluids and lavas. *Earth Planet. Sci. Lett.* **120**, 265–282.
- Hora J. M., Singer B. S. and Wörner G. (2007) Volcano evolution and eruptive flux on the thick crust of the Andean Central Volcanic Zone: $^{40}\text{Ar}/^{39}\text{Ar}$ constraints from Volcán Parímacota, Chile. *Geol. Soc. Am. Bull.* **119**, 343–362.
- Houston J. and Hartley A. J. (2003) The central Andean west-slope rain shadow and its potential contribution to the origin of hyper-aridity in the Atacama Desert. *Int. J. Climatol.* **23**(12), 1453–1464.
- Koppers A. A. (2002) ArArCALC—software for $^{40}\text{Ar}/^{39}\text{Ar}$ age calculations. *Comput. Geosci.* **28**, 605–619.
- Kuiper K., Deino A., Hilgen F., Krijgsman W., Renne P. and Wijbrans J. (2008) Synchronizing rock clocks of Earth history. *Science* **320**, 500–504.
- Kurz M. D. (1986) In situ production of terrestrial cosmogenic helium and some applications to geochronology. *Geochim. Cosmochim. Acta* **50**, 2855–2862.
- Kurz M. D., Colodner D., Trull T. W., Moore R. B. and O'Brien K. (1990) Cosmic ray exposure dating with in situ produced cosmogenic ^3He : results from young Hawaiian lava flows. *Earth Planet. Sci. Lett.* **97**, 177–189.
- Laj C., Kissel C. and Beer J. (2004) High resolution global paleointensity stack since 75 kyr (GLOPIS-75) calibrated to absolute values. In *Timescales of the Paleomagnetic Field*, pp. 255–265.
- Lal D. (1991) Cosmic ray labelling of erosion surfaces: in situ nuclide production rates and erosion models. *Earth Planet. Sci. Lett.* **104**, 424–439.
- Lee J.-Y., Marti K., Severinghaus J. P., Kawamura K., Yoo H.-S., Lee J. B. and Kim J. S. (2006) A redetermination of the isotopic abundances of atmospheric Ar. *Geochim. Cosmochim. Acta* **70**, 4507–4512.
- Licciardi J., Kurz M., Clark P. and Brook E. (1999) Calibration of cosmogenic ^3He production rates from Holocene lava flows in Oregon, USA, and effects of the Earth's magnetic field. *Earth Planet. Sci. Lett.* **172**, 261–271.
- Licciardi J., Kurz M. and Curtice J. (2006) Cosmogenic ^3He production rates from Holocene lava flows in Iceland. *Earth Planet. Sci. Lett.* **246**, 251–264.
- Lifton N. (2016) Implications of two Holocene time-dependent geomagnetic models for cosmogenic nuclide production rate scaling. *Earth Planet. Sci. Lett.* **433**, 257–268.
- Lifton N. A., Bieber J. W., Clem J. M., Duldig M. L., Evenson P., Humble J. E. and Pyle R. (2005) Addressing solar modulation and long-term uncertainties in scaling secondary cosmic rays for in situ cosmogenic nuclide applications. *Earth Planet. Sci. Lett.* **239**, 140–161.
- Lifton N., Sato T. and Dunai T. J. (2014) Scaling in situ cosmogenic nuclide production rates using analytical approximations to atmospheric cosmic-ray fluxes. *Earth Planet. Sci. Lett.* **386**, 149–160.
- Ludwig K. (2003) *User Manual for Isoplot 3.0*. Berkeley Geochronology Center Special Publication 4.
- Masarik J. and Reedy R. (1996) Monte Carlo simulation of in-situ-produced cosmogenic nuclides. *Radiocarbon* **38**, 163–164.
- Martin L. C. P., Blard P. H., Lavé J., Braucher R., Lupker M., Condom T., Charreau J., Mariotti V., Team A. and Davy E. (2015) In situ cosmogenic ^{10}Be production rate in the High Tropical Andes. *Quat. Geochronol.* **30**(Part A), 54–68.
- Matsuda J., Matsumoto T., Sumino K., Nagao K., Yamamoto J., Miura Y., Kaneoka I., Takahata N. and Sano Y. (2002) The $^3\text{He}/^4\text{He}$ ratio of the new internal He standard of Japan (HESJ). *Geochem. J.* **36**, 191–195.
- Muscheler R., Beer J., Kubik P. W. and Synal H.-A. (2005) Geomagnetic field intensity during the last 60,000 years based on ^{10}Be and ^{36}Cl from the Summit ice cores and ^{14}C . *Quatern. Sci. Rev.* **24**, 1849–1860.
- National Oceanic and Atmospheric Administration (1976) *National Aeronautics and Space Administration, and the United States Air Force. Washington DC*.
- Nomade S., Renne P., Vogel N., Deino A., Sharp W., Becker T., Jaouni A. and Mundil R. (2005) Alder Creek sanidine (ACs-2): a quaternary $^{40}\text{Ar}/^{39}\text{Ar}$ dating standard tied to the Cobb Mountain geomagnetic event. *Chem. Geol.* **218**, 315–338.
- Nomade S., Gauthier A., Guillou H. and Pastre J.-F. (2010) $^{40}\text{Ar}/^{39}\text{Ar}$ temporal framework for the Alleret maar lacustrine sequence (French Massif-Central): volcanological and paleoclimatic implications. *Quat. Geochronol.* **5**, 20–27.
- O'Callaghan L. J. and Francis P. W. (1986) Volcanological and petrological evolution of San Pedro volcano, Provincia El Loa, North Chile. *J. Geol. Soc.* **143**, 275–286.
- Phillips F. M., Argento D. C., Bourlès D. L., Caffee M. W., Dunai T. J., Goehring B., Gosse J. C., Hudson A. M., Jull A. T. and Kelly M. (2016) Where now? Reflections on future directions for cosmogenic nuclide research from the CRONUS Projects. *Quat. Geochronol.* **31**, 155–159.
- Renne P. R., Balco G., Ludwig K. R., Mundil R. and Min K., et al. (2011) Response to the comment by WH Schwarz, on “Joint determination of ^{40}K decay constants and $^{40}\text{Ar}/^{40}\text{K}$ for the Fish Canyon sanidine standard, and improved accuracy for $^{40}\text{Ar}/^{39}\text{Ar}$ geochronology” by PR Renne et al. (2010). *Geochim. Cosmochim. Acta* **75**, 5097–5100.
- Scarsi P. (2000) Fractional extraction of helium by crushing of olivine and clinopyroxene phenocrysts: effects on the $^3\text{He}/^4\text{He}$ measured ratio. *Geochim. Cosmochim. Acta* **64**, 3751–3762.
- Schäfer J. M., Ivy-Ochs S., Wieler R., Leya I., Baur H., Denton G. H. and Schlüchter C. (1999) Cosmogenic noble gas studies in the oldest landscape on earth: surface exposure ages of the Dry Valleys, Antarctica. *Earth Planet. Sci. Lett.* **167**, 215–226.
- Staiger J., Gosse J., Toracinta R., Oglesby B., Fastook B. and Johnson J. V. (2007) Atmospheric scaling of cosmogenic nuclide production: climate effect. *J. Geophys. Res.* **112**(B2) B02205.

- Steiger R. H. and Jäger E. (1977) Subcommittee on geochronology: convention on the use of decay constants in geo- and cosmochronology. *Earth Planet. Sci. Lett.* **36**, 359–362.
- Stone J. O. (2000) Air pressure and cosmogenic isotope production. *J. Geophys. Res. Solid Earth* **105**, 23753–23759.
- Thorpe R. S., Potts P. J. and Francis P. W. (1976) Rare Earth data and petrogenesis of andesite from the North Chilean Andes. *Contrib. Mineral. Petrol.* **54**, 65–78.
- Uppala S. M., Källberg P., Simmons A., Andrae U., Bechtold V., Fiorino M., Gibson J., Haseler J., Hernandez A. and Kelly G. (2005) The ERA-40 re-analysis. *Q. J. R. Meteorol. Soc.* **131**, 2961–3012.
- Valet J.-P., Meynadier L. and Guyodo Y. (2005) Geomagnetic dipole strength and reversal rate over the past two million years. *Nature* **435**, 802–805.
- Valkiers S., Vendelbo D., Berglund M. and De Podesta M. (2010) Preparation of argon primary measurement standards for the calibration of ion current ratios measured in argon. *Int. J. Mass Spectrom.* **291**, 41–47.
- von Blanckenburg F. and Willenbring J. K. (2014) Cosmogenic nuclides: dates and rates of Earth-surface change. *Elements* **10**, 341–346.
- Williams A. J., Stuart F. M., Day S. J. and Phillips W. M. (2005) Using pyroxene microphenocrysts to determine cosmogenic ^3He concentrations in old volcanic rocks: an example of landscape development in central Gran Canaria. *Quatern. Sci. Rev.* **24**, 211–222.
- Wörner G., Hammerschmidt K., Henjes-Kunst F., Lezaun J. and Wilke H. (2000) Geochronology ($^{40}\text{Ar}/^{39}\text{Ar}$, K–Ar and He-exposure ages) of Cenozoic magmatic rocks from Northern Chile (18–22°S): implications for magmatism and tectonic evolution of the central Andes. *Rev. Geol. Chile* **27**, 205–240.
- Zimmermann L., Blard P. H., Burnard P., Medynski S., Pik R. and Puchol N. (2012) A new single vacuum furnace design for cosmogenic ^3He dating. *Geostand. Geoanal. Res.* **36**, 121–129.

Associate editor: David L. Shuster

9.3.4 Développement d'un outil ArcGis de calcul pour les taux d'érosion

Au cours de cette thèse, j'ai contribué au développement d'un outil ArcGis - nommé Basinga - destiné au calcul du taux de production moyen attaché à un bassin versant. Cette valeur est nécessaire aux calculs de taux de dénudations se basant sur les concentrations des sédiments en isotopes cosmogéniques (un autre pouvoir incroyable des isotopes cosmogénique que cette thèse ne traite pas). Basinga propose donc de calculer rapidement et facilement ce taux de production moyen en tenant compte de l'hypsométrie du bassin mais également des variations de l'activité du champ magnétique terrestre.

J'ai contribué à cette étude en aidant Jena, qui a développé le programme, à intégrer les corrections paléomagnétiques aux calculs du taux de production.

Cette étude a fait l'objet d'un article soumis auprès de la revue Quaternary Geochronology où il est actuellement en révision.

*Manuscript

[Click here to view linked References](#)

BASINGA: a cell-by-cell arcGIS® toolbox to compute BASIN average scaling factors, ^{10}Be cosmogenic production and denudation rates

Jena Zumaque^{1*}, Julien Charreau^{1**}, Pierre-Henri Blard¹, Léo Martin¹ and Pauline Collon²

¹ CRPG, UMR 7358, CNRS, Université de Lorraine, 54501 Vandoeuvre-lès-Nancy, France

² GeoRessources, UMR 7359, Université de Lorraine – CNRS -CREGU, ENSG, 2 rue du Doyen Marcel Roubault, TSA 70605, 54518 Vandoeuvre-lès-Nancy, France

**corresponding author: Julien Charreau (charreau@crpg.cnrs-nancy.fr)

key words: scaling factors, ^{10}Be cosmogenic production rates, denudation rates, ArcGIS

Highlights

- Basinga is a new, freely available and easy handle ArcGIS® toolbox
- Basinga includes two python script tools named *Production rates* and *Denudation*
- The *Production rates* tool may compute in few minutes the average scaling factor and ^{10}Be production rates on several tens of drainage basins
- The *Production rates* tool provides several options to correct for topographic shielding, ice cover, lithology and paleomagnetic changes
- The *Denudation rates* tool computes the ^{10}Be basin average denudation rates and their uncertainties and includes both the spallogenic and the muonic productions

Abstract

Denudation is a critical parameter controlling the evolution of landscape, mountain building and climate. The analysis of terrestrial cosmogenic nuclides (TCN) in river sediment is a powerful tool to quantify basin scale average denudation rates. However, it requires a rigorous calculation of the basin average cosmogenic production rates which should account for the whole altitudinal distribution of the watershed. This paper describes a new and easy handle ArcGIS® toolbox- Basinga- freely available from the online supplementary information or upon request to the authors. It includes two tools named *Production rates* and *Denudation rates* which are both Python-based geoprocessing scripts. The former computes the average scaling factors and ^{10}Be

cosmogenic production rates. It averages the cell-by-cell local scaling factor and ^{10}Be production rates calculated following the scheme of *Lal/Stone* (*Lal*, 1991; *Stone*, 2000) using the local altitude and latitude derived from a Digital Elevation Model (DEM) of the studied basin. It may calculate automatically and in few minutes these average parameters on several tens of drainage basins together. It also provides several optional tools to correct for topographic shielding, ice cover and lithology. We also developed an original approach to correct the ^{10}Be cosmogenic rates for past variations in the Earth magnetic field. We tested this algorithm calculating the ^{10}Be cosmogenic production rates on several watersheds from regions of high reliefs where the rates have been previously estimated from several self-built calculators and scripts. We found an average difference of about 5% between our estimates and production rates calculated by the previous authors. Our results also suggest that the correction for paleomagnetic variations is relatively high (10-30%) when included in the calculation while it is almost always overlooked in the denudation rate estimates from cosmogenic analyses. At last the *Denudation rates* tool computes the ^{10}Be basin average denudation rates based on the ^{10}Be cosmogenic production rates and includes both the spallogenic and the muonic productions. Using a simple text editor, both Python scripts can be easily changed and the cosmogenic parametrization updated for homogenization and standardization if needed. *Basinga* is therefore a robust tool to accurately, quickly and automatically estimate basin average scaling factors, ^{10}Be production and denudation rates. It may enable the homogenous treatment of large dataset but also the compilation and normalization of previous published cosmogenic data.

1. Introduction

Landscape evolution is mainly controlled by the complex interactions between tectonic uplift, climate changes and surface processes which include denudation and sedimentation (e.g. *Raymo and Ruddiman*, 1992; *Whipple*, 2009; *Willett*, 2010). Understanding such a dynamic requires an accurate quantification of the numerous processes involved. Among others, denudation rates can be derived from various techniques including for example thermochronology (e.g. *Safran*, 1998; *Reiners and Brandon*, 2006; *Herman et al.*, 2010) or sediment gauging (e.g. *Kirchner et al.*, 2001;

Lupker et al., 2011, 2012). However, although they respectively provide reliable estimates for both long and short timescales, the former remains spatially limited and restricted to the source area while the latter is sensitive to human impact and/or catastrophic events. The analysis of terrestrial cosmogenic nuclides (TCN) in river sediment (Figure 1), such as ^{10}Be , is a powerful tool to infer basin scale denudation rates at intermediate time scale (10^2 to 10^5 , depending on the erosion rate) (e.g. *Brown et al.*, 1995; *Bierman and Steig*, 1996; *Granger et al.*, 1996; *von Blanckenburg*, 2005). Hence, this method is now widely used in the Earth science community in a broad variety of geological setting (*Portenga et al.*, 2011).

However, a rigorous calculation of the denudation rates at the basin scale requires an accurate estimate of the cosmogenic production rate over the entire surface of the exposed watershed (Figure 1) and thus a complete consideration of the basin topography (*Balco et al.*, 2008). The CRONUS-Earth online calculators (*Balco et al.*, 2008; *Marrero et al.*, 2015) and other open-source routines (*Zreda et al.*, 2008; *Vermeesch et al.*, 2007) may compute local erosion rates, but they were not designed to calculate basin scale denudations. Due to the non-linear dependence between production rates and elevation, calculating the cosmogenic production rate using only the mean altitude and latitude of the drainage basin may induce important biases. Such inaccuracies are larger in high-elevated large basins with important differences in elevation. Several authors (i.e. *Delunel et al.*, 2010; *Godard et al.*, 2012; *Lupker et al.*, 2012; *Scherler et al.*, 2014), studying various basins of the Himalayas and French Alps, have therefore developed their own self-built calculator. They derive basin scale denudation rates from a cell-by-cell approach where the elevation is extracted from each cell of a Digital Elevation Model and the production rates calculated accordingly. Figure 2 compares the production rates of *Delunel et al.* (2010) and *Scherler et al.* (2014) calculated using a cell by cell approach to the ^{10}Be production rates inferred using the mean altitude and latitude of the watershed. The calculated deviations between those two approaches range from ~50% to ~70%. Therefore, in high elevated regions it is critical to estimate denudation rates based on a cell-by-cell calculation. Nonetheless, this approach is not straightforward and the cosmogenic parametrization is also relatively complex. Hence, throughout the last 20 years this latter has never really been standardized nor homogenized which yielded to

large artificial discrepancies between the studies (*Portenga et al.*, 2011). For example, many studies calculated the denudation rates based on the spallogenic production only while it is critical to account for the muonic production as well, especially for high denudation rates (Fig. 2b). Nonetheless, to our knowledge, there is no available code in the literature to easily perform such homogenous and standardized calculation accounting for the muons production and the whole hypsometry of the drainage basin.

The aim of this study is therefore to provide an easy handle tool, freely available to the Earth Science community that automatically derives the scaling factors, ^{10}Be nuclide production rates and denudation rates at the scale of an entire catchment. Since these calculations strongly rely on geographical and geomorphological parameters, it shall use a widespread and frequently used geographic information system (GIS). It also demands complex calculations and iterative processes which require a numerical computing environment and a programming language that can be associated to the GIS. Python is an open-source language that can be directly integrated into ArcGIS for geoprocessing tool development in order to build user-friendly interfaces.

To this end, we created a new ArcGIS® toolbox named **Basinga (BASIN** *averaGe* scaling factors, cosmogenic production and denudation *rAtes*) which includes two Python-script-based geoprocessing tools: *Production rates* and *Denudation rates*. The basin-scale production rate is calculated by averaging the cell-by-cell local values calculated following the scheme of *Lal/Stone* (*Lal*, 1991; *Stone*, 2000) using the local altitude and latitude of the Digital Elevation Models (DEM) of the studied basin. Following several previous studies (i.e. *Delunel et al.*, 2010; *Godard et al.*, 2012; *Lupker et al.*, 2012; *Scherler et al.*, 2014), we also included in our tool the possibility to correct for topographic shielding, ice cover and lithology. Furthermore, we developed a new paleomagnetic correction tool to correct for the past variations in the Earth magnetic field (*Nishiizumi et al.*, 1989; *Muscheler et al.*, 2005). All these potential corrections remain optional and can be applied independently from each other. The denudation rates are then derived from the resultant production rates via the *Denudation rates* tool.

At last, we tested this algorithm calculating the cosmogenic production rates on several watersheds from the Himalayas (*Godard et al.* (2012), *Lupker et al.* (2012) and *Scherler et al.* (2014)) and the French Alps (*Delunel et al.* (2010)). We compared our

results to the previous rates calculated by these authors and found an average difference of ~5% with these previous studies. This observation suggests that our approach provides accurate estimates of the cosmogenic production rates.

2. Theory and basis

2.1 Basin scale denudation rates

Terrestrial cosmogenic nuclides (TCNs) such as ^{10}Be are continually produced in the uppermost meters of the Earth's surface as a result of secondary cosmic flux bombardment (*Lal and Peters, 1967; Lal, 1988, 1991*). The local concentration N (atoms.g $^{-1}$) of any TCN at surface undergoing denudation can be expressed as follows (*Lal, 1991*):

$$N = \frac{1}{\varepsilon} \cdot \left(\frac{P_{spall}}{Z_{spall} + \lambda} + \frac{P_{sm}}{Z_{sm} + \lambda} + \frac{P_{fm}}{Z_{fm} + \lambda} \right) \quad (1)$$

Where ε (cm.yr $^{-1}$) is the local erosion rate, λ (yr $^{-1}$) the decay constant of the cosmogenic nuclide, P is the *in situ* production rate at the surface (atoms.g $^{-1}$.yr $^{-1}$) and $Z = A/\rho$ (cm) where ρ is the density of the target rock (g.cm $^{-3}$) and A the attenuation length of the particles in the rock (g.cm $^{-2}$). The three subscripts for both P and Z indicate the three production pathways they are associated with (i.e. *spall* for production by spallation; *sm* and *fm* for production by slow and fast muon captures respectively). However, this equation remains valid only if erosion is constant, and if exposure time is long enough (i.e. $t \gg 1/(\lambda + \varepsilon\rho/A)$) to ensure that the nuclide concentration reaches a steady state.

River sediment collected at one given outlet averages the concentrations of all the eroded sub-catchments in the drainage basin (*Brown et al., 1995; Bierman and Steig, 1996; Granger et al., 1996; von Blanckenburg, 2005*) (Fig. 1). It is therefore possible to extrapolate the denudation rate to an entire watershed from the single analysis of one stream river sediment sample (*Brown et al., 1995*). Nevertheless, this requires several assumptions: (1) erosion rate of each sub-basin must be constant over time (even if not uniform from one to another); (2) river sediment must be well-mixed; (3) the target mineral (i.e. quartz) is assumed to be uniformly distributed through the entire basin; (4) the time scale of sediment transfer is negligible compared to denudation rate's integration

time; (5) the erosion rates must be low enough to ensure that the measured denudation rates are smaller than the ^{10}Be decay constant ($\epsilon\rho/\Lambda \gg \lambda$ where $\lambda = \log(2)/t_{1/2}$). This last condition is requested to prevent the loss of cosmogenic nuclides through radioactive decay so that λ in equation (2) becomes negligible (*Brown et al.*, 1995). The watersheds also need to be large enough so that stochastic events as landslides are adequately averaged and do not bias the ^{10}Be -derived denudation rate (cf. *Niemi et al.*, 2005; *Yanites et al.*, 2009).

If these conditions are encountered, the average ^{10}Be concentration \bar{N} (atoms.g $^{-1}$) of sediment collected at the outlet of a basin can be expressed by:

$$\begin{aligned}\bar{N} &= \frac{\sum N_i \epsilon_i A_i}{\sum \epsilon_i A_i} \\ \bar{N} &= \frac{\sum \left(\frac{P_{i\text{spall}}}{Z_{\text{spall}}} + \frac{P_{i\text{sm}}}{Z_{\text{sm}}} + \frac{P_{i\text{fm}}}{Z_{\text{fm}}} \right) A_i}{\sum \epsilon_i A_i} \\ \bar{N} &= \frac{1}{\bar{\epsilon}} \left(\frac{\overline{P_{\text{spal}}}}{\overline{Z_{\text{spall}}}} + \frac{\overline{P_{\text{sm}}}}{\overline{Z_{\text{sm}}}} + \frac{\overline{P_{\text{fm}}}}{\overline{Z_{\text{fm}}}} \right)\end{aligned}\quad (2)$$

where i represents every sub-catchments, A their corresponding area, $\bar{\epsilon}$ (cm.yr $^{-1}$) is the average erosion rate over the entire watershed and $\overline{P_{\text{spal}}}$, $\overline{P_{\text{sm}}}$, $\overline{P_{\text{fm}}}$ are the associated average ^{10}Be production rates for spallation, slow muons and fast muons (atoms.g $^{-1}$.yr $^{-1}$), respectively.

Therefore, to derive the basin scale denudation rate from equation (2) it is critical to accurately estimate the average cosmogenic production rate \bar{P}_i of the watershed.

2.2 The scaling factor and the cosmogenic production rates

As it goes through interaction with matter, *in situ* production of cosmogenic nuclide ^{10}Be appears to be decreasing exponentially with depth so that the nuclide production rate P (atoms.g $^{-1}$.yr $^{-1}$) at any depth x (cm) can be written as follows (*Lal*, 1991):

$$P(x) = P_{0\text{spallation}} \cdot e^{-\left(\frac{x\rho}{\Lambda_{\text{spallation}}}\right)} + P_{0\text{slow muon}} \cdot e^{-\left(\frac{x\rho}{\Lambda_{\text{slow muon}}}\right)} + P_{0\text{fast muon}} \cdot e^{-\left(\frac{x\rho}{\Lambda_{\text{fast muon}}}\right)} \quad (3)$$

where P_0 is the nuclide production rate at the surface (atoms.g^{-1}).

The *in situ* cosmogenic production rates are dependent on latitude as the incoming quantity of cosmic flux is controlled by the strength of the geomagnetic field (Fig. 1) (Lal, 1991). However, elevation remains the main parameter as the cosmic neutrons are attenuated both in flux and energy in the atmosphere (Lal, 1991). Several scaling schemes have been created to correct for these variations in spallogenic production rates with altitude and latitude (e.g. Lal, 1991; Stone, 2000). The most commonly used scheme was defined by (Stone, 2000) and corrects the spallogenic scaling factor for latitude and atmospheric pressure effects as follow:

$$S_p = \left(a + b \cdot e^{\frac{-P^o}{150}} + c \cdot P^o + d \cdot P^{o2} + e \cdot P^{o3} \right) \quad (4)$$

where S_p is the ^{10}Be production by spallation ($\text{atoms.g}^{-1}.\text{yr}^{-1}$) and P is the atmospheric pressure (hPa). This pressure can be directly linked to the elevation, using the standard atmosphere model (see Equation (1) in Stone (2000)). a, b, c, d, e are the scaling equation coefficients for the latitudes (see Table 1 of Stone (2000)). The cosmogenic spallogenic production rate can be calculated by multiplying this scaling factor by the normalized surface production rate at Sea Level and High Latitude (SLHL). Since the dependence between the production rates and the spatial parameters is not linear, an accurate estimate of the basin-scale denudation rate requires considering the whole distribution of elevation and latitude of the studied watershed, using a cell-by-cell distributed computation.

2.3 Limitation and additional corrections

Several limitations must be considered when using this approach. First, it assumes uniform concentration of quartz throughout the catchment area. Otherwise, if the quartz content of eroded lithologies varies across the studied basin, equation (2) is no longer valid. However, if it remains relatively difficult to quantify the concentration of quartz from every eroded lithology, one may at least exclude the lithology without quartz from the calculation (e.g. Delunel *et al.*, 2010).

Additionally, some authors (e.g. *Lal*, 1991; *Dunne et al.*, 1999; *Gosse and Phillips*, 2001) have highlighted the importance of the geometry of the exposed surface. Indeed, the quantity of the incoming cosmic ray flux received at a geographic point strongly depends on the topographic shielding that involves both surrounding reliefs and local slope.

Moreover, ice and snow cover might reduce, or, in case of the presence of an ice cap, totally shield the cosmic ray delivered to the ground surface preventing or annealing the ^{10}Be *in situ* production. The potential impact of both topographic and snow/ice cover is particularly significant in high elevated mountain ranges, and may induce a reduction of the overall production rate of 5 to 10% (e.g. *Schildgen et al.*, 2005; *Scherler et al.*, 2014). It requests complex physical model (e.g. *Schildgen et al.*, 2005) coupled to years remote sensing monitoring of snow cover that need to be calibrated using ground based records and measurements. The snow thickness may also be estimated from Precipitation Daily Data (PDD) derived from Global Climate Models (GCM).

At last, the Earth magnetic field has strongly varied over time (*Dunai*, 2001; *Pigati and Lifton*, 2004). These variations have impacted the cosmogenic production itself. For typical equivalent exposure of several ka they may induce bias of up to 20% in the integrated cosmogenic production rates (e.g. *Lifton*, 2016; *Martin et al.*, *submitted*). If overlooked, this effect may yield significant inaccuracies in the derived denudation rates.

3. Implementation in Basinga

3.1 Calculation of the scaling factor and cosmogenic production rates

3.1.1 General workflow and required input data

The **Basinga** toolbox comprises a tool named *Production rates* created through an independent Python script. This tool calculates the average basin-wide scaling factors and the ^{10}Be *in situ* production rates from a cell-by-cell approach using a DEM. To execute the main core of the program, users need at least a DEM (Figure 3 and 4) and a polygon shape file of the studied watersheds. Among the data retrieved, latitude and altitude of each cell are used to calculate the cosmogenic production rate at each point of the basin according to the scaling scheme.

The cosmogenic nuclide production rates can be corrected for several factors including topographic shielding, lithology, ice covering and paleomagnetic variations. Each correction can be applied independently from each other. The parameters obtained for each cell (i.e., latitude, altitude, atmospheric pressure, scaling factors, ^{10}Be production rates by spallation and fast and slow muon capture, and the associated sum) are then averaged over the catchment and stored in the attribute table of the edited input shape file (Figure 3 and 5), following the nomenclature described in Table 1. The raw data required by each corrective option are described below.

3.1.2 Scaling scheme and associated parametrization

In **Basinga**, to calculate the cosmogenic production rates we use the scaling scheme developed by *Stone* (2000) (following *Lal* (1991) equation 4). We however modified the parameters describing the slow and fast muon scaling factors following *Braucher et al.* (2011):

$$M_{slow\ muon} = e^{\left[\frac{(1013.25 - P^\circ)}{\Lambda_{slow\ muon}}\right]} \quad (5)$$

$$M_{fast\ muon} = e^{\left[\frac{(1013.25 - P^\circ)}{\Lambda_{fast\ muon}}\right]} \quad (6)$$

where M is the ^{10}Be production by muon capture ($\text{atoms.g}^{-1}.\text{yr}^{-1}$) and Λ the atmospheric attenuation length. P° remains the atmospheric pressure as in equation (4) and is also calculated following equation (1) of *Stone* (2000). The subscripts *fast* and *slow* indicate the nature of the muon.

Then, the local scaling factor is calculated as follow:

$$S_i(x, y) = S_p(x, y) + M_{slow\ muon}(x, y) + M_{fast\ muon}(x, y) \quad (7)$$

and the basin average scaling factor derived accordingly:

$$\bar{S} = \frac{1}{A} \iint_A S_i(x, y). F(x, y). dx dy \quad (8a)$$

where A is the area of the drainage basin which may exclude the lithology without quartz. F refers to any correcting factor to account for ice and snow cover or topographic shielding. As the production rates are computed for each individual cells of the extracted basin DEM this equation is similar to:

$$\bar{S} = \frac{\sum S_i}{n_{cells}} \quad (8b)$$

where n_{cells} represents the number of cells of the DEM corresponding to the studied watershed.

Again, as for the spallogenic production rates, the muons production rates can be calculated by multiplying both scaling factors by their corresponding associated surface production at SLHL (atoms.g⁻¹.yr⁻¹). The local cosmogenic production rate is then calculated as follow:

$$P_i(x, y) = S_{SLHL} \cdot S_p(x, y) + M_{SLHL_{slow\ muon}} \cdot M_{slow\ muon}(x, y) + M_{SLHL_{fast\ muon}} \cdot M_{fast\ muon}(x, y) \quad (9)$$

where S_{SLHL} and M_{SLHL} are the surface production at SLHL (atoms.g⁻¹.yr⁻¹) for spallogenic and muons production, respectively. The basin average production rates can be easily calculated similarly to equations (8).

For ¹⁰Be we used a SLHL surface production rate of 3.9 at.g⁻¹.y⁻¹ for spallation, which is the average value of the most recent calibration studies (e.g. *Balco et al.*, 2009; *Stroeven et al.*, 2015; *Putnam et al.*, 2010; *Martin et al.*, submitted; *Kelly et al.*, 2015; *Kaplan et al.*, 2011 ; *Lifton et al.*, 2014), and 0.034 at.g⁻¹.y⁻¹ for fast muon induced production and 0.010 at.g⁻¹.y⁻¹ for production by slow muon capture, respectively (*Braucher et al.*, 2011). Atmospheric attenuation length values of 260 and 510 (g.cm⁻²) were attributed for slow and fast muons respectively (*Braucher et al.*, 2011). However,

these parameters can be easily modified or updated if needed (see the "Getting started" in the online Supplementary Informations).

The catchment-averaged scaling factor and production rate without any additional correction are calculated with $F=1$ and A corresponding to the whole surface of the drainage basin. Thus they only represent first order estimates of the true values, which should account for the multiple effects described above and treated below.

3.1.3 Lithology

In order to exclude the regions where the eroded lithology does not bear quartz, we built an additional option to remove the corresponding area from the studied watershed (Figure 3). Using an independent polygon shape file of the geology which includes, in the attribute table, lithological information and more specifically whether quartz is present or not, one may exclude the region without this mineral using a SQL interface and expression (Figure 6). Once selected, the corresponding quartz free regions are cut from the original polygon and the tool creates a new polygon shape file of the studied watershed to correct the cosmogenic production rate. The surface A in equation 8a is therefore restricted to the region including quartz only. The calculated parameters are stored in the attribute table of this new created shape file (Table 1, Figures 3 and 5b).

3.1.4 Ice cover

Basinga also enables correcting for ice covering when computing the scaling factor and cosmogenic production rate. We assume the ice cover being sufficiently thick to fully shield the cosmic ray and hence that no cosmogenic isotope are produced below. However, ice erosion may be relatively efficient. Therefore, the area covered by ice may deliver sediment to the main stream as well. However, as previously shielded by ice those sediments are supposed to be free from cosmogenic isotope. Therefore, the corresponding factor F in equation 8a can either be equal to 1 or 0 only and equation (8a) rewritten as follow:

$$\overline{S}_{ice} = \frac{1}{A} \iint_{A_{ice\ free}} P_i(x, y) . dx dy \quad (10)$$

where $A_{\text{ice free}}$ is the basin area not covered by ice. The surface A may include or not the lithology without quartz. To run this optional tool, the ice cover must be inputted as a polygon shape file (Figure 3). The modern ice cover can be downloaded as a shape file free of charge from the Global Land Ice Measurements from Space (GLIMS) website (<http://www.glims.org>) which provides a thorough frequently updated glacier database (Armstrong *et al.*, 2005; Raup *et al.*, 2007). Moreover, cosmogenic nuclides may average denudation rates over long time scales (10^2 - 10^5) especially in slow eroding areas. Yet, the glacial coverage has changed over time which may induce a significant bias in the calculated production rate. Therefore, Delunel *et al.* (2010) have found more relevant to consider ancient glacial extent reconstruction rather than modern glacial coverage and built a polygon shape file accordingly.

Once the glacial cover shape file is selected, the tool will first execute the main process to provide the total number of cells of the whole drainage basin, and then recalculate the mean production rate excluding the glacial zones. A new shape file of the drainage basin is created including an attribute table which provides the results of the calculation (Figure 3 and 5c). Even if the ice cover correction has been checked, the uncorrected raw ^{10}Be production rate and scaling factors remain stored in the attribute table as before along with the corrected values for ice cover (Figure 5c). Note that, again, this correction for ice can be applied independently from the other options no matter if the correction for topographic shielding and/or lithology has been carried out. If the areas free of quartz were excluded, the correction for ice is applied to this restricted area only.

3.1.5 Topographic correction

A third option was built to correct for the topographic shielding. It requires an additional raster providing the shielding factor (from 0 to 1) for each cell of the studied region (Figure 3) which represents the correcting factor F in equations (8). This correction can be applied either to the whole watershed or only to the restricted regions excluding quartz-free lithologies and areas covered by ice. If this optional tool has been checked and used, the basin average topographic factor is then stored in the attribute table as “Topo_fc” (see Table 1) either in the original shape file of the watershed (Figure 5a) or

in the new created shape file which excludes the quartz free areas and areas covered by ice (Figure 5b).

The shielding factor raster can be independently computed in ArcGIS® using the approach developed by *Codilean (2006)*, which is available upon request to this author and can thus be easily integrated in **Basinga** without any further work. This tool is based on the Relief Shadow Modelling method accounting for both Self-shadows and Cast-shadows (*Codilean, 2006*). The user is however free to choose any other topographic shielding computation as long as it can be converted into a raster file of ArcGIS format. It must share the same resolution and shape of the original DEM.

3.1.6 Paleomagnetic correction

As foresaid, time variations in the Earth magnetic are responsible for changes in the cosmic flux (e.g. *Nishiizumi et al., 1989; Dunai, 2001; Pigati and Lifton, 2004*) and eventually in the cosmogenic nuclide production rates. To correct for these effects the *Production rates* tool proposes to account for the geomagnetic field variations thanks to the formula of *Nishiizumi (1989)* as proposed in *Balco et al. (2008)*.

First, one must estimate the effective time during which the analyzed sample has been exposed to cosmic flux. According to *Lal (1991)* the average time scale T_{average} is equal to z^* / ε ($T_{\text{average}} = z^* / \varepsilon = N(0)/P(0)$), where z^* is the mean attenuation length. Therefore, the production rate must be a priori known to estimate the denudation rates accordingly and hence T_{average} . Thus, this corrective option will only work if the main process that encompasses all the other possible corrections has been run first in order to estimate an a priori production rate (Figure 7). The ^{10}Be concentration must also be provided as an individual field of the attribute table of the input shape file. As one unique concentration is provided for a given drainage basin, the program assumes there is only one effective time for a given river bed sample.

Then, knowing the time variations of the earth magnetic field intensity (*Guyodo and Valet, 1996, 1999*) and assuming a dipole magnetic field (*McElhinny and McFadden, 1997*), the successive paleo-geomagnetic latitudes of the present sample location are estimated following *Nishiizumi et al. (1989)*:

$$\cos \overline{\lambda_M(t)} = \left[\frac{M_0}{M(t)} \right]^{1/4} \cdot \cos \overline{\lambda_s} \quad (10)$$

where, $\overline{\lambda_M(t)}$ is the basin average paleo-geomagnetic latitude at time t and $M(t)$ is the dipole field intensity at time t at this location. $\overline{\lambda_s}$ is the basin average present latitude, M_0 the present dipole intensity at this location and t varies from 0 to T_{average} . Three different Virtual Dipole Moment (VDM) databases may be selected to compute this paleomagnetic correction: *Muscheler et al.* (2005), *Laj et al.* (2004) (i.e. GLOPIS-75) and *Valet et al.* (2005). Then, using the same scheme of *Stone* (2000), the calculated paleo-geomagnetic latitudes and the basin mean atmospheric pressure values previously calculated, one may integrate the mean cosmogenic production rate time-scale since T_{average} (*Nishiizumi et al.*, 1989):

$$P_{\text{mag}} = \frac{1}{T_{\text{average}}} \int_0^{T_{\text{average}}} P(t) dt \quad (11a)$$

This production rate will be corrected by the averaged topographic shielding factor if the option has been activated:

$$P_{\text{mag}} = \overline{F_{\text{topo}}} \cdot \frac{1}{T_{\text{average}}} \int_0^{T_{\text{average}}} P(t) dt \quad (11b)$$

Note that if the correction for ice or lithology has been checked it has been included ahead when calculating the basin average time scale and is hence considered when averaging the latitude and atmospheric pressure.

3.2 Calculation of the ^{10}Be denudation rates

The *Denudation rates* tool computes the mean basin-wide denudation rates based on equation (2) given above (*Brown et al.*, 2005). It uses the results and calculations of the *Production rates* tool which needs to be run before. The user must also provide the ^{10}Be concentration measurements and their uncertainties to run this program. To compute the denudation rates, values of 160, 4320 and 1500 $\text{g}\cdot\text{cm}^{-2}$ were attributed to the A

absorption mean free path for neutrons, fast and slow muons, respectively (*Braucher et al.*, 2011). At last, a default value (2.7 g.cm^{-3}) of the density is also proposed but can be easily modified in the user's interface (Fig. 8).

This tool also provides an estimation of the uncertainties. It however only propagates the error on the cosmogenic production rates and the measured concentration as follow:

$$\delta\bar{\epsilon} = \sqrt{\left[\frac{\delta C}{C^2} \left(\frac{P_{spal}}{Z_{spal}} + \frac{P_{sm}}{Z_{sm}} + \frac{P_{fm}}{Z_{fm}}\right)\right]^2 + \left(\frac{P_{spal} \cdot \delta P_{spal}}{C Z_{spal}}\right)^2 + \left(\frac{P_{sm} \cdot \delta P_{sm}}{C Z_{sm}}\right)^2 + \left(\frac{P_{fm} \cdot \delta P_{fm}}{C Z_{fm}}\right)^2}$$

(13)

where C , δC and $\delta\bar{\epsilon}$ are the measured concentration of ^{10}Be , its 1σ uncertainty and the error on denudation rates, respectively. δP_i represent the uncertainties on the ^{10}Be cosmogenic production rates for spallation and muons. **Basinga** attaches an uncertainty of 9% to the spallogenic production parameters (*Balco et al.*, 2008). This accounts for the variability both resulting from these production rate calibrations and from the spatial scaling (*Balco et al.*, 2008). Since the uncertainties related to the muonic production remain highly variable in the literature (e.g. Heisinger et al., 2002a, Heisinger et al., 2002b, Braucher et al., 2003, Braucher et al., 2011, Braucher et al. 2013), we attached a conservative value of 50% for both muons. This latter can be easily changed and updated if needed (see online supplementary information).

A more rigorous approach would consider all parameters included in equation (2) and their related uncertainties but would require a laborious partial derivation. This could also be done using a numerical approach based on a Monte Carlo simulation that explores the range of all the input parameters. Such approach would involve further developments that are beyond the scope of the present tool.

4. Application to high elevated and high relief watersheds

4.1 General setting

In order to test the reliability of **Basinga**, we computed the production rates of four catchments analyzed in previous studies located in high elevated and high relief regions (*Delunel et al.*, 2010; *Godard et al.*, 2012; *Lupker et al.*, 2012; *Scherler et al.*, 2014). Three of the four sets of catchments are located in the Himalaya (*Godard et al.*, 2012; *Lupker et al.*, 2012; *Scherler et al.*, 2014) whereas the watersheds analysed by *Delunel et al.* (2010) are located in the French Western Alps. We selected studies that used the same scaling scheme (i.e. Lal/Stone, *Stone* (2000)) and employed a cell-by-cell approach. The studies carried out in Himalaya have corrected the basin scale average cosmogenic production rate for topographic shielding (*Godard et al.*, 2012; *Lupker et al.*, 2012; *Scherler et al.*, 2014) and ice cover (*Godard et al.*, 2012). Only *Delunel et al.* (2010) also provides a correction for lithology and represents therefore the most complete analysis to test our tools. Moreover *Delunel et al.* (2010) also exclude in their calculations the low slope areas ($<3^\circ$) which were considered as depositional areas not delivering sediment to the main river stream. Additional information and more details of the studied watersheds can be found in the original paper. Whenever possible, we applied the same corrections as the original study and used the same input DEM. In our study watershed polygons were computed by us using ArcGIS® and the sampling coordinates provided in the original papers. However, the software and procedure used to extract the watershed in the original papers was not specified and if different may yield to some discrepancies. To ensure homogeneity, the neutronic SLHL production rate of $3.9 \text{ at.g}^{-1}.\text{y}^{-1}$ was used for the four tested watersheds.

4.2 Production rates results

All cosmogenic production rates calculated using **Basinga** are compared to the rates calculated in the original studies in Table 2 and Figure 9.

The **Basinga**-derived ^{10}Be production rate values are a little bit higher for two sets of catchments. In the French Alps, deviation values from the initial study ranges from -3.9% to -7.2% whereas in the Himalayas, the deviation percentages between both cases are smaller and more constant with values around -2% for most watersheds. Only three basins with mean elevation above 2000m show strong differences in production rates with deviation values up to -29%.

By contrast, the large Yamuna basin analysed by Lupker et al. (2012) which encompasses all the catchments treated in the above paragraph presents a ~5% higher ^{10}Be production rate than the one inferred with **Basinga**. Interestingly, its mean production rate of about $20 \text{ atoms.g}^{-1}.\text{yr}^{-1}$ is really close to the ^{10}Be production rate of the catchment associated with sample DS7-044 (Scherler et al., 2014), both basins sharing approximatively the same mean elevation (i.e. ~2500 m). Likewise, the ^{10}Be production rate values inferred with **Basinga** are lower than the originals for all but one catchment analysed by Godard et al. (2012). The deviation percentages range from -6% to 6% with a mean deviation of about 4%.

4.5 Results of the paleomagnetic correction

We also corrected the production rates of each studied basin for paleomagnetism based on the measured concentration reported in the original papers. For homogeneity all calculations were done using the same VDM (i.e. GLOPIS-75, Laj et al. (2004)). Table 3 and figure 9 present the average time and compare those derived corrected production rates to the previous results. The times over which the ^{10}Be production rates have been integrated show a high variability from one basin to another which is related to the variable measured concentrations. Accordingly, the deviations from the previous rates remain variable but is almost always relatively high with production rates corrected for paleomagnetism lower by ~0.8% to ~39% with a mean deviation of 15%. Only one catchment shows higher production rate values after paleomagnetic corrections (i.e. DS6-008 from Scherler et al. (2014)).

5. Discussion

5.1 Origins of the discrepancies

The differences between our calculated production rates and the rates previously calculated in the original papers are relatively low and in average below 5%. This is reassuring and shows that our approach and tool provide accurate estimations of the cosmogenic production rate especially in regions of high reliefs where it is critical to account for the basin hypsometry. Our tools can therefore be applied in many different settings. Besides, as it was relatively difficult to compute the production rates in the

same exact conditions, those observed discrepancies may have several external origins not related to the calculation methods.

First, the authors probably used multiple different GIS treatments which are not specified in the corresponding papers. To extract the drainage basin from the DEM and then to extract the elevation of each basin accordingly, several different softwares (ArcGIS, MapInfo, GrassGIS, QGIS, Matlab...) can be used. This may yield to discrepancies in the geometry of the studied watershed or alteration of the elevation data due to a resampling of the original DEM. Indeed, in several basins we have found relatively different mean elevations (Table 2) from the literature which indicates that the geometry of the drainage basins and the extracted elevations remained different.

Besides, a strong source of uncertainty may be related to the calculation of the topographic factor. A striking feature observable in all cases is that our topographic factors are higher than the previous findings (Table 2). Interestingly, to compute topographic factor values all follow the shielding by obstruction method developed by *Dunne et al.* (1999). In contrast, we used the approach of *Codilean*, (2006) that follows the relief shadow modelling method initiated by *Burrough and McDonell* (1998). *Codilean* (2006) compared both method (see *Codilean* (2006) for detailed discussion) and highlighted a difference of about 0.1 between the generated factors. The deviation between our results and the previous factor are in average lower (0.02-0.1).

In **Basinga**, as the production rates rely on altitude but more importantly on latitude, all production rates calculations are done using raster projected in a Geographical system (i.e. X,Y coordinates in degrees while Z is in meter). Therefore, to compute the topographic factor, which requires the same X,Y and Z units in meter (*Codilean*, 2006), we apply a Z-factor to change the X,Y coordinates. Such correction probably yields to an additional discrepancy between the calculated topographic factors.

Moreover, *Lupker et al.*, (2012) also correct for topographic bias induced by the approximate representation of the terrain topography within each DEM cell (*Norton and Vanacker*, 2009). This might also contribute to the observed discrepancies between the factors. However, this correction is not yet implemented in **Basinga**.

At last both *Godard et al.* (2012) and Scherler et al., (2014) also corrected their ^{10}Be production rate values for snow cover, a correction that cannot be performed with **Basinga**.

5.3 The paleomagnetic correction: ambitions and limits

In order to correct the production rates from past variations in the Earth magnetic field, the paleomagnetic correction integrates the *in situ* production rates over the exposure time. Such integration strongly impacts the resultant ^{10}Be production rates. If not considered it may lead to important errors especially in slow eroding environments where exposure time may extend beyond the Holocene period during which geomagnetic field intensity was higher than present (*Gosse and Phillips, 2001*) (Figure 7d).

However, this correction strongly relies on an accurate estimation of the exposure time. Table 3 highlights how much its variations of a few decades to a few centennials can yield to very different values of integrated production rates. Yet, at the basin scale the exposure time must be highly variable but we can only estimate a unique ^{10}Be concentration value (atoms.g^{-1}) for each basin and hence a unique time of exposure. The magnitude of the error generated on integrated ^{10}Be production rates and derived denudation rates remains hard to estimate. Therefore, caution must be taken when using this correcting option and the derived results should be considered more as complementary data.

5.4 Limits and cautions with the glacial correction

Caution needs also to be taken in glacial environments especially since the glacial correction relies on the hypothesis that glaciated areas provide sediment with a null ^{10}Be concentration (*Wittmann et al., 2007*). In nature, processes of glacial erosion are way much more complicated, with notably, supra-glacial hillslopes providing sediments whose ^{10}Be concentration strongly differ from 0 (*Godard et al., 2012*).

The users are also to be warned when using the paleomagnetic correction, especially when times of exposure encompass periods of important climatic changes that strongly affect glacial extensions (e.g. *Denton and Karlén, 1973; Ruddiman, 1977; Heinrich, 1988; Bond et al., 1992, 1993, 1997; Dansgaard et al., 1993; Kiefer et al.,*

2002; Dyke, 2004; Hemming, 2004; Wolff *et al.*, 2010; Austin and Hibbert, 2012). The isostatic rebound that follows a glacial retreat (e.g. *Walcott*, 1973; *Stern et al.*, 2005; *Champagnac et al.*, 2007) can also bias the integrated ^{10}Be production rate values by modifying the altitude of the terrain and thus the atmospheric pressure. However, accounting for these parameters would require glacial and crustal numerical modelling which is way beyond the purpose of this work.

6. Conclusion and perspectives

Basinga is a freely available ArcGIS toolbox which provides two independent tools to compute the basin average cosmogenic scaling factors, ^{10}Be cosmogenic rates and ^{10}Be denudation rates. It can be easily downloaded from the Online supplementary information and installed following the "Getting Started" document also provided online. It is based on friendly interfaces which are provided with a thorough help and instruction and does not request any particular skills in programming. The parametrization can be easily updated or changed if needed following the instruction given in the "Getting Started" document. Moreover, **Basinga** computes the scaling factor and ^{10}Be cosmogenic rates in few minutes (Table 4) on several catchments together and enables a quick treatment of large datasets. The *Denudation tool* accounts for both the spallogenic and the muonic production which ensures a more rigorous estimate of the denudation rates. However, some improvement could be done in the future.

First, *Stone* (2000) highlighted that the major atmospheric systems may modify the atmospheric pressure and hence impact modern ^{10}Be *in situ* production rates (*Stone*, 2000; *Staiger et al.*, 2007). To avoid potential bias in the cosmogenic nuclide production rate calculations, it might be relevant to account for these major pressure changes. However, if the atmospheric pressure likely changed during the past (*Staiger et al.*, 2007), it remains difficult to accurately reconstruct those variations. Nevertheless, one may average the surface atmospheric pressure measured for the past 40 years (*Uppala et al.*, 2005) and calculate the production rates accordingly.

Second, in the *Production Rates* tool the average values are computed by summing all individual scaling factors or ^{10}Be cosmogenic rate calculated for each cells. This sum is then divided by the total number of cells of the region of interest (equation

8b). However, in such approach all individual cells are considered to have the same area. Yet, this is rigorously incorrect as the latitude change. This approximation may yield to significant errors for very large basin. Therefore, an additional development of the code would be needed to apply the tool to very large basins.

At last, as considered in several studies (e.g. *Godard et al.*, 2012; *Scherler et al.*, 2014), in high elevated regions, snow cover shielding factor should be calculated and corrected for. However, this factor can be computed independently and integrate to **Basinga** by multiplying it to the topographic shielding factor for example via the Raster Calculator tool box available in ArcGIS®. Hence, snow correction will be included in the overall calculation if the correction for topographic shielding is selected during the process. Finally, the cosmogenic production rate of other nuclide as ^{26}Al , ^3He , ^{36}Cl or ^{21}Ne can be easily done by changing the corresponding SLHL parameters (see Getting started in the Online Supplementary Information).

Acknowledgements

We thank Jérôme Lavé and Maarten Lupker for fruitful discussions and Romain Delunel for kindly providing his original data on the Pelvoux. We also thank Vincent Godard for discussion and complementary information about his paper. We dedicate this work to the almost Nobel price Sheldon Cooper from Caltech who greatly inspired the name of our tool. This is CRPG contribution XXX.

References

- Armstrong, R., Raup, B., Khalsa, S., Barry, R., Kargel, J., Helm, C., & Kieffer, H. (2005). GLIMS glacier database. Boulder, Colorado USA: National Snow and Ice Data Center. *Digital media*.
- Austin, W. E., & Hibbert, F. D. (2012). Tracing time in the ocean: a brief review of chronological constraints (60–8 kyr) on North Atlantic marine event-based stratigraphies. *Quaternary Science Reviews*, 36, 28-37.
- Balco, G., Stone, J. O., Lifton, N. A., & Dunai, T. J. (2008). A complete and easily accessible means of calculating surface exposure ages or erosion rates from ^{10}Be and ^{26}Al measurements. *Quaternary geochronology*, 3(3), 174-195.
- Balco, G., Briner, J., Finkel, R.C., Rayburn, J.A., Ridge, J.C., Schaefer, J.M., 2009. Regional beryllium-10 production rate calibration for late-glacial northeastern North America. *Quat. Geochronol.* 4. 93–107. 10.1016/j.quageo.2008.09.001.

- Bierman, P., & Steig, E. J. (1996). Estimating rates of denudation using cosmogenic isotope abundances in sediment. *Earth surface processes and landforms*, 21(2), 125-139.
- Bond, G., Broecker, W., Johnsen, S., McManus, J., Labeyrie, L., Jouzel, J., & Bonani, G. (1993). Correlations between climate records from North Atlantic sediments and Greenland ice. *Nature*(365), 143-147.
- Bond, G., Heinrich, H., Broecker, W., Labeyrie, L., McManus, J., Andrews, J., . . . Simet, C. (1992). Evidence for massive discharges of icebergs into the North Atlantic ocean during the last glacial period.
- Bond, G., Showers, W., Cheseby, M., Lotti, R., Almasi, P., Priore, P., . . . Bonani, G. (1997). A pervasive millennial-scale cycle in North Atlantic Holocene and glacial climates. *science*, 278(5341), 1257-1266.
- Braucher, R., Brown, E.T., Bourlès, D.L., Colin, F., 2003. In situ produced ^{10}Be measurements at great depths: implications for production rates by fast muons. *Earth Planet. Sci. Lett.* 211, 251–258.
- Braucher, R., Merchel, S., Borgomano, J., & Bourlès, D. (2011). Production of cosmogenic radionuclides at great depth: A multi element approach. *Earth and Planetary Science Letters*, 309(1), 1-9.
- Braucher, R., Bourlès, D., Merchel, S., Vidal Romani, J., Fernandez-Mosquera, D., Marti, K., Léanni, L., Chauvet, F., Arnold, M., Aumatre, G., Keddadouche, K., 2013. Determination of muon attenuation lengths in depth profiles from in situ produced cosmogenic nuclides. *Nucl. Instruments Methods Phys. Res. Sect. B Beam Interact. with Mater. Atoms* 294, 484–490. doi:10.1016/j.nimb.2012.05.023
- Brown, E. T., Stallard, R. F., Larsen, M. C., Raisbeck, G. M., & Yiou, F. (1995). Denudation rates determined from the accumulation of in situ-produced ^{10}Be in the Luquillo Experimental Forest, Puerto Rico. *Earth and Planetary Science Letters*, 129(1), 193-202.
- Burrough, P., & McDonnell, R. (1998). Creating continuous surfaces from point data. *Principles of Geographic Information Systems*. Oxford University Press, Oxford, UK.
- Champagnac, J., Molnar, P., Anderson, R., Sue, C., & Delacou, B. (2007). Quaternary erosion-induced isostatic rebound in the western Alps. *Geology*, 35(3), 195-198.
- Codilean, A. T. (2006). Calculation of the cosmogenic nuclide production topographic shielding scaling factor for large areas using DEMs. *Earth surface processes and landforms*, 31(6), 785-794.
- Dansgaard, W., Johnsen, S., Clausen, H., Dahl-Jensen, D., Gundestrup, N., Hammer, C., . . . Jouzel, J. (1993). Evidence for general instability of past climate from a 250-kyr ice-core record. *Nature*, 364(6434), 218-220.
- Delunel, R., Van Der Beek, P. A., Carcaillet, J., Bourlès, D. L., & Valla, P. G. (2010). Frost-cracking control on catchment denudation rates: Insights from in situ produced ^{10}Be concentrations in stream sediments (Ecrins–Pelvoux massif, French Western Alps). *Earth and Planetary Science Letters*, 293(1), 72-83.
- Denton, G. H., & Karlén, W. (1973). Holocene climatic variations—their pattern and possible cause. *Quaternary Research*, 3(2), 155-205.

- Dunai, T. (2001). Influence of secular variation of the geomagnetic field on production rates of in situ produced cosmogenic nuclides. *Earth and Planetary Science Letters*, 193(1), 197-212.
- Dunne, J., Elmore, D., & Muzikar, P. (1999). Scaling factors for the rates of production of cosmogenic nuclides for geometric shielding and attenuation at depth on sloped surfaces. *Geomorphology*, 27(1), 3-11.
- Dyke, A. S. (2004). An outline of North American deglaciation with emphasis on central and northern Canada. *Quaternary glaciations: extent and chronology*, 2, 373-424.
- Godard, V., Burbank, D., Bourlès, D., Bookhagen, B., Braucher, R., & Fisher, G. (2012). Impact of glacial erosion on ^{10}Be concentrations in fluvial sediments of the Marsyandi catchment, central Nepal. *Journal of Geophysical Research: Earth Surface* (2003–2012), 117(F3).
- Gosse, J. C., & Phillips, F. M. (2001). Terrestrial in situ cosmogenic nuclides: theory and application. *Quaternary Science Reviews*, 20(14), 1475-1560.
- Granger, D. E., Kirchner, J. W., & Finkel, R. (1996). Spatially averaged long-term erosion rates measured from in situ-produced cosmogenic nuclides in alluvial sediment. *The Journal of Geology*, 249-257.
- Guyodo, Y., & Valet, J.-P. (1996). Relative variations in geomagnetic intensity from sedimentary records: the past 200,000 years. *Earth and Planetary Science Letters*, 143(1), 23-36.
- Guyodo, Y., & Valet, J.-P. (1999). Global changes in intensity of the Earth's magnetic field during the past 800 kyr. *Nature*, 399(6733), 249-252.
- Heinrich, H. (1988). Origin and consequences of cyclic ice rafting in the northeast Atlantic Ocean during the past 130,000 years. *Quaternary Research*, 29(2), 142-152.
- Heisinger, B., Lal, D., Jull, A.J.T., Kubik, P., Ivy-Ochs, S., Knie, K., Nolte, E., 2002a. Production of selected cosmogenic radionuclides by muons; 2. Capture of negative muons. *Earth Planet. Sci. Lett.* 200 , 357–369.
- Heisinger, B., Lal, D., Jull, A.J.T., Kubik, P., Ivy-Ochs, S., Neumaier, S., Knie, K., Lazarev, V., Nolte, E., 2002b. Production of selected cosmogenic radionuclides by muons; 1. Fast muons. *Earth Planet. Sci. Lett.* 200, 345–355.
- Hemming, S. R. (2004). Heinrich events: Massive late Pleistocene detritus layers of the North Atlantic and their global climate imprint. *Reviews of Geophysics*, 42(1).
- Herman, F., Copeland, P., Avouac, J. P., Bollinger, L., Mahéo, G., Le Fort, P., ... & Henry, P. (2010). Exhumation, crustal deformation, and thermal structure of the Nepal Himalaya derived from the inversion of thermochronological and thermobarometric data and modeling of the topography. *Journal of Geophysical Research: Solid Earth*, 115(B6).
- Kaplan, M. R., Strelin, J. A., Schaefer, J. M., Denton, G. H., Finkel, R. C., Schwartz, R., . . . Travis, S. G. (2011). In-situ cosmogenic ^{10}Be production rate at Lago Argentino, Patagonia: Implications for late-glacial climate chronology. *Earth and Planetary Science Letters*, 309(1), 21-32.
- Kelly, M.A., Lowell, T.V., Applegate, P. J., Phillips, F.M. , Schaefer, J.M., Smith, C.A. , Kim, H., Leonard, K.C. , Hudson, A. M. (2015) A locally calibrated, late glacial ^{10}Be production rate from a low-latitude, high-altitude site in the Peruvian Andes. *Quaternary Geochronology*, Volume 26, February 2015, Pages 70-85

- Kiefer, T., Lorenz, S., Schulz, M., Lohmann, G., Sarnthein, M., & Elderfield, H. (2002). Response of precipitation over Greenland and the adjacent ocean to North Pacific warm spells during Dansgaard–Oeschger stadials. *Terra Nova*, 14(4), 295-300.
- Kirchner, J. W., Finkel, R. C., Riebe, C. S., Granger, D. E., Clayton, J. L., King, J. G., & Megahan, W. F. (2001). Mountain erosion over 10 yr, 10 ky, and 10 my time scales. *Geology*, 29(7), 591-594.
- Laj, C., Kissel, C., & Beer, J. (2004). High Resolution Global Paleointensity Stack Since 75 kyr (GLOPIS-75) Calibrated to Absolute Values. *Timescales of the Paleomagnetic Field*, 255-265.
- Lal, D. (1988). In situ-produced cosmogenic isotopes in terrestrial rocks. *Annual Review of Earth and Planetary Sciences*, 16, 355-388.
- Lal, D. (1991). Cosmic ray labeling of erosion surfaces: in situ nuclide production rates and erosion models. *Earth and Planetary Science Letters*, 104(2), 424-439.
- Lal, D., & Peters, B. (1967). Cosmic ray produced radioactivity on the earth *Kosmische Strahlung II/Cosmic Rays II* (pp. 551-612): Springer.
- Lifton, N., Sato, T., & Dunai, T. J. (2014). Scaling in situ cosmogenic nuclide production rates using analytical approximations to atmospheric cosmic-ray fluxes. *Earth and Planetary Science Letters*, 386, 149-160.
- Lifton, N., (2016), Implications of two Holocene time-dependent geomagnetic models for cosmogenic nuclide production rate scaling, *Earth and Planetary Science Letters*, Volume 433, 257-268
- Lupker, M., Blard, P.-H., Lavé, J., France-Lanord, C., Leanni, L., Puchol, N., . . . Bourlès, D. (2012). 10 Be-derived Himalayan denudation rates and sediment budgets in the Ganga basin. *Earth and Planetary Science Letters*, 333, 146-156.
- Lupker, M., France-Lanord, C., Lave, J., Bouchez, J., Galy, V., Métivier, F., . . . Mugnier, J. L. (2011). A Rouse-based method to integrate the chemical composition of river sediments: Application to the Ganga basin. *Journal of Geophysical Research: Earth Surface* (2003–2012), 116(F4).
- Marrero, S. M., Phillips, F. M., Borchers, B., Lifton, N., Aumer, R., & Balco, G. (2015). Cosmogenic nuclide systematics and the CRONUScal program. *Quaternary geochronology*.
- Martin, L.C.P., Blard, P.-H., Lave, J., Balco, G., Delunel, R., The CREp program, a fully parametrizable program to compute exposure ages., Submitted. to *Quat. Geochronol*
- McElhinny, M. W., & McFadden, P. L. (1997). Palaeosecular variation over the past 5 Myr based on a new generalized database. *Geophysical Journal International*, 131(2), 240-252.
- Muscheler, R., Beer, J., Kubik, P. W., & Synal, H.-A. (2005). Geomagnetic field intensity during the last 60,000 years based on 10 Be and 36 Cl from the Summit ice cores and 14 C. *Quaternary Science Reviews*, 24(16), 1849-1860.
- Niemi, N. A., Oskin, M., Burbank, D. W., Heimsath, A. M., & Gabet, E. J. (2005). Effects of bedrock landslides on cosmogenically determined erosion rates. *Earth and Planetary Science Letters*, 237(3), 480-498.
- Nishiizumi, K., Winterer, E., Kohl, C., Klein, J., Middleton, R., Lal, D., & Arnold, J. (1989). Cosmic ray production rates of 10Be and 26Al in quartz from glacially

- polished rocks. *Journal of Geophysical Research: Solid Earth (1978–2012)*, 94(B12), 17907-17915.
- Norton, K. P., & Vanacker, V. (2009). Effects of terrain smoothing on topographic shielding correction factors for cosmogenic nuclide-derived estimates of basin-averaged denudation rates. *Earth surface processes and landforms*, 34(1), 145-154.
- Pigati, J. S., & Lifton, N. A. (2004). Geomagnetic effects on time-integrated cosmogenic nuclide production with emphasis on in situ ^{14}C and ^{10}Be . *Earth and Planetary Science Letters*, 226(1), 193-205.
- Portenga, E. W., & Bierman, P. R. (2011). Understanding Earth's eroding surface with ^{10}Be . *GSA Today*, 21(8), 4-10.
- Putnam, A., Schaefer, J., Barrell, D., Vandergoes, M., Denton, G., Kaplan, M., . . . Kelley, S. (2010). In situ cosmogenic ^{10}Be production-rate calibration from the Southern Alps, New Zealand. *Quaternary geochronology*, 5(4), 392-409.
- Raup, B., Racoviteanu, A., Khalsa, S. J. S., Helm, C., Armstrong, R., & Arnaud, Y. (2007). The GLIMS geospatial glacier database: a new tool for studying glacier change. *Global and Planetary Change*, 56(1), 101-110.
- Raymo, M., & Ruddiman, W. F. (1992). Tectonic forcing of late Cenozoic climate. *Nature*, 359(6391), 117-122.
- Reiners, P. W., & Brandon, M. T. (2006). Using thermochronology to understand orogenic erosion. *Annu. Rev. Earth Planet. Sci.*, 34, 419-466.
- Ruddiman, W. F. (1977). Late Quaternary deposition of ice-rafted sand in the subpolar North Atlantic (lat 40 to 65 N). *Geological Society of America Bulletin*, 88(12), 1813-1827.
- Safran, E. B. (1998). *Channel network incision and patterns of mountain geomorphology*.
- Scherler, D., Bookhagen, B., & Strecker, M. R. (2014). Tectonic control on ^{10}Be -derived erosion rates in the Garhwal Himalaya, India. *Journal of Geophysical Research: Earth Surface*, 119(2), 83-105.
- Schildgen, T., Phillips, W., & Purves, R. (2005). Simulation of snow shielding corrections for cosmogenic nuclide surface exposure studies. *Geomorphology*, 64(1), 67-85.
- Staiger, J., Gosse, J., Toracinta, R., Oglesby, B., Fastook, J., & Johnson, J. V. (2007). Atmospheric scaling of cosmogenic nuclide production: climate effect. *Journal of Geophysical Research: Solid Earth (1978–2012)*, 112(B2).
- Stern, T., Baxter, A., & Barrett, P. (2005). Isostatic rebound due to glacial erosion within the Transantarctic Mountains. *Geology*, 33(3), 221-224.
- Stone, J. O. (2000). Air pressure and cosmogenic isotope production. *Journal of Geophysical Research: Solid Earth (1978–2012)*, 105(B10), 23753-23759.
- Stroeven, A.P., Heyman, J., Fabel, D., Björck, S., Caffee, M. W., Fredin, O., Harbor, J.M. (2015). A new Scandinavian reference ^{10}Be production rate, *Quaternary Geochronology*, 29, 104-115.
- Uppala, S.M., Källberg, P.W., Simmons, a. J., Andrae, U., Bechtold, V.D.C., Fiorino, M., Gibson, J.K., Haseler, J., Hernandez, a., Kelly, G. a., Li, X., Onogi, K., Saarinen, S., Sokka, N., Allan, R.P., Andersson, E., Arpe, K., Balmaseda, M. a., Beljaars, a. C.M., Berg, L. Van De, Bidlot, J., Bormann, N., Caires, S., Chevallier, F., Dethof, a., Dragosavac, M., Fisher, M., Fuentes, M., Hagemann, S., Hólm, E., Hoskins, B.J., Isaksen, L., Janssen, P. a. E.M., Jenne, R., McNally, a. P., Mahfouf, J.-F., Morcrette,

- J.-J., Rayner, N. a., Saunders, R.W., Simon, P., Sterl, a., Trenberth, K.E., Untch, a., Vasiljevic, D., Viterbo, P., Woollen, J., (2005). The ERA-40 re-analysis. *Q. J. R. Meteorol. Soc.* 131, 2961–3012. doi:10.1256/qj.04.176.
- Valet, J.-P., Meynadier, L., & Guyodo, Y. (2005). Geomagnetic dipole strength and reversal rate over the past two million years. *Nature*, 435(7043), 802-805.
- Vermeesch, P. (2007). CosmoCalc: An Excel add-in for cosmogenic nuclide calculations. *Geochemistry, Geophysics, Geosystems*, 8(8).
- Von Blanckenburg, F. (2005). The control mechanisms of erosion and weathering at basin scale from cosmogenic nuclides in river sediment. *Earth and Planetary Science Letters*, 237(3), 462-479.
- Walcott, R. I. (1973). Structure of the earth from glacio-isostatic rebound. *Annual Review of Earth and Planetary Sciences*, 1, 15.
- Whipple, K. X. (2009). The influence of climate on the tectonic evolution of mountain belts. *Nature Geoscience*, 2(2), 97-104.
- Willet, S. D. (2010). Erosion on a line. *Tectonophysics*, 484(1), 168-180.
- Wittmann, H., von Blanckenburg, F., Kruesmann, T., Norton, K. P., & Kubik, P. W. (2007). Relation between rock uplift and denudation from cosmogenic nuclides in river sediment in the Central Alps of Switzerland. *Journal of Geophysical Research: Earth Surface (2003–2012)*, 112(F4).
- Wolff, E. W., Chappellaz, J., Blunier, T., Rasmussen, S. O., & Svensson, A. (2010). Millennial-scale variability during the last glacial: The ice core record. *Quaternary Science Reviews*, 29(21), 2828-2838.
- Yanites, B. J., Tucker, G. E., & Anderson, R. S. (2009). Numerical and analytical models of cosmogenic radionuclide dynamics in landslide-dominated drainage basins. *Journal of Geophysical Research: Earth Surface (2003–2012)*, 114(F1).
- Zreda, M., Desilets, D., Ferré, T., & Scott, R. L. (2008). Measuring soil moisture content non-invasively at intermediate spatial scale using cosmic-ray neutrons. *Geophysical Research Letters*, 35(21).

Figure and tables:

Figure 1. (a) Digital elevation model of a given watershed. At each localities j the denudation ε_j is function of the local cosmogenic production rates $P_{i,j}$ (i represents the neutron, slow muon and fast muon) and the in situ cosmogenic concentration N_j in surficial rocks. The average denudation rate of the whole basin can be quantified by measuring the in situ cosmogenic concentration in a stream river sand sampled at the outlet of the basin (photo); **(b)** Schematic diagram showing the shielding effect of the earth magnetic field; **(c)** Cosmic ray intensity as function of elevation Z and latitude. Due to cosmic ray absorption in the atmosphere (c) and shielding of the earth magnetic field, the local cosmogenic production rate at a given location j increases with elevation and latitude.

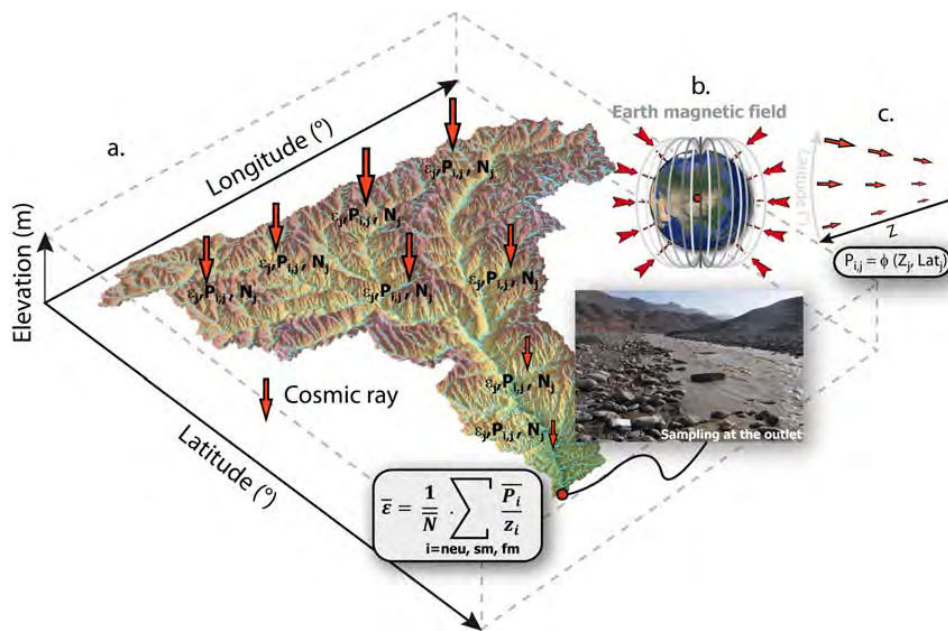


Figure 1

Figure 2. a. Mean elevation of drainage basins against the deviations between the production rates calculated using the mean altitude and latitude and the production rates calculated using a cell by cell approach (Scherler *et al.* (2014); Delunel *et al.* (2010)); b. True denudation against underestimation of denudation at different elevations if muons are not included during the calculation.

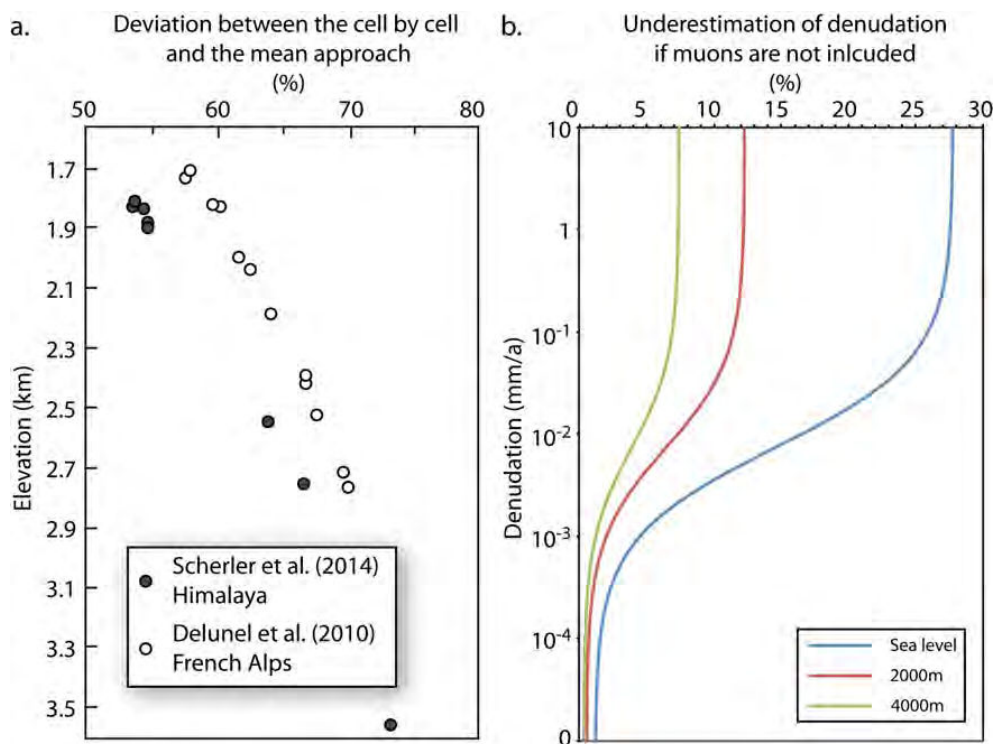


Fig. 2

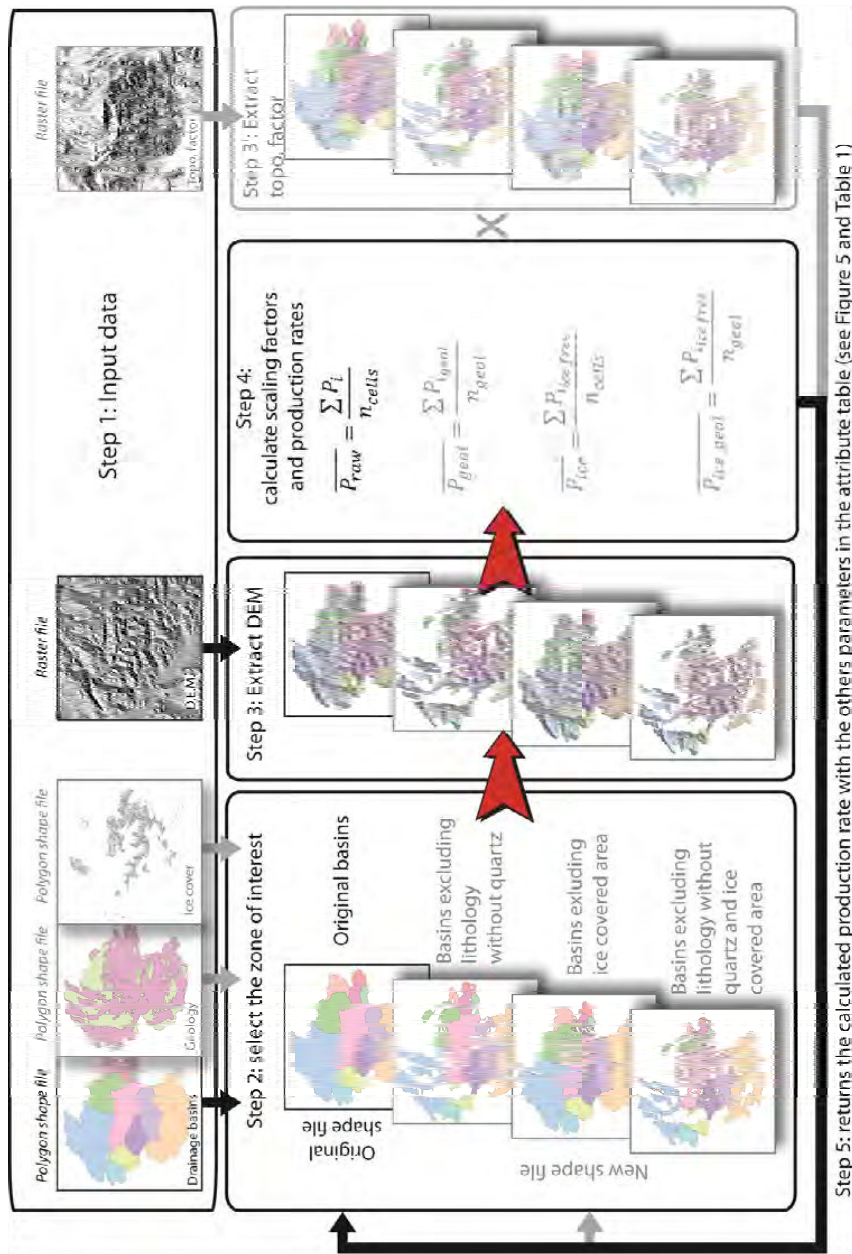


Figure 3: Work flow of the *Production rates* tool. This tool mainly works in 5 steps. The user must first provide the input data corresponding to the corrective options chosen (Step 1). Then the tool first selects and extracts the corresponding zone of interest (Steps 2 and 3). During this step it may create a new shape file if the correction for geology and ice have been checked. After that it calculates the cosmogenic scaling factors and ¹⁰Be cosmogenic production rates for each individual cell and averages other basins. At last it returns the calculated values to the attribute table either of the original shape file or to a new shape file created when the region of interest has been selected.

Figure 4: *Production rates* tool interface in ArcMap. This is the main interface where the users must specify at least the shape file of the drainage basin, the DEM and the path for the output file. The other fields remain optional and can be activated or not by checking the corresponding boxes. A detailed help is provided for each of the fields and can be shown on the right side of the tool by clicking "Show Help" at the right lower corner.

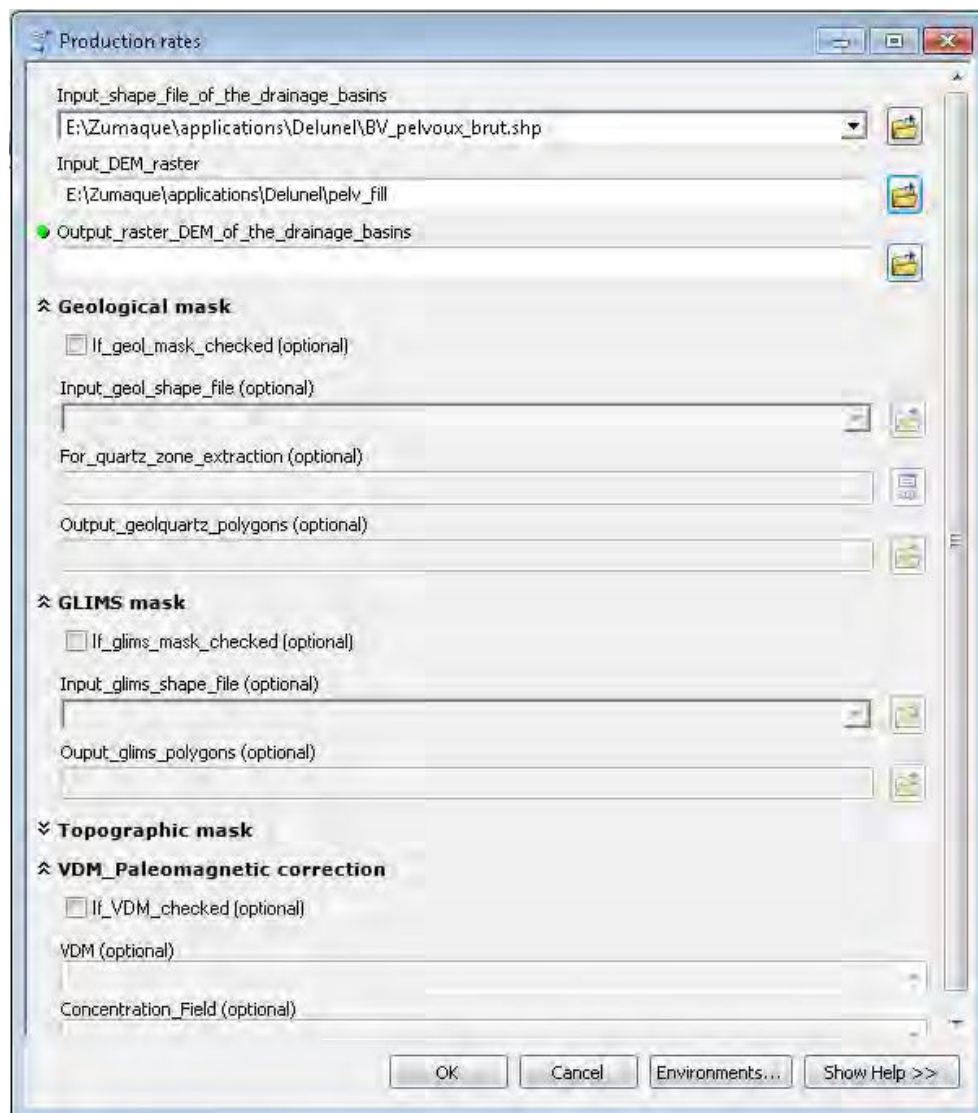


Figure 5: Examples of attribute tables and associated field (i.e. columns) where the results of calculations are stored accordingly to the correctives options chosen. The tables will also include three fields named SFn_, SFf_ and SFs_ which provide the spallogenic, fast muons and slow muons scaling factors, respectively.

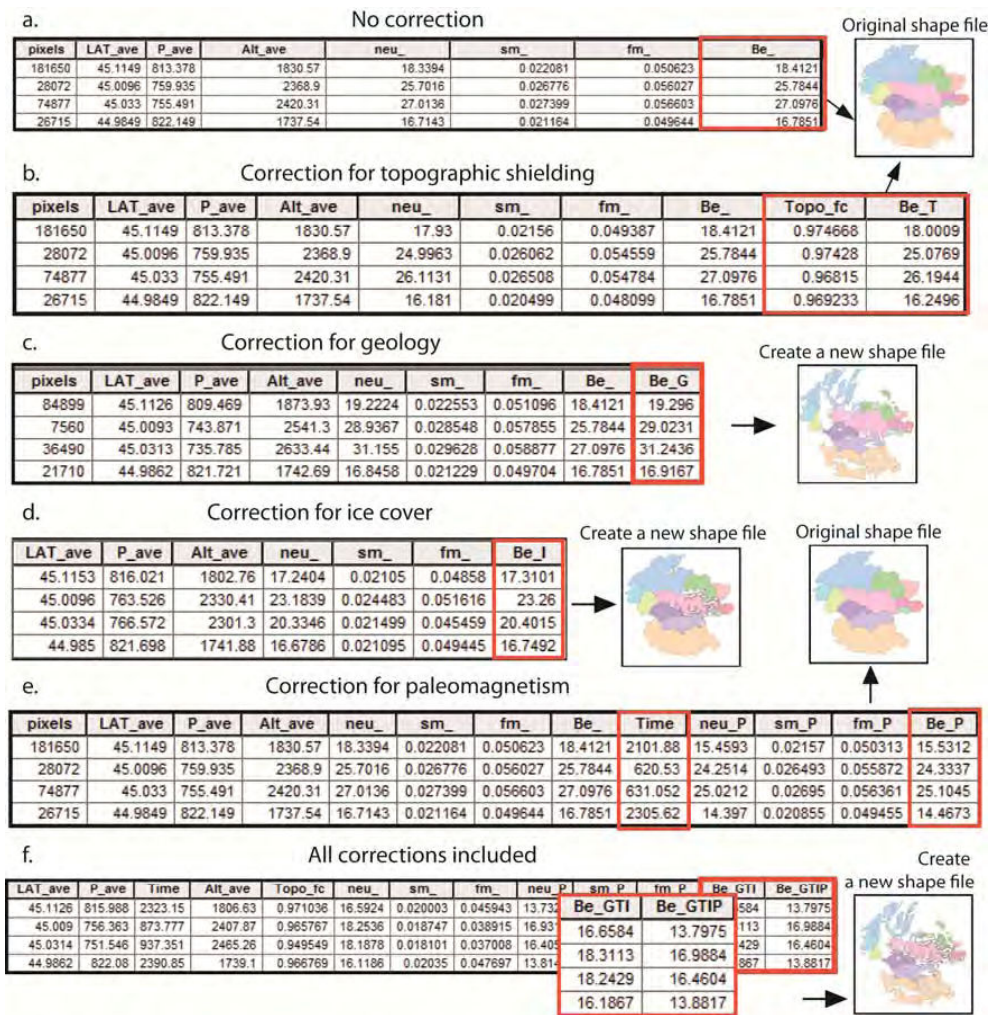


Fig. 5

Figure 6: a. Example of an attribute table which provides lithological information and specify the presence or absence of quartz in an independent field (e.g. field named 'Quartz'); b. Example of a shape file providing the polygons associated to the attribute table where the lithological information are given (after Delunel et al. (2010)); c. SQL interface open once the correction for lithology is selected. To compute the production rate in the region with quartz only (e.g. 'Crystalline basement') the user must specified a SQL expression (e.g. 'Quartz' = 'yes') which selects the right polygons of the shape file accordingly.

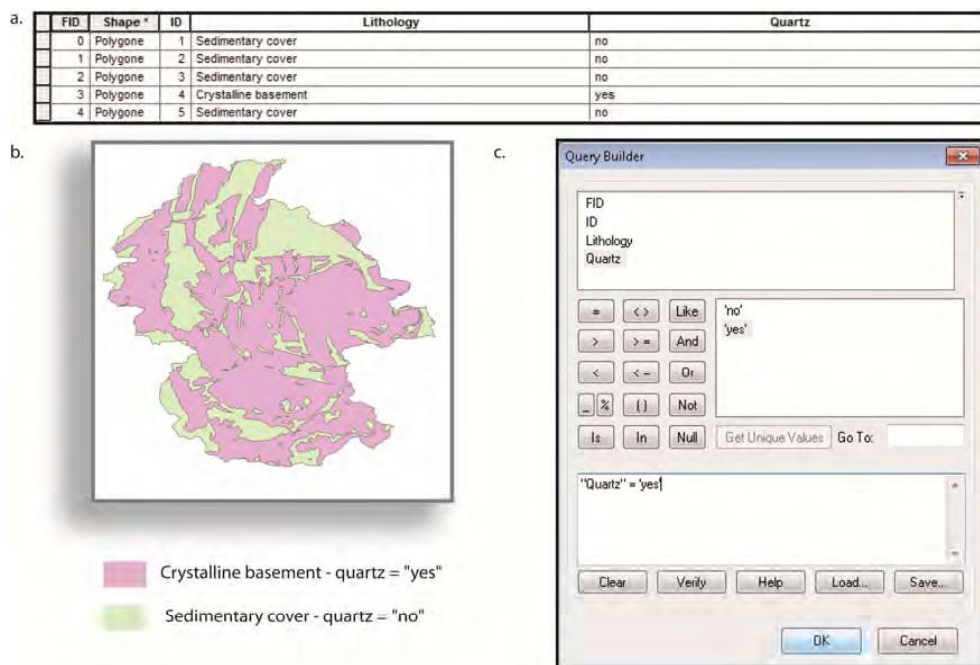


Fig. 6

Figure 7: Work flow of the paleomagnetic correction. The attribute table of the original shape file must include a field providing the measured concentrations for each studied watershed. The basin average production rate without any correction for paleomagnetism is calculated first (Step 1). Then the time average is computed accordingly to this later and the concentration (Step 2). At last, based on the paleomagnetic database chosen (here *Muscheler et al. (2005)*) the average cosmogenic production rate is integrated since this average time (Step 3) and stored in the attribute table with a suffix '_P' (Step 4).

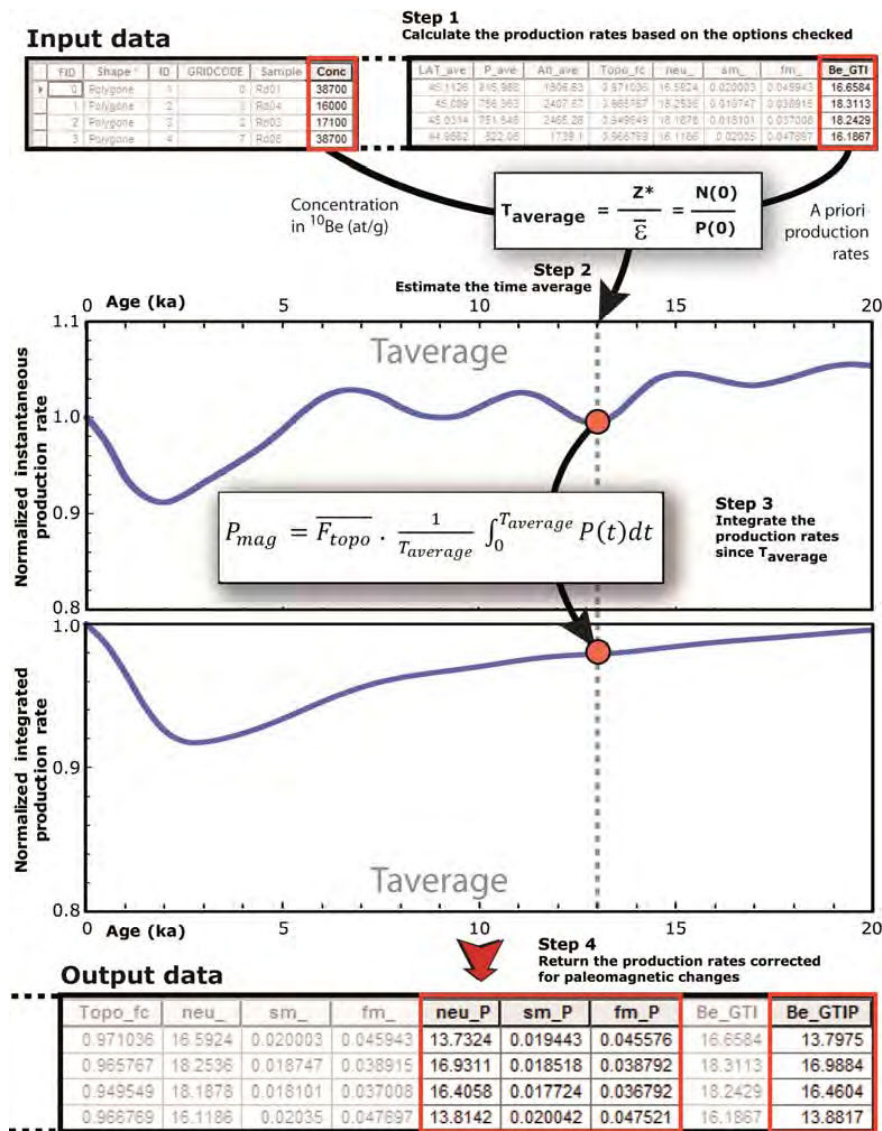


Fig. 7

Figure 8: *Denudation rates* tool interface. The user must specify the path to the shape file where the concentration in ^{10}Be and their uncertainties are stored. This file must include the ^{10}Be cosmogenic production rates calculated using the *Production rates* tool. The field of the ^{10}Be concentrations and their uncertainties must be specified and the box checked if the correction for paleomagnetism has been carried out during the previous calculations.

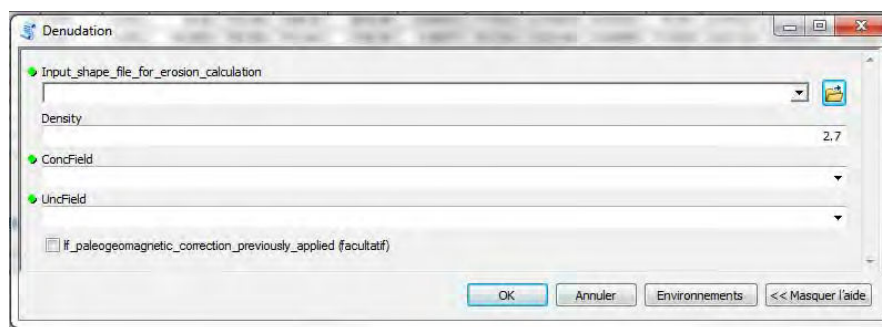


Figure 9: ^{10}Be cosmogenic production rates calculated using Basinga compared to the previous cosmogenic rates calculated in the original studies either with no correction for paleomagnetism (left) or including a correction for paleomagnetism (right).

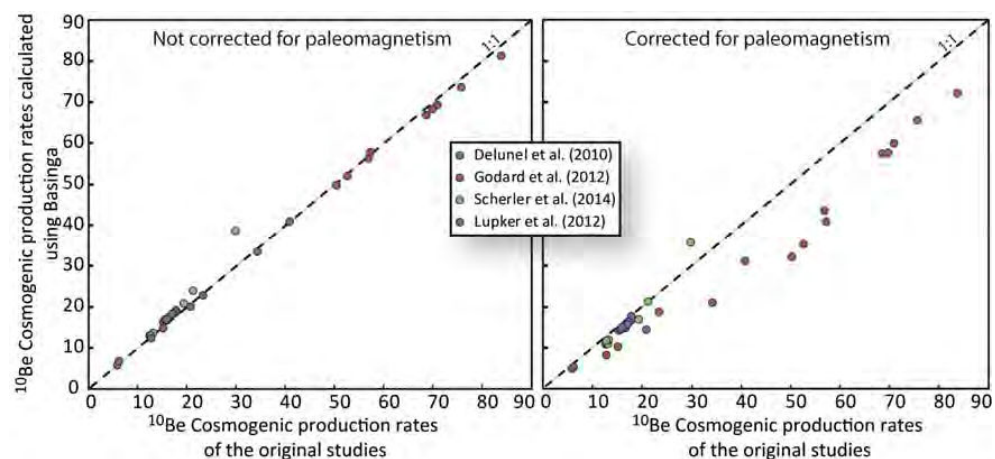


Table 1. List and description of the different fields generated by the *Production rates* and *Denudation rates* tools.

Fields	Description	Units
Pixels	Number of cells encountered in the area of the original catchment ^a	-
Alt_ave	Catchment-averaged altitude ^b	(DEM unit)
LAT_ave	Catchment-averaged latitude ^b	Decimal degrees ^c
P_ave	Catchment-averaged atmospheric pressure ^b	hPa
Time	Time of exposure ^d	Yr
Topo_fc*	Catchment-averaged topographic shielding factor	-
pixfreeI*	Number of ice free cells from the original catchment	-
Be_ ¹	Catchment-averaged ¹⁰ Be production rates ^b	atoms.g ⁻¹ .yr ⁻¹
neu_ ²	Catchment-averaged ¹⁰ Be nuclides produced by spallation ^b	atoms.g ⁻¹ .yr ⁻¹
sm_ ²	Catchment-averaged ¹⁰ Be nuclides produced by slow muon capture ^b	atoms.g ⁻¹ .yr ⁻¹
fm_ ²	Catchment-averaged ¹⁰ Be nuclides produced by fast muon capture ^b	atoms.g ⁻¹ .yr ⁻¹
SFn_ ¹	Catchment-averaged scaling factor for spallogenic production	-
SFf_ ¹	Catchment-averaged scaling factor for fast muonic production	-
SFs_ ¹	Catchment-averaged scaling factor for slow muonic production	-

*These fields are directly related to two different corrective options and might not appear if not requested.

^a If the correction for lithology has been activated, this number exclude the zones without quartz.

^b The calculation details are explained in section 4.1 and 4.2.

^c Negative values represent south latitudes.

^d The calculation details are explained in section 4.6.

¹ The “Be_“ and “SFn_”, “SFf_”, “SFs_” may be followed by one or more indicative letters accordingly to the optional correction selected by the user (G: Geology (lithology); T: Topographic shielding factor; I: Ice cover shielding factor; P: Paleomagnetic changes). Noteworthy, as the paleomagnetic results are computed independently (see section 4.6), anytime this option is selected, these fields will appear twice: first referred with all the options activated but the paleomagnetic changes, and second with a “P” at the end providing the rate corrected for past variations in the earth magnetic field.

² These three fields represents the details of the “Be_“ sum field described above. They are not followed by an indicative letter since the “Be_“ field already provides this information. However, as it is stated right above, they will appear twice if a correction for paleomagnetic changes is requested, the second “neu_”, “sm_” and “fm_” fields being referred with a supplementary "P".

Table 2. Table of the initial published cosmogenic results (I) (Delumel et al., 2010; Godard et al., 2012; Lupker et al., 2012; Scherler et al., 2014) compared to our results computed using Basinga (II).
 * only the basin average production rates for spallation are compared

Catchment	Sample name	Sample location		Basin area (km ²)	Mean Elevation (m)		Topographic shielding factor		Quartz	Ice/snow correction	Mean production rates (at/g/yr)		Deviation (%)
		Lat. (°N)	Long. (°E)		(I)	(II)	(I)	(II)			(I)	(II)	
<i>Delumel et al. (2010)</i>													
Romanche	Rd01	45.0512	5.8513	613	2222	2093	0.93	0.96	yes/yes	yes/yes	16.64	17.63	-6
Veneon	Rd02	45.0139	6.0636	260	2413	2283	0.92	0.95	yes/yes	yes/yes	17.24	18.26	-6
Up. Romanche	Rd03	45.0372	6.2074	100	2616	2465	0.93	0.95	yes/yes	yes/yes	17.16	18.24	-6
Tabuc	Rd04	44.9846	6.4781	21	2510	2433	0.94	0.97	yes/yes	yes/yes	17.89	19.19	-7
Saint Pierre	Rd05	44.8911	6.4461	44	2765	2639	0.91	0.94	yes/yes	yes/yes	16.77	17.60	-5
Celse Niere	Rd06	44.8822	6.443	19	2674	2454	0.91	0.94	yes/yes	yes/yes	17.96	18.66	-4
Gyr	Rd07	44.8708	6.4853	84	2603	2438	0.92	0.95	yes/yes	yes/yes	17.43	18.22	-5
Roizonne	Rd08	44.9401	5.8598	62	1741	1739	0.94	0.97	yes/yes	yes/yes	15.36	16.19	-5
Bonne	Rd09	44.8909	5.9075	156	1836	1820	0.93	0.96	yes/yes	yes/yes	15.76	16.77	-6
Upper Bonne	Rd10	44.8812	5.9893	102	1995	1957	0.93	0.95	yes/yes	yes/yes	17.1	18.01	-5
Drac	Mb130	44.7934	5.9724	545	1825	1797	0.95	0.97	yes/yes	yes/yes	15.96	16.70	-5
Severaisse	Mb146	44.7843	6.0629	159	1980	1916	0.93	0.96	yes/yes	yes/yes	16.07	16.90	-5
<i>Godard et al. (2012)*</i>													
Chepe	NEP080	28.0595	84.4842	309	1800	1821	0.94	0.99	no/no	yes/no	15.21	14.51	5
Chudi	NEP030	27.9546	84.4188	110	700	709	0.94	0.996	no/no	yes/no	5.85	5.48	6
Darondi	NEP003	27.9066	84.5397	614	1400	1428	0.93	0.99	no/no	yes/no	12.87	12.18	5
Dordi	NIB-975-44	28.168	84.4483	353	2900	2569	0.9	0.98	no/no	yes/no	34.32	33.20	3
Dudh	NIB-975-10	28.5289	84.3599	389	4700	4381	0.86	0.97	no/no	yes/no	68.64	66.61	3
Khudi	NIB-975-02	28.2818	84.355	136	2600	2598	0.91	0.99	no/no	yes/no	23.4	22.64	3
Marsyandi	NEP124	28.3875	84.4022	2416	4700	4450	0.89	0.98	no/no	yes/no	70.98	69.17	3
Marsyandi	NEP151	28.6185	84.145	560	4900	4670	0.9	0.98	no/no	yes/no	75.66	73.41	3
Marsyandi	NIB-975-06	28.3216	84.4006	2482	4600	4387	0.88	0.98	no/no	yes/no	69.81	68.10	2
Marsyandi	NEP106	28.1036	84.4437	3462	4000	3791	0.89	0.98	no/no	yes/no	56.94	56.05	2
Marsyandi	NIB-975-52	28.0642	84.4751	3487	4000	3680	0.89	0.98	no/no	yes/no	57.33	57.65	-1
Marsyandi	NEP065	27.9872	84.4295	3877	3700	3432	0.9	0.98	no/no	yes/no	52.65	51.79	2

Marsyandi	NEP006	27.9042	84.5338	4082	3600	3280	0.9	0.98	no/no	yes/no	50.31	49.59	1
Nar	NEP138	28.5587	84.2591	880	5200	4962	0.9	0.98	no/no	yes/no	83.85	81.14	3
Nyadi	NEP118	28.3233	84.4068	215	3500	3227	0.88	0.98	no/no	yes/no	40.95	40.78	0
Paudi	NEP099	28.1131	84.4262	83	1000	950	0.95	0.99	no/no	yes/no	6.24	6.58	-5
<i>Scherler et al. (2014)</i>													
	DS7-048	30.5734	78.0073	100	1808	1805	0.97	0.99	no/no	yes/no	12.647	12.88	-2
	DS7-049	30.6416	78.0069	168	1840	1836	0.97	0.98	no/no	yes/no	12.959	13.23	-2
	DS6-AR3	30.7222	78.088	89	1881	1879	0.97	0.99	no/no	yes/no	13.246	13.50	-2
	DS7-051/	30.7222	78.0871	89	1881	1879	0.97	0.99	no/no	yes/no	13.246	13.50	-2
	DS7-061	30.7998	78.112	210	1893	1892	0.97	0.99	no/no	yes/no	13.326	13.61	-2
	DS7-045	30.8203	78.2074	9	1832	1826	0.97	0.99	no/no	yes/no	12.794	12.97	-1
	DS7-044	30.8729	78.3037	25	2539	2542	0.95	0.98	no/no	yes/no	19.502	20.77	-7
	DS6-006	30.8882	78.3054	55	2738	2750	0.94	0.98	no/no	yes/no	21.285	23.87	-12
	DS6-008	30.9334	78.4009	160	3558	3560	0.94	0.98	no/no	yes/no	29.943	38.56	-29
<i>Lupker et al. (2012)</i>													
Yamuna	YAM Q3	30.443	77.674	7620	2420	2234	0.96	0.989	no/no	no/no	20.922	19.99	4

Table 3. Table of the initial published cosmogenic rates (*Delunel et al., 2010; Godard et al., 2012; Lupker et al., 2012; Scherler et al., 2014*) (I) compared to our results calculated with Basinga and including a paleomagnetic correction (II).

Catchment	Sample name	^{10}Be (at/g)	Time of exposure (yr)	Mean production rates (atoms.g ⁻¹ .yr ⁻¹)		Deviation percentages (%)
				(I)	(II)	
<i>Delunel et al. (2010)</i>						
Romanche	Rd01	38700±6700	2195	16.64	14.9	10.44
Veneon	Rd02	25000±4400	1369	17.24	15.96	7.45
Upper Romanche	Rd03	17100±3000	937	17.16	16.29	5.06
Tabuc	Rd04	16000±3300	833	17.89	17.6	1.64
Saint Pierre	Rd05	22300±4300	1267	16.77	15.54	7.35
Celse Niere	Rd06	19800±3400	1061	17.96	16.6	7.56
Gyr	Rd07	14500±2500	796	17.43	16.29	6.54
Roizonne	Rd08	38700±6800	2391	15.36	14.2	7.55
Bonne	Rd09	50700±9300	3024	15.76	14.33	9.11
Upper Bonne	Rd10	41100±8200	2282	17.1	15.68	8.26
Drac	Mb130	22400±4200	1341	15.96	14.62	8.4
Severaisse	Mb146	24700±4500	1461	16.07	14.91	7.22
<i>Godard et al. (2012)</i>						
Chepe	NEP080	16390±1160	1134	15.21	10.27	32.5
Chudi	NEP030	60090±2690	10909	5.85	4.97	15.09
Darondi	NEP003	9130±540	757	12.87	8.09	37.17
Dordi	NIB-975-44	12200±650	376	34.32	20.94	38.99
Dudh	NIB-975-10	8860±680	137	68.64	57.42	16.35
Khudi	NIB-975-02	5570±1180	248	23.4	18.63	20.38
Marsyandi	NEP124	8330±800	123	70.98	59.79	15.77
Marsyandi	NEP151	15830±1420	220	75.66	65.49	13.44
Marsyandi	NIB-975-06	11340±680	170	69.81	57.54	17.58
Marsyandi	NEP106	6150±770	109	56.94	43.48	23.65
Marsyandi	NIB-975-52	7920±680	144	57.33	40.79	28.84
Marsyandi	NEP065	9520±800	188	52.65	35.27	33.02
Marsyandi	NEP006	9540±1030	196	50.31	32.25	35.89
Nar	NEP138	23720±1210	298	83.85	71.98	14.15
Nyadi	NEP118	7390±490	186	40.95	31.13	23.97
Paudi	NEP099	16740±790	2537	6.24	5.39	13.62
<i>Scherler et al. (2014)</i>						
	DS7-048	18700±670	1452	12.65	10.81	14.53
	DS7-049	66370±1660	5018	12.96	10.93	15.69
	DS6-AR3	74700±1580	5533	13.25	11.43	13.68

	DS7-051/	49010±1250	3630	13.25	10.95	17.34
	DS7-061	85240±2130	6265	13.33	11.81	11.37
	DS7-045	139030±3460	10716	12.79	11.71	8.44
	DS7-044	47410±1200	2283	19.5	16.88	13.47
	DS6-006	13690±320	574	21.29	21.11	0.81
	DS6-008	4760±190	124	29.94	35.68	-19.14
	<i>Lupker et al. (2012)</i>					
Yamuna	YAM Q3	21400±2100	1071	20.92	14.46	30.89

Table 4. Computing times results with respect to the computer performances, the area of the watersheds analysed, and also the corrective options requested. Computer (a): Desktop computer, Windows7, 8GB memory, Processor: Intel Core i7-2600 CPU 3.4 GHz; Computer (b): Laptop PC, Windows7, 8GB memory, Processor: Intel Core CPU 2.9 GHz

*G: Quartz locations; T: Topographic shielding factor; I: Ice cover shielding factor; P: Paleomagnetic changes

References	Computing times		Treated area (km ²)	Requested options*
	Computer (a)	Computer (b)		
<i>Delunel et al., 2010</i>	3 min 11 seconds	5 min 36 seconds	2165	Q; T; I
<i>Lupker et al., 2012</i>	1 min 3 seconds	2 min 11 seconds	7620	T
<i>Lupker et al., 2012</i>	1 min 24 seconds	—	7620	T; P
<i>Godard et al., 2012</i>	5 min 52 seconds	14 min 7 seconds	23455	T
<i>Scherler et al., 2014</i>	26.55 seconds	1 min 42 seconds	905	T

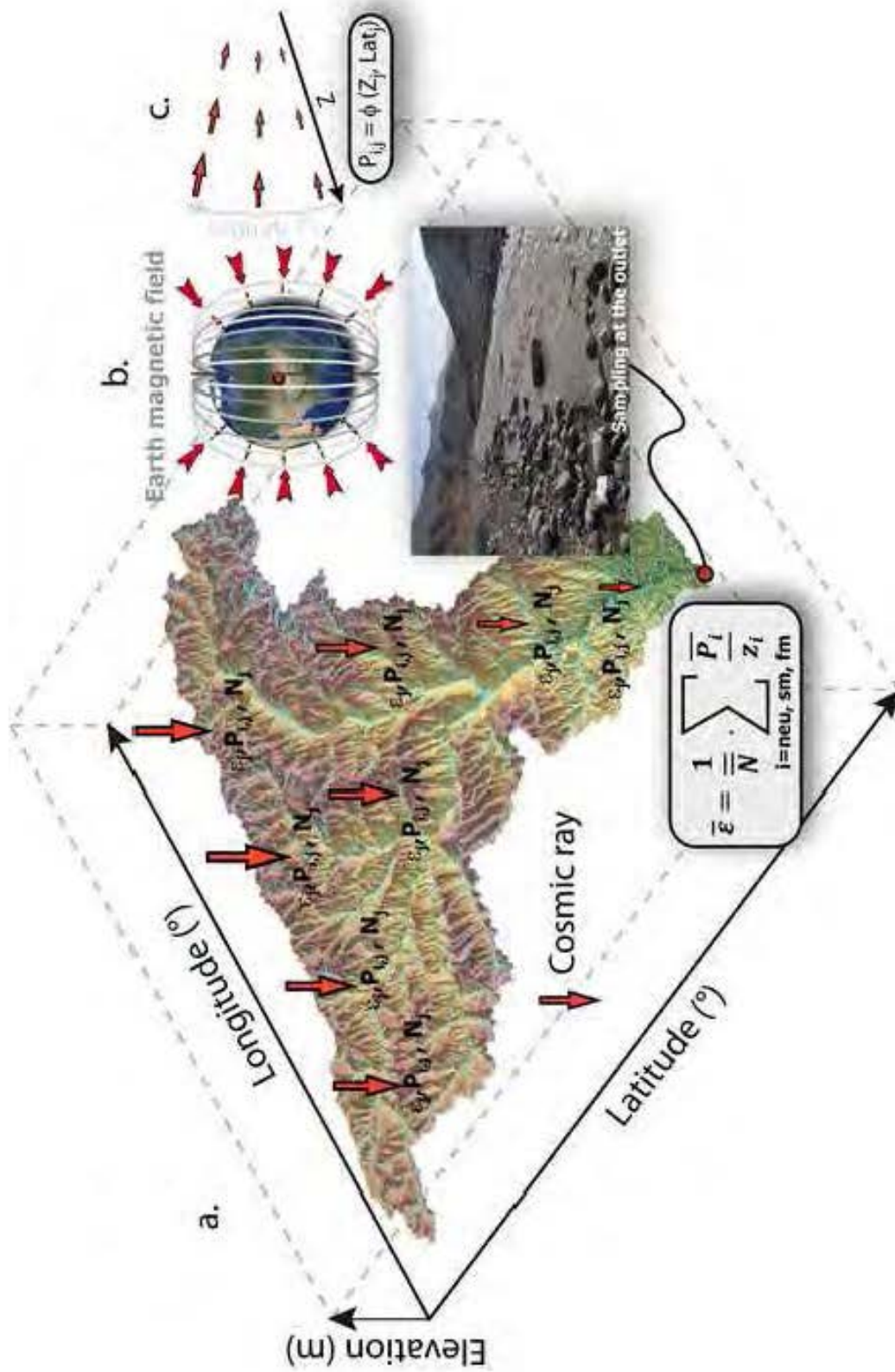


Figure 1

Figure1
[Click here to download high resolution image](#)

Figure2

[Click here to download high resolution image](#)

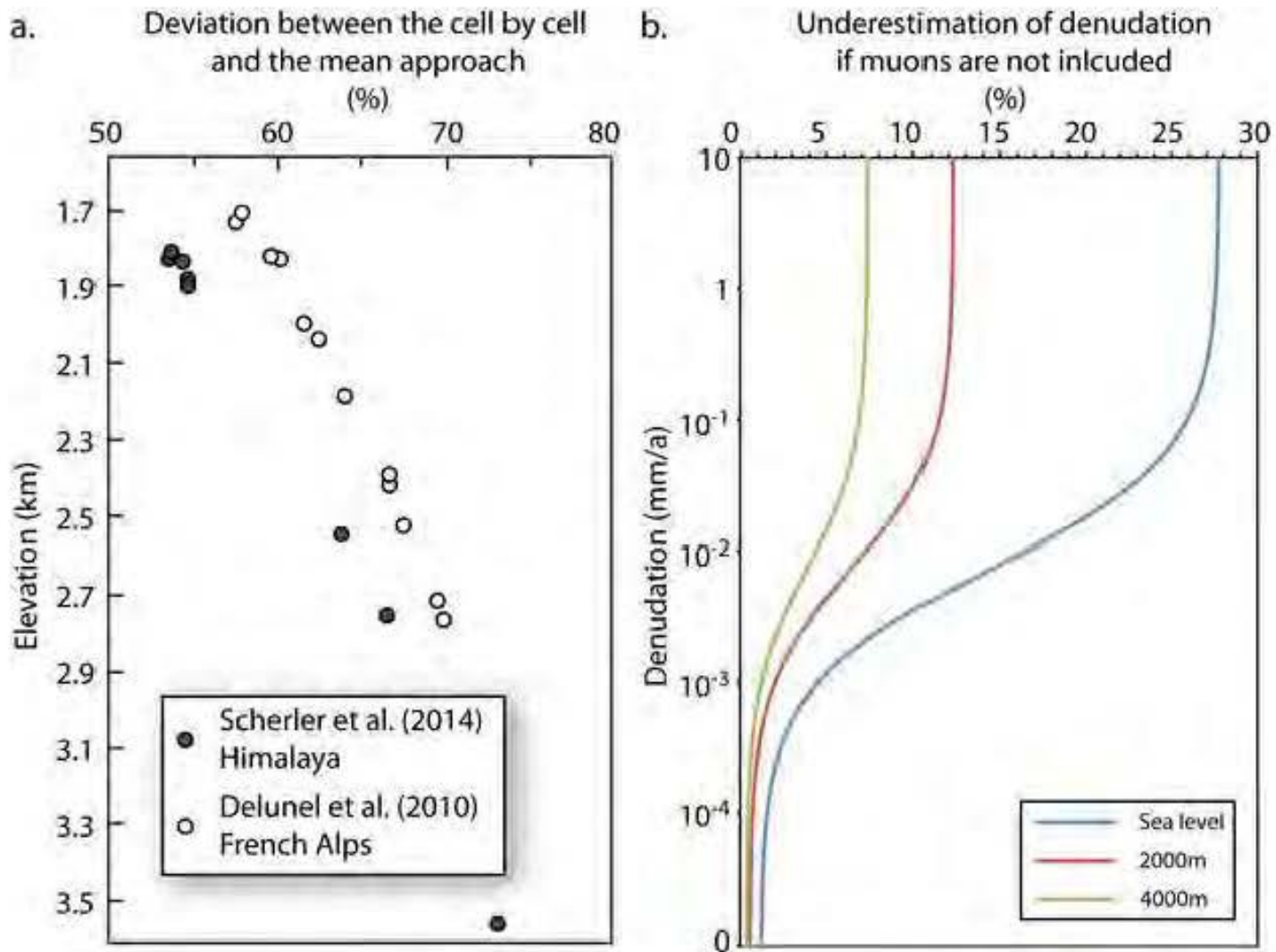


Fig. 2

Figure3
[Click here to download high resolution image](#)

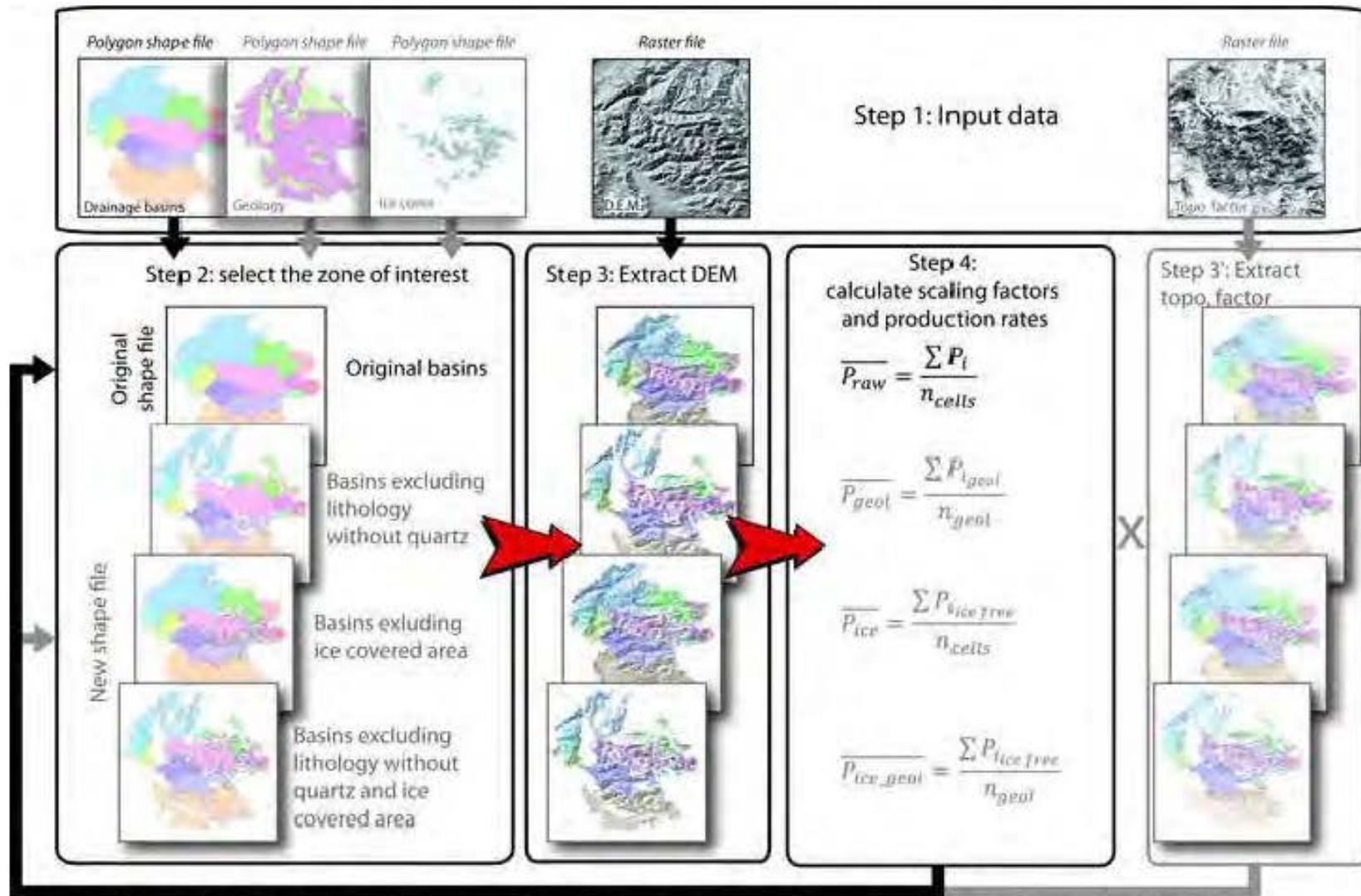


Figure4

[Click here to download high resolution image](#)

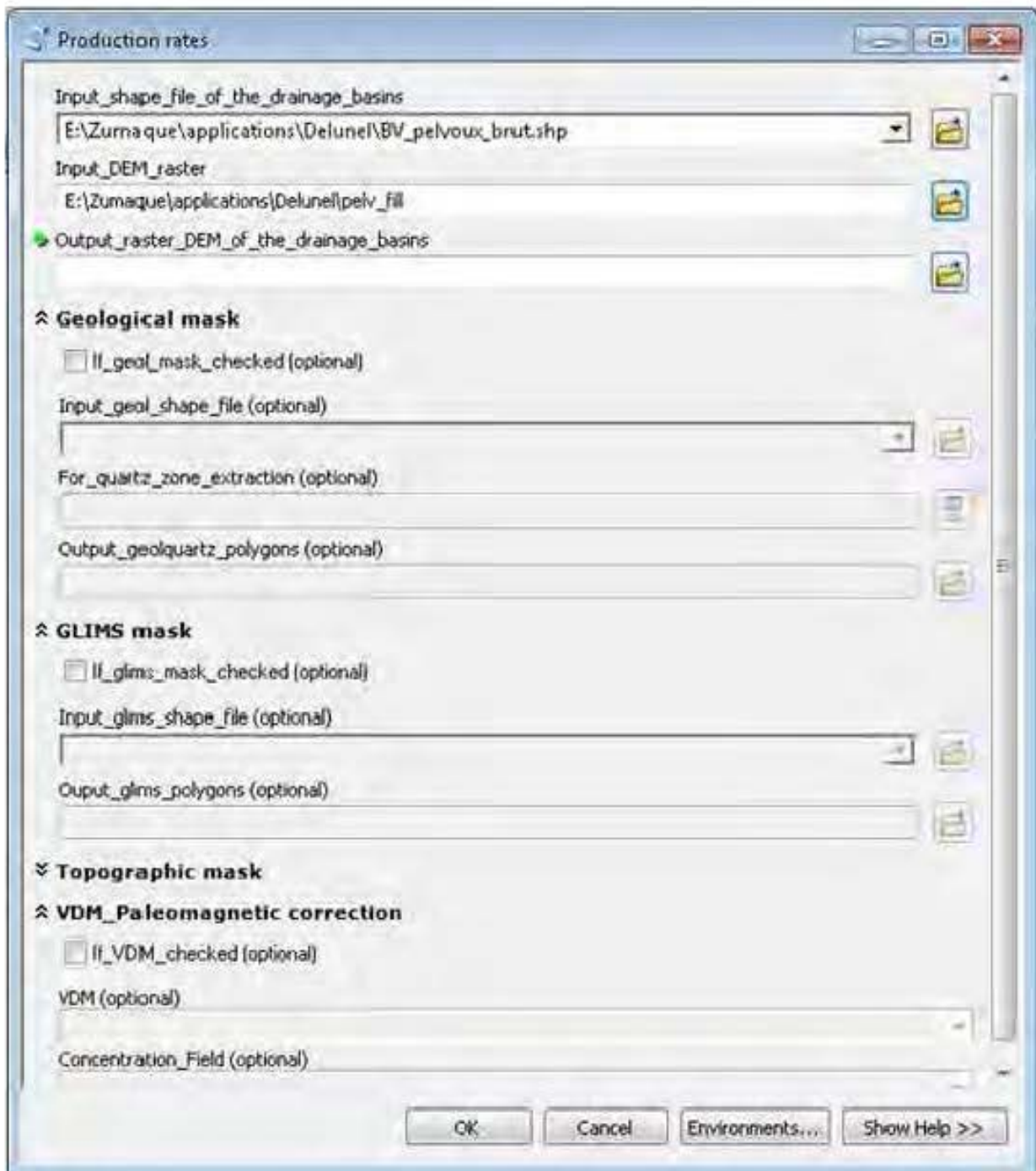


Figure5

[Click here to download high resolution image](#)

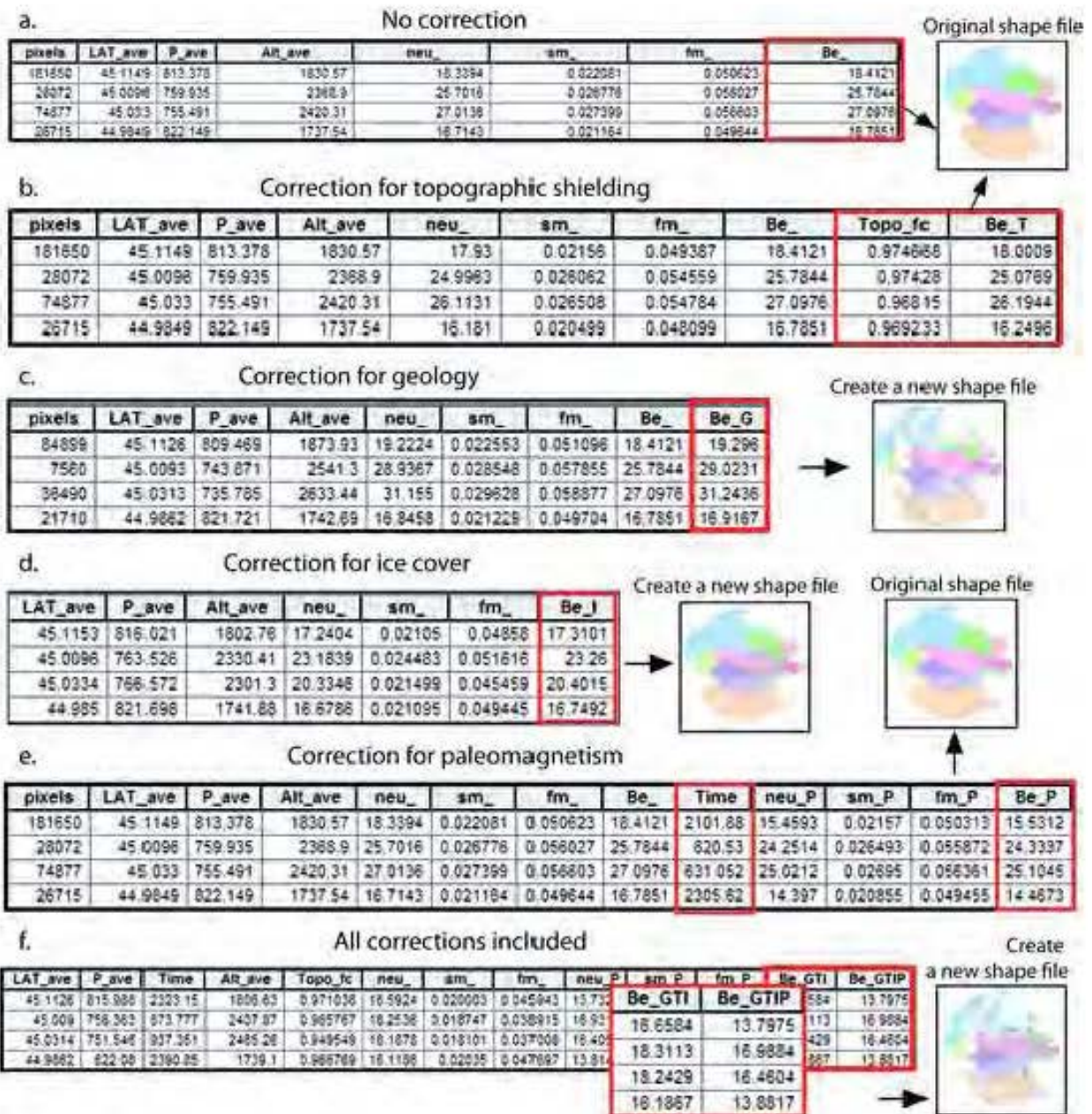


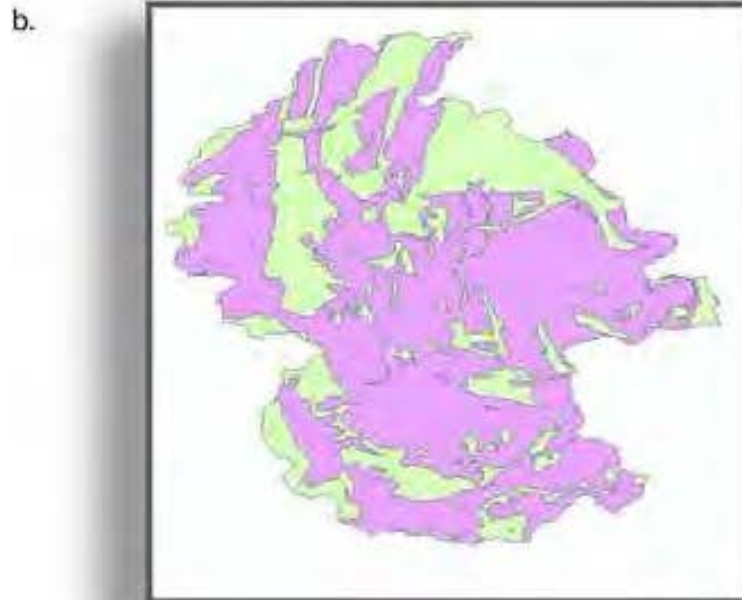
Fig. 5

Figure6

[Click here to download high resolution image](#)

a.

FID	Shape *	ID	Lithology	Quartz
0	Polygone	1	Sedimentary cover	no
1	Polygone	2	Sedimentary cover	no
2	Polygone	3	Sedimentary cover	no
3	Polygone	4	Crystalline basement	yes
4	Polygone	5	Sedimentary cover	no



Crystalline basement - quartz = "yes"

Sedimentary cover - quartz = "no"

c.

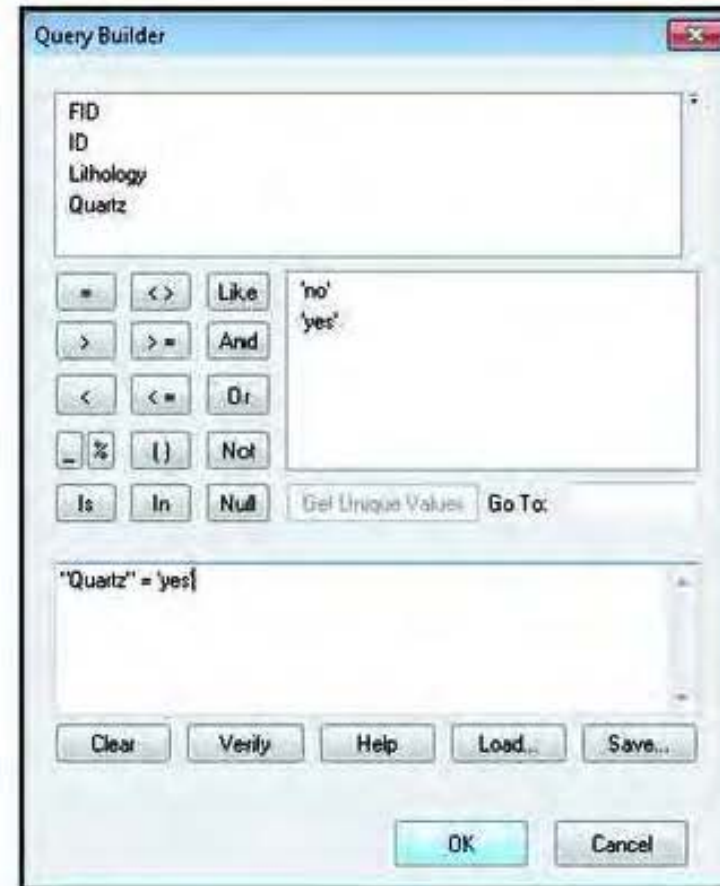


Fig. 6

Figure7

[Click here to download high resolution image](#)

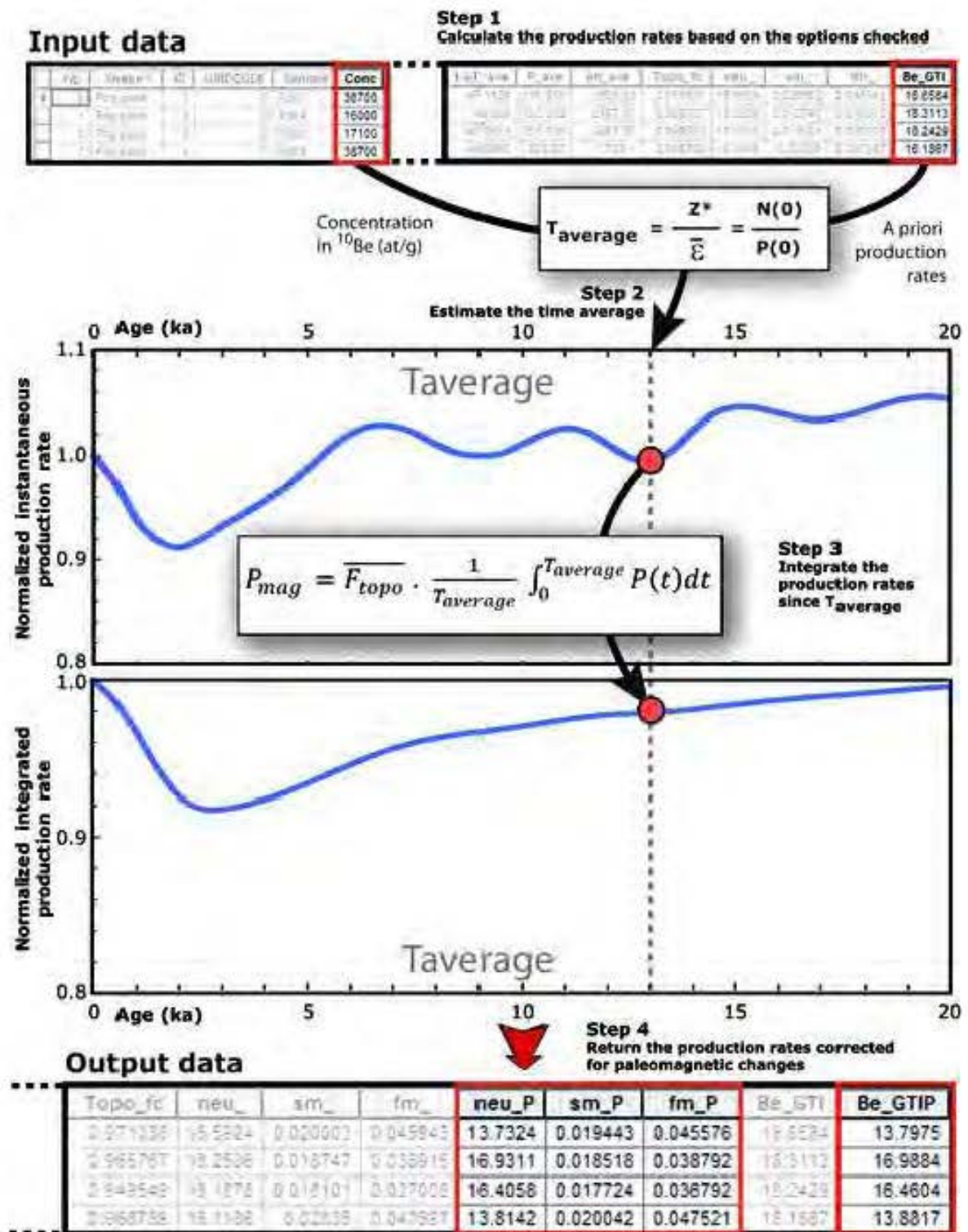


Fig. 7

Figure8
Click here to download high resolution image



Figure9
[Click here to download high resolution image](#)

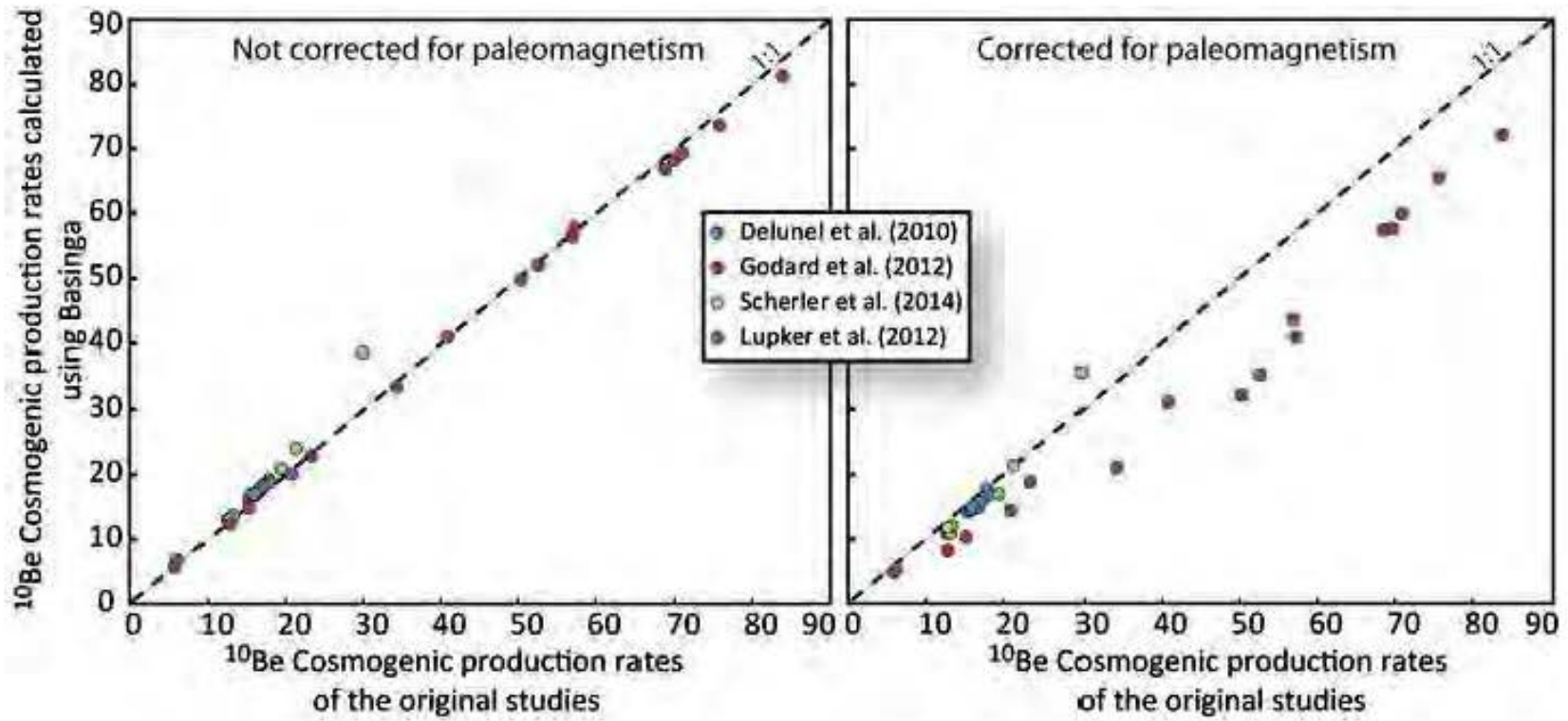


Table des figures

1.1	Mise en contexte paléoclimatique de la période tardiglaciaire.	16
1.2	L'Altiplano et les sites étudiés pendant cette thèse.	17
1.3	Synthèse des taux ^{10}Be andins.	18
1.4	Fonctionnement du programme CREp.	19
1.5	Reconstruction de paléotempératures.	20
1.6	Champ des précipitations pendant le haut niveau Tauca.	21
2.1	$\delta^{18}\text{O}$ des foraminifères benthiques.	24
2.2	Mise en contexte paléoclimatique de la période tardiglaciaire.	25
2.3	Caractéristiques d'un glacier de montagne.	28
2.4	Synthèse ACR - YD.	29
3.1	Formation des isotopes cosmogéniques.	32
3.2	Dépendance spatiale du taux de production.	33
3.3	Le VDM terrestre depuis 60 ka.	34
9.1	Localisation du volcan Chiar-Khota.	249
9.2	Localisation des moraines et des échantillons à Chiar-Khota.	250

Bibliographie

- Andersen, K. K., Azuma, N., Barnola, J.-M., Bigler, M., Biscaye, P., Caillon, N., Chappellaz, J., Clausen, H. B., Dahl-Jensen, D., Fischer, H., Flückiger, J., Fritzsche, D., Fujii, Y., Goto-Azuma, K., Grønbold, K., Gundestrup, N. S., Hansson, M., Huber, C., Hvidberg, C. S., Johnsen, S. J., Jonsell, U., Jouzel, J., Kipfstuhl, S., Landais, a., Leuenberger, M., Lorrain, R., Masson-Delmotte, V., Miller, H., Motoyama, H., Narita, H., Popp, T., Rasmussen, S. O., Raynaud, D., Rothlisberger, R., Ruth, U., Samyn, D., Schwander, J., Shoji, H., Siggard-Andersen, M.-L., Steffensen, J. P., Stocker, T., Sveinbjörnsdóttir, a. E., Svensson, a., Takata, M., Tison, J.-L., Thorsteinsson, T., Watanabe, O., Wilhelms, F., and White, J. W. C. (2004). High-resolution record of Northern Hemisphere climate extending into the last interglacial period. *Nature*, 431(7005) :147–51.
- Baker, P. a., Rigsby, C. a., Seltzer, G. O., Fritz, S. C., Lowenstein, T. K., Bacher, N. P., and Veliz, C. (2001a). Tropical climate changes at millennial and orbital timescales on the Bolivian Altiplano. *Nature*, 409(6821) :698–701.
- Baker, P. a., Seltzer, G. O., Fritz, S. C., Dunbar, R. B., Grove, M. J., Tapia, P. M., Cross, S. L., Rowe, H. D., and Broda, J. P. (2001b). The history of South American tropical precipitation for the past 25,000 years. *Science (New York, N. Y.)*, 291(5504) :640–3.
- Balco, G., Stone, J. O., Lifton, N. a., and Dunai, T. J. (2008). A complete and easily accessible means of calculating surface exposure ages or erosion rates from ^{10}Be and ^{26}Al measurements. *Quaternary Geochronology*, 3(3) :174–195.
- Banderas, R., Alvarez-Solas, J., Robinson, A., and Montoya, M. (2014). An interhemispheric mechanism for glacial abrupt climate change. *Climate Dynamics*, pages 2897–2908.
- Bard, E., Rostek, F., Turon, J., and Gendreau, S. (2000). Hydrological impact of heinrich events in the subtropical northeast atlantic. *Science (New York, N. Y.)*, 289(5483) :1321–4.
- Barker, S., Chen, J., Gong, X., Jonkers, L., Knorr, G., and Thornalley, D. (2015). Icebergs not the trigger for North Atlantic cold events. *Nature*, 520(7547) :333–336.
- Bennett, M. and Glasser, N. (2009). *Glacial Geology, Ice Sheets and Landforms*. 2nd editio edition.
- Blard, P.-H., Lavé, J., Farley, K., Fornari, M., Jiménez, N., and Ramirez, V. (2009). Late local glacial maximum in the Central Altiplano triggered by cold and locally-wet conditions during the paleolake Tauca episode (17–15ka, Heinrich 1). *Quaternary Science Reviews*, 28(27-28) :3414–3427.
- Blard, P.-H., Lave, J., Farley, K. a., Ramirez, V., Jimenez, N., Martin, L. C., Charreau, J., Tibari, B., and Fornari, M. (2014). Progressive glacial retreat in the Southern Altiplano (Uturuncu volcano, 22°S) between 65 and 14ka constrained by cosmogenic ^3He dating. *Quaternary Research*, 82(1) :209–221.
- Blard, P.-H., Lavé, J., Sylvestre, F., Placzek, C., Claude, C., Galy, V., Condom, T., and Tibari, B. (2013). Cosmogenic ^3He production rate in the high tropical Andes (3800 m, 20°S) : Implications for the local last glacial maximum. *Earth and Planetary Science Letters*, 377-378 :260–275.
- Blard, P.-H., Sylvestre, F., a.K. Tripathi, Claude, C., Causse, C., Coudrain, a., Condom, T., Seidel, J.-L., Vimeux, F., Moreau, C., Dumoulin, J.-P., and Lavé, J. (2011). Lake highstands on the Altiplano (Tropical Andes) contemporaneous with Heinrich 1 and the Younger Dryas : new insights from ^{14}C , U–Th dating and d^{18}O of carbonates. *Quaternary Science Reviews*, 30(27-28) :3973–3989.

- Blunier, T. and Brook, E. J. (2001). Timing of Millennial-Scale climate change in Antarctica and Greenland during the last glacial period. *Science*, 291(2001) :109–112.
- Bond, G., Heinrich, H., Broecker, W., Labeyrie, L., McManus, J., Andrews, J., Huon, S., Jantschik, R., Clasen, S., Simet, C., Tedesco, K., Klas, M., Bonani, G., and Ivy, S. (1992). Evidence for massive discharges of icebergs into the North Atlantic ocean during the last glacial period. *Nature*, 360(6401) :245–249.
- Broecker, W. S. (1998). Paleocean circulation during the Last Deglaciation : A bipolar seesaw ? *Paleoceanography*, 13(2) :119.
- Buizert, C. and Schmittner, A. (2015). Southern Ocean control of glacial AMOC stability and Dansgaard-Oeschger interstadial duration. *Paleoceanography*, (OCTOBER) :n/a–n/a.
- Chiang, J. C. H., Lee, S. Y., Putnam, A. E., and Wang, X. (2014). South Pacific Split Jet, ITCZ shifts, and atmospheric North-South linkages during abrupt climate changes of the last glacial period. *Earth and Planetary Science Letters*, 406 :233–246.
- Christopherson, R. W. (2010). *Geosystems : An Introduction to Physical Geography*. Pearson edition.
- Clapperton, C., Clayton, J., and Benn, D. (1997). LATE QUATERNARY GLACIER ADVANCES AND PALAEOLAKE HIGHSTANDS IN THE BOLIVIAN ALTIPLANO. *Quaternary ...*, 6182(96) :49–59.
- Clayton, J. D. and Clapperton, C. M. (1995). The last glacial cycle and palaeolake synchrony in the southern bolivian altiplano : cerro azanaques case study.
- Clayton, J. D. and Clapperton, C. M. (1997). Broad synchrony of a Late-glacial glacier advance and the highstand of palaeolake Tauca in the Bolivian Altiplano. *Journal of Quaternary Science*, 12(3) :169–182.
- Crowley, T. (1992). North Atlantic deep water cools the southern hemisphere. *Paleoceanography*, 7(4) :489–497.
- De Deckker, P., Moros, M., Perner, K., and Jansen, E. (2012). Influence of the tropics and southern westerlies on glacial interhemispheric asymmetry. *Nature Geoscience*, 5(4) :266–269.
- Denton, G. H., Anderson, R. F., Toggweiler, J. R., Edwards, R. L., Schaefer, J. M., and Putnam, A. E. (2010). The Last Glacial Termination. *Science*, 328(5986) :1652–1656.
- Desilets, D. and Zreda, M. (2003). Spatial and temporal distribution of secondary cosmic-ray nucleon intensities and applications to in situ cosmogenic dating. *Earth and Planetary Science Letters*, 206(1-2) :21–42.
- Desilets, D., Zreda, M., and Prabu, T. (2006). Extended scaling factors for in situ cosmogenic nuclides : New measurements at low latitude. *Earth and Planetary Science Letters*, 246(3-4) :265–276.
- Dubois, N., Kienast, M., Normandeau, C., and Herbert, T. D. (2009). Eastern equatorial Pacific cold tongue during the Last Glacial Maximum as seen from alkenone paleothermometry. *Paleoceanography*, 24(4) :1–12.
- Dunai, T. (2001). Influence of secular variation of the geomagnetic field on production rates of in situ produced cosmogenic nuclides. *Earth and Planetary Science Letters*, 193(1-2) :197–212.
- Dunai, T. (2010). *Cosmogenic Nuclides Principles, Concepts and Applications in the Earth Surface Sciences*. University of Edinburgh, cambridge edition.
- Farber, D. L., Hancock, G. S., Finkel, R. C., and Rodbell, D. T. (2005). The age and extent of tropical alpine glaciation in the Cordillera Blanca, Peru. *Journal of Quaternary Science*, 20(7-8) :759–776.
- Foucault, A. (2009). *CLIMATOLOGIE et PALEOCLIMATOLOGIE*. Dunod edition.
- Garreaud, R., Vuille, M., and Clement, A. C. (2003). The climate of the Altiplano : observed current conditions and mechanisms of past changes. *Palaeogeography, Palaeoclimatology, Palaeoecology*, 194(1-3) :5–22.

- Gibbons, F. T., Oppo, D. W., Mohtadi, M., Rosenthal, Y., Cheng, J., Liu, Z., and Linsley, B. K. (2014). Deglacial $\delta^{18}\text{O}$ and hydrologic variability in the tropical Pacific and Indian Oceans. *Earth and Planetary Science Letters*, 387 :240–251.
- Glasser, N. F., Clemmens, S., Schnabel, C., Fenton, C. R., and Mchargue, L. (2009). Tropical glacier fluctuations in the Cordillera Blanca , Peru between 12 . 5 and 7 . 6 ka from cosmogenic ^{10}Be dating. *Quaternary Science Reviews*, 28(27-28) :3448–3458.
- Gosse, J. C., Klein, J., Lawn, B., Middleton, R., and Evenson, E. B. (1995). Beryllium-10 dating of the duration and retreat of the last pinedale glacial sequence. *Science (New York, N.Y.)*, 268(5215) :1329–33.
- Gosse, J. C. and Phillips, F. M. (2001). Terrestrial in situ cosmogenic nuclides : theory and application. *Quaternary Science Reviews*, 20(14) :1475–1560.
- Guyodo, Y. and Valet, J. (1999). Global changes in intensity of the Earth's magnetic field during the past 800 kyr. *Nature*, 399(May) :249–252.
- Hall, S. R., Farber, D. L., Ramage, J. M., Rodbell, D. T., Finkel, R. C., Smith, J. A., Mark, B. G., and Kassel, C. (2009). Geochronology of Quaternary glaciations from the tropical Cordillera. *Quaternary Science Reviews*, 28(25-26) :2991–3009.
- Han, Z., Li, X., Yi, S., Stevens, T., Chen, Y., Wang, X., and Lu, H. (2015). Extreme monsoon aridity episodes recorded in South China during Heinrich Events. *Palaeogeography, Palaeoclimatology, Palaeoecology*, 440 :467–474.
- Heinrich, H. (1988). Origin and consequences of cyclic ice rafting in the Northeast Atlantic Ocean during the past 130,000 years. *Quaternary Research*, 29(2) :142–152.
- Ivanochko, T. S., Ganeshram, R. S., Brummer, G. J. A., Ganssen, G., Jung, S. J. A., Moreton, S. G., and Kroon, D. (2005). Variations in tropical convection as an amplifier of global climate change at the millennial scale. *Earth and Planetary Science Letters*, 235(1-2) :302–314.
- Jomelli, V., Favier, V., Vuille, M., Braucher, R., Martin, L., Blard, P.-H., Colose, C., Brunstein, D., He, F., Khodri, M., Bourlès, D. L., Leanni, L., Rinterknecht, V., Grancher, D., Francou, B., Ceballos, J. L., Fonseca, H., Liu, Z., and Otto-Bliesner, B. L. (2014). A major advance of tropical Andean glaciers during the Antarctic cold reversal. *Nature*.
- Jomelli, V., Khodri, M., Favier, V., Brunstein, D., Ledru, M.-P., Wagnon, P., Blard, P.-H., Sicart, J.-E., Braucher, R., Grancher, D., Bourlès, D. L., Braconnot, P., and Vuille, M. (2011). Irregular tropical glacier retreat over the Holocene epoch driven by progressive warming. *Nature*, 474(7350) :196–9.
- Jouzel, J., Masson-Delmotte, V., Cattani, O., Dreyfus, G., Falourd, S., Hoffmann, G., Minster, B., Nouet, J., Barnola, J. M., Chappellaz, J., Fischer, H., Gallet, J. C., Johnsen, S., Leuenberger, M., Loulergue, L., Luethi, D., Oerter, H., Parrenin, F., Raisbeck, G., Raynaud, D., Schilt, A., Schwander, J., Selmo, E., Souchez, R., Spahni, R., Stauffer, B., Steffensen, J. P., Stenni, B., Stocker, T. F., Tison, J. L., Werner, M., and Wolff, E. W. (2007). Orbital and Millennial Antarctic Climate Variability over the Past 800,000 Years. *Science*, 317(5839) :793–796.
- Jouzel, J., Vaikmae, R., Petit, J. R., Martin, M., Duclos, Y., Stievenard, M., Lorius, C., Toots, M., M? ?li ? ?res, M. A., Burckle, L. H., Barkov, N. I., and Kotlyakov, V. M. (1995). The two-step shape and timing of the last deglaciation in Antarctica. *Climate Dynamics*, 11(3) :151–161.
- Kelly, M. a., Lowell, T. V., Applegate, P. J., Phillips, F. M., Schaefer, J. M., Smith, C. a., Kim, H., Leonard, K. C., and Hudson, A. M. (2013). A locally calibrated, late glacial ^{10}Be production rate from a low-latitude, high-altitude site in the Peruvian Andes. *Quaternary Geochronology*, pages 1–16.
- Kelly, M. a., Lowell, T. V., Applegate, P. J., Smith, C. a., Phillips, F. M., and Hudson, a. M. (2012). Late glacial fluctuations of Quelccaya Ice Cap, southeastern Peru. *Geology*, 40(11) :991–994.
- Laj, C., Kissel, C., and Beer, J. (2004). High Resolution Global Paleointensity Stack Since 75 kyr (GLOPIS-75) Calibrated to Absolute Values. *Timescales of the Paleomagnetic Field*, 145 :255–265.

- Lal, D. (1991). Cosmic ray labeling of erosion surfaces : in situ nuclide production rates and erosion models. *Earth and Planetary Science Letters*, 104(2-4) :424–439.
- Lifton, N. (2015). Implications of two Holocene time-dependent geomagnetic models for cosmogenic nuclide production rate scaling. *Earth and Planetary Science Letters*, 433 :257–268.
- Lifton, N., Sato, T., and Dunai, T. J. (2014). Scaling in situ cosmogenic nuclide production rates using analytical approximations to atmospheric cosmic-ray fluxes. *Earth and Planetary Science Letters*, 386 :149–160.
- Lifton, N. a., Bieber, J. W., Clem, J. M., Duldig, M. L., Evenson, P., Humble, J. E., and Pyle, R. (2005). Addressing solar modulation and long-term uncertainties in scaling secondary cosmic rays for in situ cosmogenic nuclide applications. *Earth and Planetary Science Letters*, 239(1-2) :140–161.
- Lisiecki, L. E. and Raymo, M. E. (2005). A Pliocene-Pleistocene stack of 57 globally distributed benthic $\delta^{18}O$ records. *Paleoceanography*, 20(1) :1–17.
- Malone, A. G. O., Pierrehumbert, R. T., Lowell, T. V., Kelly, M. A., and Stroup, J. S. (2015). Constraints on southern hemisphere tropical climate change during the Little Ice Age and Younger Dryas based on glacier modeling of the Quelccaya Ice Cap, Peru. *Quaternary Science Reviews*, 125 :106–116.
- May, J. H., Zech, J., Zech, R., Preusser, F., Argollo, J., Kubik, P. W., and Veit, H. (2011). Reconstruction of a complex late Quaternary glacial landscape in the Cordillera de Cochabamba (Bolivia) based on a morphostratigraphic and multiple dating approach. *Quaternary Research*, 76(1) :106–118.
- McManus, J. F., Francois, R., Gherardi, J.-M., Keigwin, L. D., and Brown-Leger, S. (2004). Collapse and rapid resumption of Atlantic meridional circulation linked to deglacial climate changes. *Nature*, 428(6985) :834–837.
- Mix, A. C., Years, B. P., Ruddiman, F., and McIntyre, A. (1986). L Mean Sea-Surface. 1(1) :43–66.
- Mölg, T. and Kaser, G. (2011). A new approach to resolving climate-cryosphere relations : Downscaling climate dynamics to glacier-scale mass and energy balance without statistical scale linking. *Journal of Geophysical Research Atmospheres*, 116(16) :1–13.
- Montade, V., Kageyama, M., Combourieu-Nebout, N., Ledru, M. P., Michel, E., Siani, G., and Kissel, C. (2015). Teleconnection between the intertropical convergence zone and southern westerly winds throughout the last deglaciation. *Geology*, 43(8) :735–738.
- Moreno, P. I., Jacobson, G. L., Lowell, T. V., and Denton, G. H. (2001). Interhemispheric climate links revealed by late-glacial cooling episode in southern Chile. *Nature*, 409(6822) :804–8.
- Muscheler, R., Beer, J., Kubik, P. W., and Synal, H.-a. (2005). Geomagnetic field intensity during the last 60,000 years based on ^{10}Be and ^{36}Cl from the Summit ice cores and ^{14}C . *Quaternary Science Reviews*, 24(16-17) :1849–1860.
- New, M., Lister, D., Hulme, M., and Makin, I. (2002). A high-resolution data set of surface climate over global land areas. *Climate Research*, 21(1) :1–25.
- N.O.A.A. (1976). U.S. Standard Atmosphere. *US Government Printing Office*.
- Paterson, W. S. B. (1994). *The Physics of Glaciers. 3rd Edition*. Pergamon, Oxford.
- Pausata, F. S. R., Battisti, D. S., Nisancioglu, K. H., and Bitz, C. M. (2011). Chinese stalagmite $\delta^{18}O$ controlled by changes in the Indian monsoon during a simulated Heinrich event. *Nature Geoscience*, 4(7) :474–480.
- Peterson, L. C. (2000). Rapid Changes in the Hydrologic Cycle of the Tropical Atlantic During the Last Glacial. *Science*, 290(5498) :1947–1951.
- Placzek, C., Quade, J., and Patchett, P. J. (2006). Geochronology and stratigraphy of late Pleistocene lake cycles on the southern Bolivian Altiplano : Implications for causes of tropical climate change. *Geological Society of America Bulletin*, 118(5-6) :515–532.

- Quesada, B., Sylvestre, F., Vimeux, F., Black, J., Paillès, C., Sonzogni, C., Alexandre, A., Blard, P.-H., Tonetto, A., Mazur, J.-C., and Bruneton, H. (2015). Impact of Bolivian paleolake evaporation on the d18O of the Andean glaciers during the last deglaciation (18.5-11.7 ka) : diatom-inferred d18O values and hydro-isotopic modelling. *Quaternary Science Reviews*, 120 :93–106.
- Rupper, S. and Roe, G. (2008). Glacier changes and regional climate : A mass and energy balance approach. *Journal of Climate*, 21(20) :5384–5401.
- Servant, M. and Fontes, J.-C. (1978). Les lacs quaternaires des hauts plateaux des Andes boliviennes - premières interprétations paléoclimatiques. *Cahiers O.R.S.T.O.M., Série Géologie*, X(1) :9–23.
- Sirocko, F., Garbe-Schonberg, D., McIntyre, A., and Molino, B. (1996). Teleconnections Between the Subtropical Monsoons and High-Latitude Climates During the Last Deglaciation. *Science*, 272(5261) :526–529.
- Smith, C. a., Lowell, T. V., Owen, L. a., and Caffee, M. W. (2011). Late Quaternary glacial chronology on Nevado Illimani, Bolivia, and the implications for paleoclimatic reconstructions across the Andes. *Quaternary Research*, 75(1) :1–10.
- Smith, J. a. and Rodbell, D. T. (2010). Cross-cutting moraines reveal evidence for North Atlantic influence on glaciers in the tropical Andes. *Journal of Quaternary Science*, 25(3) :243–248.
- Smith, J. a., Seltzer, G. O., Farber, D. L., Rodbell, D. T., and Finkel, R. C. (2005). Early local last glacial maximum in the tropical Andes. *Science (New York, N. Y.)*, 308(5722) :678–81.
- Soruco, A., Vincent, C., Francou, B., Ribstein, P., Berger, T., Sicart, J. E., Wagnon, P., Arnaud, Y., Favier, V., and Lejeune, Y. (2009). Mass balance of Glaciar Zongo, Bolivia, between 1956 and 2006, using glaciological, hydrological and geodetic methods. *Annals of Glaciology*, 50(50) :1–8.
- Stone, J. O. (2000). Air pressure and cosmogenic isotope production. *Journal of Geophysical Research*, 105(B10) :23753.
- Stríkis, N. M., Chiessi, C. M., Cruz, F. W., Vuille, M., Cheng, H., Barreto, E. A. S., Mollenhauer, G., Kasten, S., Karmann, I., Edwards, R. L., Bernal, J. P., and Sales, R. (2015). Timing and structure of Mega-SACZ events during Heinrich Stadial 1. *Geophysical Research Letters*, pages 1–8.
- Sylvestre, F., Servant, M., Servant-Vildary, S., Causse, C., Fournier, M., and Ybert, J.-P. (1999). Lake-Level Chronology on the Southern Bolivian Altiplano (18°–23°S) during Late-Glacial Time and the Early Holocene. *Quaternary Research*, 51(1) :54–66.
- Thompson, L. G., Davis, M. E., Mosley-Thompson, E., Sowers, T. A., Henderson, K. A., Zagorodnov, V. S., Lin, P., Mikhailenko, V. N., Campen, R. K., Bolzan, J. F., Cole-Dai, J., and Francou, B. (1998). A 25,000-Year Tropical Climate History from Bolivian Ice Cores. *Science*, 282(December) :1858–1864.
- Toggweiler, J. R. (2009). CLIMATE CHANGE : Shifting Westerlies. *Science*, 323(5920) :1434–1435.
- Uppala, S. M., Kallberg, P. W., Simmons, a. J., Andrae, U., Bechtold, V. D. C., Fiorino, M., Gibson, J. K., Haseler, J., Hernandez, a., Kelly, G. a., Li, X., Onogi, K., Saarinen, S., Sokka, N., Allan, R. P., Andersson, E., Arpe, K., Balmaseda, M. a., Beljaars, a. C. M., Berg, L. V. D., Bidlot, J., Bormann, N., Caires, S., Chevallier, F., Dethof, a., Dragosavac, M., Fisher, M., Fuentes, M., Hagemann, S., Hólm, E., Hoskins, B. J., Isaksen, L., Janssen, P. a. E. M., Jenne, R., McNally, a. P., Mahfouf, J.-F., Morcrette, J.-J., Rayner, N. a., Saunders, R. W., Simon, P., Sterl, a., Trenberth, K. E., Untch, a., Vasiljevic, D., Viterbo, P., and Woollen, J. (2005). The ERA-40 re-analysis. *Quarterly Journal of the Royal Meteorological Society*, 131(612) :2961–3012.
- Vuille, M. (1999). Atmospheric circulation over the Bolivian Altiplano during dry and wet periods and extreme phases of the southern oscillation. *International Journal of Climatology*, 19(14) :1579–1600.
- Wagnon, P., Ribstein, P., Francou, B., and Sicart, J. E. (2001). Anomalous heat and mass budget of Glaciar Zongo , Bolivia , during the 1997 / 98 El Ni · o year. *October*, 47(156) :21–28.

- Wang, X., Auler, A. S., Edwards, R. L., Cheng, H., Cristalli, P. S., Smart, P. L., Richards, D. a., and Shen, C.-C. (2004). Wet periods in northeastern Brazil over the past 210 kyr linked to distant climate anomalies. *Nature*, 432(7018) :740–3.
- Wang, X., Auler, A. S., Edwards, R. L., Cheng, H., Ito, E., Wang, Y., Kong, X., and Solheid, M. (2007). Millennial-scale precipitation changes in southern Brazil over the past 90,000 years. *Geophysical Research Letters*, 34(23) :1–5.
- Wang, Y. J., Cheng, H., Edwards, R. L., An, Z. S., Wu, J. Y., Shen, C. C., and Dorale, J. a. (2001). A high-resolution absolute-dated late Pleistocene Monsoon record from Hulu Cave, China. *Science (New York, N.Y.)*, 294(5550) :2345–2348.
- Ward, D. J., Cesta, J. M., Galewsky, J., and Sagredo, E. (2015). Late pleistocene glaciations of the arid subtropical Andes and new results from the Chajnantor Plateau, northern Chile. *Quaternary Science Reviews*, 128 :98–116.
- Wunsch, C. (2006). Abrupt climate change : An alternative view. *Quaternary Research*, 65(2) :191–203.
- Zech, J., Zech, R., Kubik, P. W., and Veit, H. (2009). Glacier and climate reconstruction at Tres Lagunas, NW Argentina, based on ^{10}Be surface exposure dating and lake sediment analyses. *Palaeogeography, Palaeoclimatology, Palaeoecology*, 284(3-4) :180–190.
- Zech, R., Kubik, P. W., Veit, H., Kull, C., Kubik, P. W., and Veit, H. (2007a). of the Past Exposure dating of Late Glacial and pre-LGM moraines in the Rosa , Northern / Central Chile (31 ° S) Cordon de Do na. *Climate Of The Past*, pages 1–14.
- Zech, R., Kull, C., Kubik, P. W., and Veit, H. (2007b). LGM and Late Glacial glacier advances in the Cordillera Real and Cochabamba (Bolivia) deduced from ^{10}Be surface exposure dating. *Climate of the Past Discussions*, 3(4) :623–635.
- Zhang, R. and Delworth, T. L. (2005). Simulated tropical response to a substantial weakening of the Atlantic thermohaline circulation. *Journal of Climate*, 18(12) :1853–1860.
- Zhang, X., Lohmann, G., Knorr, G., and Purcell, C. (2014). Abrupt glacial climate shifts controlled by ice sheet changes. *Nature*, 512(7514) :290–294.
- Zhou, J. and Lau, K. M. (1998). Does a monsoon climate exist over South America? *Journal of Climate*, 11(5) :1020–1040.
- Zorzi, C., Sanchez Goñi, M. F., Anupama, K., Prasad, S., Hanquiez, V., Johnson, J., and Giosan, L. (2015). Indian monsoon variations during three contrasting climatic periods : The Holocene, Heinrich Stadial 2 and the last interglacial-glacial transition. *Quaternary Science Reviews*, 125 :50–60.

Les paléoglaciers et les paléolacs de l'Altiplano, archives climatiques de la dernière déglaciation

Mots-clés : *Paléoclimat, Paléoglaciers, Paléolacs, Âge d'exposition, Inversions Climatiques, Réorganisations Climatiques Abruptes, Paléotempératures, Paléoprécipitations*

Résumé

La période Quaternaire (2.6 Ma - Présent) est caractérisée par une forte variabilité climatique mondiale et l'alternance d'épisodes glaciaires et interglaciaires. La période tardiglaciaire (il y a 20 à 11 ka) voit se succéder des réorganisations rapides et abruptes du climat à différentes échelles. Deux épisodes froids dans l'hémisphère Nord sont synchrones du développement des paléolacs géants Tauca (17 - 14 ka) et Coipasa (13 - 11.5 ka) sur l'Altiplano bolivien. L'Altiplano est un haut plateau bordé par les Cordillères Orientale et Occidentale des Andes. Les flancs des volcans et des massifs montagneux y présentent de nombreuses preuves d'une activité glaciaire passée intense. Ces géomorphologies glaciaires, ainsi que les lignes de rivage abandonnées des paléolacs constituent de précieuses archives pour comprendre le climat passé. L'exploitation couplée de ces deux archives est au cœur de cette thèse.

Après des chapitres introductifs, le chapitre 4 porte sur la calibration du taux de production du ^{10}Be in situ dans les Hautes Andes Tropicales. Ce paramètre géochimique est nécessaire à l'emploi de la méthode des âges d'exposition utilisée dans cette thèse afin de reconstruire l'histoire des paléoglaciers. Un nouveau taux de $4.07 \pm 0.18 \text{ at.g}^{-1}.\text{a}^{-1}$ est établi à partir de l'âge et de la concentration en ^{10}Be du fan-delta de Challapata situé sur le flanc de Cerro Azanaques (18.9°S - 66.7°W). Une synthèse des taux andins est également menée et conduit à proposer un jeu de données de référence pour la calibration du ^{10}Be in-situ dans cette région.

Le chapitre 5 porte sur le développement d'un code de calcul pour les âges d'exposition. Les programmes existant à ce jour n'incluent pas les dernières avancées dans le domaine et obligent les utilisateurs à se servir de paramètres sans pouvoir les choisir et les discuter. Dans cette optique, le programme CREp offre une grande flexibilité de paramétrage. Il est de plus couplé à une base de données en ligne de taux de production afin de proposer les choix les plus pertinents pour cette valeur clé du calcul. Le programme CREp est disponible sur Internet.

Le chapitre 6 présente 4 chronologies glaciaires basées sur les âges d'exposition dans la vallée du Zongo (16.2°S - 68.1°W), au Cerro Tunupa (19.8°S - 67.6°W), au Nevado Sajama (18.1°S - 68.9°W) et au Cerro Luxar (21.0°S - 68.0°W). Elles sont couplées à une reconstitution des températures moyennes basée sur la modélisation croisée lac-glaciers. Les résultats indiquent 2 comportements glaciaires différents au cours du tardiglaciaire entre le Nord et le Sud et suggèrent une variabilité spatiale importante des précipitations. Des refroidissements de 4 - 4.5 °C et 2.5 °C sont respectivement associés aux stades Tauca et Coipasa.

Le dernier chapitre est consacré à la reconstitution du champ des précipitations sur l'Altiplano durant le stade Tauca. La modélisation croisée permet d'observer les variations de précipitation par rapport au présent pour 8 sites répartis sur l'Altiplano et d'en déduire une carte des précipitations synthétique pour la période considérée. Ces variations indiquent des précipitations 1.7 à 3.1 fois supérieures à l'actuel. La répartition des pluies révèle un apport accru de l'humidité en provenance de l'Est, et suggère une intensification et une expansion vers le sud des vents d'Est, en cohérence avec plusieurs observations actuelles et passées.

The palaeo-glaciers and palaeo-lakes from the Bolivian Altiplano as climatic archives for the last deglaciation

Keywords: *Palaeo-climate, Palaeo-glaciers, Palaeo-lakes, Exposure Ages, Climatic Inversions, Abrupt Climatic Reorganizations, Palaeo-temperatures, Palaeo-precipitations*

Abstract

The Quaternary period (2.6 Ma - Present) is characterized by rapid and strong worldwide climate variability and the alternating pattern of glacial and interglacial periods. Rapid and abrupt climatic reorganisations follow one another at different scales during the late glacial period (20 - 11 ka ago). Two cold episodes in the Northern Hemisphere are coeval with the rise of giant palaeo-lakes Tauca (17 - 14 ka) and Coipasa (13 - 11.5 ka) over the Bolivian Altiplano. The Altiplano is a high plateau surrounded by the eastern and western cordilleras of the Andes. The flanks of the volcanoes and mountainous massifs in the area exhibit substantial evidence of intense past glacial activity. These glacial geomorphologies, along with the abandoned palaeo-lake shorelines represent valuable archive to understand the past climate. The coupled study of these 2 archives is at the heart of this thesis project.

After introductory chapters, the chapter 4 deals with the calibration of in situ ^{10}Be production rate in the High Tropical Andes. This geochemical parameter is required to make use of the exposure age method, which is applied in this thesis to reconstruct the palaeo-glaciers history. A new production rate of $4.07 \pm 0.18 \text{ at.g}^{-1}.\text{yr}^{-1}$ is derived from the age and ^{10}Be concentration of the Challapata fan-delta, on the flank of Cerro Azanaques (18.9°S - 66.7°W). A review of the Andean production rates is also presented and leads to propose a reference calibration dataset for the in situ ^{10}Be production rate in the region.

The chapter 5 deals with the development of a calculation code for exposure ages. Actual programs do not account for the latest advances in this domain and force users to use fixed parameters without being able to change or discuss them. In this view the CREp program offers an important flexibility in the parameterization. Furthermore, it is coupled with an online production rate database so as to offer the most relevant choices concerning the key parameters of the calculation. The CREp program is available online.

The chapter 6 presents 4 exposure age based glacial chronologies in the Zongo Valley (16.2°S - 68.1°W), Cerro Tunupa (19.8°S - 67.6°W), Nevado Sajama (18.1°S - 68.9°W) and Cerro Luxar (21.0°S - 68.0°W). They are coupled with lake and glacier modelling to reconstruct mean temperature evolution. Results indicate 2 different glacial behaviours during the lateglacial period between the North and the South of the Altiplano and suggest an important spatial variability of the precipitations. Coolings of 4 - 4.5 °C and 2.5 °C are respectively associated to the Tauca and Coipasa Highstands.

The last chapter presents a reconstitution of the Altiplano precipitation field during the Tauca Highstand. The lake and glacier cross-modelling enables to derive the precipitation increase compare to present for 8 sites distributed over the Altiplano and to infer a synthetic precipitation field for the period. These variations indicate 1.7 to 3.1 times stronger precipitations compared to present. The rain spatial distribution reveals enhanced moist input from the East and suggests a strengthening and southward expansion of the easterly winds, in consistence with actual and past observations.